



**HAL**  
open science

# Taking into account polydispersity for the modeling of liquid fuel injection in internal combustion engines

Damien Kah

► **To cite this version:**

Damien Kah. Taking into account polydispersity for the modeling of liquid fuel injection in internal combustion engines. Other. Ecole Centrale Paris, 2010. English. NNT : 2010ECAP0044 . tel-00618786v2

**HAL Id: tel-00618786**

**<https://theses.hal.science/tel-00618786v2>**

Submitted on 4 Oct 2011

**HAL** is a multi-disciplinary open access archive for the deposit and dissemination of scientific research documents, whether they are published or not. The documents may come from teaching and research institutions in France or abroad, or from public or private research centers.

L'archive ouverte pluridisciplinaire **HAL**, est destinée au dépôt et à la diffusion de documents scientifiques de niveau recherche, publiés ou non, émanant des établissements d'enseignement et de recherche français ou étrangers, des laboratoires publics ou privés.



## THESE

présentée par

**Damien KAH**

pour l'obtention du

GRADE de DOCTEUR

Formation doctorale : Energétique

Laboratoire d'accueil : Laboratoire d'Énergétique Moléculaire  
et Macroscopique, Combustion (EM2C)  
du CNRS et de l'ECP

### Prise en compte des aspects polydispersés pour la modélisation d'un jet de carburant dans les moteurs à combustion interne

Soutenue le 20 Décembre 2010

**Jury :**

MM	Pitsch	H.	Rapporteur
	Coquel	F.	Rapporteur
	Lance	M.	Rapporteur
	Massot	M.	Directeur de thèse
Mme	Laurent	F.	Co-Directrice de thèse
MM	Jay	S.	Encadrant IFP Energies nouvelles
	Fox	R.	Président
Mme	Cuenot	B.	Invitée
M	Candel	S.	Invité

# Contents

<b>Summary</b>	<b>19</b>
<b>General Introduction</b>	<b>20</b>
<b>I Spray modeling and simulation</b>	<b>30</b>
<b>1 Kinetic modeling for disperse spray in gaseous flow</b>	<b>32</b>
1.1 Gas phase description . . . . .	32
1.1.1 Gas equation system . . . . .	32
1.1.2 Reference quantities and dimensionless formulation . . . . .	34
1.2 Kinetic spray modeling . . . . .	35
1.2.1 Particle flow regimes . . . . .	35
1.2.2 Williams-Boltzmann kinetic equation:framework and derivation . . . . .	36
1.2.2.1 Fundamental assumptions . . . . .	36
1.2.2.2 Williams-Boltzmann Equation . . . . .	36
1.2.3 Spray equation closure . . . . .	37
1.2.3.1 Drag Force . . . . .	37
1.2.3.2 Evaporation term . . . . .	38
1.2.3.3 Collisions . . . . .	39
1.2.4 Non-dimensional formulation . . . . .	39
1.2.5 Extension to aerosols . . . . .	40
1.3 Gas/liquid coupling: flow regime characterization . . . . .	41
1.3.1 Source terms for the gas phase . . . . .	41
1.3.2 One-way coupling . . . . .	41
1.3.3 Range of particulate flow studied . . . . .	42
<b>2 Overview of the resolution strategies for spray dynamics</b>	<b>43</b>
2.1 Lagrangian methods . . . . .	43
2.1.1 Description of Lagrangian techniques . . . . .	43
2.1.2 Lagrangian limitations, need and challenges for Eulerian methods . . . . .	44
2.2 Eulerian resolution methods . . . . .	45
2.2.1 Derivation strategies for a DNS resolution . . . . .	45
2.2.2 Presuming NDF profile . . . . .	46
2.2.2.1 Size discretization . . . . .	47
2.2.2.2 Preservation of the continuous character of the size variable . . . . .	50
2.2.3 Quadrature approach . . . . .	50
<b>3 Multi-fluid model: principles, achievements, limitations</b>	<b>53</b>
3.1 Model and assumptions . . . . .	53
3.1.1 Semi-kinetic system of conservation law . . . . .	53
3.1.2 Multi-fluid system of conservation laws . . . . .	54
3.1.3 Mathematical peculiarity of the monokinetic assumption . . . . .	57

3.2	Multi-fluid numerical methods . . . . .	59
3.2.1	Operator splitting . . . . .	59
3.2.2	Physical space transport resolution: kinetic-based scheme . . . . .	61
3.2.3	Phase space transport resolution . . . . .	67
3.3	Achievements of the multi-fluid model . . . . .	68
3.3.1	Illustration on a two-dimensional vortical flow . . . . .	69
3.3.2	Validation on a free-jet configuration . . . . .	73
3.3.2.1	Comparison to Lagrangian simulations . . . . .	73
3.3.2.2	Importance of the treatment of polydispersity . . . . .	75
3.4	Limitations of the multi-fluid model and need for high order moment methods . . . . .	77
3.4.1	Accuracy shortage in the description of polydispersity . . . . .	77
3.4.2	The issue of characteristics crossing . . . . .	84
3.5	Conclusion . . . . .	85
 <b>II High order size moment method for treatment of spray polydispersity</b>		<b>86</b>
<b>4</b>	<b>Eulerian Multi Size Moment (EMSM) model: modeling and closure properties</b>	<b>88</b>
4.1	Derivation of the model and closure properties . . . . .	88
4.1.1	Spray or aerosol: the same issue . . . . .	88
4.1.2	Operator splitting strategy . . . . .	88
4.1.3	Drag closure problem and resulting transport scheme . . . . .	89
4.1.4	Physical transport model . . . . .	89
4.1.5	Evaporation model . . . . .	90
4.1.5.1	Flux at zero size . . . . .	90
4.1.5.2	Possible extension to a multi-fluid context . . . . .	91
4.2	Finite moment space property and finite Hausdorff moment problem . . . . .	91
4.2.1	Moment space . . . . .	91
4.2.2	Canonical moment space . . . . .	92
4.2.3	Some solutions to the Hausdorff finite moment problem . . . . .	93
4.2.4	Behavior at the frontier of the moment space . . . . .	96
4.3	Mathematical challenges of the system . . . . .	97
4.4	Conclusion . . . . .	97
<b>5</b>	<b>A new numerical scheme for stable and accurate moment dynamics</b>	<b>99</b>
5.1	Constant evaporation rate . . . . .	99
5.1.1	Invariance property of moment space through evaporation with zero flux . . . . .	99
5.1.2	Integrated version of the dynamical system . . . . .	100
5.1.3	Link with abscissas and weights of the lower principal representation . . . . .	102
5.1.4	Algorithm of the new scheme . . . . .	103
5.2	Link with a DQMOM approach . . . . .	104
5.2.1	DQMOM and new DQMOM formalism of the evaporation process . . . . .	105
5.2.2	Relation between the two formulations . . . . .	106
5.3	Evaporation rate depending on size, using a piecewise constant approximation . . . . .	106
5.4	Treatment of arbitrary evaporation law . . . . .	108
5.4.1	Change of variable characteristics . . . . .	108
5.4.2	Algorithm of the new scheme . . . . .	109
5.5	Results . . . . .	110
5.5.1	Constant evaporation law . . . . .	110
5.5.2	Discontinuous evaporation law . . . . .	113
5.5.3	Arbitrary evaporation law . . . . .	114
5.5.3.1	Smooth evaporation law . . . . .	114
5.5.3.2	Discontinuous evaporation law . . . . .	116
5.5.3.3	Regularity and ‘natural’ variables . . . . .	116

5.6	Conclusions . . . . .	118
<b>6</b>	<b>Numerical strategy for transport in physical space and drag</b>	<b>120</b>
6.1	General form of the kinetic scheme for moment transport . . . . .	121
6.2	First order kinetic scheme . . . . .	122
6.3	Second order kinetic scheme . . . . .	123
6.3.1	Reconstruction . . . . .	124
6.3.2	Slope limitation . . . . .	125
6.3.3	Fluxes computation . . . . .	126
6.4	Validation on a one dimensional case . . . . .	127
6.4.1	Aerosol case . . . . .	127
6.4.2	Spray case . . . . .	128
6.4.3	Order accuracy study . . . . .	129
6.4.4	Comparison with other methods present in literature . . . . .	132
6.5	General algorithm towards implementation in MUSES3D . . . . .	132
<b>7</b>	<b>Introduction of the EMSM model in MUSES3D</b>	<b>134</b>
7.1	Presentation of MUSES3D . . . . .	134
7.1.1	General characteristics . . . . .	134
7.1.2	Numerical scheme implementation . . . . .	135
7.1.2.1	Splitting strategy . . . . .	135
7.1.2.2	Physical transport resolution . . . . .	135
7.1.2.3	Phase space transport resolution . . . . .	136
7.1.3	Treatment of boundary conditions . . . . .	138
7.1.4	Data Types . . . . .	138
7.1.5	Code coupling for gas-liquid interaction . . . . .	139
7.2	Implementation of the high order moment method . . . . .	140
7.2.1	Moment Initialization . . . . .	140
7.2.2	Phase transport resolution . . . . .	141
7.2.3	Physical transport resolution . . . . .	143
7.2.3.1	Inventory of the new functions to code . . . . .	143
7.2.3.2	Implementation of the new functions . . . . .	144
7.3	Conclusion . . . . .	146
<b>8</b>	<b>Numerical validation with MUSES3D</b>	<b>148</b>
8.1	Spray in a two-dimensional Taylor-Green configuration . . . . .	148
8.2	Two-dimensional free-jet configuration in an unstationnary gaseous phase . . . . .	153
8.3	Conclusion . . . . .	154
<b>III</b>	<b>High order velocity moment method for high Knudsen number flows</b>	<b>156</b>
<b>9</b>	<b>Eulerian Multi Velocity Moment (EMVM) model</b>	<b>158</b>
9.1	Kinetic description of dilute gas-particle flows and moment transport equations . . . . .	159
9.1.1	Moment dynamic system . . . . .	159
9.1.2	Resolution strategy and challenges for the advection term resolution . . . . .	161
9.2	Quadrature-based method in one-dimension . . . . .	161
9.2.1	Quadrature-based velocity moment models for kinetic equations . . . . .	162
9.2.1.1	Quadrature inside the moment space . . . . .	162
9.2.1.2	Hyperbolic structure inside the moment space . . . . .	163
9.2.1.3	Behavior at the frontier of the moment space . . . . .	164
9.2.2	Entropy conditions . . . . .	168
9.2.3	Kinetic-macroscopic relation for smooth solutions . . . . .	171
9.2.4	Riemann problems and entropy measure solutions . . . . .	172
9.2.5	Examples of entropy solutions . . . . .	175

9.2.5.1	‘Collision’ of two particles packets . . . . .	175
9.2.5.2	‘Collision’ of four particles packets . . . . .	176
9.2.5.3	Smooth solution connected with the frontier of the moment space . . . . .	178
9.2.6	Numerical simulations via kinetic schemes . . . . .	180
9.2.6.1	Numerical quadrature strategy at the frontier of the moment space . . . . .	181
9.2.6.2	Numerical results . . . . .	182
9.3	Extension to two-dimensions . . . . .	193
9.3.1	Position of the problem . . . . .	193
9.3.2	Proposed quadrature method . . . . .	193
9.3.2.1	Cholesky decomposition . . . . .	193
9.3.2.2	Ability to treat areas of null temperature . . . . .	196
9.3.3	Discussion of the method relatively to other possible solutions . . . . .	197
9.3.3.1	Comparison of the Cholesky decomposition to other methods . . . . .	197
9.3.3.2	Comparison between different Cholesky decomposition . . . . .	198
9.3.3.3	Symmetric Cholesky method . . . . .	199
9.3.3.4	Symmetric optimised Cholesky method . . . . .	200
9.3.4	Kinetic-based numerical scheme . . . . .	201
9.4	Treatment of collision and drag terms . . . . .	202
9.5	General numerical strategy . . . . .	204
9.6	Illustration of the EMVM model . . . . .	204
9.6.1	Crossing jet . . . . .	204
9.6.2	Colliding jets . . . . .	204
9.6.3	Addition of the drag effect . . . . .	206
<b>10</b>	<b>Model coupling polydispersity and droplet crossing</b>	<b>210</b>
10.1	Presentation of the models and assumptions . . . . .	210
10.1.1	Coupling of the multi-fluid and EMVM models . . . . .	211
10.1.2	Coupling of the EMSM and EMVM models . . . . .	212
10.2	Numerical and algorithmic strategy towards implementation in MUSES3D . . . . .	214
10.2.1	Strategy for the EMFVM model implementation . . . . .	214
10.2.2	Numerical strategy for the EMSVM model . . . . .	215
10.2.3	Validation results for the EMSVM model . . . . .	216
<b>11</b>	<b>Implementation of the EMFVM model in MUSES3D</b>	<b>221</b>
11.1	Inventory of needed modifications . . . . .	221
11.2	Data structure modification and associated numerical tools implementation . . . . .	222
11.2.1	Data structure . . . . .	222
11.2.2	Associated numerical tools . . . . .	223
11.3	Modification of the initialization process . . . . .	225
11.4	Numerical scheme adaptation . . . . .	225
11.4.1	Physical transport resolution . . . . .	225
11.4.2	Phase space transport resolution . . . . .	227
11.5	Conclusion . . . . .	227
<b>12</b>	<b>Validation and results</b>	<b>230</b>
12.1	Dynamics of a droplet cloud in a Taylor-Green configuration . . . . .	230
12.1.1	Non evaporating case . . . . .	230
12.1.2	Case of a polydisperse evaporating spray . . . . .	236
12.2	Free-jet configuration . . . . .	238
12.2.1	EMFVM model versus Lagrangian models for free-jet configuration . . . . .	238
12.2.2	EMFVM model versus multi-fluid model for crossing jets . . . . .	240

<b>IV</b>	<b>Introduction of the size moment method in the code IFP-C3D</b>	<b>242</b>
<b>13</b>	<b>Adaptation of the moment method to the Arbitrary Lagrangian Eulerian formalism</b>	<b>244</b>
13.1	Equations in frame change . . . . .	245
13.1.1	Description of motion . . . . .	245
13.1.2	Equations in a moving frame . . . . .	248
13.1.2.1	Quasi-Eulerian description . . . . .	248
13.1.2.2	Description using the dilatation rate . . . . .	249
13.2	Numerical scheme . . . . .	251
13.2.1	Outline of peculiarities introduced by the ALE formalism . . . . .	251
13.2.2	Dimensional and operator splitting numerical scheme inspired from IFP-C3D . . .	252
13.3	Resolution for the gas phase . . . . .	254
13.3.1	Lagrangian phase . . . . .	254
13.3.2	Eulerian phase . . . . .	255
13.4	Resolution for aerosol and realizability condition . . . . .	257
13.4.1	Adaptation of the numerical scheme in the Eulerian phase . . . . .	257
13.4.2	Results . . . . .	259
13.5	Transport of spray and preservation of the discrete maximum principle . . . . .	262
13.5.1	Treatment of the drag term in phase A . . . . .	262
13.5.2	Phase B . . . . .	262
13.5.3	Phase C: first attempt for a stable advection scheme . . . . .	262
13.5.4	Stable second order scheme with flux coherence between $m_1$ and $\psi u_p$ . . . . .	264
13.5.5	Results . . . . .	266
13.5.5.1	Convection at uniform velocity . . . . .	266
13.5.5.2	Ability to capture $\delta$ -shocks . . . . .	266
13.5.5.3	Resolution coupling transport and evaporation . . . . .	268
13.5.5.4	Resolution coupling transport and drag . . . . .	269
<b>14</b>	<b>Introduction of the EMSM model in an industrial code, IFP-C3D</b>	<b>274</b>
14.1	Presentation of IFP-C3D . . . . .	274
14.1.1	General characteristics of the IFP-C3D code . . . . .	274
14.1.2	General algorithm and numerical scheme . . . . .	274
14.1.3	Connectivity aspect and grid evolution . . . . .	276
14.1.4	Introduced models . . . . .	277
14.1.5	Mapping of the intervention areas for the implementation of the EMSM model . .	277
14.2	Implementation of the EMSM model . . . . .	278
14.2.1	Data structure . . . . .	278
14.2.2	Initialization . . . . .	278
14.2.3	Implementation of injection boundary conditions . . . . .	279
14.2.4	Numerical scheme implementation . . . . .	279
14.2.4.1	Developments in phase A . . . . .	279
14.2.4.2	Developments in phase B . . . . .	280
14.2.4.3	Developments in phase C . . . . .	281
14.3	Numerical validations . . . . .	286
14.3.1	One-dimensional Riemann problem . . . . .	286
14.3.2	Validation of the scheme robustness through mesh movement . . . . .	286
14.3.3	Validation of the spray dynamics by comparison with the MUSES3D code . . . .	291
14.4	Feasibility of injection cases with Eulerian spray model . . . . .	296
14.4.1	Description of the case . . . . .	296
14.4.2	Computations of the size moments, and drag coefficients . . . . .	297
14.4.3	Comparison with the Lagrangian resolution method . . . . .	298
14.4.4	Spray description with the Eulerian spray model . . . . .	306
14.5	Conclusion . . . . .	314

<b>V</b>	<b>Synthesis of two-fluid models for separate-phase flows</b>	<b>315</b>
<b>15</b>	<b>Derivation of a two-fluid model</b>	<b>317</b>
15.1	Local instantaneous formulation . . . . .	317
15.2	Averaged two-fluid equations . . . . .	318
15.2.1	Averaging procedure . . . . .	318
15.2.1.1	Conservation of mass . . . . .	321
15.2.1.2	Conservation of momentum . . . . .	322
15.2.1.3	Energy equation . . . . .	323
15.2.2	The volume fraction equation . . . . .	324
15.2.3	The notion of area density to better account for the flow topology . . . . .	325
15.2.4	Closure challenges and consistency conditions . . . . .	325
15.3	General classification of two-fluid models . . . . .	326
15.3.1	The critical issue of interface description . . . . .	327
15.3.2	Mono-fluid models . . . . .	327
15.3.3	Two-fluid mixture models . . . . .	327
15.3.4	Two-fluid interface models . . . . .	328
15.4	Mathematical structure . . . . .	329
15.5	Thermodynamic consistency . . . . .	331
<b>16</b>	<b>Review on models for multi-phase flows</b>	<b>337</b>
16.1	Mixture model . . . . .	337
16.2	Two-fluid models . . . . .	339
16.2.1	Resolution of problems without an interface . . . . .	339
16.2.2	Resolution of interface problems . . . . .	340
16.2.2.1	Incompressible case . . . . .	340
16.2.2.2	Compressible case . . . . .	341
16.3	Two-fluid model implemented in the IFP-C3D code . . . . .	348
	<b>General Conclusion and Perspectives</b>	<b>350</b>
	<b>Appendices</b>	<b>354</b>
<b>A</b>	<b>Chapman-Enskog development for the resolution of the Fokker-Planck equation</b>	<b>354</b>
<b>B</b>	<b>EMSM model</b>	<b>358</b>
B.1	Resolution of the ODE system with classical methods . . . . .	358
B.2	ME reconstruction and boundaries of the moment space . . . . .	360
B.3	Moment vector advection scheme in the context of a non-structured grid . . . . .	363
<b>C</b>	<b>EMVM model</b>	<b>365</b>
C.1	Generalized Cholesky matrices decomposition . . . . .	365
C.2	Equations on centered moments . . . . .	369
<b>D</b>	<b>Arbitrary Lagrangian Eulerian formalism</b>	<b>371</b>
D.1	Counter-example of Section 13.5.3 . . . . .	371
D.2	Derivation of equations in ALE formalism in three dimensions . . . . .	372
	<b>Bibliography</b>	<b>374</b>



# List of Figures

1	Break-up steps for a liquid injection: from a liquid core to a droplet spray. . . . .	21
2	Particle mass density obtained with the multi-fluid model in a Homogeneous Isotropic Turbulence. . . . .	25
1.1	Domain of Knudsen . . . . .	35
2.1	Two classes of Eulerian models derived from the kinetic equation. . . . .	46
2.2	Resolution methods for the treatment of the size phase space . . . . .	47
2.3	Final models in the context of a size discretization . . . . .	48
2.4	Size distribution sampling . . . . .	49
2.5	Size distribution function discretization . . . . .	49
2.6	General overview of spray models based on a kinetic description . . . . .	52
3.1	Kinetic based transport scheme algorithm . . . . .	66
3.2	(left) Taylor-Green configuration for the gas vorticity field, (right) Initial condition for the droplets, composed of a motionless cloud. The droplet mass is represented, which is reconstructed from the first four size moments: $(m_0, m_1, m_2, m_3)$ . . . . .	69
3.3	(left) Initial size distribution for the particles. (right) Corresponding mass distribution . . . . .	70
3.4	Eulerian droplet mass at time $t = 1$ . . . . .	71
3.5	Eulerian droplet mass at time $t = 2$ . . . . .	72
3.6	Free-jet configuration at time $t = 20$ . . . . .	73
3.7	Non-evaporating polydisperse spray at time $t = 20$ . . . . .	74
3.8	Evaporating polydisperse spray at time $t = 20$ . . . . .	75
3.9	Comparison of the gas-phase fuel mass fraction at times $t = 15$ (left) and $t = 20$ (right). . . . .	76
3.10	Total number density of the polydisperse evaporating spray at time $t = 20$ . (Left) Multi-fluid model with one section. (Right) Multi-fluid model with ten sections. . . . .	76
3.11	Comparison of the gas-phase fuel mass fraction at times $t = 15$ (left) and $t = 20$ (right). . . . .	77
3.12	Results for spray dynamics in the gas field made of Taylor-Green vortices. Results for the multi-fluid method for 10 sections. . . . .	79
3.13	Results for spray dynamics in the gas field made of Taylor-Green vortices. Results for the multi-fluid method for 40 sections. . . . .	80
3.14	Comparison of the final mass in the two halves of the size phase space between the ten section discretization and the forty section discretization, in the evaporating case. . . . .	81
3.15	Evolution of the mean particle size through evaporation with a $d^2$ law, and comparison with the analytical solution. . . . .	82
3.16	Multi-fluid model with ten sections, at time $t = 2$ . Comparison of the final mass in the first and second section between evaporating and non evaporating case. . . . .	83
3.17	Mass density for simulation of two crossing jets using the standard multi-fluid approach (left) and the EMVM model (right) for droplets with $St = 5.29$ . Source: Fréret et al. [87]. . . . .	84
4.1	Reconstruction of a smooth NDF using different methods. . . . .	95
4.2	Cut of the moment space in the $m_2$ - $m_3$ plan. . . . .	96
4.3	Position of the EMSM model in the spray model derived from kinetic description . . . . .	98
4.4	Possibility to use the EMSM model within a sectional method . . . . .	98

5.1	Numerical solution for the problem of evaporation in the sense of characteristics. . . . .	107
5.2	Smooth NDF and ME reconstructed NDF obtained with the EMSM model with 1 section and 4 moments. . . . .	110
5.3	Evolution of the error on the moments calculated with the moment method with one section (left) or two sections (right) relatively to their initial value. . . . .	111
5.4	Evolution of the error on the mass density relatively to its initial value, calculated with the moment method with one or two sections and the multi-fluid method of order 2 with 4 or 8 sections. . . . .	111
5.5	Discontinuous NDF and ME reconstructed NDF obtained with the EMSM model with 2 sections and 4 moments. . . . .	112
5.6	Evolution of the error on the moments calculated with the moment method with one section (left) or two sections (right) relatively to their initial value. . . . .	112
5.7	Evolution of the error on the mass density relatively to its initial value, calculated with the moment method with one or two sections and the multi-fluid method of order 2 with 6 or 8 sections. . . . .	113
5.8	NDF and ME reconstructed NDF obtained with the EMSM model with 2 sections and 4 moments. . . . .	113
5.9	Evolution of the error on the moments calculated with the moment method with one section relatively to their initial value. . . . .	114
5.10	Smooth NDF (solid), ME reconstructed NDF obtained with the moments computed with the moment method with discontinuous evaporation rates with 2 sections and 4 moments. . . . .	115
5.11	Evolution of the errors on the moments calculated with the moment method with discontinuous evaporation rates, with 2 sections. . . . .	115
5.12	Evolution of the error on the moments calculated with the moment method with one section for the affine coefficient of evaporation. . . . .	116
5.13	Evolution of the error on the moments calculated with the moment method with one section for the discontinuous coefficient of evaporation. . . . .	117
5.14	Evolution of the exact moments for the equation on the radius (solid lines) and the moments calculated with the EMSM model with one or two sections; corresponding error on the moments for the one section case. . . . .	117
5.15	Evolution of the error on the moments calculated with the moment method for the equation on the radius, with two sections (left) or three sections (right) and relatively to their initial value. . . . .	118
5.16	Smooth NDF in radius, ME reconstructed NDF obtained with the moments computed with the EMSM model for 1 section and 4 moments or for 2 sections and 4 moments. . . . .	119
6.1	Evolution of aerosol particles calculated with the moment method, in a constant velocity field. . . . .	127
6.2	Evolution of a spray in a discontinuous velocity field, calculated with the moment method. . . . .	128
6.3	Evolution of a spray in a discontinuous velocity field calculated with the moment method. . . . .	129
6.4	Order accuracy study. Initial conditions. . . . .	130
6.5	Order accuracy study. Moment profile for the final time, with a 100 cell grid. . . . .	130
6.6	Order accuracy study. Profile of $m_0$ for the final time. . . . .	131
6.7	Order accuracy study. Error curves with respect to grid refinement in logarithmic scale. . . . .	131
7.1	General splitting structure. . . . .	135
7.2	Code structure for physical transport. The dashed line distinguishes the different modules. . . . .	137
7.3	Code structure for phase space transport. The dashed line distinguishes the different modules. . . . .	137
7.4	Modular block structure of MUSES3D solver, and interactions . . . . .	140
7.5	Implementation of EMSM model in the structure for phase space transport. The dashed line distinguishes the different modules. The dotted border locates the contributions. . . . .	144

7.6	Implementation of EMSM model in the structure for physical transport. The dashed line distinguishes the different modules. The dotted borders locate the contributions. The signe MF denotes the multi-fluid model . . . . .	147
8.1	Taylor-Green configuration for the gas vorticity field and Initial condition for the droplets. . . . .	149
8.2	Initial size distribution for the particles and corresponding mass distribution. . . . .	149
8.3	Results for spray dynamics dragged by the gas field made of Taylor-Green vortices, with the EMSM model, at $t = 0.5$ and time $t = 1$ . . . . .	150
8.4	Results for spray dynamics dragged by the gas field made of Taylor-Green vortices, with the EMSM model, at $t = 1.5$ and time $t = 2$ . . . . .	151
8.5	Results for spray dynamics dragged by the gas field made of Taylor-Green vortices, with the MF model, at $t = 0.5$ and time $t = 1$ . . . . .	151
8.6	Results for spray dynamics dragged by the gas field made of Taylor-Green vortices, with the MF model, at $t = 1.5$ and time $t = 2$ . . . . .	152
8.7	Evolution of the droplet mass through evaporation with a $d^2$ law, and comparison with the analytical solution; Evolution of the mean particle size through evaporation, and comparison with the analytical solution. . . . .	152
8.8	Total number density of the polydisperse evaporating spray. . . . .	154
8.9	Comparison of the gas-phase fuel mass fraction. . . . .	155
9.1	Moment dynamics in the context of a smooth transition between areas of null and non null dispersion. Initial conditions. Top-left: $M_0$ . Top-right: $M_1$ . Bottom-left: weights. Bottom-right: abscissas. The solid line corresponds to $(n_1, U_1)$ , the dashed line with circles corresponds to $(n_2, U_2)$ . . . . .	178
9.2	Moment dynamics in the context of a smooth transition between areas of null and non null dispersion. Solution at $t = 0.2$ . Top-left: $M_0$ . Top-right: $M_1$ . Bottom-left: weights. Bottom-right: abscissas. The solid line corresponds to $(n_1, U_1)$ , the dashed line with circles corresponds to $(n_2, U_2)$ . . . . .	179
9.3	Handling of the moment space border. . . . .	182
9.4	Initial fields of weights (left) and abscissas (right) for the two particle packet case. The first quadrature node is represented by solid lines whereas the second node is represented by circles. . . . .	183
9.5	Numerical and analytical solution for the two particle packet case, at $t = 0.1$ . . . . .	184
9.6	Numerical and analytical solution for the two particle packet case, at $t = 0.4$ . . . . .	185
9.7	Initial conditions for the four particle packet case. . . . .	187
9.8	Numerical and analytical moments for the four particle packet case, at $t = 0.1$ . . . . .	188
9.9	Numerical and analytical weights and abscissas for the four particle packet case, at $t = 0.1$ . . . . .	189
9.10	Four particle packet case, at time $t = 0.1$ . Left: ratio $q/(M_0e)$ . Right: ratio $q/e^{3/2}$ . . . . .	189
9.11	Moment dynamics in the context of a smooth transition between areas of null and non null dispersion, at time $t = 0.2$ : monents. . . . .	191
9.12	Moment dynamics in the context of a smooth transition between areas of null and non null dispersion, at time $t = 0.2$ : ratio $q/(M_0e)$ and $q/e^{3/2}$ . . . . .	192
9.13	Lines of iso-probability of a Maxwellian velocity distribution in two dimensions. The red points represent quadrature nodes . . . . .	194
9.14	Principle of the Cholesky decomposition. . . . .	196
9.15	Symmetric Cholesky decomposition. . . . .	200
9.16	Crossing jets, for times $t = 0.4, 0.6, 0.8, 1$ . . . . .	205
9.17	Results for collision with $\text{Kn} = 0.1$ at $t = 0.6, t = 0.8$ and $t = 1$ . . . . .	207
9.18	Results for collision with $\text{Kn} = 1$ at $t = 0.6, t = 0.8, t = 1$ . . . . .	208
9.19	Results for drag at $t = 0.8$ and $t = 1$ with $\text{St} = 1$ and $\text{St} = 0.1$ . . . . .	209
9.20	Results for drag and collision at $t = 1$ with $\text{St} = 1$ and $\text{Kn} = 1$ , and $\text{St} = 1$ and $\text{Kn} = 0.1$ . . . . .	209
10.1	Evolution of a spray in a discontinuous velocity field calculated with the EMFVm model, compared to the analytical solution of the problem. . . . .	217

10.2	Evolution of a spray in a discontinuous velocity field calculated with the EMFVM model, compared to the analytical solution of the problem. . . . .	218
10.3	Transport and evaporation of droplet clouds with PTC. . . . .	219
10.4	Overview of spray models, augmented with the models designed in this PhD. . . . .	220
11.1	Implementation of EMFVM model in the structure for physical transport. . . . .	227
11.2	Implementation of EMFVM model in the structure for phase space transport. . . . .	229
12.1	Dynamics of a monodisperse spray in Taylor-Green vortices, solved with the EMFVM model, until $t = 1$ . Corresponding droplet mass density. . . . .	232
12.2	Dynamics of a monodisperse spray in Taylor-Green vortices, solved with the EMFVM model. Corresponding x-velocity, y-velocity, and temperature, for $t = 0.5$ and $t = 1$ . . . . .	233
12.3	Dynamics of a monodisperse spray in Taylor-Green vortices, solved with the EMFVM model, from $t = 1.25$ to $t = 2$ . Corresponding droplet mass density. . . . .	234
12.4	Dynamics of a monodisperse spray in Taylor-Green vortices, solved with the EMFVM model. Corresponding x-velocity, y-velocity, and temperature, for $t = 1.5$ and for $t = 2$ . . . . .	235
12.5	Dynamics of a polydisperse evaporating spray in Taylor-Green vortices, solved with the EMFVM model, for $t = 0.5, 1, 1.5, 2$ . Corresponding droplet mass density. . . . .	236
12.6	Dynamics of a polydisperse evaporating spray in Taylor-Green vortices, solved with the EMFVM model. Corresponding droplet mass density for each size section. . . . .	237
12.7	Non-evaporating polydisperse spray with high-inertia droplets at time $t = 20$ . . . . .	238
12.8	Focus on region of the spray outlined by the rectangle in Fig. (12.7)-(bottom right). . . . .	239
12.9	Evaporating polydisperse spray with high-inertia droplets at time $t = 15$ . . . . .	240
12.10	Total number density of the non-evaporating spray at time $t = 20$ . . . . .	241
13.1	Lagrangian description of motion. . . . .	246
13.2	Lagrangian description of motion. . . . .	246
13.3	Initial condition for the moments. . . . .	260
13.4	Solution of the Riemann problem at $t = 0.1$ for the gas and the aerosol on fix and a moving grid. . . . .	261
13.5	Solution of the Riemann problem at $t = 0.1$ for the gas and the evaporating aerosol on fix and a moving grid. . . . .	261
13.6	Convection of the spray at uniform velocity with and without mesh movement. . . . .	267
13.7	$\delta$ -shock dynamics at time $t = 0.1$ for the first and second order scheme without mesh movement. . . . .	267
13.8	$\delta$ -shock dynamics at time $t = 0.1$ for the first and second order scheme with mesh movement. . . . .	268
13.9	Initial condition for the moment and the velocity. . . . .	269
13.10	Evolution of a spray in a discontinuous velocity field calculated with the moment method, compared to the analytical solution of the problem, at $t = 0.2$ and $t = 0.45$ . . . . .	270
13.11	Evolution of a spray in a discontinuous velocity field calculated with the moment method, compared to the analytical solution of the problem, at $t = 0.2$ with mesh movement. . . . .	270
13.12	Coupled transport and drag resolution. Initial condition for the moment and the gas. . . . .	271
13.13	Solution for particles with $St = 2 \cdot 10^{-3}$ . . . . .	271
13.14	Solution at time $t = 0.05$ . . . . .	272
14.1	General algorithm of the IFP-C3D code. . . . .	275
14.2	Illustration of connectivity. . . . .	276
14.3	Implementation of the EMSM in the IFP-C3D code structure. . . . .	285
14.4	Initial size distribution. . . . .	287
14.5	Initial conditions for the spray. . . . .	287
14.6	Solution for spray particles for the Riemann problem. . . . .	288
14.7	Considered piston movement during the computation. . . . .	289
14.8	Results in the case of an aerosol, for $m_0$ and $m_1$ . Results for $cad = -100, -30, 50, 180$ . . . . .	289
14.9	Results in the case of a spray, for $m_0$ and $m_1$ . Results for $cad = -100, -30, 50, 180$ . . . . .	290
14.10	Taylor-Green configuration for the gaseous flow and initial condition for the spray. . . . .	293

14.11	Comparison of the results of the IFP-C3D and MUSES3D codes, at time $t = 0.4$ .	293
14.12	Comparison of the results of the IFP-C3D and MUSES3D codes, at time $t = 1$ .	294
14.13	Comparison of the results of the IFP-C3D and MUSES3D codes, at time $t = 1.4$ .	294
14.14	Comparison of the results of the IFP-C3D and MUSES3D codes, at time $t = 2$ .	295
14.15	Illustration of Rosin-Rammler distributions, for two values of $q_{rr}$ .	296
14.16	Mesh used for the Lagrangian, and Eulerian numerical simulations.	297
14.17	Comparison of Lagrangian and Eulerian results for a monodisperse flow made of droplets of $D = 5 \mu m$ , at time $t = 5.10^{-3} s$ .	299
14.18	Comparison of Lagrangian and Eulerian results for a monodisperse flow made of droplets of $D = 5 \mu m$ , at time $t = 10^{-2} s$ .	300
14.19	Comparison of Lagrangian and Eulerian results for a monodisperse flow made of droplets of $D = 5 \mu m$ , at time $t = 1.5.10^{-2} s$ .	300
14.20	Comparison of Lagrangian and Eulerian results for a monodisperse flow made of droplets of $D = 5 \mu m$ , at time $t = 2.10^{-2} s$ .	301
14.21	Gas density field: Results for a monodisperse flow made of droplets of $D = 5 \mu m$ , at $t = 5.10^{-3} s$ and $t = 10^{-2} s$ .	301
14.22	Gas density field: Results for a monodisperse flow made of droplets of $D = 5 \mu m$ , at $t = 1.5.10^{-2} s$ and $t = 2.10^{-2} s$ .	302
14.23	Comparison of Lagrangian and Eulerian results for a monodisperse flow made of droplets of $D = 20 \mu m$ , at time $t = 5.10^{-3} s$ .	302
14.24	Comparison of Lagrangian and Eulerian results for a monodisperse flow made of droplets of $D = 20 \mu m$ , at time $t = 10^{-2} s$ .	303
14.25	Gas density field in the context of the two-way coupling considered in the Lagrangian resolution. Results for a monodisperse flow made of droplets of $D = 20 \mu m$ . Left : results for $t = 5.10^{-3} s$ ; Right : results for $t = 10^{-2} s$ .	303
14.26	Comparison of Lagrangian and Eulerian results for a polydisperse flow made of droplets of $D = 20 \mu m$ , at time $t = 5.10^{-3} s$ .	304
14.27	Comparison of Lagrangian and Eulerian results for a polydisperse flow made of droplets of $D = 20 \mu m$ , at time $t = 10^{-2} s$ .	304
14.28	Gas density field: Results for a monodisperse flow made of droplets of $D = 5 \mu m$ , at $t = 5.10^{-3} s$ and $t = 10^{-2} s$ .	305
14.29	Results of the EMSM model for a polydisperse flow with a Sauter mean radius of $D_{smr} = 5 \mu m$ , at $t = 10^{-2} s$ .	306
14.30	Results of the EMSM model for a polydisperse flow with a Sauter mean radius of $D_{smr} = 5 \mu m$ , at $t = 5.10^{-2} s$ .	307
14.31	Results of the EMSM model for a polydisperse flow with a Sauter mean radius of $D_{smr} = 5 \mu m$ , at $t = 0.1 s$ .	308
14.32	Results of the EMSM model for a polydisperse flow with a Sauter mean radius of $D_{smr} = 20 \mu m$ .	308
14.33	Results of the EMSM model for a polydisperse flow with a Sauter mean radius of $D_{smr} = 20 \mu m$ , at $t = 0.1 s$ .	309
14.34	Results of the EMSM model for a polydisperse flow with a Sauter mean radius of $D_{smr} = 80 \mu m$ at $t = 10^{-2} s$ and $t = 5.10^{-2} s$ .	309
14.35	Results of the EMSM model for a polydisperse evaporating spray with a Sauter mean radius of $D_{smr} = 5 \mu m$ , at $t = 0.1 s$ .	310
14.36	Results of the EMSM model for a polydisperse evaporating spray with a Sauter mean radius of $D_{smr} = 5 \mu m$ , at $t = 0.1 s$ .	311
14.37	Results of the EMSM model for a polydisperse evaporating spray with a Sauter mean radius of $D_{smr} = 20 \mu m$ , at $t = 0.1 s$ .	311
14.38	Results of the EMSM model for a polydisperse evaporating spray with a Sauter mean radius of $D_{smr} = 20 \mu m$ , at $t = 0.1 s$ .	312
14.39	Results of the EMSM model for a polydisperse evaporating spray with a Sauter mean radius of $D_{smr} = 80 \mu m$ , at $t = 0.1 s$ .	312

14.40	Results of the EMSM model for a polydisperse evaporating spray with a Sauter mean radius of $D_{smr} = 80 \mu m$ , at $t = 0.1 s$ .	313
15.1	Multi-species (left) vs multi-fluid configuration (right)	328
15.2	Hierarchy of two-fluid models.	330
15.3	Derivation of a two-fluid model	336
16.1	Illustration of the two types of visions: multi-fluid and multi-phase vision.	344
B.1	Analytical solution, reconstruction from its moments by maximization of entropy, and solution computed with the Runge-Kutta method, for a smooth initial distribution.	359
B.2	Analytical solution, reconstruction from its moments by maximization of entropy, and solution computed with the Runge-Kutta method, for a singular initial distribution.	359
B.3	canonical moments of the Euler Explicit solution for $dt = 0.1$ and $dt = 0.001$ for a smooth initial distribution.	360
B.4	canonical moments of the Euler Explicit solution for $dt = 0.05$ and $dt = 0.001$ for a singular initial distribution.	361
B.5	ME reconstruction with 4 moments, for $p_1 = 0.01$ (left) or $p_1 = 0.99$ (right), $p_2 = 0.5$ and $p_3 = 0.5$ and the Dirac delta functions corresponding to the lower principal representation.	361
B.6	ME reconstruction with 4 moments, for $p_1 = 0.2$ , $p_2 = 0.01$ (left) or $p_2 = 0.99$ (right) and $p_3 = 0.5$ and the Dirac delta functions corresponding to the lower principal representation.	362
B.7	ME reconstruction with 4 moments, for $p_1 = 0.2$ , $p_2 = 0.5$ and $p_3 = 0.01$ (left) or $p_3 = 0.99$ (right) and the Dirac delta functions corresponding to the lower principal representation.	362
B.8	ME reconstruction with 6 moments, for $p_1 = 0.5$ , $p_2 = 0.25$ and $p_3 = 0.5$ , $p_4 = 0.0171$ and $p_5 = 0.5$ and the Dirac delta functions corresponding to the lower principal representation.	363
B.9	Primary (left) and dual (right) mesh	363
C.1	Generalized Cholesky decomposition	365
C.2	Quadrature method and associated error for a distribution with $r = 0.9$ , $m_{30} = 0$ .	367
C.3	Quadrature method and associated error for a distribution with $r = 0$ , $m_{30} = 1$ .	367
C.4	Quadrature method and associated error for a distribution with $r = 0.9$ , $m_{30} = 1$ .	368

# Remerciements

S'engager dans une thèse, c'est s'engager dans aventure dont on arrive assez mal au début à définir les tenants et les aboutissants. C'est en cela qu'elle paraît mystérieuse, intimidante, mais aussi exaltante. On s'y plonge avec enthousiasme, détermination, mais aussi avec une certaine appréhension et l'espoir que l'on va parvenir à apporter une contribution qui soit reconnue. Si cet objectif a été atteint, c'est d'abord et avant tout grâce à la participation de nombreuses personnes. Aussi je profite de cet espace pour leur exprimer ma reconnaissance.

Je tiens d'abord à remercier les membres du jury, Rodney O. Fox, Heinz Pitsch, Michel Lance, Frédéric Coquel, Marc Massot, Frédérique Laurent, Stéphane Jay, Sébastien Candell et Bénédicte Cuenot pour l'intérêt qu'ils ont manifesté à l'égard de ce travail. Je salue en particulier Heinz Pitsch, Michel Lance et Frédéric Coquel pour le temps qu'ils ont consacré à la lecture du manuscrit dont je suis conscient de la densité, ainsi que de la qualité de leurs remarques qui ont permis une mise en perspective plus large que je n'aurais pu le faire. Je remercie enfin Rodney O. Fox de m'avoir fait l'honneur de présider le jury.

Je remercie ensuite mes différents laboratoires d'accueil qui, par les moyens humains, matériels et financiers qu'ils ont apportés, ont créé un environnement de travail de qualité. Je remercie IFP Energies nouvelles et en particulier le département Moteurs et Simulation Systèmes qui m'a financé pendant ces trois années. Merci à Stéphane Henriot de m'avoir fait confiance, ainsi qu'à Antonio Pires da Cruz qui a repris le flambeau. Je remercie également le laboratoire EM2C de m'avoir fourni tout les moyens dont j'avais besoin pendant ces trois années, et les six mois qui ont précédé durant lesquels j'ai effectué mon stage de fin d'étude. Je remercie Nasser Darabiha, directeur du laboaratoire, ainsi qu'Estelle Iacona qui lui a succédé et m'a permis de finir mon travail de thèse dans de bonnes conditions. Je remercie enfin le département de génie chimique d'Iowa State University qui m'a accueilli en son sein durant le semestre d'automne 2008.

La réussite d'une thèse est très étroitement liée à l'équipe encadrante. De ce point de vue, je remercie très chaleureusement l'équipe avec laquelle j'ai eu plaisir à évoluer tout au long de cette aventure: Marc Massot, Frédérique Laurent et Stéphane Jay. Merci à Marc et Frédérique, que j'ai connu lors de mon projet de synthèse, d'abord de m'avoir donné goût au sujet et très vite intégré dans leur équipe au laboratoire EM2C. Je salue la confiance qu'ils m'ont manifestée pendant ces trois années, ainsi que leur disponibilité et écoute alliées à un niveau d'exigence élevé. Cela a créé des conditions on ne peut plus favorables à ma progressive maîtrise du sujet et aux contributions que j'ai pu apportées. Je retiendrai aussi l'aspect chaleureux de nos échanges, à la confluence des relations maître-élève et de la camaraderie, qui ont parfois donné lieu à des épisodes aussi inattendus que savoureux, et disons le franchement, à de franches rigolades. En particulier je salue la capacité de Marc à toujours préserver un climat serein même dans des situations de tensions exacerbées (avec une spéciale dédicace à ses références à Mickey3D, "tetesàclaques" et les savoureux "instants d'innocence"). Je remercie Stéphane Jay qui a supervisé mon travail à IFP Energies nouvelles. En plus des échanges amicaux que j'ai eu avec lui, je salue la souplesse dont il a fait preuve, étant conscient de la difficulté d'encadrer cette thèse dont la configuration, entre le laboratoire EM2C et IFP Energies nouvelles, est pour le moins atypique. Plus généralement, le niveau d'implication de mes encadrants dans cette thèse en a fait un succès.

Au delà de mon encadrement officiel, j'ai eu la chance de pouvoir travailler avec des personnes dont

je tiens à souligner l'implication. Je citerai en premier lieu Stéphane de Chaisemartin. Il a été pour moi une sorte de "parrain" de thèse, tant son aide, notamment en informatique scientifique, et dans la rédaction du manuscrit a été considérable. Je le remercie pour sa disponibilité et sa gentillesse, mais aussi pour tous les bons moments passés à discuter, que ce soit de science ou d'autres choses. Éloigné de quelques bureaux de celui de Stéphane, mon maître de l'ALE, Huy Tran, ne ménageait pas ses efforts pour m'initier à cette discipline rugueuse. Je tiens à faire part de ma profonde gratitude à Huy pour avoir rendu chaque session un moment tout aussi intense qu'agréable, et pour le plaisir que j'ai eu à développer le prototype du chapitre 13 avec lui. Je remercie à présent Lucie Fréret qui m'a épaulé lors de mes timides débuts en informatique scientifique, lors du Summer Program à Stanford en juillet 2008 et de sa préparation. Je lui suis grandement reconnaissant de la patience dont elle a fait preuve à mon égard. Lucie m'a également apporté une aide précieuse à chaque fois que je la sollicitais tout au long de la thèse. J'ai aussi eu la chance de travailler avec Rodney O. Fox dans le cadre d'une collaboration ô combien stimulante. Je ne saurais assez le remercier lui, ainsi que Marc, de m'avoir permis de passer un semestre dans son laboratoire à Iowa State University, pour un séjour qui restera inoubliable à plus d'un titre. Je retiens aussi les interactions avec Christophe Chalons avec lequel j'ai eu plaisir à travailler sur un projet en analyse mathématique. Je remercie enfin Julien Bohbot, Nicolas Gillet et Anthony Velghe de m'avoir été d'un grand secours dans ma prise en main du code IFP-C3D, ainsi qu'à Grégory Font, notre expert matlab.

De manière plus générale, je remercie toutes les personnes que j'ai eu plaisir à côtoyer dans mes trois laboratoires d'accueil, et avec lesquelles j'ai eu d'intéressantes discussions et échangé conseils, anecdotes, et plaisanteries. De manière non exhaustive, je remercie à IFP Energies nouvelles Christian Angelberger, Antonio Pires da Cruz, Chawki Habchi, Rajesh Kumar, les anciens thésards Aymeric (mon compagnon d'arme de l'Eulérien, grand amateur de lipides sous toutes ses formes), Jorg (excellent lanceur de sucre et imitant à merveille le cri du cochon), Lionel (le "Grand Frère" de l'Eulérien), Jean-Baptiste (abondant pourvoyeur de blagues pourries, un très bon partenaire donc), Gopalkrisnan (le "dieu suprême", c'est apparemment la signification de son nom, enfin c'est ce qu'il dit), Alessio (Maaa, c'est pas moi qui a fait ça !), Zakaria (avec qui on refaisait le Match tous les lundi midis lors de conversations passionnées), Yohan (ou devrais je dire Monsieur 'L'Equipe') et Vahid (le "Hulk Hogan" de R102). Au laboratoire EM2C, je retiens les échanges avec Laurent Zimmer, Benoît Fiorina, Christophe Laux, mes compatriotes Lorrains (Vive le Bitcherland, le Saint-Augustin, la mirabelle et le Schnapps!), mais aussi Thierry Schuller, Anne Bourdon, Matthieu Boileau, ainsi que les anciens thésards Guillaume (alias "Buche"), Patrick, Antoine, Nicolas, Paul, Ammar, Farah. Au département de génie chimique de Iowa State University, je remercie Maulik, mon co-bureau indien qui a initié une longue relation entre moi et ce pays, Latrisha et Keeman qui m'ont initié au wallyball et aux différentes manières de processer le houblon à Ames, Alberto, Janine. J'adresse tous mes encouragements aux thésards de l'équipe: Max, François et Oguz, ainsi qu'à Pauline, Kirsten, Sabre, Hubert, Guillaume, Nicolas, Abdelillah, Carlo, Bejoy, Julien, Théodore, Frédérique, Tapish, Alessandro, Loyal, Diane.

Je fais part de toute ma gratitude à toutes les courageuses relectrices et tous les courageux relecteurs de mon manuscrit: Stéphane de Chaisemartin, Frédérique Laurent, Marc Massot, Lucie Fréret, Stéphane Jay, Huy Tran, François Doisneau, Aymeric Vie, beau-papa Kamal et Rachna. Il est la vitrine de ce travail ambitieux qu'il ne m'aurait été possible d'accomplir sans toute cette aide.

Enfin, je ne saurais conclure ces quelques lignes sans rendre hommage à l'indéfectible soutien de ma petite famille. Je pense d'abord à ma Maman Marie-Josèphe et à ma Grand-Mère Eugénie qui ont toujours cru en moi et n'ont cessé de m'insuffler force et courage. Je remercie aussi mon Grand-Père Radé, qui, de là où il est, m'a constamment soutenu. Qu'ils sachent que cette réussite, c'est la leur. Je remercie mon beau-père Patrick qui a toujours été présent et solidaire, et apporté de la bonne humeur. Je remercie enfin la petite dernière, ma femme Rachna, que j'ai rencontrée lors de mon séjour à Iowa State. En dépit des difficultés liées à l'éloignement, elle a fait preuve d'un courage et d'une patience admirables, et m'a toujours soutenu lors de mes moments de découragement. Elle a également utilisé le peu de vacances qu'elle avait pour traverser l'Atlantique afin d'assister à ma soutenance. Je remercie également ma belle-famille et mon beau-père venu spécialement d'Inde pour assister également à ma soutenance.



Je remercie enfin le lecteur pour l'intérêt qu'il porte à mon travail, en ouvrant le manuscrit déjà, et peut être avec l'intention de le lire et même de l'étudier. Si tel est le cas, je lui souhaite bon courage et qu'il ne perde pas espoir même s'il se sent submergé et qu'il a l'impression de ne pas avancer. Qu'il se rappelle de cette phrase, que j'ai pu lire un jour en haut d'un tableau lorsque j'étais en classe de math sup et qui m'accompagne désormais: "Celui qui a déplacé la montagne, c'est celui qui a commencé par enlever les petites pierres".

# Résumé

Le contexte général de cette thèse est la simulation numérique de l'injection de carburant dans un moteur à combustion interne, afin d'améliorer son rendement et de limiter la production de polluants. De manière plus générale, ce travail s'applique à tout système industriel mettant en jeu un écoulement multiphasique constitué d'un carburant liquide injecté dans une chambre occupée initialement par du gaz, comme par exemple les moteurs automobiles ou aéronautiques, ou les turbomachines.

Intrinsèquement, il est possible de simuler l'ensemble de l'écoulement avec les équations classiques de la dynamique des fluides sans avoir recours à des outils de modélisation supplémentaires liés au caractère diphasique. Mais, les tailles des structures générées pendant l'injection (gouttes de diamètre inférieur à  $10 \mu m$ ) conduisent à des temps de calculs prohibitifs pour une application industrielle. C'est pourquoi il est nécessaire d'introduire une modélisation diphasique. C'est dans ce contexte que deux régions sont formellement distinguées: le coeur liquide dense proche de l'injecteur, appelé écoulement à phases séparées, et le spray constitué d'une population de gouttes polydispense (c'est-à-dire de tailles différentes) générées après le processus d'atomisation en aval de l'injecteur.

Ce travail de thèse étudie les modèles Eulériens pour la description de spray évaporants et polydispenses, en vue d'applications industrielles. Ils représentent une alternative potentielle aux modèles Lagrangiens qui sont majoritairement utilisés en industrie mais présentant des inconvénients majeurs. Ainsi, le modèle multi-fluide est étudié dans un premier temps. Bien que prometteur, deux difficultés sont soulignées: le coût requis pour une description précise de la polydispersion, et son incapacité à décrire les croisements de gouttes (particle trajectory crossing, PTC, en anglais). La thèse propose des solutions à ces deux limitations. Ces solutions reposent chacune sur des méthodes de moments. Premièrement, le modèle appelé Eulerian Size Multi Size Moment (EMSM) permet de résoudre des sprays évaporants et polydispenses de manière bien plus efficace que le modèle multi-fluide. Des outils mathématiques sont utilisés pour fermer le système d'équations associé au modèle, et combinés à des schémas de types volumes finis appelés schémas cinétiques, afin de préserver la réalisabilité du vecteur de moments, pour le transport et l'évaporation.

Une réponse à la seconde limitation est apportée avec le modèle appelé Eulerian Multi Velocity Moment (EMVM) basé sur le transport de moments en vitesse d'ordre élevé. Une distribution bimodale peut être localement reconstruite à partir des moments en utilisant une méthode de quadrature de moments (Quadrature Method of Moment, QMOM en anglais) en une ou plusieurs dimensions d'espace. De la même manière que précédemment, l'utilisation de schémas cinétiques permet de préserver la réalisabilité du vecteur de moment. De plus, une étude mathématique approfondie de la dynamique du système en une dimension d'espace en révèle toute la complexité et représente une étape indispensable en vue de l'élaboration de schémas de transport d'ordre élevé (supérieur ou égal à 2).

Afin de les tester, ces deux modèles ainsi que les outils numériques associés sont implémentés dans MUSES3D, un code académique de simulation numérique directe (Direct Numerical Simulation DNS en anglais) dédié à l'évaluation des modèles de spray. Des résultats de grande qualité démontrent le potentiel des modèles.

L'extension du modèle EMSM dans un contexte industriel est ensuite considérée, avec son implémentation dans IFP-C3D, un code résolvant des écoulements réactifs sur des maillages non structurés et mobiles (dû au mouvement du piston) dans un formalisme RANS (Reynolds Averaged Navier Stokes) en présence de sprays. Le formalisme ALE (Arbitrary Lagrangian Eulerian en anglais) est utilisé et le modèle EMSM réécrit dans ce formalisme afin de mener des calculs en maillage mobile. De plus, une étude numérique a permis d'étendre les propriétés de précision et de stabilité obtenues en maillage fixe. La robustesse

du modèle EMSM est alors démontrée avec succès dans IFP-C3D sur un cas impliquant un mouvement de piston, ainsi que dans le cadre d'une comparaison avec le code MUSES3D. Enfin, des résultats très encourageants prouvent la faisabilité d'un calcul d'injection dans une chambre de combustion d'un spray polydisperse avec le modèle EMSM.

**Mots clés:** Ecoulements diphasiques; Sprays polydisperses; Sprays hors-équilibre; Méthodes de moments d'ordre élevé; Espace des moments; Ecoulements à phases séparées; Formalisme ALE; Schémas cinétiques; Informatique scientifique.

# Summary

The general context of the PhD is the simulation of fuel injection in an internal combustion engine, in order to improve its thermal and ecological efficiency. This work more generally concerns any industrial device involving a multiphase flow made of liquid fuel injected in a chamber filled with gaz: automotive or aircraft engines, or turbo machines. In and of itself, it is possible to simulate this flow without any modeling. However the small structures created during injection (droplets of diameter until  $10\ \mu\text{m}$  or less) lead to a prohibitive computational cost for any industrial application. Therefore modeling is necessary. In this context, two areas are formally distinguished: the dense liquid core close to the injector called separate-phase flow, and the spray made of a polydisperse droplet population (i.e. droplets with different sizes) generated after the atomization processes downstream of the injector.

This PhD work investigates Eulerian models for the description of polydisperse evaporating sprays, for industrial computations. They represent a potential alternative to Lagrangian models, widely used at present, yet suffering from major drawbacks. Thus, the Multi-Fluid model is assessed. Although it is very promising, two difficulties are highlighted: its cost for a precise description of polydispersity, and its inability to describe particle trajectory crossing (PTC).

Solutions to these two limitations are considered. Both rely on high order moment methods. First, the Eulerian Multi Size Moment (EMSM) proposes a much more efficient resolution of polydisperse evaporating sprays than the Multi-Fluid model does. Mathematical tools are used to close the model and combined with original finite volume kinetic-based schemes in order to preserve the moment-set integrity, for evaporation and advection. An answer to the second limitation is provided with the Eulerian Multi Velocity Moment (EMVM) based on high order velocity moments. A bimodal velocity distribution can be locally reconstructed for the moments using the quadrature method of moments (QMOM), in one or multi-dimensions. Here also, finite volume kinetic-based schemes are studied in order to preserve the moment set integrity. Moreover, a mathematical study of the one-dimensional dynamic system highlights its peculiarity and constitutes a necessary basis for the design of high order numerical schemes. In order to assess them, both the models and their numerical tools are implemented in the MUSES3D code, an academic DNS solver that provides a framework devoted to spray method evaluation. Achievements of the EMSM and the EMVM models are presented.

The extension of the EMSM model to an industrial context is then considered, with its implementation in the IFP-C3D code, a 3D unstructured reactive flow solver with spray. In order to perform computations within a moving domain (due to the piston movement) the Arbitrary Lagrangian Eulerian (ALE) formalism is used. A numerical study has been achieved, in order to extent to this formalism the properties of accuracy and stability of the EMSM model, which already induces strong stability condition in an Eulerian approach. The robustness of the EMSM model in the IFP-C3D code has been successfully demonstrated on a case involving a moving piston, and also on a comparison with the MUSES3D code. Moreover, very encouraging results demonstrate the feasibility of the EMSM model for spray injection.

**Keywords:** Two-phase flows; Polydisperse sprays; Non-equilibrium spray; High order moment methods; Moment space; Separate-phase two-fluid models; ALE formalism; Kinetic-based numerical schemes; Scientific computing.

# General Introduction

Taking into account two-phase flow effects has become a critical aspect for many industrial combustion devices, such as automotive engines, aeronautical turbo shaft or turbojet engines. Active research on two-phase flows is also carried out in other important fields, such as chemical engineering, nuclear engineering, or atmospheric studies. Given the cost and the complexity of experiments, a great interest for numerical simulation has emerged, not only in the academic field, but also in industry. A high maturity has been reached in the simulation of monophasic gaseous combustion or turbulent gaseous flow fields. Yet the description of two-phase effects still leads to major difficulties, particularly in combustion, as they significantly influence flame structure and pollutant production. Conscious of these issues for the future of car engines production, IFP Energies nouvelles has been leading an ambitious project aiming at simulating fuel injection in internal combustion engines. In this context, two-phase interactions as well as liquid influence on the combustion process are the main effects that must be accounted for:

- As far as phase interactions are concerned, coupled transfers occur between gas and liquid phases in the course of fuel injection.
  - The first phenomenon encountered is the break-up of the liquid core injected. This phenomenon, called primary break-up, leads to a discontinuous liquid phase constituted of ligaments, clusters and droplets with a large size range. During this stage, liquid and gas phases exchange mainly momentum. Indeed, the gas phase can contribute to the break-up of the liquid core, as in air-assisted atomizers [150]. With regards to the liquid phase, air entrainment by the jet can occur, particularly in pressure atomizer where the liquid is injected with a high velocity.
  - Afterwards, the gas phase interacts with the resulting discontinuous liquid phase. Momentum transfers still occur through interactions between the spray and the gas turbulent eddies. These interactions may lead to the secondary break-up of the liquid ligaments and clusters into smaller spherical droplets. This population of disperse spherical droplets is called *spray*. These momentum transfers may come with heat transfers. The liquid phase is heated and then vaporizes, leading to mass transfer from the liquid to the gas. Moreover, liquid-liquid interactions may occur, as collision or coalescence, acting upon the physics of the liquid phase.
- The combustion of a two-phase flow is significantly different from the purely gaseous one. If we consider that the spray is completely vaporized before burning, the combustion is considered homogeneous. This situation is often taken as a simplification assumption and can occur if the vaporizing and burning zones are separated. Otherwise, if combustion and vaporization are mixed, different spray combustion regimes are defined. A first distinction is made in [20], between external combustion, where the flame is located around the spray, and internal combustion, where each droplet burns separately. The group combustion regime is introduced in [32]. In [202], the influence of equivalent ratio and advection of the spray on combustion is taken into account. Different types of external combustion are characterized. Besides, new regimes are introduced, as group combustion of droplet clusters and hybrid regimes, combining external and group combustion. Furthermore, two-phase combustion depends on the fuel vapor repartition, driven by liquid evaporation. The dynamics of the liquid phase thus directly influences combustion, since it influences vapor fuel spatial concentration.

In order to accurately describe fuel injection, one can consider a resolution of the entire flow, using DNS techniques [236, 91, 36, 109, 110]. But the cost of these methods is the main stumbling block for their use in industrial framework. Therefore, in order to still enable a resolution of the problem, although it implies losing information on the details of the flow, reduced order models are derived. In this context, it is essential to take into account two different zones. In each zone, physical phenomena are driven by different characteristics of the flow, calling for different types of modeling best suited for each zone. They can be visualized in Fig. (1).

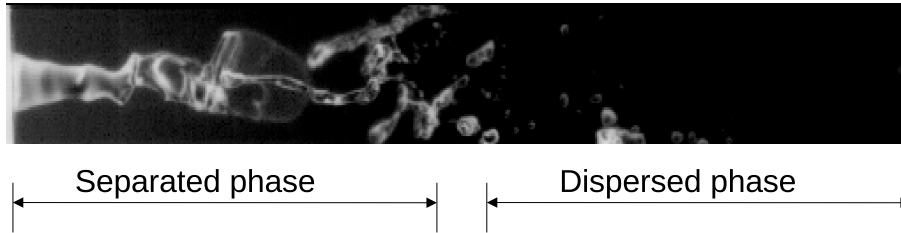


Figure 1: Break-up steps for a liquid injection: from a liquid core to a droplet spray. Source: Y. Merry, EM2C Laboratory

- In the primary break-up zone, the liquid phase being continuous, it is necessary to adopt a separate-phase flow description. In this framework, the shape of the interface between the liquid phase and the gas flow is not presumed. Therefore the description of the interface dynamics is predominant and conditions the coupling terms. The liquid can be a continuum or/and can be made of ligaments and droplets. This seems natural only in an Eulerian framework for the liquid phase, where the evolution of mean quantities, i.e density, velocity and energy of the liquid phase, are computed at fixed computational cells. There are numerous models intended to describe this area, we call them here separate-phase two-fluid models. It has first been formalized in [115, 53] and [209].
- On the other hand, in the secondary break-up zone, a disperse-phase flow description is more appropriate. In this case, the liquid phase is assumed to be composed of spherical droplets. Furthermore, the droplets are considered as point particles, so that the fluid flow is not resolved around and inside the droplets, and the coupling with the gas phase is done through source terms in the gaseous phase equations. The liquid is thus assumed to be dilute. That corresponds, in the classification established in [193], to a liquid volume fraction  $\alpha_l$ , going from  $\alpha_l = 10^{-4}$  to  $\alpha_l = 10^{-2}$ , limit where it begins to be moderately dense. Moreover, for DNS simulations, droplet size must be smaller than the smallest scale of the gas turbulence, the Kolmogorov length scale [138]. In this case, physical phenomena are conditioned by the droplet size distribution called polydispersity. In this framework a Lagrangian tracking approach is often used, and the information, i.e droplet characteristics, is tracked within the flow.

The project of IFP Energies nouvelles involves the simulation of the fuel spray injection in the entire combustion chamber, from the flow in the nozzle injector to the area downstream of the injector, after secondary break-up, where the liquid phase has the characteristic of a disperse droplet cloud population. This simulation requires the use of the different types of models, for separate-phase and disperse-phase flow area. A key challenge that can already be mentioned here is to couple these descriptions in order to carry out a full injection computation. This leads us to consider the resolution methods used in the industrial framework so far :

- A full liquid injection has been realized using an Eulerian separate-phase two-fluid model. In this case, a RANS resolution of the gas and the liquid is done as well as the description of the interface dynamics with an equation for the volume fraction. This has been done during the first stages of the project led by IFP Energies nouvelles [215, 220], in the industrial code IFP-C3D. This approach can also be found in [116] for the description of a disperse-phase flow this time. This

shows that separate-phase two-fluid models, dedicated to the description of interface dynamics and thus interface conditions of equilibrium or non-equilibrium between the phases, can be used to describe the disperse-phase as well. But in this case, since the fluid topology is accessed, if needed, only through a volume fraction and a surface area density, the polydispersity characteristic of the spray cannot be accounted for, and so some essential piece of information of the spray is missed. Therefore, separate-phase two-fluid models alone are not the solution for an accurate description of both flow areas.

- For the disperse-phase, a Lagrangian approach is used. But this resolution method is also used in the region close to the injector nozzle. This method has the advantage to be simple and easily implemented. In this case, two-fluid effects such as cavitation and atomization cannot be described. Instead these interactions have to be modeled. This liquid description is coupled to a RANS description of the gas flow [6]. When it comes to Eulerian descriptions, let us also mention the recent implementation of the Eulerian multi-fluid model in the AVBP code of CERFACS, in a LES framework [223, 221].

This brief review points out the fact that each type of model is suited for one flow area. But none of these models can describe both areas simultaneously and accurately. This assessment highlights the need for a coupling between the different methods to provide an accurate description of a full liquid injection. An interesting first answer has been given with the coupling of an Eulerian separate-phase model for the simulation of the liquid core primary break-up with a Lagrangian description of the disperse-phase in regions distant from the injector nozzle, done in the solver Eulerian Lagrangian Spray Atomization (ELSA) [54]. Such a full spray injection computation in a LES framework is today an essential contribution towards a predictive two-phase combustion simulation. Two main research directions are followed at present with this long-term objective:

- First, precise DNS of the primary break-up are conducted in order to extract more accurate information than average values of the resulting droplet size and velocity distributions. In this case, two systems are resolved by a DNS, one for the gas, and one for the liquid. The interface between the liquid and the gas phase is hence completely resolved. The interface can be described using various types of methods: Lagrangian methods, front tracking methods, or Eulerian methods (VOF, Level Set or Ghost Fluid explained in [108, 178])
- Second, studies are conducted in order to choose the most efficient resolution method for the LES of the polydisperse liquid phase. These studies concern for example Eulerian methods, that are of great interest for massively parallel computations.

The final objective is to couple these two resolution methods, in order to combine precise descriptions of the separate phase and the disperse-phase flows. At first, this description would be obtained in a DNS framework, but the eventual objective is to get a LES derivation for industrial configurations. Yet the coupling of this two types of model in a LES context is still an open question, for example concerning the type of information that should be inherited from the primary break-up simulation in the disperse-phase simulation.

This PhD, realized jointly at the EM2C laboratory, Ecole Centrale Paris, and at IFP Energies nouvelles, is a clear contribution towards this ambitious objective, in an industrial context, to couple

- a precise description of the flow and phenomena that occur close to the injector,
- and a precise and efficient description of spray polydispersity downstream of the injector.

A separate phase two-fluid model has already been implemented by [215, 220] in the CFD code of IFP Energies nouvelles for the resolution of reactive multiphase-flows, IFP-C3D. Therefore, this PhD work investigates models for polydisperse sprays having in mind the two following requirements. The first is to prepare a coupling with the separate phase two-fluid model as efficient as possible. The second concerns the efficiency in terms of computational cost of the method, that should allow computations in industrial configurations.

So far, several strategies are available for the disperse-liquid phase modeling. Two levels of modeling can be envisioned, based on a deterministic or a probabilistic approach.

- A deterministic approach can be conducted for the simulation of the liquid phase. In this case all the droplets of the spray are tracked in the flow, using a Lagrangian method. We refer to this method as the Discrete Particle Simulation (DPS) [202, 180]. Numerical particles representing one droplet are tracked in the flow, through the resolution of their characteristic evolution: size, center of mass position, velocity, temperature... This method can be coupled with different descriptions of the gaseous flow: DNS, LES or RANS. In the case of the coupling with a gas DNS, it is often considered as a two-phase flow DNS, even if not all scales are eventually resolved. Nevertheless, one has to keep in mind the modeling assumptions and restrictions associated with the disperse-phase description. A major difficulty of this approach is that it is a deterministic resolution of a spray flow, where initial conditions of the particle population can generally be accessed only statistically.
- On the other hand, a probabilistic formulation can be introduced to model liquid disperse-phase. In this case a number density function (NDF) of the spray  $f$  is introduced, the quantity  $f(t, \mathbf{x}, S, \mathbf{u}, T) dt dS d\mathbf{u} dT$  being the probable number of droplets within at time  $t$ , a position in  $[x, x + dx]$ , a size in  $[S, S + dS]$ , a velocity in  $[\mathbf{u}, \mathbf{u} + d\mathbf{u}]$ , and a temperature in  $[T, T + dT]$ . The NDF satisfies a Williams-Boltzmann equation

$$\underbrace{\partial_t f + \nabla_{\mathbf{x}} \cdot (\mathbf{u}f)}_{\text{Free Transport}} + \underbrace{\nabla_{\mathbf{u}} \cdot (\mathbf{F}f)}_{\text{Drag Force}} - \underbrace{\partial_S(Rf)}_{\text{Evaporation}} + \underbrace{\partial_T(Ef)}_{\text{Heat Transfer}} = \underbrace{\Gamma}_{\text{Collisions}} + \underbrace{Q}_{\text{Coalescence}} . \quad (1)$$

In this framework, along with the disperse-phase assumptions, we further assume that the effect of the gas on the liquid only depends on local gas properties, i.e there is no long-distance interactions. This approach is called the kinetic model, by analogy with the kinetic theory of gases. It is an Eulerian statistical approach. Eq.(1) is presented in a DNS framework, but one remarks that LES or RANS descriptions for the kinetic equation are also considered [169]. In these cases, a kinetic model 'in the mean' can be derived to take into account unresolved scales, leading to a new unclosed Williams-Boltzmann, equation, different from Eq. (1) [199]. Further modeling is thus needed to close the equation.

Nevertheless, given the high number of dimensions of the phase space (8 in 3D), a finite volume discretization of this equation, called the full spray equation method in [193], cannot be used at the scale of an industrial burner. Resolution methods have thus to be derived from this kinetic model, to obtain macroscopic models, well-suited for numerical simulations at industrial scale. Two resolution strategies were used so far.

- A stochastic Lagrangian Monte-Carlo method called Direct Simulation Monte-Carlo method, (DSMC) [16, 114], where stochastic parcels are tracked within the flow. The link between Lagrangian statistical methods and DPS has to be clearly highlighted. Indeed, statistical Lagrangian description can refer to two different levels of modeling.
  1. The most common one is associated with a coarser version of DPS, needed in industrial configurations for computational cost reasons. In this framework, a numerical particle, or parcel, represents several physical droplets [71, 193]. In this case, the computed solution does not approximate, or approximate with a lot of noise, the spray NDF and its moments, defined at the kinetic level of description. This method is referred to in this work as the Stochastic Parcel (SP) method [193].
  2. The second one, we call DSMC in this work, is a resolution method for the kinetic equation Eq. (1), as introduced in [16] for rarefied gas. In this framework we aim at achieving a converged solution approximating the NDF moment dynamics. It can be seen as equivalent to Eulerian methods derived from the kinetic model. One has nevertheless to keep in mind that, if both approaches aim at solving the same quantities, the assumptions might differ from one approach to another. The DSMC method represents a refined vision of the DPS, several statistical particles being needed, if necessary, for one physical droplet. The



numerical particle has a weight associated, adapted to the needed refinement. These methods have been developed for instance by [226] in a LES framework.

Practically speaking, the difference between DPS and statistical methods arises in collision modeling. The stochastic methods allow to compute directly the collision integrals in a statistical way, whereas collisions are seen deterministically in DPS. Besides, the different visions of the statistical methods described above leads to a major difference in the refinement used, since a converged solution, in the sense of the kinetic modeling, is expected in DSMC method.

- A wide range of Eulerian techniques are derived from the kinetic model. Various techniques are used to derive a system of equations governing the evolution of a set of moments of the spray NDF. The most common methods, for spray simulation, are two-fluid spray models (not to be confused with separate-phase two-fluid models) [80, 134], multi-fluid models [102, 146, 49], and the Direct Quadrature Method of Moments (DQMOM) [161]. Let us notice the use of moment methods for the treatment of soot particles, [185, 184]. In some LES approaches, the spatial filter is applied on the moment equations [234, 81].

At present, Lagrangian methods are widely used for the disperse-phase simulation since they combine an efficient modeling of the polydisperse phase, a high numerical efficiency, not introducing any numerical diffusion, and an easiness of implementation. Nevertheless, they suffer from important drawbacks. First, they raise the question of the coupling with the Eulerian description of the gas phase. This question is still open since it involves two ways of description that are fundamentally different. Then, if a DSMC is considered, a very high number of statistical particles has to be used for unsteady polydisperse cases. Moreover, in the framework of domain decomposition for parallel computations it is needed to use complex and costly dynamic partitioning methods, to ensure a good load balancing between the different parallel processes. Recent advances have been obtained in this field [92]. Finally, as previously mentioned, Lagrangian methods are restricted to disperse-phase flow only. In order to describe a full spray injection, Lagrangian methods, when they are used, have to be coupled with an Eulerian model for separate-phase flows. As for the coupling with the gas description this raises theoretical and numerical questions. Since the same phase is concerned, this coupling is even more crucial.

Regarding the objective of IFP Energies nouvelles to couple an existing separate-phase two-fluid model with a polydisperse spray model, the aforementioned drawbacks of Lagrangian methods make the use of an Eulerian formalism attractive for the design of a spray model. The Eulerian formalism consists of indirectly solving transport equations for the NDF by solving for selected moments the kinetic equation using a moment method. The use of moment methods results in the loss of some information but for the following two reasons the cost of such methods can potentially be much lower than that of the Lagrangian alternative. The first is due to the fact that the equation is solved for a limited number of unknowns, the second is related to the high level of optimization one can reach, when both phases are solved within an Eulerian framework [49, 88, 86]. Besides, for comparison with data in practice, the principal quantities of interest are the moments of the NDF. Finally, it appears that this kind of method allows *a priori* a much easier coupling with a separate-phase two-fluid model than Lagrangian methods.

In the literature, two types of Eulerian models for the description of spray polydispersity are provided. The first one consists in discretizing the size phase space into size intervals called “sections” since the work of Tambour and coworkers (see for example [102] and references therein). There exists a large variety of applications and methods such as multi-fluid models for sprays (see [146, 147, 145, 144] extended from sectional models of Tambour, Greenberg et al. and [168, 172, 49] for a review of recent results) or sectional approach for aerosols (see [219, 137] and references therein), also called class methods in [27]. The multi-fluid approach relies on the derivation of a semi-kinetic model from the Williams equation using a moment method for velocity conditioned by size, but keeping the size as a variable [146]. This function is then discretized using a ‘finite-volume’ approach that yields conservation equations for mass, momentum (and possibly other properties such as enthalpy) of droplets in fixed size intervals called ‘sections’ extending the original work of Tambour, Greenberg and collaborators [101, 102] for evaporating sprays. It has led to very nice realizations. An example of those is presented in Fig. (2). However, partitioning the particle phase into size sections artificially considers several phases, and so multiplies the computational cost

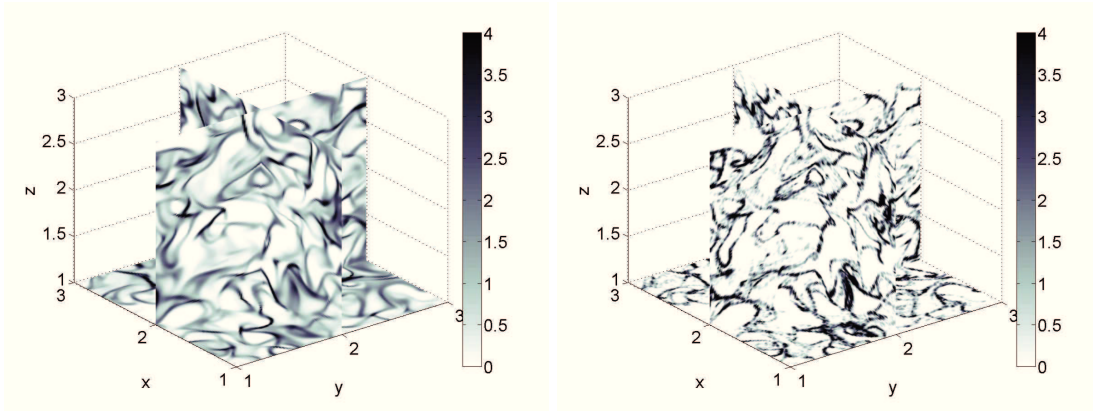


Figure 2: Particle mass density obtained with the multi-fluid model in a Homogeneous Isotropic Turbulence. The Stokes number of the particles is 1.2. (Left) Results obtained with the Eulerian model. (Right) Results obtained with the Lagrangian model. The computation was optimized to run on 512 processors

by the actual number of sections. This appears prohibitive for a use in an industrial context in terms of efficiency. This all the more true that the multi-fluid model is shown to be at most first order in the size variable [143] (extended to second order by [145, 69, 70, 59]). Thus, for applications implying a dynamics in the phase space, for example evaporation, the multi-fluid method introduces intrinsic numerical diffusion and then requires fine grids in size phase space. Therefore, in terms of computational cost, the possibility of high order moment method considering only one size section is very attractive. At present, several high order moment methods have been designed. The first one consists of solving the evolution of moments of a presumed NDF (assumed as a log-normal law) [183]. Presumably, this seems very attractive since knowing *a priori*, the profile of the NDF makes its reconstruction from the moments much easier. However, this approach leads to serious numerical instabilities thus preventing its use for the treatment of an evaporating spray, since during the computation, it might be impossible to reconstruct a log-normal distribution function from the moment set.

The second method uses Direct Quadrature Method of Moment (DQMOM) [159] wherein equations are directly written on the nodes and abscissas of the distribution function [85]. Contrary to the first one, this method is robust. But it suffers from serious accuracy problems in the resolution of the evaporation term, as pointed out in [85].

The second limitation encountered by Eulerian spray models is the difficulty to describe particle trajectory crossing (PTC). Two important parameters in fluid-particle flows are the Knudsen number  $Kn$  and the Stokes number  $St$ . The Knudsen number represents the importance of particle-particle collisions relative to free transport. For small Knudsen numbers, collisions are preponderant so that the droplet velocity distribution relaxes to a Maxwellian (or equilibrium) distribution: this is the case for dense sprays. On the other hand, for high Knudsen numbers, the flows physics is no longer conditioned by the collision rate, thus the equilibrium distribution is not a good approximate and one must solve the kinetic equation to adequately capture the flow physics. This is the case for dilute sprays. The Stokes number is defined as the ratio of the characteristic response time of the particle to the characteristic time scale of the gas flow. If the Stokes number is small, particles have nearly the same velocity as the fluid. On the other hand, for high Stokes numbers, particles barely feel the fluid and have thus their own dynamics. Consequently in the case of high Knudsen and moderate and high Stokes numbers flows, droplet trajectories may cross. Although naturally described by Lagrangian methods, these trajectories crossings are very difficult to describe with Eulerian methods, as explained in details in this work.

Indeed, most of the Eulerian methods for spray provide a description in a zero Knudsen limit where the droplet velocity distribution relaxes towards a Maxwellian distribution, that is the hydrodynamic limit [11]. Besides in some models, like the multi-fluid model, the particle velocity distribution is assumed to be locally monokinetic. On the other hand, when PTC occurs, the velocity distribution function is

locally bi-modal with values corresponding to the velocities originating from each characteristics.

According to the above discussion on advantages and drawbacks of Lagrangian and Eulerian spray models, it comes that the choice of an Eulerian model for the description of spray polydispersity is the best suited for the application targeted by IFP Energies nouvelles. Nevertheless, this discussion has highlighted two major limitations encountered by Eulerian models : a sufficiently efficient description of spray polydispersity to be used in industrial configurations, and the description of PTC.

The objectives of this PhD are thus the following. First, a high order moment method, i.e considering  $N$  moments with  $N > 2$ , has to be devised to describe an evaporating polydisperse spray efficiently. This involves, to propose a proper treatment of the evaporation term and associated numerical schemes, first in the context of a homogeneous spray, i.e without advection in the physical space. Once a proper closure for the evaporation term is found, this model has to be extended to the advection operator. Designing a finite volume robust advection scheme for the moment sequence is quite a challenge, since [231, 176] have proven that finite volume schemes using independent reconstruction for the moments lead to serious numerical instabilities, when one attempts to access the NDF from the data of the moments. This is due to the fact that the moment vector has to be realizable. Namely, each component of this vector has to be the actual moment of an NDF. The set formed by all the realizable moment vectors is called the moment space. Due to its complex geometry, any scheme based on independent advection of each of the moment is not robust.

Secondly, after assessing the potential of this method in an academic context, another part of this PhD work concerns the extension of this model and associated scheme to an industrial context. As previously mentioned, IFP Energies nouvelles has launched an ambitious project for the development in a RANS framework of numerical tools targeting the description of a full fuel injection in an internal combustion chamber. For that purpose, a separate-phase Eulerian model has been implemented in the IFP-C3D code so far. The next step of this project, as stated in [215, 220], is to implement a spray model able to account for the polydisperse character of the droplet population downstream of the injector. This work requires to take up two challenges. First, the specific numerical schemes for the new Eulerian spray model are designed in an Eulerian framework with fix grids. Yet, the algorithm used in the IFP-C3D code relies on the Arbitrary Lagrangian Eulerian formalism (ALE). This formalism is typically used when moving mesh are involved. In the applications targeted by IFP Energies nouvelles, this enables to cope with the movement of a piston in an automotive combustion chamber. Accordingly, the numerical schemes designed in the context of this PhD have to be extended to the ALE formalism. This method is enforced in the context of engine simulation in the unstructured CFD code IFP-C3D [18]. The second challenge consists in the actual implementation, from scratch, of this spray model in a code as complex as IFP-C3D, ensuring that a new major functionality has been provided, without interfering with and altering the present ones. The first step of this implementation is done in a DNS framework.

Third, one of the objectives of this PhD work is to overcome the second limitation of Eulerian spray models, that concerns PTC. This work is performed on the basis of the development of Quadrature Method of Moments (QMOM) for the description of PTC done in [84].

The final objective concerns the upcoming work devoted to couple the high order size moment method implemented in IFP-C3D with the separate-phase Eulerian model already implemented by [215, 220]. For that purpose, a precise knowledge of both Eulerian spray models and separate phase two-fluid models is required. Thus, a methodology gathering the elementary guidelines for the derivation a consistent model is needed. Very significant advances have been made over the past two decades. One can notably point out the work of Baer and Nunziato [10], paving the way for intense research activity on the description of non-equilibrium interface conditions between the liquid and the gas phase. But to our knowledge no type of comparative review currently exists. The according purpose of this PhD is to bring an humble contribution towards this synthesis work. This work is intended to prepare in the best conditions possible the forthcoming coupling work.

The answers of all these questions are organized in this manuscript as follows. First, the modeling framework considered in this work is presented in Part I, for the design and evaluation of new spray models. The two major limitations of Eulerian models relative to Lagrangian models are detailed in the context of the multi-fluid model. Solutions to each of these limitations are presented in Part II and Part III, respectively. In Part II, we explain how we have designed a high order size moment method for an

efficient description of spray polydispersity, overcoming for this occasion the first limitation. The second limitation is addressed with the design of a high order velocity moment method based on a QMOM approach, in order to describe PTC. The feasibility to couple the two above-mentioned is also studied. In Part IV, we present the work realized in order to adapt the high order size moment method exposed in Part II to the ALE formalism, and the introduction of this method in the IFP-C3D code. Finally, a study on separate-phase Eulerian two-fluid models is provided in Part V. The purpose of this part is to prepare the further coupling with the spray model by giving a background on separate-phase two-fluid models in order to understand the physical motivations for the implementation of the two-fluid model in the code IFP-C3D.

The kinetic modeling for spray and the gas description are given in Chapter 1. After characterizing the various types of flow regimes, governing equations are given for both the disperse-liquid and the gas phase in a detailed modeling framework. In order to conduct precise evaluation of the new spray models proposed in this PhD, a simplified modeling framework is defined for both the liquid and the gas phase. The existing spray resolution methods are presented in Chapter 2, where we notably highlight the link between the kinetic model and the different macroscopic Lagrangian and Eulerian methods. As far as Eulerian methods are concerned, we provide a classification based on the derivation techniques of the principal methods available at present. Chapter 3 is dedicated to the detailed presentation of the multi-fluid model. During his PhD [49], Stéphane de Chaisemartin proposed an evaluation of the multi-fluid model in the purpose of an extension to an industrial context. In this context, with the collaboration of Lucie Fréret, they developed a code dedicated to spray model evaluation, called Multi-Fluid Solver for Eulerian Spray or MUSES3D <sup>1</sup> with initially the single multi-fluid model. Part of this PhD work has consisted in characterizing the description of polydispersity provided by the multi-fluid model through the MUSES3D code. This study has highlighted its capacity to describe the size distribution as well as the size-conditioned dynamics. These results have been published in [126]. The other aspect of this work has been to highlight the limitations of the multi-fluid model relative to Lagrangian approaches. First, it does not provide a description of polydispersity efficient enough to be envisioned for industrial applications. It is based on a first order method in size with extension to second order at the most, so that a precise description of the size distribution requires a fine grid in size phase space, at the expense of computational cost. Second, it does not allow PTC. This work has been published in the journal *Flow, Turbulence and Combustion* [126], in a Lectures Series of the Von Karman Institute [172].

The first Eulerian method designed in the context of this PhD, is presented in Chapter 4. This model, referred to as Eulerian Multi Size Moment (EMSM) model relies on a high order moment method for the size variable. Its derivation, associated to the corresponding assumptions and closures are presented in Chapter 4. The philosophy of this model is different from the multi-fluid since the continuous character of the size variable is now conserved. Chapter 5 presents the design of original numerical tools that achieve a very precise resolution of the size distribution of evaporating sprays, while ensuring the strong stability condition induced by the system. First results by comparison with the multi-fluid model are very satisfactory, and show in particular that the EMSM model can treat any distribution function, giving a positive answer to the difficulty highlighted in [85]. This work has been published in the *SIAM Journal of Applied Mathematics* [173] and presented during the SIAM International Conference on Numerical Combustion, Monterey, USA (2008) [127].

The second achievement, presented in Chapter 6, has been the design of a high order finite volume scheme for the advection of the size moments, preserving the integrity of the moment set. Let us underline the challenge of this work, since this issue has already been discussed by several authors, for example [231, 176] without reaching a fully satisfactory solution. This work, with simple validation test cases, has been partially published in [172], and was presented during the ICLASS Conference, Vail, USA (2009) [128]. Third, in order to assess the potential of the EMSM model on more challenging test case, its associated numerical schemes have been implemented in the MUSES3D code, preserving its principal features: genericity, accuracy, and optimization through High Performance Computing (HPC) techniques. This is the object of Chapter 7. The corresponding results allow to draw positive conclusions

---

<sup>1</sup><http://www.projet-plume.org/fr/relier/muses3d>

in terms of precision and cost, about the potential of the EMSM model in an industrial context. This work has been submitted in Journal of Computational Physics [129].

The second limitation, highlighted in the context of the multi-fluid model, is addressed. As for the previous chapter, a high order moment method is considered, for velocity moments this time. This model referred to as Eulerian Multi Velocity Moment (EMVM) model, relies on a QMOM approach, as explained in [84]. The first aspect of this PhD work contributes to the research on high order advection schemes for the type of systems derived in Chapter 9. A mathematical study of the closed one-dimensional system is conducted in collaboration with Marc Massot and Christophe Chalons, from EM2C laboratory. This work has been submitted in the journal Communication in Mathematical Sciences [125]. Secondly, the theoretical gap between one-dimensional and multi-dimensional case is investigated. The difficulty is due to the fact that the quadrature problem does not have a unique solution any more. The two-dimensional case only is considered in this work, since the extension to three-dimensions does not bring any additional difficulties. Results of this study are exposed in Chapter 9. A third aspect of this work is to consider the possibility to couple the advances brought by the multi-fluid and EMVM models in a comprehensive model called the Eulerian Multi-Fluid and Velocity Moment (EMFVM) model, explained in Chapter 10. As done for the EMSM a numerical strategy for the EMFVM model is designed to implement it in the MUSES3D, code. Its validation work through challenging test cases has been published in the journal Flow, Turbulence and Combustion [126], in two proceedings of the Summer Program 2008 at Stanford [51, 87] and in a special issue of the Comptes Rendus Mécanique [50]. Meanwhile, we have considered the coupling of the high order moment methods for both size and velocity, referred to as Eulerian Multi Size and Velocity Moments (EMSVM) model, for which we have considered suitable numerical tools towards their implementation.

The extension of the EMSM model to an industrial framework is discussed in the last part. This work, aiming at introducing a new functionality in the IFP-C3D code, consists in two aspects. First, since the general algorithm of the IFP-C3D code is based on the ALE algorithm, a theoretical study is conducted on the adaptation of the EMSM model numerical tools to the ALE formalism. In this new context, we show, in Chapter 13, that we are able to preserve the accuracy order of the schemes designed in Part II, while ensuring the strong stability conditions imposed by the moment dynamic system. The second aspect concerns the actual implementation of the EMSM model in the IFP-C3D code. The numerical strategy is exposed in Chapter 13. The validation of this work is performed by comparison with the MUSES3D code, used a reference, since the EMSM model has previously been implemented and validated, in Chapter 8. Validation of the model on injection is performed by comparison with the Lagrangian approach and thus demonstrated the feasibility of the EMSM model in such cases. First results of this work were presented during the ICMF Conference, Tampa, USA (2010) [130], and is in preparation the International Journal of Multiphase Flows [131].

A methodology for the derivation of separate two-fluid models is provided in Chapter 15. Two-fluid models are formally obtained by averaging the conservation equations of a single phase system. The various types of averaging processes are presented, with the resulting formal system of equations. The essential difference with single-phase models, is the existence of an interface between phases. The critical quantity that allows to describe the interface dynamics is the liquid volume fraction  $\alpha_l$ . A classification of two-fluid model is given, based on the type of equilibrium assumptions made between the phases. Finally, the condition to ensure for a two-fluid model to be consistent are finally presented. Then, a short review on two-fluid models is given in Chapter 16, based on the classification established in Chapter 15.

*This present work was supported by a grant from IFP Energies nouvelles, and benefited from a support from EM2C Laboratory. Furthermore, the present research was done thanks to:*

- *an ANR (French National Research Agency) Young Investigator Award (M. Massot, 2006 – 2009, ANR-05-JC05\_42236)*
- *a financial support from Stanford University and NASA Ames Research Center during the 2008 Summer Program at the Center for Turbulence Research*

- *a financial support of the U.S. Department of Energy at Ames Lab/Iowa State University during the Fall 2008 semester*

The present Ph.D. Thesis work was awarded:

- The SMAI-GAMNI 2010 best French Ph.D. Thesis Award from the French Society for Industrial and Applied Mathematics (Société de Mathématiques appliquées et industrielles- Groupe pour l'Avancement des Méthodes Numériques de l'Ingénieur).
- The ECCOMAS (European Community in Computational Methods in Applied Sciences) best 2010 European Ph.D. Thesis in the field of Computational Methods in Applied Sciences and Engineering.

## Part I

# Spray modeling and simulation

# Introduction

The precise spray flow modeling framework of the study is given in this part. The gas phase description is coupled with a kinetic spray model. This model comes from a statistical description of the disperse liquid phase. It gives the evolution of the spray Number Density Function (NDF). This model provides a mesoscopic level of modeling: it is called kinetic by analogy with the kinetic theory of gases. Indeed, the NDF evolution equation is similar to the Boltzmann equation. The NDF evolution is driven by the physical phenomena applied to the spray. The detailed description of the kinetic modeling framework, as well as the droplet model needed for its closure, are provided in Chapter 1. Furthermore, in order to evaluate a model, as done in this work with the Eulerian Multi Size Moment (EMSM) and Eulerian Multi Velocity Moment (EMVM) models, a modeling framework is defined in Chapter 1.

The spray equation of this kinetic model cannot be resolved at the scale of industrial application, given the associated cost. Macroscopic methods for its simulation have to be introduced. These methods can use a Lagrangian approach or an Eulerian approach. They are reviewed in Chapter 2. Among them, the multi-fluid model appears as the state of the art in terms of spray polydispersity description. Therefore, Chapter 3 is dedicated to its characterization work, and also the highlight of its limitations that has motivated the work presented in Part II and Part III.



# Chapter 1

## Kinetic modeling for disperse spray in gaseous flow

The two-phase flow modeling framework is detailed in this chapter. The present work aims at assessing a method for the disperse-phase simulation. The spray is thus considered to be dilute, i.e. with a volume liquid fraction  $\alpha = 10^{-4}$ , to moderately dense,  $\alpha = 10^{-2}$ , as established by the classification done in [193]. It is essential to note that the type of flow considered is specific to dilute regimes, contrary to two-fluid models, exposed in Chapter 16, where no specification is given for  $\alpha$ . In this framework, droplets are assumed to be point particles. The gas flow just around the droplets as well as the liquid flow inside the droplets are not resolved and the coupling with the gas phase is done through source terms in the gas phase equations. Besides, a statistical description based on a kinetic equation for the spray NDF is considered. In this kinetic formulation, the effect of the gas on the spray only depends of local gas properties. Long-distance interactions between gas and liquid are thus neglected. The governing equations for the gas and liquid phases are given in this chapter, with the simplified framework in which studies are conducted in this PhD. Droplet models needed to close the source terms of the kinetic equation are provided. The kinetic formulation is then extended to the class of aerosol, referring to low inertia set of particles with a mean velocity equal to the gas one. Finally, the scope of studied particle flow regime is given, as well as the general assumptions.

### 1.1 Gas phase description

For the gas description, the Navier Stokes equations for a multi-species reactive flow are considered. Two strategies can be envisioned for their derivation. These Eulerian equations can be obtained through mass, momentum and energy balance on a control volume. This derivation can be found for example, for a general mono-species non-reactive case in [31], and in [197] for reactive multi-species flows. Another more mathematical way to obtain these equations consists in deriving this fluid level of description from the kinetic theory of gases, [94, 75, 167]. It leads to a mixed hyperbolic-parabolic system, its mathematical structure being studied in [95].

These gaseous phase equations are given in the framework of a two-phase flow, with a dispersed liquid phase. This liquid phase is assumed to be dilute enough so that its influence on the gas phase can be described by a source term addition in the gas phase equations. We decide to clearly explicit the non dimensional equation, to underline the reference quantities arising. These quantities will also drive liquid dimensionless equation derivation, in Section 1.2.

#### 1.1.1 Gas equation system

The conservative form of the Navier Stokes system describes mass, species, momentum and energy conservation. The influence of the liquid phase is taken into account through mass, momentum and energy

source terms.

The conservation of mass is given by:

$$\partial_t \rho_g + \nabla_{\mathbf{x}} \cdot (\rho_g \mathbf{u}_g) = S^{\text{fuel}}, \quad (1.1)$$

where  $\rho_g$  is the gas density,  $\mathbf{u}_g$  the velocity and  $S^{\text{fuel}}$  the mass source term from the liquid phase evaporation.

Regarding species conservation, we have, for the  $k^{\text{th}}$  species:

$$\partial_t (\rho_g Y_k) + \nabla_{\mathbf{x}} \cdot (\rho_g \mathbf{u}_g Y_k) = -\nabla_{\mathbf{x}} \cdot (\rho_g \mathbf{u}_k^{\text{diff}} Y_k) + \dot{\omega}_k + S_k^{\text{species}}, \quad (1.2)$$

where  $Y_k$ ,  $\mathbf{u}_k^{\text{diff}}$ , and  $S_k^{\text{species}}$  are the mass fraction, the diffusion velocity, and the liquid evaporation mass source term of species  $k$ , respectively. The term  $\dot{\omega}_k$  is the reactive rate of species  $k$ . By definition, one has:

$$Y_k = \frac{\rho_k}{\rho_g}, \quad \rho_g \mathbf{u}_g = \sum_{k=1}^{n_s} \rho_k \mathbf{u}_k Y_k, \quad \mathbf{u}_k^{\text{diff}} = \mathbf{u}_k - \mathbf{u}_g, \quad (1.3)$$

where  $\rho_k$  and  $\mathbf{u}_k$  are respectively the density and the hydrodynamic velocity of species  $k$ , and  $n_s$  the number of species. It yields:

$$\sum_{k=1}^{n_s} Y_k = 1, \quad \sum_{k=1}^{n_s} \rho_k \mathbf{u}_k^{\text{diff}} = 0, \quad \sum_{k=1}^{n_s} S_k^{\text{species}} = S^{\text{fuel}}. \quad (1.4)$$

Discussions about the closure of  $\mathbf{u}_k^{\text{diff}}$  can be found in [197] or [75]. As in [49] a Fick's law closure, neglecting the Soret effect is used:

$$\mathbf{u}_k^{\text{diff}} Y_k = -D_k \nabla_{\mathbf{x}} (Y_k), \quad (1.5)$$

where  $D_k$  is the diffusion coefficient of species  $k$  into the mixture.

The momentum conservation is given by:

$$\partial_t (\rho_g \mathbf{u}_g) + \nabla_{\mathbf{x}} \cdot (\rho_g \mathbf{u}_g \otimes \mathbf{u}_g) = -\nabla_{\mathbf{x}} (P_g) + \nabla_{\mathbf{x}} \cdot (\mathbf{T}) + S^{\text{mom}}, \quad (1.6)$$

with  $\mathbf{T}$  the viscous stress tensor. This tensor is closed in the context of the Navier-Stokes equations for Newtonian fluids [31].

We consider here, as done in [200, 49], an equation for sensible enthalpy,  $h_s = \int_{T_0}^{T_g} C_{p,g} dT$  in order to eliminate the chemical term due to the formation enthalpy of species:

$$\partial_t (\rho_g h_s) + \nabla_{\mathbf{x}} \cdot (\rho_g \mathbf{u}_g h_s) = -\nabla_{\mathbf{x}} \cdot (\mathbf{q}) + \partial_t (P_g) + \mathbf{T} : \nabla_{\mathbf{x}} (\mathbf{u}_g) + \dot{\omega}_T + S^{\text{enth}}, \quad (1.7)$$

$$\mathbf{q} = -\lambda_g \nabla_{\mathbf{x}} T_g + \rho_g \sum_{k=1}^{n_s} h_k D_k \nabla_{\mathbf{x}} \cdot (Y_k). \quad (1.8)$$

where  $h_k$  is the enthalpy associated to the species  $k$ .

The final gaseous phase system of equations reads:

$$\begin{aligned} \partial_t \rho_g + \nabla_{\mathbf{x}} \cdot (\rho_g \mathbf{u}_g) &= S^{\text{fuel}}, \\ \partial_t (\rho_g Y_k) + \nabla_{\mathbf{x}} \cdot (\rho_g \mathbf{u}_g Y_k) &= \nabla_{\mathbf{x}} \cdot (\rho_g D_k \nabla_{\mathbf{x}} (Y_k)) + \dot{\omega}_k + S_k^{\text{species}}, \\ \partial_t (\rho_g \mathbf{u}_g) + \nabla_{\mathbf{x}} \cdot (\rho_g \mathbf{u}_g \otimes \mathbf{u}_g) &= -\nabla_{\mathbf{x}} (P_g) + \nabla_{\mathbf{x}} \cdot (\mathbf{T}) + S^{\text{mom}}, \\ \partial_t (\rho_g h_s) + \nabla_{\mathbf{x}} \cdot (\rho_g \mathbf{u}_g h_s) &= -\nabla_{\mathbf{x}} \cdot (\mathbf{q}) + \partial_t (P_g) + \mathbf{T} : \nabla_{\mathbf{x}} (\mathbf{u}_g) + \dot{\omega}_T + S^{\text{enth}}. \end{aligned}$$

### 1.1.2 Reference quantities and dimensionless formulation

In order to introduce the dimensionless equations, we define the reference velocity  $U_0$  and length  $L_0$  as well as physical constants for a reference physical mixture  $\rho_\infty$ ,  $\mu_\infty$ ,  $P_\infty$ ,  $C_{p,\infty}$ ,  $C_{v,\infty}$ . The dimensionless parameters read:

$$\begin{aligned} \bar{x} &= \frac{x}{L_0}, & \bar{u}_g &= \frac{u_g}{U_0}, & \bar{t} &= \frac{t}{\tau_g}, & \bar{\rho}_g &= \frac{\rho_g}{\rho_\infty}, \\ \bar{\mu}_g &= \frac{\mu_g}{\mu_\infty}, & \bar{P}_g &= \frac{P_g}{P_\infty}, & \bar{C}_{p,g} &= \frac{C_{p,g}}{C_{p,\infty}}, & \bar{C}_{v,g} &= \frac{C_{v,g}}{C_{v,\infty}}, \end{aligned} \quad (1.9)$$

where  $\tau_g = \frac{L_0}{U_0}$  is the characteristic time scale of the flow.

To derive the dimensionless equations, we define a normalization Reynolds number based on the reference quantities, as well as an another formulation for the viscosity [200]:

$$Re_0 = \frac{\rho_\infty L_0 U_0}{\mu_\infty}, \quad \mu_g^* = \frac{\bar{\mu}_g}{Re_0}. \quad (1.10)$$

In the context of this Thesis, these quantities are essential, since they will be reused to define the dimensionless quantities of the spray model.

Besides, in order to close the momentum equation, we define the reference Mach number  $M$ , and the ratio  $\gamma_\infty$  between the reference heat capacities:

$$M = \frac{U_0}{\sqrt{\gamma_\infty \frac{P_\infty}{\rho_\infty}}}, \quad \gamma_\infty = \frac{C_{p,\infty}}{C_{v,\infty}}. \quad (1.11)$$

Finally, the system is also driven by:

$$Sc_k = \frac{\mu_g}{\rho_g D_k}, \quad Pr = \frac{C_{p,g} \mu_g}{\lambda_g}, \quad Le_k = \frac{\lambda_g}{\rho_g C_{p,g} D_k}. \quad (1.12)$$

The Schmidt number  $Sc_k$  for the species  $k$ , compares the mechanical diffusivity  $\mu_g/\rho_g$  of the species to the mass diffusivity  $D_k$ , whereas the Prandtl number  $Pr$  compares the mechanical diffusivity to thermal diffusivity  $\lambda_g/\rho_g C_{p,g}$ . The mass and thermal diffusivities are compared via the Lewis number,  $Le_k = Sc_k/Pr$ . In order to obtain a simple form of the dimensionless system of equations, similar to the original one, we introduce the quantities:

$$D_k^* = \frac{\bar{\mu}_g}{\bar{\rho}_g Re_0 Sc_k}, \quad \lambda_g^* = \frac{\bar{C}_{p,g} \bar{\mu}_g}{Re_0 Pr}, \quad (1.13)$$

$$\mathbf{q}^* = -\lambda_g^* \nabla_{\bar{\mathbf{x}}} T_g + \bar{\rho}_g \sum_{k=1}^{n_s} h_k D_k^* \nabla_{\bar{\mathbf{x}}} (Y_k). \quad (1.14)$$

For the sake of simplicity, the same variables are used in the original equations and the nondimensionalized ones:

$$\begin{aligned} \partial_t \rho_g + \nabla_{\mathbf{x}} \cdot (\rho_g \mathbf{u}_g) &= S^{\text{fuel}}, \\ \partial_t (\rho_g Y_k) + \nabla_{\mathbf{x}} \cdot (\rho_g (\mathbf{u}_g Y_k)) &= \nabla_{\mathbf{x}} \cdot (\rho_g D_k^* \nabla_{\mathbf{x}} (Y_k)) + \dot{\omega}_k + S_k^{\text{species}}, \\ \partial_t (\rho_g \mathbf{u}_g) + \nabla_{\mathbf{x}} \cdot (\rho_g \mathbf{u}_g \otimes \mathbf{u}_g) &= -\frac{1}{\gamma_\infty M^2} \nabla_{\mathbf{x}} (P_g) + \nabla_{\mathbf{x}} \cdot (\mathbf{T}) + S^{\text{mom}}, \\ \partial_t (\rho_g h_s) + \nabla_{\mathbf{x}} \cdot (\rho_g \mathbf{u}_g h_s) &= -\nabla_{\mathbf{x}} \cdot (\mathbf{q}^*) + \frac{\gamma_\infty - 1}{\gamma_\infty} \partial_t (P_g) + M^2 (\gamma_\infty - 1) \mathbf{T} : \nabla_{\mathbf{x}} \cdot (\mathbf{u}_g) + \dot{\omega}_T + S^{\text{enth}}. \end{aligned} \quad (1.15)$$

## 1.2 Kinetic spray modeling

The dispersed-phase assumption for the liquid, applicable for dilute sprays with volume fraction  $\alpha$  falling within the range  $10^{-4} < \alpha < 10^{-2}$ , allows the use of the so-called ‘kinetic’ spray model. This model is based on the Williams equation, [228, 229]. Although this represents a mesoscopic level of description, it is called ‘kinetic’ by analogy with the microscopic kinetic theory of gases. Indeed, the assumptions made for the spray droplets [83], are similar to the ones made for the gas molecules when deriving the kinetic model. These assumptions are recalled here. The model describes the transport of the NDF and its evolution, due to the physical phenomena like evaporation, heat transfer or particle interactions applied to the spray, as external forces. The source terms responsible for this phase space evolution of the NDF are analyzed here. Due to the above dispersed-phase assumption, the liquid influence on the gas is obtained through source terms in the gas phase equations. The expressions for such source terms are provided in the framework of kinetic spray description.

### 1.2.1 Particle flow regimes

Within the dilute limit assumption made here, the dynamics of a gas-particle flow is ruled by two major effects. First, in the absence of gas phase, the particles behave like a granular flow. The flow can then be parameterized by the Knudsen number  $\text{Kn}$  introduced in this chapter. This number represents the importance of particle-particle collisions relative to free transport, and is the equivalent of the Knudsen number defined from the gas kinetic theory [213]. Therefore, the flow behaviour is characterized by  $\text{Kn}$  like in the gas kinetic theory. The particle flow can be considered a continuous flow as long as  $\text{Kn} \ll 1$ . In such cases, the flow can be described by the Navier-Stokes equations, or by the Euler equations for even lower Knudsen number  $\text{Kn} < 0.01$ . On the contrary, when  $\text{Kn} > 0.1$ , the rate of collisions is not significant enough to ensure that the flow is at equilibrium, i.e the velocity distribution function is Maxwellian, or at a state close to equilibrium (assumption done for the derivation of the Navier-Stokes equations). In such cases, the particle flow must be described from the Boltzmann equation by other techniques [213]. The various types of description adopted according to the values of the Knudsen is represented in Fig. (1.1).

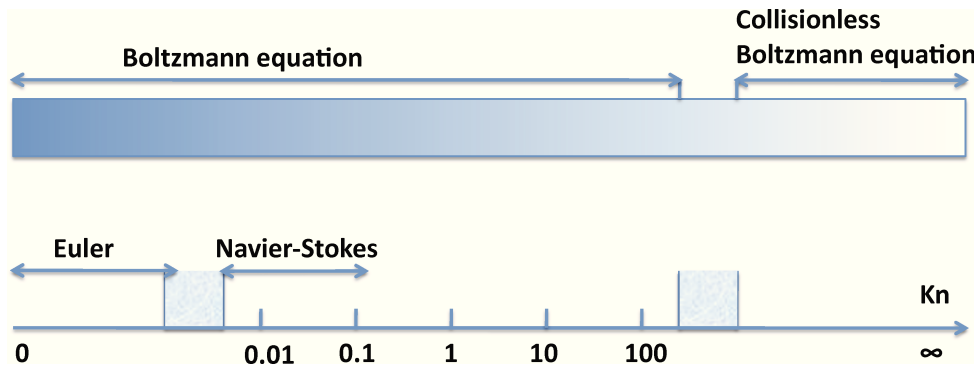


Figure 1.1: Domain of Knudsen

Secondly, adding the fluid phase introduces new physical phenomenon, and drag is the most important effect to be taken into account. It is characterized by two dimensionless numbers. For an isolated particle in a uniform fluid, the particle Reynolds number  $\text{Re}_p$  determines the net force of the fluid on the particle. The other parameter is the Stokes number  $\text{St}$  which is the ratio of the characteristic time response of the particle to the characteristic time scale of the fluid flow. If the Stokes number is small enough ( $\text{St} \ll 1$ ), the particles will have nearly the same velocity as the fluid. On the other hand, for large Stokes numbers, particles barely ‘feel’ the fluid, so that their trajectory is hardly influenced by the fluid. A precise description of particle regimes according to their Stokes number is not the objective

of this PhD. Yet we distinguish between particle having their own dynamics we call spray, and particle with a dynamics similar to the gas one we call aerosol. Although our core interest field is spray, we will show that the techniques developed in Part II, can be applied to problems where aerosol may be involved.

## 1.2.2 Williams-Boltzmann kinetic equation:framework and derivation

We present herein the framework which allows the derivation Williams “kinetic” equation for spray, see for example [228, 229].

### 1.2.2.1 Fundamental assumptions

We recall that we focus here on a dispersed liquid phase, i.e. a spray constituted of isolated droplets. We assume that the primary break-up has already occurred. Consequently, in order to simulate a full injection process in an automotive or aeronautics combustion chamber, this model needs to be coupled with a model for separated two-phase flow computing the primary break-up and giving the initial conditions of the spray, i.e., droplet sizes and velocities. These initial conditions of the spray can also be obtained by experimental results or modeled, [9]. This issue is essential in the framework of full injection computations.

In order to entirely describe the spray, we need to compute the trajectory of each particle by solving a dynamical equation. It would then be necessary to take into account all the possible interactions of the particle with the gas and with the other particles. If we consider the size and velocity evolution of one droplet, the phase space is of dimension  $N \times 2N_{\text{dim}}$  where  $N$  is the number of droplets in the spray and  $N_{\text{dim}}$  is the physical space dimension. In many applications, the order of magnitude of  $N$  is  $10^9$ , preventing to realize such computations.

We thus adopt a statistical point of view, introducing a multiple-particle joint PDF  $f_N(t, \mathbf{x}_1, \mathbf{x}_2, \dots, \mathbf{x}_n, \mathbf{u}_1, \dots, \mathbf{u}_N)$  defined from the ensemble of all realizations of the spray. We further assume droplet independence, that can be linked with the molecular chaos assumption in the kinetic theory of gases. In this framework, one has:

$$f_N(t, \mathbf{x}_1, \mathbf{x}_2, \dots, \mathbf{x}_n, \mathbf{u}_1, \dots, \mathbf{u}_N) = f_1(t, \mathbf{x}_1, \mathbf{u}_1) f_1(t, \mathbf{x}_2, \mathbf{u}_2) \dots f_1(t, \mathbf{x}_n, \mathbf{u}_n), \quad (1.16)$$

where  $f_1$  is the single-particle joint PDF. We thus only need to compute the single-particle joint PDF,  $f_1(t, \mathbf{x}_1, \mathbf{u}_1)$ . We finally define the number density function (NDF),  $f(t, \mathbf{x}, \mathbf{u})$ , as the sum over all the spray droplets of the single-particle joint PDF. We then want to solve the evolution of the NDF of the spray.

### 1.2.2.2 Williams-Boltzmann Equation

The droplets are assumed to be spherical, and are characterized by their position,  $\mathbf{x}$ , their size  $\phi$ , their velocity  $\mathbf{u}$  and their temperature  $T$ . The number density function depends on these variables and on time, the quantity  $f^\phi(t, \mathbf{x}, \phi, \mathbf{u}, T) dt d\mathbf{x} d\phi d\mathbf{u} dT$  being the probable number of droplets with, at time  $t$ , a position in  $[\mathbf{x}, \mathbf{x} + d\mathbf{x}]$ , a size in  $[\phi, \phi + d\phi]$ , a velocity in  $[\mathbf{u}, \mathbf{u} + d\mathbf{u}]$  and a temperature in  $[T, T + dT]$ . The particle size can be described either by their volume  $V$ , surface  $S$  or radius  $r$ , with the following relation:

$$f^S dS = f^r dr = f^V dV. \quad (1.17)$$

It has been shown in [145], that using the droplet surface as the variable for particle size is a good choice in the development of the multi-fluid model from the kinetic description in the framework of evaporating sprays. As explained in Chapter 4, it also proves to be a good choice for the development of the high order size moment method for the description of polydispersity. We therefore use surface  $S$  as the size variable in the following development. The number density function  $f$ , without any superscript, will then be associated to the droplet surface. The NDF function of the spray follows a transport equation, first introduced in [228], and is similar to a Boltzmann equation:

$$\partial_t f + \nabla_{\mathbf{x}} \cdot (\mathbf{u}f) + \nabla_{\mathbf{u}} \cdot (\mathbf{F}f) - \partial_S(Rf) + \partial_T(Ef) = \Gamma + Q, \quad (1.18)$$

where:

- $\partial_t f + \nabla_{\mathbf{x}} \cdot (\mathbf{u}f)$  represents the free transport of the spray;
- $\mathbf{F} = d_t(\mathbf{u})$  is the acceleration applied on droplets per unit mass;
- $R = -d_t(S)$  is the rate of change of the size  $S$  of droplets, or evaporation term;
- $E = d_t(T)$  is the rate of change of droplet temperature due to heat transfer;
- $\Gamma$  is the rate of change of distribution function  $f$  due to collisions;
- $Q$  is the rate of change of  $f$  through particle formation by secondary break-up process.

One can note the level of description of the disperse-phase kinetic model. The influence of the gas on the spray is modeled through the terms  $\mathbf{F}$ ,  $R$  and  $E$ . These terms depend on the gas temperature, velocity and composition at the position of the droplet, and therefore are dependent on space and time.

The relationship presented in Eq. (1.18) is the general formulation of the Williams-Boltzmann equation that is typically presented in the introduction of spray modeling. Nevertheless, in the context of this PhD, we focus on the following terms of Eq. (1.18): the free transport term, the external force term and the evaporation term, and potentially collision term. Isolating these effects will enable us to efficiently design numerical schemes for their resolution. Therefore, a simplified version of the Williams-Boltzmann equation is the basic kinetic equation verified by  $f(t, \mathbf{x}, S, \mathbf{u})$ , that has been studied throughout this research work:

$$\partial_t f + \nabla_{\mathbf{x}} \cdot (\mathbf{u}f) + \nabla_{\mathbf{x}} \cdot (\mathbf{F}f) - \partial_S(Rf) = \Gamma. \quad (1.19)$$

It is important to remember that this simplified framework is not due to a limitation of the proposed models. It is instead a critical step in the design of efficient Eulerian methods for spray resolution. Contrary to initial impressions of simplicity that one may harbour, these terms are the most challenging ones to solve when using high order moment methods. Indeed, recent publications point out intrinsic difficulties for the description of polydispersity through evaporation [85], and for the description of particle trajectory crossing (PTC) [84]. With high order moment method, models for collision and coalescence have been designed and proven to be very satisfactory [87, 147, 85]. The term of heat transfer, written with the same formalism as the evaporation term, can be solved with the tools explained in Chapter 5.

### 1.2.3 Spray equation closure

The evolution of the spray NDF in the phase space  $(S, \mathbf{u})$  is considered here. The terms in the spray equation leading to this evolution and representing physical phenomena are based on classical models for isolated droplets. The droplet models compatible with the kinetic description of the spray are provided here.

#### 1.2.3.1 Drag Force

Among all the terms contained in the term of force applied by unit mass  $\mathbf{F}$  (gravity and buoyancy effects, drag force, virtual mass effect, Basset force, lift force) described in [49], we will focus on the drag term  $\mathbf{D}_r$ . Indeed, as shown in [69], in a gas-liquid flow, where  $\rho_g/\rho_l$  is of the order of  $10^{-2}$  down to  $10^{-3}$ , the only external forces that need to be accounted for are drag force and gravity. Furthermore, in order to work in a simple modeling framework, we neglect gravity in the studies presented in this work.

The general expression for the drag force is given by [193, 208]:

$$\mathbf{D}_r = \frac{1}{8} \rho_g C_D S (\mathbf{u}_g - \mathbf{u}) \|\mathbf{u}_g - \mathbf{u}\|, \quad (1.20)$$

where  $C_D$  is the drag coefficient. This coefficient depends on the particle shape as well as on the flow parameters such as Reynolds number, Mach number, turbulence, etc. In the kinetic model we assume

that the particles are spherical, and we focus only on the variation of  $C_D$  with the Reynolds number based on the relative velocity:

$$\text{Re}_p = \frac{\rho_g S^{1/2} \|\mathbf{u}_g - \mathbf{u}\|}{\sqrt{\pi} \mu_g}. \quad (1.21)$$

Two flow regimes can be considered: first the Stokes flow regime where the drag coefficient varies inversely with Reynolds number, for  $\text{Re}_p < 1000$ ; second the inertial range regime where the drag coefficient approaches a nearly constant value, see [44] for details. Within the Stokes regime, for low relative velocity ( $\text{Re}_p < 1$ ), the drag coefficient is given by the Stokes law, proposed by C.G. Stokes in 1851:

$$C_D = \frac{24}{\text{Re}_p}, \quad \text{Re}_p < 1. \quad (1.22)$$

Two more regimes are identified:

$$\begin{aligned} C_D &= \frac{24}{\text{Re}_p} \left(1 + \frac{\text{Re}_p^{2/3}}{6}\right), & \text{Re}_p < 1000, \\ C_D &= 0.45, & 1000 < \text{Re}_p < 3.5 \cdot 10^5. \end{aligned} \quad (1.23)$$

In the case of a Stokes law, the drag force term can be written:

$$\mathbf{D}_r = m_p \frac{18 \pi \mu_g}{\rho_l S} (\mathbf{u}_g - \mathbf{u}) = m_p \frac{(\mathbf{u}_g - \mathbf{u})}{\tau_p}, \quad (1.24)$$

where

$$\tau_p = \frac{\rho_l S}{18 \pi \mu_g} \quad (1.25)$$

is the velocity response time. The variable  $\tau_p(S)$  represents the time required for a droplet of size  $S$  to respond to a change in gas velocity.

### 1.2.3.2 Evaporation term

We present here the closure considered to obtain the size evolution rate.

$$[\dot{m}_p]_s = -d_t \left( \frac{\rho_l S^{3/2}}{6 \sqrt{\pi}} \right) = -\rho_l \frac{S^{1/2}}{4 \sqrt{\pi}} d_t S = \rho_l \frac{S^{1/2}}{4 \sqrt{\pi}} R. \quad (1.26)$$

We neglect, in Eq. (1.26), the dilatation of the droplet, so that  $\rho_l$  is constant. Therefore, we need to compute the vapor mass flux to obtain the  $R$  expression.

In the limit of no chemical reaction,  $R$  reads [208]:

$$R = 4\pi \frac{\rho_g}{\rho_l} Sh_c D_{y_F} \ln(1 + Bm), \quad (1.27)$$

where  $Bm$  is the Spalding mass transfer number,  $Sh_c$  is the convective Sherwood number and  $D_{y_F}$  is the Fick's law binary coefficient. The definition of these terms as well as the demonstration of this result can be found in [49]. In the context of this PhD, a constant droplet-temperature model is chosen, since droplet heating is not considered. If this model is considered without taking convective corrections into account, it leads to the  $D^2$  law [97, 210], where the square of the droplet diameter  $D$  has a linear regression in time:

$$d_t(D^2) = -\xi. \quad (1.28)$$

The coefficient  $\xi$  does not depend on the droplet diameter, but depends on local gas conditions. The absence of relative velocity yields  $Sh_c = 2$ . The rate of change of size  $R$  is thus given by:

$$R = 8\pi \frac{\rho_g}{\rho_l} D_{y_F} \ln(1 + Bm). \quad (1.29)$$

More details about this law can be found in [49].

### 1.2.3.3 Collisions

Collision kinetic modeling for spray is detailed in [225, 144]. Its derivation is similar to Boltzmann equation derivation for rarefied gases, see [34, 35]. We assume binary collisions, that is verified if the spray is moderately dense. As mentioned in Section 1.2.2, these collisions will be used only in one case study, in Section 9.1.1 to show that the high order velocity moment method applies to a particle flow experiencing collisions. In this work, we will assume that the collision term is closed. For example, using the Bhatnagar-Gross-Krook (BGK) approximation [15], the collision term becomes:

$$\Gamma = \frac{1}{\tau_c}(f_{eq} - f), \quad (1.30)$$

where  $\tau_c$  is the characteristic collision time of the droplet flow, and  $f_{eq}$  the equilibrium distribution function.

### 1.2.4 Non-dimensional formulation

In order to obtain the liquid source terms for the dimensionless gas system in Eq. (1.15), we present the main elements used in deriving the liquid dimensionless formulation, focusing on the  $\mathbf{D}_r$  and  $R$  coefficients, given in Eq. (1.24) and Eq. (1.29) respectively. The liquid dimensionless formulation is driven by the gas phase one and thus we use the same reference quantities, see Section 1.1.2. Given the presence of particles, we also introduce a reference size  $S_0$  for the droplet size variable and then a dimensionless surface  $\bar{S} = S/S_0$ , and a reference droplet density  $n_0 = N_0/L_0^{N_{\text{dim}}}$ , for a physical space with  $N_{\text{dim}}$  dimensions. Thus, in addition to the gas characteristic time  $\tau_g$ , another reference time can be defined:

$$\tau_{drop} = \frac{S_0}{L_0 U_0}. \quad (1.31)$$

A dimensionless number  $R_{drop-gas}$  can then be defined:

$$R_{drop-gas} = \frac{\tau_{drop}}{\tau_g} = \frac{S_0}{L_0^2}, \quad (1.32)$$

that will naturally arise in the dimensionless droplet terms, due to the cohabitation of these gas and liquid reference quantities. In this framework, the dimensionless number density function  $\bar{f}$  can be written, for a  $N_{\text{dim}}$ -space dimension domain:

$$\bar{f}(\bar{t}, \bar{\mathbf{x}}, \bar{S}, \bar{\mathbf{u}}) = f(t, \mathbf{x}, S, \mathbf{u}) \frac{U_0^{N_{\text{dim}}} S_0}{n_0}. \quad (1.33)$$

The dimensionless formulation for the coefficients  $\mathbf{D}_r$  and  $R$  is obtained as described below:

$$\begin{aligned} \overline{\mathbf{D}_r} &= \frac{L_0}{U_0^2} \mathbf{D}_r, \\ K &= \frac{L_0}{U_0 S_0} R. \end{aligned} \quad (1.34)$$

We finally obtain the following forms:

$$\begin{aligned} \overline{\mathbf{D}_r} &= \frac{\overline{\mathbf{u}_g} - \bar{\mathbf{u}}}{\text{St}}, \\ K &= \frac{1}{R_{drop-gas}} 4\pi \frac{\rho_g}{\rho_l} Sh_c D_{yF}^* \ln(1 + Bm), \end{aligned} \quad (1.35)$$

The Stokes number, introduced in Section 1.2.1 occurs in the dimensionless drag term and reads:

$$\text{St} = \frac{\overline{\rho_l} \bar{S}}{18\pi\mu_g^* L_0^2} = \frac{\tau_p}{\tau_g}, \quad (1.36)$$



and characterizes the influence of the gaz of particles in terms of drag force. The expressions of  $\mu^*$  and  $D_{y_F}^*$  are given in Eq. (1.10) and Eq. (1.13), respectively.

For collisions, the collision operator writes, in dimensionless formulation:

$$\bar{\Gamma} = \frac{\overline{f_{eq}} - \bar{f}}{\text{Kn}}, \quad (1.37)$$

where the Knudsen number  $\text{Kn}$ , also introduced in Section 1.2.1 occurs and reads:

$$\text{Kn} = \frac{\tau_c}{\tau_g}. \quad (1.38)$$

It characterizes the rate of collision occurring in the particle flow relative to the gas dynamics.

### 1.2.5 Extension to aerosols

As mentioned in Section 1.2.1, we will show that the methods designed in Part II can be applied to the case of aerosol. It corresponds to particles with a Stokes number close to zero,  $\text{St} \rightarrow 0$ , so that their trajectory are influenced by the small scale fluctuations of the Brownian motion. As a result, the kinetic equation satisfied by the NDF is slightly different from the Williams-Boltzmann equation and contains a new term representing the effects of the Brownian motion, which creates dispersion in the velocity distribution function. This kinetic equation is called the Fokker-Planck equation, and reads:

$$\partial_t f + \nabla_{\mathbf{x}} \cdot (\mathbf{u}f) - \partial_S(Rf) = \frac{1}{\tau_p} \nabla_{\mathbf{u}} \cdot [(\mathbf{u} - \mathbf{u}_g)f + \tau_p \mathbf{Q} \nabla_{\mathbf{u}} f]. \quad (1.39)$$

The left-hand side is similar to the Williams-Boltzmann equation with transport in physical space and evaporation. The first term of the right-hand side corresponds to the classical Stokes drag. The second term of the right-hand side represents the effect of Brownian motion on the droplets.  $\mathbf{Q}$  is the matrix of the temporal correlation of forces due to Brownian motion. If  $\mathbf{F} = (F_1, F_2, F_3)^t$  is the force due to Brownian motion in three dimensions, then  $Q_{ij}(t) = \int_0^\infty F_i(t)F_j(t+\tau) d\tau$ . Its dimensionless expression writes :  $\sigma = \frac{\mathbf{Q}\tau_p}{U_0^2}$ .

As it is classical in statistical physics, a Langevin equation can be associated to the previous Fokker-Planck equation, which in the “viscous limit” or for large times compared to  $\tau_p$  when the inertial term in the equation of motion can be disregarded, reduces to a spatial diffusion as studied in the original works of Einstein and Smoluchowski [38]. Since we rather work with NDF and consider the equation (1.39) as the fundamental model of our particles/droplets, we will obtain the spatially diffusive regime as a singular perturbation using a Chapman-Enskog type of expansion. For the sake of clarity, let us thus rewrite Eq. (1.39) as :

$$\partial_t f + \nabla_{\mathbf{x}} \cdot (\mathbf{u}f) - \partial_S(Kf) = \frac{1}{\epsilon} \mathcal{J}(f), \quad \mathcal{J}(f) = \nabla_{\mathbf{u}} \cdot [(\mathbf{u} - \mathbf{u}_g)f + \sigma \nabla_{\mathbf{u}} f], \quad (1.40)$$

where we wrote  $\text{St} = \epsilon$ , and dropped the evaporation term as it does not play any role in this development. The differential operator  $\mathcal{J}$  appears to be a singular perturbation for Eq. (A.1) in the case  $\epsilon \rightarrow 0$ . The NDF is solved in this case using a Chapman-Enskog development (see classical references of kinetic theory of gases [100, 79, 42, 213]), that is to say that  $f$  is decomposed into powers of  $\epsilon$ . This development can be found in Appendix A in one-dimensional case. This development performed up to the first order of the parameter  $\epsilon$  leads to the following equation called the Schmoluchovski equation [89].

$$\partial_t \rho_p + \nabla_{\mathbf{x}} \cdot (\rho_p \mathbf{u}_g) - \partial_S(K \rho_p) = \epsilon \nabla_{\mathbf{x}} \cdot (\sigma \nabla_{\mathbf{x}} \rho_p + \rho_p D_t \mathbf{u}_g), \quad D_t = \partial_t + \mathbf{u}_g \cdot \nabla_{\mathbf{x}}. \quad (1.41)$$

where the flux at first order in  $\epsilon$  delivers a diffusion term as well as an acceleration term which can be related to a normalized pressure gradient in the framework of an incompressible flow for the gaseous

phase and which will not be considered in the following for the sake of clarity of the exposition. This allows us to write the following equation on the total number density conditioned on size,  $\rho_p(t, x, S)$ , called the Smoluchowski equation [89, 38]:

$$\partial_t \rho_p + \nabla_{\mathbf{x}} \cdot (\rho_p \mathbf{u}_g) - \partial_S (K \rho_p) = \epsilon \nabla_{\mathbf{x}} \cdot (\sigma \nabla_{\mathbf{x}} \rho_p), \quad (1.42)$$

which is valid for large time scales compared to  $\tau_p$ .

In the context of this PhD, we show that the numerical tools designed for evaporation and transport can be applied to solve the left-hand side of Eq.(1.41). Therefore, we will consider this part of the equation and the acceleration and diffusion terms can be further solved in the context of of an operator splitting algorithm. The equation considered here is then:

$$\partial_t \rho_p + \partial_x (\rho_p u_g) - \partial_S (K \rho_p) = 0. \quad (1.43)$$

## 1.3 Gas/liquid coupling: flow regime characterization

### 1.3.1 Source terms for the gas phase

The kinetic spray modeling derived above, allows computation of the source terms arising in the gaseous equations, Eq.(1.9), accounting for the influence of the dispersed liquid phase on the carrier gaseous phase. These terms represent the variation of mass density, for the mixture and for individual species, due to spray vaporization; the variation of momentum of the spray, due to spray vaporization and to external forces; and finally the variation of enthalpy per unit mass, due to spray vaporization and heat transfer.

$$\begin{aligned} S^{\text{fuel}} &= \iiint \rho_l R d_S(V) f dS d\mathbf{u} dT, \\ S_k^{\text{species}} &= \iiint \Omega_k^{\text{surf}} \rho_l R d_S(V) f dS d\mathbf{u} dT, \\ S^{\text{mom}} &= \iiint \rho_l \mathbf{u} R d_S(V) f dS d\mathbf{u} dT + \iiint \rho_l V \mathbf{F} f dS d\mathbf{u} dT, \\ S^{\text{enth}} &= \iiint \rho_l C_{p,l} T R d_S(V) f dS d\mathbf{u} dT + \iiint \rho_l V C_{p,l} E f dS d\mathbf{u} dT, \end{aligned} \quad (1.44)$$

where  $V(S) = S^{3/2}/(6\sqrt{\pi})$  is the volume corresponding to the size  $S$ . Moreover,  $\Omega_k^{\text{surf}}$  is the flux fraction for species  $k$ , from liquid surface to gas. In our study the droplets are mono-component, thus  $\Omega_k^{\text{surf}} = 0$  or  $\Omega_k^{\text{surf}} = 1$ . One has to note that to obtain the expression  $S^{\text{enth}}$ , we assume that no reaction is happening at the droplet surface. We therefore consider that droplets evaporate before burning [49].

The two-way coupling is illustrated here, the gas influence over the spray resulting in  $\mathbf{F}$  and  $R$  coefficients, depending on both gas and liquid local properties. The influence of the spray over the gas is taken into account by the source terms of Eq.(1.44).

### 1.3.2 One-way coupling

Taking into account two-way effects, i.e. influence of the spray on the gaseous carrier phase, may be of great importance for several application fields. Indeed if, e.g. the spray is dense, it may significantly modify the mass and momentum of the gas. For combustion applications, two-way coupling is necessary in order to take into account the vaporization of the droplets into the gaseous phase before burning. Nevertheless, we restrict ourselves in this study to one-way coupling. Indeed in this work our objective is to evaluate various levels of description of spray derived from the kinetic modeling, and to show the

feasibility of the corresponding models. This evaluation aims at precisely characterizing the methods, their derivation from a given kinetic model, and the numerical scheme used. Two-way effects, as well as droplet models, are done at the kinetic level of description, and the evaluation of their efficiency to reproduce a complex physics is out of the scope of this study. Furthermore, analyzing and understanding the difficulties related to the spray resolution method itself is a necessary first step in the evaluation of the whole two-phase flow description.

This evaluation will be done through comparisons with the Eulerian multi-fluid model, derived from the same kinetic model. In the case of the multi-fluid method, its efficiency has been validated in [49], and is taken as a reference. Accomodating two-way coupling will introduce a bias resulting from the difficulties in coupling Eulerian and Lagrangian descriptions. Furthermore, the comparison of two-way effects modeling in Lagrangian and Eulerian descriptions can take advantage of the present study in order to focus only on coupling effects.

Finally, the important point we wish to reiterate is that this restriction is definitely not related to any limitation of the proposed models, wherein a two way coupling can be accounted, see [170, 144, 148]. This restriction is purely imposed, by the deliberate focus on developing a simple framework for precise model characterization.

### 1.3.3 Range of particulate flow studied

As shown in Section 1.2.4, the range of particulate flows studied are characterized by their Stokes and Knudsen numbers. We detail below the types of flow targeted in the context of this PhD thesis. First, the entire ranges of Stokes numbers are addressed.

- The models dedicated to describe spray polydispersity, i.e the multi-fluid model presented in Chapter 3, and the EMSM model designed in during this PhD and presented in Chapters 4, 5 and 6, rely on a monokinetic assumption for the velocity distribution function, see Chapter 2. Accordingly, they are intended to describe low St number flow  $St \ll 1$ . However, in Chapter 3, it is proven that, thanks to the properties of the numerical scheme used for physical transport, these models can be extended to the case of higher Stokes number. The singularities engendered by the monokinetic assumption are proven to be well captured by the numerical schemes, and comparisons with Lagrangian simulation and experimental results are highly satisfactory even for moderate Stokes numbers, [49].
- Entire range of Stokes numbers are addressed in the high order velocity moment method (Chapters 9 and 10), which aims at overcoming the monokinetic assumption and at simulating particle trajectory crossing (PTC).

When it comes to the range of Knudsen numbers:

- High Knudsen numbers will almost always be considered, in order to justify the no collisions assumption. Therefore, by default and unless the opposite is stated, collision-less flow is considered. However it must be emphasized that this is not dictated by any limitation of the models. This is primarily because we choose to work in the framework containing the critical processes (i.e evaporation, physical transport, and to a smaller extend drag) for which the breakthroughs brought by our models are assessed.
- The primary interest of the EMVM model is to simulate high Knudsen flows where the equilibrium assumption cannot be done. However, all types of Knudsen flow can be simulated in the context of this model. The purpose of Section 9.1 is to demonstrate that the collision term can be solved, by solving a term that is closed by the BGK model.

## Chapter 2

# Overview of the resolution strategies for spray dynamics

This chapter discusses the choice of the resolution method for the spray among different available strategies. A natural choice for spray resolution method is a Lagrangian method where we track particles in the flow, considered as representing physical droplets. Moreover, we introduced in Chapter 1 the kinetic description of spray. Other Lagrangian methods consist then in tracking statistical particles in connection with Eq. (1.19). This widely used Lagrangian approach has proven its great efficiency to simulate complete spray dynamics without introducing any numerical diffusion, [71, 193, 6, 201, 179, 204]. However, given the encountered limitations of Lagrangian methods in terms of physics and computing discussed here, Eulerian spray descriptions represent an interesting complementary tool, given its easier coupling with the gas phase description, and its easier optimization through parallel computing, making it an interesting choice for High Performance Computing (HPC) [19, 141]. We summarize here the main Lagrangian approaches, highlighting their level of modeling in order to study their connection with the kinetic level of description. We then present the main derivation strategies leading to Eulerian moment approaches, along with the associated assumptions. We distinguish between methods explicitly presuming the profile of the size distribution and quadrature methods. Within this first class of methods, for which the literature is the most abundant, two families of models are isolated, relative to their treatment of the size variable. The first performs a discretization of the size phase space with Finite Volume procedures. On the contrary, the second family keeps the size variable continuous. The spray computations presented in this work are done in the context of Direct Numerical Simulation (DNS), and thus coupled to a DNS of the gas phase.

## 2.1 Lagrangian methods

We propose in this section to first go through the main approaches of spray Lagrangian particular descriptions, highlighting the associated level of descriptions and their link for non-collisional spray, i.e in the infinite Knudsen number. We study here DNS framework, all the scales of the gas flow are thus resolved. When considering a modeled turbulent carrier phase, extra effort has to be done to describe particle turbulent dispersion. We do not tackle this issue in this work as we focus on DNS, and we refer to [47] for a review of the turbulent dispersion modeling approaches. Finally, we point out the limitations of such methods.

### 2.1.1 Description of Lagrangian techniques

The first Lagrangian method associated to the mesoscopic dispersed-phase description is the Discrete Particle Simulation (DPS). In this framework, each Lagrangian numerical particle represents a physical droplet. A system of ODE is thus solved to obtain the evolution of the droplet parameters, size and velocity for the  $k^{th}$  droplet. This approach, called a two-phase DNS, has been introduced in [203]. Most

of the first numerical studies were dedicated to solid particle dispersion, [211, 73]. The extension to evaporating droplets in turbulent flows has been provided in [165, 201, 179], and has been used in combustion applications in [164, 202, 180]. This method, is mainly used in DNS configuration, where all the droplets contained in the physical domain can be tracked.

The second approach is a statistical approach, where numerical particles are different from physical droplets. The statistical Lagrangian description can be used in two different contexts.

- First it can be used instead of a DPS method in a configuration where the high number of physical droplets prevents to use one numerical particle for each droplet, given the high computational cost associated. In this framework, the numerical particle, also called parcel, represent several physical droplets. This description has been introduced for fuel spray in [193], extending the work of [71]. This method is referred in [47] as the discrete element method, and as a multicontinua method in [208], where the parcels are defined as classes of droplets. The computational cost of this method is obviously linked to the chosen number of tracked parcels. The cost of the method is thus well controlled, and it is therefore broadly used to compute industrial configurations. This method is implemented for instance in the KIVA code, [6], and is used in many industrial computational codes at present. We refer to this method in this work as Stochastic Parcel (SP) method, as done in [193].
- On the other hand, the statistical Lagrangian method can be seen as a resolution method of the Williams kinetic equation. This approach is called Direct Simulation Monte-Carlo method (DSMC), and is originally introduced in [16] for rarefied gas. This approach aims at describing the evolution of the spray NDF moments, and thus a high number of statistical particles are needed to obtain a converged solution. In this case, several numerical particles may be needed to represent one physical droplet. The numerical particle has a weight associated, adapted to the needed refinement. This method provides directly the ensemble average, in terms of initial condition, and then the reconstructed Eulerian fields correspond to the same level of information than the one provided by a Eulerian method.

In cases without collision, the difference between the two methods, is only the level of refinements provided. Indeed, the convergence expected in the DSMC method demands a high number of statistical particles, leading to a higher refinement level than in DPS. On the contrary, the SP method aims at coarsening the DPS description. The number of statistical parcels is thus set by the computational cost limitation, without drawing any links with kinetic level of description.

### 2.1.2 Lagrangian limitations, need and challenges for Eulerian methods

At present, Lagrangian methods are widely used for the disperse-phase simulation since they combine an easy modeling of the phase polydispersity, a high numerical efficiency, not introducing numerical diffusion, and an easiness of implementation. Nevertheless, they suffer from some shortcomings, in terms of modeling and computing.

The first type of problems, when using Lagrangian methods, is the coupling between the Lagrangian particles and the Eulerian description of the gaseous phase. Moreover, with the solver Eulerian Lagrangian Spray Atomization (ELSA) [54], but also with the project of IFP Energies nouvelles, efforts are done toward the simulation of a whole injection process. This requires a spray model for the description of the droplet population that occurs after the atomization processes. This requires also a separate two-fluid model like the models presented in Part V for the description of the separate-phase area close to the injector. These models are based on an Eulerian approach, and again rise the issue of coupling with a Lagrangian approach for the disperse-phase. Yet, if not impossible, this coupling could be done *a priori* much easier if one considers an Eulerian approach for the disperse-phase also. Furthermore, in the framework of domain decomposition for parallel computations, Lagrangian approaches need the use of complex and costly dynamic partitioning methods, in order to ensure a good load balancing between the numerous parallel processes. One can nevertheless highlight recent advances in this field [92].

Eulerian methods for disperse-phase modeling, derived from the kinetic model exposed in Chapter 1,

provide thus a very promising complementary tool to Lagrangian methods, since they can easily be coupled with the gas phase and their coupling with a Eulerian two-fluid method for separate-phase modeling is much more conceivable than for a Lagrangian method. Moreover, Eulerian methods are well-suited for massively parallel computations.

But if Eulerian models appear to be a potential answer to the shortages of Lagrangian methods, they nevertheless face two major stumbling blocks, in comparison with Lagrangian methods. The first one lies in the description of polydispersity, which is naturally done by Lagrangian methods, but far from being plain-sailing in an Eulerian framework, since its cost may be prohibitive, even with parallel computations capabilities. The second obstacle lies in the ability to describe particle trajectory crossing (PTC) in the case of high Knudsen numbers. This is also naturally done by Lagrangian methods, but is a serious issue for Eulerian methods, since the classical methods locally considers only a the mean particle velocity (a monomodal velocity distribution) and do not account for multi-modal velocity distribution. It is at the price of the resolution of these two obstacles that Eulerian methods for spray can become a serious alternative to Lagrangian methods.

## 2.2 Eulerian resolution methods

The alternative to Lagrangian particle tracking is the resolution of spray Eulerian global quantities, as number or mass density, momentum. These Eulerian methods can be seen as moment methods derived from the kinetic equation Eq.(1.19). We propose to present here the main derivation strategies and resulting methods in the framework of spray. We highlight in this presentation the key issues of Eulerian spray modeling in combustion context, that are velocity and size distribution description. Indeed these two issues condition the ability of Eulerian methods to describe polydispersion and out-of-equilibrium velocity distribution, i.e, droplet trajectory crossing description. The derivation strategies are presented in a laminar framework, in order to highlight the key points of the moment equation derivation, without introducing extra modeling complexity. We then discuss the extension to turbulent flows.

### 2.2.1 Derivation strategies for a DNS resolution

The full resolution with finite volume of the kinetic equation, Eq.(1.19), named by O'Rourke the full spray equation method [193], can difficultly be used given its cost related to the high number of phase space dimensions. Indeed in a 3-D case, the phase space is of dimension seven (3 for space, 3 for velocity, 1 for size). Nevertheless, in many cases the knowledge of the full kinetic description of the spray is not needed, and it is sufficient to know the evolution of global quantities, the NDF moments. For a given function  $\psi(y)$ , the  $k^{th}$  order moment  $m_k$  is defined by:

$$m_k = \int_y y^k \psi(y) dy. \quad (2.1)$$

Therefore, for the NDF we introduce the moment  $\mathcal{M}$ :

$$\mathcal{M}_{k,l,m,n} = \int_S \int_{\mathbf{u}} S^k u_x^l u_y^m u_z^n dS d\mathbf{u} \quad (2.2)$$

of order  $k$  in size,  $(l, m, n)$  for each component of the velocity, respectively.

The evolution of these spray global quantities can therefore be derived from the Williams kinetic equation Eq.(1.19), in the following way:

$$\int_S \int_{\mathbf{u}} \text{Eq.(1.19)} S^k u_x^l u_y^m u_z^n dS d\mathbf{u}. \quad (2.3)$$

Nevertheless, one has to notice that the moment equation derivation leads to a loss of information and that, without any peculiar assumption, the system of equations for moments is not closed, even if the kinetic model was. Indeed, some quantities can not be expressed in function of the set of moments resolved; for example with regard to velocity moments, the equation for the  $p^{th}$  order moment (with

$p = l + m + n$ ) introduces the moments of order  $p + 1$ . Therefore taking one first order moment  $\mathcal{M}_{0,1,0,0}$  introduces the second order moments  $\mathcal{M}_{0,2,0,0}, \mathcal{M}_{0,1,1,0}, \mathcal{M}_{0,1,0,1}$ . Assumptions have then to be done on the form of the NDF to close the moment evolution system. For most of the spray Eulerian methods, the derivation of the moment system, along with its associated closures can be divided into two steps. First a form for the NDF in velocity is presumed for each fixed size, leading to the derivation of an intermediate closed system of conservation laws, the semi-kinetic system. The second step is devoted to the size-phase space treatment, and there exist several methods introducing different types of conservation law systems and closures. However, we can also find methods using a one step moment equations derivation with quadrature-based approximations of the NDF, obtaining the unclosed moments by quadrature formula. These two classes of methods are shown in Fig. (2.1).

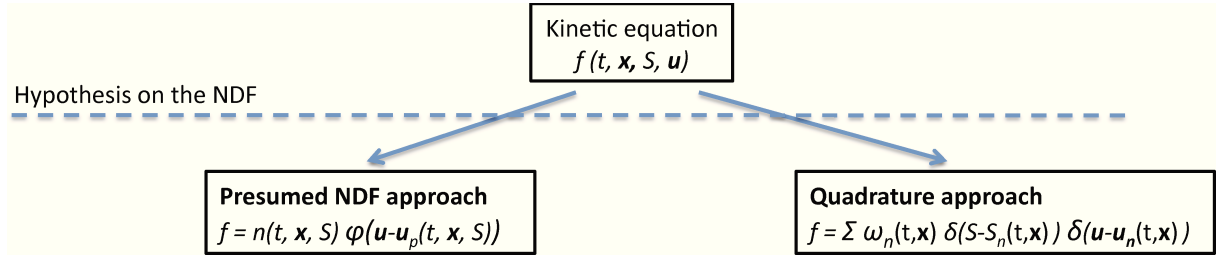


Figure 2.1: Two classes of Eulerian models derived from the kinetic equation.

### 2.2.2 Presuming NDF profile

For modeling purposes, the basis of several Eulerian spray resolution methods is to presume the form of the velocity distribution at the kinetic level. Two levels of assumptions are done. The first assumption is that the velocity distribution profile is independent from the size variable. The NDF can thus be written:

$$f(t, \mathbf{x}, S, \mathbf{u}) = n(t, \mathbf{x}, S) \phi(\mathbf{u} - \mathbf{u}_p(t, \mathbf{x}, S)), \quad \int_{\mathbb{R}} \phi(\mathbf{u}) d\mathbf{u} = 1, \quad (2.4)$$

where  $\mathbf{u}_p$  is the mean velocity, conditioned by size. One has to notice that at this level, the model is still size-conditioned, i.e., the mean values depend on the size of the droplets. From this approximation, we can derive a system of moment equations for the spray taking the moments in velocity of order zero:  $\mathcal{M}_{0,0,0,0} = n$ , and one:  $\mathcal{M}_{0,1,0,0} = n u_x$ ,  $\mathcal{M}_{0,0,1,0} = n u_y$  and  $\mathcal{M}_{0,0,0,1} = n u_z$  in the following way:

$$\begin{aligned} \int_{\mathbf{u}} \text{Eq.(1.19)} d\mathbf{u}, \\ \int_{\mathbf{u}} \mathbf{u} \text{Eq.(1.19)} d\mathbf{u}. \end{aligned} \quad (2.5)$$

It gives the following semi-kinetic system:

$$\begin{aligned} \partial_t n + \nabla_{\mathbf{x}} \cdot (n \mathbf{u}_p) &= \partial_S (n \tilde{R}), \\ \partial_t (n \mathbf{u}_p) + \nabla_{\mathbf{x}} \cdot (n \mathbf{u}_p \otimes \mathbf{u}_p + \mathbf{P}) &= \partial_S (n \tilde{R} \mathbf{u}_p) + n \tilde{D}_r, \end{aligned} \quad (2.6)$$

where the notation  $(\tilde{\cdot})$ , defines the mean quantities:

$$\tilde{g}(t, \mathbf{x}, S) = \int_{\mathbf{u}} g(t, \mathbf{x}, S, \mathbf{u}) \phi(\mathbf{u} - \mathbf{u}_p(t, \mathbf{x}, S)) d\mathbf{u}, \quad (2.7)$$

$\mathbf{P}$  is a tensor equivalent to a pressure term, describing the velocity dispersion of the droplets:

$$\mathbf{P} = \int_{\mathbf{u}} n \phi(\mathbf{u} - \mathbf{u}_p) (\mathbf{u} - \mathbf{u}_p) \otimes (\mathbf{u} - \mathbf{u}_p) d\mathbf{u}. \quad (2.8)$$

In the DNS framework, the function  $\phi$  is taken as a Dirac delta-function:

$$f(t, \mathbf{x}, S, \mathbf{u}) = n(t, \mathbf{x}, S) \delta(\mathbf{u} - \mathbf{u}_p(t, \mathbf{u}, S)). \quad (2.9)$$

In this context, there is no velocity dispersion around the mean value and  $\mathbf{P} = 0$ . Furthermore, the quantities  $(\cdot)$  are the point-wise values of the functions at  $\mathbf{u} = \mathbf{u}_p$ :

$$\tilde{R} = R(\mathbf{u}_p) = R_p, \quad \tilde{D}_r = D_r(\mathbf{u}_p) = D_{r,p}. \quad (2.10)$$

Once a closure has been established for the velocity distribution, two types of approaches exist for the resolution of the size variable, see Fig. (2.2).

- The size phase space is discretized into small intervals or samples wherein the size NDF  $n$  is presumed. In this case, only one moment per section, corresponding to droplet mass, is solved
- The size variable is kept continuous. In that case, several size moments are solved, and the size NDF, for which the profile may be presumed, is reconstructed from the data of the moments.

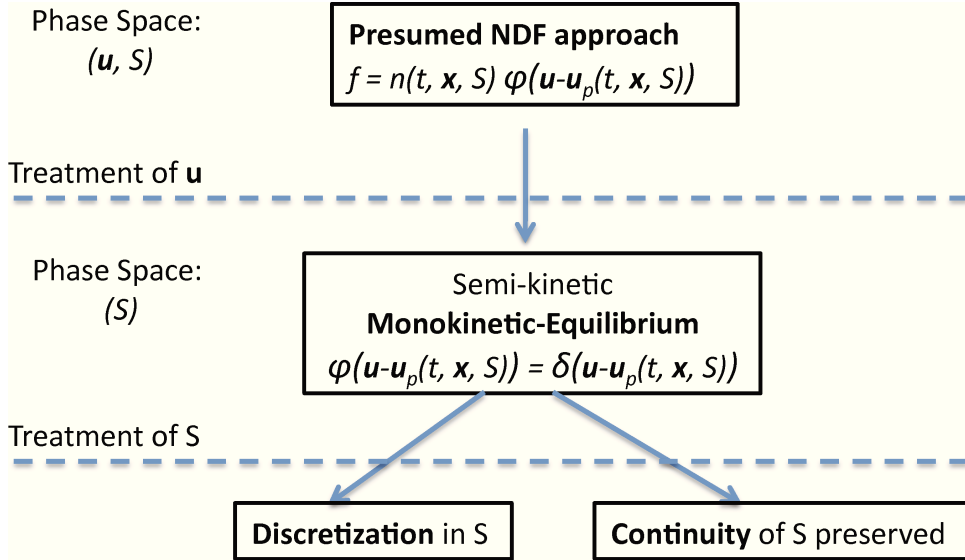


Figure 2.2: Resolution methods for the treatment of the size phase space

### 2.2.2.1 Size discretization

**Two-fluid model** The two-fluid model, for dispersed liquid case framework, is based on a presumed PDF in velocity. It must be taken great care of the fact that this two-fluid model is fundamentally different from the two-fluid model for the separate-phase, presented in Chapter 15 and Chapter 16. Indeed, disperse-phase two-fluid models are dedicated to dilute and disperse droplet flow, whereas separate-phase ones do not assume the topology of the liquid phase flow. This model is studied in [65, 187]. It can be derived from the semi-kinetic model, realizing an integration over the whole size phase space, see Fig. (2.3)

$$\int_S \text{Eq. (2.6)} dS, \quad (2.11)$$

assuming [69]:

$$n(t, \mathbf{x}, S) = n(t, \mathbf{x}) \delta(S - S_p(t, \mathbf{x})). \quad (2.12)$$



It gives the following evolution for the number and the mass density, as well as the momentum:

$$\begin{aligned}\partial_t n + \nabla_{\mathbf{x}} \cdot (n \mathbf{u}_p) &= 0, \\ \partial_t (\alpha \rho_l) + \nabla_{\mathbf{x}} \cdot (\alpha \rho_l \mathbf{u}_p) &= -\dot{m}_p, \\ \partial_t (\alpha \rho_l \mathbf{u}_p) + \nabla_{\mathbf{x}} \cdot (\alpha \rho_l \mathbf{u}_p \otimes \mathbf{u}_p) &= -\frac{1}{St} \alpha \rho_l (\mathbf{u}_p - \mathbf{u}_g) - \dot{m}_p \mathbf{u}_p,\end{aligned}$$

where  $\alpha$  is the liquid volume fraction and  $\dot{m}_p$  is the mass flux due to evaporation. In this framework, a mean size can be defined for the droplets by the following formula:

$$r = \left( \frac{3\alpha}{4\pi n} \right)^{1/3}. \quad (2.13)$$

Nevertheless, the information on the size distribution and on the size-velocity correlation is lost in this derivation. Closures are thus needed for the terms  $\dot{m}_p$ ,  $\alpha$ . In this framework, the droplet interaction terms, needed to account for secondary breakup, collisions and coalescence, cannot be included directly but can only be treated by rough approximations.

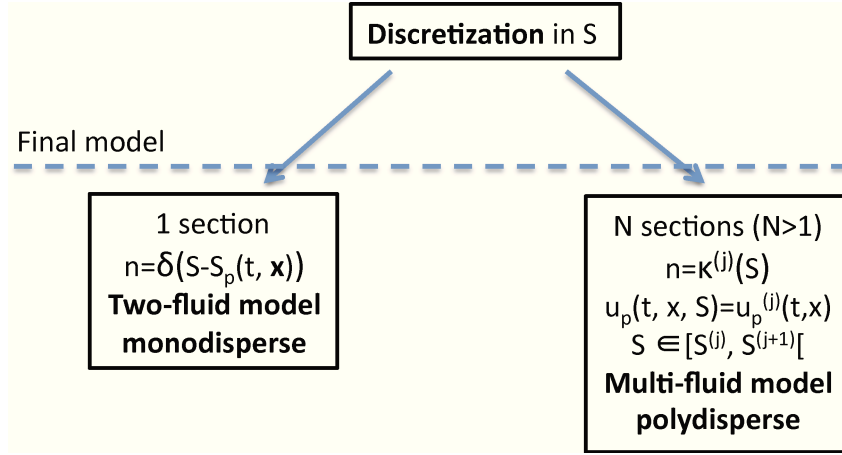


Figure 2.3: Final models in the context of a size discretization

An extension of the two-fluid model consists in realizing a sampling of the distribution and to define  $N$  samples by:

$$n(t, \mathbf{x}, S, \mathbf{u}) = \sum_{i=1}^N f(t, \mathbf{x}) \delta(S - S_{p,i}(t, \mathbf{x})) \delta(\mathbf{u} - \mathbf{u}_{p,i}(t, \mathbf{x})), \quad (2.14)$$

each sample having its mean size,  $S_{p,i}$  and velocity,  $\mathbf{u}_{p,i}$ . The system of equations for each sample is derived in the way used for the classical two-fluid method, presuming the shapes of the velocity and size distributions. It thus results in  $N$  systems of equations similar to Eq. (2.13). This sampling is illustrated in Fig. (2.4). Nevertheless, one has to notice that the sampled sizes are not interacting and thus the description of the phenomena inducing coupling in the size phase space, as coalescence or secondary breakup, are not taken into account. This model allows fast computation but only accesses a mean droplet size. Moreover, in the context of a monokinetic assumption for the velocity distribution function, no PTC can be described.

**Multi-fluid model** The multi-fluid method, introduced in [102] and characterized in [146], proposes to conserve information on the size distribution as well as on the size-velocity correlations, discretizing the size phase space. The semi-kinetic system Eq. (2.6) is averaged on fixed size intervals  $[S^{(j)}, S^{(j+1)}[$ ,  $j \in [1, N_s]$  called sections, where  $N_s$  is the number of sections. We thus solve the evolution of moments of

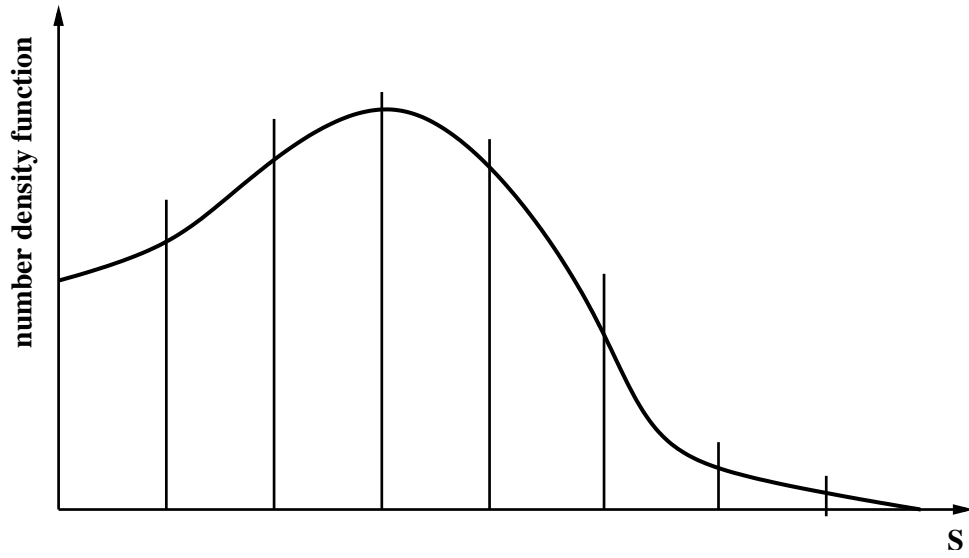


Figure 2.4: Size distribution sampling

the NDF in each section, the sections being coupled by exchange of mass and momentum, see Fig. (2.5) and Fig. (2.2).

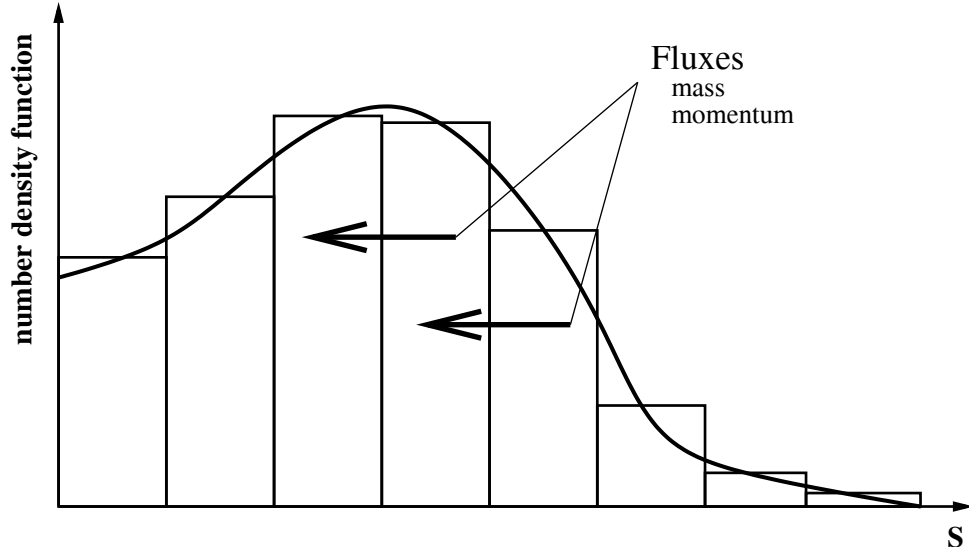


Figure 2.5: Size distribution function discretization

For each section  $j$ , a system of conservation law for the mass and momentum, given by:

$$\begin{aligned}
 m^{(j)}(t, \mathbf{x}) &= \int_{S^{(j)}}^{S^{(j+1)}} \rho_l \frac{S^{3/2}}{6\sqrt{\pi}} n(t, \mathbf{x}, S) dS, \\
 m^{(j)}(t, \mathbf{x}) \mathbf{u}_p^{(j)}(t, \mathbf{x}) &= \int_{S^{(j)}}^{S^{(j+1)}} \rho_l \frac{S^{3/2}}{6\sqrt{\pi}} n(t, \mathbf{x}, S) \mathbf{u}_p(t, \mathbf{x}, S) dS,
 \end{aligned}
 \tag{2.15}$$

is derived from the semi-kinetic system:

$$\int_{S^{(j)}}^{S^{(j+1)}} \rho_l \frac{S^{3/2}}{6\sqrt{\pi}} \text{Eq. (2.6)} \, dS. \quad (2.16)$$

The detailed equations for the multi-fluid model are given in Chapter 3, and we just give here the key elements concerning its derivation. As far as closures are concerned, the size phase space discretization allows to take into account evaporation or droplet interactions phenomena coupling droplets of different sizes. The number distribution in one section,  $n(t, \mathbf{u}, S)$ ,  $S \in [S^{(j)}, S^{(j+1)}]$ , is unclosed as we only solve one moment in size of this distribution. We thus presume the profile of  $n$  in a given section, as a function of the droplet geometry only:

$$n(t, \mathbf{x}, S) = m^{(j)}(t, \mathbf{x}) \kappa^{(j)}(S), \quad S \in [S^{(j)}, S^{(j+1)}]. \quad (2.17)$$

The size distribution function is generally approximated by a piecewise constant function,  $\kappa^{(j)} = \text{cte}$ . In our framework  $\kappa^{(j)}$  is constant relative to the droplet surface variable. It must be noticed though that, in general, the form of  $\kappa^{(j)}$  depends of the choice for the size variable, and will be different for the droplet volume, surface, or radius. Meanwhile, the velocity  $\mathbf{u}_p(t, \mathbf{x}, S)$  is assumed to not depend on size in a section:  $\mathbf{u}_p^{(j)}(t, \mathbf{x})$ . This is known as the fundamental sectional assumption, [102, 146]. Unlike the presumed size distribution method, the form of the size distribution is assumed only within a section in the multi-fluid model. This model thus describes the polydispersion as well as the size velocity correlation, a key issue in evaporating spray simulations.

However, the main drawback of this method is the cost associated to the resolution of  $N_s$  systems of conservation laws, needed to obtain the evolution of the sections. Indeed, it has been shown that the multi-fluid model is a first order method regarding evaporation [145], and thus a high number of sections, typically ten to twenty, may be needed to obtain a precise description of the evaporation process. This drawback can be avoided by using methods of higher order for the description of evaporation in multi-fluid framework. A second important limitation, comes from the description of same section droplet trajectories crossing, that can not be done with standard multi-fluid method, as with all presumed velocity PDF based Eulerian method. These two limitations are the basis of this PhD. They will be developed in Chapter 3.

### 2.2.2.2 Preservation of the continuous character of the size variable

The other way to obtain a description of the size distribution is to preserve the continuous characteristic of the size variable, and thus to directly solve the NDF. But until now, all these methods are based on presumed size NDF, as done in [9, 183]. The idea is to presume a form for the size distribution and to solve the evolution of a set of moments of this distribution. Nevertheless, this approach suffers from severe problems coming from both the evaporation process and the coupling with the velocity conditioned by size. Indeed it is necessary to presume a form of the spray NDF, for instance a log-normal form, and to resolve the evolution of this log-normal parameters. Nevertheless, the form of the NDF is not conserved through evaporation: an initially log-normal distribution evaporating has no reason to stay a log-normal distribution. Therefore severe singularities occur in the equations governing the evolution of the log-normal parameters.

## 2.2.3 Quadrature approach

As we mentioned in Section 2.2.1, an alternative to the presumed velocity PDF Eulerian method for the simulation of spray is the Direct Quadrature Method of Moments (DQMOM), introduced in [159]. In this framework, the NDF of the spray is assumed to have the form:

$$n(t, \mathbf{x}, S, \mathbf{u}) = \sum_{n=1}^N \omega_n \delta(S - S_n) \delta(\mathbf{u} - \mathbf{u}_n), \quad (2.18)$$

and a system of conservation laws is derived directly for the weights and abscissas  $(\omega_n, S_n, \mathbf{u}_n)$ :

$$\begin{aligned}\partial_t \omega_n + \nabla_{\mathbf{x}} \cdot (\omega_n \mathbf{u}_n) &= a_n, \\ \partial_t (\omega_n S_n) + \nabla_{\mathbf{x}} \cdot (\omega_n S_n \mathbf{u}_n) &= b_n, \\ \partial_t (\omega_n S_n \mathbf{u}_n) + \nabla_{\mathbf{x}} \cdot (\omega_n S_n \mathbf{u}_n \otimes \mathbf{u}_n) &= c_n,\end{aligned}\tag{2.19}$$

where the source terms  $(a_n, b_n, c_n)$  are obtained from the source terms of the Williams equation Eq. (1.19), writing conservation equations on a set of chosen moments. It results in a  $5N \times 5N$  linear system giving these source terms [159].

The DQMOM method, along with the multi-fluid method, have been compared to a Lagrangian description in the framework of a 1-D vaporizing and coalescing laminar spray [85]. It has been shown that the DQMOM method, first introduced in the context of aerosol dynamics and aggregation-breakage processes, can be implemented for a vaporizing spray described by a Williams equation, Eq. (1.19), as also tackled in [83]. The DQMOM reveals to be very efficient to describe spray coalescence, more efficient than the multi-fluid due to its limited numerical diffusion in the size phase space. As far as evaporation is concerned, the method is shown to be robust but the importance to treat precisely the problem of the evaporative flux due to droplet disappearance is highlighted. An efficient solution to this problem, common to several moment methods for fluid-particle flows, is tackled in [173].

Finally, up to now, the DQMOM fails to treat droplet trajectory crossings, [84].

Figure (2.6) offers a general synthetic overview of these models.

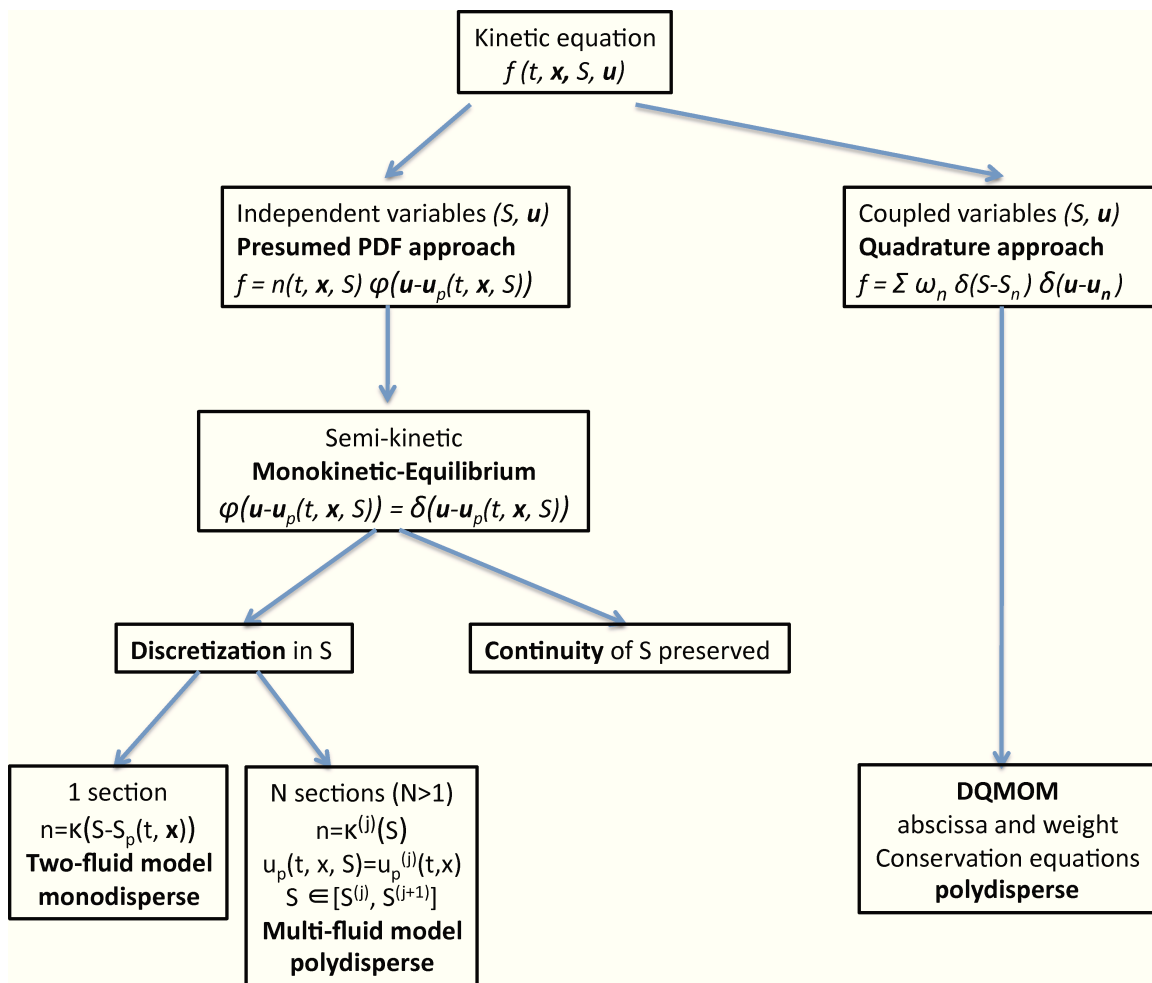


Figure 2.6: General overview of spray models based on a kinetic description

## Chapter 3

# Multi-fluid model: principles, achievements, limitations

The Eulerian multi-fluid model is presented in this chapter. It corresponds to a low order moment method in size and velocity, associated with a size discretization. The formalism and the associated assumptions were originally introduced in [146], extending the ideas of [102]. The multi-fluid model is the first robust model able to describe spray polydispersity. Its numerical efficiency for DNS computations has been assessed in the PhD of Stéphane de Chaisemartin who has shown impressive achievements [49]. The study of the multi-fluid has been essential in the context of this PhD for three reasons. The assessment of its limitations have been the motivation of the research work devoted to design the Eulerian Multi Size Moments (EMSM) and Eulerian Multi Velocity Moments (EMVM) models, presented in Part II and Part III respectively. Secondly, some of the numerical methods designed for the multi-fluid model and presented here are the basis for some numerical schemes designed for the EMSM and EMVM models. These methods are detailed in this chapter and will be referred to in other chapters. Finally, the configurations of the tests cases considered to assess the potential of the multi-fluid model are presented here.

The remainder of this chapter is the following. The multi-fluid model with its assumptions is presented in section Section 3.1, with a discussion on the consequences on its mathematical structure. The numerical methods are presented in Section 3.2. Particular attention is devoted to the splitting strategies and the advection schemes since they are the basis of numerical methods designed for the EMSM and the EMVM models. Then Section 3.3 discusses the achievements brought by the multi-fluid model. Finally, its two major limitations are discussed on Section 3.4. This work has been published in [126].

### 3.1 Model and assumptions

#### 3.1.1 Semi-kinetic system of conservation law

The general form of the semi-kinetic system has been given in Eq.(2.6). We highlight here the main assumptions and give its form under an equilibrium assumption with no dispersion for the velocity distribution. In this framework, the closure of the system is obtained through the following assumptions:

- [H1] For a given droplet size, at a given point  $(t, \mathbf{x})$ , there is only one characteristic averaged velocity  $\mathbf{u}_p(t, \mathbf{x}, S)$ .
- [H2] The dispersion in the distribution function around the mean velocity  $\mathbf{u}_p$  is zero in each direction, whatever the point  $(t, \mathbf{x}, S)$ .

It is equivalent to presume the following NDF conditioned by droplet size:

$$f(t, \mathbf{x}, S, \mathbf{u}) = n(t, \mathbf{x}, S)\delta(\mathbf{u} - \mathbf{u}_p(t, \mathbf{x}, S)), \quad (3.1)$$

that is to reduce the support of the NDF to a one-dimensional sub-manifold parametrized by droplet size. The semi-kinetic system is then closed, and Eq. (2.6) becomes:

$$\begin{aligned}\partial_t n + \nabla_{\mathbf{x}} \cdot (n\mathbf{u}_p) &= \partial_S(nR_p), \\ \partial_t(n\mathbf{u}_p) + \nabla_{\mathbf{x}} \cdot (n\mathbf{u}_p \otimes \mathbf{u}_p) &= \partial_S(nR_p\mathbf{u}_p) + n\mathbf{D}_{r,p},\end{aligned}\tag{3.2}$$

with, as defined in Eq. (2.10),  $R_p = R(\mathbf{u}_p)$  and  $\mathbf{D}_{r,p} = \mathbf{D}_r(\mathbf{u}_p)$ . The expressions for the terms  $R$  and  $\mathbf{D}_r$  are given in Eq. (1.29) and Eq. (1.24). It must be noticed that the two descriptions at the kinetic level and at the moment level are equivalent as long as two following conditions are satisfied. First, the NDF conditioned by droplet size stays mono-kinetic, i.e. satisfies Eq. (3.1) and associates one single velocity at a fixed position and time for a given droplet size. Second, the solution of the system of conservation equations remains regular. Indeed, the solution of Eq. (3.2) can become singular, even if the initial condition is regular, as explained in Section 3.1.3.

### 3.1.2 Multi-fluid system of conservation laws

In order to obtain the classical multi-fluid system of conservation law, the phase space is discretized. We choose a discretization  $0 = S^{(1)} < S^{(2)} < \dots < S^{(j)} < \dots < S^{(N_s+1)}$  for the droplet size phase space and we average the obtained system of conservation laws over each fixed size intervals  $[S^{(j)}, S^{(j+1)}[$ , called section. The set of droplets in one section can be seen as a fluid for which conservation equations are written. The sections exchange mass and momentum, and heat, if temperature is considered. The average in each section consists in taking one moment in size, of order 3/2 in surface, which is proportional to the droplet mass. The system of conservation laws gives us the evolution of the vector of moments of the distribution function in the phase space  $(t, \mathbf{u}, S)$ :

$$(\mathcal{M}_{3/2,0,0,0}, \mathcal{M}_{3/2,1,0,0}, \mathcal{M}_{3/2,0,1,0}, \mathcal{M}_{3/2,0,0,1})^t,\tag{3.3}$$

where the first index of the moment  $\mathcal{M}_{k,l,m,n}$  denotes the order in size, and the three following refers to the three components of the velocity, in three dimensions. The order 3/2 in size  $\mathcal{M}_{3/2,0,0,0}$ , corresponds to the mass density of droplets and it has been chosen because of its relevance to the evaporation and combustion processes. The evolution of these moments gives the evolution of mass and momentum of the spray. To close the system, the following assumptions are introduced:

[H3] In one section, droplet velocity do not depend on the size of the droplets.

[H4] The form of  $n$  as a function of  $S$  is supposed to be independent of  $t$  and  $\mathbf{x}$  in a given section, thus decoupling the evolution of the mass concentration of droplets in a section from the repartition in terms of sizes.

These assumptions are equivalent to presume the NDF in velocity and size inside each section:

$$\begin{aligned}\mathbf{u}_p(t, \mathbf{x}, S) &= \mathbf{u}_p^{(j)}(t, \mathbf{x}), \\ n(t, \mathbf{x}, S) &= m^{(j)}(t, \mathbf{x})\kappa^{(j)}(S),\end{aligned}$$

where  $m^{(j)}$  is the mass concentration of droplets in the  $j^{th}$  section, given by:

$$m^{(j)}(t, \mathbf{x}) = \int_{S^{(j)}}^{S^{(j+1)}} \rho_l \frac{S^{3/2}}{6\sqrt{\pi}} n(t, \mathbf{x}, S) dS,\tag{3.4}$$

which gives us, for the form  $\kappa^{(j)}$  in one section:

$$\int_{S^{(j)}}^{S^{(j+1)}} \rho_l \frac{S^{3/2}}{6\sqrt{\pi}} \kappa^{(j)}(S) dS = 1.\tag{3.5}$$

As mentionned in [146], there exist several possibilities to choose  $\kappa^{(j)}$  depending for example on whether a form for the NDF constant is radius is chosen, i.e.  $\kappa_R^{(j)} = \text{constant}$ , or a form for the NDF constant is surface is chosen, i.e.  $\kappa_S^{(j)} = \text{constant}$ . We expose the second formulation. The formulation for  $\kappa_R^{(j)} = \text{constant}$  can easily be figured out, thanks to the following relation, stating that the number density is conserved:

$$\kappa_R^{(j)} dR = \kappa_S^{(j)} dS, \quad (3.6)$$

leading to :

$$\kappa_R^{(j)} = \kappa_S^{(j)} 8\pi R. \quad (3.7)$$

We have, through Eq. (3.5),

$$\kappa^{(j)} = \frac{6\sqrt{\pi}}{\rho_l} \frac{5/2}{(S^{(j+1)})^{5/2} - (S^{(j)})^{5/2}}, \quad (3.8)$$

We derive the evolution of the set of moments written in Eq. (3.3) from the semi-kinetic system Eq. (2.6):

$$\int_{S^{(j)}}^{S^{(j+1)}} \rho_l \frac{S^{3/2}}{6\sqrt{\pi}} \text{Eq.(2.6)} dS, \quad (3.9)$$

and we obtain, under the assumptions [H1] to [H4]:

$$\begin{aligned} \partial_t m^{(j)} + \nabla_{\mathbf{x}} \cdot (m^{(j)} \mathbf{u}_{\mathbf{p}}^{(j)}) &= -(E_1^{(j)} + E_2^{(j)}) m^{(j)} + E_1^{(j+1)} m^{(j+1)}, \\ \partial_t (m^{(j)} \mathbf{u}_{\mathbf{p}}^{(j)}) + \nabla_{\mathbf{x}} \cdot (m^{(j)} \mathbf{u}_{\mathbf{p}}^{(j)} \otimes \mathbf{u}_{\mathbf{p}}^{(j)}) &= -(E_1^{(j)} + E_2^{(j)}) m^{(j)} \mathbf{u}_{\mathbf{p}}^{(j)} + E_1^{(j+1)} m^{(j+1)} \mathbf{u}_{\mathbf{p}}^{(j+1)} \\ &\quad + m^{(j)} \mathbf{D}_{\mathbf{r},\mathbf{p}}^{(j)}, \end{aligned} \quad (3.10)$$

where we define the averaged drag term in the  $j^{\text{th}}$  section:

$$\mathbf{D}_{\mathbf{r},\mathbf{p}}^{(j)}(t, \mathbf{x}) = \frac{1}{m^{(j)}} \int_{S^{(j)}}^{S^{(j+1)}} \rho_l \frac{S^{3/2}}{6\sqrt{\pi}} \mathbf{D}_{\mathbf{r},\mathbf{p}}(t, \mathbf{x}, S, \mathbf{u}_{\mathbf{p}}) n(t, \mathbf{x}, S) dS. \quad (3.11)$$

Since we have chosen to express the drag term with a Stokes closure, the dependance of  $\mathbf{D}_{\mathbf{r},\mathbf{p}}$  in the variable  $S$  is  $1/S$ . The expression of  $\mathbf{D}_{\mathbf{r},\mathbf{p}}^{(j)}$  becomes:

$$\mathbf{D}_{\mathbf{r},\mathbf{p}}^{(j)} = \frac{\mathbf{u}_{\mathbf{g}}(t, \mathbf{x}) - \mathbf{u}_{\mathbf{p}}^{(j)}(t, \mathbf{x})}{\text{St}_0 S_p^{(j)}}, \quad (3.12)$$

where  $\text{St}_0$  is the Stokes number associated to the characteristic size  $S_0$  defined in Section 1.2.4:

$$\text{St}_0 = \frac{\rho_l S_0}{18\pi\mu_g}. \quad (3.13)$$

Besides,  $S_p^{(j)}$ , the characteristic droplet surface of section  $j$  seen by the gas, given from the form of  $\kappa^{(j)}$ , reads:

$$S_p^{(j)} = \frac{3((S^{(j+1)})^{5/2} - (S^{(j)})^{5/2})}{5((S^{(j+1)})^{3/2} - (S^{(j)})^{3/2})}, \quad (3.14)$$

Regarding the evaporation terms,  $\int_{S^{(j)}}^{S^{(j+1)}} \rho_l \frac{S^{3/2}}{6\sqrt{\pi}} R_p n dS$ , an integration by part is conducted to separate the exchange terms between successive sections, given by:

$$\begin{aligned} E_1^{(j)} &= \rho_l \frac{(S^{(j)})^{3/2}}{6\sqrt{\pi}} R_p^{(j)} \kappa^{(j)}, \\ E_2^{(j)} &= \int_{S^{(j)}}^{S^{(j+1)}} \rho_l \frac{\partial_S (S^{3/2})}{6\sqrt{\pi}} R_p \kappa^{(j)} dS, \end{aligned} \quad (3.15)$$



that is, using Eq. (3.8),

$$\begin{aligned} E_1^{(j)} &= \frac{5(S^{(j)})^{3/2}}{2((S^{(j+1)})^{5/2} - (S^{(j)})^{5/2})} R_p^{(j)}, \\ E_2^{(j)} &= \frac{5((S^{(j+1)})^{3/2} - (S^{(j)})^{3/2})}{2((S^{(j+1)})^{5/2} - (S^{(j)})^{5/2})} R_p^{(j)}, \end{aligned} \quad (3.16)$$

with  $R_p^{(j)}(t, \mathbf{x}) = R_p(t, \mathbf{x}, \mathbf{u}_p^{(j)})$ . One can notice that to conduct the integration of Eq. (3.15),  $R_p$  is assumed to be independent of size inside the section. This assumption is legitimate in the context of a  $d^2$  evaporation law.

From the term  $E_2^{(j)}$ , it is possible to compute the fuel mass source term in the gaseous equation,  $S^{\text{fuel}}$ . We have:

$$S^{\text{fuel}} = \int_S \int_{\mathbf{u}} \rho_l R_p \frac{\partial_S(S^{3/2})}{6\sqrt{\pi}} f \, dS d\mathbf{u}, \quad (3.17)$$

and thus in the multi-fluid framework, the mass source term is given by the sum of the section contributions:

$$S^{\text{fuel}} = \sum_{j=1}^{N_s} \int_{S^{(j)}}^{S^{(j+1)}} \rho_l \frac{\partial_S(S^{3/2})}{6\sqrt{\pi}} R_p \kappa_S^{(j)} m^{(j)} \, dS = \sum_{j=1}^{N_s} m^{(j)} E_2^{(j)}. \quad (3.18)$$

In the same manner,

$$S^{\text{mom}} = \sum_{j=1}^{N_s} \int_{S^{(j)}}^{S^{(j+1)}} \int_{\mathbb{R}} \rho_l \frac{\partial_S(S^{3/2})}{6\sqrt{\pi}} R_p \mathbf{u}_p \kappa_S^{(j)} m^{(j)} \delta(\mathbf{u}_p - \mathbf{u}_p^{(j)}) \, d\mathbf{u} dS = \sum_{j=1}^{N_s} m^{(j)} \mathbf{u}_p^{(j)} E_2^{(j)}. \quad (3.19)$$

### Dimensionless formulation

The multi-fluid model is computed in a dimensionless form, obtained from the dimensionless kinetic equation introduced in Section 1.2.4. We first introduce a reference mass density for droplets  $m_0$

$$m_0 = \rho_\infty \frac{(S_0)^{3/2}}{6\sqrt{\pi}} N_0. \quad (3.20)$$

The dimensionless multi-fluid system of conservation laws is given by:

$$\begin{aligned} \frac{L_0}{U_0 m_0} \text{Eq. (3.10)a}, \\ \frac{L_0}{U_0^2 m_0} \text{Eq. (3.10)b}, \end{aligned} \quad (3.21)$$

leading to the same system as Eq. (3.10), with the following dimensionless variable

$$\begin{aligned} \overline{m^{(j)}} &= \frac{m^{(j)}}{m_0}, \\ \overline{\mathbf{u}_p^{(j)}} &= \frac{\mathbf{u}_p^{(j)}}{U_0}. \end{aligned} \quad (3.22)$$

The dimensionless form of the external forces, and the surface change rate in one section are obtained from Section 1.2.4:

$$\overline{\mathbf{D}_{r,p}^{(j)}}(\overline{t}, \overline{\mathbf{x}}) = \overline{\mathbf{D}_{r,p}}(\overline{t}, \overline{\mathbf{x}}, \overline{S_p^{(j)}}, \overline{\mathbf{u}_p^{(j)}}),$$

$$\overline{R_p^{(j)}}(\overline{t}, \overline{\mathbf{x}}) = \overline{R_p}(\overline{t}, \overline{\mathbf{x}}, \overline{S_p^{(j)}}, \overline{\mathbf{u}_p^{(j)}}). \quad (3.23)$$

$$(3.24)$$

The expression of  $\overline{D_{r,p}}, \overline{R_p}$  being given in Eq. (1.35).

The dimensionless characteristic Stokes number  $\overline{St}_0$  writes :

$$\overline{St}_0 = \frac{\overline{\rho_l}}{18\pi\mu_g^*} \frac{S_0}{L_0^2}. \quad (3.25)$$

In dimensionless formulation,  $\kappa_S^{(j)}$  becomes:

$$\overline{\kappa_S^{(j)}} = \frac{5/2}{\overline{\rho_l} \left( (\overline{S^{(j+1)}})^{5/2} - (\overline{S^{(j)}})^{5/2} \right)}, \quad (3.26)$$

so that

$$\overline{E_1^{(j)}} = \frac{5(\overline{S^{(j)}})^{3/2}}{2 \left( (\overline{S^{(j+1)}})^{5/2} - (\overline{S^{(j)}})^{5/2} \right)} \overline{R_p^{(j)}}, \quad (3.27)$$

$$\overline{E_2^{(j)}} = \frac{5(\overline{S^{(j+1)}})^{3/2} - (\overline{S^{(j)}})^{3/2}}{2 \left( (\overline{S^{(j+1)}})^{5/2} - (\overline{S^{(j)}})^{5/2} \right)} \overline{R_p^{(j)}}. \quad (3.28)$$

$$(3.29)$$

In the following of this chapter, and in Part II and Part III, we deal with dimensionless quantities. For the sake of legibility, we will omit the bar sign.

### 3.1.3 Mathematical peculiarity of the monokinetic assumption

In the context of the evaluation of the multi-fluid relevance for industrial applications [49], the first step was to show the ability to design a robust and efficient numerical scheme. This step requires to analyze the mathematical properties of the multi-fluid model conservation laws. This study is all the more important that the physical transport part of the dynamical system for the EMSM model presented in Chapter 4 has the same structure as the multi-fluid model. It will also be referred to in the analysis of the physical transport part structure in the context of the high order velocity moment method.

In the monokinetic multi-fluid framework chosen in this study, Eq. (3.10), the transport term has a peculiar structure known as the pressureless gas system, [21]. Indeed, it is similar to an Euler gas dynamics system of equations, but without any pressure term in the momentum equation:

$$\begin{aligned} \partial_t m + \nabla_{\mathbf{x}} \cdot (m \mathbf{u}_p) &= 0, \\ \partial_t (m \mathbf{u}_p) + \nabla_{\mathbf{x}} \cdot (m \mathbf{u}_p \otimes \mathbf{u}_p) &= 0. \end{aligned} \quad (3.30)$$

This weakly hyperbolic system can be found for example in astrophysics, when describing the formation of large scale structures in the universe or in the modeling of sticky particles [235]; it has also been presented in [67] for bubbles. The structure of this system comes from the monokinetic assumption for the spray velocity distribution done at the kinetic level, Section 3.1. An interesting property in this framework is the mathematical equivalence between the kinetic and the fluid level of description for smooth solutions, Theorem 1.

**Theorem 1 (Bouchut)** *Let  $T > 0$ ,  $m(t, \mathbf{x}), \mathbf{u}_p(t, \mathbf{x}) \in C^1([0, T] \times \mathbb{R}^d)$  and define*

$$f(t, \mathbf{x}, \mathbf{u}) = m(t, \mathbf{x}) \delta(\mathbf{u} - \mathbf{u}_p(t, \mathbf{x})). \quad (3.31)$$

*Then  $(m, \mathbf{u}_p)$  solve Eq. (3.30) in  $[0, T] \times \mathbb{R}^d$  if and only if*

$$\partial_t f + \nabla_{\mathbf{x}} \cdot (\mathbf{u} f) = 0 \quad \text{in } [0, T] \times \mathbb{R}^d \times \mathbb{R}^d, \quad (3.32)$$

where  $d$  is the number of physical space dimensions. This equivalence is shown in [21]. Therefore the solutions of the macroscopic system Eq. (3.30) are the solution of the kinetic equation Eq. (3.32) as long as the distribution is monokinetic, Eq. (3.31). Bouchut also showed that the velocity verifies a maximum property.

A key point is thus to know whether an initially monokinetic distribution stays monokinetic as times evolves. These issues are discussed in [117], where a kinetic equation with a Stokes drag force source term is considered:

$$\partial_t f + \nabla_{\mathbf{x}} \cdot (\mathbf{u}f) = -\nabla_{\mathbf{u}} \cdot \left( \frac{\mathbf{u}_g - \mathbf{u}}{\text{St}} f \right). \quad (3.33)$$

This work considers on open domain with Lipschitz boundary. In the framework of our study, it is not needed to consider domain boundary, for periodicity reasons. The whole space  $\mathbb{R}^d$  is thus considered. It is shown that, under normalization conditions on the initial velocity field  $\mathbf{u}_{p_0}$  and on the gas velocity field  $\mathbf{u}_g$ ,  $f$  remains monokinetic, Theorem 2. These conditions are based on the Stokes number.

**Theorem 2 (Jabin)** *Assume  $m_0 \in L^1(\mathbb{R}^d)$  and*

$$\begin{aligned} m &\in L^\infty([0, \infty], L^1(\mathbb{R}^d)), \\ \mathbf{u}_p &\in L^\infty([0, \infty], W^{1,\infty}(\mathbb{R}^d)), \\ \|\mathbf{u}_{p_0}\|_{W^{1,\infty}(\mathbb{R}^d)} &\leq \frac{1}{2d\text{St}}, \\ \|\mathbf{u}_g\|_{L^\infty([0,\infty], W^{1,\infty}(\mathbb{R}^d))} &\leq \frac{1}{4d\text{St}}. \end{aligned} \quad (3.34)$$

*Then there exist unique  $m$  and  $\mathbf{u}_p$  defined on the time interval  $[0, \infty]$ , solutions to Eq. (3.30).*

A precise framework is thus defined where the equivalence between the kinetic and the fluid level of description stands. If the provided conditions are not fulfilled, this equivalence is no longer valid and singularities may occur at the fluid level of description. These singularities, caused by the breaking of the monokinetic assumption, are called  $\delta$ -shocks. It corresponds to a discontinuity in velocity which leads to Dirac delta function concentrations in density. In fact, for smooth solutions, the equation on the velocity itself is decoupled from the conservation of mass and takes the form of the Burger's classical equation:

$$\partial_t \mathbf{u}_p + \mathbf{u}_p \cdot \nabla_{\mathbf{x}} \mathbf{u}_p = 0. \quad (3.35)$$

A shock may then arise, leading to the concentration of density at its interface. The breaking of the monokinetic assumption is related to droplet trajectory crossings (PTC). As mentioned in introduction of this manuscript, in the infinite Knudsen limit taken in the applications, cluster of droplets are crossing each other, without colliding. It is associated, in a Eulerian description of the spray, to a bimodal distribution at the kinetic level, leading to two droplet velocities at the same space and time location. In the resolution of the whole problem, as formulated in Eq. (3.10), the drag term will decrease the occurrence of such crossings, attracting droplet velocity toward gas velocity. Nevertheless, for droplets inertial enough, influence of drag is weaker and crossings may still occur. As we already mentioned in the assumption [H1], Section 3.1, at a given point there is only one averaged velocity, preventing the description of droplet crossings. In the two-fluid model, also based on one averaged velocity, the same problem occurs and droplet crossings can neither be described. However, in the multi-fluid model, as presented in assumption [H1], we have one averaged velocity at a given size. Consequently, the polydispersion described in the multi-fluid model allows crossing of droplets provided they do not belong to the same size interval. Nevertheless, equally-sized droplet crossings are out of the limits of the multi-fluid model and can not be described.

This observation has two consequences. First one wants to be able to control droplet dynamics for a given gaseous flow. Indeed for turbulent flows or even for laminar flows with contra-rotative vortices or impinging jets, equally-sized droplet crossings may occur. One would like to be able, through a limitation on the Stokes number of the droplets, to foresee these crossing occurrences. To do so, Theorem 2 is used in 2-D vortical flows to illustrate the conditions leading to droplet trajectory crossings. This study is conducted in Section 3.3.1. Second, a robust numerical method must be developed to cope with the

velocity discontinuities and density concentration arising if equally-sized droplet crossings do still occur at rare occasions in the flow.

Along with the previously described singularities, the system can lead to creation of vacuum. One can note that it is important to be able to cope efficiently with vacuum zones since they represent areas of the flow where no droplet is to be found and are commonly encountered in most applications. Furthermore, the positivity of density and the maximum principle on velocity are preserved. One can note that configurations challenging to compute may arise, even when no singularity occurs, for example due to the concentration of density in an area of the flow. This situation occurs for example when droplets are ejected from the core of vortices and accumulated in weak vorticity areas.

A specific numerical method is consequently needed, for the transport part of the multi-fluid method, requiring:

- to stand high gradients even up to the situation where all the mass density would be concentrated in one cell,
- to preserve the positivity of mass density,
- to reproduce a discrete maximum principle on the velocity,
- to deal with vacuum zones in the computational domain.

Furthermore, the best compromise between robustness, precision and computational cost is required. The development of such a numerical method is presented in Section 3.2.

## 3.2 Multi-fluid numerical methods

The numerical scheme designed for the multi-fluid method must deal with the complex mathematical structure of the governing system of equations, described and illustrated in Section 3.1. Furthermore, the numerical scheme has to present the best compromise between precision and cost, in order to tackle more complex 2-D jet or 3-D configurations, Section 3.3.2, [49]. In order to treat efficiently the different difficulties of the multi-fluid system, that are a complex transport term and stiff source terms, we use an operator splitting, [212, 17, 55]. It allows to design efficient numerical methods for each contribution. Furthermore, one takes advantage of the structured grids used in this study to introduce a dimensional splitting to treat multi-dimensional configurations, leading to a high efficiency. Particular attention is devoted to the description of the splitting algorithm and the physical transport resolution method, since these algorithms are reused for the numerical scheme designed for the EMSM (Section 6.3) and the EMVM models (Section 9.5).

We are however aware of the fact that methods devoted to unstructured grids would be required for industrial realizations. Nevertheless, albeit this work aims at studying the relevance of the multi-fluid method for industrial scale configurations, it focuses on a still academic context. This is a needed first step toward industrial applications, and with a clear gap in terms of configuration complexity compared to the multi-fluid computations provided up to now. Furthermore, this academic context is needed to provide precise analysis and validations of the model, Chapter 4, Chapter 9. Finally, its relative simplicity, allows to rapidly settle a configuration. When extension to industrial configuration is required, one will take advantage of extension methods to unstructured grids proposed in the literature.

### 3.2.1 Operator splitting

Phenomena involved in our problem are decoupled: transport induces an evolution in the physical space without leading to any change in the phase space, whereas transport in internal coordinate space, i.e., size and velocity through evaporation and drag, induces an evolution without any coupling with the spatial coordinates. It is then interesting to separate them using an operator-splitting method. The multi-fluid system, Eq. (3.10), is then split into two systems, one for the physical space and one for the phase space.

On one hand, the evolution in the physical space for the multi-fluid size section  $j$  reads:

$$\begin{aligned}\partial_t m^{(j)} + \nabla_{\mathbf{x}} \cdot (m^{(j)} \mathbf{u}_{\mathbf{p}}^{(j)}) &= 0, \\ \partial_t (m^{(j)} \mathbf{u}_{\mathbf{p}}^{(j)}) + \nabla_{\mathbf{x}} \cdot (m^{(j)} \mathbf{u}_{\mathbf{p}}^{(j)} \otimes \mathbf{u}_{\mathbf{p}}^{(j)}) &= 0.\end{aligned}\tag{3.36}$$

On the other hand, the phase space evolution, in internal coordinate space, reads for section  $j$ :

$$\begin{aligned}d_t m^{(j)} &= -(E_1^{(j)} + E_2^{(j)})m^{(j)} + E_1^{(j+1)}m^{(j)}, \\ d_t (m^{(j)} \mathbf{u}_{\mathbf{p}}^{(j)}) &= -(E_1^{(j)} + E_2^{(j)})m^{(j)} \mathbf{u}_{\mathbf{p}}^{(j)} + E_1^{(j+1)}m^{(j)} \mathbf{u}_{\mathbf{p}}^{(j)} + m^{(j)} \mathbf{D}_{\mathbf{r}, \mathbf{p}}^{(j)}.\end{aligned}\tag{3.37}$$

The operator-splitting method consists in solving alternatively these simpler problems Eq. (3.36) and Eq. (3.37) in order to approximate the solution of the full problem, Eq. (3.10). The easier splitting algorithm is the Lie algorithm [152]: it alternates phase and physical space transport:

- Phase space transport: solve Eq. (3.36) during  $\Delta t$ ,
- Physical space transport: solve Eq. (3.37) during  $\Delta t$ ,

but it only provides first order precision in time. Assuming that the steps are second order in time, the Strang splitting, with the following structure [55]:

- Phase space transport: solve Eq. (3.36) during  $\Delta t/2$ ,
- Physical space transport: solve Eq. (3.37) during  $\Delta t$ ,
- Phase space transport: solve Eq. (3.36) during  $\Delta t/2$ ,

guaranties a second order precision in time.

As mentioned in [152], this Strang splitting can also be obtained with an algorithm based on a Lie splitting. The Lie splitting is composed of two steps of length  $\Delta t$ . The Strang splitting is constructed with these two steps but it alternates the order in which they are performed:

1. iteration  $2n$

- Phase space transport: solve Eq. (3.36) during  $\Delta t$ ,
- Physical space transport: solve Eq. (3.37) during  $\Delta t$ ,

2. iteration  $2n+1$

- Physical space transport: solve Eq. (3.37) during  $\Delta t$ ,
- Phase space transport: solve Eq. (3.36) during  $\Delta t$ .

This alternated splitting is in fact a classical Strang splitting with a splitting timestep  $2\Delta t$ . Indeed it can be written:

- Phase space transport: solve Eq. (3.36) during  $\Delta t$ ,
- Physical space transport: solve Eq. (3.37) during  $2\Delta t$ ,
- Phase space transport: solve Eq. (3.36) during  $\Delta t$ .

The error due to the splitting increases, but the steps are of length  $\Delta t$ . Furthermore, to advance the solution of  $\Delta t$  we need to perform only two steps and not three, and it can lead to a benefit in the computational efficiency of the algorithm.

### 3.2.2 Physical space transport resolution: kinetic-based scheme

As mentioned in Section 3.1.3, the transport part of the multi-fluid system of equations has a peculiar structure. Indeed the system for the physical transport of the  $j^{\text{th}}$  multi-fluid section, Eq. (3.36), is similar to the pressureless gas system Eq. (3.30). In order to explain the choice made for the multi-fluid transport scheme, one first focuses on this pressureless gas system. The kinetic finite volume scheme derived in [24] is presented in a 1-D case. This general presentation gives the basis to derive the numerical method used for the multi-fluid transport. This transport term resolution is presented regardless of the multi-fluid section discretization, as physical transport is local in size phase space.

#### Finite volume kinetic schemes for pressureless gas system

The general framework of pressureless gas system is used to introduce finite volume kinetic methods, in 1-D and multi-dimensional cases.

**Conservative methods** We refer to [151, 152, 96], as reference manuals on conservative methods for hyperbolic problems. To introduce finite volume methods, we choose the 1-D system of conservation laws for pressureless gas dynamics:

$$\begin{aligned}\partial_t m + \partial_x(mu_p) &= 0, \\ \partial_t(mu_p) + \partial_x(mu_p^2) &= 0.\end{aligned}\tag{3.38}$$

This system can be written in the form:

$$\partial_t \mathbf{p} + \partial_x(\mathbf{g}(\mathbf{p})) = 0,\tag{3.39}$$

where

$$\mathbf{p} = \begin{pmatrix} m \\ m u_p \end{pmatrix}, \quad \mathbf{g}(\mathbf{p}) = u_p \mathbf{p}.\tag{3.40}$$

In order to cope with the discontinuous solutions arising from the non linear conservation law Eq. (3.39), a finite volume method is well-suited. In fact, finite difference methods can be expected to break down near discontinuities in the solution, where the partial differential equation form of the conservation law, Eq. (3.39) does not hold in the classical sense, but in the sense of distributions. Finite volume methods are based on the integral form of the conservation law, instead of the differential equation. The integral form of Eq. (3.39) is given, for any two points  $x_1$  and  $x_2$ :

$$d_t \int_{x_1}^{x_2} \mathbf{p}(t, x) dx = \mathbf{g}(\mathbf{p}(t, x_1)) - \mathbf{g}(\mathbf{p}(t, x_2)).\tag{3.41}$$

In the finite volume methods, rather than point-wise approximations at grid points, the domain is broken into grid cells, and the cell average of  $\mathbf{p}$  is approximated over each grid cell. The classical finite volume discretization gives evaluation at the center of the cells:  $0 < x_1 < x_2 < \dots < x_N$ , if  $N$  cells are considered. Therefore a cell corresponds to  $[x_{i-1/2}, x_{i+1/2}]$ , where:  $0 \leq x_{1/2} < \dots < x_{i-1/2} < \dots < x_{N+1/2}$ . The  $i^{\text{th}}$  cell average  $\mathbf{p}_i^n$  of  $\mathbf{p}$  at time  $t^n$ , is defined by the integral of  $\mathbf{p}$  divided by the length of the cell:

$$\mathbf{p}_i^n = \frac{1}{\Delta x} \int_{x_{i-1/2}}^{x_{i+1/2}} \mathbf{p}(t^n, x) dx.\tag{3.42}$$

These values are modified by the flux through the edge of the grid cells:

$$\mathbf{p}_i^{n+1} = \mathbf{p}_i^n - \frac{\Delta t}{\Delta x} (\mathbf{F}_{i+1/2} - \mathbf{F}_{i-1/2}),\tag{3.43}$$

where  $\mathbf{F}$  is called the numerical flux function. This form can be naturally obtained by integrating over time interval  $[t^n, t^{n+1}]$  the integral form Eq. (3.41). Therefore the numerical flux function can be seen as an average flux through  $x_{i+1/2}$  over the time interval, [151]:

$$\mathbf{F}_{i+1/2} = \frac{1}{\Delta t} \int_{t^n}^{t^{n+1}} \mathbf{g}(\mathbf{p}(t, x_{i+1/2})) dt. \quad (3.44)$$

The primary problem in finite volume methods is to determine good numerical flux functions that approximate the correct fluxes reasonably well, based on the approximate cell averages, the only data available. Note that in order to obtain high order resolution methods, the cell averages are used to reconstruct a piecewise linear function, used to obtain a more precise evaluation of the numerical flux function. It gives a better accuracy for smooth function, nevertheless, it fails near discontinuities where oscillations are generated. Slope limiters are thus used to detect discontinuity and to avoid local extrema creation. In our case, two main slope limiters are used, that gives, for the example of the mass,  $m = \mathbf{p}(1)$ , the slope  $D_{m_i^n}$  [152]:

- the minmod slope, defined by:

$$D_{m_i^n} = \text{minmod} \left( \frac{m_i^n - m_{i-1}^n}{\Delta x_i}, \frac{m_{i+1}^n - m_i^n}{\Delta x_{i+1}} \right), \quad (3.45)$$

where

$$\text{minmod}(a, b) = \begin{cases} a & \text{if } |a| < |b| \text{ and } ab > 0, \\ b & \text{if } |b| < |a| \text{ and } ab > 0, \\ 0 & \text{if } ab \leq 0, \end{cases} \quad (3.46)$$

- the Monotonized Central-difference limiter (MC limiter), first introduced in [218] defined by:

$$D_{m_i^n} = \text{minmod} \left( \left( \frac{m_{i+1}^n - m_{i-1}^n}{\Delta x_{i-1} + \Delta x_{i+1}} \right), 2 \left( \frac{m_i^n - m_{i+1}^n}{\Delta x_i} \right), 2 \left( \frac{m_{i+1}^n - m_i^n}{\Delta x_{i+1}} \right) \right). \quad (3.47)$$

Furthermore, we want a numerical method able to cope with the delta-shock formation and the emergence of vacuum, described in Section 3.1.3. We then want a method that guaranties a maximum principle on the velocity the positivity of density, and is able to stand cases where the density tends to zero. These requirements enforces us to use a method of at most second-order.

Bouchut *et al.* proposed, in [24], a second-order kinetic scheme designed to solve the pressureless gas system, thus ensuring positivity of density and maximum principle on velocity. They propose first- and second-order kinetic schemes for 1-D and 2-D pressureless gas systems.

**1-D kinetic scheme algorithm** A 1-D finite volume kinetic scheme is developed in [24] for this system. It is based, for  $t \in [t^n, t^{n+1}]$ , on the equivalence between a macroscopic and a microscopic level of description, see Theorem 1:

$$\begin{cases} \partial_t f + u \partial_x f = 0, \\ f(t^n, x, u) = m^n(t^n, x) \delta(u - u_p(t^n, x)). \end{cases} \iff \begin{cases} \partial_t m + \partial_x(mu_p) = 0, \\ \partial_t(mu_p) + \partial_x(mu_p^2) = 0. \end{cases} \quad (3.48)$$

The values of  $m$  and  $u_m$  are then recovered from  $f$  by the formula:

$$\begin{pmatrix} m \\ mu_p \end{pmatrix} (t^{n+1}, x) = \int_{\mathbb{R}} \begin{pmatrix} 1 \\ u \end{pmatrix} f(t^{n+1}, x, u) du. \quad (3.49)$$

In order to obtain the kinetic conservative scheme for the density and the momentum, we thus integrate the equivalent kinetic equation Eq. (3.48) (left) on the control volume  $[x_{i-1/2}, x_{i+1/2}]$  for all the velocities

$u \in \mathbb{R}$  and for time  $t \in [t^n, t^{n+1}]$ , that is to say we take the moment of order zero and one in velocity of the kinetic equation:

$$\int_{x_{i-1/2}}^{x_{i+1/2}} \int_{\mathbb{R}} \int_{t^n}^{t^{n+1}} \begin{pmatrix} \partial_t f \\ u \partial_t f \end{pmatrix} dt dx du + \int_{x_{i-1/2}}^{x_{i+1/2}} \int_{\mathbb{R}} \int_{t^n}^{t^{n+1}} \begin{pmatrix} u \partial_x f \\ u^2 \partial_x f \end{pmatrix} dt dx du = 0. \quad (3.50)$$

Let us define:

$$\begin{pmatrix} m_i^n \\ q_i^n \end{pmatrix} = \frac{1}{\Delta x} \int_{x_{i-1/2}}^{x_{i+1/2}} \begin{pmatrix} m(t^n, x) \\ q(t^n, x) \end{pmatrix} dx, \quad (3.51)$$

with  $q_i^n = m_i^n u_{p_i}^n$  and  $q = m u$ . With these definitions, the integration Eq. (3.50) of the kinetic equation leads to the following scheme:

$$\begin{pmatrix} m_i^{n+1} \\ q_i^{n+1} \end{pmatrix} = \begin{pmatrix} m_i^n \\ q_i^n \end{pmatrix} - \frac{\Delta t}{\Delta x} (\mathbf{F}_{i+1/2} - \mathbf{F}_{i-1/2}), \quad (3.52)$$

with the fluxes given by:

$$\mathbf{F}_{i+1/2} = \begin{pmatrix} F_{i+1/2}^{(1)} \\ F_{i+1/2}^{(2)} \end{pmatrix} = \frac{1}{\Delta t} \int_{t^n}^{t^{n+1}} \int_{\mathbb{R}} \begin{pmatrix} 1 \\ u \end{pmatrix} u f(t, x_{i+1/2}, u) du dt. \quad (3.53)$$

In addition, one can compute the integrals over  $\mathbb{R}^+$  and  $\mathbb{R}^-$  separately, and then the numerical flux can be written in the flux vector splitting form:

$$\mathbf{F}_{i+1/2} = \mathbf{F}_{i+1/2}^+ + \mathbf{F}_{i+1/2}^-. \quad (3.54)$$

These fluxes are obtain under the CFL condition:

$$\Delta t \sup_x |u_p(x)| \leq \min_i \Delta x. \quad (3.55)$$

The comparison with the flux expression for classical finite volume numerical schemes points out that the flux  $\mathbf{g}$  is replaced by  $\int_{\mathbb{R}} f(t, x_{i+1/2}, u) du$ . Indeed, a kinetic scheme involves the NDF  $f$  of the kinetic description for the resolution of the macroscopic quantities,  $m_i$  and  $u_i$ . In order to compute these fluxes, an evaluation of the function  $f$  is needed at some points of the grid. This is done by reconstructing this function from the averaged values  $m_i^n$  and  $q_i^n$ . Let us denote  $\tilde{f}$  this reconstructed function. This function is given at Eq. (3.48). For a first order scheme,  $\tilde{f}$  is piecewise constant so that we have:

$$\mathbf{F}_{i+1/2}^+ = \frac{1}{\Delta t} \int_{t^n}^{t^{n+1}} \int_{\mathbb{R}^+} u \begin{pmatrix} 1 \\ u \end{pmatrix} m_i \delta(u - u_{p_i}^n) du dt = \begin{pmatrix} m_i^n (u_{p_i}^n)_+ \\ m_i^n u_{p_i}^n (u_{p_i}^n)_+ \end{pmatrix}, \quad (3.56)$$

For a second order scheme,  $\tilde{f}$  is piecewise linear, with the adequate slopes:

$$\begin{cases} m^n(x) = m_i^n + D_{m_i^n}(x - x_i), \\ u_p^n(x) = \bar{u}_{p_i}^n + D_{u_{p_i}^n}(x - x_i), \end{cases} \quad (3.57)$$

with

$$\bar{u}_{p_i}^n = u_{p_i}^n - \frac{D_{m_i^n} D_{u_{p_i}^n}}{12 m_i^n} (\Delta x)^2, \quad u_{p_i}^n = \frac{q_i^n}{m_i^n}, \quad (3.58)$$

The bar value  $\bar{u}_{p_i}^n$  is introduced to ensure conservation of momentum, i.e., to satisfy Eq. (3.51). One needs then to evaluate this reconstructed function  $\tilde{f}$ , at time  $t$ . The interest of this approach is that, since  $\tilde{f}$  is solution of Eq. (3.48) for  $t \in [t^n, t^{n+1}]$ , we have  $\tilde{f}(t, x, u) = \tilde{f}(t^n, x - u(t - t^n), u)$ . Therefore, the flux of Eq. (3.53) can be transformed by a change of variable leading to an integral over space [24]:

$$\mathbf{F}_{i+1/2}^+ = \frac{1}{\Delta t} \int_{x_{i+1/2}^L}^{x_{i+1/2}} \begin{pmatrix} m^n(x) \\ m^n(x) u_p^n(x) \end{pmatrix} dx, \quad (3.59)$$



where  $x_{i+1/2}^L$  is the abscissa of the last droplets reaching  $x_{i+1/2}$  at  $\Delta t$ :

$$x_{i+1/2}^L = x_{i+1/2} - \Delta t \frac{(\bar{u}_{p_i}^n + \frac{\Delta x}{2} D_{u_{p_i}^n})_+}{1 + \Delta t D_{u_{p_i}^n}}, \quad (3.60)$$

and

$$\mathbf{F}_{i+1/2}^- = -\frac{1}{\Delta t} \int_{x_{i+1/2}}^{x_{i+1/2}^R} \begin{pmatrix} m^n(x) \\ m^n(x) u_p^n(x) \end{pmatrix} dx, \quad (3.61)$$

where  $x_{i+1/2}^R$  is the abscissa of the last droplets reaching  $x_{i+1/2}$  at  $\Delta t$ :

$$x_{i+1/2}^R = x_{i+1/2} - \Delta t \frac{(\bar{u}_{p_{i+1}}^n - \frac{\Delta x}{2} D_{u_{p_{i+1}}^n})_-}{1 + \Delta t D_{u_{p_{i+1}}^n}}. \quad (3.62)$$

The fluxes, Eq. (3.53), can now be computed, their form depend on the chosen reconstruction. Different reconstructions are described in [24]. In order to ensure the non-negativity of  $m$ , one needs that:

$$|D_{m_i^n} \frac{\Delta x}{2}| \leq m_i^n, \quad (3.63)$$

To guarantee the maximum principle property on the velocity:

$$v_i \leq u(x) \leq V_i, \quad x \in (x_{i-1/2}, x_{i+1/2}), \quad (3.64)$$

where

$$v_i = \min(u_{p_{i-1}}^n, u_{p_i}^n, u_{p_{i+1}}^n), \quad \text{and} \quad V_i = \max(u_{p_{i-1}}^n, u_{p_i}^n, u_{p_{i+1}}^n). \quad (3.65)$$

We need that:

$$\begin{cases} v_i \leq u_{p_i}^n + \frac{\Delta x}{2} D_{u_{p_i}^n} (1 - \frac{D_{m_i^n} \Delta x}{6m_i^n}) \leq V_i. \\ v_i \leq u_{p_i}^n - \frac{\Delta x}{2} D_{u_{p_i}^n} (1 + \frac{D_{m_i^n} \Delta x}{6m_i^n}) \leq V_i. \end{cases} \quad (3.66)$$

An additional condition applies to the velocity. This condition enables us to get an explicit expression of the fluxes by assuming that, piecewise, the velocity slope is such that the droplets do not overtake each other. This condition writes :  $\Delta t D_{u_{p_i}^n} > -1$ . Therefore, we have the restrictions on the slope of  $u_p$ :

$$\begin{aligned} D_{u_{p_i}^n} &\leq \min \left( \frac{V_i - u_{p_i}^n}{\left(1 - \frac{D_{m_i^n} \Delta x}{6m_i^n}\right) \frac{\Delta x}{2}}, \frac{u_{p_i}^n - v_i}{\left(1 + \frac{D_{m_i^n} \Delta x}{6m_i^n}\right) \frac{\Delta x}{2}} \right), \\ D_{u_{p_i}^n} &\geq \max \left( \frac{u_i - u_{p_i}^n}{\left(1 - \frac{D_{m_i^n} \Delta x}{6m_i^n}\right) \frac{\Delta x}{2}}, \frac{u_{p_i}^n - V_i}{\left(1 + \frac{D_{m_i^n} \Delta x}{6m_i^n}\right) \frac{\Delta x}{2}} \right). \end{aligned} \quad (3.67)$$

The slope  $D_{m_i^n}$  is obtain here using a MC limiter to limit the numerical diffusion [49]:

$$D_{m_i^n} = \begin{cases} \min \left( 2 \frac{m_{i+1}^n - m_i^n}{\Delta x}, 2 \frac{m_i^n - m_{i-1}^n}{\Delta x}, \frac{m_{i+1}^n - m_{i-1}^n}{2\Delta x} \right) & \text{if } m_{i-1}^n < m_i^n < m_{i+1}^n \\ \max \left( 2 \frac{m_{i+1}^n - m_i^n}{\Delta x}, 2 \frac{m_i^n - m_{i-1}^n}{\Delta x}, \frac{m_{i+1}^n - m_{i-1}^n}{2\Delta x} \right) & \text{if } m_{i-1}^n > m_i^n > m_{i+1}^n \\ 0 & \text{otherwise} \end{cases}. \quad (3.68)$$

This is different to what is done in [24] where a minmod limiter was used.

The velocity slope  $D_{u_{p_i}^n}$  writes:

$$D_{u_{p_i}^n} = \frac{1}{2} \left( \text{sgn}(u_{p_{i+1}}^n - u_{p_i}^n) + \text{sgn}(u_{p_i}^n - u_{p_{i-1}}^n) \right) \times \min \left\{ \frac{|u_{p_{i+1}}^n - u_{p_i}^n|}{(1 - \Delta x D_{m_i^n} / 6m_i^n) \Delta x}, \frac{|u_{p_i}^n - u_{p_{i-1}}^n|}{(1 + \Delta x D_{m_i^n} / 6m_i^n) \Delta x}, \frac{1}{\Delta t} \right\}, \quad (3.69)$$

To give the fluxes at the interface  $x_{i+1/2}$ , let us denote  $m_{i+1/2}^L$ ,  $m_{i+1/2}^R$ ,  $u_{i+1/2}^L$ ,  $u_{i+1/2}^R$ , the corresponding values of  $m^n(x)$  and  $u_p^n(x)$  at the left and the right of interface  $x_{i+1/2}$  between the cells  $i$  and  $i+1$ :

$$\begin{aligned} m_{i+1/2}^L &= m_i^n + \frac{\Delta x}{2} D_{m_i^n}, \\ m_{i+1/2}^R &= m_{i+1}^n - \frac{\Delta x}{2} D_{m_{i+1}^n}, \\ u_{i+1/2}^L &= \bar{u}_{p_i}^n + \frac{\Delta x}{2} D_{u_{p_i}^n}, \\ u_{i+1/2}^R &= \bar{u}_{p_{i+1}}^n - \frac{\Delta x}{2} D_{u_{p_{i+1}}^n}, \end{aligned} \quad (3.70)$$

so we can have an easy expression for the fluxes:

$$\begin{aligned} F_{i+1/2}^+ &\stackrel{(1)}{=} m_{i+1/2}^L (\alpha_{i+1/2}^L)_+ - \frac{\Delta t}{2} (\alpha_{i+1/2}^L)_+^2 \Gamma_{i+1/2}^+ \stackrel{(1)}{=} m_{i+1/2}^R (\alpha_{i+1/2}^R)_- - \frac{\Delta t}{2} (\alpha_{i+1/2}^R)_-^2 \Gamma_{i+1/2}^- \stackrel{(1)}{=} \\ F_{i+1/2}^- &\stackrel{(1)}{=} m_{i+1/2}^R (\alpha_{i+1/2}^R)_- - \frac{\Delta t}{2} (\alpha_{i+1/2}^R)_-^2 \Gamma_{i+1/2}^- \stackrel{(1)}{=} m_{i+1/2}^L (\alpha_{i+1/2}^L)_+ - \frac{\Delta t}{2} (\alpha_{i+1/2}^L)_+^2 \Gamma_{i+1/2}^+ \stackrel{(2)}{=} \\ F_{i+1/2}^+ &\stackrel{(2)}{=} m_{i+1/2}^L (\alpha_{i+1/2}^L)_+^2 - \frac{\Delta t}{2} (\alpha_{i+1/2}^L)_+^2 \Gamma_{i+1/2}^+ \stackrel{(2)}{=} m_{i+1/2}^R (\alpha_{i+1/2}^R)_-^2 - \frac{\Delta t}{2} (\alpha_{i+1/2}^R)_-^2 \Gamma_{i+1/2}^- \stackrel{(2)}{=} \\ F_{i+1/2}^- &\stackrel{(2)}{=} m_{i+1/2}^R (\alpha_{i+1/2}^R)_-^2 - \frac{\Delta t}{2} (\alpha_{i+1/2}^R)_-^2 \Gamma_{i+1/2}^- \stackrel{(2)}{=} m_{i+1/2}^L (\alpha_{i+1/2}^L)_+^2 - \frac{\Delta t}{2} (\alpha_{i+1/2}^L)_+^2 \Gamma_{i+1/2}^+ \end{aligned} \quad (3.71)$$

with the following definitions:

$$\begin{aligned} (\alpha_{i+1/2}^L)_+ &= \frac{(u_{i+1/2}^L)_+}{1 + \Delta t D_{u_{p_i}^n}}, & (u_{i+1/2}^L)_+ &= \max(0, u_{i+1/2}^L), \\ (\alpha_{i+1/2}^R)_- &= \frac{(u_{i+1/2}^R)_-}{1 + \Delta t D_{u_{p_{i+1}}^n}}, & (u_{i+1/2}^R)_- &= \min(0, u_{i+1/2}^R), \end{aligned} \quad (3.72)$$

and

$$\begin{aligned} \Gamma_{i+1/2}^+ &= \begin{pmatrix} \Gamma_{i+1/2}^+ \stackrel{(1)}{=} \\ \Gamma_{i+1/2}^+ \stackrel{(2)}{=} \end{pmatrix} = \begin{pmatrix} D_{m_i^n} \\ -m_{i+1/2}^L D_{u_{p_i}^n} + (\alpha_{i+1/2}^L)_+ D_{m_i^n} + \frac{\Delta t}{3} D_{m_i^n} D_{u_{p_i}^n} (\alpha_{i+1/2}^L)_+ \end{pmatrix}, \\ \Gamma_{i+1/2}^- &= \begin{pmatrix} \Gamma_{i+1/2}^- \stackrel{(1)}{=} \\ \Gamma_{i+1/2}^- \stackrel{(2)}{=} \end{pmatrix} = \begin{pmatrix} D_{m_i^n} \\ -m_{i+1/2}^R D_{u_{p_i}^n} + (\alpha_{i+1/2}^R)_- D_{m_i^n} + \frac{\Delta t}{3} D_{m_i^n} D_{u_{p_i}^n} (\alpha_{i+1/2}^R)_- \end{pmatrix}. \end{aligned} \quad (3.73)$$

This kinetic scheme can be summarized as illustrated in Fig. (3.1), with the three steps allowing the scheme derivation and the flux computation: kinetic function reconstruction from average values, analytical kinetic evolution of the reconstruction, average values evolution, through numerical fluxes.

Let us now consider the transport of a passive scalar  $\psi$  by the particle mean velocity field  $u_p$ . The number density function then writes:

$$f(t^n, x, u, \psi) = m^n(t^n, x) \delta(u - u_p(t^n, x)) \delta(\psi - \psi_p(t^n, x)),$$

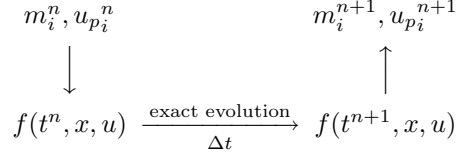


Figure 3.1: Main steps of the kinetic based transport scheme.

where  $\psi_p$  is the mean value of the quantity  $\psi$ .

The system of equations at the macroscopic level writes:

$$\begin{aligned}
\partial_t m + \partial_x(mu_p) &= 0, \\
\partial_t(mu_p) + \partial_x(mu_p^2) &= 0, \\
\partial_t(m\psi_p) + \partial_x(m\psi_p u_p) &= 0,
\end{aligned} \tag{3.74}$$

so that, except at shock locations,  $\psi_p$  verifies a transport equation:  $\partial_t \psi_p + u_p \partial_x(\psi_p) = 0$ .

Another component is added to the fluxes vector:

$$F_{i+1/2}^{(3)} = \frac{1}{\Delta t} \int_{t^n}^{t^{n+1}} \int_{\mathbb{R}} \int_{\mathbb{R}} u \psi f(t, x_{i+1/2}, u) d\psi du dt, \tag{3.75}$$

and after the change of variable leading to an integral over space:

$$F_{i+1/2}^{+(3)} = \frac{1}{\Delta t} \int_{x_{i+1/2}^L}^{x_{i+1/2}^R} m^n(x) \psi_p^n(x) dx, \tag{3.76}$$

where  $x_{i+1/2}^L$  is defined in (3.62). For a first order scheme,

$$F_{i+1/2}^{+(3)} = m_i^n \psi_{p_i}^n (u_{p_i}^n)_+, \tag{3.77}$$

where  $\psi_{p_i}^n$  is the mean value of  $\psi_p$  in the  $i^{th}$  cell. For a second order scheme,  $\psi$  is reconstructed like in (3.57):

$$\psi_p^n(x) = \psi_{p_i}^{\bar{n}} + D_{\psi_{p_i}^n}(x - x_i), \tag{3.78}$$

where

$$\psi_{p_i}^{\bar{n}} = \psi_{p_i}^n - \frac{D_{m_i} D_{\psi_{p_i}^n}(\Delta x)^2}{12m_i^n}, \quad \psi_{p_i}^n = \frac{(m\psi)_i^n}{m_i^n}. \tag{3.79}$$

The flux  $F_{i+1/2}^{(3)}$  reads:

$$\begin{aligned}
F_{i+1/2}^{+(3)} &= m_{i+1/2}^L \psi_{p_{i+1/2}}^L (\alpha_{i+1/2}^L)_+ - \frac{\Delta t}{2} (\alpha_{i+1/2}^L)_+^2 \Gamma_{i+1/2}^{+(3)}, \\
F_{i+1/2}^{-(3)} &= m_{i+1/2}^R \psi_{p_{i+1/2}}^R (\alpha_{i+1/2}^R)_- - \frac{\Delta t}{2} (\alpha_{i+1/2}^R)_-^2 \Gamma_{i+1/2}^{-(3)},
\end{aligned} \tag{3.80}$$

and

$$\begin{aligned}
\Gamma_{i+1/2}^{+(3)} &= m_{i+1/2}^L D_{\psi_{p_i}^n} + \psi_{p_{i+1/2}}^L D_{m_i^n} - \frac{2\Delta t}{3} D_{m_i^n} D_{\psi_{p_i}^n} (\alpha_{i+1/2}^L)_+, \\
\Gamma_{i+1/2}^{-(3)} &= m_{i+1/2}^R D_{\psi_{p_i}^n} + \psi_{p_{i+1/2}}^R D_{m_i^n} - \frac{2\Delta t}{3} D_{m_i^n} D_{\psi_{p_{i+1/2}}^n} (\alpha_{i+1/2}^R)_-.
\end{aligned} \tag{3.81}$$

Given the difficulties linked to the multi-dimensional kinetic schemes, and since we aim at computing academic configurations with quadrilateral grids, the **dimensional splitting**, also called alternating direction technique (ADI), see [96] and [152] and references therein, appears as a very interesting alternative. Indeed, it offers:

- an easy implementation,
- a great efficiency, since second order method with linear reconstruction can be used, as we perform a mono-dimensional transport,
- an easy extension to the aimed configurations, i.e. to 2-D, 2-D axisymmetric and 3-D domains. The two last types of configurations are used in [49].

Moreover, since each transport is done with step  $\Delta t$ , there is no CFL reduction. One can note that this technique cannot be used for unstructured grids, nearly always encountered in industrial realizations. Therefore the study of a numerical scheme, with the greater efficiency in multi-dimensional configurations with unstructured mesh, is still to be done. For example, the detailed analysis of the numerical schemes implemented in the semi-industrial code AVBP, co-developed at IFP Energies nouvelles and CERFACS, provided in [141], shows the necessity to develop a finite volume cell-vertex formulation of the kinetic scheme. Nevertheless, this is not the aim of the present work, where first realizations of the multi-fluid methods are given, providing ideas on the feasibility of such computations.

### 3.2.3 Phase space transport resolution: full ODE system with Radau5, and simplified framework for drag-evaporation resolution

The phase transport step corresponds to the resolution of the ODE system Eq. (3.37). The polydispersion resolution leads to a multi-scale problem. Indeed, droplets of different sizes have different response time to the physical phenomena. The ODE integrator must then be carefully chosen.

As mentioned in Section 1.2, in the context of this PhD, the phase space dynamics is limited to evaporation and drag with simple models, in order to precisely evaluate the resolution models and methods proposed in Part II and Part III. On the other hand, in the context of the PhD of Stéphane de Chaisemartin the phase space transport is solved in a more general context, with more complex models for evaporation and drag force, and possibly heat transfer and particle interactions. An ODE resolution scheme is then used.

#### Radau5 Program

The evolution of the droplet behavior with their inertia can lead to several time scales in the problem, and then to stiffness. The Runge-Kutta implicit methods are particularly well suited for stiff problems, see for example [106]. It is designed to solve equations of the following profile:

$$d_t(y) = \Psi(t, y), \quad (3.82)$$

The implicit Runge Kutta method based on Radau quadrature is called Radau IIA. We choose a 5<sup>th</sup> order version of this integrator. This method is shown to be A-stable in [106]. Furthermore, this method is L-stable, that allows a very fast convergence, with a fast high frequency absorption. This property is of importance for multi-fluid simulation as low inertia droplet velocity relaxes very rapidly to gas velocity, under drag force effect. This Radau IIA method is implemented in the program RADAU5, written by Hairer, see [106]. We refer to [106] and [49] for details.

#### Drag-evaporation simplified framework

One of the achievements of the PhD of Stéphane de Chaisemartin has been to implement the Radau5 algorithm in the MUSES3D code dedicated to spray resolution Chapter 7. Our purpose is to implement the methods explained in Part II and Part III in this code to evaluate their potential. Unfortunately, as explained in Chapter 5, in the context of the high order size moment method, the stability conditions

imposed by the model prevents the use of an ODE solver for the resolution of the evaporation terms. Therefore, a simplified framework is considered for phase space transport including drag and evaporation. We use, in this approximation, a modified Strang splitting and we will treat separately the two terms in a phase space transport step, alternating the order with iterations:

1. iteration  $2n$ 
  - solve evaporation term during  $\Delta t$ ;
  - solve drag term during  $\Delta t$ ;
2. iteration  $2n+1$ 
  - solve drag term during  $\Delta t$ ;
  - solve evaporation term during  $\Delta t$ .

**Drag term** We need to solve, for the drag term, the following system:

$$\begin{aligned}\partial_t m^{(j)} &= 0, \\ \partial_t(m^{(j)} \mathbf{u}_p^{(j)}) &= m^{(j)} \mathbf{D}_{r,p}^{(j)},\end{aligned}\tag{3.83}$$

with:

$$\mathbf{D}_{r,p}^{(j)} = \frac{1}{St_0 S_{\text{mean}}^{(j)}} (\mathbf{u}_g - \mathbf{u}_p^{(j)}),\tag{3.84}$$

One notes that in the case of a steady gas phase, system Eq.(3.83) can be solved exactly for a stationary gas velocity:

$$\begin{aligned}m^{(j),n+1} &= m^{(j),n}, \\ m^{(j),n+1} \mathbf{u}_p^{(j),n+1} &= m^{(j),n} \left( \mathbf{u}_g + (\mathbf{u}_p^{(j),n} - \mathbf{u}_g) \exp\left(-\frac{\Delta t}{St_0 S_{\text{mean}}^{(j)}}\right) \right).\end{aligned}\tag{3.85}$$

But to be general, we will still consider the resolution of the drag term through `Radau5`.

**Evaporation method** The numerical method used to solve the evaporation in the context of multi-fluid resolution is based on a  $\theta$ -scheme. Since the method derived for the high order size moment method is completely different there is no interest to present it in the context of this work. We refer to [144] and [145] for explanations on that scheme.

### 3.3 Achievements of the multi-fluid model

Some of the major achievements of the multi-fluid model are presented in this section. These achievements are presented with results obtained in two configurations with the `MUSES3D` code presented in Chapter 7. The first configuration involves a spray flow in a gaseous velocity field constituted by the Taylor-Green vortices. The second one involves a free-jet in an unsteady flow configuration. The detail of these configurations are presented here. They will be reused to assess the potential of the `EMSM` and `EMVM` in the following.

The simulations are conducted with an academic solver, `MUSES3D` [49, 172], using the models presented in this chapter, and presented in Chapter 7. The Reynolds number based on  $U_0$ ,  $\nu_0$  and  $L_0$  is 1,000, where  $U_0$  is the injection velocity and  $L_0$  is the jet width. We consider a characteristic velocity of  $U_0 = 1$  m/s and  $L_0 = 1.5 \times 10^{-2}$  m, as well as a typical value of  $\nu_0 = 1.6 \times 10^{-5}$  m<sup>2</sup>/s. The gas and the liquid density are such that  $\rho_l/\rho_g = 565$ . Finally, we denote by  $d_0$  the the diameter corresponding to the typical droplet surface  $S_0$  used in the computation of the Stokes number.

### 3.3.1 Illustration on a two-dimensional vortical flow

This test case shows the ability of the multi-fluid to describe dynamics conditioned by size. We set up the Taylor-Green vortices configuration described above, for the gas phase, and a motionless droplet field Fig. (3.2). The size distribution for the droplets is the constant size distribution represented on Fig. (3.3). The value of the size distribution is set in order that the total droplet mass is initiated at 1 Fig. (3.2)-right. The multi-fluid is run with ten sections, with a characteristic diameter  $d_0 = 37.5\mu m$ , with a corresponding Stokes number  $St_0 = 0.185$ . In the context of the size constant size discretization explained in Section 3.1.2, the Stokes numbers of the sections range from  $St = 0.167$  for  $j = 10$  to  $St = 0.01$  for  $j = 1$ .

Meanwhile, as explained in [49], there exists a critical value of the Stokes number  $St_c$  under which particles are not inertial enough to be ejected from the vortices. The theoretical value of  $St_c$  is  $1/8\pi \approx 0.04$ . Above this value, particles can be ejected from the vortices. Crossing trajectories may then occur, so that, in the context of Taylor-Green vortices, the number  $St_c$  sets the limit of the validity domain of the equivalence between the kinetic and macroscopic levels of description stated in Section 3.2.2.

One can notice that  $St < St_c$  for section 1 whereas  $St \gg St_c$  for section 10. One expects thus to see a segregation due to droplet size, first in seeing different dynamics according to their size, but also, in seeing that droplets of the first size sections stay in vortices, whereas the other droplets are ejected from them. For this computation we consider a  $200 \times 200$  grid, with periodic boundary conditions on each edge. The CFL is set to 1. The computation is run until  $t = 2$ , which corresponds to one lap of the vortex.

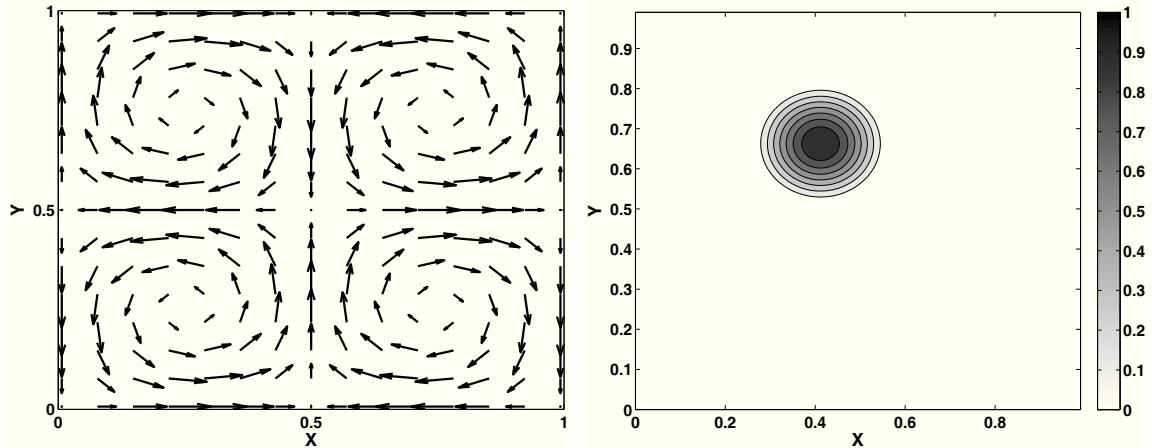


Figure 3.2: (left) Taylor-Green configuration for the gas vorticity field, (right) Initial condition for the droplets, composed of a motionless cloud. The droplet mass is represented, which is reconstructed from the first four size moments:  $(m_0, m_1, m_2, m_3)$

The mass field for each section is displayed in Fig. (3.4) and Fig. (3.5). For the sake of clarity, we choose to display the mass corresponding to odd-number sections only, from the lowest ( $j = 1$  to the highest  $j = 9$ ). Results are shown for two instants,  $t = 1$ , and  $t = 2$ .

Focusing on Fig. (3.4), for  $t = 1$ , one can assess the different of mass field from each section to another. It first shows that droplets belonging to section 1 are captured by the vortices, as predicted. Since the cloud has been initiated between two different vortices areas, the top-left and top-right, they are dragged within each of these vortices, the highest particle number being in the top-left vortex. Concerning the other sections, the observed different dynamics are due to the drag relaxation times, increasing with the section number. Physically, particles are first dragged by the top-left vertex, until they reach the left edge of the domain. Because of periodic boundary conditions, they enter the right vortices (top and bottom). Since their dynamics is opposed to the vortices (their x-velocity is negative, whereas the right vortices x-velocity is positive), they are decelerated. Therefore, the bigger the particle size is, the deeper

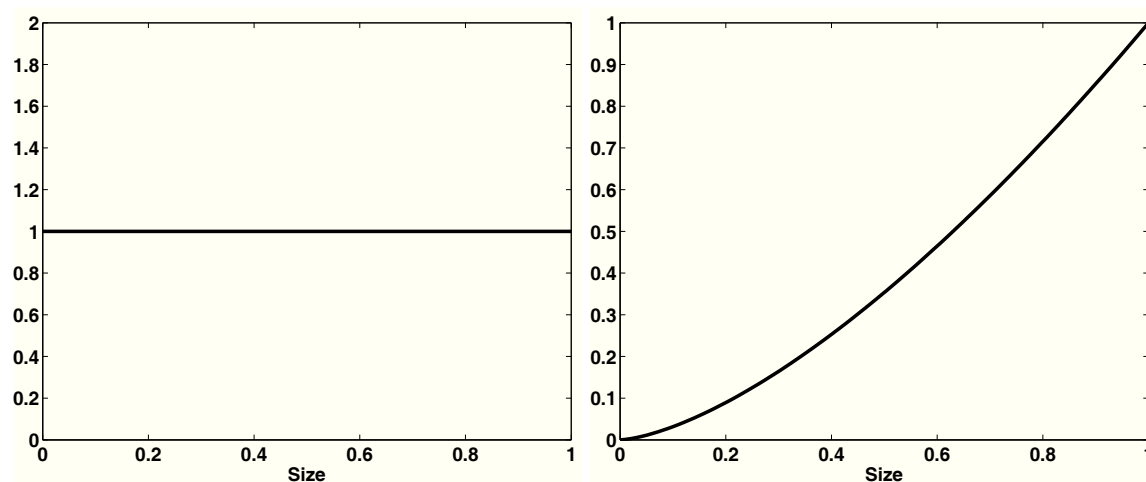


Figure 3.3: (left) Initial size distribution for the particles. (right) Corresponding mass distribution

the particle penetrate into the vortices. The same explanation goes for Fig. (3.5).

This test case also assesses the capacity of the scheme to capture  $\delta$ -shocks, some of which appearing already at time  $t = 1$ . We already mentioned that, when they enter the top-right vertex, droplet have a dynamics opposed to the gaseous velocity field. For example, in Fig. (3.4), accumulation of particles occur at the front of the field when entering the right vortices. One can note the robustness of the advection scheme in these situations.

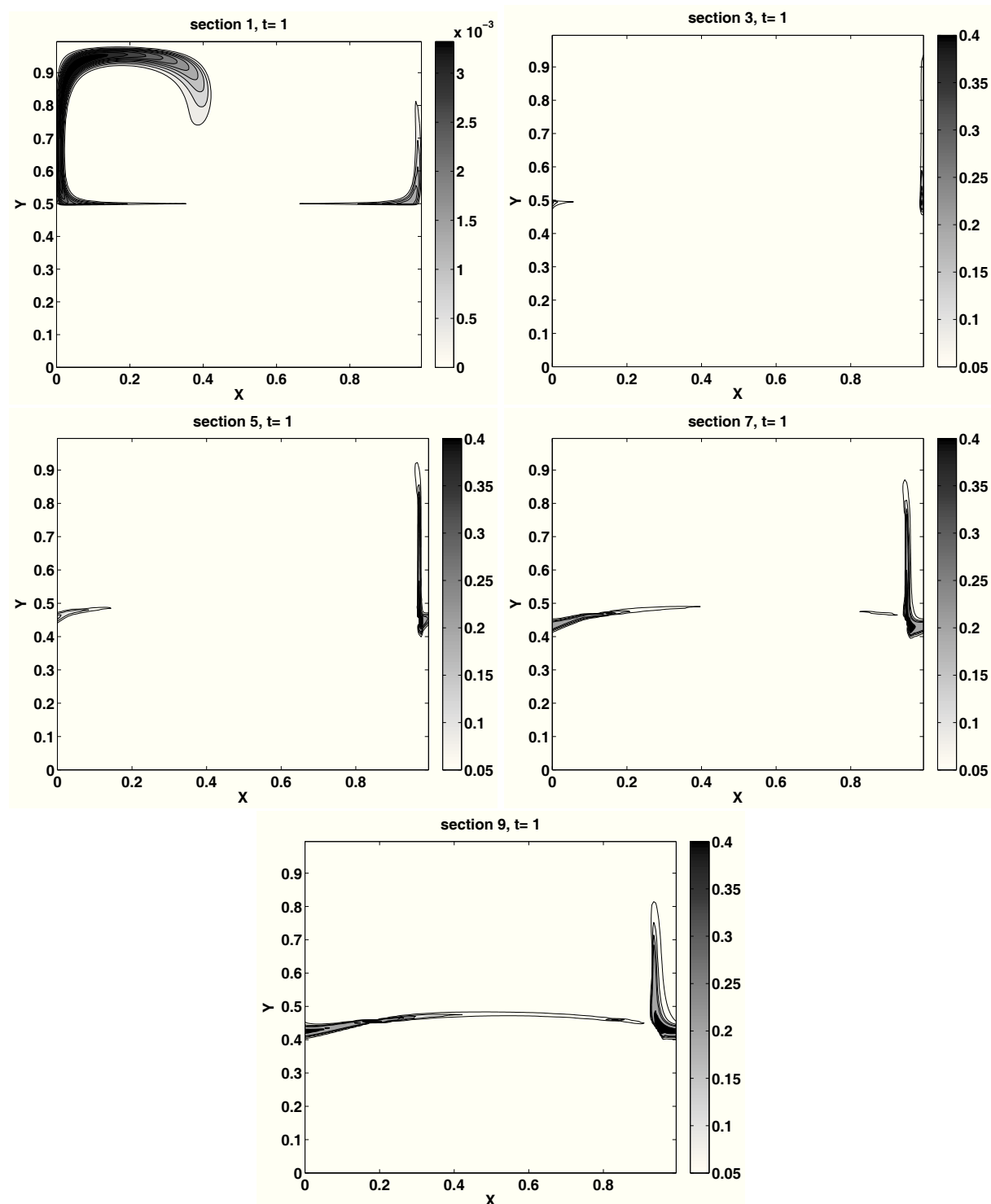


Figure 3.4: Eulerian droplet mass at time  $t = 1$ . Results for section 1, 3, 5, 7, 9. 6 iso-contours for the values  $2 \cdot 10^{-2}$ ,  $5 \cdot 10^{-2}$ , 0.1, 0.2, 0.3, 0.4, for sections 3 to 9, and 10 iso-contours from 0 to the maximum value for section 1



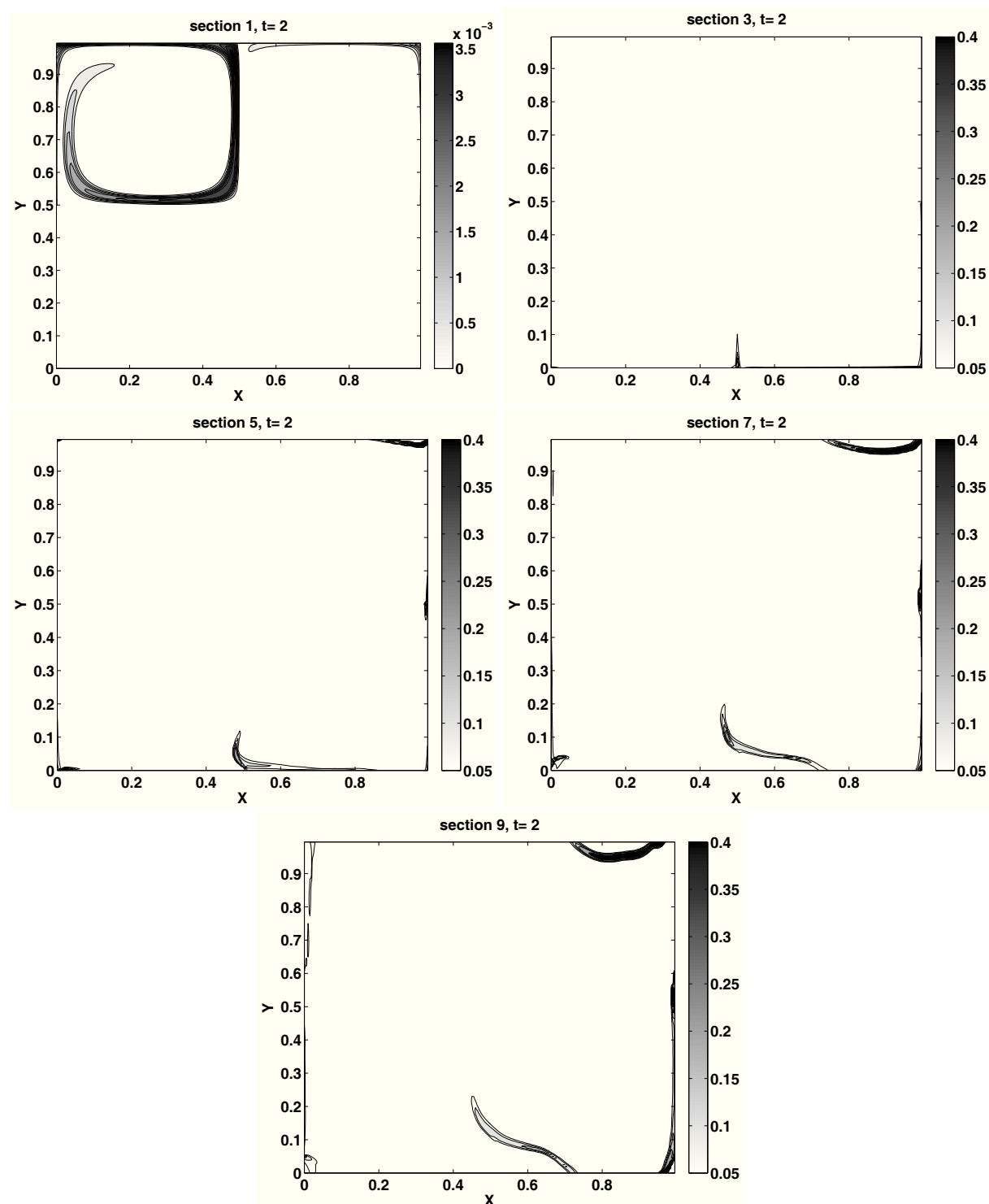


Figure 3.5: Eulerian droplet mass at time  $t = 2$ . Results for section 1, 3, 5, 7, 9. 6 iso-contours for the values  $2 \cdot 10^{-2}$ ,  $5 \cdot 10^{-2}$ , 0.1, 0.2, 0.3, 0.4, for sections 3 to 9, and 10 iso-contours from 0 to the maximum value for section 1

### 3.3.2 Validation on a free-jet configuration

In order to assess the Eulerian methods we focus on a 2-D free jet. A polydisperse spray is injected in the jet core. The simulations are conducted with an academic solver, coupling the ASPHODELE solver [200] with the multi-fluid solver MUSES3D. The ASPHODELE solver couples a Eulerian description of the gas phase with a Lagrangian description of the spray. One of the key features of this simulation tool is to allow, in the framework of one-way coupling, the simultaneous computation of the gas phase as well as both Lagrangian and Eulerian spray descriptions within the same code.

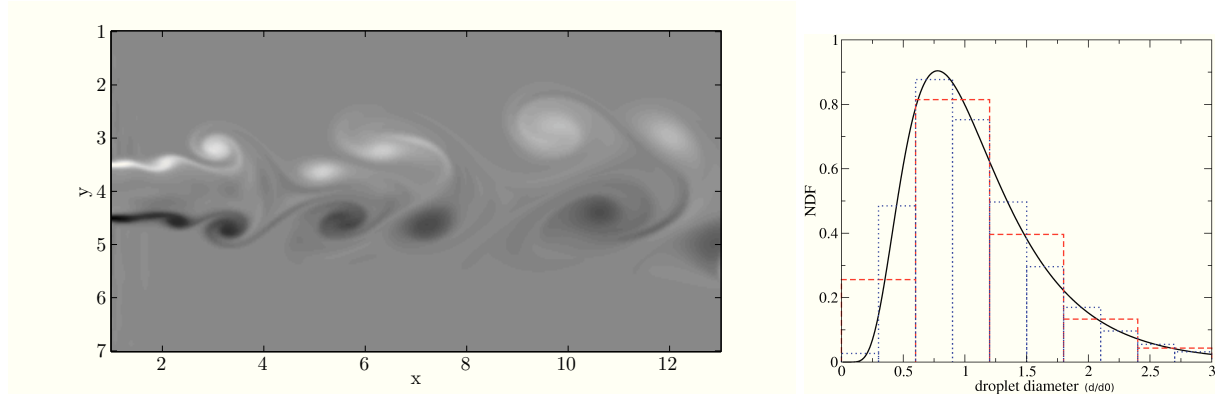


Figure 3.6: Free-jet configuration at time  $t = 20$ . (Left) Gas vorticity on a  $400 \times 200$  grid. (Right) Polydisperse lognormal distribution discretized with 5 and 10 sections.

As far as the gas phase is concerned, we use a 2-D Cartesian low Mach number compressible solver. The gas jet is computed on a  $400 \times 200$  uniformly spaced grid. To destabilize the jet, we inject turbulence using the Klein method with 10% fluctuations [135]. We use the same characteristic quantities as presented in Section 3.3.1. The gas vorticity is presented in Fig. (3.6)-left. Since we aim at validating the Eulerian models through comparisons to a Lagrangian simulation, and to show the importance of the description of the polydispersity, we restrict ourselves to one-way coupling.

#### 3.3.2.1 Comparison to Lagrangian simulations

In this first case, the lognormal distribution Figure 3.6-right is used for the injected spray. We take as a reference solution for the liquid phase a Lagrangian DPS with particle numbers in the computational domain ranging from 10,000 to 70,000 depending on the case. The number of droplets for each case is determined by stoichiometry. We provide comparisons between the Lagrangian reference and the Eulerian multi-fluid computations by plotting the Lagrangian particle positions versus the Eulerian number density. Using the multi-fluid description, we perform the comparisons for different ranges of droplet sizes and thus for different Stokes numbers, for evaporating and non-evaporating cases.

**3.3.2.1.1 Free-jet non-evaporating test case** For the non-evaporating case we use five sections for the multi-fluid simulation (see Fig. (3.6)-right). We have 70,000 Lagrangian particles in the computational domain at the considered time. We first present a comparison for low-inertia droplets and find a very good agreement for the droplets with a Stokes range from 0.011 to 0.12, corresponding to diameters between  $9 \mu\text{m}$  and  $30 \mu\text{m}$ , as shown in Fig. (3.7)-left. The multi-fluid model is thus shown to simulate well the dynamics of a polydisperse spray for relatively small Stokes numbers. Droplet dynamics are close to the gas dynamics for this range of sizes, and therefore the model remains in its domain of validity (see Section 3.1). For higher Stokes numbers the droplets are ejected from the vortices and trajectories crossings are likely to occur, breaking the monokinetic multi-fluid assumption described in Section 3.1. Nevertheless, the dynamics are still very well reproduced for high-inertia droplets. The results are plotted in Fig. (3.7)-right for Stokes numbers from 0.48 to 1.1, corresponding to diameters from  $60 \mu\text{m}$  to  $90 \mu\text{m}$ .

One can notice that the number density is concentrated in a few cells in this case and that the numerical method does not encounter any problems to capture the distribution, illustrating its robustness.

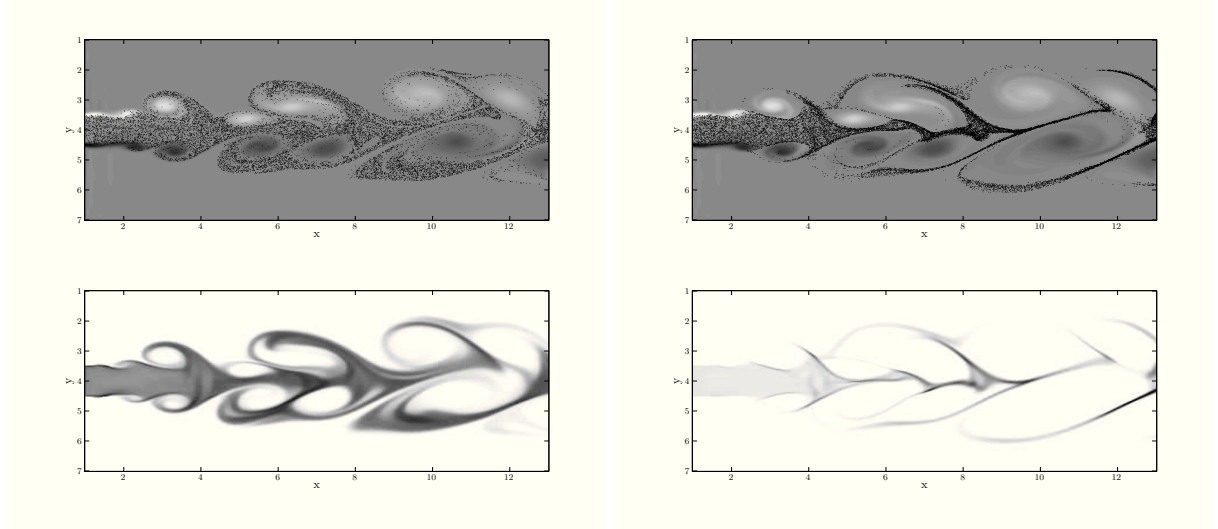


Figure 3.7: Non-evaporating polydisperse spray at time  $t = 20$ . (Left) Low-inertia droplets with Stokes 0.011 to 0.12, corresponding to diameters from 9 to 30  $\mu\text{m}$ . (Right) High-inertia droplets with Stokes 0.48 to 1.1, corresponding to diameters from 60 to 90  $\mu\text{m}$ . (Top) Lagrangian particle positions with 40,000 particles over gas vorticity. (Bottom) Eulerian number density on a  $400 \times 200 \times 5$  grid.

**3.3.2.1.2 Free-jet evaporating test case** The free-jet case is assessed here with an evaporating spray. For the  $d^2$  law, we take a constant mass-transfer number  $Bm = 0.1$ . The corresponding non-dimensional evaporation coefficient is  $K = 0.07$ . The results are presented in the same manner as for the non-evaporating case. In order to describe accurately the evaporation process, we take ten sections for the multi-fluid simulation, whereas 30,000 Lagrangian particles are present in the domain at the time considered. As in the non-evaporating case, we find a very good agreement between the Eulerian and the Lagrangian descriptions. For low-inertia droplets, the comparison is shown in Fig. (3.8)-left, with Stokes numbers from 0.011 to 0.12, corresponding to diameters  $d_0 = 9 \mu\text{m}$  to  $d_0 = 30 \mu\text{m}$ . For high-inertia droplets, the comparison is shown in Fig. (3.8)-right, with Stokes number from 0.48 to 1.1, corresponding to diameters from 60  $\mu\text{m}$  to 90  $\mu\text{m}$ .

The polydisperse evaporating free-jet case shows the ability of the multi-fluid method to treat more complex flows, closer to realistic configurations. Using these comparisons, we demonstrate that the multi-fluid model captures size-conditioned dynamics that carry droplets of different sizes to different locations. It is then essential to evaluate the ability of the Eulerian model to capture the evaporation process as a whole.

**3.3.2.1.3 Gas-phase fuel mass fraction** Our interest being in combustion applications, a key issue of evaporating spray modeling is the prediction of the gas-phase fuel mass fraction. We thus present comparisons between the gas-phase fuel mass fraction obtained from the Lagrangian and Eulerian descriptions of the spray. These results are found with the same coupled codes used in the previous section, the spray being described on the one hand by the Lagrangian method and on the other hand by the multi-fluid model. These simulations are again done using one-way coupling. As a consequence, the evaporated fuel is not added as a mass source term in the gas-phase equations, but is stored in two passive scalars, one for each description of the spray, that are transported by the flow. The Lagrangian gas-phase fuel mass fraction is obtained through a projection of the droplet evaporation over the neighbor cells of the computational mesh. This procedure is described in [49]. These two fields are plotted in Fig. (3.9). One

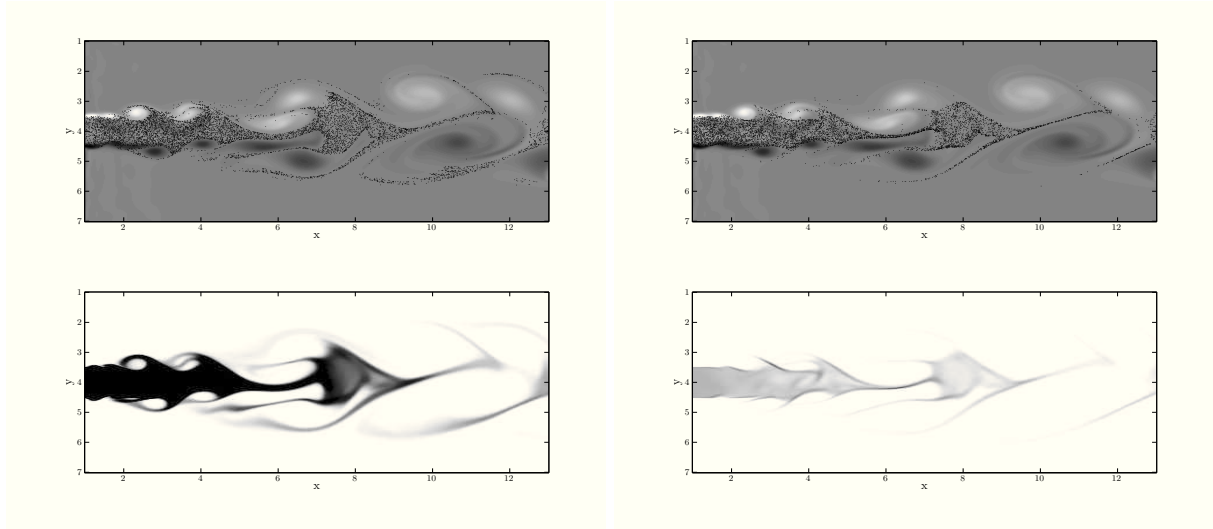


Figure 3.8: Evaporating polydisperse spray at time  $t = 20$ . (Left) Low-inertia droplets with Stokes 0.011 to 0.12, corresponding to diameters from 9 to 30  $\mu\text{m}$ . (Right) High-inertia droplets with Stokes 0.48 to 1.1, corresponding to diameters from 60 to 90  $\mu\text{m}$ . (Top) Lagrangian particle positions with 40,000 particles over gas vorticity. (Bottom) Eulerian number density on a  $400 \times 200 \times 5$  grid.

can see the very good agreement of both descriptions for spray evaporation. This comparison underlines the efficiency of the multi-fluid model in describing polydisperse evaporating sprays. Furthermore, as can be seen on Fig. (3.9), the Eulerian description provides a smoother field than the Lagrangian one. This illustrates the difficulties that arise when coupling the Lagrangian description of the liquid to the Eulerian description of gas, and underlines the advantage of the Eulerian description of the spray for the liquid-gas coupling. These results represent a first step towards combustion computations with full two-way coupling.

### 3.3.2.2 Importance of the treatment of polydispersity

Our objective in this section is to highlight the key role of polydispersity in the description of the dynamics of the droplets. We consider the same free-jet configuration as detailed previously but with a constant size distribution of the injected spray. We compare results obtained using one and ten size sections for the evaporative case. The constant mass-transfer number is set as  $Bm = 0.1$ . The corresponding non-dimensional evaporation coefficient is  $K = 0.07$ . The Stokes number of the droplets in the one-section case is  $St = 1.88$  ( $d_0 = 119 \mu\text{m}$ ). In the case of ten sections, the Stokes number ranges from  $St = 0.0188$  ( $d_0 = 12 \mu\text{m}$ ) to 2.86 ( $d_0 = 147 \mu\text{m}$ ). Two results are provided, the first shows the spray number density, and the second the gas-phase fuel mass fraction.

When focusing on the number density (Fig. (3.10)), it is obvious that the global evaporation rate strongly depends on the refinement of the description of polydispersity. The evaporation, when considering one section, is highly underestimated in comparison to the evaporation when considering ten sections. This can be understood by considering the transfer coefficients given in Eq. (3.16). For the higher sections, the evaporative coefficients  $E_2^{(j)}$  are lower than the global coefficient in the case with one section. The opposite is true for the lower sections. Adding the fact that there is a mass flux from the higher sections to the lower ones leads us to the result of Fig. (3.10). Backing up this conclusion, it can be seen in Fig. (3.11) that the gas-phase fuel mass is higher in the computation with ten sections.

Furthermore, the dynamics observed are quite different from the spray with one section to the spray with ten sections. First, as can be seen in Figure 3.11, when we focus on the free outlet zone, the gas-phase fuel mass fraction is higher with one section than with ten sections, whereas the opposite is true everywhere else in the domain. Indeed, the high evaporation rate has almost made the totality

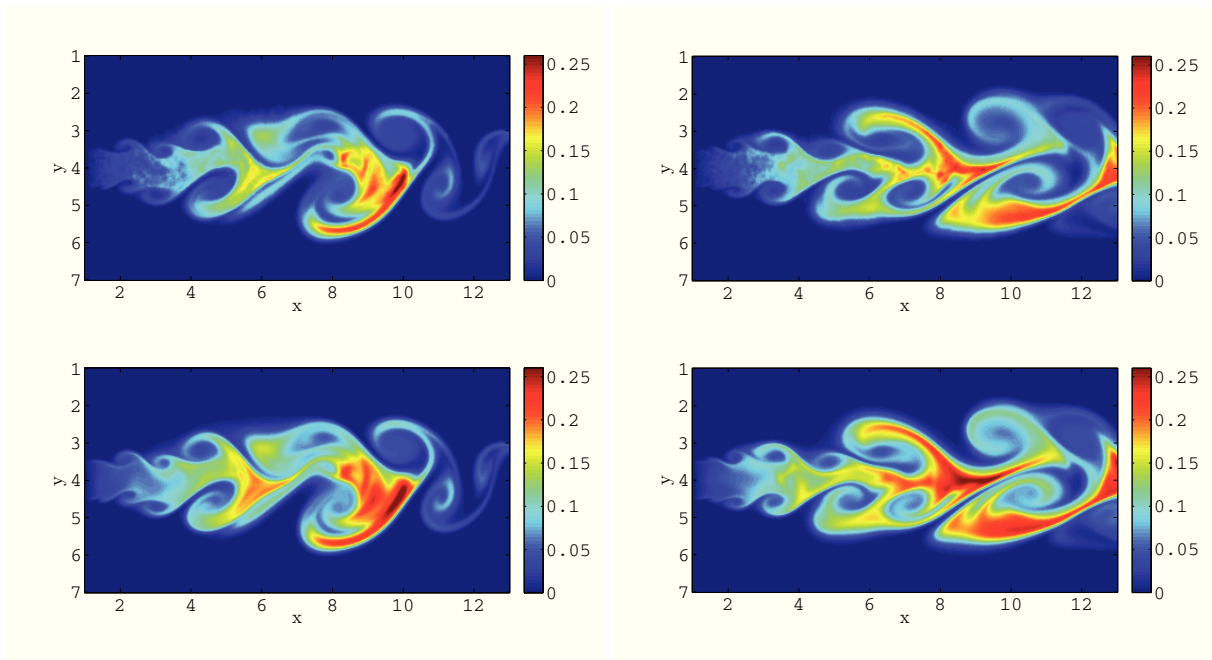


Figure 3.9: Comparison of the gas-phase fuel mass fraction at times  $t = 15$  (left) and  $t = 20$  (right). (Top) Lagrangian method with 30,000 droplets. (Bottom) Eulerian multi-fluid model on  $400 \times 200 \times 10$  mesh.

of the spray disappear, so that at the very end of the jet, only small droplets with low mass remain. On the contrary, with one section, the spray does not evaporate at as high a rate, which leads to the situation where the remaining liquid mass is much higher with one section than with ten sections. Thus the evaporation rate, proportional to the mass, becomes higher with one section.

A purely dynamic effect is observed in the gas-phase vortex interacting with the droplets whose repartition within the vortex depends on their size. For the one-section case, there is no segregation as a unique size is considered. In particular, there are no droplets at the center of the vortex. In contrast, with ten sections the segregation by size is significant. The bigger droplets are on the outer edge of the vortex, whereas the smaller ones remain near the center. These differences between the two models with respect to polydispersity have far-reaching consequences, since the accurate representation of the spatial distribution of the gas-phase fuel mass fraction is a key requirement for combustion applications.

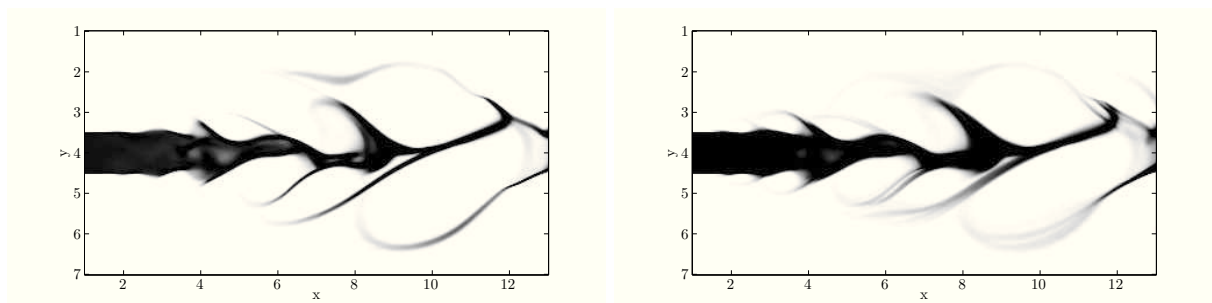


Figure 3.10: Total number density of the polydisperse evaporating spray at time  $t = 20$ . (Left) Multi-fluid model with one section. (Right) Multi-fluid model with ten sections.

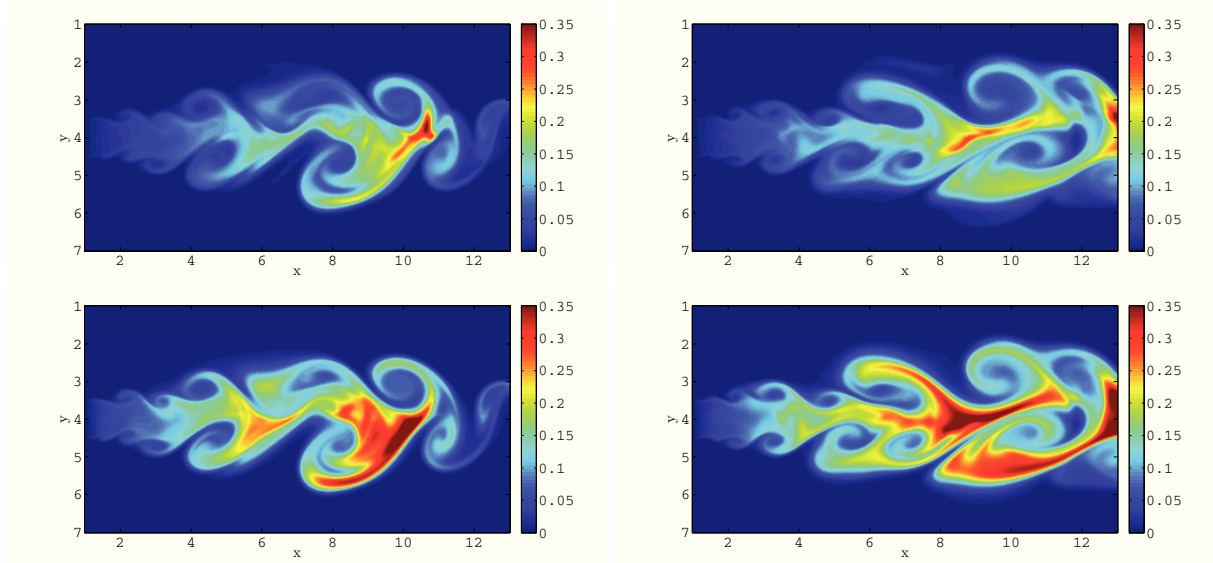


Figure 3.11: Comparison of the gas-phase fuel mass fraction at times  $t = 15$  (left) and  $t = 20$  (right). (Top) Multi-fluid model with one section. (Bottom) Multi-fluid model with ten sections.

### 3.4 Limitations of the multi-fluid model and need for high order moment methods

In the history of spray models, the multi-fluid represented a breakthrough, as it was able to describe polydispersity without assuming the general form of the size NDF (even though a size NDF is presumed in each section with the function  $\kappa^{(j)}$ ), as well as the size velocity correlation, a key issue in evaporating spray simulations. Moreover, through his PhD thesis, Stéphane de Chaisemartin showed that three dimensional computations were possible with the multi-fluid model in a reasonable time. However, the multi-fluid model still suffers from two major drawbacks, regarding the objective of proposing a serious alternative to Lagrangian methods for industrial computations: the precision of the size distribution, reconstruction, and its inability to describe particle trajectory crossing (PTC).

#### 3.4.1 Accuracy shortage in the description of polydispersity

##### Cost of the method

The main drawback of the multi-fluid model is the cost associated to the resolution of the  $N_s$  systems of conservation laws, needed to obtain the evolution of the droplet mass in the sections. Indeed it has been shown [49] that the multi-fluid model is a first order method in size, with potential extension to second order [145], and thus a high number of sections, with a minimum at ten sections, may be needed to obtain a precise description of the evaporation process. This raises a twofold problem, in terms of theory and of practical computation. First, in terms of applied mathematics, one may want to overcome this low order limitation and thus to design a high order method in size. Moreover, as shown in Fig. (3.11), the results are very different whether one or ten sections are considered. These results tend to show that a minimum number of sections is required to get an acceptable accuracy. Although this number varies according to the physical case studied, the number of 10 sections can be considered a milestone for acceptable polydispersity description. But then the computational cost is multiplied by 10, and is way too prohibitive in an industrial context.

This accuracy shortage has two aspects:

- The first one and most critical is diffusion in the size phase space when evaporation is involved

- The second one, not exclusive to the multi-fluid model, is diffusion in physical space.

We provide an illustration in a configuration emphasizing this shortage. The Taylor-Green configuration for the gas phase is taken up, with a motionless droplet cloud, but, contrary to Section 3.3.1, here the maximum droplet diameter is  $d_0 = 15\mu m$ , a much smaller value than in Section 3.3.1. This value of maximum droplet diameter is chosen in order that the Stokes number of the biggest droplets  $St = 0.03$  is still lower than the critical Stokes number  $St_c = 1/8\pi$ . Results are provided for different discretizations of the size phase space: 10 and 40 sections. The sprays are evaporating, with an evaporation coefficient  $K = 0.27$ .

### Diffusion in size phase space

Figures Fig. (3.12) and Fig. (3.13) display the dynamics of the spray equi-distributed between  $t = 0.5$  and  $t = 2$ , for the multi-fluid model with 10 and 40 sections, respectively. Focusing on the results for the final time, one can first notice that the results are similar for the two types of discretization. However, this is not the expected result. Indeed, Fig. (3.15) exhibits the evolution of the mean particle surface of the total distribution through evaporation, in the analytical case, and for the multi-fluid model with 10 and 40 sections. Although the multi-fluid model with 40 still overestimates the mean particle surface, it is closer to the analytical solution than the multi-fluid model with 10 sections. The explanation for this surprising similarity is given in Fig. (3.14) displaying the resulting mass of particles such as  $S^{(j)} < 0.5$  (the first 5 sections in the 10 section case, and the first 20 sections in the 40 section case) first, and  $S^{(j)} > 0.5$  (the remaining sections) then. These results are shown for  $t = 2$ , when, given the value of the evaporation coefficient, there must be almost no particle such as  $S^{(j)} > 0.5$ . If this is the case for the 40 section model, there is still a considerable mass of this droplets in the 10 section case. This resulting mass is due to diffusion in size phase space. The second conclusion to be drawn from Fig. (3.14) is that the dynamics of particles such as  $S^{(j)} < 0.5$  have the expected behavior, i.e they are more dragged by the gas in the 40 section case than in the 10 section case.

### Size conditioned physical space numerical diffusion

One the other, hand, still in Fig. (3.14), one can notice that particles such as  $S^{(j)} > 0.5$  seem to be more dragged in the 10 section case than in the 40 section one. This is actually not due to drag but to numerical diffusion. Indeed, since each section has its own dynamics, local CFL numbers condition the physical transport resolution section by section. In the chosen configuration, the droplets of the lowest section (i.e the smallest droplets) have the highest velocity, because they have the lowest Stokes number. As a result, the higher the section is, the lower its local CFL number is, and the bigger the numerical diffusion is. Therefore, discretization of the size phase space inevitably brings some numerical diffusion. These two types of diffusion, in size phase space and in physical space, overshadow the expected dynamics of the particles such as  $S^{(j)} < 0.5$ . The combination of these effects leads to the observed results in Fig. (3.12) and Fig. (3.13).

### Coupled phase and physical space diffusions

These two types of diffusion are coupled. Indeed, after a deeper analysis of Fig. (3.12) and Fig. (3.13), although the maximum diameter is taken such that all the particle Stokes number is lower than the critical Stokes number, one can observe a non-negative mass field into the bottom vortices. This reveals the fact that some droplets have been ejected from the top vortices. What happens is that the resolution of the evaporation term results in mass and momentum fluxes between sections, see Section 3.1.2. Accordingly, droplets present in section  $j$  at a given time may originate from sections  $j + p$  ( $p \geq 1$ ). Thus, following a droplet trajectory, one will notice that its Stokes number dynamically evolves as it may change section because of its size decrease. This coupling is illustrated in Fig. (3.16), where mass fields of section 1 and 2 are displayed at time  $t = 2$  in an evaporating case and a non-evaporating case. Numerical diffusion always occurs for particles of the second section. But for the first section, there is no particle ejection in the non-evaporating case, and in the evaporating case, ejection is due to the evaporation flux from

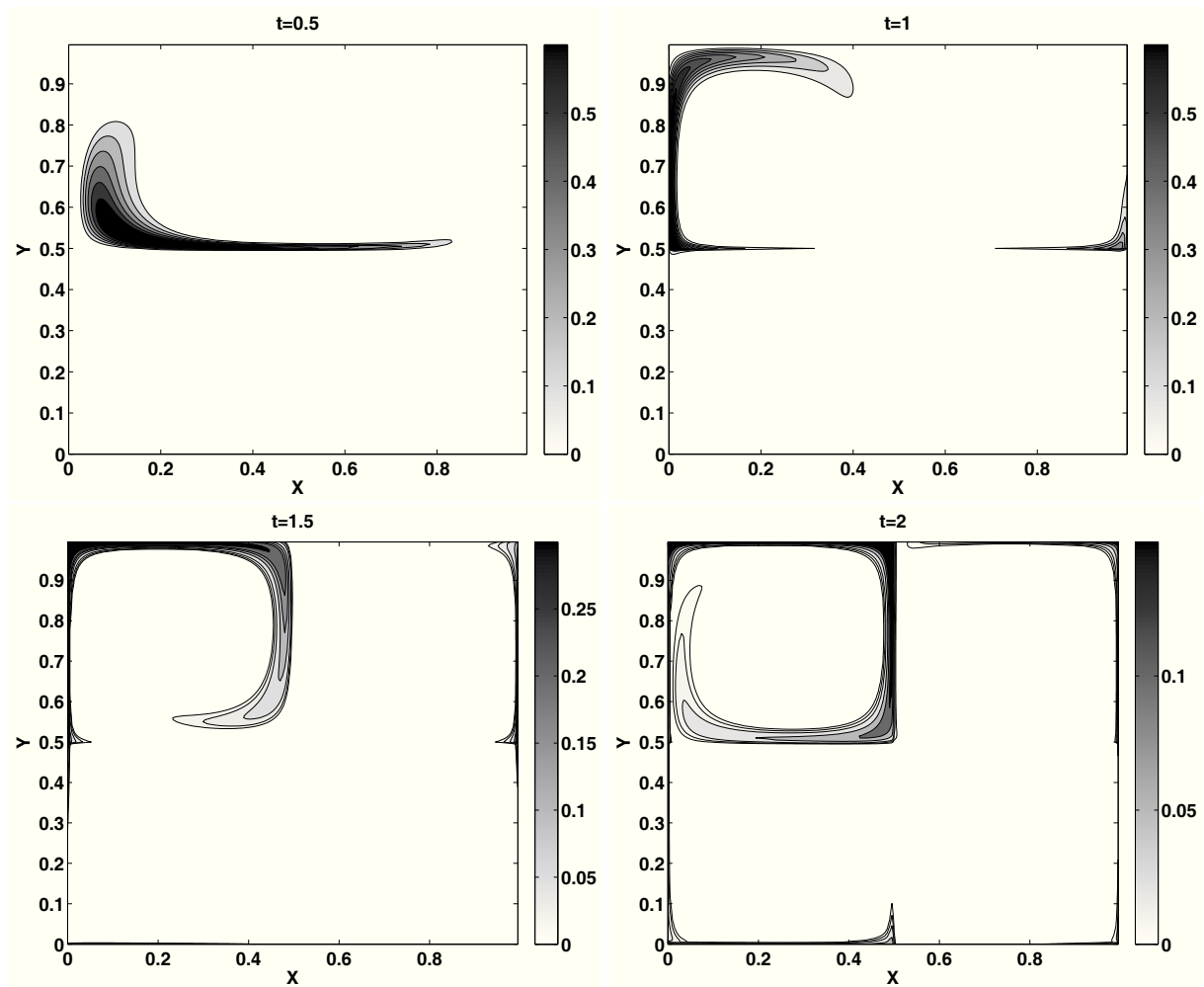


Figure 3.12: Results for spray dynamics in the gas field made of Taylor-Green vortices. Results for the multi-fluid method for 10 sections. (Top-left) Droplet mass at time  $t = 0.5$ . (Top-right) Droplet mass at time  $t = 1$ . (Bottom-left) Droplet mass at time  $t = 1.5$ . (Bottom-right) Droplet mass at time  $t = 2$ . The computation is carried out in a  $200 \times 200$  grid.

section 2.

These conclusions call for a method able to reach a good accuracy in description of polydispersity with a reduced number of sections. The EMSM model, presented in Chapter II precisely answers this issue by showing outstanding results without even discretizing the size phase space.



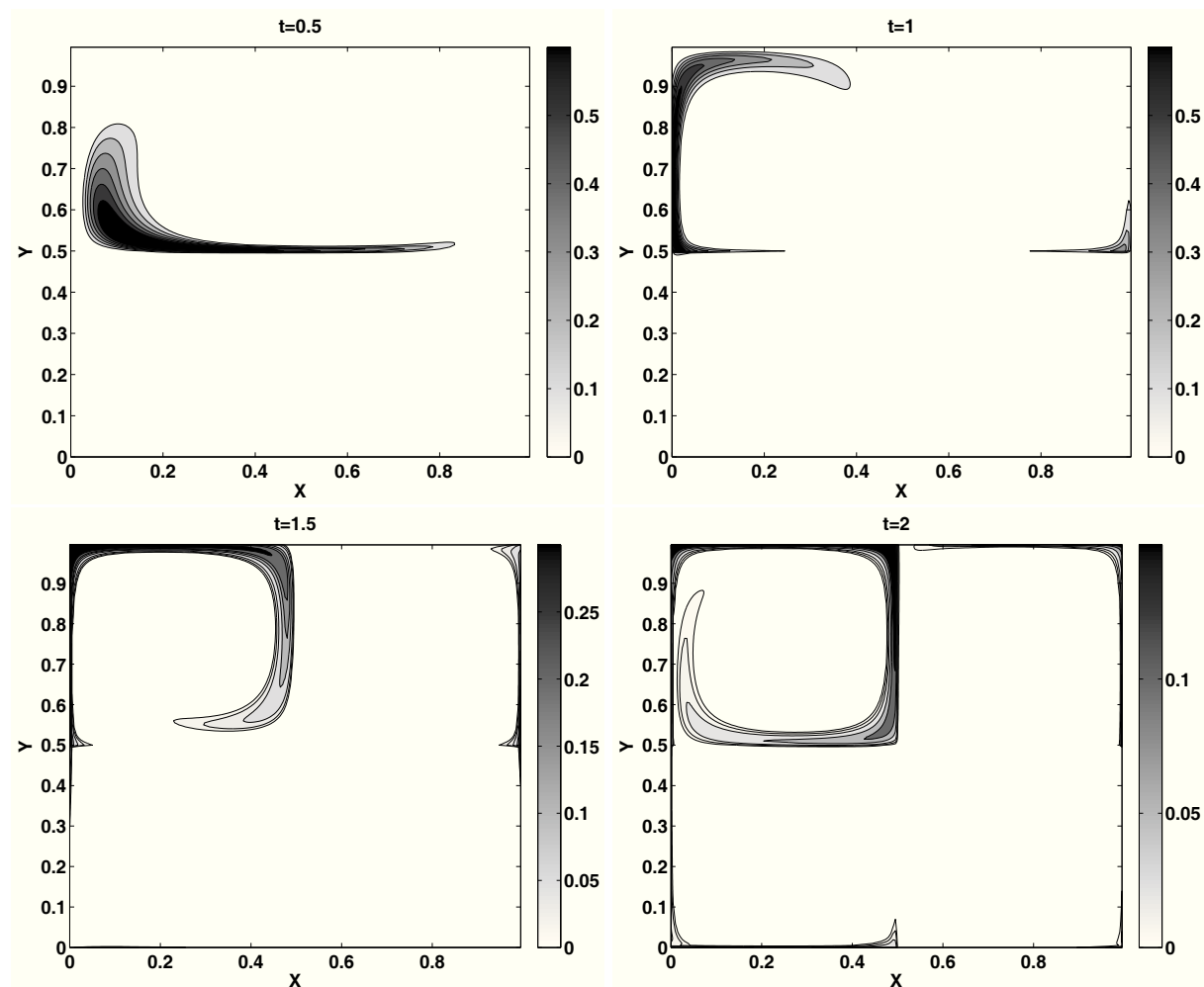


Figure 3.13: Results for spray dynamics in the gas field made of Taylor-Green vortices. Results for the multi-fluid method for 40 sections. (Top-left) Droplet mass at time  $t = 0.5$ . (Top-right) Droplet mass at time  $t = 1$ . (Bottom-left) Droplet mass at time  $t = 1.5$ . (Bottom-right) Droplet mass at time  $t = 2$ . The computation is carried out in a  $200 \times 200$  grid.

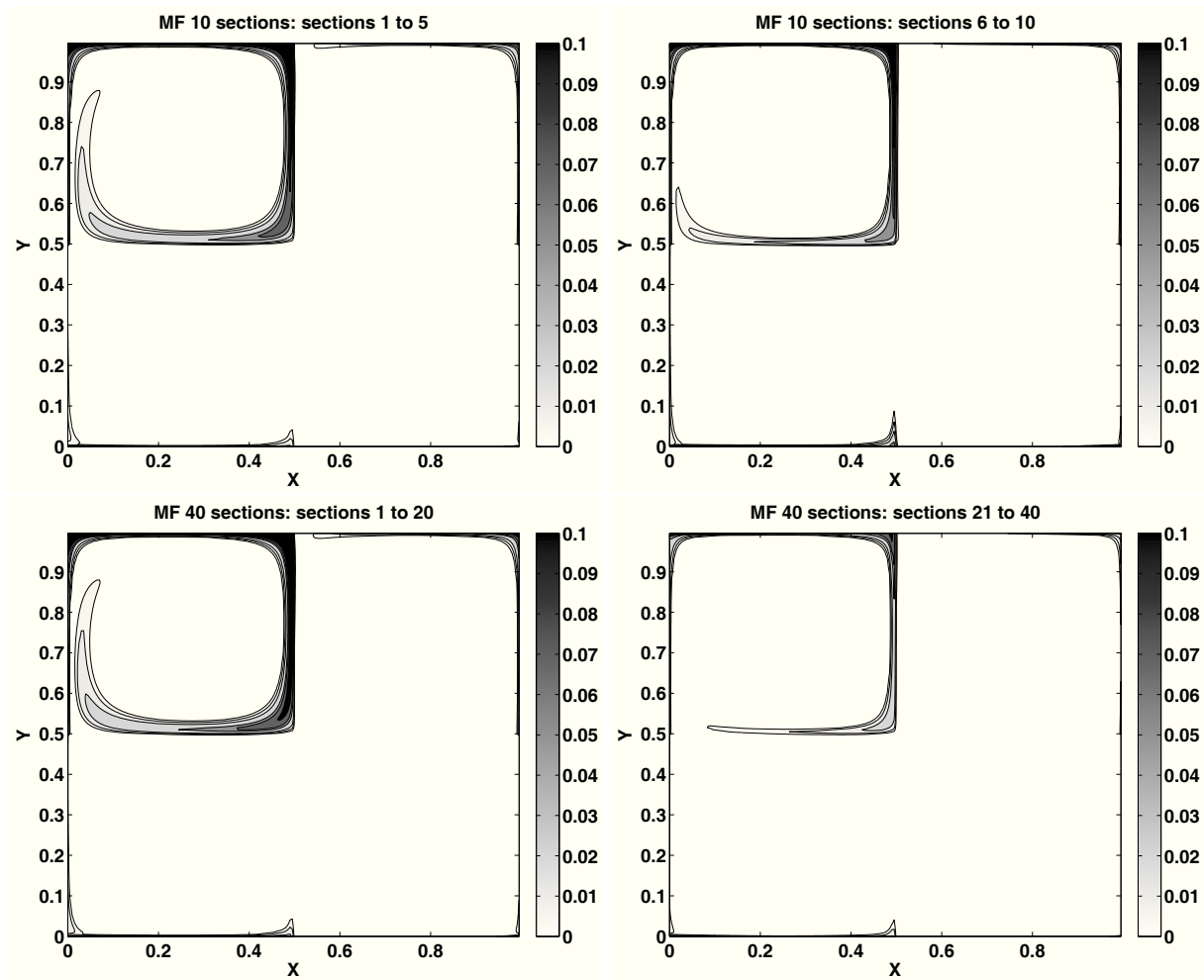


Figure 3.14: Comparison of the final mass in the two halves of the size phase space between the ten section discretization and the forty section discretization, in the evaporating case. (top) ten section discretization; (left) mass in the first half of the size phase space (section 1 to 5) (right) mass in the first half of the size phase space (section 6 to 10). (bottom) forty section discretization; (left) mass in the first half of the size phase space (section 1 to 20) (right) mass in the first half of the size phase space (section 21 to 40)

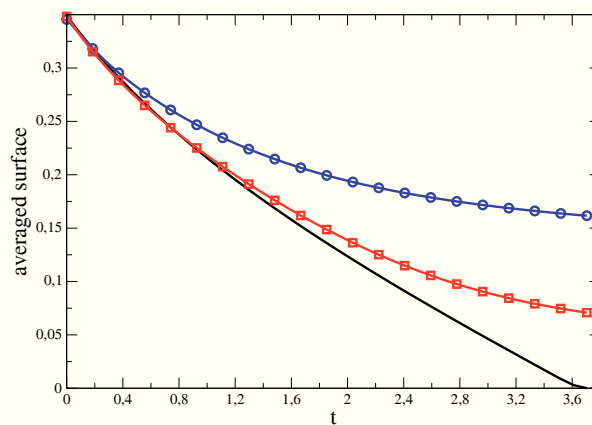


Figure 3.15: Evolution of the mean particle size through evaporation with a  $d^2$  law, and comparison with the analytical solution. Black curve: analytical solution; dashed blue curve: high order moment method; blue curve with circles: multi-fluid model with 10 sections; red curve with squares: multi-fluid model with 40 sections.

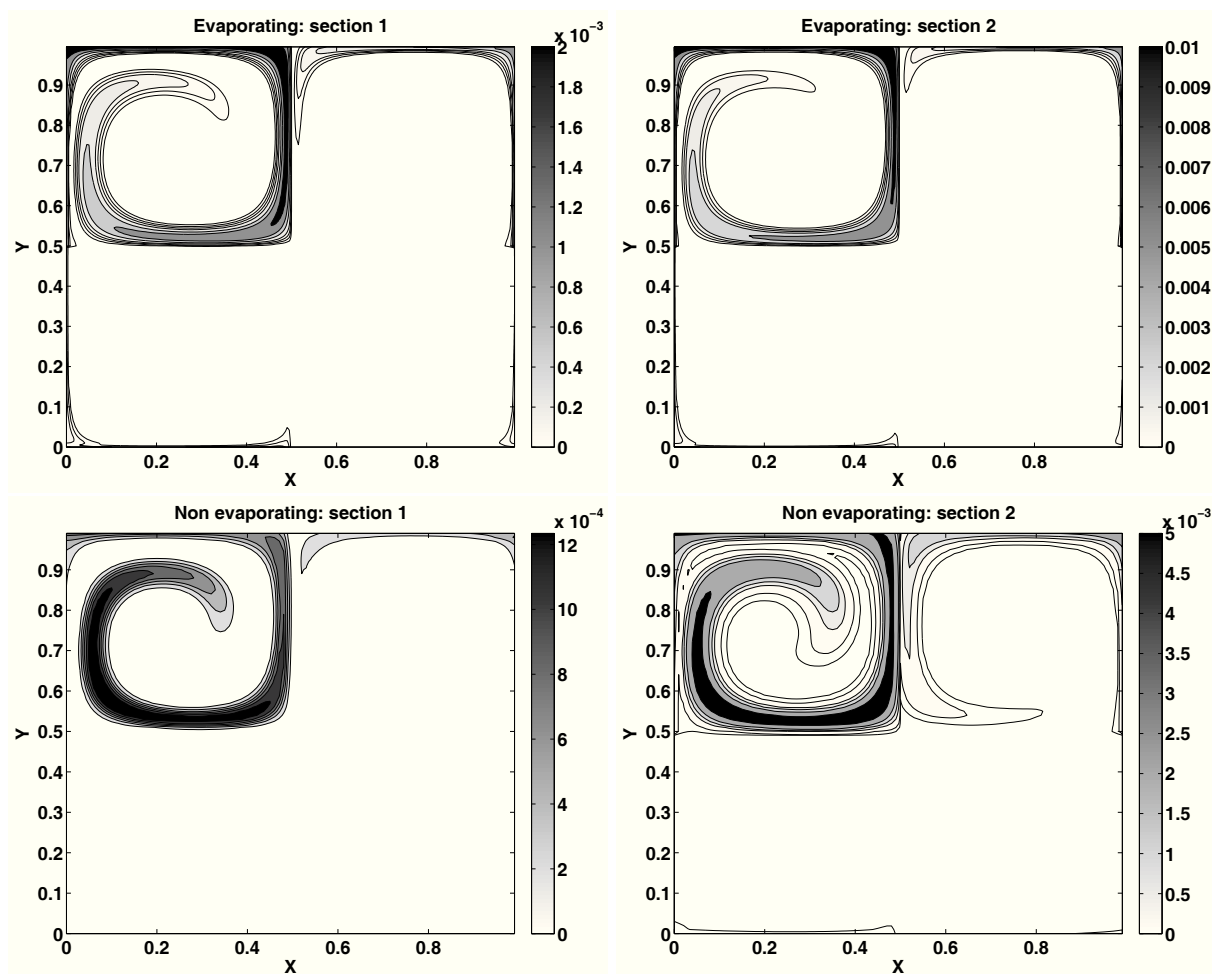


Figure 3.16: Multi-fluid model with ten sections, at time  $t = 2$ . Comparison of the final mass in the first and second section between evaporating and non evaporating case. (Top) Evaporating test case; (left): section one, (right): section two. (Bottom) Non evaporating test case; (left): section one, (right): section two.

### 3.4.2 The issue of characteristics crossing

The other limitation of the multi-fluid model concerns the description of PTC. One typical configuration for which the multi-fluid model predicts an artificial spatial averaging is when two droplet jets cross for a monodisperse spray. Indeed, at the crossing point, there exist at the same space and time location two velocities leading to a bi-modal velocity distribution that is out of equilibrium, and cannot be represented by the multi-fluid model, because of the monokinetic assumption [H1]. Only different size droplets can experience crossings within the multi-fluid framework. If the multi-fluid model is used to describe dilute (non-collisional) flows, it results in the artificial collisional “zero-Knudsen” limit presented in Fig. (3.17)-left where a  $\delta$ -shock is created (i.e., mass accumulates on 1-D spatial structures). The presence of  $\delta$ -shocks is especially problematic for fully two-way coupled systems because mass accumulation at a  $\delta$ -shock can induce strong (unphysical) changes in the gas-phase fluid dynamics. For this reason, it is necessary to develop Eulerian models for non-equilibrium velocity distributions. The EMVM model, presented in Part III addresses this issue.

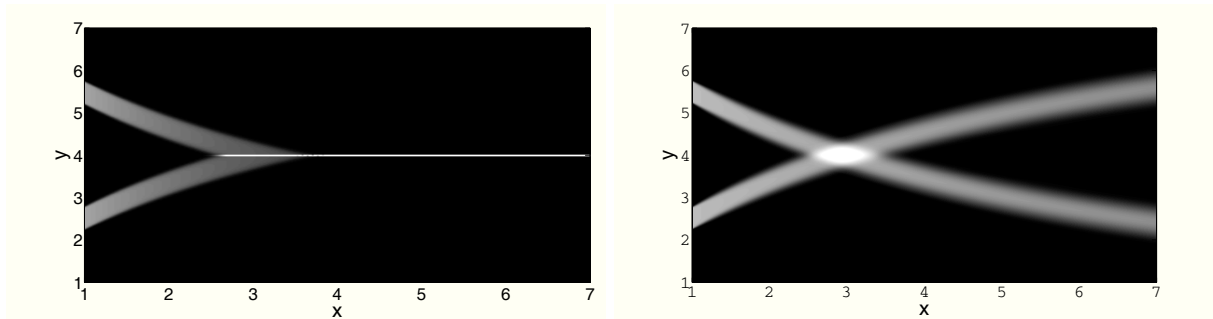


Figure 3.17: Mass density for simulation of two crossing jets using the standard multi-fluid approach (left) and the EMVM model (right) for droplets with  $St = 5.29$ . Source: Fréret et al. [87].

## 3.5 Conclusion

This chapter presents the multi-fluid model with its assumptions. The monokinetic approach for droplets belonging to the same section is particularly important since it yields the peculiar pressureless gas formalism for the final system of equations. The critical aspect of this formalism is to generate singularities called  $\delta$ -shocks as well as vacuum zones, even when starting with regular functions. Adapted numerical strategies to cope with these features have thus been designed. They rely on an operator splitting algorithm between physical and phase transport resolutions. An innovative method, relying on kinetic-based schemes, is designed for physical space transport. Although it can be used in full multi-dimensional schemes, it is presented in the context of dimensional splitting. Indeed it offers a simplified framework that will be used, as a first step, for the development of numerical schemes for the EMSM and EMVM models. Finally, the phase space transport resolution is done with an ODE solver, and since this leads to a multi-scale problem, an implicit Runge-Kutta method is used (Radau5). Another alternative is presented, based on operator splitting within the phase space resolution that will be useful for the EMSM model. The multi-fluid model is successful in describing differentiated droplet dynamics according to their size (i.e., the section they belong to). This is illustrated on a test case in a two-dimensional gaseous vortical flow made of Taylor-Green vortices. This ability of the multi-fluid model to treat polydispersity has also been assessed on a more complex configuration where a free jet is injected in a destabilized gaseous phase. This work has been published in [126]. But this method suffers from two major limitations: this is a first order method in size, leading to substantial diffusion in phase space and thus to a prohibitive computational cost in industrial context; besides it is unable to describe PTC between particles of a same section. It is to overcome these two limitations that the EMSM model, Part II and the EMVM model, Part III, have been designed in the context of this PhD.

## Part II

# High order size moment method for treatment of spray polydispersity

# Introduction

Chapter 3 has demonstrated the capability of the Eulerian multi-fluid model to capture the physics of polydisperse dense evaporating sprays. However, even though this approach has recently been extended to second order by Laurent [145] and Dufour [69, 70] for evaporating sprays, the necessity to discretize the size phase space can be a stumbling block for applications implying a drift velocity in the size phase space such as evaporation, since it introduces intrinsic numerical diffusion and then requires a fine discretization of the size phase space.

On the other hand, Moment methods such as DQMOM introduced by [159] do not encounter this limitation and have proved in [85] to perform quite well for coalescence. But it suffers from important accuracy shortage when evaporation is involved. Nevertheless, this latter method was very interesting in the sense that it was intended to overcome the abovementioned limitation of the multi-fluid model. The motivation of this work has then been to design a moment method in the same framework, providing a precise evaluation of the evaporation term. This model designed in the context of this PhD is the EMSM model. Its key interest relative to all the other Eulerian spray models encountered in literature is to provide a precise description of polydispersity without discretizing the size phase space. This makes it a good candidate in terms of efficiency.

The EMSM model is presented in Chapter 4. Its assumptions, closures and the mathematical challenges for numerical schemes (moment space preservation) are discussed. The numerical scheme is based on an operator splitting algorithm as presented in Section 3.2.1. Therefore, the numerical method, dedicated to the treatment of the evaporation term is discussed in Chapter 5, and the advection scheme in Chapter 6. The EMSM model and associated tools are then tested on challenging tests cases, presented in Section 3.3. This first requires to implement the model in the Multi-fluid Solver for Eulerian Spray, MUSES3D. Chapter 7 presents then the implementation strategy in the MUSES3D code. Finally, results presented in Chapter 8 evaluate the potential of the model.



## Chapter 4

# Eulerian Multi Size Moment (EMSM) model: modeling and closure properties

This chapter introduces the Eulerian Multi Size Moments (EMSM) model. Its framework, core assumptions and the provided closures are presented. A last section presents the mathematical challenges induced by the resulting dynamics system for the design of numerical schemes.

### 4.1 Derivation of the model and closure properties

#### 4.1.1 Spray or aerosol: the same issue

The basis kinetic equation for the case of spray is the transport equation in Section 1.2.4 with no collision for the joint size, velocity number density function  $f(t, \mathbf{x}, S, \mathbf{u})$

$$\partial_t f + \nabla_{\mathbf{x}} \cdot (\mathbf{u}f) - \partial_S(Kf) + \nabla_{\mathbf{u}} \cdot (\mathbf{D}_r f) = 0, \quad (4.1)$$

where  $K$  is the evaporation rate,  $\mathbf{D}_r$  is the drag force acting on the droplet. As mentioned in Section 1.2.3, the evaporation coefficient  $K$  is given by the classical  $d^2$  evaporation law  $K(S) = K^0 \mathbb{1}_{[0, +\infty[}(S)$ , where  $K^0$  does not depend on droplet size. The drag term is a Stokes drag term. The techniques developed here for evaporation and transport can also be applied in the context of aerosol particles solution of Eq. (1.43):

$$\partial_t n + \nabla_{\mathbf{x}} \cdot (n\mathbf{u}_g) - \partial_S(Kn) = 0. \quad (4.2)$$

#### 4.1.2 Operator splitting strategy

Let us remark, already in the modeling step, that we adopt the operator splitting strategy, defined in Section 3.2.1, between all the operators intervening in Eq. (4.1): advection, evaporation and drag. This is legitimate by the fact that designing schemes for evaporation and advection involves a high level of complexity, see Chapter 5, and Chapter 6. Therefore, solving each term separately is a relevant choice. In order to be consistent with the splitting strategy, we decide to separate the terms already in the presentation of the model.

In addition to the operator splitting, we consider, in the advection step, a dimensional splitting strategy, as presented in Section 3.2.2. This allows us to treat each direction independently. Let us insist that it does not mean that this is the only possible way to design numerical tools for the EMSM model. Nevertheless, this simplified framework allows to focus exclusively on issues linked with moment transport and to propose stable and accurate tools in this context, without the additional difficulties due to fully multi-dimensional schemes.

### 4.1.3 Drag closure problem and resulting transport scheme

Drag is involved only in the case of spray particles, i.e. with their own inertia. The resulting equation on momentum reads:

$$d_t(m_0 \mathbf{u}_p) = \mathbf{D}_{r,p}. \quad (4.3)$$

We now focus on the difficulty induced by expressing the drag term force  $\mathbf{D}_{r,p}$  in the momentum equation, the momentum being defined by  $m_0 \mathbf{u}_p$ ,  $\mathbf{D}_{r,p}$  writes:

$$\mathbf{D}_{r,p} = \int_{S_{\min}}^{S_{\max}} \frac{\mathbf{u}_g - \mathbf{u}}{St_0 S} n \, dS. \quad (4.4)$$

The presence of  $S$  at the denominator makes the formulation Eq.(4.4) unclosed. The solution considered here is to defined the momentum as  $m_1 \mathbf{u}_p$  instead of  $m_0 \mathbf{u}_p$ . The definition of the mean particle velocity  $\mathbf{u}_p$  thus changes from a number-average velocity to a size-average velocity. Accordingly, the drag terms then writes:

$$\mathbf{D}_{r,p} = \int_{S_{\min}}^{S_{\max}} \frac{\mathbf{u}_g - \mathbf{u}}{St_0} n \, dS = m_0 \frac{\mathbf{u}_g - \mathbf{u}_p}{St_0}. \quad (4.5)$$

Finally, an algorithm is here designed for the resolution of the following system for spray:

$$\partial_t(m_1 \mathbf{u}_p) + \partial_x(m_1 \mathbf{u}_p \otimes \mathbf{u}_p) = m_0 \frac{\mathbf{u}_g - \mathbf{u}_p}{St_0}, \quad (4.6)$$

where  $m_1$  is the size moment of order one of the distribution function. For the sake of legibility, from now on, the particle velocity is referred to as  $\mathbf{u}_p$ , irrespective of aerosols or sprays.

### 4.1.4 Physical transport model

We focus here on the advection term. Accordingly, the basis kinetic equation for the size velocity NDF  $f(t, \mathbf{x}, S, \mathbf{u})$  writes:

$$\partial_t f + \nabla_{\mathbf{x}} \cdot (u f) = 0, \quad (4.7)$$

while in the case of aerosols, it writes:

$$\partial_t n + \nabla_{\mathbf{x}} \cdot (n \mathbf{u}_g) = 0. \quad (4.8)$$

Let us note that in the case of aerosols, the internal variables of the NDF  $n(t, \mathbf{x}, S)$  only contain droplet size.

In the case of sprays, the first step is to reduce the phase space dimension by writing equations on mean quantities relative to velocity, but still conditioned by droplet size. This derivation is exactly the same type of derivation done in the context of the multi-fluid model. In particular, the critical assumption done in that context, the monokinetic assumption is taken up, i.e.  $f$  is projected on a distribution with a single velocity conditioned by size Eq.(3.1)

$$f(t, \mathbf{x}, S, \mathbf{u}) = n(t, \mathbf{x}, S) \delta(\mathbf{u} - \mathbf{u}_p(t, \mathbf{x}, S)), \quad (4.9)$$

The semi-kinetic equations write:

$$\begin{aligned} \partial_t n + \nabla_{\mathbf{x}} \cdot (n \mathbf{u}_p) &= 0, \\ \partial_t (n \mathbf{u}_p) + \nabla_{\mathbf{x}} \cdot (n \mathbf{u}_p \otimes \mathbf{u}_p) &= 0. \end{aligned} \quad (4.10)$$

As done in Section 4.1.5, we consider size moments of system (4.10) and Eq.(4.8). For inertial particles, as the moments are advected with their own velocity and not with the gas velocity, an additional equation

is needed. Since an accurate description of the particle dynamics conditioned by size is beyond the scope of the paper, this phenomenon will be described, here, by one averaged velocity only. In fact, the velocity of the particles  $\mathbf{u}_p$  is assumed not to depend on particle size. When a size discretization is used, as for multi-fluid methods [146], this assumption is done in each size interval. Here, a discretization can still be done, but the interest of the method comes from the possibility to reduce the number of size intervals (till eventually the case of only one interval) by a better description of each interval through a higher number of moments. The assumption of a ‘‘constant’’ velocity in each size section can then appear unjustified. But, as it will be shown in the Chapter 8, the better description of the granulometry through the use of several moments allows to have a good description of the spray dynamic thanks to an improvement of the approximation of the drag force.

The moment system of equations then reads:

$$\begin{array}{c} \text{Aerosols} \\ \left\{ \begin{array}{l} \partial_t(m_0) + \partial_x(m_0 \mathbf{u}_g) = 0 \\ \partial_t(m_1) + \partial_x(m_1 \mathbf{u}_g) = 0 \\ \partial_t(m_2) + \partial_x(m_2 \mathbf{u}_g) = 0 \\ \vdots \\ \partial_t(m_N) + \partial_x(m_N \mathbf{u}_g) = 0. \end{array} \right. \end{array} \quad \begin{array}{c} \text{Spray} \\ \left\{ \begin{array}{l} \partial_t(m_0) + \partial_x(m_0 \mathbf{u}_p) = 0 \\ \partial_t(m_1) + \partial_x(m_1 \mathbf{u}_p) = 0 \\ \partial_t(m_2) + \partial_x(m_2 \mathbf{u}_p) = 0 \\ \vdots \\ \partial_t(m_N) + \partial_x(m_N \mathbf{u}_p) = 0 \\ \partial_t(m_1 \mathbf{u}_p) + \partial_x(m_1 \mathbf{u}_p \otimes \mathbf{u}_p) = 0. \end{array} \right. \end{array} \quad (4.11)$$

### 4.1.5 Evaporation model

Since we focus in this section on the difficulties associated with evaporation process, we will reduce this equation to the ‘model’ partial differential equation (PDE) on a homogeneous number distribution function  $f(t, S)$  which satisfies:

$$\partial_t n - \partial_S (K n) = 0, \quad (4.12)$$

#### 4.1.5.1 Flux at zero size

The evaporation coefficient  $K$  also called drift velocity in the case of aerosol, is negative and has been non-dimensionalized to  $-1$ . The method will be first derived for this drift velocity before being extended to more general one.

It can be noted that this is a transport equation with discontinuous coefficients and that it has well-defined measure solutions [23]. Roughly speaking, the jump in velocity from zero for negative sizes to one for positive sizes creates the crossing of characteristics and results in a measure concentration at zero size. Consequently, it can be shown that the exact solution of equation (4.12) with a positive initial data  $f^0(S)$  on  $[0, +\infty)$  (eventually a positive measure) reads :

$$n(t, S) = \mathcal{N}^0(t) \delta(S) + n^0(S + t), \quad S \geq 0, \quad (4.13)$$

where  $\mathcal{N}^0(t) = \int_0^t f^0(S) dS$  is exactly the number of droplets/particles which have disappeared at time  $t$ . Thus this number density concentration is well defined mathematically in the sense of duality solution [23].

The principle of moment methods is to be able to write, potentially using quadrature formulas, a set of dynamical equations on a set of moments of the NDF. We illustrate this point of view in the context of the model PDE. For  $N$  a given integer, let  $\mathbf{m}$  denote the vector of surface moments:

$$\mathbf{m} = \begin{pmatrix} m_0 \\ \vdots \\ m_N \end{pmatrix}, \quad m_k(t) = \int_0^{S_{\max}} S^k n(t, S) dS. \quad (4.14)$$

where  $S_{\max}$  is the given maximal size. Using a natural integration by parts, we get the following set of ordinary differential equations for the evolution of the vector of moments  $\mathbf{m}$  :

$$d_t \mathbf{m} = -\mathbf{A} \mathbf{m} - \phi_-, \quad (4.15)$$

where besides the flux at zero size  $\phi_-$ , we introduce the translation nilpotent matrix  $A$  :

$$\phi_- = n(t, 0) \begin{pmatrix} 1 \\ 0 \\ \vdots \\ 0 \end{pmatrix}, \quad \mathbf{A} = \begin{bmatrix} 0 & & & & \mathbf{0} \\ 1 & 0 & & & \\ & 2 & \ddots & & \\ & & \ddots & \ddots & \\ \mathbf{0} & & & N & 0 \end{bmatrix}.$$

It is important to note that this form of the system is not closed since the value of the flux *can not* be found directly from the values of  $\mathbf{m}$ . The knowledge of the value of  $f(t, S)$  at the zero boundary for all  $t$  is equivalent to fully solving the original “kinetic” problem. These values then have to be provided as functions of  $\mathbf{m}(t)$ , which constitutes the challenge. The problem we just raised is similar if one wants to use a DQMOM method, since the source terms for the evolution of abscissas and weights are found from the equations of the moments and the DQMOM dynamics is then completely related to a choice for the form of the flux  $f(t, 0)$  in terms of moments or abscissas and weights [85].

The measure concentration at zero size has no impact on higher moments than the total number density and does not result in any complex behavior, except that the flux of disappearing droplet which concentrate in a Dirac delta function at zero size results in a modification of the whole set of moments through the coupling matrix  $\mathbf{A}$ .

#### 4.1.5.2 Possible extension to a multi-fluid context

In fact, the question of evaluating the flux at a given size can be considered in a more general framework. We consider, as in the multi-fluid model, “sections”, a section being defined by a fixed size interval  $[S_{\min}, S_{\max}]$ . For  $N$  a given integer, let  $\mathbf{m}$  denote the vector of  $N$  droplet surface moments which is the same as in (4.14) but with  $m_k(t) = \int_{S_{\min}}^{S_{\max}} S^k n(t, S) dS$ . The size phase space can be discretized into several sections [146, 145]. The moment dynamics then read :

$$d_t \mathbf{m} = -\mathbf{A} \mathbf{m} - \phi_- + \phi_+, \quad (4.16)$$

$$\phi_- = n(t, S_{\min}) \begin{pmatrix} 1 \\ S_{\min} \\ \vdots \\ S_{\min}^N \end{pmatrix}, \quad \phi_+ = n(t, S_{\max}) \begin{pmatrix} 1 \\ S_{\max} \\ \vdots \\ S_{\max}^N \end{pmatrix},$$

Solutions have already been proposed in order to define reasonable fluxes up to order two by taking moment vectors of dimension one [146, 145] or two [70, 145]. These solutions have been proposed in the framework of size phase space discretization. Yet, the core interest of this present work is to exhibit a new scheme for which there is no need to discretize the size phase space into sections to obtain very good accuracy.

## 4.2 Finite moment space property and finite Hausdorff moment problem

### 4.2.1 Moment space

For the sake of simplicity, we consider the non-dimensional size interval  $[0, 1]$ . If  $\mathcal{P}$  denotes the set of all probability measures on the Borel sets of the interval  $[0, 1]$ , then the  $N$ th-moment space  $\tilde{\mathbb{M}}_N$  on the interval  $[0, 1]$  denotes the set of moment vector of dimension  $N$ ,  $\tilde{\mathbb{M}}_N \subset [0, 1]^N$  :

$$\tilde{\mathbb{M}}_N = \{\mathbf{c}_N(\mu) | \mu \in \mathcal{P}\}, \quad \mathbf{c}_N(\mu) = (c_1(\mu), \dots, c_N(\mu))^t, \quad c_k(\mu) = \int_0^1 x^k d\mu(x).$$

Let us recall that, since we consider probability measures, we always have  $c_0 = 1$ . This set is convex but has a complex geometry.

However, the major challenge for numerical methods designed for evaporation and transport is to keep the integrity of the moment vector  $\mathbf{c}_N$ , i.e to ensure that  $\mathbf{c}_N$  belongs to  $\tilde{\mathbb{M}}_N$  at any time of the resolution process. Necessary and sufficient conditions for existence of a non unique  $n(t, x, S)$  are non negative Hankel determinants as stated by Wright [231], from the theory of canonical moment [58].

$$\underline{H}_{2m+d} = \begin{vmatrix} c_d & \cdots & c_{m+d} \\ \vdots & & \vdots \\ c_{m+d} & \cdots & c_{2m+d} \end{vmatrix}, \quad \overline{H}_{2m+d} = \begin{vmatrix} c_{1-d} - c_{2-d} & \cdots & c_m - c_{m+1} \\ \vdots & \vdots & \vdots \\ c_m - c_{m+1} & \cdots & c_{2m-1+d} - c_{2m+d} \end{vmatrix}, \quad (4.17)$$

with  $d = 0, 1$ ;  $m \geq 0$ ,  $\underline{H}_{-1} = \overline{H}_{-1} = \underline{H}_0 = \overline{H}_0 = 1$ . The Hankel determinants rely on the more general theory of canonical moment space, described in the following section.

### 4.2.2 Canonical moment space

For  $\mathbf{c}_N \in \mathbb{M}_N$ , let  $\mathcal{P}(\mathbf{c}_N)$  denote the set of all measures  $\mu \in \mathcal{P}$  with moments up to the order  $N$  equal to  $\mathbf{c}_N = (c_1, \dots, c_N)^t$  and

$$c_{N+1}^+(\mathbf{c}_N) = \max_{\mu \in \mathcal{P}(\mathbf{c}_N)} c_{N+1}(\mu), \quad c_{N+1}^-(\mathbf{c}_N) = \min_{\mu \in \mathcal{P}(\mathbf{c}_N)} c_{N+1}(\mu),$$

If  $\mathbf{c}_N$  is in the interior of  $\mathbb{M}_N$  then  $c_{N+1}^- < c_{N+1}^+$  and  $\mathcal{P}(\mathbf{c}_N)$  is infinite [58]. A canonical moment sequence  $(p_k)_{k \leq N+1}$  can then be defined by :

$$p_k = \frac{c_k - c_k^-(\mathbf{c}_{k-1})}{c_k^+(\mathbf{c}_{k-1}) - c_k^-(\mathbf{c}_{k-1})}. \quad (4.18)$$

Note that the canonical moments vary in the interval  $[0, 1]$  and they remain invariant under a linear transformation of the measure. Moreover,  $p_{N+1}$  is 0 or 1 if and only if  $\mathbf{c}_{N+1}$  is at the boundary of  $\mathbb{M}_{N+1}$  and  $\mathcal{P}(\mathbf{c}_{N+1})$  is then a singleton. An algorithm is given in [58] in order to go from moments to canonical moments and conversely.

In our case, since we are dealing with number density functions over an interval  $(S_{\min}, S_{\max})$ . Let us first denote  $\mathbb{M}_N(S_{\min}, S_{\max})$  the  $N$ th-moment space corresponding to this interval. For any non zero moment vector  $\mathbf{m} = (m_0, m_1, \dots, m_N)^t \in \mathbb{R}^{N+1}$ , we define the vector of normalized moments  $\tilde{\mathbf{m}} \in \mathbb{M}_N(S_{\min}, S_{\max}) \subset \mathbb{R}^N$  by  $\tilde{\mathbf{m}} = (m_1/m_0, \dots, m_N/m_0)^t$ . Let us then denote  $\tilde{\mathbb{M}}(S_{\min}, S_{\max})$  the  $N$ th-moment space of such moment vectors  $\mathbf{m}$ . Moreover, the first canonical moments can be written :

$$p_1 = \frac{m_1 - S_{\min}m_0}{(S_{\max} - S_{\min})m_0}, \quad p_2 = \frac{m_0m_2 - m_1^2}{(m_1 - S_{\min}m_0)(S_{\max}m_0 - m_1)},$$

$$p_3 = \frac{(S_{\max}m_0 - m_1)[(m_1 - S_{\min}m_0)m_3 - (m_2 - S_{\min}m_1 - S_{\min}^2m_0)m_2 - S_{\min}^2m_1^2]}{(S_{\max} - S_{\min})(m_0m_2 - m_1^2)(-m_2 + (S_{\max} + S_{\min})m_1 - S_{\max}S_{\min}m_0)}.$$

In the case of  $S_{\min} = 0$  and  $S_{\max} = 1$ , the canonical moments expression becomes:

$$p_1 = \frac{m_1}{m_0},$$

$$p_2 = \frac{m_0m_2 - m_1^2}{m_1 - m_0},$$

$$p_3 = \frac{(m_0 - m_1)(m_1m_3 - m_2^2)}{(m_0m_2 - m_1^2)(m_1 - m_2)}. \quad (4.19)$$

so the actual moments reads:

$$\begin{aligned} m_1 &= m_0 p_1, \\ m_2 &= m_0 p_1 [(1 - p_1)p_2 + p_1], \\ m_3 &= m_0 p_1 [(1 - p_1)(1 - p_2)p_2 p_3 + [(1 - p_1)p_2 + p_1]^2]. \end{aligned} \quad (4.20)$$

The geometry of the space of the canonical moments vectors is much more simpler than the one of the moments since it is then the cube  $[0, 1]^N$ . The canonical moments are then very useful in order to check the belonging to the moment space.

### 4.2.3 Some solutions to the Hausdorff finite moment problem

The Hausdorff finite moment problem for the moments  $\mathbf{m}$  is : finding a positive real valued function  $n_{\mathbf{m}}$  defined on  $[S_{\min}, S_{\max}]$  such that

$$\mathbf{m} = \int_{S_{\min}}^{S_{\max}} n_{\mathbf{m}}(x) \begin{pmatrix} 1 \\ x \\ \vdots \\ x^N \end{pmatrix} dx. \quad (4.21)$$

As seen in the previous Section, if  $\mathbf{m}$  belongs to the interior of  $\mathbb{M}_N(S_{\min}, S_{\max})$ , there is an infinity of solutions.

Similar problems were tackled in different ways in the context of solving the problem (4.12). With the use of only one moment, a fixed profile can be used [146], like a constant, leading to an at most first order method in term of the size discretization [143, 145]. Note that the moment of interest is then the moment of order 3/2 and the positivity of such moment is sufficient in order to stay in the moment space. Two kinds of extension of such methods were developed. First, in [145],  $N$  moments were used, with some polynomial functions for  $n_{\mathbf{m}}$ , in order to obtain a  $N^{\text{th}}$  order method. But the moment space of positive polynomial functions is only a sub-space of the moment space and a modified method is introduced in this article in the case of two moments, using a reconstruction with a bi-affine function instead of an affine one. An other extension were developed in [70] with the use of moments of order 0 and 3/2. It is then shown that a function of the type  $\exp(ax + b)$  can be used and a preservation of the moment space was also taken for.

Here, some reconstructions are introduced for an arbitrary number of moments in link with the structure of the moment space.

**Lower principal representation** For any point in the interior of the  $N$ th-moment space  $\mathbb{M}_N(S_{\min}, S_{\max})$ , with  $N = 2s - 1$ , it can be shown that there exists a unique lower principal representation (i.e. for which the moment  $m_{N+1}$  is minimal;  $(m_0, \dots, m_{N+1})$  then belongs to the boundary of  $\mathbb{M}_{N+1}(S_{\min}, S_{\max})$ ) under the form of a sum of  $s$  weighted Dirac delta function, the support or roots of which are in  $(S_{\min}, S_{\max})$ . This support can be shown to be the root of some orthogonal polynomials associated to Hankel determinants [58]. It is this lower principal representation that is used in quadrature method of moments (QMOM) introduced in [175] and further used in the DQMOM [159].

Then, for any  $\mathbf{m} \in \text{Int}(\mathbb{M}_N(S_{\min}, S_{\max}))$ , there exists one unique representation of the vector of moments by using weights  $(\omega_i)_{i \in [1, n]}$  and abscissas  $(\mathcal{S}_i)_{i \in [1, n]}$  such that :

$$\mathbf{m} = \begin{pmatrix} m_0 \\ m_1 \\ \vdots \\ m_N \end{pmatrix} = \begin{pmatrix} \sum_{i=1}^s \omega_i \\ \sum_{i=1}^s \omega_i \mathcal{S}_i \\ \vdots \\ \sum_{i=1}^s \omega_i \mathcal{S}_i^N \end{pmatrix}, \quad (4.22)$$

The corresponding number density function is then :

$$n_{\mathbf{m}}^-(S) = \sum_{i=1}^n \omega_i \delta(S - \mathcal{S}_i). \quad (4.23)$$

Abscissas  $\mathcal{S}_i$  are the roots of the polynomial  $P = X^n + \sum_{k=0}^{n-1} \sigma_k X^k$  with the  $\sigma_k$  given by :

$$\begin{bmatrix} m_0 & m_1 & \dots & m_{s-1} \\ m_1 & & & \vdots \\ \vdots & & & \vdots \\ m_{s-1} & \dots & \dots & m_{2s-1} \end{bmatrix} \begin{pmatrix} \sigma_0 \\ \sigma_1 \\ \vdots \\ \sigma_{n-1} \end{pmatrix} = - \begin{pmatrix} m_s \\ m_{s+1} \\ \vdots \\ m_{2s} \end{pmatrix}.$$

The weights are then solutions of a linear system. A Product Difference (PD) algorithm is given in [175] to compute these weights and abscissas.

Such a reconstruction is used for quadrature formulas [159]. But it cannot be used to solve our evaporation problem, since it requires to find the value of the flux  $n_{\mathbf{m}}$ , which is a punctual value of the NDF.

**NDF reconstruction through the Maximum Entropy formalism** A smooth approximated NDF can be obtained by the Maximum Entropy (ME) reconstruction [177]. The ME method yields a smooth distribution which maximizes the following Shannon entropy from information theory :

$$\mathcal{H}[f] = - \int_{S_{\min}}^{S_{\max}} f(x) \ln f(x) dx.$$

The existence of such ME distribution is shown in [214] as soon as the vector of moments  $\mathbf{m}$  belongs to the interior of the moment space  $\mathbb{M}_N(S_{\min}, S_{\max})$ . This is a standard constrained optimization problem, leading to the following explicit representation of the ME approximate :

$$\tilde{n}_{ME}(x) = \exp \left( - \sum_{j=0}^N \xi_j x^j \right). \quad (4.24)$$

to be supplemented by the condition (4.21). It can be seen as a generalization of the reconstruction used in [70] except that the considered moments were moments of order 0 and 3/2 instead of integer moments here. The coefficients  $\xi_0, \dots, \xi_N$  are the Lagrange's multipliers. We then just need to minimize the following convex potential :

$$\Delta = \int_{S_{\min}}^{S_{\max}} \left[ \exp \left( - \sum_{j=0}^N \xi_j x^j \right) - 1 \right] dx + \sum_{j=0}^N \xi_j m_j.$$

Indeed, its stationary points are given by

$$\frac{\partial \Delta}{\partial \xi_i} = 0 \quad \Rightarrow \quad \int_{S_{\min}}^{S_{\max}} x^i \exp \left( - \sum_{j=0}^N \xi_j x^j \right) dx = m_i.$$

Numerically, a Newton method is used, as in [177] : starting from initial choices  $\xi = (\xi_0, \dots, \xi_N)'$ , updated  $\xi$ 's are defined from

$$\xi^+ = \xi - H^{-1}(\mathbf{m}^0 - \langle X \rangle_{\xi}),$$

where  $\langle X \rangle_{\xi} = (\langle x^0 \rangle_{\xi}, \dots, \langle x^N \rangle_{\xi})'$  is the vector of approximated moments, with

$$\langle x^k \rangle_{\xi} = \int_{S_{\min}}^{S_{\max}} x^k \exp \left( - \sum_{j=0}^N \xi_j x^j \right) dx. \quad (4.25)$$

and  $H$  is the Hessian matrix defined by  $H_{i,j} = \frac{\partial^2 \Delta}{\partial \xi_i \partial \xi_j} = \langle x^{i+j} \rangle_\xi$  for  $i, j = 0, \dots, N$ .

The used numerical procedure is the same as in [177]. In this paper, they found that a double-precision 24-point Gaussian quadrature method very efficiently produces the demanded accuracy for  $\langle x^k \rangle_\xi$ . The quadrature points are computed once for the interval  $[0, 1]$  and a change of variable is used for all the integrals in order to come back to this interval. Because  $H$  is symmetric positive definite, a classical Choleski decomposition is used in order to solve the linear system [198]. A number of iterations from 4 to 15 is needed for the Newton method to converge, with an accuracy of  $10^{-6}$  on the normalized moments, from the initial value  $\xi = (-\ln(m_0)/(S_{\max} - S_{\min}), 0, \dots, 0)'$  corresponding to a constant reconstruction preserving the moment of order 0. This number of iterations depends on the distance to the boundary of the moment space : the closest the moment vector is to this boundary, the largest this number of iterations is. Since this issue is not treated in [177], we propose to treat it in the next paragraph in details. Finally such a reconstruction provides a value for the flux at zero size and thus a closure for problem (4.15) in terms of the moment vector.

An example is given in Fig. 4.1-bottom in case  $N = 3$  and we propose a comparison in Fig. 4.1-top left with a one moment (of order 3/2) constant reconstruction in 12 sections, like in [146] and a reconstruction in Fig. 4.1-top right using two moments and a bi-affine shape on each 4 sections, like in [145]. Let us note that the numerical method using the constant by part reconstruction needs 12 moments, while with the affine by part reconstruction one we need 8 moments and with the ME reconstruction we need 4 moments. The accuracy of the resulting approaches will be analysed in Chapter 5 where all the results and discussion are gathered.

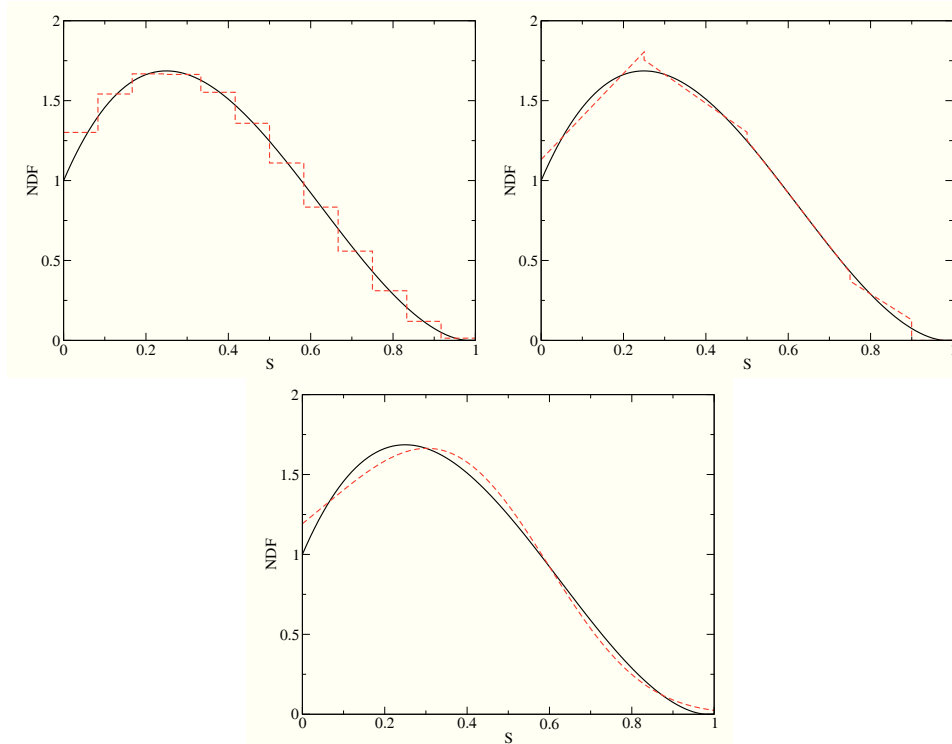


Figure 4.1: Smooth NDF (solid line) and the constant reconstruction using its moments of order 3/2 on 12 sections (top-left figure, dashed line) or the bi-affine reconstruction using its 2 first moments on 4 sections (top-right figure, dashed line) or ME reconstruction using its 4 first moments (bottom figure, dashed line).



#### 4.2.4 Behavior at the frontier of the moment space

Let us note that such an algorithm can lead to numerical difficulties due to ill-conditioned  $H$  matrices appearing in two cases. Such a bad condition number is encountered for moment vectors too close to the boundary of the moment space and results in highly oscillating  $\xi$  coefficients in the ME approximation for a reasonable number of moments. It can also appear in the case of a large vector of moments as a consequence of the peculiar high-dimensional geometry of the moment space. However, in the present contribution, we will remain low-dimensional, typically considering up to 6 moments, for which the algorithm will prove to be very efficient as long as we stay away from the frontier of the moment space. Since distributions at the frontier of the moment space consist in a sum of Dirac delta functions for which the ME reconstruction is not possible, we have to clarify the distance between such measure distributions and the closed subset of the interior of the moment space for which our formalism is operational, and eventually to make the link between the frontier and such a subset.

A first piece of answer is provided with Figure 4.2. Indeed, for a reconstruction with 4 moments, the ME reconstruction can be done, even for moment vector quite close to the boundary of the moment space. For three values of the first normalized moment, 0.1, 0.5 and 0.9, we compare a 2D-cut of the moment space in the  $(m_2, m_3)$  plane (the three traces of these cuts in the  $(m_1, m_2)$  plane are presented in Figure 4.2 bottom-right) with the set of moments in this place which can be attained with the ME formalism within an error for the moment vector evaluation below 1% with the presented Gaussian quadrature approach. In fact the quasi-totality of the moment space can be covered using such an approach.

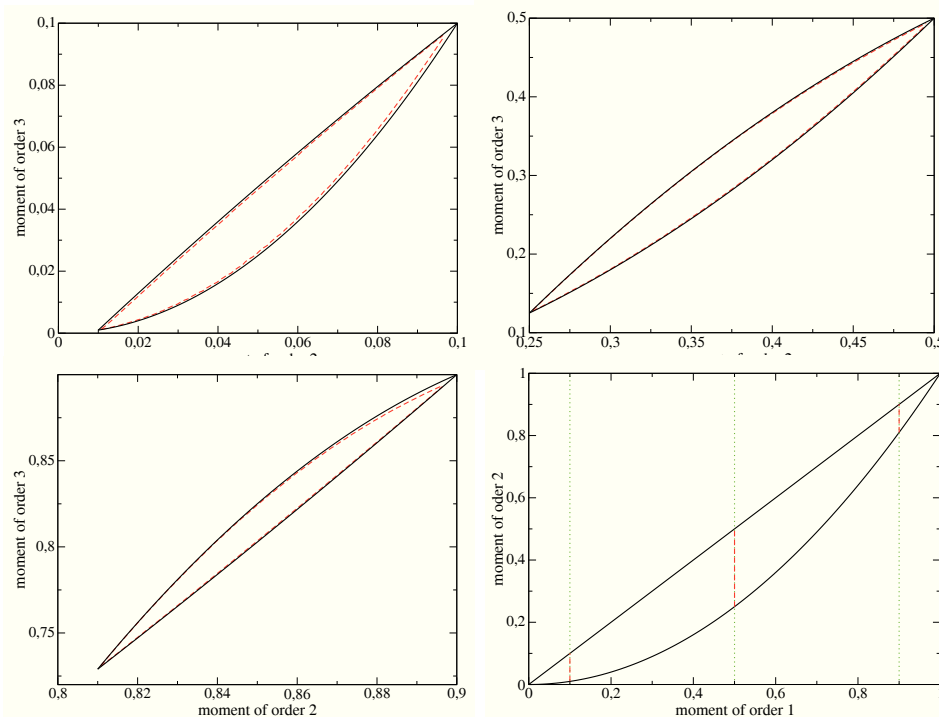


Figure 4.2: Cut of the moment space in the  $m_2$ - $m_3$  plan (bounded by solid lines) and cut of the moment space numerically attained with an error smaller than 1%, with the ME reconstruction using the Gaussian quadrature for the computation of the integrals (bounded by dashed lines) for  $m_1 = 0.1$  (top-left figure),  $m_1 = 0.5$  (top-right figure) and  $m_1 = 0.9$  (bottom-left figure); (bottom-right figure) projection of the moment space boundary in the  $m_1$ - $m_2$  plan (solid lines) and representation in this plan of the cuts (dashed lines).

However, there is a second numerical difficulty when approaching the frontier of the moment space and it comes from the lack of accuracy of the Gaussian quadrature for the computation of the integrals used in the algorithm through equation (4.25). It is quite obvious when seeing the type of reconstruction obtained in such cases (see Section 5.5.1 and Appendix B.2). Moreover, using a more precise integration method for the evaluation of the Hessian matrix allows ME reconstructions for moment vectors close at least till 1% of the boundary (that is to say, at least when all canonical moment are in the interval  $[0.01, 0.99]$ ). Thus, it becomes clear that we are able to reach almost the entire moment space with the proposed formalism and we can even quantify the small subset for which a ME formalism is out of reach. Within this context, the last question to be answered is how to use the algorithm proposed in this paper for this small subset, where distribution functions become Dirac distributions. We provide a final answer to this question in Appendix B.2, where such distributions are also illustrated for the sake of completeness.

### 4.3 Mathematical challenges of the system

As mentioned in Section 4.1, although the high order size moment method can be coupled with a multi-fluid approach leading to the size phase space discretization, the core interest of this method lies in its capacity to describe polydispersity without discretizing the size phase space, by keeping the continuous character of the size variable. Corollary, if the high order size moment method is coupled to a size discretization, the level of accuracy of this method with a very reduced number section (two for example) is unreachable by the multi-fluid model within reasonable computation time, see Section 5.5.

Nevertheless, this very promising ability of the presented model goes hand in hand with some mathematical difficulties in the structure of the system of equations for evaporation, system (4.16), and transport system (4.6). These difficulties require the use of very specific numerical methods. First, similarly to the multi-fluid model, the monokinetic assumption done in the case of sprays introduces the pressureless gas formalism in the transport system. The second difficulty, inherent to high order moment method where we recall that  $N$  moments ( $N > 2$ ) are considered, is to ensure, at any time of the resolution method that the moment sequence  $\mathbf{m} = (m_0, \dots, m_N)$  belongs to the moment space. This is of major importance, since, in the evaporation process through Entropy Maximization (see Section 4.2.3), a distribution function is explicitly reconstructed from the data of the vector  $\mathbf{m}$ . This reconstruction, and then the whole resolution process fails if the moment space is not preserved. We will refer to this condition as the realizability condition.

### 4.4 Conclusion

This section has been dedicated to the introduction of the model and the underlying assumptions on the basis of a new high order size moment method able to precisely describe a population of spray, soot, or aerosol particles in the context of evaporation transport and drag. This method is fundamentally different from the multi-fluid model presented in Chapter 3. Indeed, contrary to the multi-fluid model which, like any sectional method, introduces a discretization of the size space phase, this high order size moment method preserves the continuous characteristic of the size variable to account for polydispersity. Nevertheless, the high order size moment method can also be used in the context of a size discontinuity preserving then the continuous character of the size variable in a section.

But in the context of the collaboration with IFP Energies nouvelles, the potential efficiency of this high order size moment method showed here represents an outstanding interest. First, the final objective set by IFP Energies nouvelles is to be able to describe a fuel spray in real injection conditions in an internal combustion engine. Therefore computational efficiency is a critical criteria in the selection of the method. Only one size section might be used with the EMSM model for an even more accurate description of polydispersity than with a multi-fluid model with ten sections, as showed in Section 5.5. The computational cost can definitely not be divided by ten, since much more complex algebraic tools are used than in the multi-fluid model, but a method three, four or five times faster for a three-dimensional computation for a better description of polydispersity would already be a dramatic achievement. This estimation is done only considering the reduced framework of evaporation transport and drag. When

other terms are considered, like turbulent interaction terms (since injection occurs at turbulent regime), this gain will skyrocket, since a unique term will have to be considered for the high order size moment method whereas ten terms would have to be considered each time with the multi-fluid model.

But the mathematical difficulties of these systems make compulsory to design specific schemes, in order to cope both with the pressureless gas formalism and the realizability condition. It has been explained, in Section 3.2, that a specific precise scheme for transport, robust relative to occurrences of singularities due to the pressureless gas formalism, relies on a kinetic scheme, and is used apart from the other resolution schemes for phase space evolution.

Here again, two very different strategies are used for evaporation, and transport, since dedicated solvers are used to cope with stability conditions stated in Section 4.3. This is why an operator splitting has been adopted. The two next chapters present the numerical schemes designed for evaporation, Chapter 5, and advection of the moments Chapter 6.

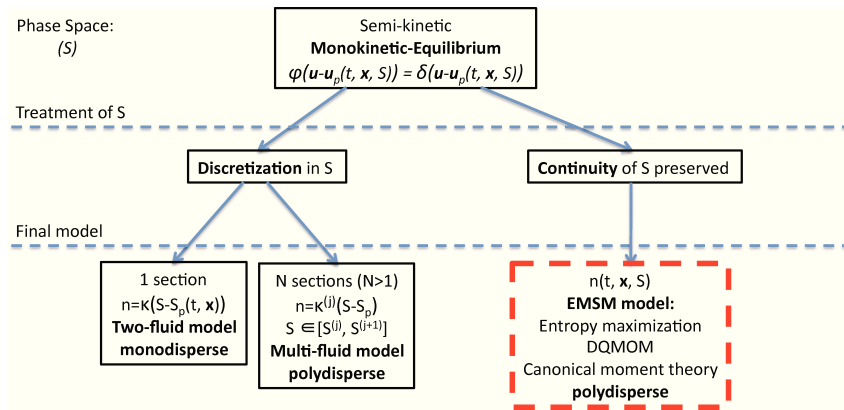


Figure 4.3: Position of the EMSM model in the spray model derived from kinetic description

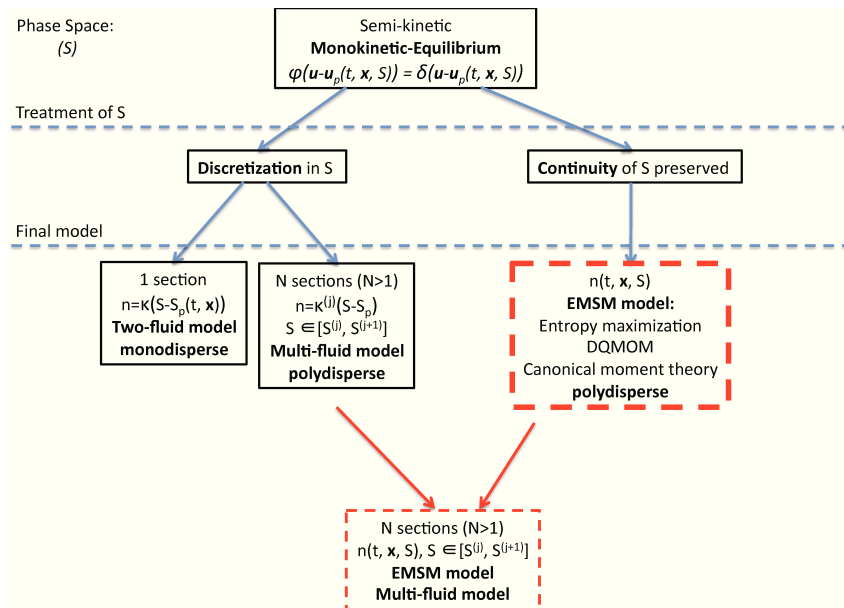


Figure 4.4: Possibility to use the EMSM model within a sectional method

## Chapter 5

# A new numerical scheme with flux evaluation for stable and accurate moment dynamics

This chapter presents the numerical scheme for the resolution of the evaporation term derived in Section 4.1.5, first with a constant evaporation rate and then with a general one. This work is inserted in the development of general scheme for the complete NDF equation, physical transport and transport in space phase being treated separately through splitting method [171, 52, 172]. Eventually, validations of the proposed tools are showed on purely evaporative test cases. This work has lead to a publication in SIAM Journal of Applied Mathematics [173] and a presentation during the SIAM International Conference on Numerical Combustion, Monterrey, USA (2008) [127].

### 5.1 Constant evaporation rate

The case of a constant evaporation law is first studied in order to present the principle of the new numerical schemes. In the following, we will see how this schemes can be extended to more general evaporation laws.

As soon as a reconstruction is done for the NDF from its moments, problem (4.16) could be solved directly with the pointwise value of this reconstruction at  $S = S_{\min}$ , using a dedicated stiff ODE-solver. But it can be shown that the stability is then not warranted. Indeed, classical ODE solvers, like for example explicit Runge-Kutta scheme or explicit Euler scheme, can not preserve the moment space: at some point, the moments can no more correspond to a positive function (in other words, the corresponding canonical moments defined by Eq. (4.18) do not stay between 0 and 1). This leads to a divergence of the method, see Appendix B.

Before introducing the first key ingredient of the numerical scheme which guarantee this stability, let us underline an invariance property which is strongly related to the linear transport equation (4.12).

#### 5.1.1 Invariance property of moment space through evaporation with zero flux

**Lemma 1** *As long as the fluxes  $\phi_-(\Delta t)$  and  $\phi_+(\Delta t)$  remain zero, the evolution of the NDF at the kinetic level is a pure translation in the size phase space and the dynamical evolution of the moments is in closed*

form. Moreover, we have:

$$\mathbf{m}(\Delta t) = \exp(-\Delta t \mathbf{A}) \mathbf{m}(0), \quad \exp(\Delta t \mathbf{A}) = \begin{bmatrix} 1 & & & & & \mathbf{0} \\ \Delta t & 1 & & & & \\ \Delta t^2 & 2 \Delta t & \ddots & & & \\ \vdots & C_{i-1}^{j-1} \Delta t^{i-j} & \ddots & \ddots & & \\ \Delta t^N & \dots & \dots & N \Delta t & 1 & \end{bmatrix}.$$

Let us note that the assumption  $\phi_-(\Delta t)$  remain zero implies that  $f(0, S) = 0$  for  $S \in [S_{\min}, S_{\min} + \Delta t]$ . This lemma has a strong implication: when the dynamics of evaporation is described by a translation in the size phase space (i.e. no fluxes of droplets appearing or disappearing) and when we choose a set of incremental moments in this “natural” evaporation variable, the moment space is invariant by this dynamics. Thus, it is not necessary to invoke quadrature methods since the dynamics is closed. It is then interesting to characterize the related evolution of the abscissas and weights since we are sure to remain in the interior of the moment space of order  $N$ .

**Lemma 2** *The evolution equation on the moments can be written in terms of the abscissas and weights in the following form :*

$$\begin{bmatrix} \sum_{i=1}^s \omega_i(\Delta t) \\ \sum_{i=1}^s \omega_i(\Delta t) \mathcal{S}_i^*(\Delta t) \\ \vdots \\ \sum_{i=1}^s \omega_i(\Delta t) \mathcal{S}_i^{*N}(\Delta t) \end{bmatrix} = \begin{bmatrix} \sum_{i=1}^s \omega_i(0) \\ \sum_{i=1}^s \omega_i(0) \mathcal{S}_i(0) \\ \vdots \\ \sum_{i=1}^s \omega_i(0) \mathcal{S}_i^N(0) \end{bmatrix}, \quad (5.1)$$

where the transport term associated to the exponential has been directly included in the new abscissas  $\mathcal{S}_i^*(\Delta t) = \mathcal{S}_i(\Delta t) + \Delta t$ .

*Proof.* The proof is straightforward once it has been noticed that we have the following equality :

$$\exp(\Delta t \mathbf{A}) \begin{bmatrix} \sum_{i=1}^s \omega_i(\Delta t) \\ \sum_{i=1}^s \omega_i(\Delta t) \mathcal{S}_i(\Delta t) \\ \vdots \\ \sum_{i=1}^s \omega_i(\Delta t) \mathcal{S}_i^N(\Delta t) \end{bmatrix} = \begin{bmatrix} \sum_{i=1}^s \omega_i(\Delta t) \\ \sum_{i=1}^s \omega_i(\Delta t) (\mathcal{S}_i(\Delta t) + \Delta t) \\ \vdots \\ \sum_{i=1}^s \omega_i(\Delta t) (\mathcal{S}_i(\Delta t) + \Delta t)^N \end{bmatrix}. \blacksquare \quad (5.2)$$

### 5.1.2 Integrated version of the dynamical system

Since the pointwise definition of the boundary fluxes is difficult to evaluate, we change the point of view and try to construct, like in the kinetic schemes for hyperbolic equations, an integral formulation making use of the underlying kinetic equation.

The integral formulation of the preceding system (4.16) of ODE’s is the following one:

$$\exp(\Delta t \mathbf{A}) \mathbf{m}(\Delta t) = \mathbf{m}(0) + \int_0^{\Delta t} \exp(\eta \mathbf{A}) (-\phi_-(\eta) + \phi_+(\eta)) d\eta. \quad (5.3)$$

We then want to use the peculiar structure of the integral form of the solution in order to obtain a more convenient form of the fluxes through two arguments : the characteristic solution of the original conservation equation (such as in the kinetic schemes [196]) as well as a moment formulation of the fluxes. This is the purpose of the following lemma.

**Lemma 3** *The integral form of the solution can be rewritten :*

$$\exp(\Delta t \mathbf{A}) \mathbf{m}(\Delta t) = \mathbf{m}(0) - \Phi_-(\Delta t) + \Phi_+(\Delta t), \quad (5.4)$$

where the fluxes read :

$$\Phi_{-}(\Delta t) = \int_{S_{\min}}^{S_{\min}+\Delta t} n(0, \beta) \begin{bmatrix} 1 \\ \beta \\ \vdots \\ \beta^N \end{bmatrix} d\beta, \quad \Phi_{+}(\Delta t) = \int_{S_{\max}}^{S_{\max}+\Delta t} n(0, \beta) \begin{bmatrix} 1 \\ \beta \\ \vdots \\ \beta^N \end{bmatrix} d\beta.$$

*Proof.* Let us first focus on the flux of disappearing droplets :

$$\int_0^{\Delta t} \exp(\eta \mathbf{A}) \phi_{-}(\eta) d\eta = \int_0^{\Delta t} n(\eta, S_{\min}) \begin{bmatrix} 1 \\ \eta & 1 & \mathbf{0} \\ \eta^2 & 2\eta & \ddots \\ \vdots & C_{i-1}^{j-1} \eta^{i-j} & \ddots & \ddots \\ \eta^N & \dots & \dots & N\eta & 1 \end{bmatrix} \begin{bmatrix} 1 \\ S_{\min} \\ \vdots \\ S_{\min}^N \end{bmatrix} d\eta.$$

Using on the one side:

$$\begin{bmatrix} 1 \\ \eta & 1 & \mathbf{0} \\ \eta^2 & 2\eta & \ddots \\ \vdots & C_{i-1}^{j-1} \eta^{i-j} & \ddots & \ddots \\ \eta^N & \dots & \dots & N\eta & 1 \end{bmatrix} \begin{bmatrix} 1 \\ S_{\min} \\ \vdots \\ S_{\min}^N \end{bmatrix} = \begin{bmatrix} 1 \\ \eta + S_{\min} \\ \vdots \\ (\eta + S_{\min})^N \end{bmatrix},$$

and the fact that along the characteristics curves, the solution is constant so that we have  $n(\eta, S_{\min}) = n(0, \eta + S_{\min})$ ; we then get :

$$\int_0^{\Delta t} \exp(\eta \mathbf{A}) \phi_{-}(\eta) d\eta = \int_0^{\Delta t} n(0, \eta + S_{\min}) \begin{bmatrix} 1 \\ \eta + S_{\min} \\ \vdots \\ (\eta + S_{\min})^N \end{bmatrix} d\eta.$$

A simple change of variable  $\beta = \eta + S_{\min}$  allows to conclude on the first equality. The treatment of the gain term is readily the same. ■

There are several important points that have to be underlined. First, it can be easily shown that in the configuration where the fluxes are both set to zero, the right variable is then  $\exp(\Delta t \mathbf{A}) \mathbf{m}(\Delta t)$ , which is invariant, the evolution of the moments being then only modified by transport through the multiplication by  $\exp(-\Delta t \mathbf{A})$ . The integral form of the ODE system (5.4) then decouples the transport per se from the evolution of the moments through the fluxes.

The second point relates to the numerical scheme to be used in order to resolve the system (4.15). It should be noted that in the situation where  $f(t, S_{\max}) = 0$ , i.e. when there is no flux coming from the upper sections and when  $S_{\min} = 0$ , a flux based on pointwise value of  $f$  only participates in the evolution of the zeroth order moment, since  $S_{\min}^N = 0$  for  $N$  greater than zero. With this new integral form, we then get another way of integrating the system of ODEs without the need for a pointwise reconstruction for which the stability is not warranted. The integral form allows to remain in the moment space  $\mathbb{M}_N(S_{\min}, S_{\max})$  of order  $N$  as presented in the following proposition.

**Proposition 1** *For a given set of moments  $\mathbf{m}(0) = \mathbf{m}^0$  at time  $t = 0$  such that  $m_0 > 0$ , we assume that the vector of normalized moments  $\widehat{\mathbf{m}}^0$  belongs to the interior of the moment space of order  $N$  associated to the interval  $[S_{\min}, S_{\max}]$ , that is  $\mathbf{m}^0 \in \text{Int}(\mathbb{M}_N(S_{\min}, S_{\max}))$ . Then, for any measurable positive function  $f_{\mathbf{m}^0}$  defined on the interval  $[S_{\min}, S_{\max} + T]$  and solution of the Hausdorff finite moment problem (4.21) in the interval  $[S_{\min}, S_{\max}]$ , we have*

$$\mathbf{m}(\Delta t) \in \text{Int}(\mathbb{M}_N(S_{\min}, S_{\max})), \quad (5.5)$$

as long as  $\Delta t \in [0, T]$ .

*Proof.* We use the integral form (5.4) and notice that

$$\mathbf{m}^0 = \int_{S_{\min}}^{S_{\max}} n_{\mathbf{m}^0}(\eta) \begin{bmatrix} 1 \\ \eta \\ \vdots \\ \eta^N \end{bmatrix} d\eta.$$

Consequently, we obtain that:

$$\exp(\Delta t \mathbf{A}) \mathbf{m}(\Delta t) = \int_{S_{\min} + \Delta t}^{S_{\max} + \Delta t} n_{\mathbf{m}^0}(\eta) \begin{bmatrix} 1 \\ \eta \\ \vdots \\ \eta^N \end{bmatrix} d\eta.$$

This last equality implies that  $\exp(\Delta t \mathbf{A}) \mathbf{m}(\Delta t)$  belongs to the interior of the moment space  $\mathbb{M}_N(S_{\min} + \Delta t, S_{\max} + \Delta t)$  so that naturally,  $\mathbf{m}(\Delta t)$  belongs the moment space  $\mathbb{M}_N(S_{\min}, S_{\max})$  and the proof is complete. ■

The choice of such function  $n_{\mathbf{m}^0}$  was discussed in the previous section and we use then the ME reconstruction in such a way that the flux can be given by:

$$\Phi_-(\Delta t) = \int_{S_{\min}}^{S_{\min} + \Delta t} \tilde{n}_{ME}(\beta) \begin{bmatrix} 1 \\ \beta \\ \vdots \\ \beta^N \end{bmatrix} d\beta. \quad (5.6)$$

Let us remark that, as explained in Section 4.2.3, the ME reconstruction is not easy to obtain for moment vectors closed to the boundary of the moment space. But, as presented in Appendix B.2, when the moment vector becomes closer to a point of this boundary, the ME reconstruction becomes closer and closer to the lower principal representation and to the sole solution of the Hausdorff moment problem corresponding this point, that is to say a sum of Dirac delta functions. Let us denote  $\sum_i \omega_i \delta_{S_i}$  one of these functions. Then, the flux can be computed from this reconstruction:

$$\Phi_-(\Delta t) = \sum \omega_i (1, S_i, \dots, S_i^N)^t, \quad (5.7)$$

where the sum is taken for all  $i$  such that  $S_i \in [S_{\min}, S_{\min} + \Delta t]$ . It can be seen that this type of flux will allow the preservation of the moment space as it will be shown in the following for the flux (5.6).

### 5.1.3 Link with abscissas and weights of the lower principal representation

We know that for any  $\mathbf{m}^0 \in \text{Int}(\mathbb{M}_N)$ , there exists one unique lower principal representation of the vector of moments by using weights  $(\omega_i)_{i \in [1, n]}$  and abscissas  $(S_i)_{i \in [1, n]}$ . Since we know that the evolution of the vector of moments takes place in the interior of the moment space  $\text{Int}(\tilde{\mathbb{M}}_N)$ , we can write:

$$\exp(\Delta t \mathbf{A}) \begin{bmatrix} \sum_{i=1}^s \omega_i(\Delta t) \\ \sum_{i=1}^s \omega_i(\Delta t) S_i(\Delta t) \\ \vdots \\ \sum_{i=1}^s \omega_i(\Delta t) S_i^N(\Delta t) \end{bmatrix} = \begin{bmatrix} \sum_{i=1}^s \omega_i(0) \\ \sum_{i=1}^s \omega_i(0) S_i(0) \\ \vdots \\ \sum_{i=1}^s \omega_i(0) S_i^N(0) \end{bmatrix} - \Phi_-(\Delta t) + \Phi_+(\Delta t).$$

This formulation can be considered as very interesting since it can be readily seen from it that in the presence of zero fluxes, the weights remain unchanged and the abscissas are only translated at the right velocity. The key variable is not  $S_i(\Delta t)$  but in fact  $S_i(\Delta t) + \Delta t$ . This will be confirmed in the next Section where we make the link between the present approach and the DQMOM approach.

Moreover, this formulation will allow us to emphasize an algorithm for the scheme. It needs the calculation of abscissas and weights from moments. It can be noted that the computation of  $\mathbf{m}(\Delta t)$  from

$\mathbf{m}(0)$  does not need the separation between flux and transport and could be done, like in [145] or [70], using directly the following formula :

$$\mathbf{m}(\Delta t) = \exp(-\Delta t \mathbf{A}) \mathbf{m}(0) - \exp(-\Delta t \mathbf{A}) \Phi_{-}(\Delta t) + \exp(-\Delta t \mathbf{A}) \Phi_{+}(\Delta t).$$

However, the calculation of abscissas and weights is not an expensive operation if we only have  $n = 2$  or  $n = 3$  like for the results presented in this paper. Moreover, they can be very useful for more general problems where phenomena like collision have to be taken into account, which can be done through a quadrature method using these abscissas and weights.

#### 5.1.4 Algorithm of the new scheme

The new scheme introduces a discretization  $0 = S_0 < S_1 < \dots < S_K = S_{\max}$  of the support  $[0, S_{\max}]$  of the distribution function. The initial moments  $m_k(0)$  on each interval  $[S_{k-1}, S_k]$ , called section as for the classical multi-fluid method, are known. The resolution algorithm corresponding to the integral formula (5.4) is used in order to find the moments in each section after a time  $\Delta t$ . This algorithm is :

1. In each section  $[S_{k-1}, S_k]$ , a reconstruction  $f^k$  is done of the distribution from its moments  $\mathbf{m}^k(0)$  by the ME method and the flux  $\Phi_{-}^k(\Delta t)$  with the section  $k-1$  is computed by (5.6) with  $\tilde{n}_{ME} = n^k$ .
2. The weights  $\omega_i^k$  and the abscissas  $S_i^k$  corresponding to the moments  $\mathbf{m}^k(0) - \Phi_{-}^k(\Delta t) + \Phi_{+}^{k+1}(\Delta t)$  are computed using the PD algorithm. Since these moments are in fact the moments of  $\sum_j n^j(S) 1_{[S_{j-1}, S_j]}(S)$  on  $[S_{k-1} + \Delta t, S_k + \Delta t]$ , the abscissas are in  $]S_{k-1} + \Delta t, S_k + \Delta t[$ .
3. The moments  $\mathbf{m}^k(\Delta t)$  corresponding to the weights  $\omega_i^k$  and the abscissas  $S_i^k - \Delta t$  are computed. It gives an approximation of the moments of  $n(\Delta t, \cdot)$  on  $]S_{k-1}, S_k[$ .

In practice, a time discretization associated to the CFL like condition  $K\Delta t \leq \Delta S$  is introduced and the previous algorithm governs the time evolution of both the moments in the various sections as well as the associated abscissas and weights.

The cost of this algorithm is essentially the cost of the ME reconstruction in each section by the Newton method and the cost of the PD algorithm. Since the number of moment we will use is small, and since the Newton method generally only requires around five iterations in order for the moments of the approximated number density function to be at a maximum relative error up to  $10^{-6}$  from the original moments, the cost of the method is very moderate.

Let us underline once more that such a method has the major advantage, with a very moderate cost, to preserve the moment vector in the singular transport equation with a very stable model for the flux of disappearing droplets/particles. Moreover, after making the link between such a scheme and the DQ-MOM approach for a better understanding of the novelty of the present contribution, we will see how this algorithm can be easily extended to more general evaporation laws, with the same type of steps.

In the general strategy of operator splitting presented in Section 4.1.2 for the resolution of the complete system Eq. (4.1), the treatment of the evaporation part is not complete if the momentum  $m_1 u$  evolution is not treated. A resolution scheme is proposed here, in a 1D case since each direction can be treated independently here. As mentioned in Section 4.1.5, because of the monokinetic assumption Eq. (4.9) in a section and since velocity does not directly interfere in the evaporation part, the same results can then be formulated on these moments like Prop. (1) with the following fluxes:

$$\begin{aligned} \Phi_{u,-}(\Delta t) &= \int_{S^{(j-1)} + \Delta t}^{S^{(j-1)} + \Delta t} \int_{\mathbb{R}} u \beta f(0, \beta, u) du d\beta, & \Phi_{u,+}(\Delta t) &= \int_{S^{(j)} + \Delta t}^{S^{(j)} + \Delta t} \int_{\mathbb{R}} u \beta f(0, \beta, u) du d\beta \\ &= u_p^{(j)} \underbrace{\int_{S^{(j-1)}}^{S^{(j-1)} + \Delta t} u \beta n(0, \beta, u) d\beta}_{\Phi_{-2}}, & &= u_p^{(j+1)} \underbrace{\int_{S^{(j)}}^{S^{(j)} + \Delta t} u \beta n(0, \beta, u) d\beta}_{\Phi_{+2}}, \end{aligned} \quad (5.8)$$



Moreover, the assumption of a constant velocity inside a section is done, as for the classical multi-fluid model, see Section 4.1.4. It also induces that the velocity can only evolve through exchanges between the sections. So nothing has to be done in the case where only one section is considered like in the following. However, for the sake of completeness, let us give a numerical scheme able to deal with the velocity evolution.

The resolution of the momentum leads to an additional evolution equation in system (4.15):

$$\partial_t(m_1^{(j)}u_p^{(j)}) = -m_0^{(j)}u_p^{(j)} - n(t, S^{(j-1)})S^{(j-1)}u_p^{(j)} + n(t, S^{(j)})S^{(j)}u_p^{(j+1)}, \quad (5.9)$$

So that system (5.4) holds, but with a different definition of matrix  $\mathbf{A}$  and fluxes  $\Phi_-$  and  $\Phi_+$ :

$$\mathbf{A} = \begin{bmatrix} 0 & & & & & & & \mathbf{0} \\ 1 & 0 & & & & & & \\ & 2 & \ddots & & & & & \\ & & \ddots & \ddots & & & & \\ & & & \ddots & \ddots & & & \\ & & & & N & 0 & & \\ & & & & & 0 & & \\ \mathbf{0} & & & & & 1 & 0 & \end{bmatrix},$$

where two dimensions have been added to the rank of  $\mathbf{A}$ , corresponding to the quantities  $m_0u_p^{(j)}$  and  $m_1u_p^{(j)}$ .

$$\Phi_-(\Delta t) = \int_{S^{(j-1)}}^{S^{(j-1)}+\Delta t} n(0, \beta, u) \begin{bmatrix} 1 \\ \beta \\ \vdots \\ \beta^N \\ 0 \\ \beta u_p^{(j)} \end{bmatrix} d\beta, \quad \Phi_+(\Delta t) = \int_{S^{(j)}}^{S^{(j)}+\Delta t} n(0, \beta, u) \begin{bmatrix} 1 \\ \beta \\ \vdots \\ \beta^N \\ 0 \\ \beta u_p^{(j+1)} \end{bmatrix} d\beta.$$

The last component of this new system reads:

$$\left[ m_1^{(j)}(\Delta t) + \Delta t m_0^{(j)}(\Delta t) \right] u_p^{(j)}(\Delta t) = m_1^{(j)}(0)u_p^{(j)}(0) - \Phi_{u,-}(\Delta t) + \Phi_{u,+}(\Delta t). \quad (5.10)$$

Meanwhile, the second equations of system (4.15) writes:

$$m_1^{(j)}(\Delta t) + \Delta t m_0^{(j)}(\Delta t) = m_1^{(j)}(0) - \Phi_{-2}(\Delta t) + \Phi_{+2}(\Delta t), \quad (5.11)$$

with  $\Phi_{-2}(\Delta t)$  denoting the second component of the vector  $\Phi_-(\Delta t)$ .

Then the updated value of  $u_p^{(j)}$  writes:

$$u_p^{(j)}(\Delta t) = \frac{m_1^{(j)}(0) - \Phi_{-2}(\Delta t)}{m_1^{(j)}(\Delta t) + \Delta t m_0^{(j)}(\Delta t)} u_p^{(j)}(0) + \frac{\Phi_{+2}(\Delta t)}{m_1^{(j)}(\Delta t) + \Delta t m_0^{(j)}(\Delta t)} u_p^{(j+1)}(0). \quad (5.12)$$

The quantity  $u_p^{(j)}(\Delta t)$  is a convex sum (because of Eq. (5.11)) of the quantities  $u_p^{(j)}(0)$  and  $u_p^{(j+1)}(0)$ , which ensures the stability of the scheme. Moreover, in the particular case of  $u_p^{(j+1)} = 0$ , i.e. when only one section is considered, it comes from Eq. (5.11) that  $\partial_t u_p^{(j)} = 0$ .

## 5.2 Link with a DQMOM approach

For the sake of completeness, let us first recall the DQMOM approach in order to resolve the evaporation dynamics in the size phase space and then adapt it to the particular structure of our problem.

### 5.2.1 DQMOM and new DQMOM formalism of the evaporation process

In order to solve the transport equation (4.12) using DQMOM, we consider the following approximation of  $n$ :

$$\bar{n}(t, S) = \sum_{i=1}^s \omega_i(t) \delta(S - \mathcal{S}_i(t)), \quad (5.13)$$

from which we have:

$$\partial_t \bar{n} = \sum_{i=1}^s a_i(t) \delta(S - \mathcal{S}_i(t)) - \sum_{i=1}^n (b_i(t) - \mathcal{S}_i(t) a_i(t)) \delta'(S - \mathcal{S}_i(t)), \quad (5.14)$$

where we have defined for commodity

$$\begin{aligned} a_i(t) &= d_t \omega_i(t), \\ b_i(t) &= d_t (\omega_i(t) \mathcal{S}(t)). \end{aligned} \quad (5.15)$$

The evolution of the approximated moments  $\bar{m}_k$  depends linearly on the  $a_i$  and  $b_i$ :

$$d_t \bar{m}_k = \sum_{i=1}^s (1-k) a_i(t) \mathcal{S}_i^k(t) + \sum_{i=1}^s k b_i(t) \mathcal{S}_i^{k-1}(t). \quad (5.16)$$

However, the variables for which we have the simplest evolution equation are  $\exp(t \mathbf{A}) \mathbf{m}(t)$ , so that it is interesting to look at the system of ODE's satisfied by  $\exp(t \mathbf{A}) \bar{\mathbf{m}}(t)$ .

**Lemma 4** *The evolution equation of the translated approximated moments reads :*

$$d_t (\exp(t \mathbf{A}) \bar{\mathbf{m}}) = \sum_{i=1}^s (1-k) a_i (\mathcal{S}_i + t)^k + \sum_{i=1}^s k (b_i + \omega_i + t a_i) (\mathcal{S}_i + t)^{k-1}, \quad (5.17)$$

Considering the new variables:

$$b_i^* = b_i + \omega_i + t \quad a_i = d_t [\omega_i (\mathcal{S}_i + t)], \quad \mathcal{S}_i^* = \mathcal{S}_i + t, \quad (5.18)$$

the new constraints of DQMOM defining the source terms are given by :

$$\sum_{i=1}^s (1-k) a_i (\mathcal{S}_i^*)^k + \sum_{i=1}^s k b_i^* (\mathcal{S}_i^*)^{k-1} = -n(t, S_{min}) S_{min}^k + n(t, S_{max}) S_{max}^k. \quad (5.19)$$

*Proof.* Let us first notice that:

$$d_t [\exp(t \mathbf{A}) \mathbf{m}] = \exp(t \mathbf{A}) [\mathbf{A} \mathbf{m} + d_t \mathbf{m}],$$

and

$$(\mathbf{A} \mathbf{m} + d_t \mathbf{m})_k = \sum_{i=1}^s [(1-k) a_i \mathcal{S}_i^k + k b_i \mathcal{S}_i^{k-1} + k \omega_i \mathcal{S}_i^{k-1}],$$

Consequently, we obtain:

$$(\exp(t \mathbf{A}) [\mathbf{A} \mathbf{m} + d_t \mathbf{m}])_k = \sum_{i=1}^s [(1-k) a_i (\mathcal{S}_i + t)^k + k (b_i + \omega_i + t a_i) (\mathcal{S}_i + t)^{k-1}],$$

and the proof is complete. ■

Let us emphasize that we obtain exactly the same form of linear system as the one obtained in the classical formulation. However, two advantages are to be underlined. First, we have isolated the transport

part from the flux part as already mentioned. Second, and it is clearly related, the abscissas appearing in the matrix to be solved do not evolve with transport in time but only change due to the fluxes so that the conditioning of the matrix, for scaled abscissas, can be controlled easily [85].

Finally, it is important to realize that we still have a differential form of the DQMOM system of equations, a remark we already mentioned earlier as far as the moment equations were concerned. In the situation of a zero upper flux and with  $S_{\min} = 0$ , we see that the flux will only influence the zeroth order moment. The difference between the two approaches can be seen to be the same one as the difference between the kinetic schemes (for which we work with a time integrated version of the dynamical system and invoke the kinetic evolution in order to evaluate the fluxes) and the method of lines (for which the integration is only performed in the size variable and where the time is kept a continuous variable, thus leading to a system of ordinary differential equation to be resolved by a standard ODE integrator) in the framework of hyperbolic system of conservation laws [151, 152].

### 5.2.2 Relation between the two formulations

Instead of working with a differential form of the system of abscissas and weights and plugging it in a LSODE like solver for ordinary differential equations, and encountering difficulties as far as stability is concerned, we make the link between the previous DQMOM formulation and the original integral form of the system developed in the previous Section in the following Lemma.

**Lemma 5** *Remembering the DQMOM new formulation in differential form (5.19), one can find a first integral for each  $k$  :*

$$\int_0^{\Delta t} \left[ \sum_{i=1}^s (1-k) a_i(t') \mathcal{S}_i^{*k}(t') + \sum_{i=1}^s k b_i^*(t') (\mathcal{S}_i^{*k-1}(t')) \right] dt' = \int_0^{\Delta t} d_{t'} \left[ \sum_{i=1}^s \omega_i(t') (\mathcal{S}_i^*(t'))^k \right] dt'.$$

*Proof.* Let us define  $\mathcal{B} = k (\mathcal{S}_i^*)^{k-1} d_{t'}(\omega_i \mathcal{S}_i^*) + (1-k) d_{t'}[\omega_i (\mathcal{S}_i^*)^k]$ . It is sufficient to note that:

$$\begin{aligned} \mathcal{B} &= k (\mathcal{S}_i^*)^{k-1} [d_{t'}(\omega_i \mathcal{S}_i^*) - \mathcal{S}_i^* d_{t'}\omega_i] + (\mathcal{S}_i^*)^k d_{t'}\omega_i \\ &= k (\mathcal{S}_i^*)^{k-1} \omega_i d_{t'}\mathcal{S}_i^* + (\mathcal{S}_i^*)^k d_{t'}\omega_i \\ &= \omega_i d_{t'}(\mathcal{S}_i^*)^k + (\mathcal{S}_i^*)^k d_{t'}\omega_i \end{aligned}$$

which completes the proof. ■

Thus, we have in fact an *exact* solution in time of the modified DQMOM differential system (5.17) through equation (5.1) once the fluxes  $\Phi_{\pm}$  have been evaluated. The link with a DQMOM formulation is then complete and we are also able to fully compare the two approaches and appreciate the novelty of the proposed numerical scheme.

## 5.3 Evaporation rate depending on size, using a piecewise constant approximation

In this Section, our aim is to treat a general evaporation law of the form

$$\partial_t n - \partial_S (K n) = 0, \quad (5.20)$$

with a piecewise constant coefficient  $K(S)$  which can approximate a continuous but non constant law. This appears naturally when considering more realistic evaporation law like in [146], which continuously depends on droplet temperature; this temperature, continuously depending of the droplet size because of the thermal inertia, is approximated by a piecewise constant function in multi-fluid method developed there, in such a way that the evaporation rate is then also a piecewise constant function. Our goal is to show how this phenomena can be simulated by the algorithm developed in this article.

In order to get a numerical solution based on the evolution of the moments, without lost of completeness, we will consider two size sections  $[0, 0.5]$  and  $[0.5, 1]$ , in which the evaporation is taken constant. So

far, the method based on moment dynamics has been displayed for a case where the evaporation rate was constant all over the size interval. The algorithm presented in Section 5.1.4 must be modified in order to preserve the moment space. Indeed, in step 3, the abscissas, initially in  $[S_{k-1} + \Delta t, S_k + \Delta t]$ , are shifted by  $-\Delta t$  so that they lie in  $[S_{k-1}, S_k]$  at the end of the algorithm. Let us take in the first section  $K = -1$  and in the second section  $K = -2$ . With the previous algorithm, the size abscissas of the first section would then be in  $[S_0 + \Delta t, S_1 + 2\Delta t]$ , so that at the end they lie in  $[S_0, S_1 + \Delta t]$ . There is no guarantee that the corresponding vector of moment in  $[S_0, S_1 + \Delta t]$  is a vector of moment in  $[S_0, S_1]$ .

In order to devise the algorithm to solve that problem, we do an analogy with the pressureless gaz. Let consider a NDF  $f(\Delta t, S, u)$  depending on the evaporation velocity  $u$ . It is solution of the following equation :

$$\partial_t f + u \partial_S f = 0.$$

We then state that  $f(t, S, u) = n(t, S) \delta(K(t, S) - u)$ , in such a way that  $K$  is a velocity in the size phase space. If we take the 0<sup>th</sup> and 1<sup>st</sup> order moment with respect to  $K$  of the kinetic transport equation, we get

$$\begin{cases} \partial_t n(t, S) + \partial_S n(t, S) K = 0, \\ \partial_t n(t, S) K + \partial_S n(t, S) K^2 = 0. \end{cases} \quad (5.21)$$

With the initial condition that  $K$  is discontinuous, this appears to be a Riemann problem for the density  $n$  and the evaporation rate  $K$  (which is also a velocity). The scheme we use consists in solving a Riemann problem between each size interval and for each time step. Let us notice that the second equation of system (5.21) is not an equation of the initial problem. The evaporation rate just depends on the size and is constant over time. The reason why we artificially transport  $K$  during a time step is because the piecewise approximation on  $K$  generate shocks in the scheme. If  $K$  is not transported, then a shock occurs at the limit between the sections so that it is impossible to know in which section it belongs to. Moreover, it is compatible with a Lagrangian view of the droplets which goes from a section to another. Figure 5.1 displays the solution in the sense of the characteristics that is computed.

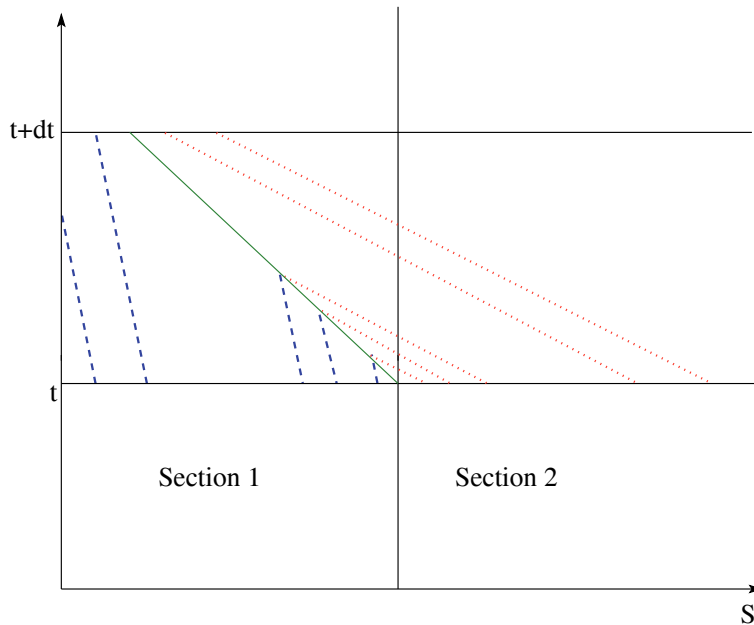


Figure 5.1: Numerical solution in the sense of characteristics. The characteristics of section 1 are represented by dashed lines and the ones of section 2 by dotted lines. The solid line stands for the  $\delta$ -shock. The characteristics close to the border enter the shock.

The first step of the algorithm is exactly the same as for the one described in Section 5.1.4. But on the contrary to the previous algorithm, we don't have to calculate two fluxes any more ( $\Phi_-^k(\Delta t)$  and  $\Phi_-^{k+1}(\Delta t)$ ), but five:

1. the evaporative flux going out of section 1 ( corresponding to  $\Phi_-^k(\Delta t)$ )
2. the flux of the droplets from section 1 whose characteristics go into the  $\delta$ -shock
3. the flux resulting from the droplets from section 1 which are in the  $\delta$ -shock
4. the flux of the droplets from section 2 whose characteristics go into the  $\delta$ -shock ( corresponding to  $\Phi_-^{k+1}(\Delta t)$ )
5. the evaporative flux entering section 1 but not going into the  $\delta$ -shock

By adding these fluxes computing the corresponding weights and abscissas and shifting them at the correct evaporation rate, we are able to construct the solution of the Riemann problem. The velocity of the  $\delta$ -shock is given in [21]

$$u = \begin{cases} \frac{K^+(0.5)(\sqrt{f^+(0.5)+K^-(0.5)}\sqrt{f^-(0.5)}}{\sqrt{f^+(0.5)+\sqrt{f^-(0.5)}}} & \text{if } f^-(0.5) \neq f^+(0.5), \\ \frac{K^+(0.5)+K^-(0.5)}{2} & \text{if } f^-(0.5) = f^+(0.5). \end{cases} \quad (5.22)$$

## 5.4 Treatment of arbitrary evaporation law

Here, our aim is to treat a general evaporation law of the form

$$\partial_t n - \partial_S (K n) = 0, \quad (5.23)$$

for which the form of the evaporation coefficient is given as a function of  $S$  in general form  $K = K(S)$ . Our aim in this Section is to directly generalize the algorithm defined in Section 5.1.4 to this kind of arbitrary but smooth evaporation laws in a sense that will be defined in the following.

First, we will evaluate the characteristics and show that some restrictions have to be imposed on the profile of function  $K$  from both the modeling and the mathematical point of view. The key issue is the behavior near zero size. Let us make the following set of assumptions on the evaporation law. We assume that we deal with real evaporation, that is,  $K(S) > 0$  for  $S > 0$  and since droplets/particles of negative size do not evaporate, we assume  $K(S) = 0$ ,  $S < 0$ . Consequently, there are two cases. The first one is the case of a discontinuous evaporation coefficient, where we assume that  $K(S)$  is globally Lipschitz on the interval  $[0, S_{\max}]$  and admits a limit at zero size which is positive. This yields measure solution with a measure concentration of droplet number density at zero size. The second case, where  $K(S)$  is globally Lipschitz on every compact subset of the interval  $[0, S_{\max}]$ , includes the continuous one, where  $K(0) = 0$ , as well as cases with infinite values at zero size (the typical example is the  $d^2$ -law with (5.23) written for the radius of the droplets  $R$ , in such a way that  $K(R) = \frac{cst}{8\pi R}$ ).

### 5.4.1 Change of variable characteristics

In this context, let us consider the characteristic curves defined by

$$\frac{d\Xi}{dt} = K(\Xi). \quad (5.24)$$

For any  $S_0 > 0$ , with the considered regularity of  $K$ , they are defined for all  $t$  as long as the curve does not crosses  $S_0$ . We then define  $\gamma(S)$  a primitive of the function  $1/K(S)$ ; it is a bijection of  $[S_0, S_{\max}]$  onto its range. We also define  $\Psi(\gamma)$ , a function such that  $f(t, S)dS$  and  $\Psi(t, \gamma)d\gamma$  define the same measure on their respective intervals; this implies that  $\Psi(t, \gamma) = K(S)f(t, S)$  and

$$\partial_t \Psi - \partial_\gamma \Psi = 0. \quad (5.25)$$

We then obtain the usual transport equation (4.12). However, two key questions arise, the first one concerns the behavior of the evaporation law around zero size and the second, related to the first, do the droplet disappear in finite time due to evaporation, or do their size approach zero asymptotically?

It is clear that the disappearance in finite time of the droplet occurs if the limit of  $K$  as  $S$  approaches zero is positive and even infinite. Assuming that the evaporation law behaves like  $a S^\alpha$  in the neighborhood of zero, the limiting value of  $\alpha$  is 1. For  $\alpha = 1$ , the size of one droplet approaches zero asymptotically and exponentially. For any positive  $\varepsilon$ ,  $\alpha = 1 + \varepsilon$  leads also to an asymptotic decrease towards zero, nevertheless algebraically, whereas  $\alpha = 1 - \varepsilon$  leads to a disappearance of droplets in finite time. This kind of behavior was observed already in [85]. However, the problem of the flux of droplet number at zero size has only to be treated when  $\alpha = 1 - \varepsilon$ . Consequently we restrict our study to this case. In such a case we can take  $\gamma$  as the primitive of  $1/K$  which is zero at  $S = 0$ ; this yields a one to one correspondence between  $S$  and the characteristic variable  $\gamma$ , for  $S \in [0, S_{\max}]$ . Finally, the theory presented before can easily be extended to the characteristic system in the  $\Psi$  variable instead of  $f$ .

Examples :  $K(S) = c/S$ ,  $\gamma = S^2/2$ , this is the case of the droplet radius with  $c = 1/8\pi$  and  $\gamma$  is the droplet surface.  $\varepsilon = 1/2$ ,  $a = 1$ ,  $\Xi(t) = (\Xi(0)^{1/2} - t/2)^2$  which leads to an evaporation time of 2 if the initial size is 1,  $\gamma = 2S^{1/2}$ .

### 5.4.2 Algorithm of the new scheme

The algorithm presented in Section 5.1.4 can be generalized to arbitrary evaporations laws, still assuring the preservation of the moment space, in the following way : a discretization  $0 = S_0 < S_1 < \dots < S_N = S_{\max}$  of the support  $[0, S_{\max}]$  is introduced. Let us assume that the moments  $\mathbf{m}^k(t)$  on each interval  $[S_{k-1}, S_k[$  and at time  $t$  are known. The moments at time  $t + \Delta t$  is computed by:

1. In each section  $[S_{k-1}, S_k]$ , a reconstruction  $f^k$  is done of the distribution from its moments  $\mathbf{m}^k(0)$  by the ME method. Let then define the characteristics  $\Xi_k$  by:

$$\frac{d\Xi_k}{dt} = K(\Xi_k), \quad \Xi_k(0) = S_k. \quad (5.26)$$

An ODE solver can be used to obtain  $\Xi_k(\Delta t)$ . The flux  $\Phi_-^k(t + \Delta t)$  with the section  $k - 1$  is computed by:

$$\Phi_-^k(t + \Delta t) = \int_{S_{k-1}}^{\Xi_{k-1}(\Delta t)} n^k(\beta) \begin{bmatrix} 1 \\ \beta \\ \vdots \\ \beta^N \end{bmatrix} d\beta. \quad (5.27)$$

2. The weights  $\omega_{i,k}$  and the abscissas  $\mathcal{S}_{i,k}$  corresponding to the moments  $\mathbf{m}^k(t) - \Phi_-^k(t + \Delta t) + \Phi_-^{k+1}(t + \Delta t)$  are computed using the QD algorithm. Since these moments are in fact the moments of  $\sum_i n^i(S) \mathbb{1}_{[S_{i-1}, S_i[}(S)$  on  $[\Xi_{k-1}(\Delta t), \Xi_k(\Delta t)]$ , the abscissas are in  $[\Xi_{k-1}(\Delta t), \Xi_k(\Delta t)]$ .

3. Let then define the characteristics  $Y_{i,k}$  by:

$$\frac{dY_{i,k}}{dt} = -K(Y_{i,k}), \quad Y_{i,k}(0) = \mathcal{S}_{i,k}. \quad (5.28)$$

The moments  $\mathbf{m}^k(t + \Delta t)$  corresponding to the weights  $\omega_{i,k}$  and the abscissas  $Y_{i,k}(\Delta t)$  are computed. The abscissas  $Y_{i,k}(\Delta t)$  necessarily belong to the interval  $[\xi_{k-1}, \xi_k[$ , so that  $\mathbf{m}^k(t + \Delta t)$  belongs to the moment space corresponding to this interval. It gives then an approximation of the moments of  $n(t + \Delta t, \cdot)$  on  $]S_{k-1}, S_k[$ .

This algorithm is valid for a CFL-like condition  $\max_S(K(S))\Delta t < \Delta S$ . In fact, it is still valid for a less restrictive condition :  $\Xi_k(\tau) \in [S_k, S_{k+1}]$  for  $\tau \in [0, \Delta t]$ .

Moreover, one can notice that it is also valid for discontinuous evaporation rate (as soon as each discontinuity is at the boundary of a section  $[\xi_{k-1}, \xi_k[$ ). This situation can appear in multi-fluid method, for evaporation law depending on the temperature of the droplet, this temperature being taken constant inside a section but being able to vary between the sections.

## 5.5 Results

### 5.5.1 Constant evaporation law

The method described in Section 5.1.4 is tested on three kinds of initial distributions : a smooth one, presented in Fig. (5.2), a discontinuous one, presented in Fig. (5.5) and a distribution corresponding to moments close to the boundary of the moment space  $\mathbb{M}_2$  in Fig. (5.8) (it is the ME-reconstruction corresponding to canonical moments  $p_1 = 0.8$ ,  $p_2 = 0.01$  and  $p_3 = 0.5$ , see Appendix B.2). A discretization into sections is introduced and the moments inside each section are computed for the initial distribution in order to initialize the simulation with our moment method. The evolution of the obtained moments can be compared with the moments of the exact solution (4.13). Moreover, since, at each time step a ME reconstruction  $\tilde{n}_{ME}(S)$  of the distribution is performed, we can easily compare such an approximated distribution from the data of moments to the exact distribution, even if the computed variables are the sole moments. Finally, the variable of interest for the spray is its mass density, which corresponds to a moments of order  $3/2$ . This fractional moment is not resolved but can be calculated through the ME reconstruction of the distribution by  $\int_0^{S_{max}} S^{3/2} \tilde{n}_{ME}(S) dS$ . This variable will be compared with the moment of order  $3/2$  of the exact solution but also with the one obtained with another numerical method: a multi-fluid method of order two derived in [145].

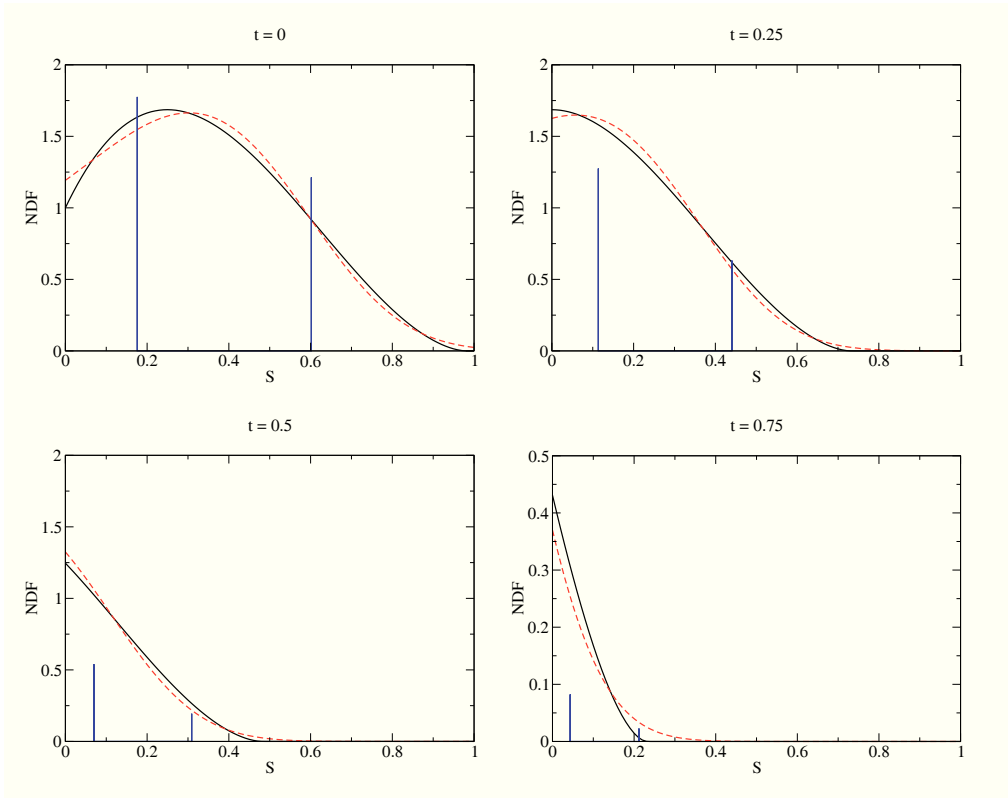


Figure 5.2: Smooth NDF (solid), ME reconstructed NDF obtained with the moments computed with the moment method with 1 section and 4 moments (dashed line) and corresponding peaks, at times  $t = 0$ ,  $t = 0.25$ ,  $t = 0.5$  and  $t = 0.75$ .

In Fig. (5.2), one can see the evolution of the smooth distribution. A simulation is also done with the scheme previously described with only 1 section and 4 moments. The time step is here  $\Delta t = 0.025$  but it can be seen that the accuracy results do not depend of the time discretization. The ME reconstruction as well as the peaks showing the abscissas and the weights corresponding to the moments are drawn. One can see that the ME reconstruction follows very well the exact distribution, with a total evaporation at approximatively the same time (see the scales of the figures). Moreover, the error on the moments is

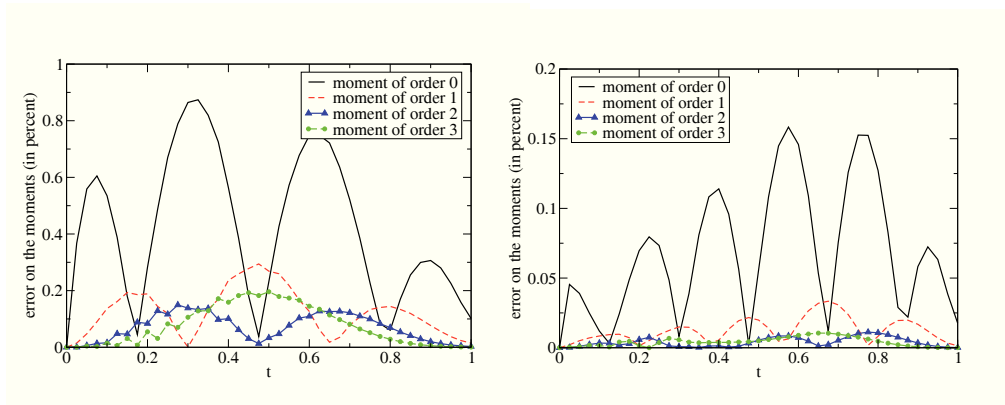


Figure 5.3: Evolution of the error on the moments calculated with the moment method with one section (left) or two sections (right) relative to their initial value.

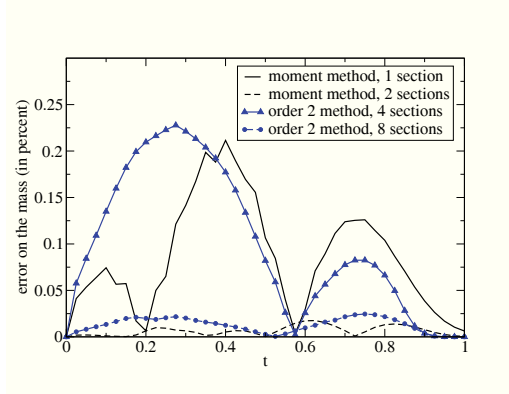


Figure 5.4: Evolution of the error on the mass density relative to its initial value, calculated with the moment method with one or two sections and the multi-fluid method of order 2 with 4 or 8 sections.

smaller than one percent of each initial moment as shown in Fig. (5.3)-left. This error decreases under 0.2% of each initial moment if two sections  $[0, 1/2]$  and  $[1/2, 1]$  are used (see Fig. (5.3)-right). With these two sections, the ME reconstruction can almost not be distinguished from the exact solution. Concerning the mass density, the error is smaller than 0.25% for a simulation with the moment method with 1 section and 4 moments and still ten times smaller with 2 sections, as seen in Fig. (5.4). In order to have the same level of accuracy, four sections are needed with the multi-fluid method of order two, that is to say twice as more moments. Moreover, the multi-fluid method giving directly equations on moments of order  $3/2$  on each section, developed in [146], were also tested, using a constant reconstruction on each section. It can be seen that our new scheme is much more accurate than this method, while using a number of moments three times smaller (like in Fig. 4.1-left).

In Fig. (5.5), one can see the evolution of the discontinuous distribution. A simulation is also done with the moment method with only 2 sections and 4 moments per section. One can see that the method is still able to reproduce a good estimation of this kind of distribution but with a lower level of accuracy. However, the accuracy of the moment is good as shown in Fig. (5.6) for calculations with one or two sections. In fact, except for the moment of order 0, the accuracy is even very good. But the difference between the two discretizations is not as large as for the regular case. Concerning the mass density, the error is smaller than 0.3% for a simulation with the moment method with 1 section and 4 moments and two times smaller with 2 sections, as seen in Fig. (5.4). In order to have the same level of accuracy, six sections are needed with the multi-fluid method of order two in the first case and twelve in the second case, that is to say a number of moments three of two times larger.

In Fig. (5.8), one can see the evolution of the distribution corresponding to moments close to the boundary of the moment space  $\mathbb{M}_2$ . The initial distribution is chosen as the ME-reconstruction corre-



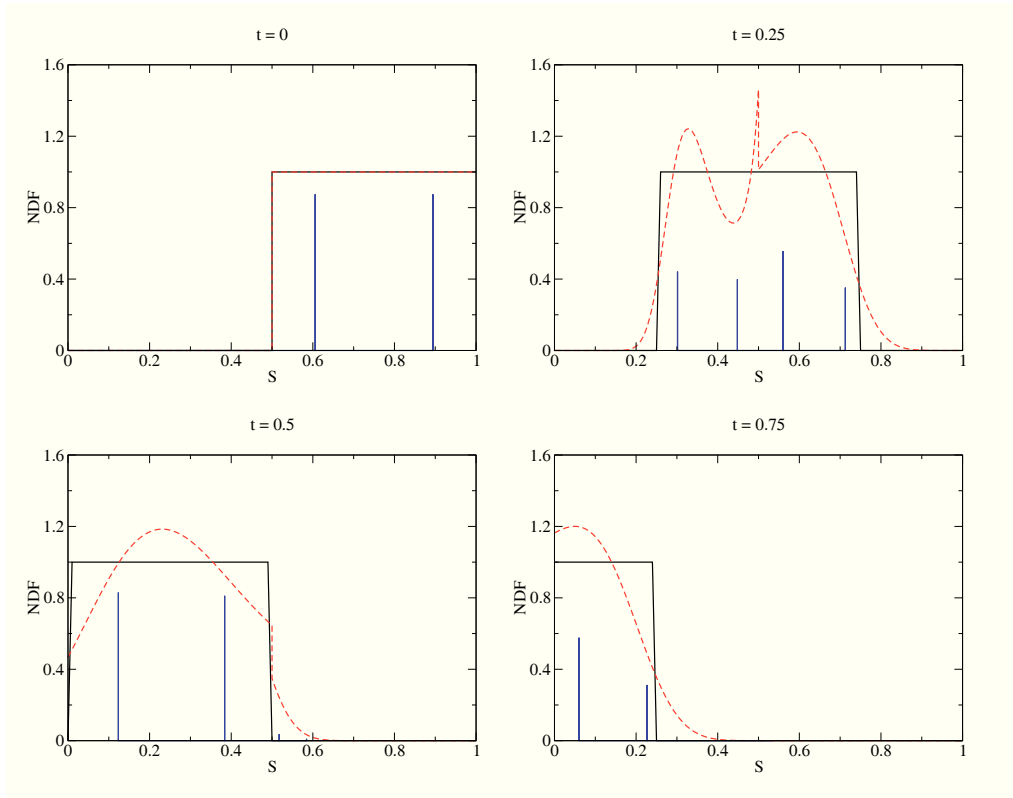


Figure 5.5: Discontinuous NDF (solid), ME reconstructed NDF obtained with the moments computed with the moment method with 2 sections and 4 moments (dashed line) and corresponding peaks, at times  $t = 0$ ,  $t = 0.25$ ,  $t = 0.5$  and  $t = 0.75$ .

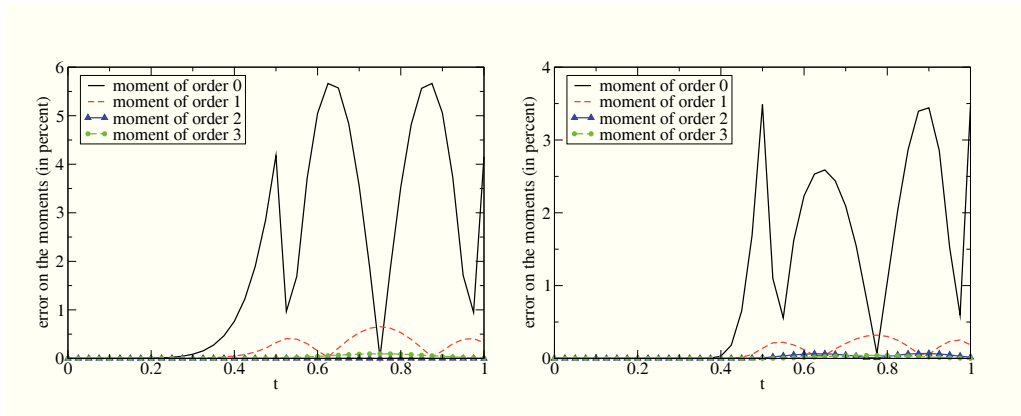


Figure 5.6: Evolution of the error on the moments calculated with the moment method with one section (left) or two sections (right) relatively to their initial value.

sponding to canonical moments  $p_1 = 0.8$ ,  $p_2 = 0.01$  and  $p_3 = 0.5$ , as done in Appendix B.2. In this case, the computation of integrals  $\langle x^k \rangle_S$ , Eq. (4.25), as well as the flux (5.6) are no more done with a Gaussian quadrature, which is not precise enough. Instead, Simpson formula are used here on 1000 sub-intervals of the integration interval; it is too much, but the aim was just to test the method.

The results are very good, since the analytical evolution of the initial distribution and the ME-reconstruction of the moments obtained by the computation can not be distinguished on Fig. (5.8). More precisely, the accuracy on the moments is greater than 2%, as shown in Fig. (5.9).

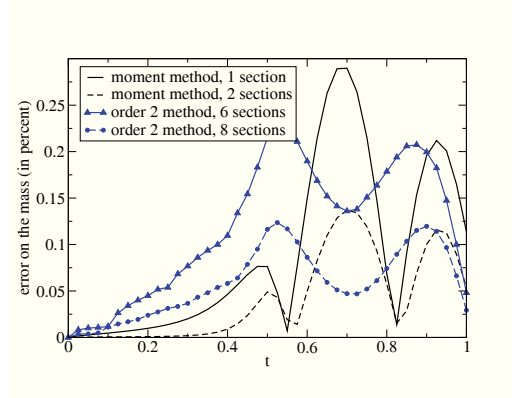


Figure 5.7: Evolution of the error on the mass density relatively to its initial value, calculated with the moment method with one or two sections and the multi-fluid method of order 2 with 6 or 8 sections.

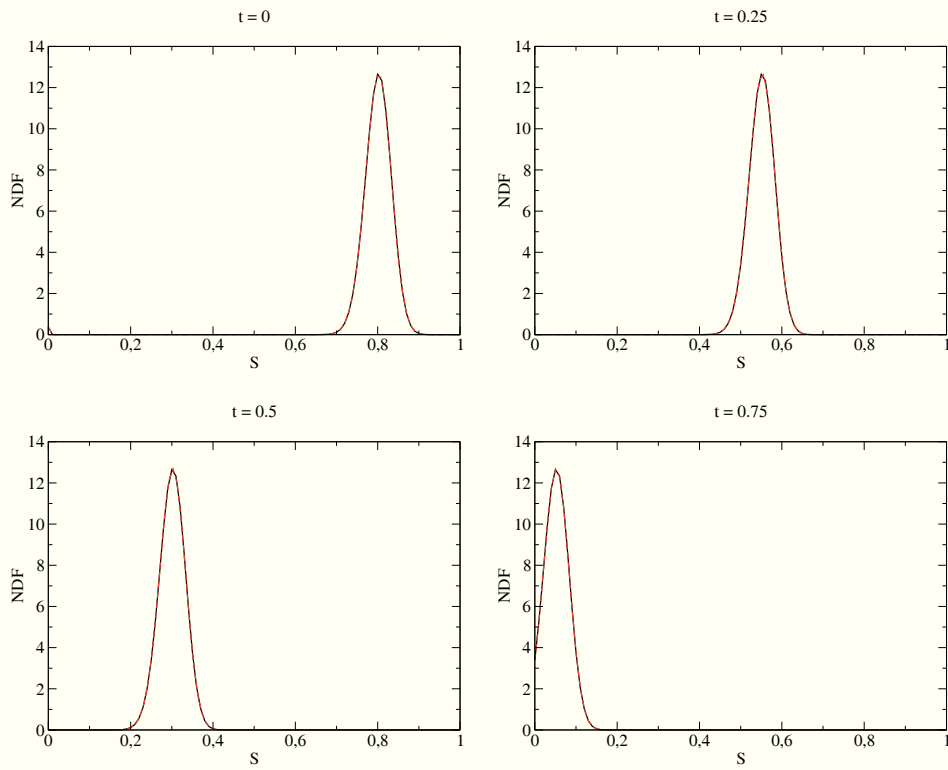


Figure 5.8: NDF (solid), ME reconstructed NDF obtained with the moments computed with the moment method with 2 sections and 4 moments (dashed line) and corresponding peaks, at times  $t = 0$ ,  $t = 0.25$ ,  $t = 0.5$  and  $t = 0.75$ .

### 5.5.2 Discontinuous evaporation law

We assume here that the evaporation rate has a linear profile and writes  $K = K^0(1 + \alpha S)$ , with  $K^0 = 0.5$  and  $\alpha = 2$ . We show now a comparison between the analytical solution and the numerical solution of Eq. (5.23). Using the change of variable proposed in Section 5.4.1, the solution writes:

$$n(\Delta t, S) = \frac{K(\gamma^{-1}(\gamma(S) + \Delta t))}{K(S)} n^0(\Delta t, \gamma^1(\gamma(S) + \Delta t)), \quad (5.29)$$

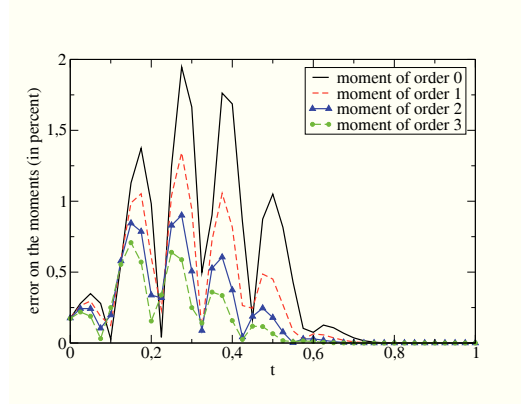


Figure 5.9: Evolution of the error on the moments calculated with the moment method with one section relatively to their initial value.

where

$$\gamma(S) = \int_1^S \frac{dS'}{K(S')} = \frac{1}{\alpha K^0} \log \frac{1 + \alpha S}{1 + \alpha}, \quad (5.30)$$

as we consider the size interval  $[0, 1]$ .

We approximate  $K$  by its averaged values on each interval: 0.75 on the first interval and 1.25 on the second one. Simulation is done with a time step  $\Delta t = 0.025$ . Fig. (5.10) displays the analytical and numerical number density at different times. The ME reconstruction as well as the peaks showing the abscissas and the weights are drawn. One can see that the ME reconstruction describes well the exact distribution. Fig. (5.11) displays the errors on the moments, compared to the analytical solution with the discontinuous evaporation rate or to the one with the affine evaporation rate. The errors compared to the affine evaporation rate are smaller than 8% of each initial moment; moreover, this error is smaller than 1% for moments of order greater than one. The accuracy is lower than in the case of a uniform evaporation rate, but this is a very difficult case because the rate  $K$  has a large variation and is approximated by piecewise constant function only on 2 sections. This result is quite encouraging and validates our method.

### 5.5.3 Arbitrary evaporation law

Algorithm of Section 5.4.2 is tested here for different kind of evaporation laws, with always a smooth initial NDF, presented in Fig. (5.2).

#### 5.5.3.1 Smooth evaporation law

The algorithm described in the previous Section is tested on two kinds of coefficient of evaporation : an affine one  $K(S) = 0.5 + S$  and a “square root” one  $K(S) = \sqrt{0.5 + S}$ . Let us note  $f_0$  the initial NDF. Using the characteristics, it can be shown that the solution of Eq. (5.23) is then given by :

$$n(t, S) = n_0(\Xi(t; 0, S)) \frac{K(\Xi(t; 0, S))}{K(S)},$$

where  $\Xi(\Delta t; 0, S)$  is the solution at time  $\Delta t$  of Eq. (5.24) with  $\Xi(0) = S$ . For the affine coefficient of evaporation, it is given by :

$$\Xi(\Delta t; 0, S) = (0.5 + S) \exp(\Delta t) - 0.5, \quad (5.31)$$

and for the square root one :

$$\Xi(\Delta t; 0, S) = \left( \frac{\Delta t}{2} + \sqrt{0.5 + S} \right)^2 - 0.5. \quad (5.32)$$

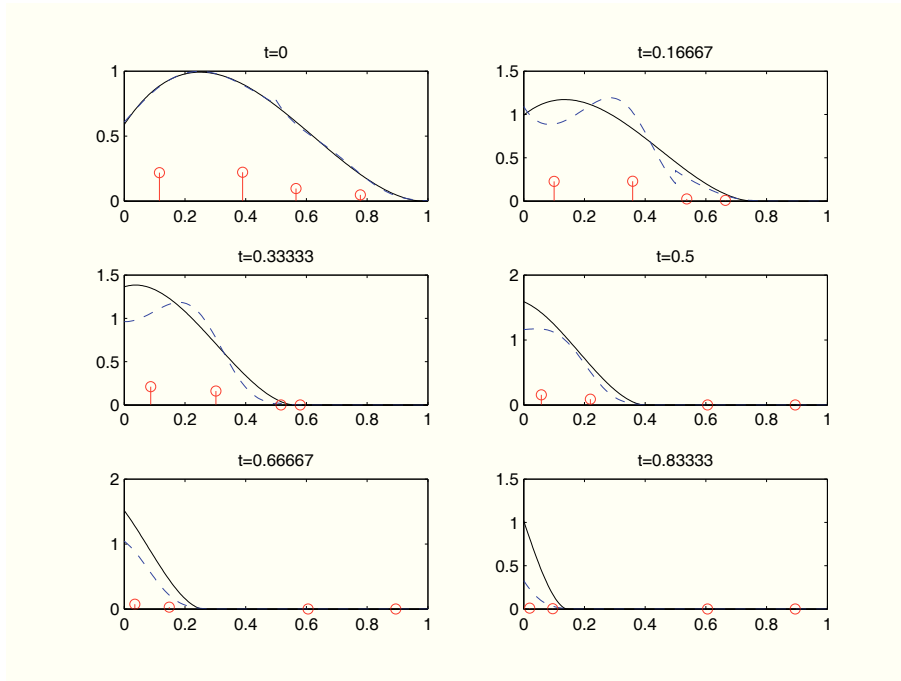


Figure 5.10: Smooth NDF (solid), ME reconstructed NDF obtained with the moments computed with the moment method with discontinuous evaporation rates with 2 sections and 4 moments (dashed line), and corresponding peaks, at times  $t = 0$ ,  $t = 0.17$ ,  $t = 0.33$ ,  $t = 0.5$ ,  $t = 0.67$  and  $t = 0.83$

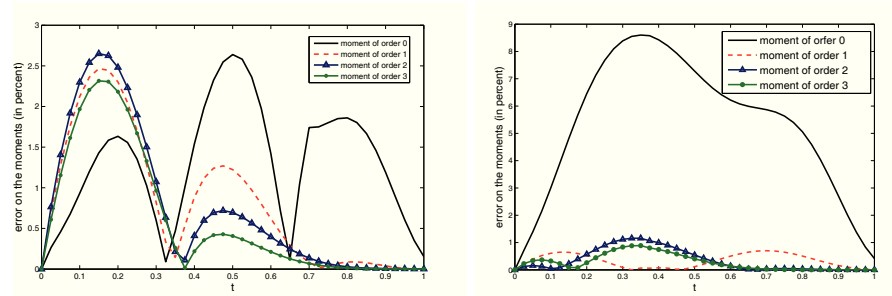


Figure 5.11: Evolution of the errors on the moments calculated with the moment method with discontinuous evaporation rates, with 2 sections and compared to the analytical solution with the discontinuous evaporation law in absolute value (left) or to the analytical solution with the affine evaporation law (right).

The initial NDF is the smooth one, presented in Fig. (5.2).

The moment method is then applied with only one section and four moments. In practice, a second order explicit Runge-Kutta method is used to solve the ODEs (5.26) and (5.28), the explicit Euler method inducing a double value of the error. Moreover, an analytic solution of such equations, given here by Eq. (5.31) or Eq. (5.32) does not bring more accuracy here. The important property to be verified by the ODE solver is that it is accurate enough to avoid characteristic crossing (which will be always the case with a monotone function  $K$ ).

The evolution of the error on the 4 considered moments are plotted in Fig. (5.12)-left for the affine coefficient of evaporation and in Fig. (5.12)-right for the square root one. It shows a level of accuracy similar to the one obtained with the constant evaporation law in Section 5.5.1.

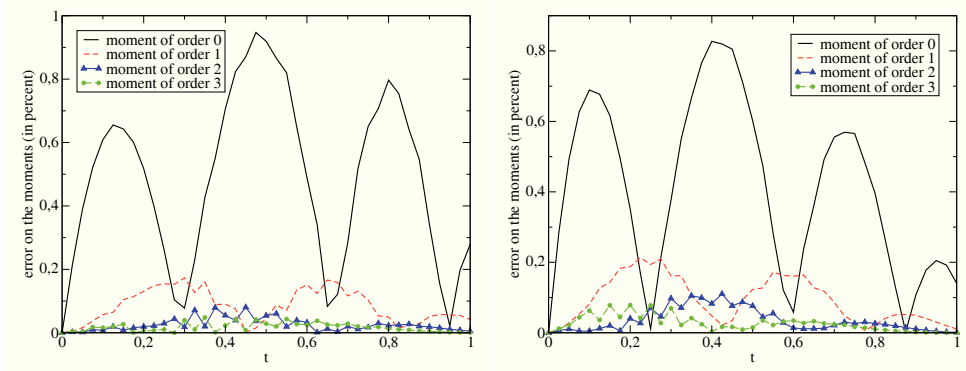


Figure 5.12: Evolution of the error on the moments calculated with the moment method with one section for the affine coefficient of evaporation (left) or for the square root coefficient of evaporation (right) relative to their initial value.

*Note:* An approximation of the integral of Eq. (5.27) by

$$(\Xi_{k-1}(\Delta t) - S_{k-1})n^k(\beta) \begin{bmatrix} 1 \\ \beta \\ \vdots \\ \beta^N \end{bmatrix}, \quad \beta = \frac{\Xi_{k-1}(\Delta t) + S_{k-1}}{2},$$

could be envisioned since it is less costly than the computation of this integral by the double-precision 24-point Gaussian quadrature method. But it is not accurate enough to allow the conservation of the moment space, since it is like approximating  $f^k$  by an affine function, which can be negative.

### 5.5.3.2 Discontinuous evaporation law

Let us now consider a general evaporation law with a piecewise constant coefficient  $K(S)$  which can approximate a continuous but non constant law. This appears naturally when considering more realistic evaporation law like in [146], which continuously depends on droplet temperature; this temperature, continuously depending of the droplet size because of the thermal inertia, is approximated by a piecewise constant function in multi-fluid method developed there, in such a way that the evaporation rate is then also a piecewise constant function. Our goal is to show that our algorithm is able to treat this kind of piecewise constant function.

We assume here that the evaporation rate has a linear profile and writes  $K = K^0(1 + \alpha S)$ , like in Section 5.5.2, so that  $n(t, S)$  is given by Eq. (5.29) and Eq. (5.30). The algorithm of Section 5.4.2 can then be applied directly. The precision of such computation, with 2 sections and 4 moments in each section, is presented in Fig. (5.13)-left. The error is smaller of the percent. However, as seen in Fig. (5.13)-right, the accuracy of this kind of approximation of the affine coefficient of evaporation by a piecewise constant one induces an error of 10% on the number and less than 2% for the other moments. But, this is a very difficult case because the rate  $K$  has a large variation and is approximated by piecewise constant function only on 2 sections.

### 5.5.3.3 Regularity and ‘natural’ variables

A more general formulation of the kinetic equation can be written using a variable  $\phi$  for the droplets size. The NDF is then  $f^\phi(t, x, \phi, u)$ . The parameter  $\phi$  denotes for example the volume  $V$  as in [102], the surface  $S$  as in [61] or the radius  $R$  ( $f^R dR = f^S dS = f^V dV$ ). Let us assume that  $\phi = S^\beta$ . In the case of a  $d^2$  evaporation law for a purely evaporative case, the simple solution  $f^S(\Delta t, S) = f^S(0, S + \Delta t) + n^0(\Delta t)\delta(S)$

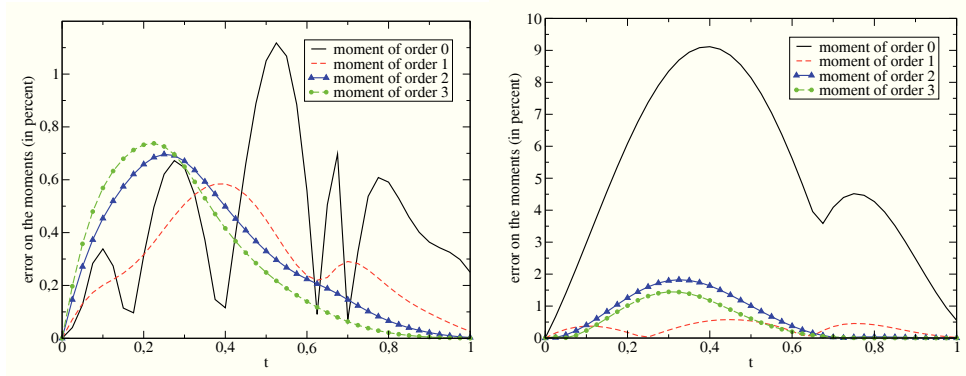


Figure 5.13: Evolution of the error on the moments calculated with the moment method with one section for the discontinuous coefficient of evaporation relatively to their initial value (left) and absolute value of the difference between the moments obtained analytically with the affine coefficient of evaporation and the moments obtained analytically with the discontinuous one, relatively to their initial value (right).

becomes for the variable  $\phi$  :

$$f^\phi(\Delta t, \phi) = \frac{(\phi^{1/\beta} + \Delta t)^{\beta-1}}{\phi^{1-1/\beta}} f^\phi(0, (\phi^{1/\beta} + \Delta t)^\beta) + n^0(\Delta t)\delta(\phi).$$

This leads to a singularity as soon as  $\beta > 1$ , like for the choice of the volume as the size variable.

For the choice of the radius as the size variable, the generalized algorithm described in Section 5.4.2 can be directly applied. The coefficient of evaporation is then  $K(R) = 1/(8\pi R)$  and the CFL-like condition can be written  $\Delta t < 4\pi(\Delta R)^2$ . The evolution of the corresponding moments are plotted in Fig. (5.14) (from the biggest to the lowest, there are the moments of order 0, 1, 2 and 3). It can be seen that computation with one section (but with the exact resolution of the ODEs for the characteristics) is not very accurate. In fact, as seen on Fig. (5.15) it is necessary to use at least 3 sections to have the same

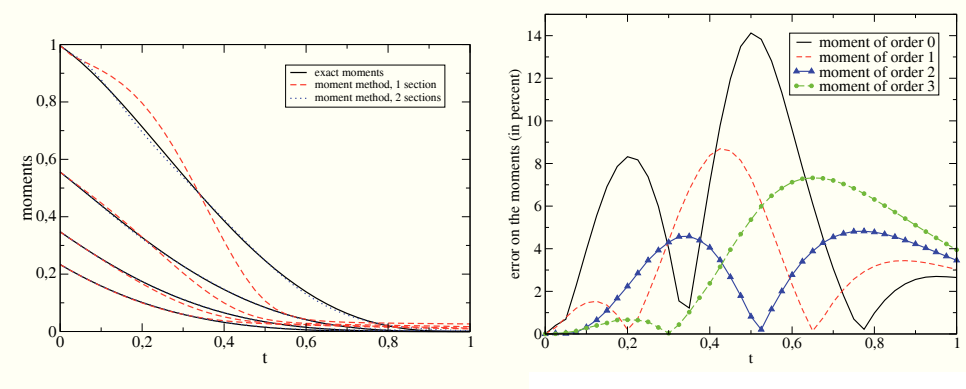


Figure 5.14: (left figure) Evolution of the exact moments for the equation on the radius (solid lines) and the moments calculated with the moment method with one section (dashed lines) or two sections (dotted lines); (right figure) Evolution of the error on the moments calculated with the moment method for the equation on the radius, with one section relatively to their initial value.

level of accuracy on the number and the mass (moments of order 0 and 3, here) as for the resolution on the equation on the surface, Section 5.5.1. In Fig. (5.16), the evolutions of corresponding analytical NDF and reconstructed NDF are plotted, illustrating the loss of accuracy of the computation with one section,

when time increases. The conclusion of this test case is that it is more efficient to use the ‘natural’ variable  $S$  than other variables like the radius. Indeed, theorems showing the separation between the transport per se in the size phase space and the evolution of moments through the fluxes are only exact for the constant evaporation rate. If the generalized algorithm gives good results, it is however better to be able to work with a variable for which the evaporation rate is constant or close to a constant.

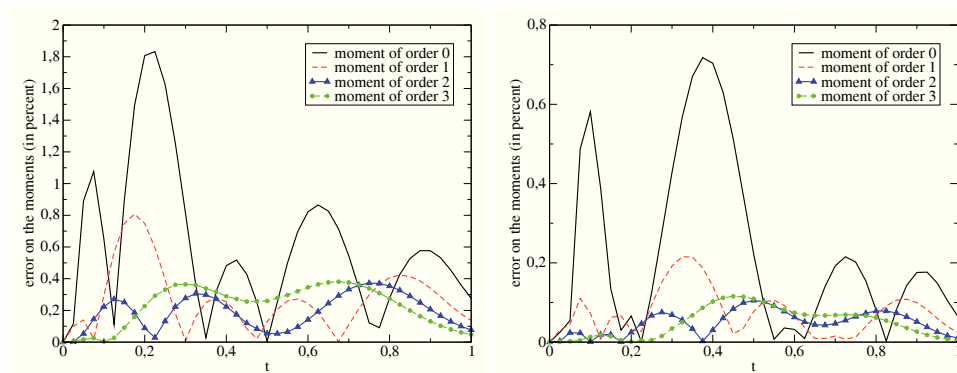


Figure 5.15: Evolution of the error on the moments calculated with the moment method for the equation on the radius, with two sections (left) or three sections (right) and relatively to their initial value.

## 5.6 Conclusions

An extension of Eulerian multi-fluid method is given here in a purely evaporating case, using ideas from DQMOM Methods and considering at least 4 moments of the NDF in each section instead of one in [146] or two in [145, 70]. Two difficulties have been resolved. The first one is the evaluation of disappearance rate of evaporating spray which is represented by a pointwise value of the NDF whereas the considered variables are its moments. The second one is the derivation of a scheme insuring the preserving of the moment space. This is done through a kinetic scheme whereas classical ODE solvers are unstable. The resulting scheme is shown to be very precise, with a total number of variables smaller than for the previous methods.

The extension of our new scheme to arbitrary evaporation laws is straightforward (see Section 5.4.2). The ideas developed in this paper can easily be extended to two internal coordinates for example for soots, the only limiting point being the ability of the ME reconstruction to work in such configuration; however, this has already been treated in the literature and does not provide additional difficulties [3] except that the study at the boundary of the moment space should be updated to this new configuration and in the context of such a study of the rate of disappearance for moment methods.

This work is inserted in the development of general scheme for the complete NDF equation, physical transport and transport in space phase being treated separately through splitting method [171, 52, 172]. The total number of variable is then important for the total cost of the method since these variables have to be transported in the physical space [128, 129, 172].

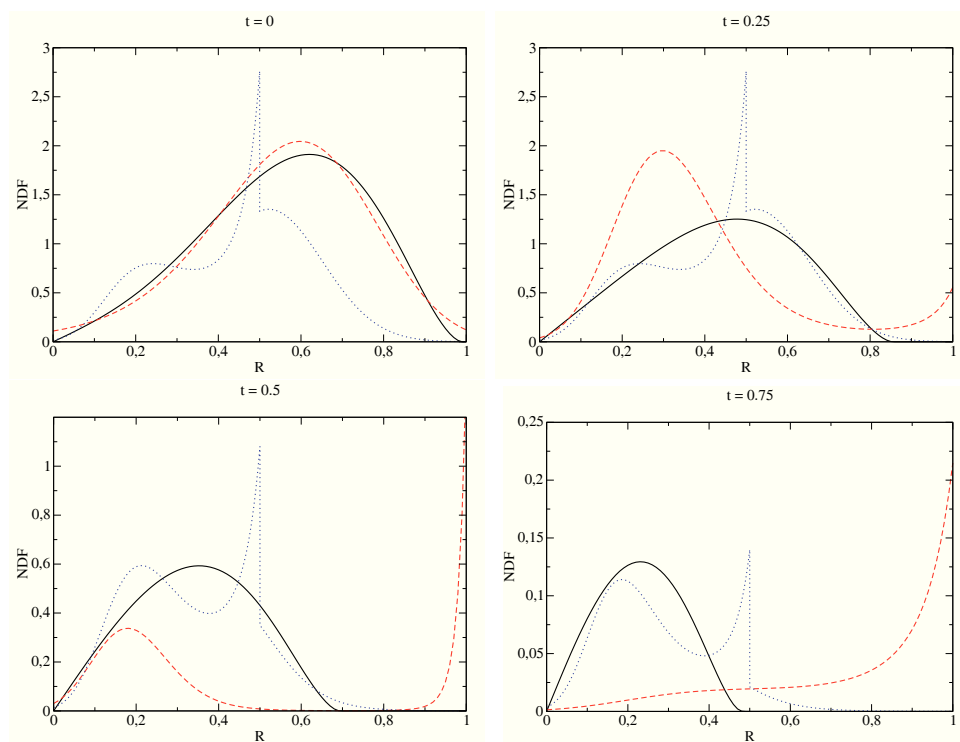


Figure 5.16: Smooth NDF in radius (solid), ME reconstructed NDF obtained with the moments computed with the moment method for 1 section and 4 moments (dashed line) or for 2 sections and 4 moments (dotted lines), at times  $t = 0$ ,  $t = 0.25$ ,  $t = 0.5$  and  $t = 0.75$ .



## Chapter 6

# Numerical strategy for transport in physical space and drag

In this section, we present the numerical scheme used to discretize the equations of system (4.11) in the case of an aerosol, and its extension to treat the case of a spray. Because of the conservative form of system (4.11), the finite-volume method [152] is a natural candidate for its discretization. Moreover, since the computations we present are enforced in a cartesian mesh, we use a dimensional splitting algorithm explained by Strang [212], preserving the second order in time of the scheme and also its properties. Thus, for example in a 2D framework, in order to solve the system on a time step  $\Delta t$ , the transport in the first direction is solved for  $\Delta t/2$  then the transport in the second direction is solved for  $\Delta t$  and finally, the transport in the first direction is solved for  $\Delta t/2$ . An alternated Lie splitting (equivalent to a Strang splitting on 2 time steps) can also be used with the advantage of using the 1D transport algorithm with the same time step in each direction [49]. So, without loss of generality, the scheme is then presented in a one dimensional framework.

Usually, high order finite volume methods use some non-constant reconstructions of the variables to evaluate the fluxes between the cells. But, the properties of the scheme are conditioned by the expression of the fluxes. Two difficulties arise here. The first one concerns the way to do the reconstruction of the moments in order to keep the integrity of the moment set. It has been seen that for a high order in space scheme, an independent reconstruction of each moment does not insure that the moment space is preserved [231, 176]. This will not inevitably lead to instabilities in the convective transport algorithm, but the physical information about the size distribution is lost. This would ban any coupling with a solver which requires a reconstruction of a distribution function from the moment, like evaporation (Chapter 5), collisions, coalescence. Assuming this being achieved, a second difficulty concerns the computation of the fluxes from the reconstructed quantities. If an approximate time solver is used (Explicit Euler, Runge-Kutta), the fluxes computation will introduce truncature errors for non constant reconstructions, and the preservation of the moment space would not be guaranteed any more. In order to meet this condition, we design a kinetic-based numerical scheme using the ideas developed by Bouchut [24]. In this context, we propose a spatial reconstruction of the distribution function meeting the realizability condition everywhere in the cell. The time solver is based on an exact resolution of the PDE in time, leading to the fact that the fluxes introduce no truncature error with respect to the spatial reconstruction. An exact computation of the fluxes is obtained using the fact that the equations on moments can be derived from a kinetic equation. This work has been the object of a proceeding of the ICLASS Conference, Vail, USA (2009) [128], and a publication in Journal of Computational Physics [129].

We recall here the dynamics system we want to solve:

$$\left\{ \begin{array}{l} \partial_t(m_0) + \partial_x(m_0 u_p) = 0 \\ \partial_t(m_1) + \partial_x(m_1 u_p) = 0 \\ \partial_t(m_2) + \partial_x(m_2 u_p) = 0 \\ \vdots \\ \partial_t(m_N) + \partial_x(m_N u_p) = 0 \\ \partial_t(m_1 u_p) + \partial_x(m_1 u_p \cdot u_p) = 0. \end{array} \right. \quad (6.1)$$

## 6.1 General form of the kinetic scheme for moment transport

Like in [24], a kinetic scheme is developed, based on the equivalence between the “macroscopic” equation on the size distribution  $n(t, x, S)$ :

$$\partial_t n + \partial_x(n u_p) = 0, \quad (6.2)$$

where  $u_p$  is the particle velocity for the spray and the gas velocity for aerosols, which then is a solution of:

$$\partial_t(n u_p) + \partial_x(n u_p^2) = 0, \quad (6.3)$$

and the kinetic equation on  $f(t, x, \xi, S)$ :

$$\partial_t f + \partial_x(u f) = 0, \quad (6.4)$$

with  $f(t, x, S, u) = n(t, x, S)\delta(u - u_p(t, x))$ . This kinetic equation has the exact solution  $f(t, x, S, u) = f(0, x - ut, S, u)$ . The strategy to develop the scheme is then the same one as in [24], with the difference that here, the “macroscopic” system of interest (4.11) is not directly (6.2) or (6.2, 6.3) but a system induced by taking the size moments of these equations.

In order to obtain discrete values over a mesh of constant size  $\Delta x$ , one defines the averages  $m_{k,i}^n$ , and  $u_{p_i}^n$  for inertial particles, with the usual definitions:

$$m_{k,i}^n = \frac{1}{\Delta x} \int_{x_{i-1/2}}^{x_{i+1/2}} m_k(t^n, x) dx, \quad k = 0, \dots, N, \quad (6.5)$$

$$q_i^n = m_{1,i}^n u_{p_i}^n = \frac{1}{\Delta x} \int_{x_{i-1/2}}^{x_{i+1/2}} m_1(t^n, x) u_p(t^n, x) dx, \quad (6.6)$$

Let us denote  $\mathbf{m}_N = (m_0, \dots, m_N)^t$  the vector of moments. The discretized equations are obtained in a conservative form by integrating Eq. (6.4) multiplied by  $(1, S, \dots, S^N, \xi)^t$  over  $(t, x, S, u) \in (t^n, t^{n+1}) \times (x_{i-1/2}, x_{i+1/2}) \times \mathbb{R} \times (0, 1)$ :

$$\begin{aligned} \mathbf{m}_{N,i}^{n+1} &= \mathbf{m}_{N,i}^n - \frac{\Delta t}{\Delta x} (\mathbf{F}_{i+1/2} - \mathbf{F}_{i-1/2}), \\ q_i^{n+1} &= q_i^n - \frac{\Delta t}{\Delta x} (G_{i+1/2} - G_{i-1/2}), \end{aligned} \quad (6.7)$$

where the fluxes for the size moments  $\mathbf{F}_{i+1/2}$  can be decomposed in  $\mathbf{F}_{i+1/2} = \mathbf{F}_{i+1/2}^+ + \mathbf{F}_{i+1/2}^-$  with:

$$\mathbf{F}_{i+1/2}^\pm = \frac{1}{\Delta t} \int_{t^n}^{t^{n+1}} \int_{\pm u \geq 0} \int_0^1 \begin{pmatrix} 1 \\ S \\ \vdots \\ S^N \end{pmatrix} u f(t, x_{i+1/2}, S, u) dS du dt, \quad (6.8)$$

and in the same way, the flux for the momentum in the case of inertial particles is  $G_{i+1/2} = G_{i+1/2}^+ + G_{i+1/2}^-$  with:

$$G_{i+1/2}^\pm = \frac{1}{\Delta t} \int_{t^n}^{t^{n+1}} \int_{\pm u \geq 0} \int_0^1 S u^2 f(t, x_{i+1/2}, S, u) dS du dt. \quad (6.9)$$

To evaluate the fluxes, the exact solution of the kinetic scheme is used:

$$\begin{aligned} \begin{pmatrix} \mathbf{F}_{i+1/2}^\pm \\ \mathbf{G}_{i+1/2}^\pm \end{pmatrix} &= \frac{1}{\Delta t} \int_0^{\Delta t} \int_{\pm u \geq 0} \int_0^1 \begin{pmatrix} 1 \\ S \\ \vdots \\ S^N \\ Su \end{pmatrix} u n(t^n, x_{i+1/2} - ut, S) \delta(u - u_p(t^n, x_{i+1/2} - ut)) dS du dt \\ &= \frac{1}{\Delta t} \int_0^{\Delta t} \int_{\pm u \geq 0} \begin{pmatrix} m_0(t^n, x_{i+1/2} - ut) \\ m_1(t^n, x_{i+1/2} - ut) \\ \vdots \\ m_N(t^n, x_{i+1/2} - ut) \\ m_1(t^n, x_{i+1/2} - ut)u \end{pmatrix} u \delta(u - u_p(t^n, x_{i+1/2} - ut)) du dt. \end{aligned}$$

Let us develop the computation for  $(\mathbf{F}_{i+1/2}^+, \mathbf{G}_{i+1/2}^+)$ . A change of variable between  $t$  and  $x = x_{i+1/2} - ut$  gives:

$$\begin{aligned} \begin{pmatrix} \mathbf{F}_{i+1/2}^+ \\ \mathbf{G}_{i+1/2}^+ \end{pmatrix} &= \frac{1}{\Delta t} \int_{\pm u \geq 0} \int_{x_{i+1/2} - u\Delta t}^{x_{i+1/2}} \begin{pmatrix} m_0(t^n, x) \\ m_1(t^n, x) \\ \vdots \\ m_N(t^n, x) \\ m_1(t^n, x)u \end{pmatrix} \delta(u - u_p(t^n, x)) du dx \\ &= \frac{1}{\Delta t} \int_{x_{i-1/2}}^{x_{i+1/2}} \begin{pmatrix} m_0(t^n, x) \\ m_1(t^n, x) \\ \vdots \\ m_N(t^n, x) \\ m_1(t^n, x)u_p(t^n, x) \end{pmatrix} \mathbb{1}_{\{x, x_{i+1/2} - u_p(t^n, x)\Delta t \leq x \leq x_{i+1/2}\}}(x) dx. \end{aligned} \quad (6.10)$$

$$(6.11)$$

the last expression being valid under the CFL condition:  $\Delta t \sup_x |u_p(t^n, x)| \leq \Delta x$ . In the same way, the other part of the fluxes are:

$$\begin{pmatrix} \mathbf{F}_{i+1/2}^- \\ \mathbf{G}_{i+1/2}^- \end{pmatrix} = -\frac{1}{\Delta t} \int_{x_{i-1/2}}^{x_{i+1/2}} \begin{pmatrix} m_0(t^n, x) \\ m_1(t^n, x) \\ \vdots \\ m_N(t^n, x) \\ m_1(t^n, x)u_p(t^n, x) \end{pmatrix} \mathbb{1}_{\{x, x_{i+1/2} \leq x \leq x_{i+1/2} - u_p(t^n, x)\Delta t\}}(x) dx. \quad (6.12)$$

The fluxes are then written with the variables of interest: the moments  $m_k$  of the size distribution  $n$ . The difficulty is now to reconstruct the moments  $m_k(t^n, \cdot)$  from the  $m_{k,i}^n$  in such a way that the moment space is preserved. In order to show how this scheme is built in a simple case, we will first compute the convective fluxes in the context of a first order kinetic scheme. But a first order scheme is not satisfactory, as our goal is to design a scheme with small diffusion. We will finally explain the reconstruction in the context of a second order in space scheme.

## 6.2 First order kinetic scheme

For a first order kinetic scheme, piecewise constant data are reconstructed:

$$\text{for } x_{i-1/2} < x < x_{i+1/2}, \quad \begin{cases} m_k(t^n, x) = m_{k,i}^n, & k = 0, \dots, N \\ u_p(t^n, x) = u_{p,i}^n. \end{cases} \quad (6.13)$$

Under the CFL condition  $\Delta t \sup_i |u_{p_i}^n| \leq \Delta x$ , the expression of the fluxes (6.10,6.12) are straightforward:

$$\mathbf{F}_{i+1/2}^+ = \mathbf{m}_{N,i}^n (u_{p_i}^n)_+, \quad \mathbf{G}_{i+1/2}^+ = m_{1,i}^n u_{p_i}^n (u_{p_i}^n)_+, \quad (6.14)$$

and

$$\mathbf{F}_{i+1/2}^- = \mathbf{m}_{N,i+1}^n (u_{p_{i+1}}^n)_-, \quad \mathbf{G}_{i+1/2}^- = m_{1,i}^n u_{p_{i+1}}^n (u_{p_{i+1}}^n)_-, \quad (6.15)$$

with the convention  $u_{p,+} = \max\{u_p, 0\}$ ,  $u_{p,-} = \min\{u_p, 0\}$ .

With piecewise constant reconstructions, the first order scheme considerably simplifies the reconstruction step as it eludes the problem of preservation of the moment space which arises when non constant reconstruction are considered. Indeed, this first order scheme can be written:

$$\mathbf{m}_{N,i}^{n+1} = \left(1 - \frac{\Delta t}{\Delta x} |u_{p_i}^n|\right) \mathbf{m}_{N,i}^n - \frac{\Delta t}{\Delta x} (u_{p_{i+1}}^n)_- \mathbf{m}_{N,i+1}^n + \frac{\Delta t}{\Delta x} (u_{p_{i-1}}^n)_+ \mathbf{m}_{N,i-1}^n \quad (6.16)$$

$$= \int_0^1 \begin{pmatrix} 1 \\ S \\ \vdots \\ S^N \end{pmatrix} \left[ \left(1 - \frac{\Delta t}{\Delta x} |u_{p_i}^n|\right) f_i - \frac{\Delta t}{\Delta x} (u_{p_{i+1}}^n)_- f_{i+1} + \frac{\Delta t}{\Delta x} (u_{p_{i-1}}^n)_+ f_{i-1} \right] (S) \, dS, \quad (6.17)$$

where  $f_i$  is a distribution function with the moments of order 0 to  $N$  given by  $\mathbf{m}_{N,i}^n$ . Under the CFL condition, the coefficients before each  $f_i$  are non negative and then,  $\mathbf{m}_{N,i}^{n+1}$  is a moment vector. In the case of a spray, the first order scheme also satisfies the maximum principle on the velocity. Other properties, like entropy inequalities or the TVD property on the velocity, can also be proved, see [21].

The first order scheme is easy to design, and robust, but, as it is well known, this scheme brings a lot of numerical diffusion. That is why a second order scheme, with low diffusion, is explained.

### 6.3 Second order kinetic scheme

For the purpose of a second order scheme, a piecewise linear reconstruction is considered. Like in [24], we would like to do that on the droplet number density,  $m_0$  and on transported quantities like the velocity. But this cannot be done directly on the normalized moments, independently, since this would lead to a dead end [231]: considering the complexity of the moment space, such reconstruction can not induce moment vectors inside the moment space for all the points of the cell. The solution comes from the fact that, from system (6.1), it can be proven that the canonical moments are transported quantities:

**Proposition 2** *Let  $u_p(t, x)$  be a  $C^1$  function. If the moment vector  $(m_0, m_1, \dots, m_N)$  is a  $C^1$  function of  $t$  and  $x$  belonging to the interior of the moment space and such that*

$$\begin{cases} \partial_t(m_0) + \partial_x(m_0 u_p) = 0 \\ \partial_t(m_1) + \partial_x(m_1 u_p) = 0 \\ \partial_t(m_2) + \partial_x(m_2 u_p) = 0 \\ \vdots \\ \partial_t(m_N) + \partial_x(m_N u_p) = 0. \end{cases} \quad (6.18)$$

*then the corresponding canonical moments are transported quantities, which means that they verify the transport equation:  $\partial_t p_k + u_p \partial_x p_k = 0$ .*

**Proof 1** *According to Corollary 1.4.6 of [58],  $p_k$  is a rational fraction of the moments  $c_k$ . Moreover, since the moment vector is in the interior of the moment space, the denominator can never be equal to zero. Therefore,  $p_k(c_k)$  is differentiable relative to each  $c_j, j \leq k$ . Thus we have the relation:*

$$\partial_t p_k + u_p \partial_x p_k = \sum_{j \leq k} \partial_{c_j} p_k [\partial_t c_j + u_p \partial_x c_j]. \quad (6.19)$$

But since the  $c_j$  are transported quantities, we have:

$$\partial_t p_k + u_p \partial_x p_k = 0. \quad (6.20)$$

■

Thus, reconstructing the canonical moments enables to preserve the integrity of the moment set at each point of the cell. Indeed, as they are proven to be transported quantities by system (4.11), they satisfy a maximum principle. They also have the property, as explained in Section 4.2.2, to live in  $]0, 1[^k$  and not in a subset of it. In the context of this work, we will restrict ourselves on the case  $N = 3$ . A greater value for  $N$  could be considered, but leading to more complex algebra.

### 6.3.1 Reconstruction

The reconstruction writes:

$$\text{for } x_{i-1/2} < x < x_{i+1/2} \quad \left\{ \begin{array}{l} m_0(x) = m_{0,i} + D_{m_{0,i}}(x - x_i) \\ p_1(x) = \overline{p_{1,i}} + D_{p_{1,i}}(x - x_i) \\ p_2(x) = \overline{p_{2,i}} + D_{p_{2,i}}(x - x_i) \\ p_3(x) = \overline{p_{3,i}} + D_{p_{3,i}}(x - x_i) \\ u_p(x) = \overline{u_{p_i}} + D_{u_{p_i}}(x - x_i), \end{array} \right. \quad (6.21)$$

where  $x_i = (x_{i+1/2} + x_{i-1/2})/2$  is the center of the  $j^{\text{th}}$  cell and where, to simplify the notation, the  $t^n$  dependance of each function is implicit. The quantities with bars are different from the canonical moments  $p_{k,i}$  corresponding to the moment vector  $\mathbf{m}_i^n$  and from the mean velocity  $u_{p_i}^n$ . In order to have the conservation property, they are defined in such a way that (according to (Eq. (4.20))):

$$\begin{aligned} m_{1,i}^n &= \frac{1}{\Delta x} \int_{x_{i-1/2}}^{x_{i+1/2}} m_0(x) p_1(x) dx, \\ m_{2,i}^n &= \frac{1}{\Delta x} \int_{x_{i-1/2}}^{x_{i+1/2}} m_0(x) p_1(x) [(1 - p_1)p_2 + p_1](x) dx, \\ m_{3,i}^n &= \frac{1}{\Delta x} \int_{x_{i-1/2}}^{x_{i+1/2}} m_0(x) p_1(x) \{(1 - p_1)(1 - p_2)p_2 p_3 + [(1 - p_1)p_2 + p_1]^2\}(x) dx, \\ m_{1,i}^n u_{p_i}^n &= \frac{1}{\Delta x} \int_{x_{i-1/2}}^{x_{i+1/2}} m_0(x) p_1(x) u_p(x) dx. \end{aligned} \quad (6.22)$$

For the first canonical moment, it is easy to see that:

$$\overline{p_{1,i}} = \frac{m_{1,i}^n}{m_{0,i}^n} - \frac{D_{p_{1,i}} D_{m_{0,i}} \Delta x^2}{m_{0,i}^n}. \quad (6.23)$$

When considering higher order canonical moments  $\overline{p_{2,i}}$  and  $\overline{p_{3,i}}$ , and the velocity, their expression are more difficult to figure out, since high order polynomials must be integrated, (up to order 4 for  $\overline{p_{2,i}}$  and  $\overline{u_{p_i}}$ , and 6 for  $\overline{p_{3,i}}$ ). The expression of  $\overline{p_{2,i}}$  and  $\overline{p_{3,i}}$  are written:

$$\overline{p_{2,i}} = a_{2,i} + b_{2,i} D_{p_{2,i}}, \quad \overline{u_{p_i}} = a_{u_{p,i}} + b_{u_{p,i}} D_{u_{p_i}}, \quad \overline{p_{3,i}} = a_{3,i} + b_{3,i} D_{p_{3,i}}. \quad (6.24)$$

where  $a_{2,i}$  and  $b_{2,i}$  are independent of  $D_{p_{2,i}}$ ,  $a_{u_{p,i}}$  and  $b_{u_{p,i}}$  are independent of  $D_{u_{p_i}}$ , and  $a_{3,i}$  and  $b_{3,i}$  are

independent of  $D_{p_{3,i}}$ . They are given by:

$$a_{2,i} \int_{x_{i-1/2}}^{x_{i+1/2}} \{m_0 p_1 [1 - p_1]\}(x) dx = m_{2,i}^n \Delta x - \int_{x_{i-1/2}}^{x_{i+1/2}} m_0(x) p_1^2(x) dx, \quad (6.25)$$

$$b_{2,i} \int_{x_{i-1/2}}^{x_{i+1/2}} \{m_0 p_1 [1 - p_1]\}(x) dx = - \int_{x_{i-1/2}}^{x_{i+1/2}} \{m_0 p_1 [1 - p_1]\}(x)(x - x_i) dx, \quad (6.26)$$

$$(6.27)$$

$$a_{u_p,i} \int_{x_{i-1/2}}^{x_{i+1/2}} \{m_0 p_1\}(x) dx = q_i^n \Delta x, \quad (6.28)$$

$$b_{u_p,i} \int_{x_{i-1/2}}^{x_{i+1/2}} \{m_0 p_1\}(x) dx = - \int_{x_{i-1/2}}^{x_{i+1/2}} \{m_0 p_1\}(x)(x - x_i) dx, \quad (6.29)$$

$$(6.30)$$

and

$$a_{3,i} \int_{x_{i-1/2}}^{x_{i+1/2}} \{m_0 p_1 (1 - p_1)(1 - p_2) p_2\}(x) dx = m_{3,i}^n \Delta x - \int_{x_{i-1/2}}^{x_{i+1/2}} \{m_0 p_1 [(1 - p_1) p_2 + p_1]^2\}(x) dx, \quad (6.31)$$

$$b_{3,i} \int_{x_{i-1/2}}^{x_{i+1/2}} \{m_0 p_1 (1 - p_1)(1 - p_2) p_2\}(x) dx = - \int_{x_{i-1/2}}^{x_{i+1/2}} \{m_0 p_1 (1 - p_1)(1 - p_2) p_2\}(x)(x - x_i) dx, \quad (6.32)$$

$$(6.33)$$

The computation of these coefficients is achieved using Maple (Maplesoft, a division of Waterloo Maple, Inc 2007). Their expression is quite heavy, but, as it is just an algebraic relation, the corresponding CPU cost is low. In a general way, let us write  $\overline{p_{k,i}} = a_{k,i} + b_{k,i} D_{p_{k,i}}$  for  $i = 1, \dots, 3$ , and  $\overline{u_{p_i}} = u_{p_i}^n + b_{u_p,i} D_{u_{p_i}}$ , since  $a_{u_p,i} = u_{p_i}^n$ .

### 6.3.2 Slope limitation

Once the conservativity of the scheme is ensured, the slopes are determined using limiters in order to satisfy maximum principles for the transported quantities and positivity for the number density. First, for the positivity of number density, the slope  $D_{m_{0,i}}$  must verify;

$$|D_{m_{0,i}} \frac{\Delta x}{2}| < m_{0,i}^n. \quad (6.34)$$

To guarantee the maximum principle on the canonical moments ( $i = 1, 2, 3$ ):

$$r_{k,i} \leq p_{k,i}(x) \leq R_{k,i}, \quad x \in (x_{i-1/2}, x_{i+1/2}),$$

where  $r_{k,i} = \min(p_{k,i-1}, p_{k,i}, p_{k,i+1})$  and  $R_{k,i} = \max(p_{k,i-1}, p_{k,i}, p_{k,i+1})$ , we must have:

$$\begin{cases} r_{k,i} \leq a_{k,i} + b_{k,i} D_{p_{k,i}} + \frac{\Delta x}{2} D_{p_{k,i}} \leq R_{k,i} \\ r_{k,i} \leq a_{k,i} + b_{k,i} D_{p_{k,i}} - \frac{\Delta x}{2} D_{p_{k,i}} \leq R_{k,i}. \end{cases} \quad (6.35)$$

From (6.23), (6.26) and (6.32), it is easy to see that  $|b_{k,i}| < \Delta x/2$  for all  $i = 1, 2, 3$ . The slopes must then verify:

$$\begin{cases} D_{p_{k,i}} \leq \min\left(\frac{R_{k,i} - a_{k,i}}{b_{k,i} + \Delta x/2}, \frac{a_{k,i} - r_{k,i}}{\Delta x/2 - b_{k,i}}\right) \\ D_{p_{k,i}} \geq \min\left(\frac{r_{k,i} - a_{k,i}}{b_{k,i} + \Delta x/2}, \frac{a_{k,i} - R_{k,i}}{\Delta x/2 - b_{k,i}}\right). \end{cases}$$

In practice, we use the following slope limiter to satisfy all the conditions:

$$\begin{aligned} D_{m_{0,i}} &= \frac{1}{2}(\text{sgn}(m_{0,i+1}^n - m_{0,i}^n) + \text{sgn}(m_{0,i}^n - m_{0,i-1}^n)) \times \min\left(\frac{|m_{0,i+1}^n - m_{0,i}^n|}{\Delta x}, \frac{|m_{0,i}^n - m_{0,i-1}^n|}{\Delta x}, \frac{2m_{0,i}^n}{\Delta x}\right), \\ D_{p_{k,i}} &= \frac{1}{2}(\text{sgn}(p_{k,i+1}^n - p_{k,i}^n) + \text{sgn}(p_{k,i}^n - p_{k,i-1}^n)) \times \min\left(\frac{|p_{k,i+1}^n - a_{k,i}|}{\Delta x + 2b_{k,i}}, \frac{|a_{k,i} - p_{k,i-1}^n|}{\Delta x - 2b_{k,i}}\right). \end{aligned} \quad (6.36)$$

The velocity can be treated like  $p_2$ , with an additional condition linked to the CFL limitation. The chosen slope is then:

$$Du_j = \frac{1}{2}(\text{sgn}(u_{p_{i+1}}^n - u_{p_i}^n) + \text{sgn}(u_{p_i}^n - u_{p_{i-1}}^n)) \times \min\left(\frac{|u_{p_{i+1}}^n - u_{p_i}^n|}{\Delta x + 2b_{u_p,i}}, \frac{|u_{p_i}^n - u_{p_{i-1}}^n|}{\Delta x - 2b_{u_p,i}}, \frac{1}{\Delta t}\right).$$

### 6.3.3 Fluxes computation

Then we can proceed with the evaluation of the fluxes:

$$\begin{pmatrix} \mathbf{F}_{i+1/2}^+ \\ \mathbf{G}_{i+1/2}^+ \end{pmatrix} = \frac{1}{\Delta t} \int_{x_{i+1/2}^L}^{x_{i+1/2}} m_0(x) \begin{pmatrix} 1 \\ p_1 \\ p_1[(1-p_1)p_2 + p_1] \\ p_1\{(1-p_1)(1-p_2)p_2p_3 + [(1-p_1)p_2 + p_1]^2\} \\ p_1u \end{pmatrix} (x) dx, \quad (6.37)$$

where  $x_{i+1/2}^L$  is the location of the last droplets reaching  $x_{i+1/2}$  at  $\Delta t$ .

$$x_{i+1/2}^L = x_{i+1/2} - \Delta t \frac{(\bar{u}_{p_i} + \frac{\Delta x}{2} D_{u_{p_i}})_+}{1 + \Delta t D_{u_{p_i}}}. \quad (6.38)$$

Similarly,

$$\begin{pmatrix} \mathbf{F}_{i+1/2}^- \\ \mathbf{G}_{i+1/2}^- \end{pmatrix} = -\frac{1}{\Delta t} \int_{x_{i-1/2}}^{x_{i+1/2}^R} m_0(x) \begin{pmatrix} 1 \\ p_1 \\ p_1[(1-p_1)p_2 + p_1] \\ p_1\{(1-p_1)(1-p_2)p_2p_3 + [(1-p_1)p_2 + p_1]^2\} \\ p_1u \end{pmatrix} (x) dx, \quad (6.39)$$

with

$$x_{i+1/2}^R = x_{i+1/2} - \Delta t \frac{(\bar{u}_{p_{i+1}} - \frac{\Delta x}{2} D_{u_{p_{i+1}}})_-}{1 + \Delta t D_{u_{p_{i+1}}}}. \quad (6.40)$$

The calculation of these fluxes is also achieved using Maple (Maplesoft, a division of Waterloo Maple, Inc 2007). Their expression is quite tedious, but, as it is just an algebraic relation, the corresponding CPU cost is low.

This kinetic based scheme, using the property of the canonical moments, preserves the moment space directly, without the use of an additional projection algorithm. The need to preserve the realizability condition comes from the use of dedicated solvers in the size phase space which require access to a distribution function. In particular, our purpose is to evaporate the droplets, which leads us to couple this scheme to the evaporation solver explained in Chapter 5. In the next section, some one-dimensional validation test-cases are presented.

## 6.4 Validation by comparison with the analytical solution for a one dimensional transport

### 6.4.1 Aerosol case

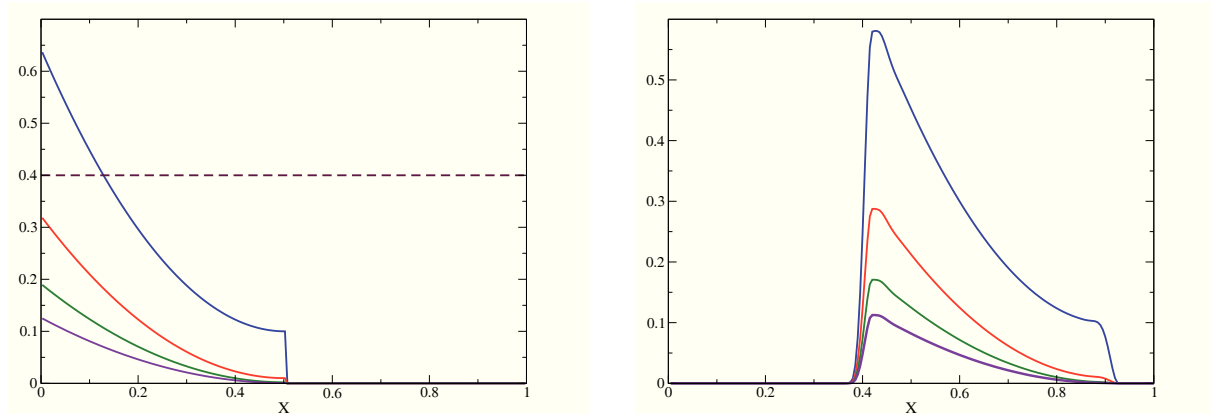


Figure 6.1: Evolution of aerosol particles calculated with the moment method, in a constant velocity field. (left) Initial condition; the plain curves represent, with decreasing ordering in terms of value, the four first moments from the  $0^{th}$  order (highest) to the  $3^{rd}$  (lowest). The plain curves are scaled by the left Y-axis and the dashed curve representing the velocity field, is scaled by the right Y-axis. (right) Solution at time  $t = 0.4$  compared to the analytical solution of the problem represented by symbols.

Let us first test the transport at constant velocity of a polydisperse aerosol. The gas velocity is then constant and equal to one everywhere and an aerosol is initially existing in half of the domain  $[0, 1]$ , the boundary conditions being periodic. Its size distribution has initially a concave shape at  $x = 0$  (part of the sinusoid) and a convex one at  $x = 0.5$  (decreasing exponential) and evolve continuously between these two points:

$$n(t = 0, x, S) = \begin{cases} \lambda(x) \sin(\pi S) + (1 - \lambda(x)) \exp(-10 S) & \text{if } x \leq 0.5, \\ 0 & \text{otherwise.} \end{cases} \quad (6.41)$$

where  $\lambda(x) = 4(0.5 - x)^2$ . The moments of order zero to three of this initial distribution are displayed on Fig. 6.1-left. The constant velocity field is also represented. According to this velocity field, we expect a translation of all the moments at velocity one. That is indeed what we obtain at Fig. 6.1-right, the numerical simulation being performed in a 200 cells grid with a convective CFL equal to one. The first conclusion, that we can draw from this trivial test case is that only numerical diffusion alters



the accuracy of the moment resolution. We must highlight the fact that this is done without an extra projection algorithm, yet yields a very high precision.

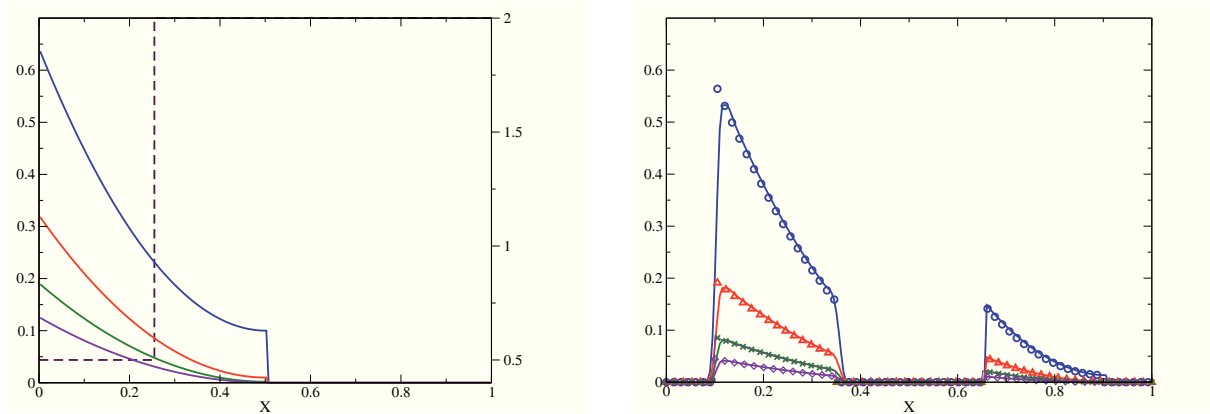


Figure 6.2: Evolution of a spray in a discontinuous velocity field, calculated with the moment method, compared to the analytical solution of the problem. (left) Initial condition; the plain curves represent, with decreasing ordering in terms of value, the four first moments from the  $0^{th}$  order (highest) to the  $3^{rd}$  (lowest). The plain curves are scaled by the left Y-axis and the dashed curve representing the velocity field, is scaled by the right Y-axis. (right) Solution at  $t = 0.2$  compared to the analytical solution of the problem represented by symbols.

### 6.4.2 Spray case

In the second test case, a quantitative comparison with an analytical solution of the transport of an evaporating spray of ballistic droplets is performed. For this problem, we choose the same size distribution as before, but now the particles have their own velocity, initiated by:

$$u(x) = \begin{cases} 0.5 & \text{if } x \leq 0.25, \\ 2 & \text{if } x > 0.25. \end{cases} \quad (6.42)$$

The initial conditions are displayed in Fig. 6.2-left. As we consider ballistic droplets, the particle dynamic is not influenced by any gas. Besides, the droplets are assumed to be evaporated at a rate  $K = 1$ . The velocity discontinuity within the droplet cloud makes it spread into two separate clouds with two distinct velocities. This configuration shows the ability of the method to handle the vacuum zone generated by the separation of the clouds. Moreover, because of periodic boundary conditions, the faster cloud will meet the slower one once it has re-entered on the left side. Figure 6.2-right displays the four analytical size moments, and the size moments given by the calculation at the time  $t = 0.2$ , performed in a 200 cells grid with a convective CFL equal to one. Figure 6.3 display the four moments at times  $t = 0.4$ . We can notice that one, the numerical solution perfectly matches the analytical one, and two, that *a fortiori* the moment space is preserved. The initial distribution breaks into two parts. Vacuum is created at the initial velocity discontinuity. At  $t=0.4$ , the fastest portion catches up the slower one. As we consider a pressureless gas formalism for the particles, nothing prevents the particles from accumulating. However, it must be kept in mind that we do not take collision into account, and the real physical solution would result in a crossing of the clouds, which is represented by the analytical solution. Simulating jet crossing is an issue in Eulerian models and new methods have been recently designed in the literature. After the shock has developed, our model is no more valid and the scheme would have been extended to treat this case, in the same way as it was done in [51] for the multi-fluid model. This is the material of a forthcoming paper.

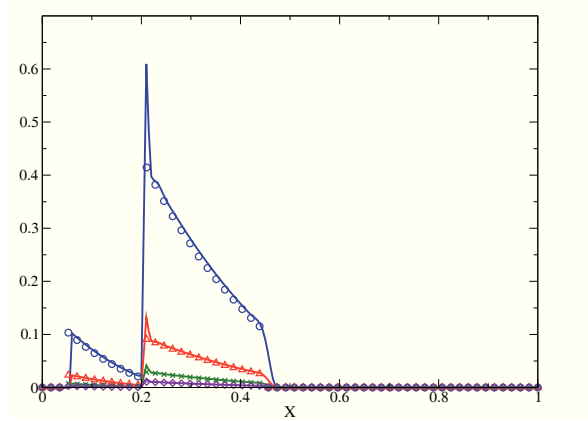


Figure 6.3: Evolution of a spray in a discontinuous velocity field calculated with the moment method, compared to the analytical solution of the problem. Solution at time  $t = 0.4$  compared to the analytical solution of the problem represented by symbols.

### 6.4.3 Order accuracy study

An order accuracy study is performed for the first and second order kinetic schemes for pure advection of a moment set. The initial size distribution has the following profile:

$$n(t = 0, x, S) = \begin{cases} \alpha(x) (\alpha(x) \sin((1-x)\pi S) + (1-\alpha(x)) \exp(-10(1-x)S)), & x \leq 0.5, \\ 0, & x > 0.5, \end{cases} \quad (6.43)$$

where  $\alpha(x) = \exp - \frac{(0.25-x)^2}{\sigma^2}$ , where  $\sigma = 0.12$ . The moments are then scaled by  $m_0$ :

$$m_k(x) \mapsto m_k(x) = \frac{m_k(x)}{m_0(x)}, \quad (6.44)$$

so that the moments  $m_0$  have a smooth profile, and particularly  $m_0$  has a gaussian profile. Such a spatial and size distribution with nonlinear coupling can be considered as general enough for an accuracy study in order to quantify the order of convergence of the proposed scheme. The velocity field is initiated as shown in Fig. 6.4-right. It writes:

$$u(t = 0, x) = \begin{cases} 1-x, & x \leq 0.5, \\ 0, & x > 0.5, \end{cases} \quad (6.45)$$

The negative slope of its linear profile leads to a compression of the moment field at the rate given by solving the equation  $d_t m/m = -\partial_x u = 0.5/(0.5 - 0.5t)$ . As the final computational time is 0.5, the final value of the moments is  $m_k(t = 0.5, x) = 2m_k(t = 0, x_0)$ , where  $x$  is the point, at  $t = 0.5$ , of the characteristic containing the point  $(t = 0, x_0)$ . The computation is run with  $CFL = 1$ .

Two types of results are given. The first type gives the final profile of the moments, comparing the results for the first and second order schemes, for the 100 cell grid, with the analytical results, see Fig. 6.5. This clearly shows the gain of accuracy brought by second order scheme in comparison to first order scheme. Grid convergence studies for the first and second order advection schemes are presented in Fig. 6.6. For both the schemes, the profile of  $m_0$  obtained using different grid resolutions is compared to the analytical solution. Four different uniform grids have been considered with the number of cells equal to 25, 50, 100 and 200. Figure 6.6-left shows grid convergence for the first order scheme, and Fig. 6.6-right shows grid convergence for the second order scheme. A remarkable result is the low numerical diffusion level of the second order scheme. Generally, numerical diffusion has two origins: the reconstruction step and the flux time integration computation at the cell interfaces in cell center finite volume schemes. The proposed second order kinetic scheme involves an exact time integration of the flux, preventing any

numerical diffusion to occur at this level. This comes from the fact that the velocities of the waves of the system are explicitly known at time  $t_n$  since they are not modified by any acoustic effect: this result is specific to the pressureless gas formalism considered here.

Table 6.1 and 6.2 show the numerical order results for both schemes and provide detailed results for the four moments. The mean order is the slope of the straight line given by a linear regression of the four error results per moment. For the first order scheme, the numerical order is lower than one (0.76). Such a result is rather classical for such a class of finite volume method (see [224] for example). For the second order scheme, the numerical order for  $m_0$  is little lower than two (1.82). Second order is reached for all other moments. Figure 6.7 displays the order curves for the first and second order schemes, highlighting the precision difference between both methods and showing the high level of accuracy reached by the second order method. Such results can be considered as very satisfying compared to other existing methods.

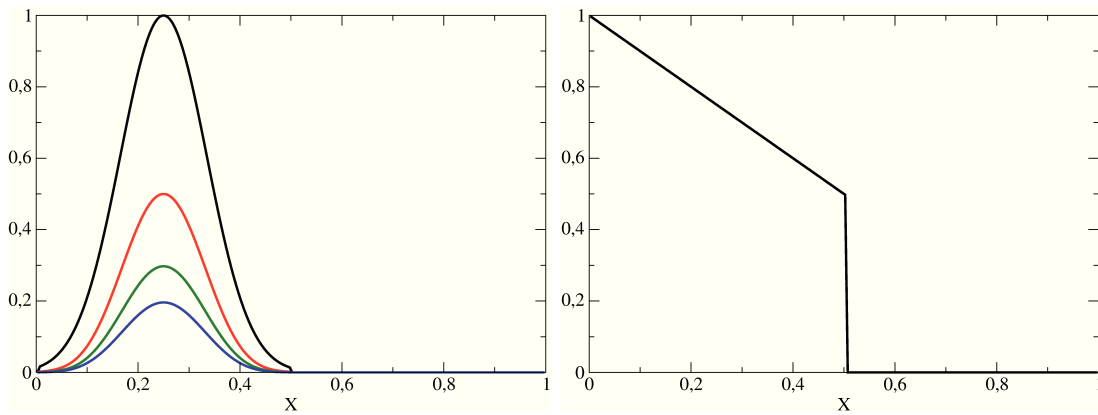


Figure 6.4: Order accuracy study. Initial conditions. Left: Initial moment field. The plain curves represent, with decreasing ordering in terms of value, the four first moments from the  $0^{th}$  order (highest) to the  $3^{rd}$  (lowest) Right: Initial velocity field

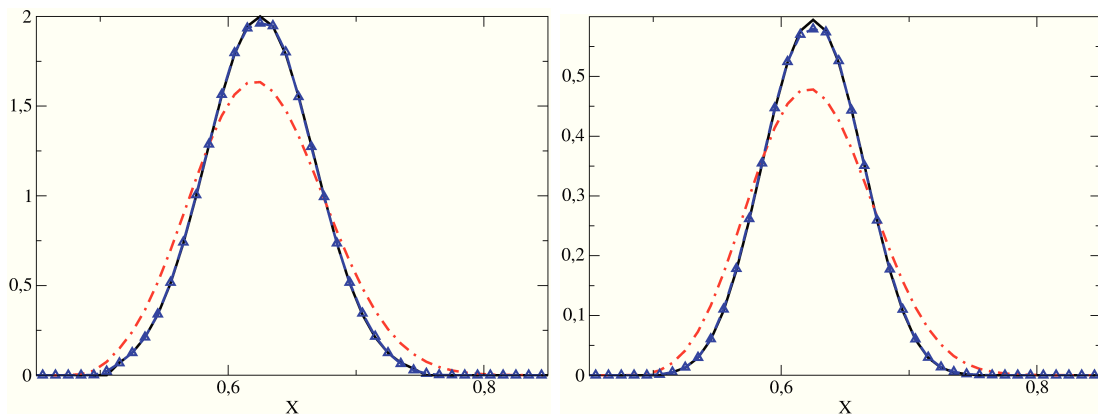


Figure 6.5: Order accuracy study. Moment profile for the final time, with a 100 cell grid. Comparison of the first and second order scheme with the analytical solution. The plain black curve represents the analytical solution, the dashed blue curve with triangles and the dotted-dashed red curve represent the numerical solution respectively for second and first order scheme. Left:  $m_0$ . Right:  $m_2$ .

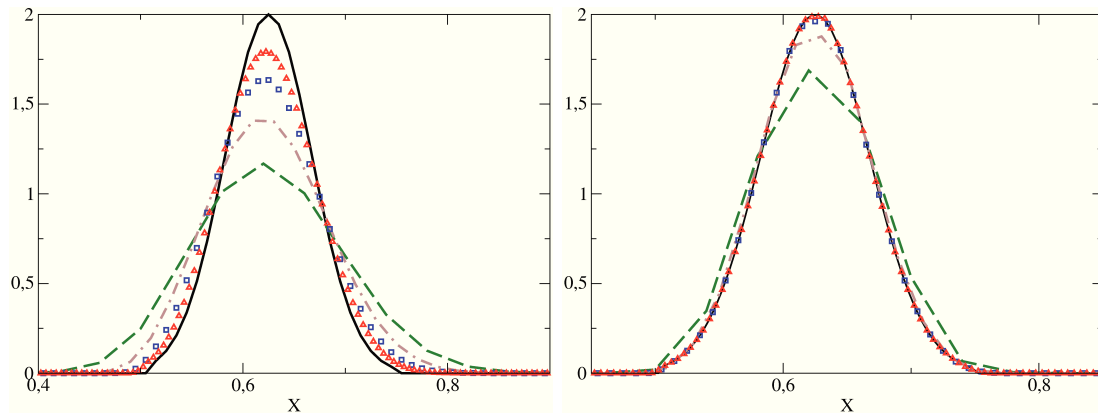


Figure 6.6: Order accuracy study. Profile of  $m_0$  for the final time. Results are displayed for 200 cells (red triangles), 100 cell (blue squares), 50 (dotted-dashed brown curve), 25 (dashed green curve). Left: first order. Right: second order.

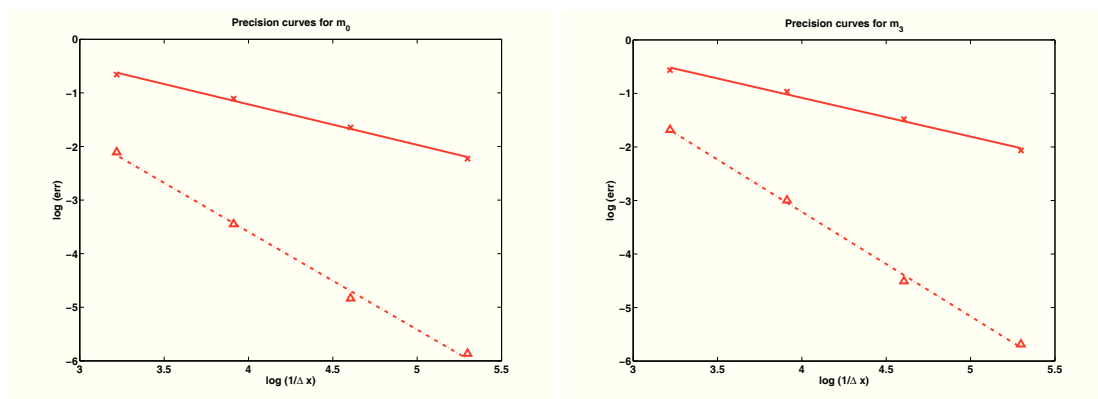


Figure 6.7: Order accuracy study. Error curves with respect to grid refinement in logarithmic scale. The solid line represents the first order scheme, the dotted-dashed represents the second order scheme. The symbols represents the logarithm of the error given by the computation. Left: results for  $m_0$ ; Right: results for  $m_3$ .

Grid size	25	50	100	200	Order
$m_0$	0.5176	0.3306	0.1932	0.1077	0.76
$m_1$	0.5534	0.3673	0.2182	0.1214	0.74
$m_2$	0.5658	0.3764	0.2247	0.1250	0.73
$m_3$	0.5686	0.3802	0.2274	0.1268	0.72

Table 6.1:  $L_1$  error and order of accuracy of the first order kinetic scheme.

Grid size	25	50	100	200	Order
$m_0$	0.1216	0.0318	0.0079	0.0028	1.82
$m_1$	0.1667	0.0436	0.0093	0.0025	2.04
$m_2$	0.1798	0.0478	0.0102	0.0028	2.01
$m_3$	0.1864	0.0499	0.0110	0.0034	1.95

Table 6.2:  $L_1$  error and order of accuracy of the second order kinetic scheme.

#### 6.4.4 Comparison with other methods present in literature

The ground difference between the scheme developed here for the advection of a moment set and the type of schemes presented in [231] and [176] is that the moment set integrity is preserved by the scheme itself. Thus, no additional numerical test or additional algorithm needs to be performed. This difference is sufficiently important so that no further numerical comparisons are relevant.

In [224], Vikas et. al design a second order quadrature-based scheme for the transport of a velocity moment vector. Whereas they are mainly interested in designing a second order scheme for the transport of velocity moment vectors, their ideas can be applied for the transport of size moments. Let us remark first that, in this article, we tackle the issue of the transport of an evaporating spray. Indeed, evaporation is an essential process to take into account in the description of spray dynamics. Therefore, if the main achievement of this paper concerns a second-order advection scheme preserving the moment set integrity, it is also very important that this scheme can be coupled to the evaporation solver presented in Section 5. However, even if it could be envisioned to couple, through an operator splitting, our evaporation algorithm to the transport algorithm proposed in [224], we still want to make sure that the accuracy is sufficient in order to obtain a global scheme that is competitive with multi-fluid models and methods. The transport presented here is dedicated to structured grids. However, it can be extended to non-structured grids, with some adjustments, as explained in Appendix B.3.

### 6.5 General algorithm towards implementation in MUSES3D

We detail here the structure of numerical scheme for a complete resolution of Eq. (4.1) (including transport, drag and evaporation) in preparation for its implementation in the MUSES3D code explained in Chapter 7. The three characteristics of this scheme, based on the numerical scheme for the multi-fluid model explained in Section 3.2 are the following. It relies on an operator splitting strategy, allowing separate treatments for the physical transport and the phase space transport. The physical transport resolution scheme, detailed in Section 6.3, is based on the kinetic-based scheme used for the multi-fluid. The phase space transport resolution is itself based on an operator splitting algorithm to treat separately the evaporation term and the drag term.

The operator splitting algorithms explained in Section 3.2 are reused in this context. We recall that its interest is to solve each operator with a dedicated numerical tool, in terms of stability and accuracy. For example, the Lie algorithm reads:

- Phase space transport: solve  $\partial_t f - \partial_S (K f) + \nabla_{\mathbf{u}} \cdot (\mathbf{D}_r f) = 0$  during  $\Delta t$ ,
- Physical space transport: solve  $\partial_t f + \nabla_{\mathbf{x}} \cdot (u f) = 0$  during  $\Delta t$ ,

The physical transport resolution is based on the kinetic scheme developed for the multi-fluid model. Yet, as explained in Section 6.3, the actual second order advection scheme for the EMSM reaches a higher

level of complexity. The reconstruction step, the slopes and the fluxes computation are finally very different in terms of algorithmic than in the context of the multi-fluid model. Reconstruction procedures for the canonical moments will have to be created from scratch, as well as the velocity reconstruction procedure and the fluxes computations. This will require a heavy computing work.

For the phase space transport resolution, it has been shown in Appendix B.1 that an ODE solver does not ensure the realizability condition applying to the size moment vector during the evaporation term treatment. Therefore, within the phase space transport resolution, the evaporation and drag operators are splitted. The evaporation term is solved with the dedicated numerical scheme presented in Chapter 5. Concerning the drag term, there are two options to treat it, as explained in Section 3.2. Since only drag is involved, one can either analytically solve the ODE, as suggested in Section 3.2. Or, one can rely on the resolution through the Radau5 solver, since drag is not the critical step for the insurance of the realizability condition. This last option is taken. In conclusion, the phase space transport requires to set the splitting algorithm, and to include the tools presented in Chapter 5, and design the interface between these new functions and the existing functions of the MUSES3D code.

## Chapter 7

# Introduction of the EMSM model in MUSES3D

The two previous sections introduced an interesting new numerical strategy for the Eulerian Multi Size Moments (EMSM) model. The following step is to assess the potential of this method on academic but challenging cases (presented in Section 3.3.1 and Section 3.3.2), in order to justify its extension to an industrial context. This is why the numerical tools developed for the EMSM model in Chapter 5 and Chapter 6 are implemented in the Multi-Fluid Solver for Eulerian Spray designed by MUSES3D. The MUSES3D code, designed by Stéphane de Chaisemartin and Lucie Fréret, is an academic platform with a high level of genericity, dedicated to evaluate Eulerian spray models. Moreover, its algorithmic strategy combined with precise numerical schemes leads to a very low level of numerical diffusion for Eulerian resolution methods. The purpose of this chapter is to present the computing strategy in order to implement the EMSM in the MUSES3D code preserving as much as possible its genericity, and performance in terms of numerical diffusion. The chapter is organized as follow. In a first part, a synthetic presentation of the code highlights the precise locations where modifications or contribution have to be made. A second part exposes the actual implementation work.

**Notation:** The various kinds of structure considered in the MUSES3D code are denoted with the following convention:

- arrays are written with normal characters,
- derived data types as well as the subroutines are written in italic characters,
- routines are written in italic bold characters,
- module names are written in bold characters.

## 7.1 Presentation of MUSES3D

### 7.1.1 General characteristics

The MUSES3D code is a generic platform dedicated to the evaluation of Eulerian spray models. Physical transport is solved with finite volume schemes, and is coupled with phase space solvers through an operator splitting algorithm. The numerical schemes studied in the context of this PhD are exposed in Section 3.2, and an complete review can be found in [49]. The design of these schemes as well as their implementation strategy in the code allow to run computations with  $CFL = 1$ , and so to reach an excellent level of spatial accuracy relative to Eulerian models.

The second major characteristic is its generic structure, that allows to consider, within the same code, various types of resolution methods, numerical schemes, model frameworks, various computational

domains and configurations. Initially containing the single multi-fluid model, the MUSES3D code has been written so that its enrichment with new resolution methods, can directly be brought in its structure. This has the advantage of focusing on the sole coding work of the method itself, inheriting the various model frameworks, and the configurations for test cases, for example. The code also proposes various numerical schemes when considering the same model. For example the dimensionalized splitting algorithm may take different forms. Furthermore, albeit dimensionalized splitting clearly represents the most efficient way for multi-dimensional configurations, fully multi-dimensional schemes have been designed in the solver for the multi-fluid model. The other reason advocating this essential modularity, is that only a dedicated numerical scheme might be stable for a given model : this is typically the case for the EMSM with the evaporation scheme presented in Chapter 5. Since the evaluation of resolution method is progressive, with an increasing level of physical complexity, the code provides various model framework with different levels of complexity. Once the model and the numerical schemes are implemented they can be tested on several computation domains, like for example 2-D, 2-D axisymmetric and 3-D cases. The code also provides the possibility to assess the methods on several configurations, among them the one involving Taylor-Green vortices for the gaseous phase, with periodic boundary conditions and the free jet configuration, presented in Section 3.3, and that we will reuse to evaluate the EMSM model.

Finally the MUSES3D code has been optimized through High Performance Computing (HPC) techniques, allowing to evaluate the multi-fluid method efficiency in a parallel framework, and also to address more realistic configurations, as explained in [49]. This parallel framework is transparent for the implementation of a new spray model.

## 7.1.2 Numerical scheme implementation

### 7.1.2.1 Splitting strategy

As explained in Section 3.2.1, the whole numerical strategy developed in the MUSES3D code relies on an operator splitting algorithm. This is an essential feature for genericity, since it allows to use dedicated resolution schemes for a given operator. Three types of splitting algorithms are presented in Section 3.2.1, all implemented in the code. The choice procedure of the splitting algorithm detailed in [49] is independent from the phase space transport and physical transport. To be fully generic vis-a-vis to further implementations this splitting strategy is combined with a modular computing structure where the different numerical schemes are contained in separate modules. This general structure is illustrated in Fig. (7.1). In the figures displayed in this chapter, the modules are framed and the routines are written in normal characters.

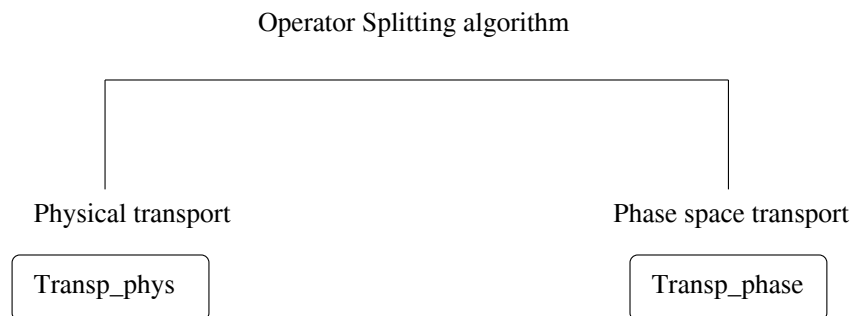


Figure 7.1: General splitting structure.

### 7.1.2.2 Physical transport resolution

The resolution of physical transport is handled by a general modular structure exclusively devoted to finite volume schemes. The achievement in MUSES3D is to be able to easily implement any conservative



scheme in the form

$$\mathbf{U}_i^{n+1} = \mathbf{U}_i^n - \frac{\Delta t}{\Delta x} (\mathbf{F}_{i+1/2} - \mathbf{F}_{i-1/2}), \quad (7.1)$$

at least for first, and also second order method in space and time. The resolution scheme, explained in Section 3.2.2, is specially suited for advection models, like the multi-fluid and the EMSM models, involving the pressureless gas formalism, see Section 3.1.3. This resolution strategy brings into play the successive steps of a finite volume resolution scheme:

- the slope computation step provides the values of the quantities present in the expression of the reconstructed variables Eq. (3.57):

$$\begin{cases} m^n(x) = m_i^n + D_{m_i^n}(x - x_i), \\ u_p^n(x) = \bar{u}_{p_i}^n + D_{u_{p_i}^n}(x - x_i), \end{cases} \quad (7.2)$$

which are the slopes and the values of  $\bar{u}_{p_i}^n$ , the modified averaged velocity in order to ensure conservation of momentum.

- The reconstruction step computations provides the actual value of the reconstructed quantities on the cell interface.
- The flux computation step provides an explicit value of the fluxes  $\mathbf{F}_{i+1/2}$  Eq. (3.53) and  $\mathbf{F}_{i-1/2}$ .
- The update procedure eventually computes the conservative terms at time  $t^{n+1}$  by adding the fluxes.

In addition, a dimensionalized splitting algorithm is considered, see Section 3.2.2, so that these steps can be considered in a one-dimensional case.

Fulfilling genericity requirement, the numerical tools corresponding to each of these steps are contained in distinct modules. The interest of this structure is obvious, since it allows to target and modify the needed procedure independently from the others.

For the time integrator, two possibilities are offered: Explicit-Euler or Runge-Kutta techniques. The choice of the time solver is independent of the finite volume resolution. We will consider here only the Explicit-Euler solver, the extension to the Explicit Runge-Kutta scheme being straightforward. The modular structure of the physical transport resolution method is illustrated in Fig. (7.2).

### 7.1.2.3 Phase space transport resolution

For the reasons given in Section 3.2.3, phase space transport, in the context of the multi-fluid model, is solved using the Radau5 solver first proposed by Hairer [105] and detailed in [49]. Concretely, this program solves the equation:

$$d_t \mathbf{Y} = \Phi(t, \mathbf{Y}). \quad (7.3)$$

The initialization of vector  $\mathbf{Y}$  is done in the module **Transp\_phase**, since it only requires the data of the moments. The actual Radau5 solver being very complex and written in a different language from the code one (Fortran 77, whereas the code is written in Fortran 90), it has been chosen to encapsulate it into a Fortran 90 interface that can be easily called (i.e with an easier set of input arguments, and argument type checking) : this routine is called *driver\_radau*, it calls the Radau5 solver, contained in another module. Finally, a strategy has to be built in order to compute the source term  $\Phi$  preserving its modular character. The source term computation involves physical data, such as the evaporation coefficient or the drag coefficient. Besides, as previously mentioned, the code provides various physical models. They are thus contained in a module dedicated to the computation of the source term of Eq. (7.3), **spray\_eq**. The call to the physical models of **spray\_eq** from the routine *driver\_radau* is handled by the interface

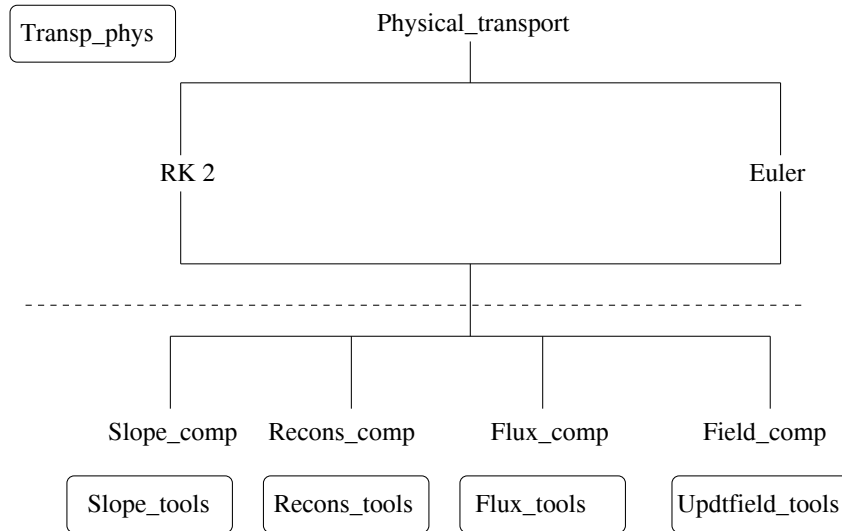


Figure 7.2: Code structure for physical transport. The dashed line distinguishes the different modules.

routine, *mf\_eq* containing the information of physical models used for the computation. This information includes, first, the considered physical framework, and then the type of the physical models. This structure is illustrated in Fig. (7.3).

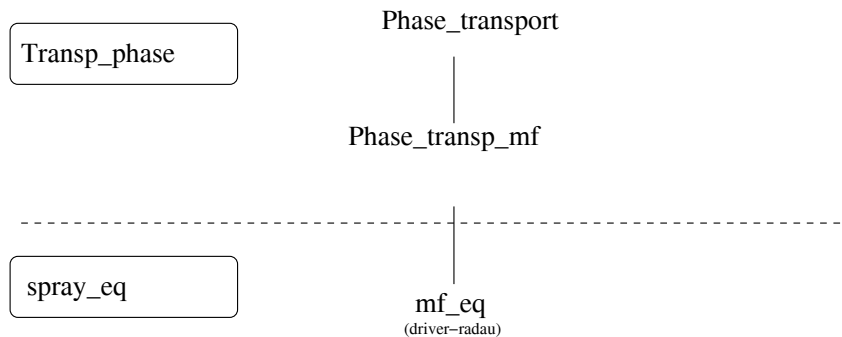


Figure 7.3: Code structure for phase space transport. The dashed line distinguishes the different modules.

This synthetic description of the code numerical structure highlights the precise location of the needed modifications to bring in order to implement the EMSM model. Concerning the physical transport resolution, referring to Fig. (7.1) and Fig. (7.2), the implementation work will concern the hierarchical level of the modules **Slope\_tools**, **Recons\_tools**, **Flux\_tools** and **Update\_tools**. We point out here the remarkably low hierarchical level of intervention (the 4<sup>th</sup> level according to the Fig. (7.1) and Fig. (7.2)), resulting from the well designed strategy of genericity. The intervention procedure for phase space transport is more challenging, since, as seen in Chapter 5, the Radau5 solver cannot be used to treat the evaporation term in the context of the EMSM model since it does not ensure the realizability condition for the moment set. For genericity purposes again, it has been decided, as explained in Section 6.5, to use an operator splitting algorithm between the drag and the evaporation term. The actual implementations are discussed in Section 7.2.

### 7.1.3 Treatment of boundary conditions

In order to ensure an easy increase of numerical schemes implemented and of type of configurations simulated, the treatment of boundary conditions is isolated from the scheme implementation. In total, four different types of boundary conditions are available in the code: injection, periodicity, symmetry and free outlet. In an injection case, the content of the ghost cells at the boundary is read in a file that is created in the initialization of the run. Treating injection case with the EMSM model will require to adapt the creation procedure of this file in this new context. On the other hand, a general procedure, *extract\_field*, handles periodicity, symmetry, or free outlet boundary conditions and couple them to the advection scheme. This coupling is fully generic and is transparent for our implementation work. An important consequence is that we benefit from the HPC structure designed in [49] for the treatment of boundary conditions.

### 7.1.4 Data Types

The high level of genericity achieved in the treatment of numerical schemes and boundary conditions goes hand in hand with a data structure common to all the spray models used. The achievement done in the MUSES3D code and explained here, is the ability to conserve the same data structure, irrespective of the spray model and associated numerical schemes. This is possible through, first, the definition of derived data types, and, second, operator overloading.

The whole data structure is based on the single type of field, *Field* defined in Algo. (1):

---

#### Algorithm 1 Field data structure

---

```

structure Field
  array sizemom, velmom
end structure Field

```

---

The array *sizemom* contains the size moments considered in the model. Typically, the size moments considered in the EMSM model will be in this array. On the other hand, the array *velmom* contains all the velocity moments considered. These are the momentum quantities. Let us remark the mass moment of the multi-fluid model, although a size moment, is included in *velmom*. This will make conditional loops easier to define between the multi-fluid and the EMSM models, as it is shown in the following. Four categories of fields can be distinguished:

- The basis field, the field *Spray*, containing the discrete values of the moments in each computational cell, has five dimensions, so that *array* reads:

$$\text{array}(N_x, N_y, N_z, N_S, N_{mom}), \quad (7.4)$$

where  $(N_x, N_y, N_z)$  covers the physical domain,  $N_S$  stands for the number of size sections in the multi-fluid context, and  $N_{mom}$  is the number of considered moments. The values of  $N_{mom}$  differs whether the array of size or velocity moment is considered. In the case of size moments,  $N_{mom} = N_{mom\_sizes}$ , and in the case of velocity moments,  $N_{mom} = N_{mom\_vel}$ .

- The numerical flux *Flux*, the slopes of the reconstructed quantities *Slope* and the reconstructed quantities *Recons*, are, contrary to *Spray*, fields of six dimensions. They write:

$$\text{array}(N_x, N_y, N_z, N_S, N_{mom}, N), \quad (7.5)$$

where, for *Flux* and *Slope*, the new values  $N$  stands for the number of transported dimension within the scheme of transport in physical space. In the case of a fully multi-dimensional scheme,  $N$  is the number of dimensions of the domain. In the case of a dimensionalized splitting, where we will exclusively work into for the implementation of the high order moment method for spray polydispersity,  $N = 1$ . For the structure *Recons*,  $N$  is equal to twice the number of transported dimensions i.e in our case,  $N = 2$ .

- The ghost cell values *Bound\_spray*, associated to the spray boundary conditions. The array that constitute it is of rank four, as it writes:

$$\text{array}(N_1, N_2, N_S, N_{mom}), \quad (7.6)$$

where  $(N_1, N_2)$  is the two-dimensionalized space extracted from the three-dimensionalized space of the domain relative to the orientation of its orthogonal vector. Thus  $(N_1, N_2)$  is  $(N_x, N_y)$  for the z -direction boundary.

- The numerical flux, slopes and reconstruction for the boundary conditions. They respectively write *Bound\_Flux*, *Bound\_Slope* and *Bound\_Recons*. The array that constitutes this kind of structure is of rank five, as it writes

$$\text{array}(N_1, N_2, nS, N_{mom}, N). \quad (7.7)$$

Three different fields are therefore defined according to their arrays dimension: *Field\_6d*, *Field\_5d*, *Field\_4d*. The different structures of MUSES3D are summarize here:

```
type(field_5d)  ::  spray
type(field_4d)  ::  Bound_spray
type(field_6d)  ::  Recons, Slope, Flux
type(field_5d)  ::  Bound_Recons, Bound_Slope, Bound_Flux
```

In order to handle these structures, dedicated procedures are defined completing:

- structure allocation/deallocation,
- structure arithmetical operations,
- structure read/write operations,
- structure initialization.

In the code, the definition of the derived types and their dedicated procedures are written in a same module **field\_class**. The structure *Spray* has a particular status as it has to be initialized and also, in case of injection, boundary condition have to be stored. Therefore a module **spray\_class** contains the definition of the structure *Spray* as well as its dedicated procedures. Since the initialization procedure is done only in the multi-fluid context, the possibility to initialize moments for in the context of the EMSM model has to be brought in the module **spray\_class**.

The major interest of defining fields generic to any model is that the data structure used in the numerical schemes and boundary conditions is independent of the model, so that the data structure will be transparent during the implementation of the EMSM. The high level of genericity reached by the MUSES3D code requires a generic structure for each of these elements: the numerical schemes the boundary conditions and the data structure. But also, the interactions between these elements, illustrated in Fig. (7.4) have to be defined in a generic manner. An example of a generic interaction is provided in Algo. (2) displaying the general structure of the finite volume scheme for physical transport resolution (the slope computation is included in *Reconstruction*).

### 7.1.5 Code coupling for gas-liquid interaction

The code MUSES3D performs spray simulation, the gas field being stationary. A natural evolution for the solver was to be coupled with a gas solver to realize two-phase flow simulations, with an unstationary gas field. This has been achived by Stéphane de Chaisemartin during his PhD, creating a multi-fluid library used by the gas solver ASPHODELE developed by J. Reveillon and co-workers [200]. This coupling has enabled some beautiful computations. Let us cite comparisons between Eulerian and Lagrangian models on a free jet configuration, a 3D computation in a Homogeneous Isotropic Turbulence (HIT) configuration, [49, 88].

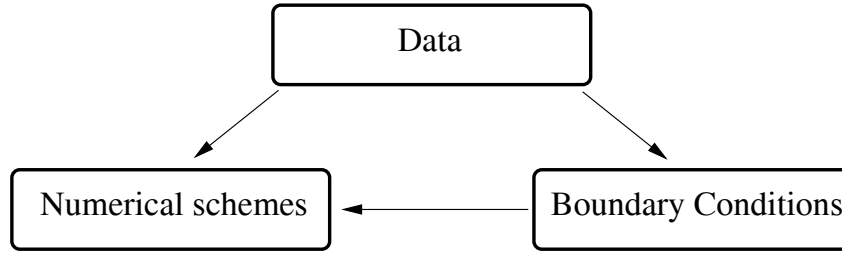


Figure 7.4: Modular block structure of MUSES3D solver, and interactions

**Algorithm 2** Transport timestep procedure

---

```

procedure Transport_timestep(Spray)
  ...
  %Reconstruction step
  call Reconstruction(Recons,Slope,Mean,Spray)
  ...
  %Fluxes computation
  call Flux_evaluation(Flux,Recons,Slope,Mean,Spray)
  ...
  %Field evolution
  call Update_field(Flux,Recons,Slope,Mean,Spray)
  ...
end procedure Transport_timestep
  
```

---

## 7.2 Implementation of the high order moment method

The previous section has highlighted the fields of intervention in order to implement the EMSM model into the MUSES3D code. This work can be split into three tasks: moment initialization, phase space transport resolution, and physical transport resolution.

**Notation:** For the sake of legibility, the profil of the arrays contained in the derived data types, which is noted in Section 7.1.4  $array(1 : N_x, 1 : N_y, 1 : N_z, 1 : N_S, 1 : N_{mom}, 1 : N)$  is written, in the algorithm illustrations under a simplified form. Indeed, given the framework described in Section 3.2, the physical transport is done in the context of a dimensionalized splitting, so there is only one transported dimension implying that  $N = 1$  and only one space dimension is mapped. Moreover, only one size section is considered, so  $N_S = 1$ . Thus, without loss of generality, the slope and the flux arrays are noted  $array_i(1 : N_{mom})$ , denoting the value of  $array$  in the  $i^{th}$  cell of the transported dimension.

### 7.2.1 Moment Initialization

In order to do quantitative comparisons between results given by the two models, and thus to validate the implementation of the high order moment method, the size moments have to be initialized so that the corresponding reconstructed mass is equal to the mass initialized for the multi-fluid model. Therefore, let us first focus on the moment initialization in the context of the EMSM model. The size distribution function  $f_{size}$ , and the total droplet mass,  $mass$ , are set by the user as parameters. Since the distribution  $f_{size}$  and the parameter mass are not correlated, the initialization takes two steps:

- the first steps corresponds to the computation of the moments of  $f_{size}$ :

$$m_{3/2}^{(j)} = \int_{S^{(j)}}^{S^{(j+1)}} S^{3/2} f_{size} dS, \quad (7.8)$$

- then, the value of  $m_{3/2}$  is adjusted relative to  $mass$ , i.e  $m_{3/2} = \alpha m_{3/2}$ , with  $\alpha$  such as

$$\alpha = \frac{mass}{\int_0^1 S^{3/2} f_{size} dS}. \quad (7.9)$$

The actual initialization of the mass moment is illustrated in Algo. (3). The moment initialization is done in the field *Spray*. Let us note that, as discussed in Section 7.1.4 for computation with the multi-fluid model, only the array *velmom* is considered, so that  $N_{mom\_sizes} = 0$ . The mass moment is thus considered as the first component of the moment velocity array.

---

**Algorithm 3** Initialization of the mass moment of the multi-fluid model

---

```

procedure Spray_init(Spray)
...
% Moment of fsize
for  $j = 1, N_S$  do
    mom_vel(1,  $j$ ) = Int( $f_{size}, 3/2, S^{(j)}, S^{(j+1)}$ )
end for

% Adjustement to mass
 $\alpha = mass / \sum_j mom\_vel(1, j)$ 
for  $j = 1, N_S$  do
    mom_vel(1,  $j$ ) =  $\alpha * mom\_vel(1, j)$ 
end for
...
end procedure Spray_init

```

---

In the context of the EMSM model, several size moments of the distribution function are initialized and are contained in the vector *mom\_sizes*. The initialization procedure is based on the procedure for the multi-fluid model, but in this case, only one section is considered. Moreover, the switch between the two types of initialization is based on the value of the parameter  $N_{mom\_sizes}$ . This is illustrated in Algo. (4). The initialization of the momentum vector is unchanged from what is done in the multi-fluid context.

---

**Algorithm 4** Initialization procedure with the two possible types of initialization

---

```

procedure Spray_init(Spray)
...
if  $N_{mom\_sizes} > 0$  then
     $\alpha = mass / Int(fsize, 3/2, 0, 1)$ 
    for  $k = 1, N_{mom\_sizes}$  do
        mom_sizes(k) = Int( $fsize, k, 0, 1$ )
        mom_sizes( $k$ ) =  $\alpha mom\_sizes(k)$ 
    end for
else
    % Mass moments, cf Algo. (3)
end if
...
end procedure Spray_init

```

---

## 7.2.2 Phase transport resolution

As explained in Section 7.1.2, it has been decided to create, within phase space transport algorithm an operator splitting algorithm between evaporation and drag for resolution with the EMSM model.

This splitting operator is of a high hierarchical level in phase space transport algorithm structure. Therefore, it is included in the module **Transp\_phase**. The routine *phase\_tr\_mms* parallel to the routine *phase\_tr\_mf*. The structure of this routine is shown in Algo. (5).

---

**Algorithm 5** General structure of the routine *phase\_tr\_mms*

---

```

procedure phase_tr_mms(mom_sizes,mom_vel)
...
  Nstep = number of steps of the splittingalgorithm
...
  if (Lie type splitting) then
    dtevap = (1, 0)
    dtdrag = (0, 1)
  else if (Strang-type splitting) then
    dtevap = (0, 1, 0)
    dtdrag = (0, .5, 0, 0.5)
  else if (Modified Strang-type splitting) then
    if evaporation first then
      dtevap = (1, 0)
      dtdrag = (0, 1)
    else
      dtevap = (0, 1)
      dtdrag = (1, 0)
    end if
  end if
...
  for  $i = 1, Nstep$  do

    if evaporation then
      call evap_emsm(mom_sizes,mom_vel,dtevap(i))
    end if
    if drag then
       $t_{end} = t_0 + dt_{drag}(i)$ 
      % Computation of Y
      call driver_radau(Y,  $t_0$ ,  $t_{end}$ )
      mom_vel = Y
    end if
  end for
end procedure phase_tr_mms

```

---

Since the resolution of the evaporation, term necessitates all the numerical tools presented in Chapter 5, the question of its introduction and its interface with the code arises. Concerning its introduction, we take benefit from the modular organization and include a new module dedicated to the resolution of the evaporation term in the context of the EMSM model : **Evaporation\_emsm**.

The complimentary work is now to create routines ensuring communication with the code structure. Since the evaporation resolution procedure is called already in the module **Transp\_phase**(see Algo. (5)), a first interface with this module is done through the routine *evap\_emsm*. Yet, information concerning the physics of the flow, gathered in the module **spray\_eq**, is needed, in order to compute the evaporation term  $K$ . Therefore, a second routine, *evap\_mixte*, establishes an interface between the modules **spray\_eq** and **Evaporation\_emsm**.

The ultimate physical data which is crucial to provide a good description for is the mass fraction of evaporated liquid in the vapor phase. This data will then condition the flame structure occurring in combustion case [49]. The computation of this data is done in the multi-fluid model and has to be done as well for the EMSM. This computation is included in the module **Evaporation\_emsm**. Since the

computation of  $Y_F$  is not systematical and is chosen by the user, a corresponding flag is inserted in the routine *evap\_mixte*, illustrated in Algo. (6). In the case of a computation of the optional argument  $Y_F$ , the evaporated mass, *evap\_mass*, is computed in addition to the resulting size and velocity moments.

---

**Algorithm 6** Evaporation with the high order moment method
 

---

```

procedure evap_mms(mom_sizes,mom_vel)
  % Compute the evaporationcoefficient
  % Computation of  $R_{si}$  using physical correlation
  call drop_model(t)
   $R = R_{si}$ 
  %Check if need to compute  $Y_F$ 
  if present  $Y_F$  then
    call evap_mixte(mom_sizes,mom_vel,R, evap_mass)
    evap_mass = evap_mass/ $\Delta t$ 
  else
    call evap_mixte(mom_sizes,mom_vel,R)
  end if
  %Computation of evaporated fuel mass fraction
   $Y_F = \text{evap\_mass}$ 
end procedure evap_mms
  
```

---

The vector  $\mathbf{Y}$  has to contain the first four size moments  $(m_0, m_1, m_2, m_3)^t$ , and the components of the momentum  $m_1 \mathbf{u}_p$ . Inversely, an update procedure has to compute the values of the moments from the output value of  $\mathbf{Y}$  at the end of the resolution. This is handled directly in the routine *phase\_tr\_mms*, as shown in Algo. (5). The computation of the sources terms, requiring the value of physical parameters, is done in the module *spray\_eq*. The interface routine created, *mms\_eq* has a structure similar to the corresponding interface in the case of the multi-fluid model. The structure update of the code structure needed by the implementation of the EMSM model is illustrated in Fig. (7.5).

### 7.2.3 Physical transport resolution

The context for physical transport resolution is clearer than phase space transport since, as seen in Section 7.1.2, the implementations directly integrate the successive step of a finite volume scheme. A direct consequence is that it allows the new developments to benefit from the existing parallel computing algorithm based on Domain Decomposition [49]. The intervention concerns the modules **Slope\_tools**, **Flux\_tools**, **Update\_tools**. Let us focus now on the actual developments to be made in these modules, with respect the scheme presented in Section 6.3 in comparison with the existing schemes presented in Section 3.2.2.

#### 7.2.3.1 Inventory of the new functions to code

In the reconstruction step, except the *zero*<sup>th</sup> order moment that is treated the same way as the mass moment in the multi-fluid approach, all the slope computations scheme have to be coded:

$$\begin{cases} p_1(x) = \overline{p_{1,i}} + D_{p_{1,i}}(x - x_i) \\ p_2(x) = \overline{p_{2,i}} + D_{p_{2,i}}(x - x_i) \\ p_3(x) = \overline{p_{3,i}} + D_{p_{3,i}}(x - x_i) \\ u_p(x) = \overline{u_{p,i}} + D_{u_{p,i}}(x - x_i), \end{cases} \quad (7.10)$$

this involves to compute the bar values that ensure that the scheme is conservative, and the slope computation. This step concerns the canonical moments which do not intervene in the multi-fluid resolution, but also the velocity as the momentum is defined as  $m_1 \mathbf{u}_p = m_0 p_1 \mathbf{u}_p$  in the EMSM model, formally different from the expression  $m_0 \mathbf{u}_p$  since it involves the reconstruction of  $p_1$  in addition to



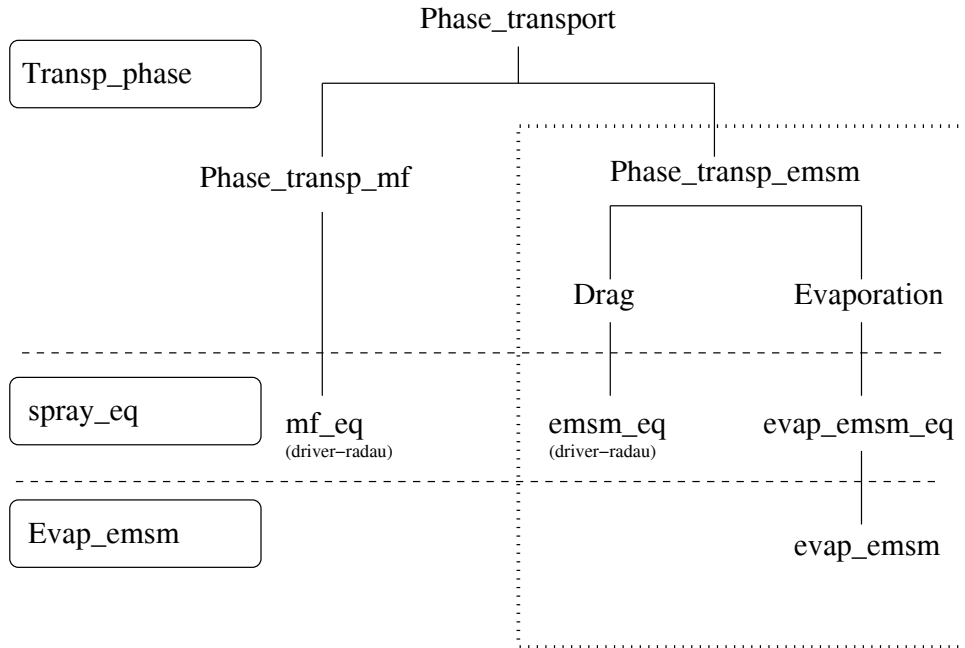


Figure 7.5: Implementation of EMSM model in the structure for phase space transport. The dashed line distinguishes the different modules. The dotted border locates the contributions.

the reconstruction of  $m_0$  in the computation of the velocity slope. The new reconstruction schemes for these variables go hand in hand with the design of new dedicated fluxes computation schemes for these variables. These two steps requires then a considerable work, contrary to the update step, where only a slight modification has to be done in order to account for the presence of size moments in the array `mom_sizes`, and of the different definition of the momentum in the case of the EMSM model.

### 7.2.3.2 Implementation of the new functions

The computation of the size moment slopes and of the velocity slope are treated in different routines. The main routine for slope computation, `slope_comp`, calls routines dedicated to size moment slope computation, `size_slope`, and to velocity computation, `vel_slope`. With this structure only velocity moment reconstruction are concerned in the context of the multi-fluid model, whereas in the context of the EMSM model, the additional quantities, the canonical moments, are reconstructed in the routine for size moments. The coding of the structure for the size moment computation has been initiated by Stéphane de Chaisemartin, and completed during this PhD. The structure, of the velocity, moment has been adapted to handle both cases of multi-fluid and EMSM models. The updated structure of `slope_comp` is represented in Algo. (7). As shown in Algo. (7), the major motivation for differentiating the treatment of size moments from velocity moments is the difference of their input argument vectors signature.

Like in the slope computation, the structure for the size flux computation distinguishes size moments and velocity moments. Algo. (8) displays the new structure of the flux computation routine `flux_comp`. Since it involves polynomial of increasing degree with the order the canonical moment considered, the flux computation function for canonical moments becomes rapidly heavy.

Eventually, the update procedure, contained in the module `Update_tools`, computes the new value of `array` at the end of the timestep. The new procedure, adapted to the case of the high order moment method is shown in Algo. (9). Contrary to the multi-fluid case, where the momentum is defined by  $m_{3/2}\mathbf{u}_p$ , in the case of the high order moment method, it is defined by  $m_1\mathbf{u}_p$ . This is taken into account in the routine `field_comp`. The implementation of the high order moment method for phase

---

**Algorithm 7** Slope computation algorithm

---

```

procedure slope_comp(Slope,Mean,Spray)
  for  $i = 1, N_x(N_y \text{ or } N_z)$  do
    if  $N_{mom\_sizes} > 0$  then
      call size_slope(Slope%sizes $i$ (:),Mean%sizes $i$ (:),Spray%sizes $i$ (:),Spray%sizes $i-1$ (:),
        Spray%sizes $i+1$ (:))
    end if
    if  $N_{mom\_vel} > 0$  then
      call vel_slope(Slope%vel $i$ (:),Mean%vel $i$ (:),Spray%vel $i$ (:),Spray%vel $i-1$ (:),
        Spray%vel $i+1$ (:),Slope%sizes $i$ (:),Mean%sizes $i$ (:),Spray%sizes $i$ (:))
    end if
  end for
end procedure slope_comp

```

---



---

**Algorithm 8** Flux computation

---

```

procedure flux_comp(Flux,Spray,Slope,Recons,Mean)
  ...
  for  $i = 1, N_x(N_y \text{ or } N_z)$  do
    if  $N_{mom\_sizes} > 0$  then
      call size_flux(Flux%sizes $i$ (:), Spray%sizes $i$ (:), Mean%sizes $i$ (:), Slope%sizes $i$ (:), Slope%vel $i$ (:),
        Recons%vel $i$ (:), Spray%sizes $i-1$ (:), Slope%sizes $i-1$ (:), Mean%sizes $i-1$ (:),
        Slope%vel $i-1$ (:), Recons%vel $i-1$ (:))
    end if
    ...
    if  $N_{mom\_vel} > 0$  then
      call vel_flux(Flux%vel $i$ (:), Recons%vel $i$ (:), Recons%vel $i-1$ (:), Slope%vel $i$ (:),
        Spray%sizes $i$ (:), Spray%sizes $i-1$ (:), Mean%sizes $i$ (:), Mean%sizes $i-1$ (:), Mean%vel $i$ (:),
        Mean%vel $i-1$ (:), Slope%sizes $i$ (:), Slope%sizes $i-1$ (:))
    end if
    ...
  end for
end procedure flux_comp

```

---

space transport can be seen in Fig. (7.6).

---

**Algorithm 9** Update procedure

---

```

procedure field_comp(Sprayn,Sprayn+1)
  for i = 1, Nx(Ny or Nz) do
    if Nmom_sizes > 0 then
      % EMSM model update
      % Update of size moments
      Spray*%sizesi(:)=Sprayn%sizesi(:)
      call euler(Spray*%sizesi(:))
      Sprayn+1%sizesi(:)=Spray*%sizesi(:)
      ...
      % Update of velocity
      Spray*%veli(2 : Nmom_vel) = Sprayn%sizesi(2) * Spray*%veli(2 : Nmom_vel)
      call euler(Spray*%veli(:))
      Sprayn+1%veli(2 : Nmom_vel) = Spray*%veli(2 : Nmom_vel)/Sprayn+1%sizesi(2)
      ...
    else if Nmom_sizes = 0 then
      % multi-fluidupdate
      ...
    end if
  end for
  ...
end procedure field_comp

```

---

## 7.3 Conclusion

This chapter presents the challenges and the computing strategy for the implementation of the EMSM in the MUSES3D code. In a first part, a synthetic presentation of the code highlights the critical aspects to consider. Then, on the basis of the existing structure and of the numerical constraints brought by the numerical tools designed for the EMSM model the principal choices for implementation of the new model are explained. They respect the genericity of the MUSES3D code, and, as it can be assessed in Chapter 8, they preserve its property of low numerical diffusion. Finally, although this issue is not addressed in this PhD, the implementation method benefits from the HPC algorithm designed in [49].

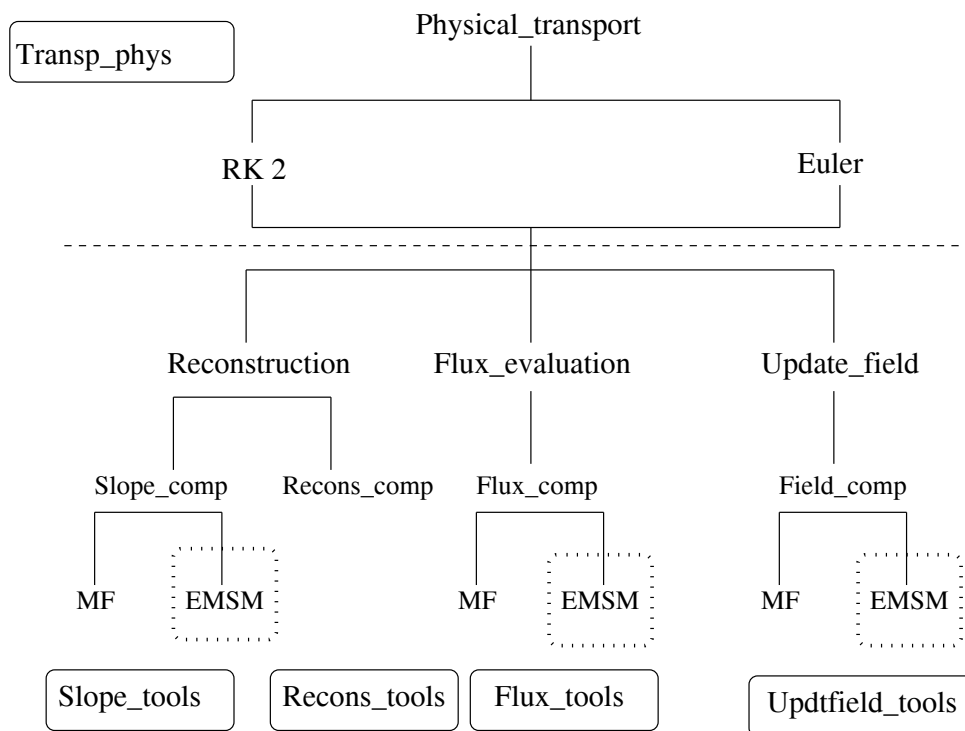


Figure 7.6: Implementation of EMSM model in the structure for physical transport. The dashed line distinguishes the different modules. The dotted borders locate the contributions. The signe MF denotes the multi-fluid model

## Chapter 8

# Numerical validation with MUSES3D

The purpose of this chapter is to assess the potential of the EMSM model through academic test cases conducted with MUSES3D (Chapter 7). In Chapter 6, one-dimensional results have already validated the numerical schemes for evaporation and advection of the moments. The results presented here validate their implementation in MUSES3D, see Chapter 7. The accuracy and efficiency in terms of CPU cost of the EMSM model relative to the multi-fluid model is appraised in the context of the two configurations presented in Section 3.3.1 and Section 3.3.2: the Taylor-Green configuration for the gaseous phase, and the free jet configuration.

Finally, let us notice that this is the first step of validation realized on an academic code, in a framework of structured grids, pure Eulerian formalism relative to the Arbitrary Lagrangian Eulerian (ALE) formalism presented in Chapter 13. Moreover, computations are run with low numerical diffusion since the schemes for physical transport allow computations with a convective CFL up to 1. This is the preliminary and necessary step towards implementation in the industrial IFP-C3D code, involving additional difficulties in terms of modeling and computing, see Chapter 13 and Chapter 14.

### 8.1 Dynamics of an evaporating spray in a two-dimensional Taylor-Green configuration for the continuous phase

Here, we focus on a case where the analytical gaseous velocity field corresponds to the Taylor Green vortices. For the computation we have chosen a  $200 \times 200$  grid cell, in order to ensure that we have a sufficiently detailed description of the field. As in the earlier cases, the CFL number is equal to one. The initialisation of the spray corresponds to a stationary cloud overlapping two different vortex areas. Periodic boundary conditions are set on the edge of the domain. In the following discussion, in order to do comparisons with the multi-fluid model, the quantity describing the liquid is the particle mass, that is to say the moment or order  $3/2$ , reconstructed from the actual solved moments:  $(m_0, m_1, m_2, m_3)$ . The initially motionless droplet cloud is dragged by the gas. We recall the gaseous configuration and the initial condition for the moments on Figures (8.1)-left and (8.1)-right. The initial NDF as well as the corresponding mass distribution function are also recalled in Fig. (8.2).

A cloud of aerosol particles is first initialized in the domain. The dimensional time is given by  $\tau_g$  and the computation is run until non dimensional time  $t = 2$ . In this configuration,  $\tau_g$  is the time taken by a particle moving at  $U_0$  to cross the domain. Two sets of computations are launched, one for the high order moment method and the other one for the multi-fluid model with ten sections. The results of the multi-fluid model are used as the reference to validate our method.

The particle Stokes number of the distribution is 0.017 for the high order moment method, and ranges from  $2.810^{-3}$  to 0.045 for the multi-fluid model with ten sections. The spray evaporation rate is set to

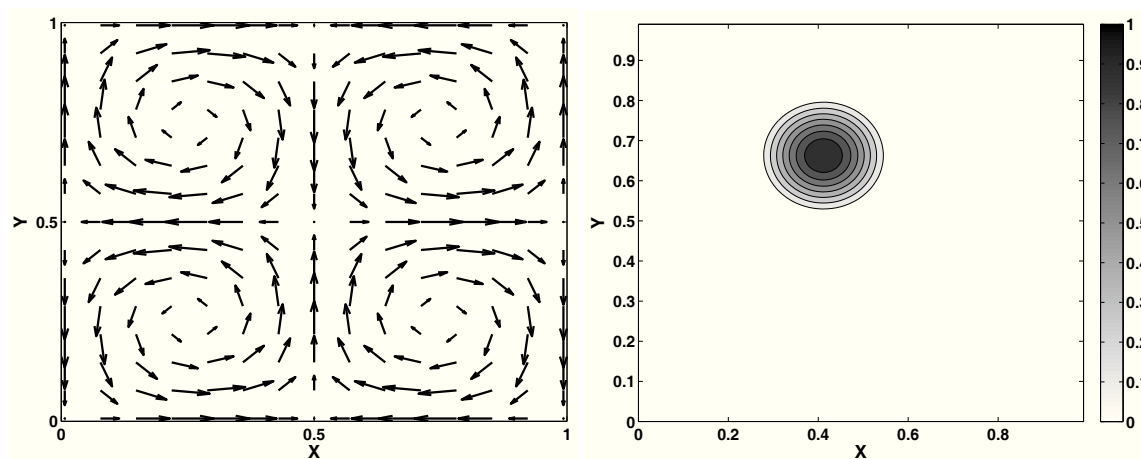


Figure 8.1: (left) Taylor-Green configuration for the gas vorticity field, (right) Initial condition for the droplets, composed of a motionless cloud. The droplet mass is represented. It is reconstructed from the first four size moments:  $(m_0, m_1, m_2, m_3)$

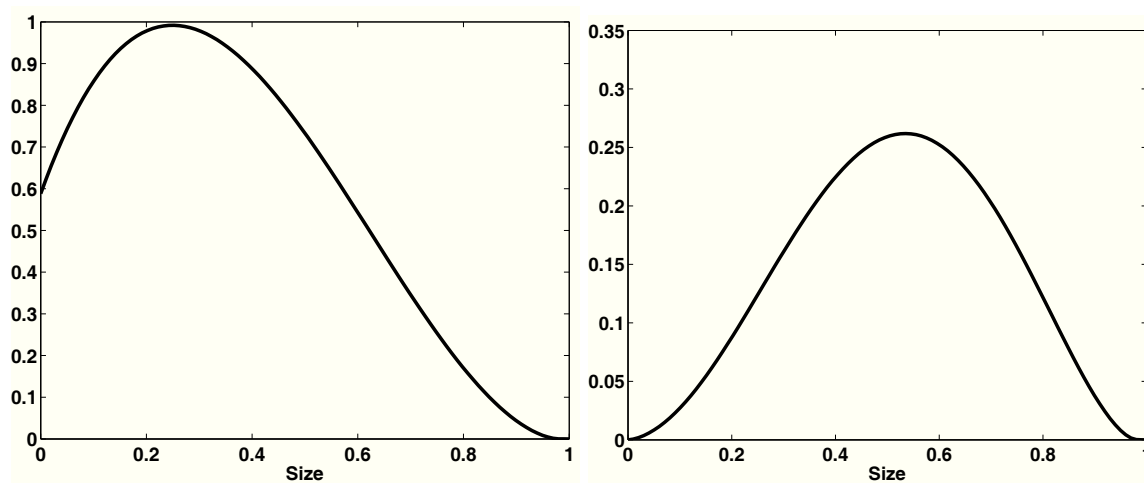


Figure 8.2: (left) Initial size distribution for the particles. (right) Corresponding mass distribution

$K = 0.27$ . Due to the cloud initial location, two parts of it are dragged by two different vortices. That is why the main part of the cloud is dragged in the top-left vortex, whereas a smaller part of the cloud is dragged in the top-right vortex. As it is shown in [49] that the critical Stokes number for the wellposedness of this problem is  $St_c = 1/8\pi$ . This value is the number under which the particles stay in the vortices so that their characteristics do not cross. Above  $St_c$ , particle inertia makes them being ejected from the vortices. However, although the particles Stokes number are less than  $St_c$ , it can be seen in both cases that some particles crosses: this is a pure numerical diffusion effect on the particle velocity.

The general notice is that the level of comparison is very good. Indeed, results at  $t = 0.5$  and  $t = 1$  are very similar between the two methods. At time  $t = 1.5$  and  $t = 2$ , the fact that the droplets are dragged faster in the case of the high order moment method comes from the computation of the drag term. In both models, the Stokes number writes  $St_0 \bar{S}$ , where  $St_0$  is defined in Section 3.1.2 and  $\bar{S}$  is the average droplet surface of the distribution. As indicated in Fig. (8.2)-right, the sections with the highest mass are between  $\bar{S} = 0.4$  and  $\bar{S} = 0.6$ . In the case of the the high order moment method,  $\bar{S} = m_1/m_0 = 0,3487$ . In terms of dynamics, our model only considers the particle mean velocity. Meanwhile, ten sections are considered for this case in the multi-fluid model, which amounts to ten different fluids with their own velocity. The spray dynamics conditioned by size is thus better solved in the multi-fluid model. Nevertheless, in order to assess the accuracy of the models in terms of mean dynamics of the droplets, some studies have been performed on the evolution of the mean droplet size through evaporation. First, Fig. (8.7)-left displays the evolution of the droplet mass through evaporation of a motionless cloud. It can be concluded that the multi-model, with ten sections, is not as accurate as the high order moment method. Further comparisons and conclusions can be found in [173]. In a second study, the evolution through evaporation of the mean particle size, given by both the models, are compared. It can be seen in Fig. (8.7)-right that the high order moment method is more accurate than the multi-fluid model in assessing the dynamical value of  $\frac{m_1}{m_0}$ . This means that, the term of mean drag, and thus the mean particle velocity is better solved by the high order moment method than the multi-fluid model. Remarkably enough, even with 40 sections, the multi-fluid model does not give as good results as the high order moment method.

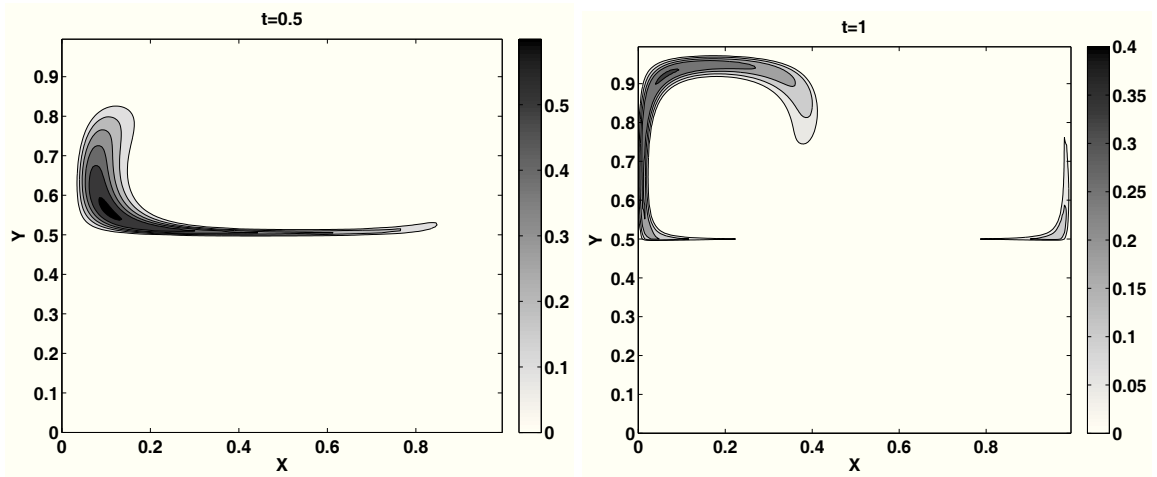


Figure 8.3: Results for spray dynamics dragged by the gas field made of Taylor-Green vortices. Results for the high order moment method. (left) Droplet mass at time  $t = 0.5$ . (right) Droplet mass at time  $t = 1$ . The computation is carried out in a  $200 \times 200$  grid.

The critical question of time efficiency has been addressed in a study comparing the computation time required for the high order moment method and for the multi-fluid model with ten sections, on that configuration described above. Three different computations are launched, first on a 50, then on a  $100 \times 100$  and finally on a  $200 \times 200$  cell grid. For each computation, the total CPU time is assessed. Moreover, in order to evaluate the relative importance of the phase space and physical space transport, the time spent in each and every routine is recorded. Table (8.1) displays the results of the analysis on

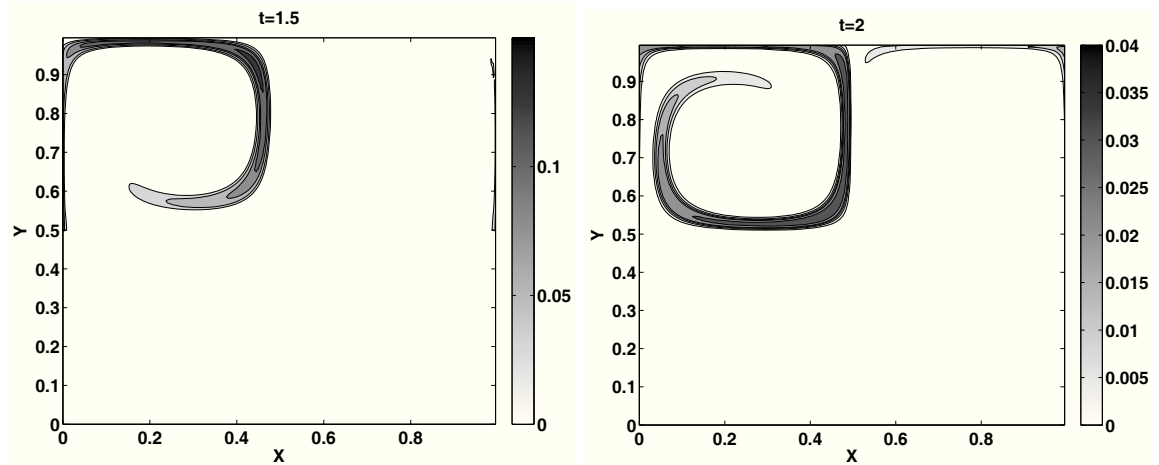


Figure 8.4: Results for spray dynamics dragged by the gas field made of Taylor-Green vortices. Results for the high order moment method. (left) Droplet mass at time  $t = 1.5$ . (right) Droplet mass at time  $t = 2$ . The computation is carried out in a  $200 \times 200$  grid.

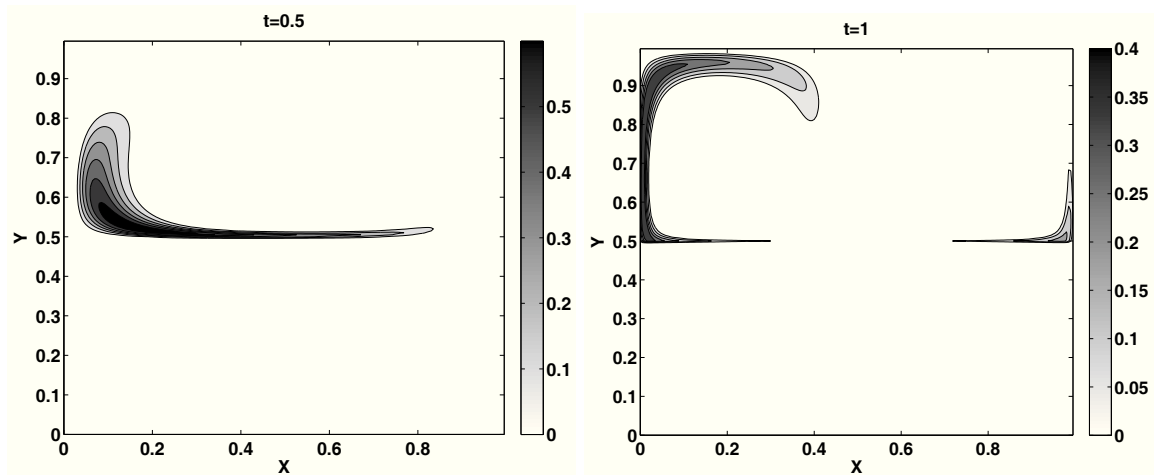


Figure 8.5: Results for spray dynamics dragged by the gas field made of Taylor-Green vortices. Results for the multi-fluid method for ten sections. (left) Droplet mass at time  $t = 0.5$ . (right) Droplet mass at time  $t = 1$ . The computation is carried out in a  $200 \times 200$  grid.

the total computation time and the relative time spent for the resolution of transport in phase space and physical space, respectively. This analysis points out the time efficiency of the high order moment method, which is about 3.6 faster than the multi-fluid method. This is a real achievement, given the quality of the comparison of the results displayed at Fig. (8.3), Fig. (8.4) for the high order moment method and Fig. (8.5), Fig. (8.6). The second result provided is that the relative importance of phase space transport decreases as the cell number increases. Moreover, Table (8.2) compares the number of variables solved for each operator resolution, for both models. For phase transport, six variables must be solved in the case of the high order moment method (the four size moments and the two components of the velocity), while  $\tilde{n}_{ME}$ , the reconstructed NDF is obtained from the moments by an iterative solver. On the other hand, three variables per section, the mass (denoted  $m_{3/2}$  as it is proportional to the size moment of order  $3/2$ ) and the two components of the velocity, are explicitly solved in the case of the multi-fluid model, which amounts to thirty variables in total. For physical transport, six variables



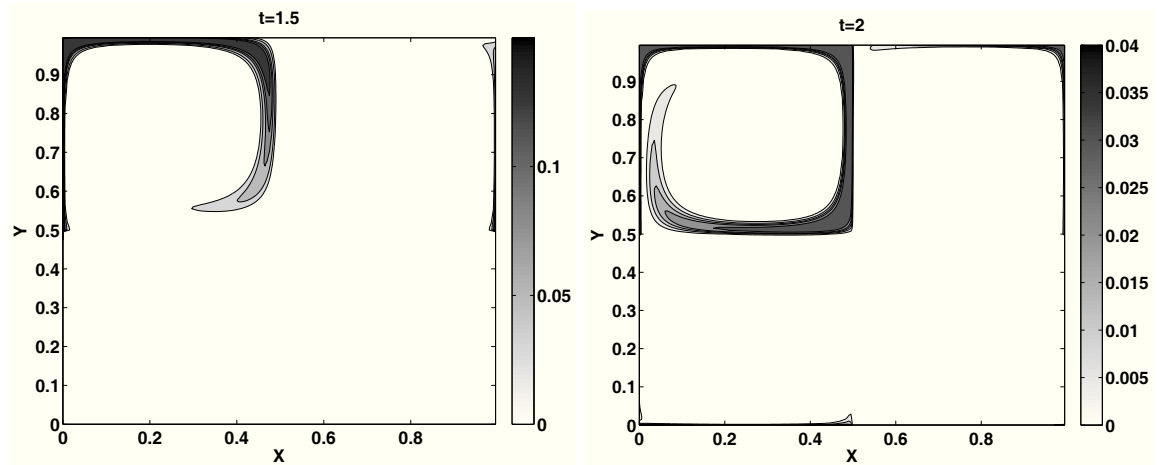


Figure 8.6: Results for spray dynamics dragged by the gas field made of Taylor-Green vortices. Results for the multi-fluid method for ten sections. (left) Droplet mass at time  $t = 1.5$ . (right) Droplet mass at time  $t = 2$ . The computation is carried out in a  $200 \times 200$  grid.

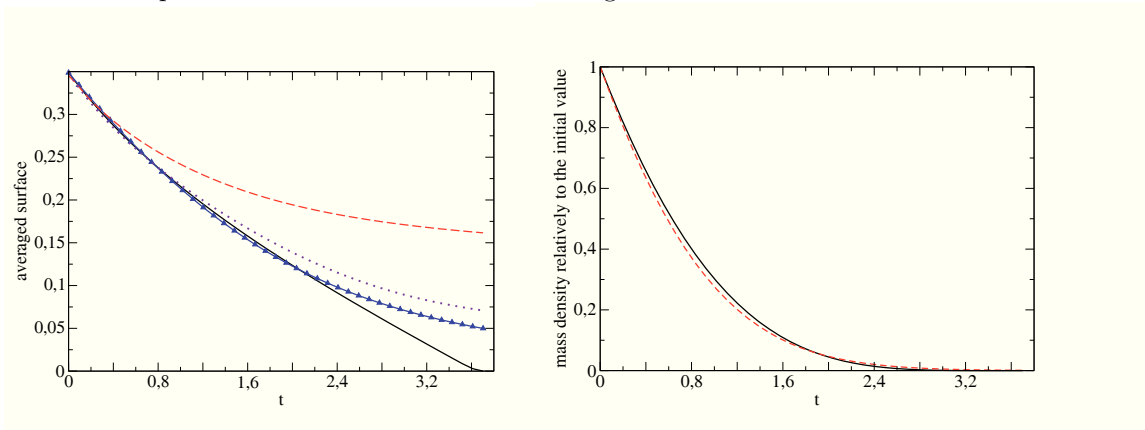


Figure 8.7: (Left) Evolution of the droplet mass of a motionless cloud through evaporation with a  $d^2$  law, and comparison with the analytical solution. Black curve: analytical solution; triangles: high order moment method; dashed red curve: multi-fluid model with ten sections. (Right) Evolution of the mean particle size through evaporation, and comparison with the analytical solution. Black curve: analytical solution; dashed blue curve: high order moment method; blue curve with triangles: multi-fluid model with ten sections; red curve with circles: multi-fluid model with 40 sections.

must be solved in the case of the high order moment method, whereas, the same thirty unknowns must be solved in the case of the multi-fluid model. It also gives the ratio between the computation times of the multi-fluid and the high order moment method. It comes from Table (8.2) that the phase space transport is, on average, 4.4 times faster in the EMSM model than the multi-fluid model, while the physical transport is, in average, 3.6 times faster. This can be understood by the fact that, in phase space transport velocity variables are only impacted by drag and not by evaporation, so that they do not require the same computation time as the moments. For physical transport the algebraic relation for the computation of slopes and fluxes of the moments and momentum, heavier than in the multi-fluid model, explain why we do not reach a time ratio of 5 as Table (8.2) could have led to expect. The time ratio is a bit lower, 3.6, but still very significant. Extrapolating from these results, we can legitimately expect that this ratio will become higher in three dimensions, and that our new method will be much faster than the multi-fluid model, especially since most of the computation time will be devoted to physical transport. We also notice that the phase space transport can easily be parallelized. As a result, our new

method proves to be very attractive for three-dimensional configurations. These very satisfactory results demonstrate the efficiency of the EMSM model relatively to the multi-fluid model.

Grid	50 × 50			100 × 100			200 × 200		
	Phase	Physical	Total (s)	Phase	Physical	Total (s)	Phase	Physical	Total (s)
EMSM	49.6 %	50.4%	52	43%	57%	318	34.5%	65.5%	2140
MF	56.79%	43.21%	205	47.25%	52.75%	1269	38.39%	61.61%	8461
Ratio time	4.5	3.4	3.9	4.4	3.7	4	4.4	3.7	3.9

Table 8.1: Computation time comparison between the high order moment method (EMSM) and the multi-fluid method (MF). Phase denotes the relative time (in pourcent of the total time) spent for phase space transport (evaporation and drag). Physical denotes the relative time (in pourcent of the total time). Total denotes the total computation time (in seconds)

	EMSM	MF	Ratio time
Phase	$m_0, m_1, m_2, m_3, +\tilde{n}_{ME},$ $u, v$ = 6 variables + $\tilde{n}_{ME}$	$10 \times (m_{3/2}, u, v)$ = 30 variables	4.4
Physical	$m_0, m_1, m_2, m_3,$ $u, v$ = 6 variables	$10 \times (m_{3/2}, u, v)$ = 30 variables	3.6

Table 8.2: Comparison of the number of variables for the high order moment (EMSM) and the multi-fluid (MF), for phase space and physical space transport. The last column represents the approximate ratio of the computational time spent for the multi-fluid model to the time spent for high order moment method, in the phase and physical transport respectively

## 8.2 Two-dimensional free-jet configuration in an unstationnary gaseous phase

In this third test case the high order moment method is assessed on a 2-D Cartesian free jet. A poly-disperse spray is injected in the jet core with the size distribution represented in Fig. (8.2)-left. The simulations are conducted with an academic solver, coupling the ASPHODELE solver, developed at CORIA by Julien Reveillon and collaborators [200], with the Eulerian solver MUSES3D [49, 172] developped at EM2C Laboratory, using the models and the numerical scheme presented in these articles. The ASPHODELE solver couples a Eulerian description of the gas phase with a Lagrangian description of the spray.

This free jet case is computed with an evaporating spray having an evaporation coefficient  $K = 0.07$ . The particle Stokes number is 0.275 for the high order moment method, corresponding to a diameter  $d_0 = 75\mu m$ , and ranges from  $St = 0.047$  to  $St = 0.75$  for the multi-fluid model with ten sections, corresponding to diameters from  $d_0 = 5\mu m$  to  $d_0 = 85\mu m$ . In order to correctly describe the evaporation process with the multi-fluid model, ten sections are considered, whereas only one section is required in the computation using the high order moment model. The computation runs until  $t = 20$ . Figure (8.8) displays the final mass fields for the spray, at times  $t = 10, 15$  and  $20$ . The level of comparison between the two resulting fields is very good. One can nevertheless notice a slight difference. In the case of the multi-fluid model with ten sections, the spray evaporates less.

Since, our primary interest is in combustion applications, the paramount objective of evaporating spray modeling is prediction of the gas-phase fuel mass fraction. Therefore we present comparisons between the gas-phase fuel mass fraction obtained from the high order moment model and multi-fluid descriptions of the spray. These simulations were once again accomplished using one-way coupling. As a consequence, the evaporated fuel is not added as a mass source term in the gas-phase equations, but is stored in passive scalars for the gas. The two fields are plotted in Fig (8.9). These results confirm the quality of the previous results. The present comparison, by showing clear similarity between the two model, highlights the efficiency of the Eulerian high order moment model and the associated numerical schemes in describing polydisperse evaporating sprays. These results are a first significant step towards combustion computations with full two-way coupling.

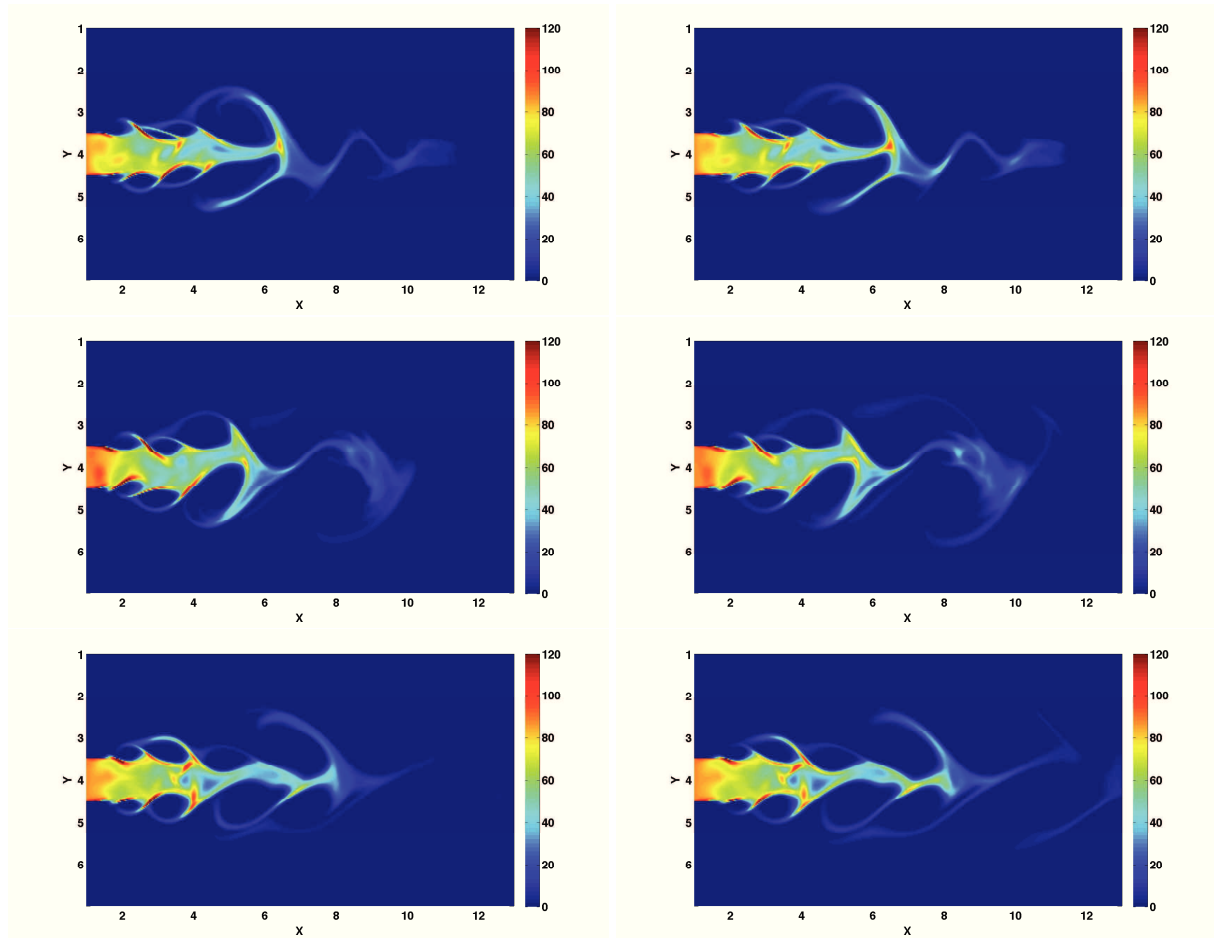


Figure 8.8: Total number density of the polydisperse evaporating spray. (Top) Results at time  $t = 10$ . (Medium) Results at time  $t = 15$ . (Bottom) Results at time  $t = 20$ . (Left) High order moment method. (Right) Multi-fluid model with ten sections. The computation is carried out in a  $400 \times 200$  grid

### 8.3 Conclusion

The results exposed in this section demonstrate the potential of the high order size moment method for the description of the dynamics of a polydisperse spray in terms of accuracy and also efficiency. Consequently they validate the numerical schemes developed for phase space transport and physical transport presented in Chapter 5 and Chapter 6 and their implementation done in the MUSES3D

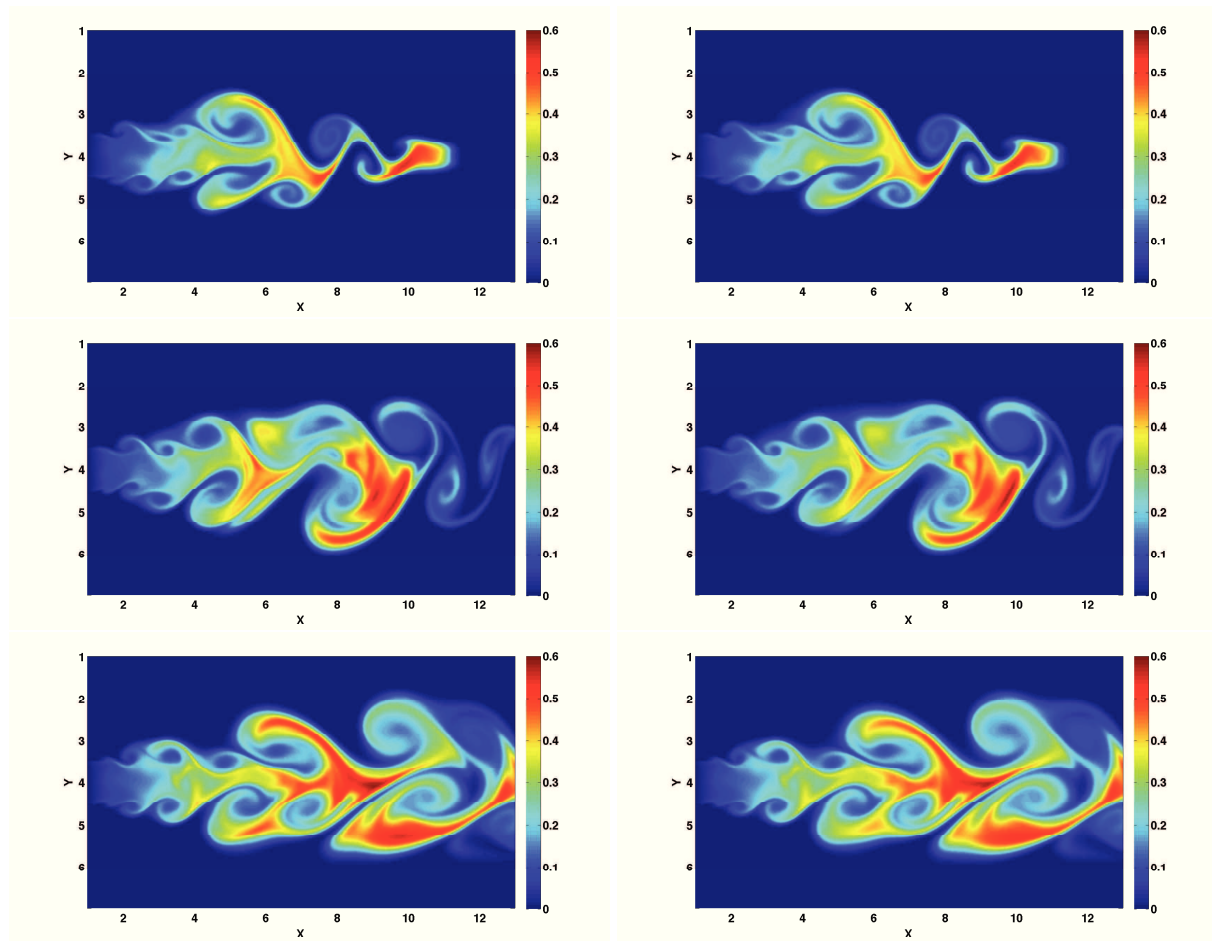


Figure 8.9: Comparison of the gas-phase fuel mass fraction. (Top) Results at time  $t = 10$ . (Medium) Results at time  $t = 15$ . (Bottom) Results at time  $t = 20$ . (Left) High order moment method. (Right) Multi-fluid model with ten sections. The computation is carried out in a  $400 \times 200$  grid

code, see Chapter 7. Two critical questions had to be answered to obtain this quality of result. The first was to ensure the realizability condition for the moments, in the treatment of evaporation, term, and during the advection scheme. This last issue has been the subject of some publications [231, 176]. Here, we propose an advection scheme preserving the integrity of the moment set *per se*. The second critical issue of our study was the efficiency in terms of CPU cost of our method relative to the multi-fluid model. It has been assessed, relatively to the multi-fluid model with 10 sections, on a study case of spray dynamics in a Taylor-Green configuration for the gaseous phase, and has given very satisfactory results. Moreover, comparisons in a free jet case with unstationary whirling gas phase show a very good level of similarity between the EMSM model and the multi-fluid model with 10 sections. This result can be found in [129].

It must nevertheless be kept in mind that these tests, performed with an academic code, are only a first step towards the implementation for spray resolution in industrial configurations. In this PhD framework the objective is to implement this method in the IFP-C3D code, with two major differences with the MUSES3D code. First, the code IFP-C3D is unstructured. Then its resolution algorithm is based on the ALE formalism. An important work has to be done in order to adapt the numerical schemes for high order size moment method in this new context, coping with the two critical conditions: the realizability condition and the stability through  $\delta$ -shock appearance. This work is explained in Chapter 13 and Chapter 14.

## Part III

# High order velocity moment method for treatment of high Knudsen number flows

# Introduction

This part investigates the possibility, for a Eulerian spray model, to describe Particle Trajectory Crossings (PTC). This constitutes the answer to the second of the two limitations formulated in Section 3.4 of Eulerian spray models relative to Lagrangian models.

Chapter 9 presents the Eulerian Multi Velocity Moment model, referred to as the EMVM model. It relies on the same idea as the Eulerian Multi Size Moment model (EMSM model) explained in Part II, i.e a high order moment method. Advection of velocity moments up to third order are considered, and methods to express the unclosed terms are discussed.

In Chapter 10, the coupling of the EMVM model with the multi-fluid or the EMSM model is presented, leading, for the first time, to Eulerian spray models able to describe both polydispersity and PTC. These new models are named, first, the Eulerian Multi-Fluid and Velocity Moment (EMFVM) model, second, the Eulerian Multi Size and Velocity Moment model.

In order to evaluate the EMFVM model, on challenging test cases such as the case presented in Section 3.3, it has to be implemented in the MUSES3D code. Its implementation strategy is then described in Chapter 11.

Finally, Chapter 12 displays and discusses the corresponding results.

## Chapter 9

# Eulerian Multi Velocity Moment (EMVM) model: modeling, mathematical properties, and numerical scheme

In the context of this work, a particle flow is characterized by two dimensionless numbers, the Knudsen and the Stokes numbers  $\text{Kn}$  and  $\text{St}$ , as explained in Section 1.2.1. In the limit of small Knudsen number, collisions are dominant and the particle velocity distribution function is very near the equilibrium distribution. In this context, in the so-called hydrodynamic limit [123], it is possible to describe the flow by velocity moments up to second order. The larger Knudsen number case is by far the most challenging case as the equilibrium distribution is no longer a good approximation and, eventually, one must solve the Boltzmann equation to adequately capture the flow physics of a non-equilibrium granular particle flow. For wall-bounded flows, non-equilibrium effects can be important near the walls, because the velocity distribution function is composed of incoming and outgoing particles in such a way that velocity is far from equilibrium.

Moreover, the greater the Stokes number is, the smaller the impact of the fluid on particles is. Then, for large enough Stokes and Knudsen numbers, particle trajectory crossing (PTC) will occur. Locally, the velocity distribution will be bimodal, with values corresponding to the velocities originating from each side of the plane. These effects are naturally considered by Lagrangian methods. But, in the vast majority of cases, when it comes to Eulerian methods, equilibrium closure for velocity moments will predict  $\delta$ -shocks [21] in the local number density when in fact no such behavior is present in the flow [57]. It is necessary to extend the moment closure to eliminate this unphysical behavior brought by the inaccurate equilibrium assumption.

The range of Knudsen, Stokes and Reynolds numbers is very wide in real gas-particle flow. However the case of high Stokes number is isolated, since our aim is to isolate the critical role of non-equilibrium effects in moment closures, and to investigate their treatment using quadrature-based moment closures. Moreover, within this assumption, velocity fluctuations due to gas-phase turbulence can be neglected.

In order to provide a closure for velocity moment of order greater than two, the quadrature method of moments (QMOM) is envisaged. It was introduced by [175] as a closure for population balance equations (PBE) involving a number density function (NDF)  $f(t, \mathbf{x}, \xi)$  with independent variable  $\xi$  representing the particle volume or mass. As seen in Chapter 2, the PBE that governs the NDF is difficult to resolve numerically, and thus moment methods are used. But in most cases, the derived moment equations are not closed and a closure step is required. Using QMOM, the moments are expressed in terms of a finite

set of  $N$  weights  $n_\alpha(t, \mathbf{x})$  and abscissas  $\xi_\alpha(t, \mathbf{x})$ . defined such that:

$$m_k = \sum_{\alpha=1}^N n_\alpha \xi_\alpha^k, \quad k = 0, \dots, 2N - 1. \quad (9.1)$$

The key feature of QMOM is the inversion algorithm used to find the weights and abscissas from the moments. Indeed, a direct non-linear solver is poorly conditioned. However, the algorithm proposed in [175] using the Product-Difference (PD) algorithm overcomes this difficulty by replacing the non-linear solver with a computationally efficient eigenvalue-eigenvector problem that is well-conditioned even for large  $N$ . Using this algorithm, it is possible to solve a spatially dependent NDF using standard flow codes to transport the moments [160, 161, 82, 227, 237]. Unfortunately, the PD algorithm only works for uni-variate distribution functions, but not for bi-variate where  $f(t, \mathbf{x}, \xi, \mu)$  depends on two internal coordinates. In order to overcome this limitation, one can directly work with transport equations of the weights and abscissas (direct quadrature method of moment or DQMOM). This method works well when  $\xi$  and  $\mu$  are passive scalars. For non-equilibrium gas-solid flows such as those considered in this work, DQMOM can be used with the velocity moments to rewrite the moment transport equations in terms of transport equations for the weights and abscissas. The resulting transport equations, in the absence of collision, have the form of the pressureless gas dynamics equation [21]. Although the DQMOM formulation works well in most of the flow domain, it fails at points where singularities occur, making the velocity abscissas change discontinuously [56]. Remarkably, a quadrature-based moment closure for the velocity distribution function is robust at such points [56, 57]. However, for multi-dimensional velocity distributions the key challenge of inverting the moments to find the weights and velocity abscissas remains.

This chapter is organized as follows. The first section presents the complete dynamic system treated in this chapter. Then it points out the mathematical issues faced for its resolution: the characterization of the entropic solution of the advection problem and the multi-dimensional quadrature of velocity moment vector. Section 9.2 focuses on the one dimension advection case where a mathematical analysis of the closed system is provided, as well as a numerical scheme. This work has been published in [125]. Section 9.3 addresses the issue of extending the QMOM to a multi-dimensional configuration and presents the adopted quadrature strategy in two dimensions. Section 9.4 focuses on the resolution of the interaction and source terms present in the basis kinetic equation. Section 9.5 exposes the numerical strategy for the complete system in two dimensions. Eventually, some basis results of impinging jet are presented in Section 9.6. This work has partially been published in [172].

## 9.1 Kinetic description of dilute gas-particle flows and moment transport equations

### 9.1.1 Moment dynamic system

We consider here only dynamic effects of a monodisperse flow, experiencing drag and collision monitored by its Stokes and Knudsen number respectively. Consider then the following kinetic equation for the velocity distribution function  $f(t, \mathbf{x}, \mathbf{u})$  of dilute monodisperse solid particles in gas phase:

$$\partial_t f + \nabla_{\mathbf{x}} \cdot (\mathbf{u} f) + \nabla_{\mathbf{u}} \cdot (\mathbf{D}_r f) = \Gamma, \quad (9.2)$$

where  $\mathbf{u}$  is the particle velocity,  $D_r$  is the drag term and  $\Gamma$  is the particle-particle collision term.

In this section, we will assume that the collision term is already closed, using the Bhatnagar-Gross-Krook (BGK) approximation [15], see Section 1.2.3. The collision term reads:

$$\Gamma = \frac{1}{\text{Kn}} (f_{eq} - f), \quad (9.3)$$



where  $f_{eq}$  is the equilibrium (Maxwellian) distribution. In 2 dimensions,  $f_{eq}$  is given by:

$$f_{eq}(\mathbf{u}) = \frac{M_{0,0}}{2\pi\sigma_{eq}} \exp\left(-\frac{\mathbf{v}^2}{2\sigma_{eq}}\right), \quad (9.4)$$

where  $\sigma_{eq}$  is the equilibrium variance and we recall that  $\mathbf{v} = \mathbf{u} - \mathbf{u}_p$ . Although for real particles, collisions are usually unelastic, for the sake of simplicity, we will consider here that  $\sigma_{eq}$  is conserved. Indeed, our primary aim is to show that the high order velocity moment method can be coupled to a collision term, the study of the collision terms being a secondary work. Note that the Knudsen number  $\text{Kn}$  is proportional to the collision time  $\tau_c$ , so that the velocity distribution function is equal to  $f_{eq}$  when  $\text{Kn} = 0$ . In the opposite limit, the particles are collision-less and the velocity distribution function will be determined by the remaining term in Eq. (9.2), and hence can be far from equilibrium.

The drag term is approximated by the Stokes closure  $\mathbf{D}_r = \frac{1}{\text{St}}(\mathbf{u}_g - \mathbf{u})$ .

In this work, we consider dynamic equations on velocity up to third order, and up to two dimensions. Let us then introduce the notations used throughout this chapter:

- $M_{l,m}$  denotes the velocity moment vector, in two dimensions:

$$M_{l,m} = \int u_1^l u_2^m f \, d\mathbf{u}, \quad l + m \leq 3, \quad (9.5)$$

- $\mathbf{W}_{N_{\text{dim}}}$  denotes the velocity moment vectors in  $N_{\text{dim}}$  dimension(s),
- $\mathbf{W}_{N_{\text{dim}}}^*$  denotes the vector of controlled moments,
- $\beta$  denotes the number of quadrature nodes,
- $\mathbf{V}_\beta$  denotes the set of weights and abscissas of the quadrature,
- $\mathbf{V}_\beta^*$  denotes the set of weights and abscissas of the quadrature in the frame of the Cholesky decomposition
- $\mathcal{W}^{N_{\text{dim}}}$  denotes the set of velocity moments up to third order in  $N_{\text{dim}}$  dimensions,
- $\mathcal{W}^{N_{\text{dim}},\dagger}$  denotes the set of representable moments by the set of weights and abscissas in  $N_{\text{dim}}$  dimensions.

In one dimension four moments are considered:

$$\mathbf{W}_1 = (M_0, M_1, M_2, M_3). \quad (9.6)$$

The system of equations verified by  $\mathbf{W}_1$  writes:

$$\begin{cases} \partial_t M_0 + \partial_x M_1 = 0, \\ \partial_t M_1 + \partial_x M_2 = 0, \\ \partial_t M_2 + \partial_x \overline{M_3} = 0, \\ \partial_t M_3 + \partial_x \overline{M_4} = 0. \end{cases} \quad (9.7)$$

where the terms  $\overline{M_4}$  is unclosed.

In two dimensions ten moments are considered:

$$\mathbf{W}_2 = (M_{0,0}, M_{1,0}, M_{0,1}, M_{2,0}, M_{1,1}, M_{0,2}, M_{3,0}, M_{2,1}, M_{1,2}, M_{0,3}). \quad (9.8)$$

Considering now the transport equations for the moments of Eq. (9.2)

$$\begin{aligned}
\partial_t(M_{0,0}) + \partial_x(M_{1,0}) + \partial_y(M_{0,1}) &= 0, \\
\partial_t(M_{l,m}) + \partial_x(M_{l+1,m}) + \partial_y(M_{l,m+1}) &= D_{l,m}^1, \quad l+m=1, \\
\partial_t(M_{l,m}) + \partial_x(M_{l+1,m}) + \partial_y(M_{l,m+1}) &= D_{l,m}^2 + C_{l,m}^2, \quad l+m=2, \\
\partial_t(M_{l,m}) + \partial_x(M_{l+1,m}) + \partial_y(M_{l,m+1}) &= D_{l,m}^3 + C_{l,m}^3, \quad l+m=3.
\end{aligned} \tag{9.9}$$

The terms  $D_{l,m}^1, D_{l,m}^2, D_{l,m}^3$  denote the drag terms, and  $C_{l,m}^2, C_{l,m}^3$  denote the collision terms. Some unclosed terms appear in Eq. (9.9):  $M_{l+1,m}$  and  $M_{l,m+1}$ , and the drag terms. Finding a robust and accurate closure for these terms is one of the issues discussed in this chapter.

### 9.1.2 Resolution strategy and challenges for the advection term resolution

As done in Part II we present the closures and the numerical scheme in the context of the operator splitting algorithm described in Section 3.2.1. This enables us to focus on resolution strategies for each of the transport, drag, and collision operator. Here particularly, it allows to isolate the advection term, which is by far the term that brings the greatest issues.

Indeed, two questions have to be answered. First, in order to design precise numerical schemes for advection, the analysis of the mathematical structure of system (9.9) has to be done, as well as the characterization of the entropic solution in case of singularities. This study is presented in Section 9.2, on a one dimension configuration to begin with, since, as mentioned in the introduction, the quadrature of a mono-variate function is well known. This is not the case for multi-dimensional configurations where the quadrature problem becomes ill-posed. Therefore, the second challenge is to propose an acceptable quadrature method, numerically stable, and being used in actual computations. The answer to this question is found in Section 9.2.6.2.

## 9.2 Quadrature-based method in one-dimension: mathematical properties of the resulting system and entropy solutions

Numerical algorithms in order to simulate systems of conservations laws such as system (9.7) with the related quadrature-based closure have been proposed in [84] from the work for [24] using naturally kinetic scheme with finite volume methods. Let us also mention the work of [99] independently proposing algorithms based on delta-closure. However, many issues are still to be tackled in order to reach high order numerical schemes that preserve the whole vector of moments. In fact, such models are meant to capture a given level of complexity in the phase space which is fixed in advance by the number of moments and quadrature nodes. In some rare or particular situations, when one controls perfectly such dynamics, it can be guaranteed that the solutions will remain smooth. However, in most cases the numerical schemes have to tackle the possibility of singular solutions when the dynamics complexity goes beyond the one allowed by the model. In such cases the solution of the resulting system of PDEs is the viscosity solution and does not reproduce the exact dynamics in phase space and measure solutions are expected, for which we need a precise framework. More specifically, even if for the pressureless gas system, the work of [21] has set the correct mathematical background in order to define general entropic solutions, such a work has not yet been performed for higher order moment methods in the several cited publications. This is the purpose of the present section, organized as follows. First we characterize the mathematical structure of the system with the quadrature-based closure provided. We then define entropy conditions and provide, for smooth solutions, the one-to-one kinetic-macroscopic relation. We then tackle the Riemann problem and define entropy measure solutions. Two examples of smooth and singular solution are then provided in Section 9.6, for which we rigorously identify the entropic character of the solution and which are then reproduced numerically.

### 9.2.1 Quadrature-based velocity moment models for kinetic equations

Consider the solution  $f = f(t, x, u)$  of the free transport kinetic equation

$$\partial_t f + u \partial_x f = 0, \quad t > 0, x \in \mathbb{R}, u \in \mathbb{R} \quad (9.10)$$

with initial condition

$$f(0, x, u) = f_0(x, u).$$

The exact solution is given by

$$f(t, x, u) = f(0, x - ut, u) = f_0(x - ut, u).$$

Defining the  $i$ -order moment

$$M_i = \int_v f(t, x, u) u^i du, \quad i = 1, \dots, N, \quad N \in \mathbb{N},$$

the associated governing equations are easily obtained from (9.10) after multiplication by  $v^i$  and integration over  $v$ , and write

$$\partial_t M_i + \partial_x M_{i+1} = 0, \quad i \geq 0.$$

For the sake of simplicity, but without any restriction, we will focus our attention hereafter on the four-moment model

$$\begin{cases} \partial_t M_0 + \partial_x M_1 = 0, \\ \partial_t M_1 + \partial_x M_2 = 0, \\ \partial_t M_2 + \partial_x M_3 = 0, \\ \partial_t M_3 + \partial_x \overline{M}_4 = 0. \end{cases} \quad (9.11)$$

It will be convenient to write (9.11) under the following abstract form

$$\partial_t \mathbf{M} + \partial_x \mathbf{F}(\mathbf{M}) = 0, \quad (9.12)$$

with  $\mathbf{M} = (M_0, M_1, M_2, M_3)^t$  and  $\mathbf{F}(\mathbf{M}) = (M_1, M_2, M_3, \overline{M}_4)^t$ .

#### 9.2.1.1 Quadrature inside the moment space

This model is closed provided that  $\overline{M}_4$  is defined as a function of  $\mathbf{M}$ . In quadrature-based moment methods, the starting point to define this closure relation consists in representing the velocity distribution of  $f(t, x, u)$  by a set of two Dirac delta functions, that is a two-node quadrature :

$$f(t, x, u) = n_1(t, x) \delta(u - U_1(x, t)) + n_2(t, x) \delta(u - U_2(x, t)), \quad (9.13)$$

where the weights  $n_1(t, x) > 0$ ,  $n_2(t, x) > 0$  and the velocity abscissas  $U_1(t, x)$ ,  $U_2(t, x)$  are expected to be uniquely determined from the knowledge of  $\mathbf{M}(x, t)$ . Dropping the  $(x, t)$ -dependance to avoid cumbersome notations, such a function  $f$  has exact moments of order  $i = 0, \dots, 4$  given by  $n_1 U_1^i + n_2 U_2^i$ . The next step then naturally consists in setting

$$\overline{M}_4 = n_1 U_1^4 + n_2 U_2^4 \quad (9.14)$$

where  $n_1$ ,  $n_2$  and  $U_1$ ,  $U_2$  are defined from  $\mathbf{M}$  by the following nonlinear system :

$$\begin{cases} M_0 = n_1 + n_2, \\ M_1 = n_1 U_1 + n_2 U_2, \\ M_2 = n_1 U_1^2 + n_2 U_2^2, \\ M_3 = n_1 U_1^3 + n_2 U_2^3. \end{cases} \quad (9.15)$$

At last, it remains to prove that this system is well-posed, which is the matter of the next proposition. We refer to [124, 99, 56] for the proof.

**Proposition 3** *System (9.12)-(9.14)-(9.15) is well-defined on the convex phase space  $\Omega$ , also called the moment space, given by*

$$\Omega = \{\mathbf{M} = (M_0, M_1, M_2, M_3)^t, M_0 > 0, M_0M_2 - M_1^2 > 0\}.$$

Moreover, setting  $\mathbf{U} = (n_1, n_2, n_1U_1, n_2U_2)^t$ , the function  $\mathbf{U} = \mathbf{U}(\mathbf{M})$  is one-to-one and onto as soon as we set for instance  $U_1 > U_2$ . Moreover we have  $0 < n_1 < M_0$  and  $0 < n_2 < M_0$ .

Proposition 3 can be extended to the more general case of a  $2k$ -moment models,  $k > 1$ . The velocity distribution is represented in this situation by a set of  $k$  Dirac delta functions, leading to  $M_i = \sum_{j=1}^k n_j U_j^i$ ,  $i = 0, \dots, 2k - 1$ , and  $\overline{M_{2k}} = \sum_{j=1}^k n_j U_j^{2k}$ .

### 9.2.1.2 Hyperbolic structure inside the moment space

The two-moment model, corresponding to  $k = 1$ , that is the one-node quadrature, writes

$$\begin{cases} \partial_t n + \partial_x n U = 0, \\ \partial_t n U + \partial_x n U^2 = 0, \end{cases}$$

which is nothing but the well-known pressureless gas dynamics system. Recall that this model is only weakly hyperbolic (the jacobian matrix is not diagonalizable) with  $v$  as unique eigenvalue, the characteristic field being linearly degenerate. Since there can be areas in the solution where a single quadrature node is sufficient at the frontier of the moment space in order to describe the dynamics, the solution in such zones will satisfy the previous degenerated system of two conservation laws. However for the time being, we will work inside the moment space and leave the behavior at the frontier for the next subsection.

Actually, we will observe in the course of the next section that the four-moment model (9.12) is equivalent for smooth solutions (only) to two decoupled pressureless gas dynamics systems associated with  $(n_1, n_1U_1)$  and  $(n_2, n_2U_2)$  respectively. Then (9.12) is expected to admit two eigenvalues  $U_1$  and  $U_2$  and to be weakly hyperbolic with linearly degenerate characteristic fields, as stated in the following proposition.

**Proposition 4** ([124, 99]) *System (9.12)-(9.14)-(9.15) is weakly hyperbolic on  $\Omega$  and admits the two eigenvalues  $U_1$  and  $U_2$ ,  $U_1 \neq U_2$ . The associated characteristic fields are linearly degenerate.*

**Proof 2** *For the sake of completeness, we propose here a direct proof of the eigenvalues  $U_1$  and  $U_2$  of (9.12)-(9.14)-(9.15). By (9.15), we first easily get*

$$\begin{cases} M_0 = n_1 + n_2, \\ M_1 - U_1 M_0 = n_2(U_2 - U_1), \\ M_2 - U_1 M_1 = n_2 U_2(U_2 - U_1), \\ M_3 - U_1 M_2 = n_2 U_2^2(U_2 - U_1), \end{cases}$$

and then, setting  $\sigma_0 = U_1 U_2$  and  $\sigma_1 = -(U_1 + U_2)$ ,

$$\begin{pmatrix} M_0 & M_1 \\ M_1 & M_2 \end{pmatrix} \begin{pmatrix} \sigma_0 \\ \sigma_1 \end{pmatrix} = - \begin{pmatrix} M_2 \\ M_3 \end{pmatrix}.$$

This system is invertible in the phase space  $\Omega$  ( $M_0 M_2 - M_1^2 \neq 0$ ) and uniquely defines  $\sigma_0$  and  $\sigma_1$  with respect to  $\mathbf{M}$  :

$$\begin{pmatrix} \sigma_0 \\ \sigma_1 \end{pmatrix} = \frac{1}{M_0 M_2 - M_1^2} \begin{pmatrix} M_1 M_3 - M_2^2 \\ M_1 M_2 - M_0 M_3 \end{pmatrix}. \quad (9.16)$$

Then, we have

$$\begin{aligned}
\overline{M}_4 &= n_1 U_1^4 + n_2 U_2^4 \\
&= n_1 U_1^3 U_1 + n_2 U_2^3 U_2 \\
&= (n_1 U_1^3 + n_2 U_2^3)(U_1 + U_2) - (n_1 U_1^2 + n_2 U_2^2)U_1 U_2 \\
&= -M_2 \sigma_0 - M_3 \sigma_1,
\end{aligned} \tag{9.17}$$

which finally gives  $\overline{M}_4$  with respect to  $\mathbf{M}$ .

The Jacobian matrix  $\mathbf{J} = \nabla_{\mathbf{M}} \mathbf{F}$  is given by

$$\mathbf{J} = \begin{pmatrix} 0 & 1 & 0 & 0 \\ 0 & 0 & 1 & 0 \\ 0 & 0 & 0 & 1 \\ a & b & c & d \end{pmatrix} \quad \text{with} \quad \begin{cases} a = \partial_{M_0} \overline{M}_4, \\ b = \partial_{M_1} \overline{M}_4, \\ c = \partial_{M_2} \overline{M}_4, \\ d = \partial_{M_3} \overline{M}_4. \end{cases}$$

Using (9.16) and (9.17), the calculations of the last row coefficients eventually lead to

$$\mathbf{J} = \begin{pmatrix} 0 & 1 & 0 & 0 \\ 0 & 0 & 1 & 0 \\ 0 & 0 & 0 & 1 \\ -\sigma_0^2 & -2\sigma_0 \sigma_1 & -2\sigma_0 - \sigma_1^2 & -2\sigma_1 \end{pmatrix}.$$

Finally, the characteristic polynomial  $p(\lambda)$  of  $\mathbf{J}$  is easily shown to equal

$$p(\lambda) = (\lambda - U_1)^2 (\lambda - U_2)^2.$$

This concludes the proof.

Propositions 3 and 4 show that System (9.12)-(9.14)-(9.15) is well-defined and weakly hyperbolic only on  $\Omega$ , which gives in particular  $U_1 \neq U_2$  in the interior of the moment space. At a first sight, this might appear to be restrictive in the sense that one of the main objectives of the model is to allow particle trajectory crossing, that is in particular to deal with initial data consisting of two colliding particle packets such that  $U_1 = U_2$  at each point initially (see for instance Section 7). Thus, in the last part of the present section, we characterize the behavior at the frontier  $\Gamma$  of the moment space when  $M_0 > 0$  :  $\Gamma = \{\mathbf{M} = (M_0, M_1, M_2, M_3)^t, M_0 > 0, M_0 M_2 - M_1^2 = 0\}$ .

### 9.2.1.3 Behavior at the frontier of the moment space

As mentioned previously, it is rather natural to envision the coexistence, in a single smooth moment solution, of zones where the number of quadrature nodes are different. More specifically, we will examine the coexistence of zones where only one quadrature node is needed ( $U_1 = U_2$ ), that is where  $\mathbf{M} = (M_0, M_1, M_2, M_3)^t$  with  $M_0 > 0$  and  $M_0 M_2 - M_1^2 = 0$ , and zones where  $M_0 M_2 - M_1^2 > 0$  which are inside the moment space  $\Omega$ , whereas the vector of moments are smooth everywhere.

After easy calculations in terms of  $n_1, n_2, U_1$  and  $U_2$ , the latter equality  $M_0 M_2 - M_1^2 = 0$  writes

$$n_1 n_2 (U_1 - U_2)^2 = 0,$$

so that if the vector  $(n_1, n_2, n_1 U_1, n_2 U_2)^t$  exists, this actually corresponds to the case  $u := U_1 = U_2$  (still under the assumption  $n_1 \neq 0$  and  $n_2 \neq 0$ ) or to the case where one of the weights is zero. We also note that in both cases  $M_k = M_0 u^k$ , whatever  $k$  in this case, so that the whole set of moments should be provided once  $M_0$  and  $M_1$  are given, in close connection to the case of pressureless gas dynamics. There are in fact two possibilities :

- either  $\mathbf{M} = (M_0, M_1, M_2, M_3)^t$  is such that  $M_0 M_3 - M_1 M_2 \neq 0$  : in this case (9.15) cannot be solved and the vector  $(n_1, n_2, n_1 U_1, n_2 U_2)^t$  does not exist,
- or  $\mathbf{M} = (M_0, M_1, M_2, M_3)^t$  is also such that  $M_0 M_3 - M_1 M_2 = 0$  : in this case (9.15) can be solved and we have  $u = U_1 = U_2 = M_1/M_0$ , together with  $n_1$  and  $n_2$  defined by the one-parameter equation  $n_1 + n_2 = M_0$ . As we will see just below, the choice  $n_1 = n_2 = M_0/2$  is the most natural one when we have to deal with an isolated point at the frontier of the moment space.

In order to justify the choice  $n_1 = n_2 = M_0/2$ , we first observe that both conditions

$$\begin{cases} M_0M_2 - M_1^2 = 0, \\ M_0M_3 - M_1M_2 = 0, \end{cases}$$

are equivalent to conditions

$$\begin{cases} e = 0, \\ q = 0, \end{cases}$$

where we have set

$$\begin{cases} e = M_0M_2 - M_1^2, \\ q = (M_3M_0^2 - M_1^3) - 3M_1(M_0M_2 - M_1^2), \end{cases}$$

and we consider  $n_1, n_2, U_1$  and  $U_2$  as functions of  $(M_0, M_1, q, e)$  with  $M_0 > 0$ , and  $e > 0^1$ . We then propose to study the asymptotic behavior of these functions when  $e \rightarrow 0^+$ , considering that  $M_0 > 0, M_1$  and  $q$  are fixed. Note that

$$\Gamma = \{(M_0, M_1, e, q)^t, M_0 > 0, e = 0\}.$$

We get the following result.

**Lemma 6** *Let be given  $M_0 > 0, M_1$  and  $q$ . Then we have*

$$\begin{aligned} \lim_{e \rightarrow 0^+} n_2 &= \begin{cases} M_0 & \text{if } q > 0, \\ 0 & \text{if } q < 0, \\ \frac{M_0}{2} & \text{if } q = 0, \end{cases} & \lim_{e \rightarrow 0^+} n_1 &= \begin{cases} 0 & \text{if } q > 0, \\ M_0 & \text{if } q < 0, \\ \frac{M_0}{2} & \text{if } q = 0, \end{cases} \\ \lim_{e \rightarrow 0^+} U_2 &= \begin{cases} \frac{M_1}{M_0} & \text{if } q > 0, \\ -\infty & \text{if } q < 0, \\ \frac{M_1}{M_0} & \text{if } q = 0, \end{cases} & \lim_{e \rightarrow 0^+} U_1 &= \begin{cases} +\infty & \text{if } q > 0, \\ \frac{M_1}{M_0} & \text{if } q < 0, \\ \frac{M_1}{M_0} & \text{if } q = 0, \end{cases} \\ \lim_{e \rightarrow 0^+} n_2U_2 &= \begin{cases} M_1 & \text{if } q > 0, \\ 0 & \text{if } q < 0, \\ \frac{M_1}{2} & \text{if } q = 0, \end{cases} & \lim_{e \rightarrow 0^+} n_1U_1 &= \begin{cases} 0 & \text{if } q > 0, \\ M_1 & \text{if } q < 0, \\ \frac{M_1}{2} & \text{if } q = 0. \end{cases} \end{aligned}$$

**Proof 3** *The admissible change of variables  $(M_0, M_1, M_2, M_3) \rightarrow (M_0, M_1, e, q)$  allows to write after easy calculations*

$$U_1 = \frac{M_1}{M_0} + \frac{q + \sqrt{q^2 + 4e^3}}{2M_0e}, \quad n_2 = \frac{M_0 e(U_1 M_0 - M_1)}{\sqrt{q^2 + 4e^3}},$$

and if  $q \neq 0$

$$U_1 = \frac{M_1}{M_0} + \frac{q}{M_0e} \frac{(1 + \text{sign}(q)\sqrt{1 + 4e^3/q^2})}{2}, \quad n_2 = \frac{M_0 e}{q} \left( \frac{U_1 M_0 - M_1}{\text{sign}(q)\sqrt{1 + 4e^3/q^2}} \right),$$

where we have set

$$\text{sign}(q) = \begin{cases} 1 & \text{if } q > 0, \\ -1 & \text{if } q < 0. \end{cases}$$

*It is then an easy matter to get the expected results distinguishing between the three cases  $q < 0, q > 0$  and  $q = 0$ . It is then clear by a continuity argument that the proposed choice  $n_1 = n_2 = M_0/2$  when  $e = q = 0$  is actually natural.*

<sup>1</sup>The definitions of  $e$  and  $q$  naturally comes out after noticing that setting  $\bar{n}_1 = \frac{n_1}{M_0}, \bar{n}_2 = \frac{n_2}{M_0}, \bar{U}_1 = U_1 - \frac{M_1}{M_0}, \bar{U}_2 = U_2 - \frac{M_1}{M_0}$ , solving (9.15) is equivalent to solving

$$\begin{cases} 1 = \bar{n}_1 + \bar{n}_2, \\ 0 = \bar{n}_1 \bar{U}_1 + \bar{n}_2 \bar{U}_2, \\ e = \bar{n}_1 \bar{U}_1^2 + \bar{n}_2 \bar{U}_2^2, \\ q = \bar{n}_1 \bar{U}_1^3 + \bar{n}_2 \bar{U}_2^3, \end{cases}$$

with  $e = (M_0M_2 - M_1^2)/M_0^2$  and  $q = ((M_3M_0^2 - M_1^3) - 3M_1(M_0M_2 - M_1^2))/M_0^3$ .

An important consequence of this lemma is that in the half plane  $e > 0$ , the region close to the frontier  $\Gamma$  for a non-zero  $q$  corresponds to abscissas going to infinity with arbitrary small weights. Moreover, when the velocity distribution at the kinetic level have compact support in the initial distribution, such a property will be preserved throughout the dynamics of the system and we want to be able to switch continuously from two-node to one-node quadrature without pathological behavior on the abscissas and weights.

Let us provide a first example where such a behavior is present. We consider a path in the moment space parametrized by the variable  $x$ , such that  $n_1 = x^3$ ,  $n_2 = 1$ ,  $U_1 = 1/x$  and  $U_2 = 0$ . As  $x$  approaches zero, the smooth moment vector  $\mathbf{M} = (1 + x^3, x^2, x, 1)^t$  has a very regular limit at the frontier of the moment space along the lines presented before with an unbounded abscissa. Indeed we have here  $e = x$  and  $q = 1 - x^3$  approaches the fixed non-zero value of 1. Note that if we replace the first weight by  $n_1 = x^4$ , we still have an unbounded abscissa even if we converge toward the point  $(0, 0)$  in the  $(e, q)$  plane ( $e = x^2, q = x(1 - x^4)$ ).

We thus have to find a framework in a subset of the plane  $(e, q)$  such that the limits are better behaved. A natural choice presented above is the line  $q = 0$  but it is too restrictive. In order to naturally introduce the relevant subset of  $\Omega$ , let us consider the other example with  $n_1 = \alpha x^\beta$ ,  $n_2 = 1$ ,  $U_1 = \gamma x^\delta$  and  $U_2 = 0$ , with  $\alpha > 0$ ,  $\gamma > 0$ ,  $\beta \geq 0$  and  $\delta \geq 0$ . As  $x$  approaches zero, the moment vector  $\mathbf{M} = (1 + \alpha x^\beta, \alpha \gamma x^{\beta+\delta}, \alpha \gamma^2 x^{\beta+2\delta}, \alpha \gamma^3 x^{\beta+3\delta})^t$  reaches the frontier  $\Gamma$  of the moment space<sup>2</sup>. Two cases are interesting; firstly when  $\beta = 0$ , we reach the point  $(0, 0)$  in the  $(e, q)$  plane asymptotically along the line  $q/e^{3/2} = (1 - \alpha)/\alpha^{1/2}$  and no weight is approaching zero, whereas the two abscissas are joining (see formulas in the proof above). Secondly, when  $\delta = 0$ , one of the weights is reaching zero, whereas the two abscissas remain different at a distance of  $\gamma$  at the limit and we reach the point  $(0, 0)$  in the  $(e, q)$  plane asymptotically along the line  $q/(M_0 e) = \gamma$  at the limit  $x \rightarrow 0$  (see again formulas in the proof above). We will prove in the following proposition that the proper framework is a symmetric cone in the  $(e, q)$  plane centered at the point  $(0, 0)$  corresponding the  $|q/(M_0 e)| \leq \eta$ , where  $\eta$  is a measure of the maximal distance allowed between the two abscissas.

**Proposition 5** *We define a regular path in the moment space  $\mathbf{M}_x$  which admits a limit as  $x$  goes to zero and is at least  $C^1$  up to the limit  $\mathbf{M}_0$ . Its limit further satisfies  $e_0 = 0$  and we assume  $M_{0x} > \nu > 0$ ,  $|q_x/(M_{0x} e_x)| \leq \eta$ , where  $\eta > 0$ . We then have the following properties :*

- $\lim_{x \rightarrow 0} q_x = q_0 = 0$ .
- *the weights and abscissas admit limits  $n_{i0} = \lim_{x \rightarrow 0} n_{ix}$ ,  $U_{i0} = \lim_{x \rightarrow 0} U_{ix}$ . If we assume that  $n_{i0} > 0$  for both  $i$ , then  $U_{10} = U_{20}$ , or, if one weight approaches zero, such as  $n_{10} = 0$  then we have  $|U_{10} - U_{20}| \leq \eta$  and  $\eta$  is then a bound on the distance between the two abscissas.*
- $\mathbf{M}_0 = (M_{00}, M_{10}, M_{10}^2/M_{00}, M_{10}^3/M_{00}^2)^t$ .

**Proof 4** *It is first clear that  $\lim_{x \rightarrow 0} q_x = q_0 = 0$  since  $|q_x| \leq \eta M_{0x} e_x$  and  $e_0 = 0$ . Then, easy calculations give*

$$U_1 - U_2 = \sqrt{\frac{q^2}{M_0^2 e^2} + \frac{4e}{M_0^2}}$$

*so that denoting  $l = \lim_{x \rightarrow 0} |q_x|/(M_{0x} e_x) \geq 0$ , we clearly have  $U_{1x} - U_{2x} \rightarrow l$  when  $x \rightarrow 0$  and  $\eta$  represents an upper bound for  $U_{10} - U_{20}$ . Let us now distinguish between both cases  $l > 0$  and  $l = 0$ . We first note the following expression for  $q/(M_0 e)$  :*

$$\frac{q}{M_0 e} = (\omega_1 - \omega_2)(U_2 - U_1), \quad \omega_i = \rho_i/M_0, \quad \omega_1 + \omega_2 = 1.$$

*If  $l > 0$ , one can write*

$$|n_{1x} - n_{2x}| = \left| \frac{q_x}{M_{0x} e_x} \right| \times \frac{1}{|U_{1x} - U_{2x}|} \times M_{0x},$$

<sup>2</sup>The corresponding values of  $e$  and  $q$  are  $e = \alpha \gamma^2 x^{\beta+2\delta}$  and  $q = \alpha \gamma^3 x^{\beta+3\delta}(1 - \alpha x^\beta)$ .

and this quantity clearly tends to  $M_{00}$  as  $x$  goes to zero. Which means that one weight approaches zero,  $n_{10} = 0$  or  $n_{20} = 0$ , and the other one  $M_{00}$  (recall that  $n_{1x} + n_{2x} = M_{0x}$ ). If  $l = 0$ , it is clear by the following formula for  $U_1$  (see the proof above)

$$U_1 = \frac{M_1}{M_0} + \frac{q + \sqrt{q^2 + 4e^3}}{2M_0e}$$

that  $U_{10} = U_{20} = M_{10}/M_{00}$ . Using now the definition of  $n_1$  and  $n_2$  (see again the proof above), one easily get

$$\omega_2 = \frac{n_2}{M_0} = \frac{\sqrt{1 + 4e^3/q^2} + \text{sign}(q)}{2\sqrt{1 + 4e^3/q^2}}, \quad \omega_1 = \frac{n_1}{M_0} = \frac{\sqrt{1 + 4e^3/q^2} - \text{sign}(q)}{2\sqrt{1 + 4e^3/q^2}},$$

so that both weights have limits piloted by the limit of  $q/e^{3/2}$ .

The last claim  $\mathbf{M}_0 = (M_{00}, M_{10}, M_{10}^2/M_{00}, M_{10}^3/M_{00}^2)^t$  is clear, which completes the proof.

A very important consequence of the previous proposition is the fact that along smooth paths inside the proposed cone which reach the point  $(0, 0)$  in the  $(e, q)$  plane, the flux introduced in equation 9.12 is regular up to the frontier of the moment space, even if the mapping of  $\mathbf{M}$  onto  $\mathbf{U}$  is not<sup>3</sup>

**Proposition 6** For any regular path in the moment space satisfying the assumptions of the previous proposition, that is living in the proper cone in the  $(e, q)$  plane and reaching smoothly the point  $(0, 0)$ , the flux  $\mathbf{F}(\mathbf{M})$  is continuous up to the frontier of the moment space and  $\mathcal{C}^1$  at  $(0, 0)$  in any direction inside the proposed cone.

**Proof 5** The proof is rather straightforward when one has noticed the two equations, the first of which is the expression (9.17) of  $\overline{M_4} = -\sigma_0 M_2 - \sigma_1 M_3$  as a function of  $M_2, M_3, \sigma_0$  and  $\sigma_1$ , and the second is the expression of  $\sigma_0$  and  $\sigma_1$  :

$$\begin{pmatrix} \sigma_0 \\ \sigma_1 \end{pmatrix} = \begin{pmatrix} \frac{q}{M_0 e} \frac{M_1}{M_0} + \left(\frac{M_1}{M_0}\right)^2 - \frac{e}{M_0^2} \\ -\frac{q}{M_0 e} - 2\frac{M_1}{M_0} \end{pmatrix}.$$

Finally, following the same lines for the evaluation of the Jacobian matrix of the flux (see matrix  $\mathbf{J}$  in section 2.2), it becomes clear that the flux is continuous and continuously differentiable in any direction inside the proposed cone. Besides, it can be easily seen that the expression of the flux as a function of  $(M_0, M_1, e, q)^t$  becomes

$$\begin{aligned} \frac{\overline{M_4}}{M_0} &= -\left(\frac{q}{M_0 e} \frac{M_1}{M_0} + \left(\frac{M_1}{M_0}\right)^2 - \frac{e}{M_0^2}\right) \left(\frac{e}{M_0^2} + \left(\frac{M_1}{M_0}\right)^2\right) + \\ &\quad \left(\frac{q}{M_0 e} + 2\frac{M_1}{M_0}\right) \left(\frac{q}{M_0^3} + \left(\frac{M_1}{M_0}\right)^3 + 3\frac{M_1}{M_0} \frac{e}{M_0^2}\right). \end{aligned}$$

$\overline{M_4}/M_0$  tends to  $(M_{10}/M_{00})^4$  when  $e$  goes to  $0^+$  which concludes the proof.

**Remark 1** Let us emphasize that in the various configurations we have proposed when the convergence toward the frontier of the moment space does not lie inside the cone  $|q_x/(M_{0x} e_x)| \leq \eta$  in the  $(e, q)$  plane, the flux can dramatically loose regularity. It can either have a limit without being differentiable or even not have a limit at all. The impact of the previous proposition thus becomes clear and sets the proper framework for solutions which will reach the frontier of the moment space.

<sup>3</sup>The mapping of  $\mathbf{M}$  onto  $\mathbf{U}$  will never be smooth at point  $(0, 0)$  in the  $(e, q)$  plane since the limit of  $\mathbf{U}$  will depend on the limit of  $q/(M_0 e)$ , whereas the limit value of  $\mathbf{M}$  in the proposed cone is always fixed.



**Remark 2** In the case  $M_0 > 0$ , at the frontier of the moment space within the previous proposed framework, we have  $e = 0$ ,  $q = 0$ ; the model is made of the two unknowns  $M_0$  and  $M_1$  and then degenerates to the usual pressureless gas dynamics which is weakly hyperbolic with a single eigenvalue  $u = M_1/M_0$ . It should be noticed that for smooth solutions, the last two equations of system 9.11 on  $M_2 = M_1^2/M_0$  and  $M_3 = M_1^3/M_0^2$  are still satisfied with  $\bar{M}_4 = M_1^4/M_0^3$  coherent with the previous limit obtained for the flux. As a consequence, we can notice, that at least for smooth solutions, the system of partial differential equations (9.11) can describe the dynamics inside and at the frontier of the moment space.

### 9.2.2 Entropy conditions

In this section, we will work in the interior of the moment space and we exhibit natural entropy inequalities for the following small viscosity system associated with (9.11) :

$$\begin{cases} \partial_t M_0 + \partial_x M_1 = \varepsilon \partial_{xx} M_0, \\ \partial_t M_1 + \partial_x M_2 = \varepsilon \partial_{xx} M_1, \\ \partial_t M_2 + \partial_x M_3 = \varepsilon \partial_{xx} M_2, \\ \partial_t M_3 + \partial_x M_4 = \varepsilon \partial_{xx} M_3, \end{cases} \quad (9.18)$$

which gives in condensed form

$$\partial_t \mathbf{M} + \partial_x \mathbf{F}(\mathbf{M}) = \varepsilon \partial_{xx} \mathbf{M}. \quad (9.19)$$

Throughout this section, we will consider smooth solutions only. We thus have

$$\partial_t \mathbf{M} + \mathbf{J} \partial_x \mathbf{M} = \varepsilon \partial_{xx} \mathbf{M} \quad \text{with} \quad \mathbf{J} = \nabla_{\mathbf{M}} \mathbf{F}.$$

Setting  $\mathbf{A} = \nabla_{\mathbf{U}} \mathbf{M}$ , we then get

$$\partial_t \mathbf{U} + \mathbf{A}^{-1} \mathbf{J} \mathbf{A} \partial_x \mathbf{U} = \varepsilon \mathbf{A}^{-1} \partial_x (\mathbf{A} \partial_x \mathbf{U}). \quad (9.20)$$

Our objective is to prove that

$$\partial_t \eta + \partial_x q \leq \varepsilon \partial_{xx} \eta, \quad (9.21)$$

for a natural choice of couple  $(\eta, q)$  given by

$$\begin{cases} \eta = n_1 S(U_1) + n_2 S(U_2), \\ q = n_1 U_1 S(U_1) + n_2 U_2 S(U_2). \end{cases} \quad (9.22)$$

Here  $S$  denotes a convex function from  $\mathbb{R}$  to  $\mathbb{R}$ , and we will especially consider the case where  $S(u) = u^{2\alpha}$ ,  $\alpha \geq 0$ . Of course, the densities  $n_1, n_2$  and velocities  $U_1, U_2$  involved in (9.22) are naturally defined by means of the one-to-one and onto function  $\mathbf{U} = \mathbf{U}(\mathbf{M})$ . In the following and with a little abuse in the notations, we will consider without distinction  $\eta$  and  $q$  as functions of  $\mathbf{M}$  or  $\mathbf{U}$ .

We first observe

$$\begin{aligned} \partial_t \eta + \partial_x q &= \partial_t \eta(\mathbf{U}) + \partial_x q(\mathbf{U}) \\ &= \nabla_{\mathbf{U}} \eta \partial_t \mathbf{U} + \nabla_{\mathbf{U}} q \partial_x \mathbf{U} \\ &= \nabla_{\mathbf{U}} \eta \{ -\mathbf{A}^{-1} \mathbf{J} \mathbf{A} \partial_x \mathbf{U} + \varepsilon \mathbf{A}^{-1} \partial_x (\mathbf{A} \partial_x \mathbf{U}) \} + \nabla_{\mathbf{U}} q \partial_x \mathbf{U}. \end{aligned}$$

The following two lemmas, the proofs of which are left to the reader, will be useful in order to estimate the entropy dissipation rate  $\mathbf{D}$  defined by

$$\mathbf{D} = \nabla_{\mathbf{U}} \eta \{ -\mathbf{A}^{-1} \mathbf{J} \mathbf{A} \partial_x \mathbf{U} + \varepsilon \mathbf{A}^{-1} \partial_x (\mathbf{A} \partial_x \mathbf{U}) \} + \nabla_{\mathbf{U}} q \partial_x \mathbf{U}.$$

**Lemma 7** The matrices  $\mathbf{J}$  and  $\mathbf{A}$  are given by

$$\mathbf{J} = \begin{pmatrix} 0 & 1 & 0 & 0 \\ 0 & 0 & 1 & 0 \\ 0 & 0 & 0 & 1 \\ -U_1^2 U_2^2 & 2U_1 U_2 (U_1 + U_2) & -2U_1 U_2 - (U_1 + U_2)^2 & 2(U_1 + U_2) \end{pmatrix},$$

$$\mathbf{A} = \begin{pmatrix} 1 & 1 & 0 & 0 \\ 0 & 0 & 1 & 1 \\ -U_1^2 & -U_2^2 & 2U_1 & 2U_2 \\ -2U_1^3 & -2U_2^3 & 3U_1^2 & 3U_2^2 \end{pmatrix}$$

and we have

$$\mathbf{A}^{-1}\mathbf{J}\mathbf{A} = \begin{pmatrix} 0 & 0 & 1 & 0 \\ 0 & 0 & 0 & 1 \\ -U_1^2 & 0 & 2U_1 & 0 \\ 0 & -U_2^2 & 0 & 2U_2 \end{pmatrix}.$$

**Lemma 8** *The gradients  $\nabla_{\mathbf{U}}\eta$  and  $\nabla_{\mathbf{U}}q$  are given by*

$$\nabla_{\mathbf{U}}\eta = \begin{pmatrix} S(U_1) - U_1 S'(U_1) \\ S(U_2) - U_2 S'(U_2) \\ S'(U_1) \\ S'(U_2) \end{pmatrix}^t, \quad \nabla_{\mathbf{U}}q = \begin{pmatrix} -U_1^2 S'(U_1) \\ -U_2^2 S'(U_2) \\ S(U_1) + U_1 S'(U_1) \\ S(U_2) + U_2 S'(U_2) \end{pmatrix}^t,$$

and we have

$$\nabla_{\mathbf{U}}q = \nabla_{\mathbf{U}}\eta \mathbf{A}^{-1}\mathbf{J}\mathbf{A}.$$

Before going on, let us make the following two remarks. We first note that thanks to the first lemma, (9.20) with  $\varepsilon = 0$  inside the moment space gives :

$$\begin{cases} \partial_t n_1 + \partial_x n_1 U_1 = 0, \\ \partial_t n_2 + \partial_x n_2 U_2 = 0, \\ \partial_t n_1 U_1 - U_1^2 \partial_x n_1 + 2U_1 \partial_x n_1 U_1 = 0, \\ \partial_t n_2 U_2 - U_2^2 \partial_x n_2 + 2U_2 \partial_x n_2 U_2 = 0, \end{cases}$$

which is equivalent to

$$\begin{cases} \partial_t n_1 + \partial_x n_1 U_1 = 0, \\ \partial_t n_1 U_1 + \partial_x n_1 U_1^2 = 0, \\ \partial_t n_2 + \partial_x n_2 U_2 = 0, \\ \partial_t n_2 U_2 + \partial_x n_2 U_2^2 = 0. \end{cases} \quad (9.23)$$

Besides, at the frontier of the moment space, we obtain the pressureless gas dynamics on a single quadrature node. We then observe that for smooth solutions, thanks to the remark at the end of the previous section, the system (9.12) is nothing but either two decoupled or one single pressureless gas dynamics system of equations. We then observe that still with  $\varepsilon = 0$ ,  $\mathbf{D} = 0$ , by lemma 8, in both cases :

$$\partial_t \eta + \partial_x q = 0, \quad (9.24)$$

that is for smooth solution both inside and at the frontier of the moment space.

Let us go back to the case  $\varepsilon > 0$ . We thus have the following equality,

$$\mathbf{D} = \varepsilon \nabla_{\mathbf{U}}\eta \mathbf{A}^{-1} \partial_x (\mathbf{A} \partial_x \mathbf{U}),$$

from which it is natural to isolate  $\varepsilon \partial_{xx} \eta$  :

$$\begin{aligned} \mathbf{D} &= \varepsilon \nabla_{\mathbf{U}}\eta \mathbf{A}^{-1} \partial_x (\mathbf{A} \partial_x \mathbf{U}) \\ &= \varepsilon \nabla_{\mathbf{U}}\eta \partial_{xx} \mathbf{U} + \varepsilon \nabla_{\mathbf{U}}\eta \mathbf{A}^{-1} \partial_x \mathbf{A} \partial_x \mathbf{U} \\ &= \varepsilon \partial_x (\nabla_{\mathbf{U}}\eta \partial_x \mathbf{U}) - \varepsilon \partial_x (\nabla_{\mathbf{U}}\eta) \partial_x \mathbf{U} + \varepsilon \nabla_{\mathbf{U}}\eta \mathbf{A}^{-1} \partial_x \mathbf{A} \partial_x \mathbf{U} \\ &= \varepsilon \partial_{xx} \eta + \varepsilon (\nabla_{\mathbf{U}}\eta \mathbf{A}^{-1} \partial_x \mathbf{A} \partial_x \mathbf{U} - \partial_x (\nabla_{\mathbf{U}}\eta) \partial_x \mathbf{U}). \end{aligned}$$

By lemma 8 giving  $\nabla_{\mathbf{U}}\eta$ , we easily get

$$\partial_x (\nabla_{\mathbf{U}}\eta) \partial_x \mathbf{U} = n_1 (\partial_x U_1)^2 S''(U_1) + n_2 (\partial_x U_2)^2 S''(U_2).$$

It is now a matter to calculate  $\nabla_{\mathbf{U}}\eta\mathbf{A}^{-1}\partial_x\mathbf{A}\partial_x\mathbf{U} = \mathbf{A}^{-t}(\nabla_{\mathbf{U}}\eta)^t\partial_x\mathbf{A}\partial_x\mathbf{U}$ . We first observe that

$$\partial_x\mathbf{A}\partial_x\mathbf{U} = \begin{pmatrix} 0 \\ 0 \\ 2n_1(\partial_x U_1)^2 + 2n_2(\partial_x U_2)^2 \\ 6n_1U_1(\partial_x U_1)^2 + 6n_2U_2(\partial_x U_2)^2 \end{pmatrix}$$

so that only the last two components of  $\mathbf{A}^{-t}(\nabla_{\mathbf{U}}\eta)^t$  are actually needed. Finally, easy calculations not reported here lead to

$$\mathbf{A}^{-t}(\nabla_{\mathbf{U}}\eta)^t\partial_x\mathbf{A}\partial_x\mathbf{U} = -\frac{1}{(U_1 - U_2)^4}(2n_1(\partial_x U_1)^2 X_1 + 2n_2(\partial_x U_2)^2 X_2),$$

where we have set

$$\begin{cases} X_1 = (U_1 - U_2)^2 \left( 3(S(U_1) - S(U_2)) - 2(U_1 - U_2)S'(U_1) - (U_1 - U_2)S'(U_2) \right), \\ X_2 = -(U_1 - U_2)^2 \left( 3(S(U_1) - S(U_2)) - (U_1 - U_2)S'(U_1) - 2(U_1 - U_2)S'(U_2) \right). \end{cases}$$

The entropy inequality (9.21) is then valid if and only if

$$\nabla_{\mathbf{U}}\eta\mathbf{A}^{-1}\partial_x\mathbf{A}\partial_x\mathbf{U} - \partial_x(\nabla_{\mathbf{U}}\eta)\partial_x\mathbf{U} \leq 0,$$

that is, setting  $S_i = S(v_i)$ ,  $S'_i = S'(v_i)$  and  $S''_i = S''(v_i)$ ,  $i = 1, 2$ ,

$$\begin{aligned} & (U_1 - U_2)^2 n_1 (\partial_x U_1)^2 \left( 6(S_1 - S_2) - 4(U_1 - U_2)S'_1 - 2(U_1 - U_2)S'_2 + (U_1 - U_2)^2 S''_1 \right) \\ & \quad + \\ & (U_1 - U_2)^2 n_2 (\partial_x U_2)^2 \left( -6(S_1 - S_2) + 2(U_1 - U_2)S'_1 + 4(U_1 - U_2)S'_2 + (U_1 - U_2)^2 S''_2 \right) \\ & \geq 0. \end{aligned}$$

A sufficient condition is given by

$$\begin{cases} 6(S_1 - S_2) - 4(U_1 - U_2)S'_1 - 2(U_1 - U_2)S'_2 + (U_1 - U_2)^2 S''_1 \geq 0, \\ -6(S_1 - S_2) + 2(U_1 - U_2)S'_1 + 4(U_1 - U_2)S'_2 + (U_1 - U_2)^2 S''_2 \geq 0. \end{cases} \quad (9.25)$$

Let us focus for instance on the first inequality (the second one is treated in a similar way), and let us consider the left-hand side as a function of  $U_2$ , for any given  $U_1$  :

$$\mathcal{F}_1(U_2) = 6(S_1 - S_2) - 4(U_1 - U_2)S'_1 - 2(U_1 - U_2)S'_2 + (U_1 - U_2)^2 S''_1.$$

Differentiation yields

$$\begin{aligned} \mathcal{F}'_1(U_2) &= 4(S'_1 - S'_2) - 2(U_1 - U_2)(S''_1 + S''_2), \\ \mathcal{F}''_1(U_2) &= 2(S''_1 - S''_2) - 2(U_1 - U_2)S'''_2, \\ \mathcal{F}'''_1(U_2) &= 2(U_2 - U_1)S''''_2. \end{aligned}$$

It is then clear that  $\mathcal{F}_1(U_1) = \mathcal{F}'_1(U_1) = \mathcal{F}''_1(U_1) = \mathcal{F}'''_1(U_1) = 0$ . Then, provided that  $S''''(u) \geq 0$ ,  $\forall v$ , we easily get by a chain argument based on the sign of the derivative and the monotonicity property that  $\mathcal{F}_1(U_2) \geq 0$ ,  $\forall U_1, U_2$ . We have thus proved the following proposition :

**Proposition 7** *Smooth solutions of (9.19) satisfy the entropy inequality (9.21) for any entropy flux pair  $(\eta, q)$  defined by (9.22) provided that  $u \rightarrow S(u)$  is a smooth function from  $\mathbb{R}$  to  $\mathbb{R}$  with nonnegative fourth-order derivative. In particular, the natural choice  $S(u) = u^{2\alpha}$  with  $\alpha \geq 2$  is suitable.*

**Remark 3** Any third-order polynomial may of course be added to the leading term of  $S$ , without changing the sign of the fourth-order derivative. However, if we focus on (strictly) convex functions  $v \rightarrow S(v)$  in order to get a (strictly) convex entropy  $\eta = \eta(\mathbf{U})$ , only first-order polynomials may be added without changing the convexity property.

**Remark 4** If we consider  $S(u) = 1, u, u^2, u^3$ , it is easily checked that (9.25) holds true with two equalities. In agreement with (9.18), these choices that lead to the pairs  $(\eta, q) = (M_i, M_{i+1})$ ,  $i = 0, \dots, 3$ , are admissible.

**Remark 5** In the case  $M_0 > 0$ ,  $e = 0$ ,  $q = 0$  with the additional conditions associated with the connection between the interior and the frontier of the moment space presented in subsection 9.2.1.3, we clearly have  $M_k = M_1^k / M_0^{k-1}$ . In this case, the entropy pairs clearly work also in such a case, for smooth solutions, and admits a smooth behavior at the frontier of the moment space in the cone we have defined previously.

### 9.2.3 Kinetic-macroscopic relation for smooth solutions

For smooth solutions, we established in the previous section that the four-moment model (9.11) is equivalent to the following two decoupled pressureless gas dynamics model

$$\begin{cases} \partial_t n_1 + \partial_x n_1 U_1 = 0, \\ \partial_t n_1 U_1 + \partial_x n_1 U_1^2 = 0, \\ \partial_t n_2 + \partial_x n_2 U_2 = 0, \\ \partial_t n_2 U_2 + \partial_x n_2 U_2^2 = 0, \end{cases} \quad (9.26)$$

where  $n_1, n_2, U_1$  and  $U_2$  are defined by the nonlinear system (9.15). The aim of this section is to prove a rigorous equivalence result, still for smooth solutions, between this macroscopic model and the free transport kinetic formulation (9.10) when the velocity distribution is given by a set of two Dirac delta functions. This result is nothing but a generalization of the one given in [21] for the usual pressureless gas dynamics model.

**Proposition 8** Let  $T > 0$  and  $n_i(t, x), U_i(t, x)$  in  $C^1(]0, T[ \times \mathbb{R})$  for  $i = 1, 2$ . Let us define

$$f(t, x, u) = \sum_{i=1}^2 n_i(t, x) \delta(u - U_i(t, x)).$$

Then,  $n_i$  and  $v_i$  solve (9.11), or equivalently (9.26), in  $]0, T[ \times \mathbb{R}$  if and only if

$$\partial_t f + u \partial_x f = 0, \quad \text{in } ]0, T[ \times \mathbb{R} \times \mathbb{R} \quad (9.27)$$

in the distributional sense, that is if and only if for all  $\phi \in C_c^\infty(]0, T[ \times \mathbb{R})$  and  $\chi \in C_c^\infty(\mathbb{R})$

$$\int_0^T \int_{\mathbb{R}} \sum_{i=1}^2 n_i(t, x) \left( \partial_t \phi(t, x) + U_i(t, x) \partial_x \phi(t, x) \right) \chi(U_i(t, x)) = 0. \quad (9.28)$$

**Proof 6** Let us first assume that (9.28) holds true. Since the velocity functions  $v_i$  are in particular locally bounded, one can successively choose  $\chi \in C_c^\infty(\mathbb{R})$  such that  $\chi(u) = u^k$ ,  $k = 0, \dots, 3$  for all  $u = U_i(t, x)$  and then get

$$\int_0^T \int_{\mathbb{R}} \sum_{i=1}^2 n_i(t, x) \left( \partial_t \phi(t, x) + U_i(t, x) \partial_x \phi(t, x) \right) (U_i(t, x))^k = 0$$

for all  $\phi \in C_c^\infty(]0, T[ \times \mathbb{R})$ . Invoking the closure relation (9.15), this clearly gives the four-moment model (9.11), or equivalently (9.26), since  $n_i(t, x)$  and  $U_i(t, x)$  are smooth functions.

Conversely, let us assume that the partial differential equations of (9.26) are satisfied. Using the mass conservation equations associated with  $n_i$ , it is then usual to show that for  $i = 1, 2$

$$n_i(\partial_t U_i + U_i \partial_x U_i) = 0,$$

and then multiplying by  $\chi'$  for any smooth function  $\chi$ ,

$$\partial_t n_i \chi(U_i) + \partial_x n_i \chi(U_i) U_i = 0.$$

Summing over  $i = 1, 2$  and integrating past a test function  $\phi \in \mathcal{C}_c^\infty(]0, T[ \times \mathbb{R})$  gives the expected result (9.28). This concludes the proof.

This Proposition allows, as a corollary, to introduce a particular type of solution which will be denoted piecewise *free boundary*  $\mathcal{C}^1$  solutions. Such solutions correspond to a discontinuous connection from the interior of the moment space to the frontier through a contact discontinuity for which the Rankine Hugoniot solutions are trivially satisfied as well as the entropy conservation equation (9.24).

**Corollary 1** *We consider the following distribution at the kinetic level  $f(t, x, u) = \sum_{i=1}^2 n_i(t, x) \delta(u - U_i(t, x))$ , where  $n_1(t, x) > 0$  and  $U_1(t, x)$  are taken as constants (or sufficiently smooth in some time interval), whereas  $n_2(t, x)$  is zero except in a compact connected subset  $K_0$  at time  $t = 0$  of  $\mathbb{R}$ , where  $n_2(0, x) > 0$  and  $U_2(0, x)$  are two constants (or sufficiently smooth in some time interval) such that  $U_2 \neq U_1$ . The resulting solution at the moment level exhibits two discontinuities at the frontier of the compact set  $K_t$  which is the translation of set  $K_0$  at velocity  $U_2$ ; however the system 9.26 as well as the entropy conservation equation (9.24) are satisfied in the weak sense, that is the equations are satisfied in the usual sense where the solution is smooth and Rankine-Hugoniot conditions are satisfied at discontinuity points.*

**Proof 7** *It is clear that the moment solution will satisfy the system of conservation equations everywhere except at the frontier of the  $K_t$  set. The Rankine-Hugoniot jump conditions are trivially satisfied at the discontinuities where the mass flux associated to the first abscissa is  $n_1(U_1 - U_2)$  in the referential of the discontinuity and leads to zero jump conditions for the part of the flux associated to the first abscissa by continuity, whereas the mass flux associated to the second abscissa is zero, as usual in contact discontinuities, which also allows to conclude. The same path allows to conclude on the fact that for any entropy-flux pair, the conservation equation is satisfied in the weak sense.*

Let us underline the fact that in the region where the second weight is zero outside the compact set  $K_t$ , we have used so far the convention that in such a region where a single quadrature node is to be found, we take the two weights as equal and the two abscissas as equal. The results proposed in the previous corollary are of course independent of such a choice since the point at the frontier of the moment space is isolated. Besides, such a corollary can be extended to as many quadrature nodes as needed as long as the number of nodes allows to describe the dynamics at the kinetic level at any point and time. Finally, the collision of two particle packets presented in subsection 9.2.5.1 satisfies the assumptions of Corollary 1 and will be an entropic solution.

### 9.2.4 Riemann problems and entropy measure solutions

In this section, we focus on the Riemann problem, which is associated with the initial condition

$$\mathbf{M}(x, 0) = \begin{cases} \mathbf{M}_L & \text{if } x < 0, \\ \mathbf{M}_R & \text{if } x > 0, \end{cases} \quad (9.29)$$

for two constant states  $\mathbf{M}_L$  and  $\mathbf{M}_R$  in  $\Omega$ .

The solution of (9.12)-(9.29) is sought in the form

$$\mathbf{M}(x, t) = \begin{cases} \mathbf{M}_L & \text{if } x < \sigma_L t, \\ \mathbf{M}_L^\delta(t) \delta(x - \sigma_L t) & \text{if } x = \sigma_L t, \\ \mathbf{M}_* & \text{if } \sigma_L t < x < \sigma_R t, \\ \mathbf{M}_R^\delta(t) \delta(x - \sigma_R t) & \text{if } x = \sigma_R t, \\ \mathbf{M}_R & \text{if } x > \sigma_R t, \end{cases} \quad (9.30)$$

which corresponds to the juxtaposition of two Dirac delta functions with mass  $\mathbf{M}_\beta^\delta$  and position  $x - \sigma_\beta t$ ,  $\beta = L, R$ , and separated by a constant state  $\mathbf{M}_\star$  in  $\Omega$ . Here,  $\sigma_\beta$  denotes a real number and  $\mathbf{M}_\beta^\delta(t)$  is defined by

$$\mathbf{M}_\beta^\delta(t) = \begin{pmatrix} m_\beta(t) \\ m_\beta(t)\sigma_\beta \\ m_\beta(t)\sigma_\beta^2 \\ m_\beta(t)\sigma_\beta^3 \end{pmatrix} \quad (9.31)$$

with  $m_\beta(t) \geq 0$ ,  $m_\beta(0) = 0$  and  $\beta = L, R$ .

We introduce the following natural definitions of (entropy) measure solutions.

**Definition 1** Let  $\eta = n_1 S(U_1) + n_2 S(U_2)$  and  $q = n_1 U_1 S(U_1) + n_2 U_2 S(U_2)$  with  $S(u) = u^{2\alpha}$ ,  $\alpha \in \mathbb{N}$ . We say that (9.30) is a measure solution of (9.12)-(9.29) if and only if  $\partial_t \eta + \partial_x q = 0$  in  $\mathcal{D}'(]0, \infty[ \times \mathbb{R})$  for  $S(u) = u^{2\alpha}$  with  $\alpha = 0, \frac{1}{2}, 1, \frac{3}{2}$ , that is for  $(\eta, q) = (M_i, M_{i+1})$ ,  $i = 0, 1, 2, 3$ . We say that (9.30) is an entropic measure solution of (9.12)-(9.29) if and only if  $\partial_t \eta + \partial_x q \leq 0$  in  $\mathcal{D}'(]0, \infty[ \times \mathbb{R})$  for  $S(v) = v^{2\alpha}$  with  $\alpha = 0, \frac{1}{2}, 1, \frac{3}{2}$  and  $\alpha \geq 2$ .

We can prove the following equivalence result.

**Theorem 3** The solution given by (9.30) is a measure solution of (9.12)-(9.29) if and only if

$$\begin{cases} \sigma_L(\mathbf{M}_L - \mathbf{M}_\star)t - (\mathbf{F}(\mathbf{M}_L) - \mathbf{F}(\mathbf{M}_\star))t + \mathbf{M}_L^\delta(t) = 0 \\ \sigma_R(\mathbf{M}_\star - \mathbf{M}_R)t - (\mathbf{F}(\mathbf{M}_\star) - \mathbf{F}(\mathbf{M}_R))t + \mathbf{M}_R^\delta(t) = 0. \end{cases} \quad (9.32)$$

The solution given by (9.30) is an entropic measure solution of (9.12)-(9.29) if and only if in addition

$$\begin{cases} \sigma_L(\eta(\mathbf{M}_L) - \eta(\mathbf{M}_\star))t - (q(\mathbf{M}_L) - q(\mathbf{M}_\star))t + \eta(\mathbf{M}_L^\delta(t)) \leq 0 \\ \sigma_R(\eta(\mathbf{M}_\star) - \eta(\mathbf{M}_R))t - (q(\mathbf{M}_\star) - q(\mathbf{M}_R))t + \eta(\mathbf{M}_R^\delta(t)) \leq 0, \end{cases} \quad (9.33)$$

for all  $S(u) = u^{2\alpha}$  with  $\alpha \geq 2$ .

**Proof 8** We first recall that  $\partial_t \eta + \partial_x q = 0$  in  $\mathcal{D}'(]0, \infty[ \times \mathbb{R})$  means that for any smooth function with compact support  $\varphi \in C_c^\infty(]0, \infty[ \times \mathbb{R})$ , we have

$$\begin{aligned} & \langle \partial_t \eta + \partial_x q, \varphi \rangle = - \langle \eta, \partial_t \varphi \rangle - \langle q, \partial_x \varphi \rangle = \\ & - \int_0^\infty \int_{-\infty}^{+\infty} \eta(x, t) \partial_t \varphi(x, t) dx dt - \int_0^\infty \int_{-\infty}^{+\infty} q(x, t) \partial_x \varphi(x, t) dx dt = 0, \end{aligned}$$

where by definition (9.30)

$$\eta(x, t) = \begin{cases} \eta(\mathbf{M}_L) & \text{if } x < \sigma_L t, \\ \eta(\mathbf{M}_L^\delta(t))\delta(x - \sigma_L t) & \text{if } x = \sigma_L t, \\ \eta(\mathbf{M}_\star) & \text{if } \sigma_L t < x < \sigma_R t, \\ \eta(\mathbf{M}_R^\delta(t))\delta(x - \sigma_R t) & \text{if } x = \sigma_R t, \\ \eta(\mathbf{M}_R) & \text{if } x > \sigma_R t, \end{cases}$$

and

$$q(x, t) = \begin{cases} q(\mathbf{M}_L) & \text{if } x < \sigma_L t, \\ q(\mathbf{M}_L^\delta(t))\delta(x - \sigma_L t) & \text{if } x = \sigma_L t, \\ q(\mathbf{M}_\star) & \text{if } \sigma_L t < x < \sigma_R t, \\ q(\mathbf{M}_R^\delta(t))\delta(x - \sigma_R t) & \text{if } x = \sigma_R t, \\ q(\mathbf{M}_R) & \text{if } x > \sigma_R t. \end{cases}$$

Here we note that  $q(\mathbf{M}_\beta^\delta(t)) = \sigma_\beta \eta(\mathbf{M}_\beta^\delta(t))$  with  $\eta(\mathbf{M}_\beta^\delta(t)) = m_\beta(t)S(\sigma_\beta)$ ,  $\beta = L, R$ . For all  $\varphi \in C_c^\infty([0, \infty[ \times \mathbb{R})$  we thus have

$$\begin{aligned} & \langle \partial_t \eta + \partial_x q, \varphi \rangle = \\ & - \int_0^\infty dt \int_{-\infty}^{\sigma_L t} \eta(\mathbf{M}_L) \partial_t \varphi(x, t) dx - \int_0^\infty \eta(\mathbf{M}_L^\delta(t)) \partial_t \varphi(\sigma_L t, t) dt \\ & - \int_0^\infty dt \int_{\sigma_L t}^{\sigma_R t} \eta(\mathbf{M}_\star) \partial_t \varphi(x, t) dx - \int_0^\infty \eta(\mathbf{M}_R^\delta(t)) \partial_t \varphi(\sigma_R t, t) dt \\ & - \int_0^\infty dt \int_{\sigma_R t}^\infty \eta(\mathbf{M}_R) \partial_t \varphi(x, t) dx - \int_0^\infty dt \int_{-\infty}^{\sigma_L t} q(\mathbf{M}_L) \partial_x \varphi(x, t) dx \\ & - \int_0^\infty q(\mathbf{M}_L^\delta(t)) \partial_x \varphi(\sigma_L t, t) dt - \int_0^\infty dt \int_{\sigma_R t}^\infty q(\mathbf{M}_\star) \partial_x \varphi(x, t) dx \\ & - \int_0^\infty q(\mathbf{M}_R^\delta(t)) \partial_x \varphi(\sigma_R t, t) dt - \int_0^\infty dt \int_{\sigma_R t}^\infty q(\mathbf{M}_R) \partial_x \varphi(x, t) dx \end{aligned}$$

that is, using in particular  $q(\mathbf{M}_\beta^\delta(t)) = \sigma_\beta \eta(\mathbf{M}_\beta^\delta(t))$ ,

$$\begin{aligned} & \langle \partial_t \eta + \partial_x q, \varphi \rangle = \\ & = - \int_0^\infty dt \eta(\mathbf{M}_L) \left( \frac{d}{dt} \int_{-\infty}^{\sigma_L t} \varphi(x, t) dx - \sigma_L \varphi(t, \sigma_L t) \right) - \int_0^\infty q(\mathbf{M}_L) \varphi(\sigma_L t, t) dt \\ & - \int_0^\infty dt \eta(\mathbf{M}_\star) \left( \frac{d}{dt} \int_{\sigma_L t}^{\sigma_R t} \varphi(x, t) dx - \sigma_R \varphi(t, \sigma_R t) + \sigma_L \varphi(t, \sigma_L t) \right) \\ & - \int_0^\infty q(\mathbf{M}_\star) (\varphi(\sigma_R t, t) - \varphi(\sigma_L t, t)) dt \\ & - \int_0^\infty dt \eta(\mathbf{M}_R) \left( \frac{d}{dt} \int_{\sigma_R t}^\infty \varphi(x, t) dx + \sigma_R \varphi(t, \sigma_R t) \right) + \int_0^\infty q(\mathbf{M}_R) \varphi(\sigma_R t, t) dt \\ & - \int_0^\infty \eta(\mathbf{M}_L^\delta(t)) \frac{d}{dt} [\varphi(\sigma_L t, t)] dt - \int_0^\infty \eta(\mathbf{M}_R^\delta(t)) \frac{d}{dt} [\varphi(\sigma_R t, t)] dt \\ & = \int_0^\infty \varphi(\sigma_L t, t) (\sigma_L \eta(\mathbf{M}_L) - q(\mathbf{M}_L)) dt + \int_0^\infty \varphi(\sigma_R t, t) (\sigma_R \eta(\mathbf{M}_\star) - q(\mathbf{M}_\star)) dt \\ & - \int_0^\infty \varphi(\sigma_L t, t) (\sigma_L \eta(\mathbf{M}_\star) - q(\mathbf{M}_\star)) dt - \int_0^\infty \varphi(\sigma_R t, t) (\sigma_R \eta(\mathbf{M}_R) - q(\mathbf{M}_R)) dt \\ & - \int_0^\infty \eta(\mathbf{M}_L^\delta(t)) \frac{d}{dt} [\varphi(\sigma_L t, t)] dt - \int_0^\infty \eta(\mathbf{M}_R^\delta(t)) \frac{d}{dt} [\varphi(\sigma_R t, t)] dt \\ & = \int_0^\infty \varphi(\sigma_L t, t) (\sigma_L (\eta(\mathbf{M}_L) - \eta(\mathbf{M}_\star)) - (q(\mathbf{M}_L) - q(\mathbf{M}_\star))) dt \\ & + \int_0^\infty \varphi(\sigma_R t, t) (\sigma_R (\eta(\mathbf{M}_\star) - \eta(\mathbf{M}_R)) - (q(\mathbf{M}_\star) - q(\mathbf{M}_R))) dt \\ & - \int_0^\infty \eta(\mathbf{M}_L^\delta(t)) \frac{d}{dt} [\varphi(\sigma_L t, t)] dt - \int_0^\infty \eta(\mathbf{M}_R^\delta(t)) \frac{d}{dt} [\varphi(\sigma_R t, t)] dt \\ & = \int_0^\infty \varphi(\sigma_L t, t) \frac{d}{dt} (\sigma_L (\eta(\mathbf{M}_L) - \eta(\mathbf{M}_\star)) t - (q(\mathbf{M}_L) - q(\mathbf{M}_\star)) t + \eta(\mathbf{M}_L^\delta(t))) dt \\ & + \int_0^\infty \varphi(\sigma_R t, t) \frac{d}{dt} (\sigma_R (\eta(\mathbf{M}_\star) - \eta(\mathbf{M}_R)) t - (q(\mathbf{M}_\star) - q(\mathbf{M}_R)) t + \eta(\mathbf{M}_R^\delta(t))) dt. \end{aligned}$$

Then, since  $m_\beta(0) = 0$  and then  $\eta(\mathbf{M}_\beta^\delta(0)) = 0$ ,  $\beta = L, R$ , it is clear that (9.30) is a measure solution of (9.12)-(9.29) if and only if (9.32) is valid for all  $t \geq 0$ , and an entropic measure solution if and only if in addition (9.33) holds true for all  $t \geq 0$  and all  $\eta = n_1 S(U_1) + n_2 S(U_2)$  and  $q = n_1 U_1 S(U_1) + n_2 U_2 S(U_2)$  with  $S(u) = u^{2\alpha}$ ,  $\alpha \geq 2$ .

**Remark 6** Let us recall that  $\eta(\mathbf{M}_\beta^\delta(t)) = m_\beta(t)S(\sigma_\beta)$ . Since (9.33) is made of equalities when  $S(u) = 1$  and  $S(u) = u$  (we get in these cases the first two components of (9.32)), the validity of (9.33) for all  $S(u) = u^{2\alpha}$ ,  $\alpha \geq 2$ , is equivalent to the validity of

$$\begin{cases} \sigma_L(\eta(\mathbf{M}_L) - \eta(\mathbf{M}_*)) - (q(\mathbf{M}_L) - q(\mathbf{M}_*)) \leq 0 \\ \sigma_R(\eta(\mathbf{M}_*) - \eta(\mathbf{M}_R)) - (q(\mathbf{M}_*) - q(\mathbf{M}_R)) \leq 0, \end{cases} \quad (9.34)$$

for all  $S(u) = u^{2\alpha} - \sigma_L^{2\alpha} \frac{u - \sigma_R}{\sigma_L - \sigma_R} - \sigma_R^{2\alpha} \frac{u - \sigma_L}{\sigma_R - \sigma_L}$ ,  $\alpha \geq 2$ .

### 9.2.5 Examples of entropy solutions

In this section, we propose three particular entropic solutions. The first one models the collision of two particles packets with free boundary  $\mathcal{C}^1$  smooth solution, that is a solution for which an exact link with the kinetic level is preserved and for which the entropy equation is exactly satisfied. In such a situation the four-moment model does not develop  $\delta$ -shock Dirac delta functions and is actually able to properly represent the crossing of the two packets which correspond to the dynamics at the kinetic level. The second one models the collision of four particles packets. In this case and as expected since the number of moments is set to four, the entropic solutions involves two  $\delta$ -shock Dirac delta functions singularities. Whereas the first case corresponds to a connection from the interior of the moment space to the frontier through a contact discontinuity, or free boundary solution, resulting in an isolated point at the frontier, we consider in a third example a smooth connection to the frontier of the moment space, such that the point at the frontier is an accumulation point of a trajectory inside the moment space.

#### 9.2.5.1 ‘Collision’ of two particles packets

We consider a Riemann initial data (9.29) where  $\mathbf{M}_L = \mathbf{M}(\mathbf{U}_L)$  and  $\mathbf{M}_R = \mathbf{M}(\mathbf{U}_R)$  are such that

$$\mathbf{U}_L = \frac{1}{2} \begin{pmatrix} n_L \\ n_L \\ n_L U_L \\ n_L U_L \end{pmatrix} \quad \text{and} \quad \mathbf{U}_R = \frac{1}{2} \begin{pmatrix} n_R \\ n_R \\ n_R U_R \\ n_R U_R \end{pmatrix}$$

for two given densities  $n_L > 0$  and  $n_R > 0$  and velocities  $v_L > 0$  and  $v_R < 0$ . We recall that the function  $\mathbf{M} = \mathbf{M}(\mathbf{U})$  is defined by (9.15). We define

$$\mathbf{M}(x, t) = \begin{cases} \mathbf{M}_L & \text{if } x < U_R t, \\ \mathbf{M}_* & \text{if } U_R t < x < U_L t, \\ \mathbf{M}_R & \text{if } x > U_L t, \end{cases} \quad (9.35)$$

with  $\mathbf{M}_* = \mathbf{M}(\mathbf{U}_*)$  given by

$$\mathbf{U}_* = \begin{pmatrix} n_L \\ n_R \\ n_L U_L \\ n_R U_R \end{pmatrix}.$$

Our objective here is to prove that the following Dirac delta functions free solution is an entropy solution of (9.12)-(9.29). Conditions (9.32) and (9.33) write here

$$\begin{cases} U_R(\mathbf{M}_L - \mathbf{M}_*) - (\mathbf{F}(\mathbf{M}_L) - \mathbf{F}(\mathbf{M}_*)) = 0 \\ U_L(\mathbf{M}_* - \mathbf{M}_R) - (\mathbf{F}(\mathbf{M}_*) - \mathbf{F}(\mathbf{M}_R)) = 0. \end{cases} \quad (9.36)$$

and

$$\begin{cases} U_R(\eta(\mathbf{M}_L) - \eta(\mathbf{M}_*)) - (q(\mathbf{M}_L) - q(\mathbf{M}_*)) \leq 0 \\ U_L(\eta(\mathbf{M}_*) - \eta(\mathbf{M}_R)) - (q(\mathbf{M}_*) - q(\mathbf{M}_R)) \leq 0, \end{cases} \quad (9.37)$$



with  $\eta(\mathbf{U}) = n_1 S(U_1) + n_2 S(U_2)$  and  $q(\mathbf{U}) = n_1 U_1 S(U_1) + n_2 U_2 S(U_2)$  for all  $S(u) = u^{2\alpha}$  with  $\alpha \geq 2$ . We will focus only on the first equality of (9.36) and the first inequality of (9.37), the second ones being treated similarly. We clearly have

$$\mathbf{M}_L - \mathbf{M}_\star = \begin{pmatrix} n_L \\ n_L U_L \\ n_L U_L^2 \\ n_L U_L^3 \end{pmatrix} - \begin{pmatrix} n_L + n_R \\ n_L U_L + n_R U_R \\ n_L U_L^2 + n_R U_R^2 \\ n_L U_L^3 + n_R U_R^3 \end{pmatrix} = - \begin{pmatrix} n_R \\ n_R U_R \\ n_R U_R^2 \\ n_R U_R^3 \end{pmatrix},$$

while

$$\mathbf{F}(\mathbf{M}_L) - \mathbf{F}(\mathbf{M}_\star) = \begin{pmatrix} n_L U_L \\ n_L U_L^2 \\ n_L U_L^3 \\ n_L U_L^4 \end{pmatrix} - \begin{pmatrix} n_L U_L + n_R U_R \\ n_L U_L^2 + n_R U_R^2 \\ n_L U_L^3 + n_R U_R^3 \\ n_L U_L^4 + n_R U_R^4 \end{pmatrix} = - \begin{pmatrix} n_R U_R \\ n_R U_R^2 \\ n_R U_R^3 \\ n_R U_R^4 \end{pmatrix}.$$

It is then clear that the first equality of (9.36) holds true. Let us now check that the proposed Riemann solution fulfills the entropy condition. We clearly have

$$\begin{aligned} & U_R(\eta(\mathbf{M}_L) - \eta(\mathbf{M}_\star)) - (q(\mathbf{M}_L) - q(\mathbf{M}_\star)) = \\ & U_R(n_L S(U_L) - (n_L S(U_L) + n_R S(U_R))) - (n_L U_L S(U_L) - (n_L U_L S(U_L) + n_R U_R S(U_R))) \\ & = 0, \end{aligned}$$

which allows to prove that the proposed solution is an entropic smooth solution.

### 9.2.5.2 ‘Collision’ of four particles packets

We consider a Riemann initial data (9.29) where  $\mathbf{M}_L = \mathbf{M}(\mathbf{U}_L)$  and  $\mathbf{M}_R = \mathbf{M}(\mathbf{U}_R)$  are such that

$$\mathbf{U}_L = \frac{1}{2} \begin{pmatrix} n \\ n \\ nU_1 \\ nU_2 \end{pmatrix} \quad \text{and} \quad \mathbf{U}_R = \frac{1}{2} \begin{pmatrix} n \\ n \\ -nU_2 \\ -nU_1 \end{pmatrix}$$

for a given density  $n > 0$  and two velocities  $v_2 > v_1 > 0$ . We have

$$\begin{aligned} \mathbf{M}_L &= \frac{1}{2} \begin{pmatrix} 2n \\ n(U_1 + U_2) \\ n(U_1^2 + U_2^2) \\ n(U_1^3 + U_2^3) \end{pmatrix} \quad \text{and} \quad \mathbf{M}_R = \frac{1}{2} \begin{pmatrix} 2n \\ -n(U_1 + U_2) \\ n(U_1^2 + U_2^2) \\ -n(U_1^3 + U_2^3) \end{pmatrix} \\ \mathbf{F}(\mathbf{M}_L) &= \frac{1}{2} \begin{pmatrix} n(U_1 + U_2) \\ n(U_1^2 + U_2^2) \\ n(U_1^3 + U_2^3) \\ n(U_1^4 + U_2^4) \end{pmatrix} \quad \text{and} \quad \mathbf{F}(\mathbf{M}_R) = \frac{1}{2} \begin{pmatrix} -n(U_1 + U_2) \\ n(U_1^2 + U_2^2) \\ -n(U_1^3 + U_2^3) \\ n(U_1^4 + U_2^4) \end{pmatrix}. \end{aligned}$$

We define

$$\mathbf{M}(x, t) = \begin{cases} \mathbf{M}_L & \text{if } x < -\sigma t, \\ \mathbf{M}_L^\delta(t)\delta(x + \sigma t) & \text{if } x = -\sigma t, \\ \mathbf{M}_\star & \text{if } -\sigma t < x < \sigma t, \\ \mathbf{M}_R^\delta(t)\delta(x - \sigma t) & \text{if } x = \sigma t, \\ \mathbf{M}_R & \text{if } x > \sigma t, \end{cases} \quad (9.38)$$

with  $\sigma > 0$ ,  $\mathbf{M}_\star = \mathbf{M}(\mathbf{U}_\star)$  given by

$$\mathbf{U}_\star = \frac{1}{2} \begin{pmatrix} n_\star \\ n_\star \\ -n_\star U_\star \\ n_\star U_\star \end{pmatrix}, \quad \mathbf{M}_\star = \begin{pmatrix} n_\star \\ 0 \\ n_\star U_\star^2 \\ 0 \end{pmatrix}, \quad n_\star > 0, \quad U_\star > 0,$$

and  $\mathbf{M}_L^\delta(t)$ ,  $\mathbf{M}_R^\delta(t)$  given by

$$\mathbf{M}_L^\delta(t) = m(t) \begin{pmatrix} 1 \\ -\sigma \\ \sigma^2 \\ -\sigma^3 \end{pmatrix}, \quad \mathbf{M}_R^\delta(t) = m(t) \begin{pmatrix} 1 \\ \sigma \\ \sigma^2 \\ \sigma^3 \end{pmatrix},$$

with  $m(t) \geq 0$ . We have

$$\mathbf{F}(\mathbf{M}_\star) = \begin{pmatrix} 0 \\ n_\star U_\star^2 \\ 0 \\ n_\star U_\star^4 \end{pmatrix}.$$

The generalized Rankine-Hugoniot jump conditions (9.32) write here

$$\begin{cases} -\sigma(\mathbf{M}_L - \mathbf{M}_\star)t - (\mathbf{F}(\mathbf{M}_L) - \mathbf{F}(\mathbf{M}_\star))t + \mathbf{M}_L^\delta(t) = 0 \\ \sigma(\mathbf{M}_\star - \mathbf{M}_R)t - (\mathbf{F}(\mathbf{M}_\star) - \mathbf{F}(\mathbf{M}_R))t + \mathbf{M}_R^\delta(t) = 0. \end{cases}$$

that is, equivalently

$$\begin{cases} 2\sigma\mathbf{M}_\star - \sigma(\mathbf{M}_L + \mathbf{M}_R) + (\mathbf{F}(\mathbf{M}_R) - \mathbf{F}(\mathbf{M}_L)) + \frac{m(t)}{t} \begin{pmatrix} 2 \\ 0 \\ 2\sigma^2 \\ 0 \end{pmatrix} = 0, \\ 2\mathbf{F}(\mathbf{M}_\star) + \sigma(\mathbf{M}_R - \mathbf{M}_L) - (\mathbf{F}(\mathbf{M}_L) + \mathbf{F}(\mathbf{M}_R)) - \frac{m(t)}{t} \begin{pmatrix} 0 \\ 2\sigma \\ 0 \\ 2\sigma^3 \end{pmatrix} = 0. \end{cases} \quad (9.39)$$

This is made of eight equalities and we note that four are trivial (zero equals zero), so that four are left to determine the four unknowns  $n_\star$ ,  $U_\star$ ,  $\sigma$  and  $m(t)/t$ . We propose below to numerically solve this nonlinear system for a specific set of values for  $n$ ,  $U_1$  and  $U_2$ .

**Remark 7** *We conjecture existence and uniqueness of a solution to this nonlinear system. Indeed, the initial condition involves four different velocities while the model is able to represent two different velocities only. More precisely and by analogy with the usual pressureless gas dynamics model (see [24], [21]), velocity  $U_1$  is to "bump" into velocities  $-U_1$  and  $-U_2$  to create a first Dirac delta function. By symmetry, another Dirac delta function is expected.*

Regarding the entropy inequalities (9.33), we first remark that for  $S(u) = u^{2\alpha}$ ,

$$\begin{aligned} \eta(\mathbf{M}_L) &= \eta(\mathbf{M}_R) = \frac{n}{2}(S(U_1) + S(U_2)) \\ \eta(\mathbf{M}_\star) &= n_\star S(U_\star), \\ \eta(\mathbf{M}_L^\delta(t)) &= \eta(\mathbf{M}_R^\delta(t)) = m(t)S(\sigma), \end{aligned}$$

while

$$\begin{aligned} q(\mathbf{M}_L) &= -q(\mathbf{M}_R) = \frac{n}{2}(U_1 S(U_1) + U_2 S(U_2)) \\ q(\mathbf{M}_\star) &= 0. \end{aligned}$$

As an immediate consequence, both inequalities in (9.33) are equivalent and the entropy condition is

$$\sigma(n_\star S(U_\star) - \frac{n}{2}(S(U_1) + S(U_2))) - \frac{n}{2}(U_1 S(U_1) + U_2 S(U_2)) + \frac{m(t)}{t}S(\sigma) \leq 0. \quad (9.40)$$

**A concrete example.** We propose to take  $n = 1$ ,  $U_1 = 0.8$  and  $U_2 = 1.2$ . Numerically solving (9.39) gives  $n_* = 1.88265$ ,  $U_* = 1.06026$ ,  $\sigma = 0.87983$  and  $m(t)/t = 0.22342$ . If the left-hand side of (9.40), which represents the entropy dissipation rate associated with  $S(u) = u^{2\alpha}$ , is denoted  $D(\alpha)$ , a simple calculation gives for instance  $D(2) = -0.27324$ ,  $D(3) = -0.86854$ ,  $D(4) = -1.88678, \dots$ . The proposed solution (9.38) is then actually an entropy measure solution of the four-moment model. Such an exact entropic solution will be used in the following to prove the relevance of the numerical scheme proposed hereafter with respect to the exact solution when singularities are present.

### 9.2.5.3 Smooth solution connected with the frontier of the moment space

As a last example, we introduce a smooth solution which allows to connect zones inside the moment space with zone at the frontier within the proper framework introduced in subsection 9.2.1.3. Particles are initiated in the domain  $[0, 0.5]$ . In the domain  $[0, 0.1]$ , a monomodal velocity distribution is reconstructed, with  $U_1 = U_2 = 1$ , and  $n_1 = n_2 = 0.5$ . On the contrary, a bimodal velocity distribution is reconstructed in the domain  $[0.1, 0.4]$ , with  $n_1 = n_2 = 0.5$  and for the abscissas,  $U_1 = 1 + \frac{x-0.1}{0.3}$  and  $U_2 = 1$ . The initial conditions are represented in Fig. 9.1.

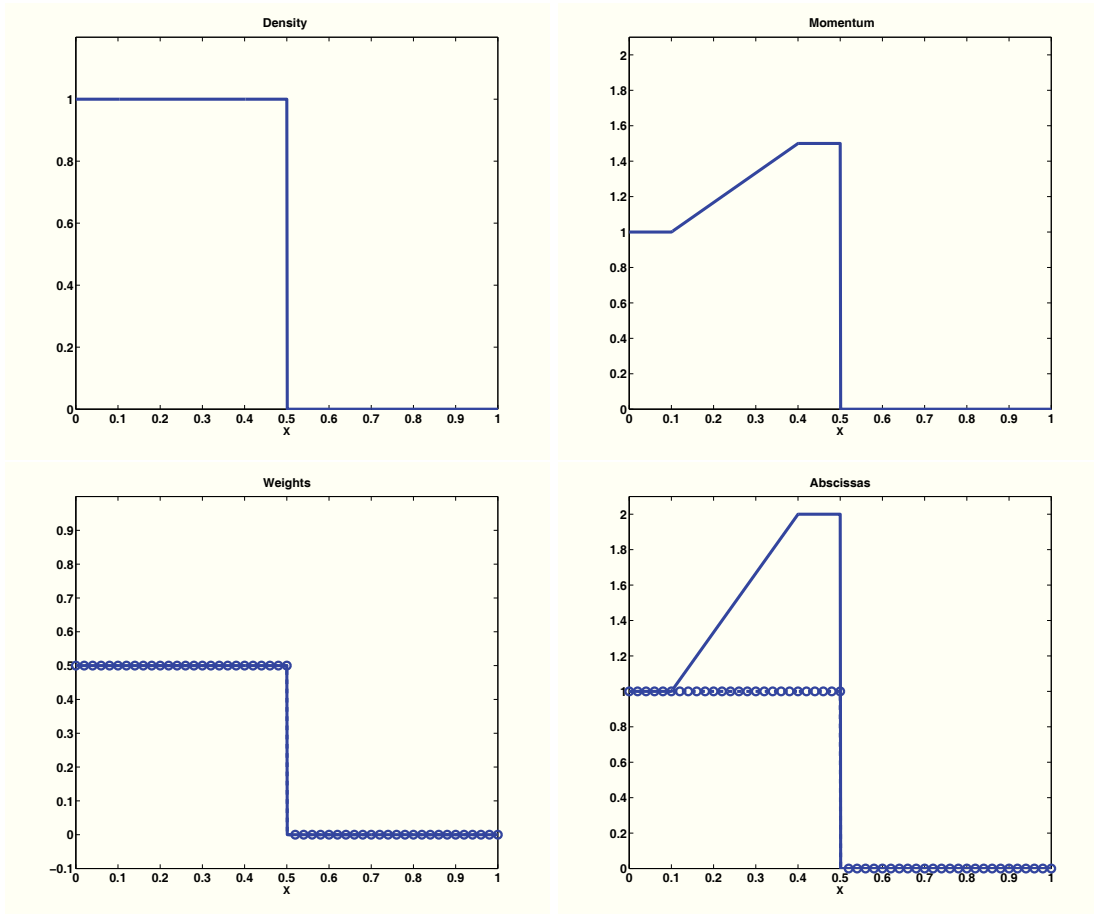


Figure 9.1: Moment dynamics in the context of a smooth transition between areas of null and non null dispersion. Initial conditions. Top-left:  $M_0$ . Top-right:  $M_1$ . Bottom-left: weights. Bottom-right: abscissas. The solid line corresponds to  $(n_1, U_1)$ , the dashed line with circles corresponds to  $(n_2, U_2)$ .

The ground difference with the first test case is that the transition between the two zones is smooth, and so the numerical strategy to account for this transition is of major importance. The analytical solution of this problem, in smooth areas, consists of a decoupled transport of each of the quadrature

nodes as two independent pressureless gas as showed in system (9.23). This comes from the fact that the number of Dirac delta functions reconstructed from the moments, two in this case, is always sufficient to capture the problem dynamics. The equivalence between the kinetic and macroscopic equations is preserved, and the solution in terms of moments satisfy the entropy equation. Therefore, the solution consists in the superposition of a particle translation at constant velocity  $U_2 = 1$ , and a particle transport with the following velocity field:

$$U_1 = \begin{cases} 1 & x \in [0, 0.1] \\ 1 + \frac{x-0.1}{0.3} & x \in [0.1, 0.4] \\ 2 & x \in [0.4, 0.5] \end{cases} \quad (9.41)$$

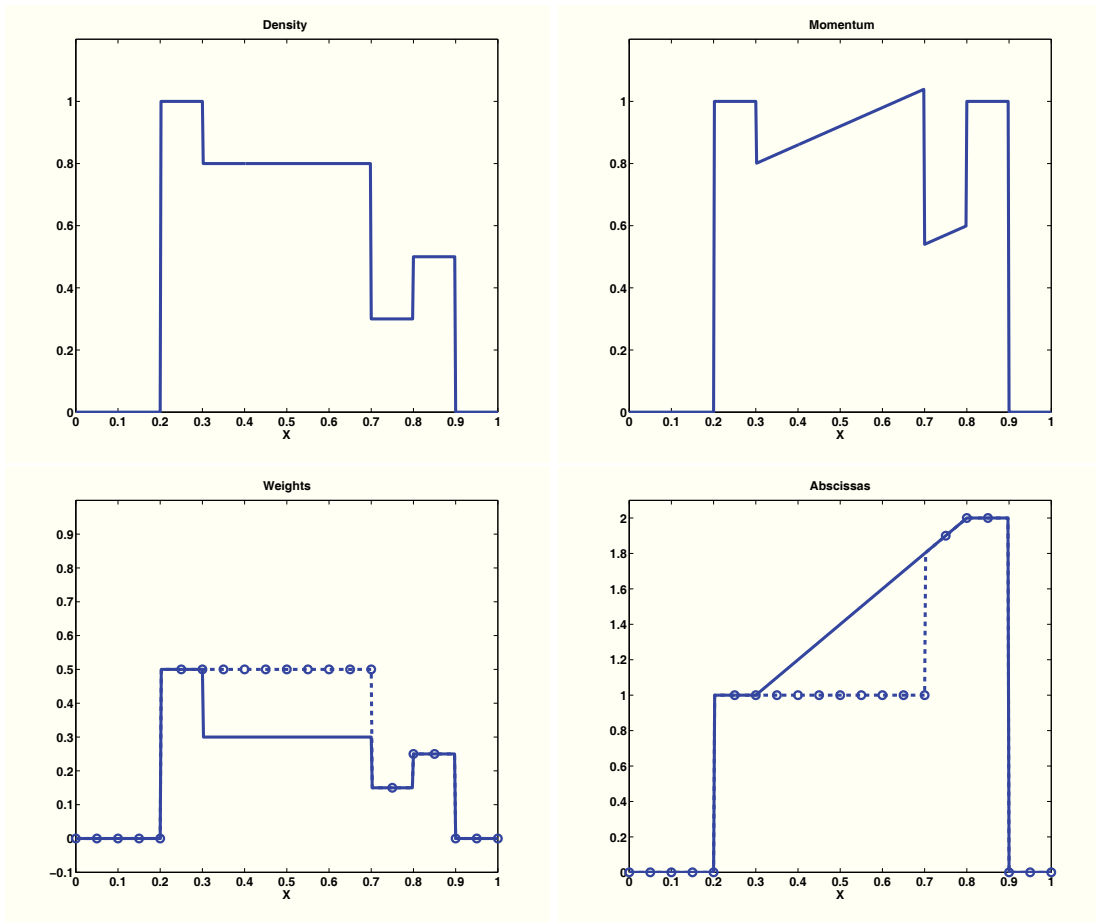


Figure 9.2: Moment dynamics in the context of a smooth transition between areas of null and non null dispersion. Solution at  $t = 0.2$ . Top-left:  $M_0$ . Top-right:  $M_1$ . Bottom-left: weights. Bottom-right: abscissas. The solid line corresponds to  $(n_1, U_1)$ , the dashed line with circles corresponds to  $(n_2, U_2)$ .

The analytical solution is displayed in Fig. 9.2. Let us first notice the fronts at  $x = 0.2$  and  $x = 0.9$  moving with a velocity  $u = 1$  and  $u = 2$  respectively. The first front corresponds to particles initiated with velocity  $u = 1$  between  $x = 0$  and  $x = 0.1$ . The second front corresponds to particles initiated with velocity  $u = 2$  between  $x = 0.4$  and  $x = 0.5$ . The square wave between  $x = 0.8$  and  $x = 0.9$  is the final location of the particles initiated with velocity  $u = 2$  between  $x = 0.4$  and  $x = 0.5$ .

The value of  $n_1$  between  $x = 0.3$  and  $x = 0.8$  corresponds to the expansion of the density field due to transport with a linear velocity field with positive slope. The value of the density in that area is the

solution of the equation  $\partial_t n_1 + U_1 \partial_x n_1 = -n_1 \partial_x U_1$ , which yields  $n_1 = 0.3$  at time  $t = 0.2$ <sup>4</sup>.

According to the initial conditions, both weights have the same profile, the quantities  $\frac{q}{M_0 e}$  and  $\frac{q}{e^{3/2}}$  are null. At time  $t = 0.2$ , the weight profiles are different in the interval  $[0.3, 0.8]$  corresponding to the expansion of  $n_1$ . Therefore,  $\frac{q}{e^{3/2}}$  is non null, as well as  $\frac{q}{M_0 e}$  since the velocities have also different values. Besides, their values can be exactly calculated.

### 9.2.6 Numerical simulations via kinetic schemes

This section is devoted to the discretization of (9.12)-(9.14)-(9.15). As already stated, we use as a building block a natural first-order kinetic scheme already proposed in the literature [124, 99, 56] and briefly recalled here for the sake of completeness.

Let us first introduce a time step  $\Delta t > 0$  and a space step  $\Delta x > 0$  that we assume to be constant for simplicity. We set  $\lambda = \Delta t / \Delta x$  and define the mesh interfaces  $x_{j+1/2} = j\Delta x$  for  $j \in \mathbb{Z}$ , and the intermediate times  $t^n = n\Delta t$  for  $n \in \mathbb{N}$ . In the sequel,  $\mathbf{M}_j^n$  denotes the approximate value of  $\mathbf{M}$  at time  $t^n$  and on the cell  $\mathcal{C}_j = [x_{j-1/2}, x_{j+1/2})$ . For  $n = 0$ , we set

$$\mathbf{M}_j^0 = \frac{1}{\Delta x} \int_{x_{j-1/2}}^{x_{j+1/2}} \mathbf{M}_0(x) dx, \quad j \in \mathbb{Z},$$

where  $\mathbf{M}_0(x)$  is the initial condition.

Let us now assume as given  $(\mathbf{M}_j^n)_{j \in \mathbb{Z}}$  the sequence in  $\Omega$  of approximate values at time  $t^n$ . In order to advance it to the next time level  $t^{n+1}$ , the kinetic scheme is decomposed into two steps.

*First step : transport ( $t^n \rightarrow t^{n+1-}$ )*

We first set  $\mathbf{U}_j^n = \mathbf{U}(\mathbf{M}_j^n)$  and define the function  $(x, u) \rightarrow f^n(x, u)$  by

$$f^n(x, u) = (n_1)_j^n \delta(v - (U_1)_j^n) + (n_2)_j^n \delta(v - (U_2)_j^n),$$

$$\forall (x, u) \in \mathcal{C}_j \times \mathbb{R}, \quad j \in \mathbb{Z}.$$

We then solve the transport equation

$$\begin{cases} \partial_t f + u \partial_x f = 0, & (x, u) \in \mathbb{R} \times \mathbb{R}, \\ f(t = 0, x, u) = f^n(x, u), \end{cases} \quad (9.42)$$

the solution of which is given by  $f(t, x, u) = f^n(x - ut, u)$ .

At last, we set  $f^{n+1-}(x, u) = f^n(x - u\Delta t, u)$ .

*Second step : collapse ( $t^{n+1-} \rightarrow t^{n+1}$ )*

The first four moments at time  $t^{n+1}$  are now naturally defined by setting

$$(M_i)_j^{n+1} = \frac{1}{\Delta x} \int_{x_{j-1/2}}^{x_{j+1/2}} \int_{-\infty}^{+\infty} u^i f^{n+1-}(x, u) du dx.$$

Then, we have  $\mathbf{M}_j^{n+1} = ((M_0)_j^{n+1}, (M_1)_j^{n+1}, (M_2)_j^{n+1}, (M_3)_j^{n+1})^t$  for all  $j \in \mathbb{Z}$ , which completes the algorithm description.

**Remark 8** *It is easy to see that this scheme preserves the moment space  $\Omega$ , see for instance [56].*

<sup>4</sup>In the interval  $[0.8, 0.9]$ , although  $n_2$  should be null (the square wave at velocity  $U_2 = 1$  should be bounded between the front  $x = 0.2$  and  $x = 0.7$ ) we computed  $n_2 = 0.5$  and  $U_2 = 2$ . We did this to be consistent with the conditions stated in Section 9.2.1.3 when the moment vector lies in the moment space border

**Remark 9** Under the natural CFL condition

$$\Delta t \max_{j \in \mathbb{Z}} ((U_1)_j^n, (U_2)_j^n) \leq CFL \Delta x,$$

with  $CFL \leq 1$ , integrating (9.42) over  $(t, x, u) \in (0, \Delta t) \times \mathcal{C}_j \times \mathbb{R}$  and against  $u^i$ ,  $i = 0, \dots, 3$  easily leads to the equivalent update formula

$$\mathbf{M}_j^{n+1} = \mathbf{M}_j^n - \frac{\Delta t}{\Delta x} (\mathbf{F}_{j+1/2}^n - \mathbf{F}_{j-1/2}^n), \quad j \in \mathbb{Z},$$

where we have set  $\mathbf{F}_{j+1/2}^n = ((M_1)_{j+1/2}^n, (M_2)_{j+1/2}^n, (M_3)_{j+1/2}^n, (M_4)_{j+1/2}^n)^t$  and  $(M_i)_{j+1/2}^n = (M_i)_{j+1/2}^{n+} + (M_i)_{j+1/2}^{n-}$ , and with

$$(M_i)_{j+1/2}^{n-} = (n_1)_{j+1}^n \min(0, (U_1)_{j+1}^n) ((U_1)_{j+1}^n)^{i-1} + \min(0, (U_2)_{j+1}^n) (n_2)_{j+1}^n ((U_2)_{j+1}^n)^{i-1},$$

$$(M_i)_{j+1/2}^{n+} = (n_1)_j^n \max(0, (U_1)_j^n) ((U_1)_j^n)^{i-1} + (n_2)_j^n \max(0, (U_2)_j^n) ((U_2)_j^n)^{i-1}.$$

### 9.2.6.1 Numerical quadrature strategy at the frontier of the moment space

This paragraph addresses the issue of how to numerically handle the transition between a vector in the interior of the moment space, and a vector lying at its frontier. For an isolated point at the frontier of the moment space  $\Gamma$ , there is no specific problem since we use a single quadrature node and the quadrature is not a problem. The two problems we have to face are related to the preservation of the cone in which we envision to work in section 2 as well as to deal with finite precision algebra in the neighborhood of the point  $(0, 0)$  in the  $(e, q)$  plane.

Consequently we introduce two constants in the numerical quadrature we use. First, for finite precision algebra and in order to avoid numerical errors, we only evaluate the two quadrature nodes when  $e/M_0^2 > \epsilon_1$ , where  $\epsilon_1$  is a small number related to machine precision. Under this threshold, the velocity dispersion is considered null ( $e = 0$ ), and the set of Dirac delta functions are reconstructed as suggested in section 2:  $n_1 = n_2 = M_0/2$ ,  $U_1 = U_2 = M_1/M_0$ .

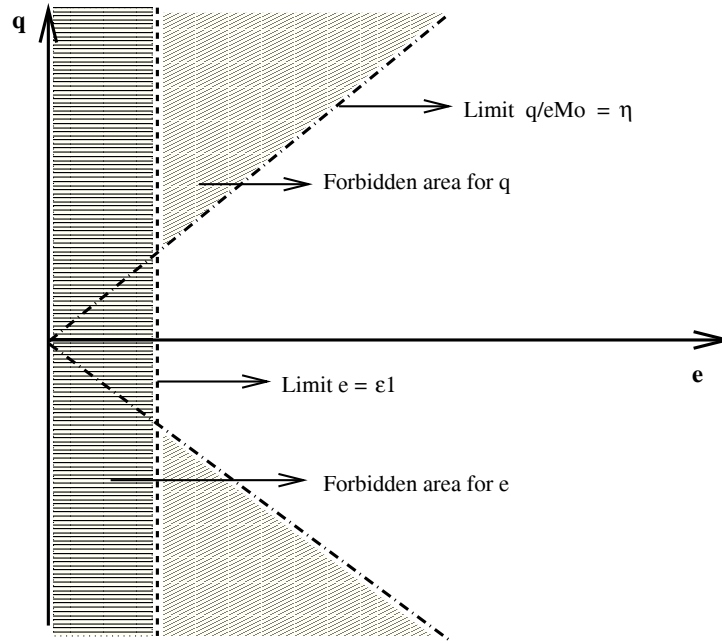


Figure 9.3: Handling of the moment space border.

Secondly, since we want to deal with compactly supported velocity distribution at the kinetic level, we will introduce another constant,  $\eta$  which is a bound for the distance between the two abscissas. In fact we impose to the solution to remain inside the cone in the  $(e, q)$  plane :  $\frac{|q|}{M_0 e} \leq \eta$ . It will be shown in the following examples that the cone is in fact automatically preserved by the proposed algorithm and that such a bound does not have to be imposed but is satisfied by the numerical solution.

If  $\frac{|q|}{M_0 e} > \eta$ , then we set  $q/(M_0 e) = \text{sign}(q) \eta$ , so that :

$$\frac{q}{M_0 e} = \text{sign}(q) \eta, \quad q = \text{sign}(q) \eta M_0 e, \quad M_3 = q + M_1 M_2 / M_0.$$

As illustrated in Fig 9.3 and explained in Section 9.2.1.3, the variable  $q$  is forced to be in a cone delimited by the straight lines of slope  $\pm\eta$  and becomes null when  $e \leq \epsilon_1$ .

Let us remark that limiting  $\frac{q}{M_0 e}$  does not lead to a limitation on the quantity  $\frac{q}{e^{3/2}}$  in such a way as to allow the possibility to reach large ratio in terms of weights (one weight can approach a zero value while the quantity  $\frac{q}{e^{3/2}}$  grows indefinitely) but without allowing the abscissas distance to grow beyond of fixed limit naturally inherited from the initial solutions at the kinetic level. We will come back to this point in the following result section. For the simulations we present, the parameters are such that:  $\epsilon_1 = 10^{-9}$  and  $\eta = 2$ .

### 9.2.6.2 Numerical results

This section is devoted to numerical illustrations of solutions to the two Riemann problems and one dedicated solution in order to study the connection to the frontier of the moment space for which we have derived analytical entropic solutions in Section 9.2.5. The solutions to the two Riemann problems involve two and four particle packets. A last result highlights the numerical strategy and the effect of numerical diffusion at the frontier of the moment space for which a free boundary connects a zone where  $e = 0$  and a zone where  $e > 0$ .

In all the figures, we choose to represent  $n_1$  and  $U_1$  by solid lines, and  $n_2$  and  $U_2$  by lines with circle markers. In the representation of weights and abscissas, values have to be assigned for  $U_1$  and  $U_2$  : we thus decide that  $U_1$  is the maximum of the relative values of velocity.

### Two packet collision

Figure 9.2.6.2 represents the initial conditions for the two particle packet case. Figures 9.5 and 9.6 presents the numerical and analytical solutions for the two particle packet case with  $n_L = n_R = 1$ , and  $U_L = 1$ ,  $U_R = -1$ . The computation is run with a 1000 cell grid on the spatial domain  $[0, 1]$ , with  $CFL = 1$ . The length of each packet is 0.4 ( $n_1 = n_2 = U_1 = U_2 = 0$  for  $x \leq 0.1$  and  $x \geq 0.9$ ) and the two packets start to collide exactly at time  $t = 0$ . Moving in opposite direction once across the other, with the same opposite speed, they then mix together and we note in particular that  $n_1 = n_2 = 1$  and  $U_1 = U_2 = 0$  in the mixing zone (see for instance the plots at time  $t = 0.1$ ). As expected, they finally get separated again and we note that a perfect agreement is obtained with the exact entropic solution.

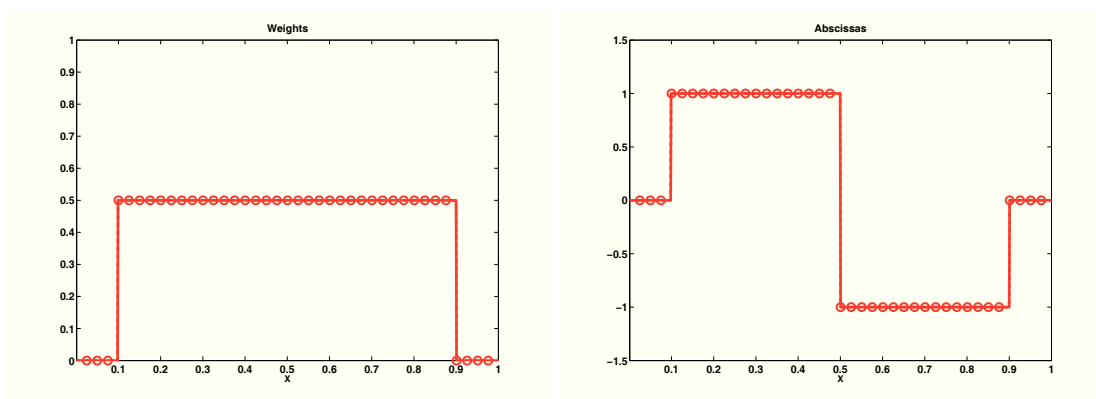


Figure 9.4: Initial fields of weights (left) and abscissas (right) for the two particle packet case. The first quadrature node is represented by solid lines whereas the second node is represented by circles.



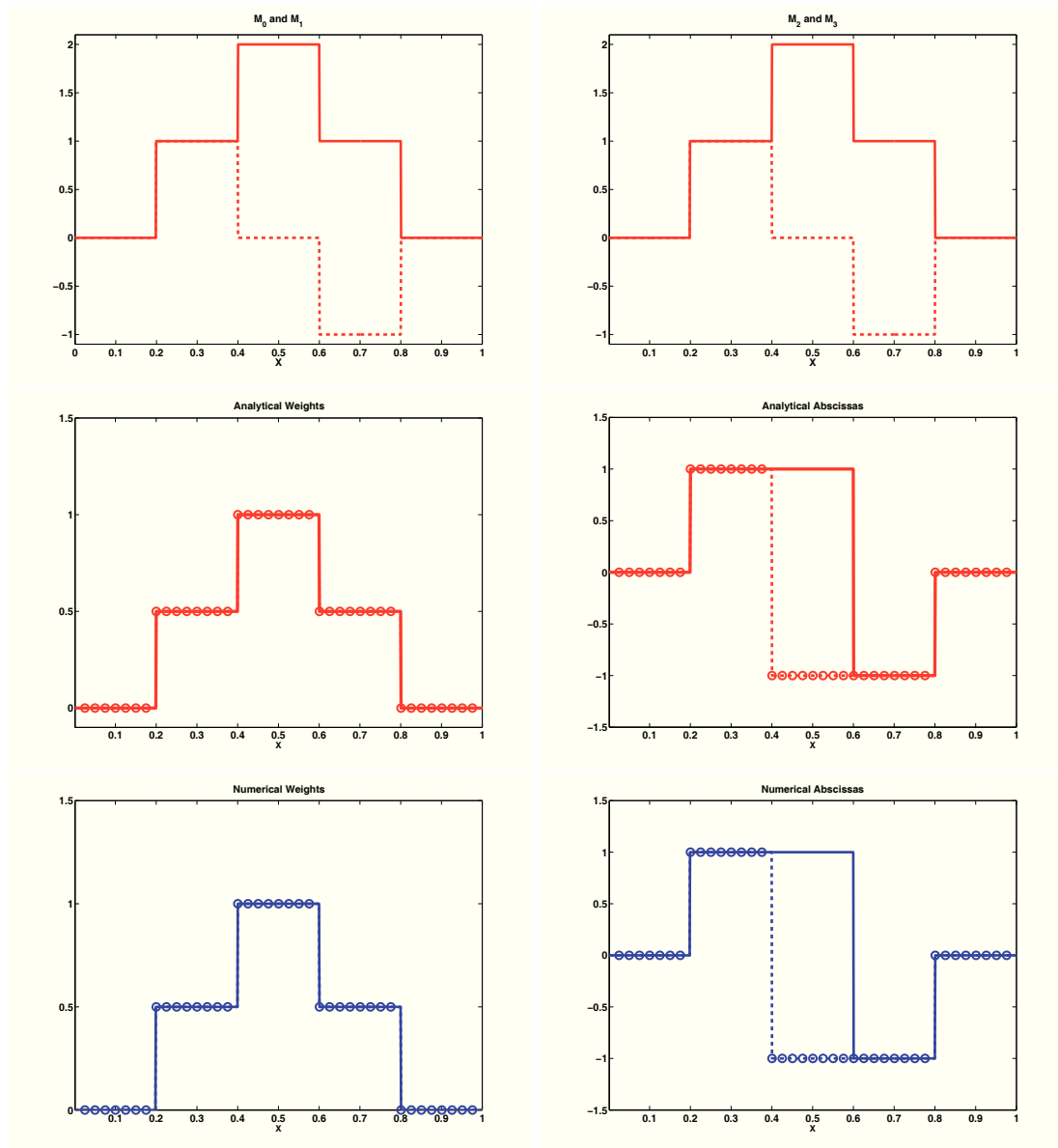


Figure 9.5: Numerical and analytical solution for the two particle packet case with  $n_L = n_R = 1$ , and  $U_L = 1$ ,  $U_R = -1$ . Results at  $t = 0.1$ . The red lines represent the analytical solution, the blue lines represent the numerical solution. The solid line corresponds to the higher abscissa, the dashed line with circle to the lower one. Top-left: Numerical results for  $M_0$  (solid line) and  $M_1$  (dashed line). Top-right: Numerical results for  $M_2$  (solid line) and  $M_3$  (dashed line). Middle-left: Analytical result for weights. Middle-right: Analytical results for abscissas. Bottom-left: Numerical results for weights. Bottom-right: Numerical results for abscissas. The computation is run in a 1000 cell grid, with  $CFL = 1$ .

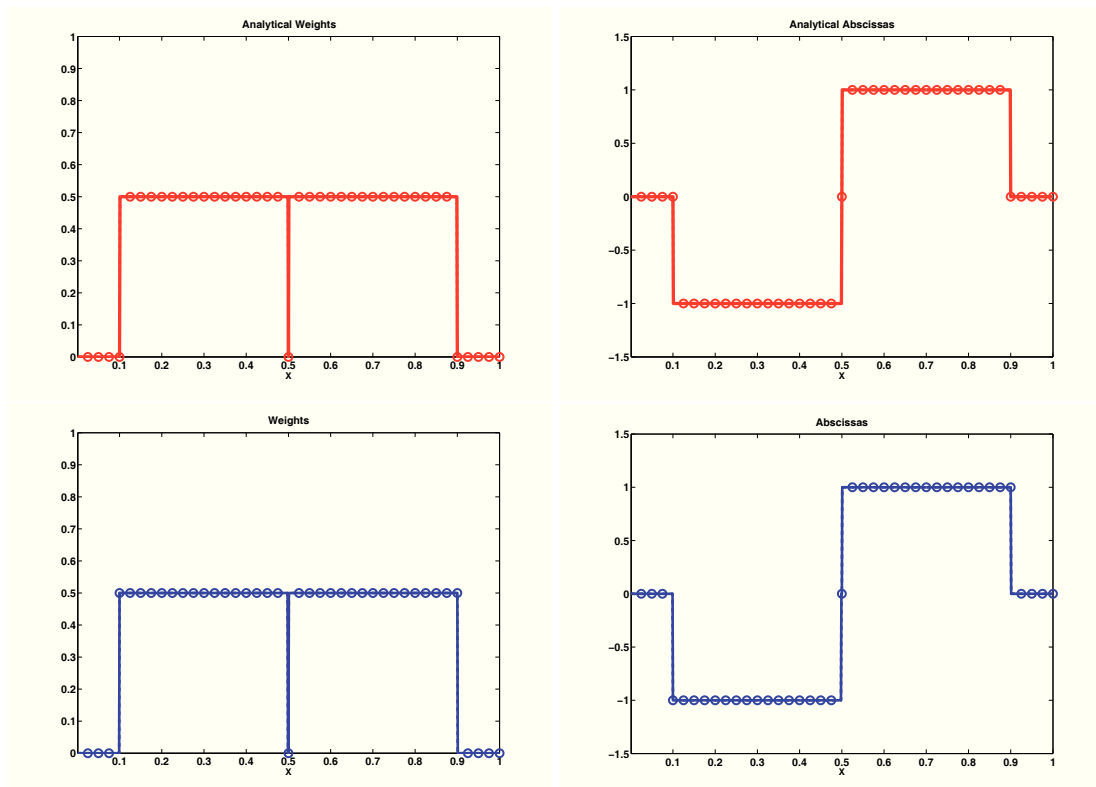


Figure 9.6: Numerical and analytical solution for the two particle packet case with  $n_L = n_R = 1$ , and  $U_L = 1$ ,  $U_R = -1$ . The red lines represent the analytical solution, the solid line corresponds to the higher abscissa, the dashed line with circles to the lower one. Results at time  $t = 0.4$ . Top-left: Analytical result for weights. Top-right: Analytical results for abscissas. Bottom-left: Numerical results for weights. Bottom-right: Numerical results for abscissas. The computation is run in a 1000 cell grid, with  $CFL = 1$ .

### Four packet collision

Figure 9.7 presents the initial conditions. Figures 9.8 and 9.9 present the numerical and analytical solutions respectively for the moments and the weights and abscissas. The computation is run with a 1000 cell grid on the spatial domain  $[0, 1]$ , at  $CFL = 1$ . Here, we observe the presence of two Dirac delta functions as already discussed in Section 9.2.5. We get a very good agreement between exact and numerical solutions for the moments, showing that the numerical solution converges to the analytical one. The disparities encountered between the analytical and numerical solution in the case of the weights and abscissas are due to the fact that the mapping  $\mathbf{U}(\mathbf{M})$  is discontinuous at the moment space border. In area of numerical diffusion ( $x \approx 0.22$  and  $x \approx 0.88$ ), when the dispersion  $e$  is under the threshold  $\epsilon_1$ , weights and abscissas are reconstructed as explained in section 2. Concerning the wave propagating at velocity 0.8, the change of weight, theoretically discontinuous, is actually smooth in the numerical case. This is due to the fact that the CFL number is based on the highest value of velocity, which is 1.2 in this studied case. Meanwhile, because of the conservation of the velocity moments, the numerical velocity jump (at  $x = 0.154$ ) happens before the analytical velocity jump (at  $x = 0.18$ ). One can here notice that the quadrature method provides the expected value of velocity in the numerical diffusion zones. The same explanation holds for the different velocity jump locations between the analytical and numerical solution at  $x = 0.82$  and  $x = 0.845$ . The same phenomenon is responsible for the disparities between the analytical and numerical solutions at the  $\delta$ -shocks locations, at  $x = 0.4$  and  $x = 0.6$ . Finally, the analytical and numerical waves propagating at velocity 1.2 coincide, since the CFL number, set at 1, is based on this velocity value. The velocity jumps of  $U_1$  and  $U_2$  observed at locations  $x = 0.22$  corresponds to the wave propagating at velocity 1.2 and separating the constants states ( $U_1 = 0.8, U_2 = 0$ ) and ( $U_1 = 1.2, U_2 = 0.8$ ). The fact that this wave leads to jump for both the abscissas is purely due to the adopted convention for the representation of  $U_1$  and  $U_2$ . The same explanation holds for the symmetric jump at location  $x = 0.78$ .

Figure 9.10 displays the final profile of the quantities  $\frac{q}{M_0 e}$  and  $\frac{q}{e^{3/2}}$  which we recall are respectively proportional to the product of weight and abscissa difference, and weight difference. Thus,  $\frac{q}{M_0 e}$  has significative values in areas where the weights and abscissa differential are important, whereas  $\frac{q}{e^{3/2}}$  reaches high value in areas where the weight ratio is important. Since in the domain, except for the singularities, the weights have the same value, both quantities are equal to zero. At the singularities, since the shocks concern one weight letting the other one unchanged, a weight difference is experienced. Therefore  $\frac{q}{e^{3/2}}$  has no zero values at singularities. And as the abscissas are different throughout the domain,  $\frac{q}{M_0 e}$  has also no zero values at singularities but is still bounded by the initial maximal difference of abscissas during the coupling of singularities and numerical diffusion.

We have thus provided numerical simulations in the two cases for which we have at our disposal an analytical entropic solution, either in the smooth case, or in the singular case where  $\delta$ -shock measure solutions are present. In the first case, the crossing of the two droplets monokinetic packets is very properly reproduced without numerical diffusion since we work at CFL one, even if this is not symptomatic of the numerical diffusion such methods will encounter with a first order method in realistic configurations [129]. In the second case, the numerical method is able to capture the creation of the measure singular solutions associated to the fact that we have limited the number of quadrature node to two and thus, as in the case of pressureless gas dynamics at a lower level, the proper physical solution, in the infinite Knudsen number limit, where the various droplet packets cross without interacting, differs from the entropic solution of the system of partial differential equations (9.11) obtained through the quadrature-based closure.

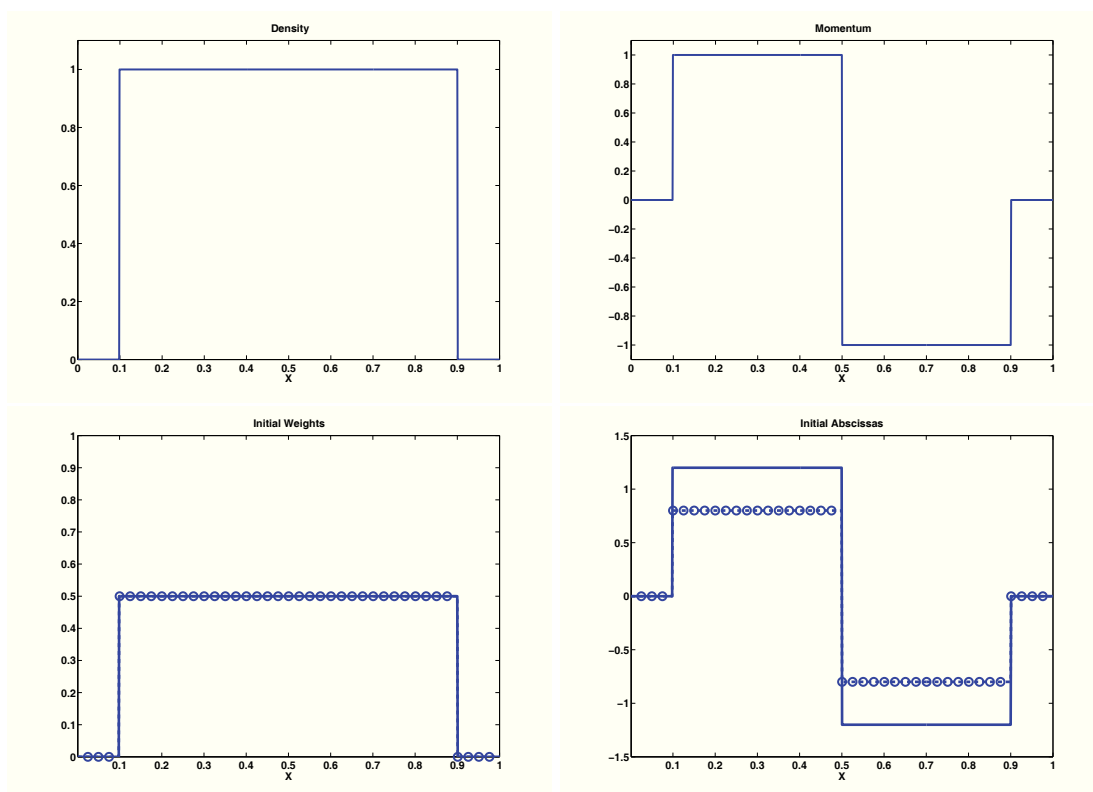


Figure 9.7: Initial conditions for the four particle packet case with  $n_L = n_R = 1$ , and  $U_1 = 1.2$ ,  $U_2 = 0.8$ . Top-left:  $M_0$ . Top-right:  $M_1$ . Bottom-left: weights. Bottom-right: abscissas. The solid line corresponds to the set  $(n_1, U_1)$ , and the dashed line with circles to the set  $(n_2, U_2)$ .

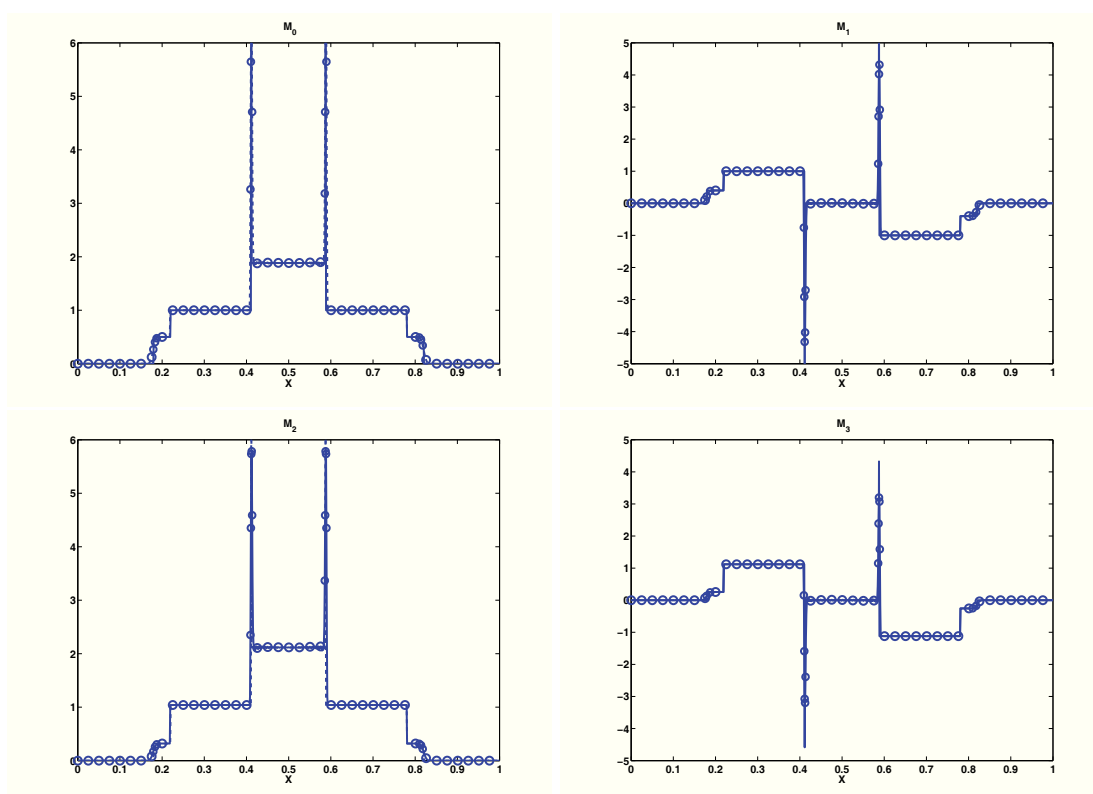


Figure 9.8: Numerical and analytical solutions for the four particle packet case with  $n_L = n_R = 1$ , and  $U_1 = 1.2$ ,  $U_2 = 0.8$ , at  $t = 0.1$ . Top-left:  $M_0$ . Top-right:  $M_1$ . Bottom-left:  $M_2$ . Bottom-right:  $M_3$ . The solid lines correspond to the analytical solution, the dashed lines with circles correspond to the numerical solution. The computation is run in a 1000 cell grid, with  $CFL = 1$ .

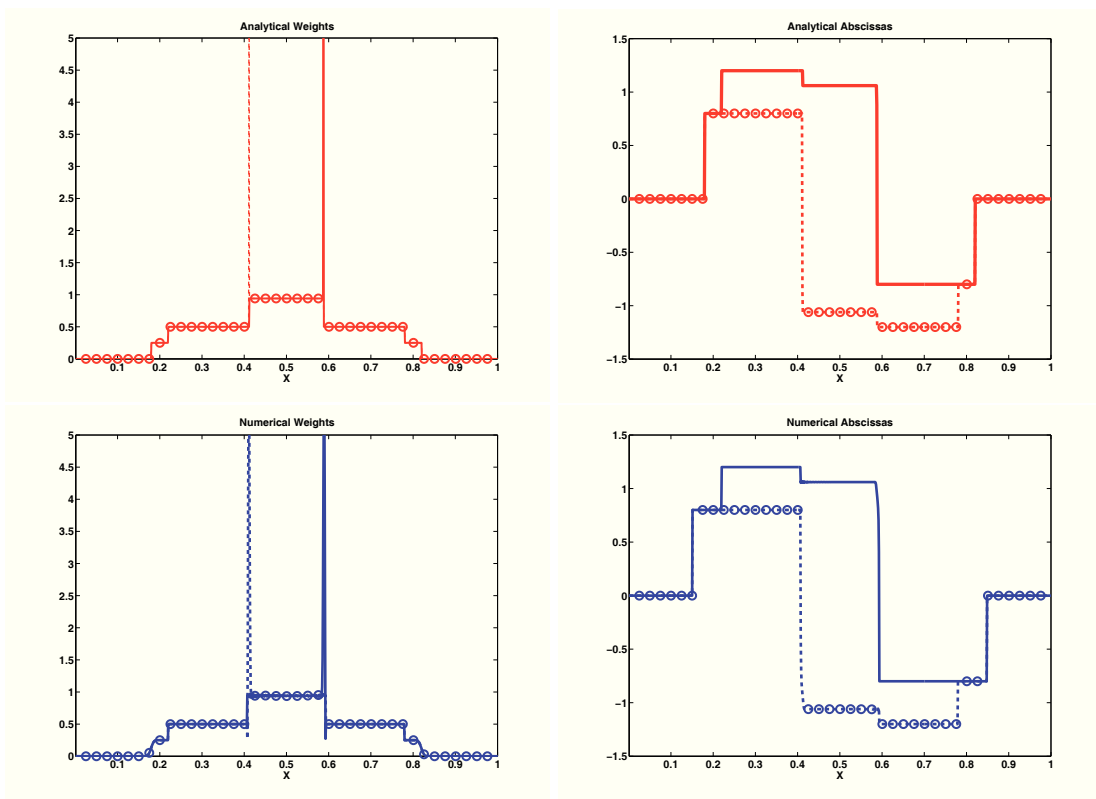


Figure 9.9: Numerical and analytical solutions for the four particle packet case with  $n_L = n_R = 1$ , and  $U_1 = 1.2$ ,  $U_2 = 0.8$ , at  $t = 0.1$ . Top-left: Analytical weights. Top-right: Analytical abscissas. Bottom-left: Numerical weights. Bottom-right: Numerical abscissas. The solid line corresponds to the set  $(n_1, U_1)$ , and the dashed line with circles to the set  $(n_2, U_2)$ . The computation is run in a 1000 cell grid, with  $CFL = 1$ .

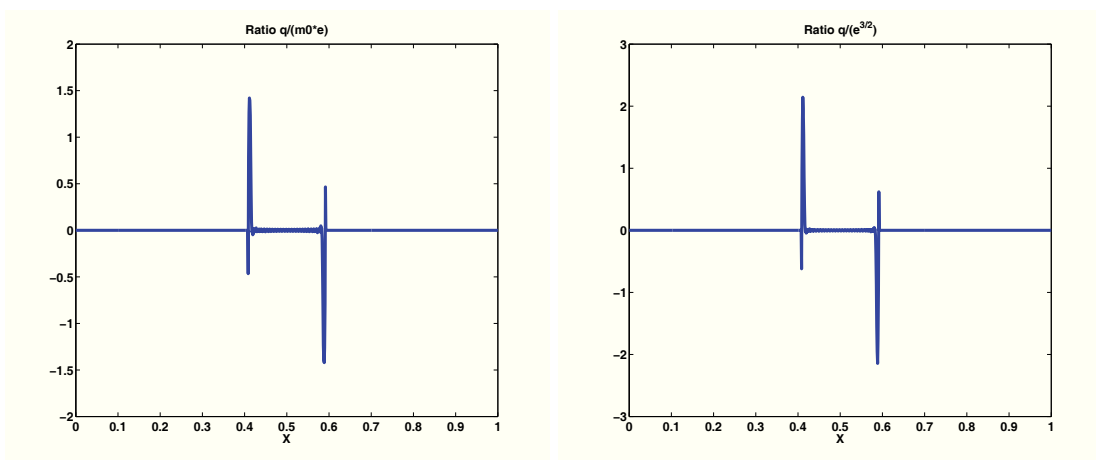


Figure 9.10: Four particle packet case, at time  $t = 0.1$ . Left: ratio  $q/(M_0e)$ . Right: ratio  $q/e^{3/2}$ .

### Free boundary case

The last test case assesses the numerical ability of the method to deal with the transition from the interior to the frontier of the moment space. The initial condition is explained in subsection 9.2.5.3. The ground difference with the first test case is that the transition between the two zones is smooth, and so the numerical strategy to account for this transition is of major importance. The analytical solution has been provided in subsection 9.2.5.3. For numerical simulations, the grid contains 400 cells, and the CFL number is set to 1. The computation is run until  $t = 0.2$ .

Results are displayed in Fig. 9.11. Let us first focus on the fronts present at  $x = 0.2$  and  $x = 0.9$  for the analytical solution. Since the CFL number is based on the highest velocity value, which is 2, the corresponding wave is not diffused at  $x = 0.9$ , contrary to the front located at  $x = 0.2$  corresponding to the square wave moving at velocity  $U_2 = 1$ . Note that in these areas,  $n_1 = n_2$ , since  $e = 0$  or  $e < \epsilon_1$ . The borders of these areas are clearly seen at  $x \approx 0.22$  and  $x = 0.8$ . The constant profiles for  $n_2$  and  $n_1$  observed respectively between  $x = 0.5$  and  $x = 0.7$  and between  $x = 0.5$  and  $x = 0.8$  correspond to the one observed in the analytical solution. In the area between  $x = 0.22$  and  $x = 0.5$ , the density profiles would be expected to be constant, with the same value as before. Instead of that, one observes a peak value for  $n_2$  and a low value for  $n_1$ , the sum  $n_1 + n_2$  begin constant. This results from a coupling between the quadrature method and numerical diffusion. Since the CFL is based on the velocity value  $u = 2$ , the computed upwind fluxes across interfaces do not contain all the particles of a cell, in the area between  $x = 0.22$  and  $x = 0.5$ . Therefore, a cell  $i$  at time  $t^n$  containing particles with velocity  $U_2 = 1$  and  $U_1 = 1 + 2\Delta_u$  contains, at time  $t^{n+1}$ , in addition to these last particles, some particles with velocity  $u = U_1 + \Delta_u$  coming from the cell  $i - 1$ . But the quadrature method projects this trimodal distribution onto a bimodal distribution. Since for  $x$  close to 0.22,  $U_1 \rightarrow U_2 = 1$ , the quadrature nodes are such that  $n_2 \approx 1$  with  $U_2 \approx 1$  and  $n_1 \ll 1$  with  $U_1 = 1 + \Delta_u$ . This effects also accounts for the small discontinuity of  $U_1$  seen at  $x = 0.22$ . It also explains the fact that  $U_2$  is not exactly equal to 1 between  $x = 0.3$  and  $x = 0.5$ , and the profile of  $U_2$  between  $x = 0.75$  and  $x = 0.8$  in a region where  $n_2 \ll n_1$ . Further and further from  $x = 0.22$  the density values tend to their analytical value. Finally, the undershoot of density value at  $x = 0.8$  is another consequence of numerical diffusion. This point marks the limit between the linear profile and the constant profile of  $U_2$ .

Figure 9.12 displays the profile of quantities  $\frac{q}{M_0 e}$  and  $\frac{q}{e^{3/2}}$  at time  $t = 0.2$ . First, it is important to note that the limitation on  $\frac{q}{M_0 e}$  with  $\eta = 2$  has no effect since the maximal value of  $|q/(M_0 e)|$  is exactly 1 from the numerical simulation. Let us underline that in the present case, the numerical scheme allows to preserve the proposed cone associated with a maximal distance between the abscissas which is also respected. Comparing the analytical value of  $|q/(M_0 e)|$  to the numerical resolution in Fig 9.12, it is instructive to observe that the numerical diffusion is creating zones where it can be far from zero, whereas it should be zero in the analytical solution. However, this is done in such a way as to preserve the maximal value foreseen as the maximal distance between the abscissa at time  $t = 0$  which is one. Let us also underline that we have rerun this case with various values of  $\epsilon_1$  varying from  $10^{-9}$  up to  $10^{-7}$  without any significant effect on the solution. It can also be noticed that the quantity  $q/e^{3/2}$  has large values in the regions of connection between the interior and the frontier of the moment space, but has no reason to be naturally limited as opposed to the previous quantity as it can be seen in Fig. 9.11-bottom left.

As a consequence, it can be seen that we have designed the proper theoretical setting for the transition from the interior of the moment space towards its frontier since the cone we have defined seems to be automatically preserved by the kinetic scheme we have used. Such a point would be worth a detailed study which is beyond the scope of the present paper.

In this section, we have extended the notion of entropic measure solution of quadrature-based moment method for kinetic equations. Such kinetic equations are frequently encountered in many application fields where a complex dynamics in phase space is involved. Following the contribution of [24] for the pressureless gas dynamics which is the one-node quadrature version of a more general system of conservation laws for quadrature-based moment models, we have been able to provide a few problem test-cases showing that the numerical solution of the resulting system of conservation laws through kinetic schemes reproduces the defined entropic solution as well as the proper theoretical setting for the

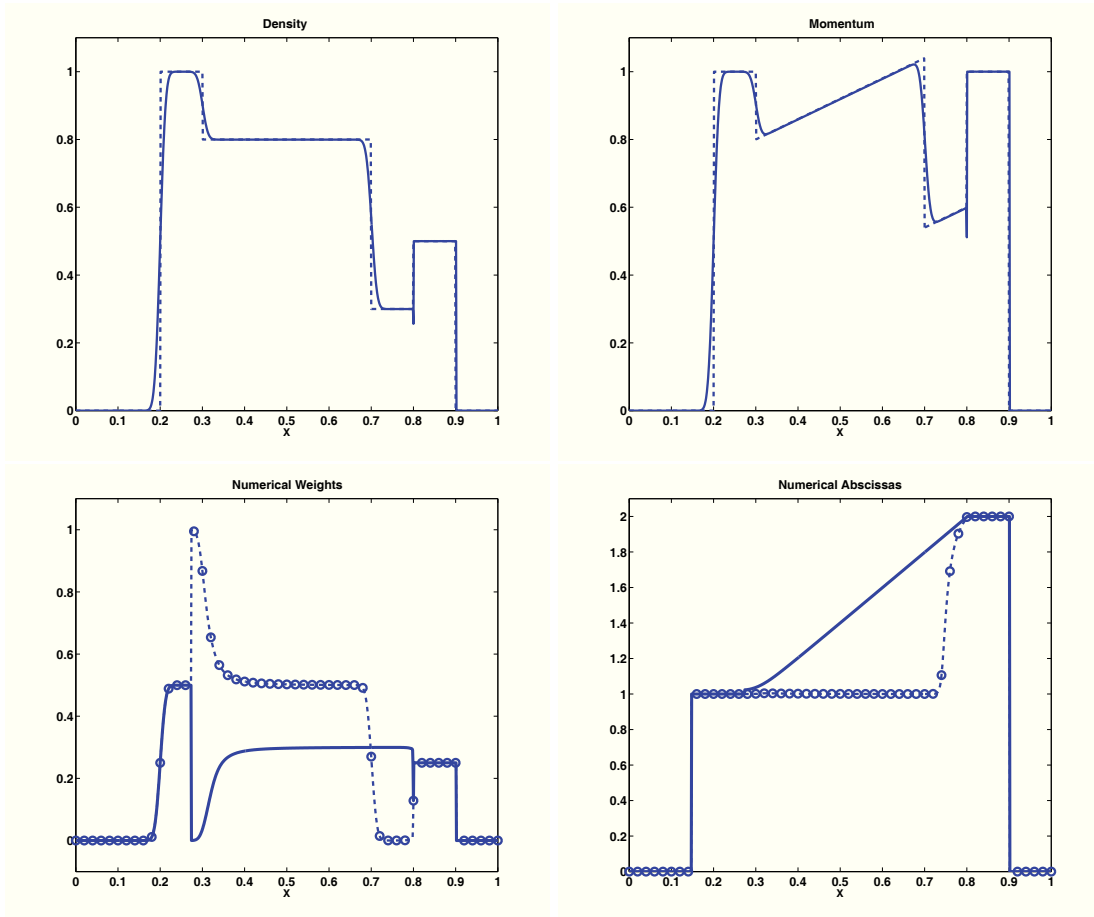


Figure 9.11: Moment dynamics in the context of a smooth transition between areas of null and non null dispersion, at time  $t = 0.2$ . Top-left:  $M_0$ . Top-right:  $M_1$ . The straight lines represent the analytical entropic solution, whereas the dashed lines represent the numerical solution. Bottom-left: weights. Bottom-right: abscissas. The solid line corresponds to the set  $(n_1, U_1)$ , and the dashed line with circles to the set  $(n_2, U_2)$ .

transition from the interior to the frontier of the moment space. It is an important point for the case of PTC where the solution remains smooth and where the scheme allows to describe the phase space dynamics properly as well as for cases where the complexity of the dynamics in phase space leads to generalized  $\delta$ -shocks, as observed for pressureless gas dynamics due to the weakly hyperbolic structure of the system of conservation laws. Two stumbling blocks still remains to be treated. First, we would need a uniqueness theory and a convergence analysis in a general framework in order to fully justify the use of the kinetic schemes for the simulation of such models. However, as explained already in [21], the framework of entropic solution is not sufficient in order to provide uniqueness since one can exhibit multiple entropic solutions for measure solutions. Let us underline that it is easy to construct the same type of measure solutions for system (9.12), which is the exact same collision case used by Bouchut, but with a motionless Dirac delta function in density localized at the collision point of the other two incoming “particles”. An infinite set of entropic solution can then be exhibited depending on the nature of the collision. As a consequence, it would be first useful to investigate such a point on the pressureless gas dynamics and then to extend it to the present system of higher order quadrature-based moment models. Besides, the construction of fully high order methods is still an open question and requires further developments. At last, let us mention that most of the results of the present paper do naturally extend to higher order



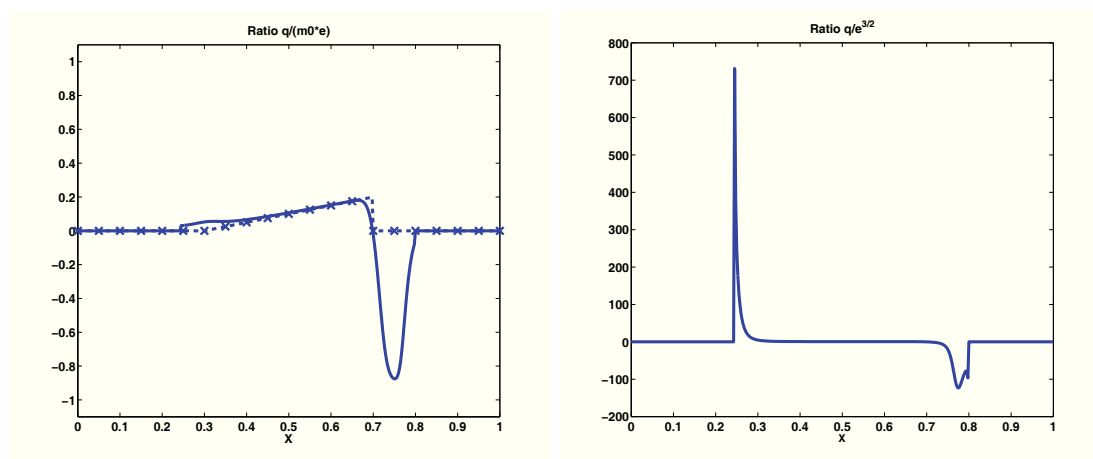


Figure 9.12: Moment dynamics in the context of a smooth transition between areas of null and non null dispersion, at time  $t = 0.2$ . Left: ratio  $q/(M_0 e)$ . The dashed line with crosses represents the analytical solution, whereas the solid line represents the numerical solution. Right: ratio  $q/e^{3/2}$ .

moment systems, but at the price of algebra complications. In fact, the key point lies in the extension of the proposed study of the behavior of the quadrature at the frontier of the moment space, namely when the two velocities  $U_1$  and  $U_2$  become equal. If we consider for instance the 6-moment model and assume that one of the three velocities  $U_1$ ,  $U_2$  and  $v_3$  is smooth while the other two become equal, we are in the same framework as in the present paper. But the case when the three velocities tend to be equal needs to be precised in a future work.

## 9.3 Extension to two-dimensions

### 9.3.1 Position of the problem

Here, we want to solve the advection part of system (9.9):

$$\partial_t(M_{l,m}) + \partial_x(M_{l+1,m}) + \partial_y(M_{l,m+1}) = 0, \quad 0 \leq l+m \leq 3, \quad (9.43)$$

by finding closure for  $M_{l+1,m}$  and  $M_{l,m+1}$ .

As noted in the introduction, closure methods can be found in the literature, such as the QMOM [175], or the DQMOM [159]. But, if algorithms used for the QMOM are efficient for one-dimensional systems, yet their extension to higher dimensions is less straightforward. For DQMOM, although it works well in most of the flow domain, it fails at PTC points, which is a problem that does not occur for quadrature-based moment methods. Quadrature-based moment methods distinguish themselves from other moment methods by the use of quadrature weights and abscissas to model unclosed terms in the moment transport equations. Thus, when developing a quadrature method, an important task is to define the algorithm for computing the weights and abscissas from the moments. The total number of nodes for a quadrature in  $N_{\text{dim}}$  dimensions is denoted by  $\beta$ . Let  $N_{\text{dim}}$  denote the number of phase space dimensions (which is in this case the number of physical space dimensions). Let  $\mathbf{V}_\beta = [(n_\alpha, \mathbf{u}_\alpha)]$  with  $\alpha \in (1, \dots, \beta)$  denote the set of weights and abscissas for the  $\beta$ -node quadrature approximation of  $f$ . Note that the vector of quadrature nodes  $\mathbf{V}_\beta$  contains  $(1 + N_{\text{dim}})\beta$  unknowns (i.e.  $\beta$  weights, and  $\beta N_{\text{dim}}$  component velocity vectors). To find the components of  $\mathbf{V}_\beta$ , we work with the velocity moments up to third order which are related to the quadrature weights and abscissas by:

$$M_{l,m} = \sum_{\alpha=1}^{\beta} n_\alpha U_{(\alpha)1}^l U_{(\alpha)2}^m. \quad (9.44)$$

In the following, since we work in two dimensions, so that  $N_{\text{dim}} = 2$ . As discussed in the beginning of this chapter, in two dimensions, the set of ten moments is defined by:

$$\mathbf{W}_2 = (M_{0,0}, M_{1,0}, M_{0,1}, M_{2,0}, M_{1,1}, M_{0,2}, M_{3,0}, M_{2,1}, M_{1,2}, M_{0,3}). \quad (9.45)$$

In the method we investigate, we assume that the number of quadrature nodes is the same for each and every direction, and is fixed at 2. Therefore, the total number of nodes in two dimensions is  $\beta = 4$ . The moment vector  $\mathbf{W}_2$  contains ten moments. On the other hand, 4 nodes, with three unknowns per node (one weight and two abscissas), leads to a total of twelve unknowns.

We denote by  $\mathcal{W}_2$  the set of third-order moments in two dimensions. Our purpose is to design a robust method for finding  $\mathbf{V}_\beta$  from  $\mathbf{W}_2$ . The inverse operation, finding  $\mathbf{W}_2$  from  $\mathbf{V}_\beta$  is Eq. (9.44), which is called *projection*, for reasons which will become apparent later. In general, it will not be possible to represent all possible moment sets in  $\mathcal{W}_2$  using weights and abscissas in  $\mathbf{V}_\beta$ . We will therefore define the set of representable moments as  $\mathcal{W}_2^\dagger \in \mathcal{W}_2$ .

### 9.3.2 Proposed quadrature method

#### 9.3.2.1 Cholesky decomposition

We begin to define the mean particle velocity vector:

$$\mathbf{u}_p = \begin{pmatrix} \frac{M_{1,0}}{M_0} \\ \frac{M_{0,1}}{M_0} \end{pmatrix}. \quad (9.46)$$

Besides, we define the relative velocity vector as

$$\mathbf{v} = \mathbf{u} - \mathbf{u}_p. \quad (9.47)$$

At equilibrium the velocity distribution function writes:

$$f(\mathbf{v}) = \frac{1}{(2\pi)\det(\boldsymbol{\sigma})} \exp\left[-\frac{1}{2}\mathbf{v}^T \boldsymbol{\sigma}^{-1} \mathbf{v}\right], \quad (9.48)$$

where the covariance matrix  $\boldsymbol{\sigma}$ , writes:

$$\boldsymbol{\sigma} = \begin{bmatrix} \sigma_{1,1} & \sigma_{1,2} \\ \sigma_{2,1} & \sigma_{2,2} \end{bmatrix}. \quad (9.49)$$

So  $\boldsymbol{\sigma}^{-1}$  writes :

$$\boldsymbol{\sigma}^{-1} = \frac{1}{\det(\boldsymbol{\sigma})} \begin{bmatrix} \sigma_{2,2} & -\sigma_{2,1} \\ -\sigma_{1,2} & \sigma_{1,1} \end{bmatrix}, \quad (9.50)$$

The coefficient of the covariance matrix are defined such that:

$$\sigma_{1,1} = \frac{M_{2,0}}{M_{0,0}} - u_{p,1}^2, \quad \sigma_{1,1} = \frac{M_{1,1}}{M_{0,0}} - u_{p,1}u_{p,2}, \quad (9.51)$$

$$\sigma_{1,2} = \frac{M_{1,1}}{M_{0,0}} - u_{p,1}u_{p,2}, \quad \sigma_{2,2} = \frac{M_{0,2}}{M_{0,0}} - u_{p,2}^2. \quad (9.52)$$

$$(9.53)$$

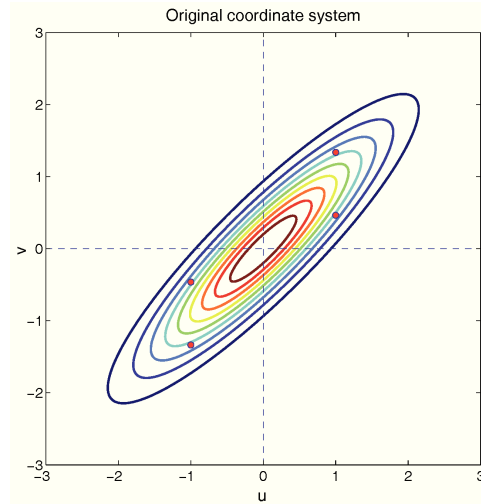


Figure 9.13: Lines of iso-probability of a Maxwellian velocity distribution in two dimensions. The red points represent quadrature nodes

The next step is to introduce a linear transformation  $\mathbf{L}$  to decompose  $\boldsymbol{\sigma}$ . The choice of the linear transformation is not unique, but for reasons that we will describe later, we choose to use a variation of the Cholesky decomposition defined such that  $\mathbf{L}^T \mathbf{L} = \boldsymbol{\sigma}$ , where  $\mathbf{L}$  is upper triangular:

$$\mathbf{L} = \begin{bmatrix} \sqrt{\sigma_{1,1}} & \frac{\sigma_{1,2}}{\sqrt{\sigma_{1,1}}} \\ 0 & \sqrt{\sigma_{2,2} - \frac{\sigma_{1,2}^2}{\sigma_{1,1}}} \end{bmatrix}. \quad (9.54)$$

With this choice we set  $\mathbf{B} = \mathbf{L}^T$  and introduce a two-component vector  $\mathbf{X} = [X_1, X_2]^T$  defined by

$$\mathbf{X} = \mathbf{B}^{-1}(\mathbf{v}), \quad \text{so that} \quad \mathbf{u} = \mathbf{B}\mathbf{X} + \mathbf{u}_p. \quad (9.55)$$

If we denote the first four moments of  $\mathbf{X}_i$  by  $m_{(i)k}$ ,  $k \in (0, 1, 2, 3)$ , then they are related to the velocity moments by

$$\begin{aligned} m_{(i)0} &= 1, \quad m_{(i)1} = 0, \quad m_{(i)2} = 1, \\ m_{(i)3} &= h_i(\mathbf{B}, \mathbf{u}_p, M_{30}/M_{00}, \dots, M_{03}/M_{00}), \end{aligned} \quad (9.56)$$

where  $h_i$  depends, in general, on all four third-order velocity moments [84].

Using the two-node quadrature formulas [84], the moments of  $X_i$  can be inverted for  $i \in (1, 2)$  to find  $(n_{(i)1}, n_{(i)2}, X_{(i)1}, X_{(i)2})$ :

$$\begin{aligned} n_{(i)1} &= 0.5 + \gamma_i, \quad X_{(i)1} = -\left(\frac{1 - 2\gamma_i}{1 + 2\gamma_i}\right)^{1/2}, \\ n_{(i)2} &= 0.5 - \gamma_i, \quad X_{(i)2} = \left(\frac{1 + 2\gamma_i}{1 - 2\gamma_i}\right)^{1/2}, \end{aligned} \quad (9.57)$$

where  $(-1/2 < \gamma_i < 1/2)$

$$\gamma_i = \frac{m_{(i)3}/2}{[(m_{(i)3})^2 + 4]^{1/2}}. \quad (9.58)$$

The four-node quadrature approximation is then defined using the tensor product of the one-dimensional abscissas as

$$\mathbf{V}_4^* = [(n_1^*, X_{(1)1}, X_{(2)1}), (n_2^*, X_{(1)1}, X_{(2)2}), (n_3^*, X_{(1)2}, X_{(2)1}), (n_4^*, X_{(1)2}, X_{(2)2})], \quad (9.59)$$

where the (as yet) unknown weights  $n_\alpha^*$  must obey the linear equations [84]

$$\begin{aligned} n_1^* - n_4^* &= n_{(1)1} - n_{(2)2}, \\ n_1^* + n_4^* &= n_{(2)2}, \\ n_3^* + n_4^* &= n_{(1)2}. \end{aligned} \quad (9.60)$$

The right-hand sides of Eq. (9.60) are known, and have the property that  $n_{(1)1} + n_{(1)2} = 1$  and  $n_{(2)1} + n_{(2)2} = 1$ .

The linear system in Eq. (9.60) has rank three. We must therefore add another linear equation to define the four weights. For this purpose, we will use the cross moment  $M_{(1)2} = \langle X_1 X_2 \rangle = 0$ , the value of which follows from the definition of  $\mathbf{B}$ . In terms of the weights and abscissas in Eq. (9.59), we have

$$X_{(1)1}X_{(2)1}n_1^* + X_{(1)1}X_{(2)2}n_2^* + X_{(1)2}X_{(2)1}n_3^* + X_{(1)2}X_{(2)2}n_4^* = 0. \quad (9.61)$$

The resulting system can be inverted analytically to find

$$\begin{aligned} n_1^* &= n_{(1)1}n_{(2)1} = (0.5 + \gamma_1)(0.5 + \gamma_2), \\ n_2^* &= n_{(1)1}n_{(2)2} = (0.5 + \gamma_1)(0.5 - \gamma_2), \\ n_3^* &= n_{(1)2}n_{(2)1} = (0.5 - \gamma_1)(0.5 + \gamma_2), \\ n_4^* &= n_{(1)2}n_{(2)2} = (0.5 - \gamma_1)(0.5 - \gamma_2). \end{aligned} \quad (9.62)$$

Note that these weights are always non-negative.

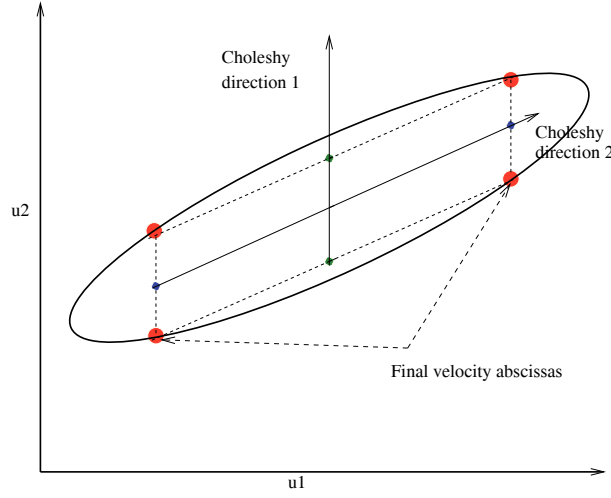


Figure 9.14: Principle of the Cholesky decomposition. The final quadrature nodes, in red, are tensorial product of the one-dimensional quadrature nodes (in green) determined in each Cholesky direction.

In summary, the weights and abscissas in  $\mathbf{V}_4$  are found from those in  $\mathbf{V}_4^*$  using Eq. (9.55) to invert the abscissas and  $n_\alpha = M_{0,0}n_\alpha^*$ . The eight moments controlled in this process are

$$\mathbf{W}_2^* = (M_{0,0}, M_{(1)0}, M_{(0)1}, M_{(2)0}, M_{(1)1}, M_{(0)2}, M_{(3)0}, M_{(0)3}).$$

Note that the two third-order moments in  $\mathbf{W}_2^*$  are a linear combination of the four third-order moments in  $\mathbf{W}_2$ . Hence,  $\mathbf{W}_2^*$  is a subset of  $\mathbf{W}_2$  containing eight independent moments (instead of ten). However, given moments in  $\mathbf{W}_2$  it is straightforward to project them (using the weights and abscissas) into  $W^{2\dagger}$ , i.e., the eight-dimensional moment subspace that can be represented by  $\mathbf{V}_4$  is  $W^{2\dagger}$ . The overall procedure can be represented as [84]

$$\mathbf{W}_2 \rightarrow \mathbf{W}_2^* \leftrightarrow \mathbf{V}_4^* \leftrightarrow \mathbf{V}_4 \leftrightarrow \mathcal{W}_2^\dagger \subset \mathcal{W}_2,$$

where a projection step is used to define  $W^{2\dagger}$ .

### 9.3.2.2 Ability to treat areas of null temperature

In the decomposition realized in Section 9.3.2 the matrix  $\mathbf{L}$  is implicitly assumed to be triangular, i.e.  $\sigma_{1,2}^2 < \sigma_{1,1}\sigma_{2,2}$ . In this section, a quadrature method is used in cases where  $\sigma_{1,2}^2 = \sigma_{1,1}\sigma_{2,2}$  so that  $\mathbf{L}$  becomes singular. In such cases, since the Cholesky decomposition is not possible, the covariance matrix  $\boldsymbol{\sigma}$  is diagonalized. We distinguish between two different cases when the velocity covariance matrix becomes singular: (i) the singularity occurs in one of the two principal directions (i.e.,  $\sigma_{1,1} = 0$  or  $\sigma_{2,2} = 0$ ), or (ii) it occurs in a non-principal direction. If the singularity occurs in a principal direction (for example let us choose  $x_1$ ), then the diagonalization is trivial. A one-dimensional quadrature is performed on the moments in direction  $x_2$  [84]. In direction  $x_1$ , one weight is set to one in order to conserve the droplet mass, while the other weight and the abscissas are null. If the singularity does not occur in a principal direction, the general relationship deduced from the fact that the velocity covariance matrix is singular is  $\sigma_{1,2}^2 = \sigma_{1,1}\sigma_{2,2}$  with  $\sigma_{1,1} \neq 0$  and  $\sigma_{2,2} \neq 0$ . Letting  $\rho = \sigma_{1,1}/\sigma_{1,2}$ , the covariance matrix can be written as

$$\boldsymbol{\sigma} = \sigma_{1,2} \begin{bmatrix} \rho & 1 \\ 1 & 1/\rho \end{bmatrix}. \quad (9.63)$$

The eigenvalues of  $\boldsymbol{\sigma}$  are  $\lambda_1 = \sigma_{1,1} + \sigma_{2,2}$  and  $\lambda_2 = 0$ . The inverse transformation matrix for this case is

$$\mathbf{B}^{-1-1} = \frac{1}{\alpha} \begin{bmatrix} \rho & 1 \\ -1 & \rho \end{bmatrix}. \quad (9.64)$$

The parameter  $\alpha$  is determined by the fact that  $m_1^2 = 1$  in order to use Eq. (9.57) in the direction associated with eigenvalue  $\lambda_1$ . Hence it comes that  $\alpha^2 = (\rho\sqrt{\sigma_{1,1}} + \sqrt{\sigma_{2,2}})^2$ , so that  $\alpha = |\rho\sqrt{\sigma_{1,1}} + \sqrt{\sigma_{2,2}}|$ . It has though to be distinguished between the cases where  $\rho > 0$  and  $\rho < 0$ , so that  $\alpha$  eventually writes:

$$\alpha = \frac{\sigma_{1,1} + \sigma_{2,2}}{\sqrt{\sigma_{2,2}}}, \quad \rho > 0,$$

$$\alpha = \frac{|\sigma_{1,1} - \sigma_{2,2}|}{\sqrt{\sigma_{2,2}}}, \quad \rho < 0. \quad (9.65)$$

$$(9.66)$$

A one-dimensional quadrature is then performed on the moments in this direction [84]. Similar to the first case, in the orthogonal direction, in order to conserve the droplet mass, one weight is set to one, the other weight and the abscissas are null. The weights and abscissas in the canonical basis are defined using the relation  $\mathbf{u} = \mathbf{B}\mathbf{X} + \mathbf{u}_p$ .

### 9.3.3 Discussion of the method relatively to other possible solutions

#### 9.3.3.1 Comparison of the Cholesky decomposition to other methods

In the two-node quadrature method of [56, 57], a different approach was used to fix the weights and abscissas. Essentially, the different lies in selecting the moments that are controlled. In [56, 57], the six moments (in two dimensions):

$$(M_{0,0}, M_{1,0}, M_{0,1}, M_{2,0}, M_{0,2}, M_{3,0} + M_{0,3}), \quad (9.67)$$

were used. Note that this moment set does not include cross moments of second order, i.e  $M_{1,1}$ . In contrast, in the formulation presented previously the covariance matrix is exactly reproduced. This of course comes at the expense of transporting more moments (ten instead of six). Note that in the case of [56, 57] the number of moments is equal to the number of unknown weights and abscissas. It might be argued that the new method could be improved for  $N_{\text{dim}} > 1$  because the number of moments controlled is less than the number of unknowns. Like wise, the eight moments in  $\mathbf{W}_2^*$  can be augmented by four additional moments:  $M_{(2)1}, M_{(1)2}, M_{(3)1}, M_{(1)3}$  to form an optimal moment set for computing  $\mathbf{V}_4^*$ . In practice, the use of the optimal moment sets introduces two new issues. First, the weights and abscissas must be found numerically by solving a nonlinear system of equations that can be poorly conditioned. Second, the optimal moment sets contain fourth and fifth order moments, all of which would have to be added to  $\mathbf{W}_2$ , i.e more moment transport equations are needed.

The use of optimal moment set has been tested in [84], where it was found that in most cases considered, the nonlinear solver was able to converge (albeit very slowly), but not always. The non-convergence cases typically have weights that are very unequal. However, it was not possible to predict in advance which moment sets would not converge. In all likelihood, the convergence problems will be more acute for  $N_{\text{dim}} = 3$  given the larger number of moments in the optimal set that are not controlled by the new method. Thus, given that the computational cost is orders of magnitude larger and convergence is not guaranteed, it is unlikely that a nonlinear solver will provide a computationally efficient method for inverting moment sets. This conclusion is consistent with the findings of [232]. In general, since moment inversion in one-dimensional is well established and reliable [175], it will be much more fruitful to increase the number of nodes and the order of moments (i.e computing  $\beta = 3^{N_{\text{dim}}}$  nodes requires fifth-order moments) to achieve greater accuracy.

Moreover, it can be noted that quadrature-based moment closures bear some resemblance to discrete velocity models [29, 93, 190] and to the Lattice-Boltzmann method (LBM) [90, 140]. However, the differences are significant. In LBM the discretizations of velocity space, physical and time are strongly coupled and determine the numerical methods and properties, while quadrature-based moments methods do not directly imply a physical space and time discretization scheme. This can be seen from the

fact that the moment equations closed by quadrature are still written as continuous functions of physical space and time. The principal similarity between quadrature methods and LBM is that both represent velocity phase space by a discrete set of velocities. However, a very significant difference between the two methods is that in LBM the discrete velocities are fixed, while in quadrature methods they are variable fields that vary in space and time according to the local flow physics (the velocities moments). Another difference is the number of unknowns available to control the moments. In LBM, only the weights are used to construct a linear mapping into the moments and so, the maximum number of moments that can be controlled is equal to the number of weights. In contrast, we have seen that by using quadrature four velocity abscissas could, in principle, control twelve moments if all the weights and abscissas were allowed to vary. However, because of the difficulty with inverting the nonlinear mapping between the moments and the quadrature nodes, the full quadrature procedure is untractable. Nevertheless, the partial quadrature method presented here still allows us to control eight moments with only four nodes.

Finally, it can be noticed that the moment-inversion method proposed here is very similar in spirit to the method proposed by [232] for aerosol applications with passive transport of a distribution function. The main difference is that they defined the linear transformation matrix  $\mathbf{B}$  in terms of the eigenvectors of the covariance matrix. In our case, using a decomposition in terms of eigenvectors would lead to  $\mathbf{B} = [\mathbf{eig}_1^T, \mathbf{eig}_2^T]$ , with  $\mathbf{eig}_1$  and  $\mathbf{eig}_2$ , the eigenvectors, writing:

$$\mathbf{eig}_1 = \begin{pmatrix} \frac{\sigma_{1,1} - \sigma_{2,2} - \sqrt{(\sigma_{1,1} - \sigma_{2,2})^2 + 4\sigma_{1,2}^2}}{2} \\ \sigma_{1,2} \end{pmatrix}, \quad (9.68)$$

(9.69)

$$\mathbf{eig}_2 = \begin{pmatrix} \sigma_{1,2} \\ \frac{\sigma_{2,2} - \sigma_{1,1} + \sqrt{(\sigma_{1,1} - \sigma_{2,2})^2 + 4\sigma_{1,2}^2}}{2} \end{pmatrix}. \quad (9.70)$$

(9.71)

This decomposition has been tested in [84]. However, because the velocity is a dynamic variable, i.e the space fluxes are computed using the velocity abscissas, the properties of the eigenvectors make them a poor choice. The fundamental difficulty is the fact that the eigenvectors of  $\boldsymbol{\sigma}$  do not vary smoothly with its components. In other words, small changes in the correlation structure cause the orientation of the eigenvectors to jump in a discontinuous manner. Thus, at two neighboring spatial locations, the resulting velocity abscissas can be completely different, even though the moments are continuous. As a result, the fluxes computed from the abscissas are then discontinuous, leading to random fluctuations in the moments. In contrast, the Cholesky matrix  $\mathbf{L}$  varies smoothly with the components of  $\boldsymbol{\sigma}$  and, hence, the fluxes are well behaved.

### 9.3.3.2 Comparison between the different types of quadrature using a Cholesky decomposition

The robustness of the quadrature-based moment method relative to other closure methods has been discussed in the previous paragraph. Nonetheless the Cholesky matrix is dependent on the ordering of the covariance matrix, and is thus different for each of the two permutations (in two dimensions) of the coordinates.

Indeed, the square root matrix of  $\boldsymbol{\sigma}$ ,  $\mathbf{L}$ , writes:

$$\mathbf{L} = \begin{bmatrix} \sqrt{\sigma_{1,1}} & \frac{\sigma_{1,2}}{\sqrt{\sigma_{1,1}}} \\ 0 & \sqrt{\sigma_{2,2} - \frac{\sigma_{1,2}^2}{\sigma_{1,1}}} \end{bmatrix}. \quad (9.72)$$

But if the axis system changes, i.e if we permute the x-axis with the y-axis, then the covariance matrix writes

$$\boldsymbol{\sigma}' = \mathbf{P}\mathbf{L}\mathbf{P} = \begin{bmatrix} \sigma_{2,2} & \sigma_{1,2} \\ \sigma_{1,2} & \sigma_{1,1} \end{bmatrix}, \quad (9.73)$$

where  $\mathbf{P}$  denotes the permutation matrix in two dimensions

So  $\mathbf{L}$  is then

$$\mathbf{L}' = \begin{bmatrix} \sqrt{\sigma_{2,2}} & \frac{\sigma_{1,2}}{\sqrt{\sigma_{2,2}}} \\ 0 & \sqrt{\sigma_{1,1} - \frac{\sigma_{1,2}^2}{\sigma_{2,2}}} \end{bmatrix}. \quad (9.74)$$

If we note  $\mathbf{B} = \text{chol}(\boldsymbol{\sigma})$ , then  $\mathbf{B}' = \text{chol}(\mathbf{P}\boldsymbol{\sigma}\mathbf{P})$ . Besides, since  $\mathbf{L} = \mathbf{B}^T\mathbf{B}$ , it is straightforward to see that  $\mathbf{B}'\mathbf{P}$  is also a Cholesky matrix for  $\mathbf{L}$ , but with  $\mathbf{B}'\mathbf{P} \neq \mathbf{B}$ . Consequently, the decomposition frame differs according to the axis permutation chosen (in two dimensions there are two possible permutations, in three dimensions there are six possible permutations). In essence, one direction is chosen as the principal direction (which is the first vector here). Therefore, the weights and abscissas reconstruction relies on the choice for the Cholesky decomposition. It would thus be desirable to replace  $\mathbf{L}$  with a permutation-invariant linear transform.

Secondly, as shown in Section 9.3, all the moments of  $\mathcal{W}_2$  are not always reached by the Cholesky decomposition. Indeed, the quadrature method only uses two linear combinations of the four third order moments, and therefore, the weights and abscissas reach the moments in  $\mathcal{W}_2^*$  which is a subspace of  $\mathcal{W}_2$ . The quadrature method is exact up to second order moment. In the case of an equilibrium distribution all the third order moments are null, and the quadrature method is exact for all the moments in  $\mathbf{W}_2$ . But in cases where the distribution is different from an equilibrium distribution, then some errors occur on the third order moments. Certain methods derived from the Cholesky decomposition have been devised to address these two difficulties, and are explained here.

The purpose of this paragraph is to present the tentative methods designed in order to address these problems.

### 9.3.3.3 Symmetric Cholesky method

The basic idea of this method comes from the following statement. If the Cholesky matrix considers a principal direction, for example say  $e_x$ , through a permutation of axis, it will then consider  $e_y$  as the principal direction. The next step is to compute two sets of weights and abscissas,  $\mathbf{V}_\beta$  and  $\mathbf{V}'_\beta$ , derived from each permutation of the axis respectively. In  $n$  dimensions, there are  $n!$  possible permutations. We get now a global set of  $2n$  weights and abscissas,  $\mathbf{V}_\beta = [(\frac{1}{2}(n_\alpha + n'_\alpha), \frac{1}{2}(\mathbf{u}_\alpha + \mathbf{u}'_\alpha))]$ . This method amounts to compute arithmetic means of the nodes given by each of the axis permutation, as we can see on the following illustration.

Since no direction is privileged any more, this method enables to preserve the isotropy of a configuration, see Section 9.6. But when the distribution is no longer gaussian, an error still occurs on the third order moments. That is not surprising as nothing was done to address this problem. Moreover, this method is no more a projection like the Cholesky method.



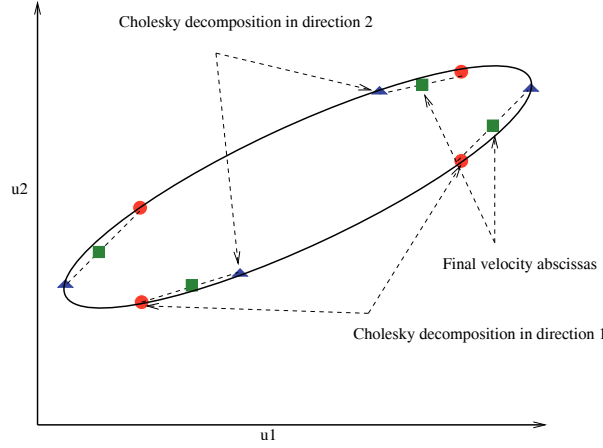


Figure 9.15: Symmetric Cholesky decomposition. The final quadrature nodes, green squares, are averaged from the nodes of the Cholesky decompositions performed in direction  $x$ , red circles, and direction  $y$ , blue triangles

### 9.3.3.4 Symmetric optimised Cholesky method

In the symmetric velocity-moment inversion algorithm, two sets of velocity weights and abscissas are generated, one for each permutation of the  $2 \times 2$  covariance matrix, each permutation having weight  $\alpha = \frac{1}{2}$ . But in the symmetric optimised Cholesky method presented here, these weights can be modified by a factor  $\beta_j$  to capture the non equilibrium in the third order moments.

For each permutation, the quadrature representations of these moments are:

$$\overline{M_{j,l,m}} = \sum_{\alpha=1}^4 n_{jq} U_{j,\alpha,1}^l U_{j,\alpha,2}^m. \quad (9.75)$$

For each permutation  $j$ , only two linear combinations of the third order moments are exactly reproduced. Thus, we will modify the permutation weights using  $\beta_j$  to minimize the quadrature error in the third order moments.

We define the quadrature errors in the third order moments:

$$N_{lm} = M_{l,m} - \frac{1}{2}(\overline{M_{1,l,m}} + \overline{M_{2,l,m}}). \quad (9.76)$$

The factor of  $1/2$  in the second term on the right hand sides of these expressions is the isotropic weight. In order to minimise the error, we will introduce the non equilibrium weights  $\beta_j$ . The latter are found by minimizing the following constrained objective function:

$$\Phi(\beta_1, \beta_2, \lambda) = \epsilon(\beta_1^2 + \beta_2^2) + \sum_{l=0, m=3-l}^3 (\beta_1 \overline{M_{1,l,m}} + \beta_2 \overline{M_{2,l,m}} - N_{lm}) - \lambda(\beta_1 + \beta_2), \quad (9.77)$$

where  $\lambda$  is the Lagrange multiplier that constrains solutions to obey  $\beta_1 + \beta_2 = 1$ . The term involving  $\epsilon$  is needed to treat the special case where all of the differences between the moments computed from 9.76 for the two permutations are null. The solution to this minimization problem yields

$$\beta_1 = \frac{A}{2\epsilon + \beta}, \beta_2 = -\beta_1, \quad (9.78)$$

where

$$\begin{aligned} A &= \sum_{l=0, m=3-l}^3 N_{lm} (\overline{M_{1,lm}} - \overline{M_{2,lm}}), \\ B &= \sum_{l=0, m=3-l}^3 (\overline{M_{1,lm}} - \overline{M_{2,lm}})^2. \end{aligned} \quad (9.79)$$

This solution is valid as long as  $0 \leq \beta_j + 1/2 \leq 1$ . Otherwise,  $\beta_1 = \text{sgn}A/2$  and  $\beta_2 = -\text{sgn}A/2$ . Note that the limits on  $\beta_j$  can be achieved by defining.

$$\epsilon = \max(\epsilon_0, |A| - B/2), \quad (9.80)$$

where  $\epsilon_0$  is needed for the case  $A = B = 0$ .

This method reduces the error on third order moments, but the computational cost is quite high. For example, for a  $50 \times 50$  mesh, the computation lasts twice as long as with the simple Cholesky method. Besides, the operation we do with this method is not a projection like the Cholesky method. Indeed, the set of abscissas obtained is not stable through the projection-inversion algorithm. This means that if we apply the projection-inversion to a set of weights and abscissas, the resulting weights and abscissas are different. Actually, the nodes converge to a set of nodes of an equilibrium distribution. This leads to unaccurate results if sub time steps are involved, which makes the set of nodes evolve artificially.

### 9.3.4 Kinetic-based numerical scheme

The numerical scheme for physical transport of the velocity moments is presented here. It is based on a dimensional splitting, so that the idea of the scheme presented in Section 9.2.6 can be reused here. The dynamic system for advection reads:

$$\partial_t \mathbf{W} + \partial_x \mathbf{H}(\mathbf{W}) = 0, \quad (9.81)$$

where

$$\mathbf{W} = \begin{pmatrix} M_{0,0} \\ M_{l,m}^1 \\ M_{l,m}^2 \\ M_{l,m}^3 \end{pmatrix}, \quad \mathbf{H}(\mathbf{W}) = \begin{pmatrix} M_{l+1,m}^1 \\ M_{l+1,m}^2 \\ M_{l+1,m}^3 \\ M_{l+1,m}^4 \end{pmatrix}, \quad (9.82)$$

Defining  $\mathbf{W}_i$  as the mean value of  $\mathbf{W}$  in the cell  $i$ , a fractional two-step, first-order explicit, finite volume scheme for Eq. (9.43) reads:

$$\mathbf{W}_i^{n+1} = \mathbf{W}_i^n - \frac{\Delta t}{\Delta x} [G(\mathbf{W}_i^n, \mathbf{W}_{i+1}^n) - G(\mathbf{W}_{i-1}^n, \mathbf{W}_i^n)], \quad (9.83)$$

where  $G$  is the corresponding numerical flux function. In this context, for advection in the first direction, it is natural to adopt the following expression for the numerical flux function

$$G(\mathbf{W}_{left}, \mathbf{W}_{right}) = Q^+(\mathbf{W}_{left}) + Q^-(\mathbf{W}_{right}), \quad (9.84)$$

with

$$Q^+(\mathbf{W}_{left}) = \sum_{\alpha=1}^{\beta} (n_{\alpha} \max(0, U_{(\alpha)1}))_{left} \begin{pmatrix} 1 \\ U_{(\alpha)1}^l U_{(\alpha)2}^m, & l+m=1 \\ U_{(\alpha)1}^l U_{(\alpha)2}, & l+m=2 \\ U_{(\alpha)1}^l U_{(\alpha)2}^m, & l+m=3 \end{pmatrix}_{left}, \quad (9.85)$$

and

$$Q^-(\mathbf{W}_{right}) = \sum_{\alpha=1}^{\beta} (n_{\alpha} \min(0, U_{(\alpha)1}))_{right} \begin{pmatrix} 1 \\ U_{(\alpha)1}^l U_{(\alpha)2}^m, & l+m=1 \\ U_{(\alpha)1}^l U_{(\alpha)2}^m, & l+m=2 \\ U_{(\alpha)1}^l U_{(\alpha)2}^m, & l+m=3 \end{pmatrix}_{right}. \quad (9.86)$$

Note that although these expressions have been written for fluxes in the  $x$  direction, the extension to other directions is straightforward. This transport scheme is directly implemented in the MUSES3D code.

## 9.4 Treatment of collision and drag terms

Considering now the part of system (9.9) involving the drag and collision terms:

$$\begin{aligned} d_t(M_{0,0}) &= 0, \\ d_t(M_{l,m}) &= D_{l,m}^1, \quad l+m=1, \\ d_t(M_{l,m}) &= D_{l,m}^2 + C_{l,m}^2, \quad l+m=2, \\ d_t(M_{l,m}) &= D_{l,m}^3 + C_{l,m}^3, \quad l+m=3, \end{aligned} \quad (9.87)$$

where

$$C_{l,m}^2 = \frac{1}{\text{Kn}} \left( \sigma_{eq} \frac{|l-m|}{2} - \sigma(l,m) \right), \quad (9.88)$$

where  $\sigma(l,m)$  is defined such as

$$\begin{aligned} \sigma(2,0) &= \sigma_{1,1}, \\ \sigma(0,2) &= \sigma_{2,2}, \\ \sigma(1,1) &= \sigma_{1,2} = \sigma_{2,1}, \end{aligned} \quad (9.89)$$

$$C_{l,m}^3 = \frac{1}{\text{Kn}} (\Delta_{lm} - M_{l,m}), \quad (9.90)$$

where

$$\begin{aligned} \Delta_{lm} &= |l-m| u_{p,\min(l,m)} + M_{0,0} u_{p,1}^l u_{p,2}^m, \quad \text{when } l \neq 0, m \neq 0, \\ \Delta_{lm} &= (l u_{p,1} + m u_{p,2}) \sigma_{eq} + M_{0,0} u_{p,1}^l u_{p,2}^m, \quad \text{when } l=0 \text{ or } m=0. \end{aligned} \quad (9.91)$$

$$(9.92)$$

Introducing the drag operator brings three unclosed terms  $D_{l,m}^1$ ,  $D_{l,m}^2$  and  $D_{l,m}^3$  which are closed thanks to the set of weights and abscissas defined through the quadrature methods:

$$\begin{aligned} D_{l,m}^1 &= \sum_{\alpha=1}^{\beta} n_{\alpha} [l D_{r(\alpha)1} + m D_{r(\alpha)2}], \\ D_{l,m}^2 &= \sum_{\alpha=1}^{\beta} n_{\alpha} [l \max(0, l-1) U_{(\alpha)1} D_{r(\alpha)1} + m \max(0, m-1) U_{(\alpha)2} D_{r(\alpha)2} + lm (U_{(\alpha)2} D_{r(\alpha)1} + U_{(\alpha)1} D_{r(\alpha)2})], \\ D_{l,m}^3 &= \sum_{\alpha=1}^{\beta} n_{\alpha} \left[ l \max(0, l-2) U_{(\alpha)1}^2 D_{r(\alpha)1} + m \max(0, m-2) U_{(\alpha)2}^2 D_{r(\alpha)2} \right. \\ &\quad \left. + \frac{lm}{2} \left( U_{(\alpha)3-l}^2 D_{r(\alpha)l} + 2 U_{(\alpha)3-l} U_{(\alpha)l} D_{r(\alpha)3-l} \right) \right], \end{aligned} \quad (9.93)$$

where  $D_{r(\alpha)d}$  is defined such as:

$$D_{r(\alpha)d} = \frac{u_{g,d} - U_{(\alpha)d}}{St}. \quad (9.94)$$

Let us focus now on the numerical resolution of these terms. The dynamic system reads:

$$\frac{d\mathbf{W}}{dt} = D(\mathbf{W}) + C(\mathbf{W}), \quad \mathbf{W}(0) = \mathbf{W}_i^*, \quad (9.95)$$

where

$$D(\mathbf{W}) = \begin{pmatrix} 0 \\ D_{l,m}^1 \\ D_{l,m}^2 \\ D_{l,m}^3 \end{pmatrix}, \quad C(\mathbf{W}) = \begin{pmatrix} 0 \\ 0 \\ C_{l,m}^2 \\ C_{l,m}^3 \end{pmatrix}, \quad (9.96)$$

and  $\mathbf{W}_i^n$  is the initial condition for the moments. A splitting algorithm is still used to solve each part independently.

To compute the first part, we note that the drag term in Eq. (9.9) are equivalent to

$$\begin{aligned} \frac{dn_\alpha}{dt} &= 0, \\ \frac{dU_{(\alpha)d}}{dt} &= D_{r(\alpha)d}. \end{aligned} \quad (9.97)$$

$$(9.98)$$

Assuming that  $u_{g,d}$  does not depend on time, this expression can be explicitly solved to find the changes in the weights and abscissas due to drag:

$$\begin{aligned} n_\alpha^* &= n_\alpha^n, \\ U_{(\alpha)d}^* &= \exp\left(-\frac{\Delta t}{St_i}\right) U_{(\alpha)d}^n + \left[1 - \exp\left(-\frac{\Delta t}{St_i}\right)\right] u_{g,d}^n. \end{aligned} \quad (9.99)$$

$$(9.100)$$

where  $n_\alpha^n$  and  $U_{(\alpha)d}^n$  are the weights and abscissas found from  $\mathbf{W}_i^n$  using quadrature and  $St_i$  is the local Stokes number.

The next step is to compute the contribution due to the collisions:

$$\frac{d\mathbf{W}}{dt} = C(\mathbf{W}), \quad \mathbf{W}(0) = \mathbf{W}_i^*. \quad (9.101)$$

This can be done explicitly:

$$\mathbf{W}_i^{**} = \exp\left(-\frac{\Delta t}{Kn_i}\right) \mathbf{W}_i^* + \left[1 - \exp\left(-\frac{\Delta t}{Kn_i}\right)\right] \Delta(\mathbf{W}_i^*). \quad (9.102)$$

where  $Kn_i$  is the local collision time and  $\Delta(\mathbf{W})$  denotes the vector of equilibrium moments. To finish up, quadrature is used to compute  $n_\alpha^{n+1}$  and  $U_{(\alpha)d}^{n+1}$  from  $\mathbf{W}_i^{**}$ ; and  $\mathbf{W}_i^{n+1}$  is computed using projection.

## 9.5 General numerical strategy

The numerical scheme for physical transport of the velocity moments is presented here. This scheme is directly implemented in the code MUSES3D, see Chapter 11. On the other hand, the expression of the drag and collision terms, given in Section 9.1.1, allow an explicit resolution. The resolution procedure of these terms is shown for the purpose of the illustrations proving the feasibility to couple the quadrature method with the resolution of source terms. The solution algorithm, as explained in [84], is based on an operator splitting algorithm, which contains the different steps:

1. Initialize the weights and abscissas in  $\mathbf{V}_4^*$  and the moments in  $\mathbf{W}^{2\dagger}$ ,
2. Advance in time  $\Delta t$  the moment in  $\mathbf{W}_2$  using the moment transport equation,
  - advance moments due to fluxes,
  - advance moments due to drag,
  - advance moments due to collisions,
3. Invert the moments in  $\mathbf{W}_2$  to find the weights and abscissas in  $\mathcal{W}_2$ ,
4. Compute the moments in  $\mathcal{W}_2^\dagger$  using  $\mathbf{V}_4$  (projection step),
5. Return to step 2.

## 9.6 Illustration of the EMVM model

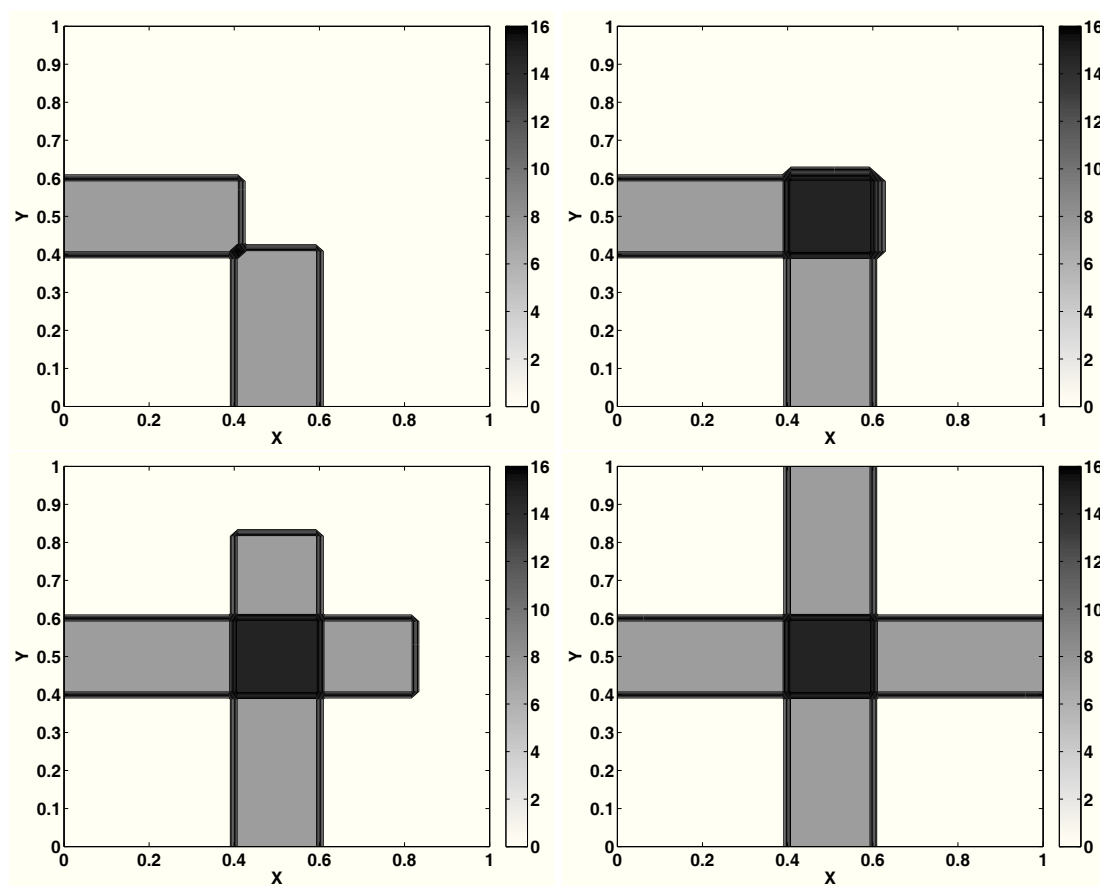
### 9.6.1 Crossing jet

We consider here the case of two crossing jets within the limit of infinite Knudsen and Stokes number. Consequently only advection is considered in this case, which gives a simple illustration of the possibilities offered by the quadrature method. We consider two jets injected from the left and the bottom side of a square  $100 \times 100$  domain. Both jets are injected with an absolute velocity of 1. Free outlet conditions are set on the other domain boundaries. The CFL number is set at 1, at the computation lasts until  $t = 1$ . The results, displayed for  $t = 0.4, 0.6, 0.8$  and 1, are displayed in Fig. (9.16).

This configuration is a typical two-dimensional configuration for which the Eulerian multi-fluid model (and also the EMSM model) predicts an artificial averaging when two droplet jets are crossing without drag nor evaporation, for a monodisperse spray. Indeed, at the collision location, there are, at the same space and time location, two velocities leading to a bi-modal velocity distribution, that is out of equilibrium. The classical multi-fluid model, because of its equilibrium assumption, can not handle this case and predicts an artificial velocity averaging which can be also interpreted as a collision of the two jets as shown in [51, 49, 50]. The EMVM model predicts the exact solution for this simple configuration for which the two jets do not see each other in the chosen infinite Knudsen limit.

### 9.6.2 Colliding jets

The dynamics of a finite Knudsen number flow is studied here. The critical point is the comparison of the results given by two different types of quadrature-based methods using different decomposition of the covariance matrix: the simple Cholesky decomposition (the first one presented), and the symmetric Cholesky decomposition, permutation-invariant. Computations are run for two values of Knudsen numbers :  $\text{Kn} = 0.1$  (Fig. (9.17)) and  $\text{Kn} = 1$  (Fig. (9.18)). Results with the symmetric Cholesky decomposition are displayed on the left column, while results with the simple Cholesky decomposition are on the right column. Three instants are considered:  $t = 0.6, t = 0.8$  and  $t = 1$ . The parameter of the simulation are the same as in the previous paragraph, In the first case for  $\text{Kn} = 0.1$ , where the collision rate is important, the velocity distribution relaxes to an equilibrium distribution fast, so that the resulting distribution is close to an Gaussian distribution. Therefore, results given by the two different decomposition are similar, with some minor distinctions at time  $t = 1$ . They become obvious for the case of  $\text{Kn} = 1$ , for which the collision rate is much less important. Accordingly, because of the relaxation to

Figure 9.16: Crossing jets, for times  $t = 0.4, 0.6, 0.8, 1$

$f_{eq}$  due to collisions, the covariance matrix can be decomposed into non singular Cholesky matrices, but yet the velocity distribution stays far from equilibrium. This is the reason why, two different parts of the flow can be distinguished in Fig. (9.18)-bottom left. One can notice, like in Fig. (9.17), the collision part of the flow, in the direction  $y = x$ . In addition, because of the persistent non-equilibrium due to the low collision rate, a crossing part can be observed at  $x = 0.5$  and  $y = 0.5$ .

Figure (9.18) gives a clear illustration of how dissimilar a reconstruction the two quadrature-based can lead to. Nevertheless, results are conform to our expectations for the symmetric method, as it perfectly respects the symmetry of the configuration. This observation conduces us to recognize the limitations of the quadrature-based moment method exposed here in terms of its ability to treat any kind of flow. Moreover, both the computations showed what we could fear about these methods, i.e some velocity abscissas become very high, and they are associated to weights with very small values. It clearly appear in this context that further developments are called for in order to consider any application for industrial cases. Nevertheless, these problems are highlighted in the case where collision effects exist. But, these cases are not in the scope of flows studied in this PhD, see Section 1.3. And it is shown in Chapter 12 that the quadrature-based moment method is legitimate for the spray dynamics studied.

### 9.6.3 Addition of the drag effect

Finally, the drag effect is added the spray dynamics. Results with the single drag effect are displayed in Fig. (9.19) for different values of  $\tau_p \cdot St = 0.1$  and  $St = 1$ . The gas velocity is constant and set to  $\mathbf{u}_g = [1, 1]^T$ . As expected, the spray dynamics is much more influenced by the gas for  $St = 0.1$ , since small particles are considered, than for  $St = 1$ , where bigger particles are considered. Notice than the resolution of the drag term does not unphysical abscissas after the reconstruction step, which where the case with the collision term. Eventually, a last computation is run, combining drag and collision effects, for  $St = 1$ , and  $Kn = 1$  and  $0.1$ , with results displayed in Fig. (9.20). One can thus assess the impact of the collision on the flow field, in comparison with Fig. (9.20).

## Conclusion

This chapter proposes an answer to the second of the two limitations of Eulerian spray models towards Lagrangian models, stated in Section 3.4. This answer, the EMVM model, relies on the transport of velocity moment up to third order, and the use of the QMOM. But there are two challenges. For one-dimensional cases, if the quadrature method is known and robust, no fully high order advection scheme has been designed so far. A partially second order scheme has been proposed in [224], reconstructing the weights resulting from the quadrature. This chapter presents a mathematical analysis of the dynamic system and analyses entropy solutions when singularities occur, in order to pave the way for the design of high order advection schemes. Moreover, the extension of the QMOM to multi-dimensional case needs to bridge the theoretical gap with the one dimension case since the quadrature problem is now ill-posed. A solution is presented in this chapter, on the basis of the work done in [84]. The model presented here is an extension of the one proposed in [84], since it can treat also treat cases when the velocity distribution degenerates into a mono-modal distribution. Numerical tools for the resolution of spray dynamics with drag and collision is explained, with some illustrations. If the method proposed is a breakthrough, since it allows to describe PTC in multi-dimensional cases in an Eulerian framework, this method has been improved in terms of stability in [233], and extended to the crossing of Gaussian velocity distributions [37].

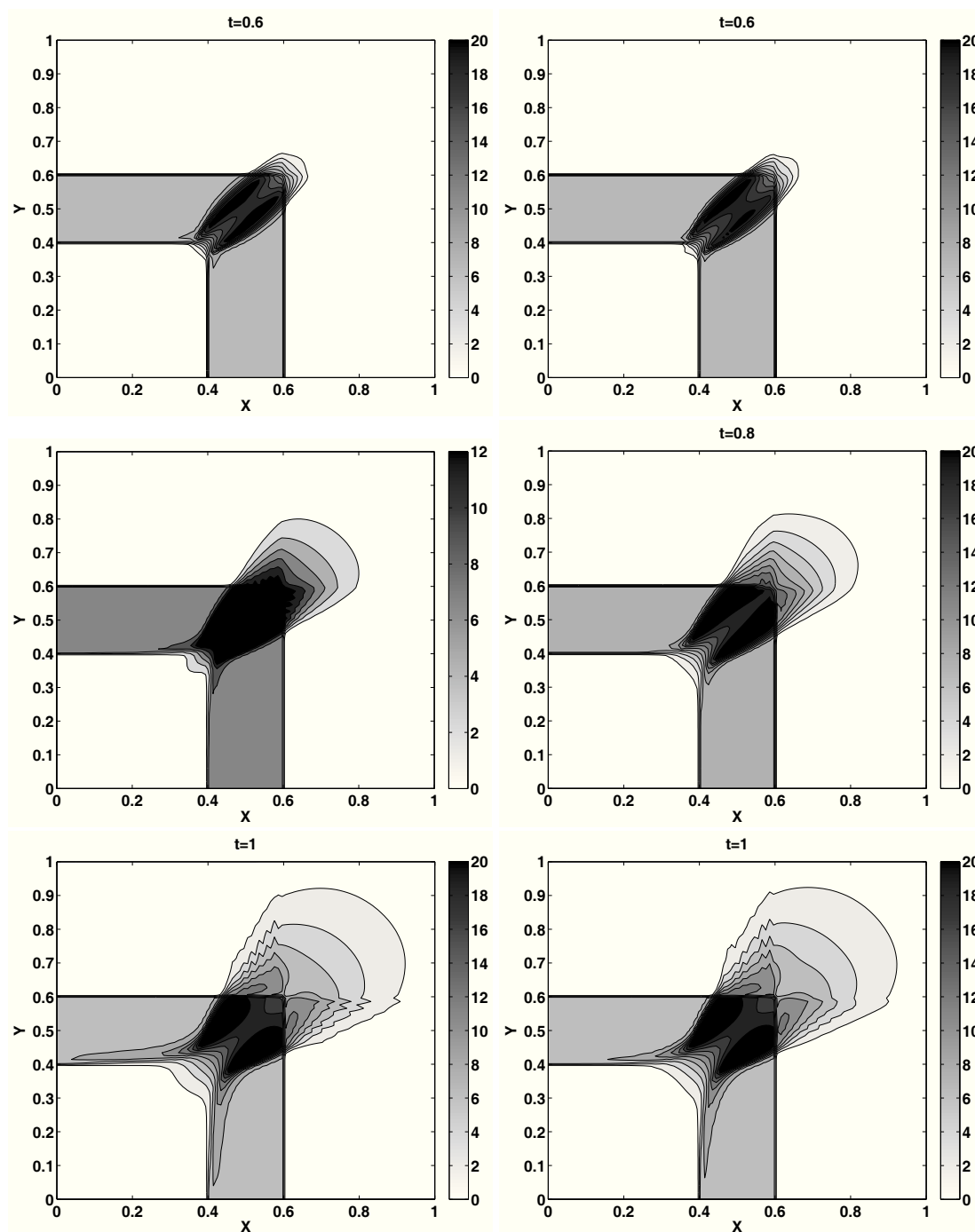
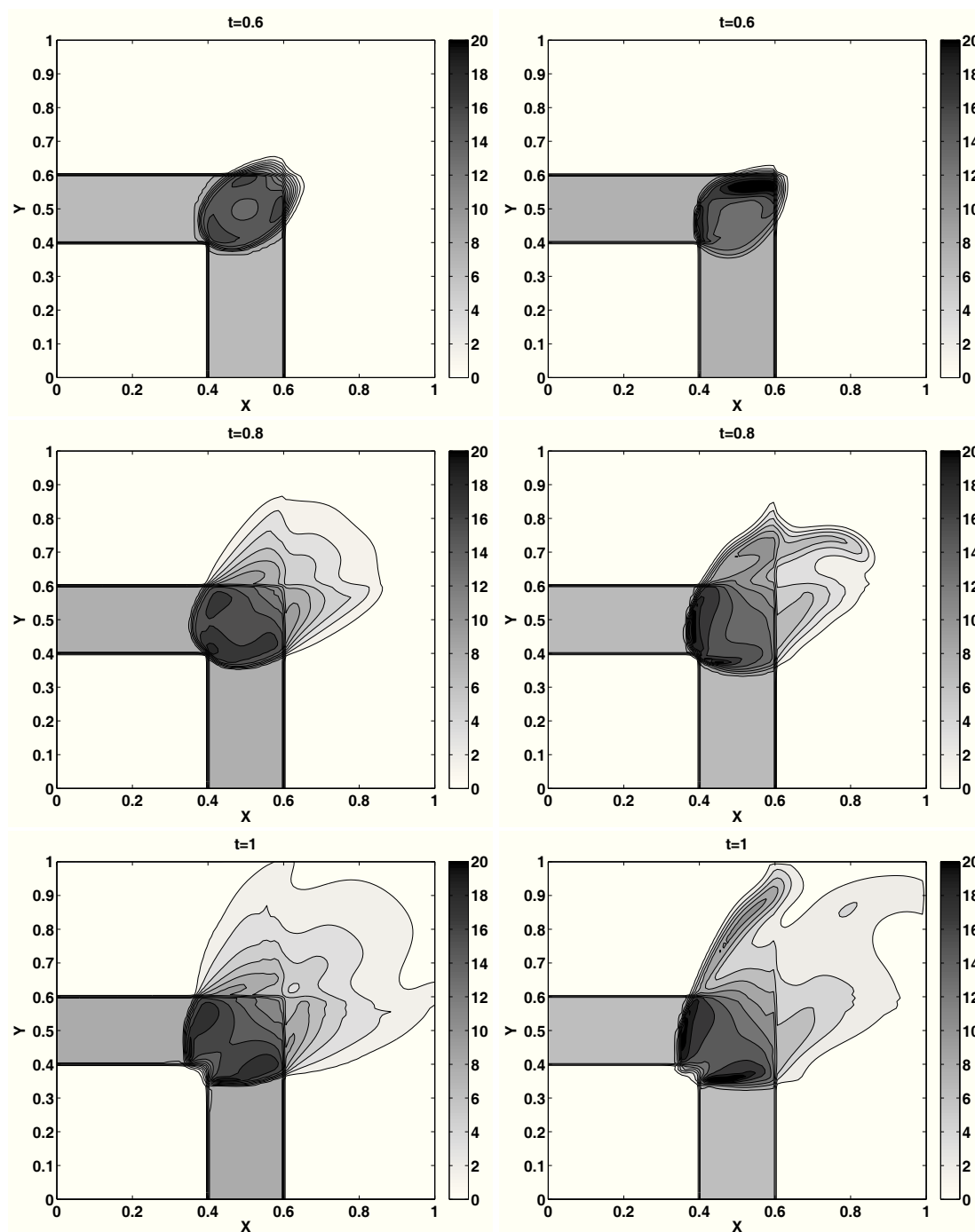


Figure 9.17: Results for collision with  $Kn = 0.1$ . (Top)  $t = 0.6$ . (Medium)  $t = 0.8$ . (Bottom)  $t = 1$



Figure 9.18: Results for collision with  $\text{Kn} = 1$ . (Top)  $t = 0.6$ . (Medium)  $t = 0.8$ . (Bottom)  $t = 1$

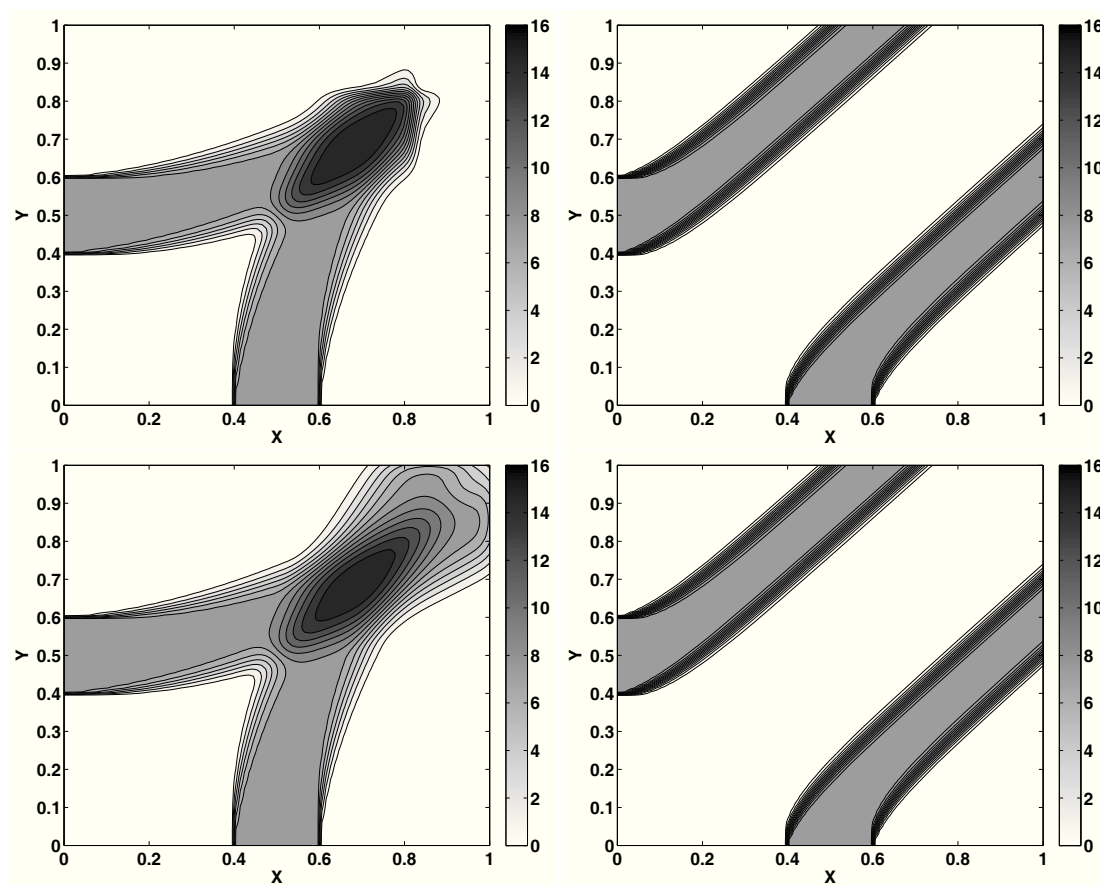


Figure 9.19: Results for drag at  $t = 0.8$  and  $t = 1$ . (Left)  $St = 1$ . (Right)  $St = 0.1$

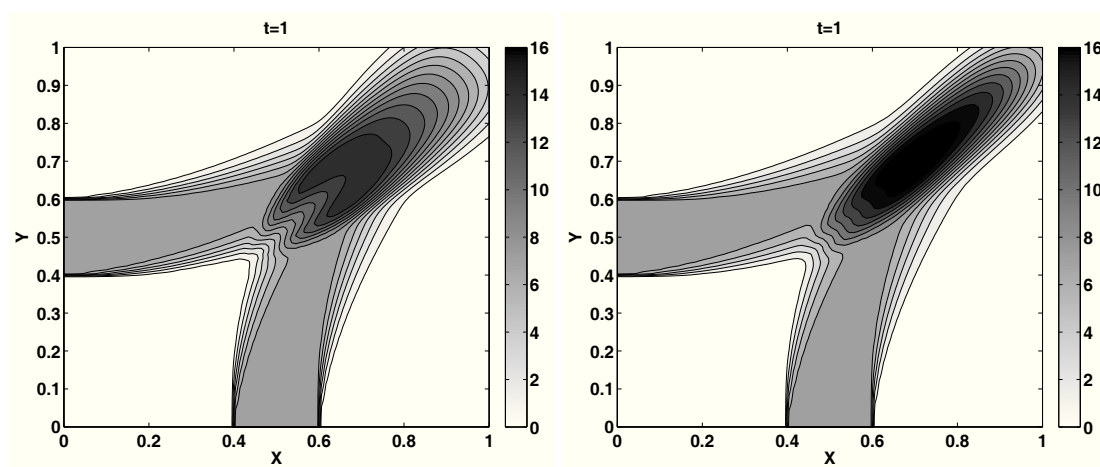


Figure 9.20: Results for drag and collision at  $t = 1$ . (Left)  $St = 1$  and  $Kn = 1$ . (Right)  $St = 1$  and  $Kn = 0.1$

## Chapter 10

# Model coupling polydispersity and droplet crossing

Chapter 9 presents the EMVM model, with the capacity to account for particle trajectory crossing (PTC). Previsouly, in Chapter 3 we presented the multi-fluid model, able to account for the polydisperse character of the droplet population. However, its computational cost makes its application in an industrial context hardly conceivable. This is why, in Part II, the EMSM is proved to describe spray polydispersity at a reasonably enough computational cost so that its application in industrial context can be envisaged. These models give positive answers to the limitations of Eulerian models relative to Lagrangian models, formulated in Section 3.4.

Yet each of these answers is independent from the other. This is the reason why, in this present chapter, we investigate the possibility of coupling these models, i.e to be able, within a single model, to describe a polydispersity spray within the limit of high Knudsen number, where PTC may occur. We show that, under assumptions made on the profile of the number density function (NDF), this coupling is possible without bringing any new difficulty in terms of modeling. Two models are presented, the Eulerian Multi-Fluid and Velocity Moment (EMFVM) model, resulting for the coupling between the multi-fluid model and the EMVM model, and the Eulerian Multi Size and Velocity Moment (EMSVM) model, resulting from the coupling of the EMSM model and the EMVM model.

Our purpose is to provide a first evaluation of these models through the MUSES3D code, see Chapter 7. Consequently, the implementation strategy of these models in the algorithm of the MUSES3D code is presented here, insisting on the EMFVM model that has actually been implemented in the code and providing very encouraging first results [51, 87, 126].

As stated in Section 1.2, the basis of our work is the following equation:

$$\partial_t f + \nabla_{\mathbf{x}} \cdot (\mathbf{u}f) + \nabla_{\mathbf{u}} \cdot (\mathbf{D}_r f) + \partial_S(Kf) = 0, \quad (10.1)$$

### 10.1 Presentation of the models and assumptions

Referring to Section 3.1, the multi-fluid model as well as the EMSM model presume the form of the NDF

$$f(t, \mathbf{x}, S, \mathbf{u}) = n(t, \mathbf{x}, S)\delta(\mathbf{u} - \mathbf{u}_p(t, \mathbf{x}, S)), \quad (10.2)$$

where the velocity distribution is reconstructed by a one-node quadrature that allows to acces only the mean particle velocity. Yet, thanks to recent developments, explained in Chapter 9, it has been shown that more complex velocity distributions can be accessed by two-node quadrature. Therefore, a more general NDF is considered in this chapter:

$$f(t, \mathbf{x}, S, \mathbf{u}) = n(t, \mathbf{x}, S)\phi(t, \mathbf{x}, S, \mathbf{u} - \mathbf{u}_p(t, \mathbf{x}, S)), \quad (10.3)$$

where  $\phi$  is the velocity probability density function (PDF), such as  $\int_{\mathbf{u}} \phi(t, \mathbf{x}, S, \mathbf{u}) d\mathbf{u} = 1, \forall(t, \mathbf{x}, S)$ . The models presented in this chapter are designed to solve the size-velocity coupled moments up to two dimensions in space:

$$\begin{aligned} \mathcal{M}_{k,l,m} &= \int_{S_{\min}}^{S_{\max}} \int_{\mathbb{R}} S^k u_x^l u_y^m f d\mathbf{u} dS \\ &= \int_{S_{\min}}^{S_{\max}} S^k n(t, \mathbf{x}, S) M_{l,m}(t, \mathbf{x}, S) dS, \end{aligned} \quad (10.4)$$

where we recall the expression of  $M_{l,m}$  given in Eq. (9.5):

$$M_{l,m} = \int u_1^l u_2^m \phi d\mathbf{u}, \quad l + m \leq 3, \quad (10.5)$$

The coupled models are presented in the framework of sectional methods, where a size section  $[S^{(j)}, S^{(j+1)}]$ , introduced in Section 3.1, is defined as a subspace of the size phase space. This implies that the size phase space must contain at least two sections. However, in Chapter 5, we shown that the EMSM model does not need to discretize the size phase space, although it can be used in a context of several sections. Since, in the present chapter, we discuss both the multi-fluid and EMSM models, we extend the meaning of section, that is to say that we add to it the possibility of containing the whole size phase space is added. From now on, we set  $S_{\min} = S^{(j)}$  and  $S_{\max} = S^{(j+1)}$ , and the superscript  $j$  refers to section  $j$ . To get an explicit expression of  $\mathcal{M}_{k,l,m}$ , the following assumption is introduced

[H1] In one section, the velocity distribution is independent of the size variable

This means that, in each section,

$$M_{l,m}^{(j)}(t, \mathbf{x}, S) = M_{l,m}^{(j)}(t, \mathbf{x}), \quad (10.6)$$

Given this hypothesis, within one section, size and velocity distributions are independent so that the  $\mathcal{M}_{k,l,m}$  is a tensorial product of size moment  $m_k$  and velocity moment  $M_{l,m}$ :

$$\mathcal{M}_{k,l,m}^{(j)} = m_k^{(j)} M_{l,m}^{(j)}, \quad (10.7)$$

with the convention  $M_{0,0}^{(j)} = 1$ .

The coupling procedure consists in putting together the capacity to describe polydispersity presented in Chapter 3 and Chapter 4, in a monokinetic context, and the capacity to describe PTC within a monodisperse spray, presented in Chapter 9, in the context of the assumption of independence of the size and velocity distributions in each section. Consequently, in a section, the velocity distribution ‘sees’ a monodisperse distribution, and can be reconstructed using exactly the same quadrature methods explained in section Section 9.2 and Section 9.3. If the size and velocity moments were fully coupled, then the phase space would have an additional dimension (which amounts to three in two dimensions in space), and the quadrature method would be even more complex.

We distinguish, at this stage, the coupling of the EMVM model with the multi-fluid model and the EMSM model.

### 10.1.1 Coupling of the multi-fluid and EMVM models

We couple here the multi-fluid and EMVM models, and designate the resulting model by Eulerian Multi Fluid and Velocity Moments (EMFVM) model. Let us work on a size section, delimited by the interval  $[S^{(j)}, S^{(j+1)}]$ . According to Eq. (10.3), the mass  $m_{3/2}^{(j)}$ , and the mean velocity  $\mathbf{u}_p^{(j)}$  are not enough to

reconstruct the NDF any more. We need, as in Section 9.3, a ten moment set, up to third-order velocity moments, as we use four sets a weights and abscissas:

$$\mathbf{W}^{(j)} = \left( m_{3/2}^{(j)}, m_{3/2}^{(j)} M_{1,0}^{(j)}, m_{3/2}^{(j)} M_{0,1}^{(j)}, m_{3/2}^{(j)} M_{2,0}^{(j)}, m_{3/2}^{(j)} M_{1,1}^{(j)}, m_{3/2}^{(j)} M_{0,2}^{(j)}, \right. \\ \left. m_{3/2}^{(j)} M_{3,0}^{(j)}, m_{3/2}^{(j)} M_{2,1}^{(j)}, m_{3/2}^{(j)} M_{1,2}^{(j)}, m_{3/2}^{(j)} M_{0,3}^{(j)} \right), \quad (10.8)$$

$$(10.9)$$

The moments are defined by:

$$m_{3/2}^{(j)} M_{l,m}^{(j)} = \int_{S^{(j)}}^{S^{(j+1)}} \frac{\rho_l S^{3/2}}{6\sqrt{\pi}} \int_{\mathbf{u}} u_x^l u_y^m f \, d\mathbf{u} dS. \quad (10.10)$$

We derive now the system of equation for the EMFVM model:

$$\partial_t \left( m_{3/2}^{(j)} M_{l,m}^{(j)} \right) + \partial_x \left( m_{3/2}^{(j)} M_{l,m}^{(j)} \right) + \partial_y \left( m_{3/2}^{(j)} M_{l,m}^{(j)} \right) = (E_1^{(j)} + E_2^{(j)}) m_{3/2}^{(j)} M_{l,m}^{(j)} \\ - E_1^{(j+1)} m_{3/2}^{(j+1)} M_{l,m}^{(j+1)} + m_{3/2}^{(j)} F_{l,m}^{(j)}, \quad (10.11)$$

where the interaction terms between size section  $E_1^{(j)}$  and  $E_1^{(j+1)}$ , as well as the interaction term with the gas phase  $E_2^{(j)}$  have exactly the same expression as obtained for the multi-fluid model, see Section 3.1. On the other hand, the drag force  $F_{l,m}^{(j)}$ , is expressed exactly the same way as in the context of the EMVM model. It depends on the indexes  $l$  and  $m$  of the velocity moment considered, and writes:

$$F_{l,m}^{(j)} = l \frac{u_{g,x} M_{l-1,m}^{(j)} - M_{l,m}^{(j)}}{\text{St}_0 S_p^{(j)}} + m \frac{u_{g,y} M_{l,m-1}^{(j)} - M_{l,m}^{(j)}}{\text{St}_0 S_p^{(j)}}, \quad (10.12)$$

where the reference Stokes number  $\text{St}_0$  and the mean size of section  $j$ ,  $S_p^{(j)}$ , are defined in Eq. (3.13) and Eq. (3.14) respectively.

The dynamics of the velocity moments is the same as explained Section 9.3, within a size section. The single difference with the EMVM model is that, instead of Eq. (9.44), the quadrature procedure has to verify the following relation:

$$m_{3/2}^{(j)} M_{l,m}^{(j)} = \sum_{\alpha=1}^{\beta} n_{\alpha} U_{(\alpha)1}^l U_{(\alpha)2}^m, \quad m_{3/2}^{(j)} = \sum_{\alpha=1}^{\beta} n_{\alpha}. \quad (10.13)$$

For the evaporation operator, the mass and momentum fluxes in the multi-fluid model are replaced by fluxes of all the moments. Because of the assumption of independence of size and velocity distributions, the physical interaction terms expression introduces no additional difficulty compared to their derivation in the context of the multi-fluid or the EMVM model.

A remarkable consequence from system (10.11) is that the velocity distribution in the section  $j$  can turn from a monomodal to a bimodal distribution, because of the fluxes from section  $j + 1$ .

### 10.1.2 Coupling of the EMSM and EMVM models

We couple here the richness of description brought by the EMSM and EMVM models. The resulting model is designated by Eulerian Multi Size and Velocity Moments (EMSVM) model. As previously recalled, this method can be used in the context of several size sections. We will present it in this context, to be consistent with the presentation of the EMFVM model. Nevertheless, let us recall that

the core interest of this model lies in its capacity to describe polydispersity using a single size section. The moment vector considered reads then :

$$\mathbf{W}^{(j)} = \left( m_0^{(j)}, m_1^{(j)}, m_2^{(j)}, m_3^{(j)}, m_1^{(j)} M_{1,0}^{(j)}, m_1^{(j)} M_{0,1}^{(j)}, m_1^{(j)} M_{2,0}^{(j)}, m_1^{(j)} M_{1,1}^{(j)}, m_1^{(j)} M_{0,2}^{(j)}, \right. \\ \left. m_1^{(j)} M_{3,0}^{(j)}, m_1^{(j)} M_{2,1}^{(j)}, m_1^{(j)} M_{1,2}^{(j)}, m_1^{(j)} M_{0,3}^{(j)} \right). \quad (10.14)$$

$$(10.15)$$

The moments are defined by:

$$\mathcal{M}_{k,l,m}^{(j)} = m_k^{(j)} M_{l,m}^{(j)} = \int_{S^{(j)}} S^k \int_{\mathbf{u}} u_x^l u_y^m f \, d\mathbf{u} dS. \quad (10.16)$$

We recall that the momentum is defined by  $m_1^{(j)} (M_{1,0}^{(j)}, M_{0,1}^{(j)})^t$  and not by  $m_0^{(j)} (M_{1,0}^{(j)}, M_{0,1}^{(j)})^t$ , so that the drag term can be explicitly solved. See Section 6.3 for details on that issue.

The system of equations for the high order size and velocity moment method is then derived:

$$\begin{aligned} \partial_t m_0^{(j)} + \partial_x \left( m_0^{(j)} M_{1,0}^{(j)} \right) + \partial_y \left( m_0^{(j)} M_{0,1}^{(j)} \right) &= -K \left( \tilde{n}_{ME}^{(j)}(t, \mathbf{x}, S^{(j)}) - \tilde{n}_{ME}^{(j+1)}(t, \mathbf{x}, S^{(j+1)}) \right), \\ \partial_t m_1^{(j)} + \partial_x \left( m_1^{(j)} M_{1,0}^{(j)} \right) + \partial_y \left( m_1^{(j)} M_{0,1}^{(j)} \right) &= -K m_0^{(j)} \\ &+ K \left( -\tilde{n}_{ME}^{(j)}(t, \mathbf{x}, S^{(j)}) S^{(j)} + \tilde{n}_{ME}^{(j+1)}(t, \mathbf{x}, S^{(j+1)}) S^{(j+1)} \right), \\ \partial_t m_2^{(j)} + \partial_x \left( m_2^{(j)} M_{1,0}^{(j)} \right) + \partial_y \left( m_2^{(j)} M_{0,1}^{(j)} \right) &= -2K m_1^{(j)} \\ &+ K \left( -\tilde{n}_{ME}^{(j)}(t, \mathbf{x}, S^{(j)}) S^{(j)2} - \tilde{n}_{ME}^{(j+1)}(t, \mathbf{x}, S^{(j+1)}) S^{(j+1)2} \right), \\ \partial_t m_3^{(j)} + \partial_x \left( m_3^{(j)} M_{1,0}^{(j)} \right) + \partial_y \left( m_3^{(j)} M_{0,1}^{(j)} \right) &= -3K m_2^{(j)} \\ &+ K \left( -\tilde{n}_{ME}^{(j)}(t, \mathbf{x}, S^{(j)}) S^{(j)3} - \tilde{n}_{ME}^{(j+1)}(t, \mathbf{x}, S^{(j+1)}) S^{(j+1)3} \right), \\ \partial_t \left( m_1^{(j)} M_{l,m}^{(j)} \right) + \partial_x \left( m_1^{(j)} M_{l+1,m}^{(j)} \right) + \partial_y \left( m_1^{(j)} M_{l,m+1}^{(j)} \right) &= -K m_0^{(j)} M_{l,m}^{(j)} \\ &+ K \left( -M_{l,m}^{(j)} \tilde{n}_{ME}^{(j)}(t, \mathbf{x}, S^{(j)}) S^{(j)} + M_{l,m}^{(j+1)} \tilde{n}_{ME}^{(j+1)}(t, \mathbf{x}, S^{(j+1)}) S^{(j+1)} \right) \\ &+ l m_0^{(j)} \frac{u_{g,x} M_{l-1,m}^{(j)} - M_{l,m}^{(j)}}{St_0} + m m_0^{(j)} \frac{u_{g,y} M_{l,m-1}^{(j)} - M_{l,m}^{(j)}}{St_0}, \quad 0 < l + m \leq 3. \end{aligned} \quad (10.17)$$

The first four equations, on size moments, are similar to the equations Eq. (4.15) and system (4.6) derived in the context of the EMSM model, whereas the remaining equations on velocity moments correspond to the equations Eq. (9.9) without the collision term, and with the addition of the evaporation term. The single difference with the EMVM model is that, instead of Eq. (9.44), the quadrature procedure has to verify the following relation:

$$m_1^{(j)} M_{l,m}^{(j)} = \sum_{\alpha=1}^{\beta} n_{\alpha}^{(j)} U_{(\alpha)1}^{l,(j)} U_{(\alpha)2}^{m,(j)}, \quad m_1^{(j)} = \sum_{\alpha=1}^{\beta} n_{\alpha}^{(j)}. \quad (10.18)$$

Because of the independence assumption between the size and velocity moments, the closure of the evaporation terms is done as presented in Section 4.2.3, and the inversion procedure of the velocity moments is done as presented in Chapter 9.

The coupled EMFVM and EMSVM models are presented in the context of the decorrelation assumption between size and velocity distributions. This assumption provides an important simplification of the problem, preventing the appearance of correlated size-velocity moments. Therefore, no additional difficulty is to mention in terms of the new models. We couple, in this chapter, the advances made in Chapter 5 and Chapter 9. Nevertheless this appears as a major contribution in the field of Eulerian spray models as it shows the feasibility of designing an Eulerian model able to overcome both the limitations underlined in the general introduction, i.e polydispersity and PTC description.

The next step is to evaluate the potential of these methods. For that purpose, Chapter 7 presented the MUSES3D code, a platform dedicated to the evaluation of spray models. The next section presents the numerical and algorithmic strategy adopted to implementation of these models in MUSES3D. Contrary to the modeling part, intrinsic difficulties, brought by the model, have to be solved.

## 10.2 Numerical and algorithmic strategy towards implementation in MUSES3D

The numerical and algorithmic strategy are presented here for the implementation of the models described in Section 10.1 in the code MUSES3D. During this PhD, the EMFVM has been fully implemented, leading to computations of jets with the same conditions as with a Lagrangian model, presented in [51, 87, 126]. The EMSVM could not be implemented by lack of time. Yet a strategy and a simplified model are exposed.

### 10.2.1 Strategy for the EMFVM model implementation

The numerical scheme is designed in the spirit of the time splitting algorithm of the code MUSES3D presented in Section 7.1, where physical transport and phase space transport are solved separately. The resolution scheme for physical transport is a first order kinetic-based scheme presented in Section 9.5, similar to the scheme present in MUSES3D, see Section 7.1.2, so that its implementation needs minor changes. Resolution of phase space transport is by far more challenging. As presented in Section 3.2, the resolution method for phase space transport is based on a Radau5 solver, for the multi-fluid model. On the other hand, considering a velocity moment vector introduces the realizability, condition stated in Prop.(3). It has been shown in Chapter 6 that the use of ODE solvers is hardly compatible with the realizability brought by the moment vector, i.e in the case of size moments, they do not preserve the moment space. Nevertheless, because of the wider support of the velocity phase space which is not compact, contrary to the size phase space, fewer conditions have to be verified when working with velocity moments. However, with the following system derived from system (10.11), and just containing the terms of phase space transport:

$$d_t \left( m_{3/2}^{(j)} M_{l,m}^{(j)} \right) = (E_1^{(j)} + E_2^{(j)}) m_{3/2}^{(j)} M_{l,m}^{(j)} - E_1^{(j+1)} m_{3/2}^{(j+1)} M_{l,m}^{(j+1)} + m_{3/2}^{(j)} F_{l,m}^{(j)}, \quad (10.19)$$

the Radau5 solver is not able to satisfy the second of this reduced set of conditions. A counter-example can easily be found, when considering a non evaporative motionless particle cloud dragged by the gas phase at velocity,  $\mathbf{u}_g = [1, 0]^T$ . At the end of the first iteration done by the Radau5 solver,  $M_{1,0}^{(j)}$  becomes positive, whereas  $M_{2,0}^{(j)}$  is still negative, leading to a negative velocity dispersion in the first direction. In order to fulfill the realizability condition through Radau5, two modifications have to be provided to the algorithm. The first intervention concerns the initialization of the argument vector  $\mathbf{y}$  of the Radau5 solver, that is solved during the procedure. Secondly, at one time during the iterative procedure the

Jacobian of the source term of the Partial Differential Equation (PDE) has to be computed, see [49] for the related explanation. The Jacobian cannot be computed with the usual numerical method of the Radau5 solver. Indeed, it introduces an arbitrary shift in the values of the velocity moments. But this arbitrary shift does not guarantee that the realizability condition to be still ensured. This modification, contrary to the first one, does not bring any numerical difficulty.

For vector  $\mathbf{y}$  initialized the idea is to considered, from second order, velocity moments in the referential frame moving at velocity the mean particle velocity  $(M_{1,0}^{(j)}, M_{0,1}^{(j)})$ :

$$m_{3/2}^{(j)} \tilde{M}_{l,m}^{(j)} = \int_{S^{(j)}}^{S^{(j+1)}} S^{3/2} \int_{\mathbf{u}} (u_{g,x} - M_{1,0}^{(j)})^l (u_{g,y} - M_{0,1}^{(j)})^m f(t, S, \mathbf{u}) d\mathbf{u} dS, \quad l + m > 2. \quad (10.20)$$

The  $\tilde{M}_{l,m}^{(j)}$  are called centered moments. Up to first order, the moments are unchanged, so that  $\tilde{M}_{0,1}^{(j)} = 1$ ,  $\tilde{M}_{1,0}^{(j)} = M_{1,0}^{(j)}$  and  $\tilde{M}_{0,1}^{(j)} = M_{0,1}^{(j)}$ . The other centered moments are deduced from the actual moments by the following relations:

$$\begin{aligned} \tilde{M}_{2,0}^{(j)} &= M_{2,0}^{(j)} - (M_{1,0}^{(j)})^2, \\ \tilde{M}_{1,1}^{(j)} &= M_{1,1}^{(j)} - M_{1,0}^{(j)} M_{0,1}^{(j)}, \\ \tilde{M}_{0,2}^{(j)} &= M_{0,2}^{(j)} - (M_{0,1}^{(j)})^2, \\ \tilde{M}_{3,0}^{(j)} &= M_{3,0}^{(j)} - 3M_{2,0}^{(j)} M_{1,0}^{(j)} + 2(M_{1,0}^{(j)})^3, \\ \tilde{M}_{2,1}^{(j)} &= M_{2,1}^{(j)} - M_{2,0}^{(j)} M_{0,1}^{(j)} - 2M_{1,1}^{(j)} M_{1,0}^{(j)} + 2(M_{1,0}^{(j)})^2 M_{0,1}^{(j)}, \\ \tilde{M}_{1,2}^{(j)} &= M_{1,2}^{(j)} - M_{0,2}^{(j)} M_{1,0}^{(j)} - 2M_{1,1}^{(j)} M_{0,1}^{(j)} + 2(M_{0,1}^{(j)})^2 M_{1,0}^{(j)}, \\ \tilde{M}_{0,3}^{(j)} &= M_{0,3}^{(j)} - 3M_{0,2}^{(j)} M_{0,1}^{(j)} + 2(M_{0,1}^{(j)})^3. \end{aligned} \quad (10.21)$$

With the relation between centered moments and actual moments, given in Eq.(10.21), it is possible to write the dynamic system verified by these centered moments from system (10.19). For the sake of legibility, the corresponding system of equations expression can be found in Appendix C.2. These two modifications in the resolution algorithm of the MUSES3D code are explained in Chapter 11.

### 10.2.2 Numerical strategy for the EMSVM model

Similarly to the previous case, the numerical scheme is devised in the context of an operator splitting algorithm. The physical transport resolution method is given in Section 9.5, and is thus the same as in the case of the EMFVM model. The schemes for the two models differ when it comes to phase space transport resolution. Indeed, we show, in Section 5.1.2 and Appendix B.1, that an ODE solver (and therefore the Radau5 solver) cannot ensure the realizability condition for the size moment vector. Therefore, within the phase space transport resolution, the evaporation and drag operators are splitted, as explained in Section 6.5. In this context, there are two options to treat the drag term. One can either rely on the resolution through the Radau5 solver, since drag is not the critical step for the insurance of the realizability condition. Or, since only drag with Stokes closure is involved, one can explicitly solve the ODE, as suggested in Section 3.2.

The critical aspect of the scheme is the resolution of the evaporation term (considered here to be expressed by a  $d^2$ -law, see Section 1.2.3). If only one section is considered, according to system (10.17), the evaporation term does not impact the velocity moments. The difficult comes when the size phase space is discretized with at least two sections. In this context, the value of the velocity moment of section  $j$  may be changed by the positive flux coming from section  $j + 1$ , like it is already the case for the EMFVM model. In this case, we propose the following simplified resolution scheme. The integral formulation of Lemma 3 is reused, for the size moments :

$$\exp(\Delta t \mathbf{A}) \mathbf{m}^{(j)}(\Delta t) = \mathbf{m}^{(j)}(0) - \Phi_-^{(j)} + \Phi_-^{(j+1)} \quad (10.22)$$



where, in comparison to the terms of Lemma 3,  $\Phi_-^{(j)} = \Phi_-$  and  $\Phi_-^{(j+1)} = \Phi_+$ .

Extending the matrix  $\mathbf{A}$  by taking into account the equations on velocity moments  $M_{l,m}^{(j)}$  (like it is done in Section 5.1.4 for the momentum), one obtains a generalization of Eq. (10.23) for the  $M_{l,m}^{(j)}$ :

$$\left[ m_1^{(j)}(\Delta t) + \Delta t m_0^{(j)}(\Delta t) \right] M_{l,m}^{(j)}(\Delta t) = m_1^{(j)}(0) M_{l,m}^{(j)}(0) - M_{l,m}^{(j)}(0) \Phi_{-2}(\Delta t) + M_{l,m}^{(j+1)}(0) \Phi_{+2}(\Delta t) \quad (10.23)$$

where the notations for the fluxes are explained in Section 5.1.4.

The same behavior as in the multi-fluid multi-velocity model is observed, i.e the distribution in section  $j$  can change from a monomodal to a bimodal distribution due to the fluxes.

The updated values of the velocity moments are convex sums of the initial moments, which, given the convex geometry of the moment space, verifies the realizability condition on the velocity moments.

### 10.2.3 Validation results for the EMSVM model

Our objective here is to do a first evaluation of the numerical tools presented for the EMSVM model. The first test case takes up the one-dimensional spray dynamics case exposed in Section 6.4.2, and shows that droplet crossing simulation is possible while preserving the quality of polydispersity description through evaporation. The second test case involves impinging droplet clouds in two-dimensions, and proves the feasibility of the quadrature in two-dimensions. This is a very important result, since there exist a theoretical gap between quadrature methods for monovariate functions and quadrature methods for multi-variate functions, see Chapter 9.

#### Transport and evaporation of a spray in the infinite Stokes limit

In this first test case, the same configuration as presented in Section 6.4.2 is considered. The objective is to show that the limitations stated in Section 6.4.2 about the non ability of Eulerian model to describe PTC can be overcome by coupling the high order size moment method with the high order velocity moment method model. In practice, the parameters of the simulation are the same, but what differs between the two results is that, in the result display in Section 6.4.2, the solved quantity is the vector:

$$\mathbf{m} = (m_0, m_1, m_2, m_3)^t, \quad (10.24)$$

containing only size moments, whereas in this actual test case, the solved quantity is the vector:

$$\mathcal{M} = (m_0 M_0, m_1 M_0, m_2 M_0, m_3 M_0, m_1 M_1, m_1 M_2, m_1 M_3)^t, \quad (10.25)$$

containing size and velocity moments. The parameters of the simulation are recalled: the computation is run in a 200 cell grid, the CFL is set at 1 and periodic boundary conditions are set. The initial conditions are recalled, and the results are displayed in Fig. (10.1) and Fig. (10.2), at the same instants as in Section 6.4.2, i.e  $t = 0.2, t = 0.4, t = 0.7$ . The solid lines represent the numerical solution, whereas the markers represent the analytical solution. At the first instant, the result is fully similar to the one in Section 6.4.2, because at the kinetic level of description the velocity distribution is mono-modal, and therefore a monokinetic macroscopic model is equivalent to the kinetic description. This is not the case at  $t = 0.4$ , where the faster cloud overtakes the lower cloud. Since the flow is assumed to be collisionless (with  $\text{Kn} \rightarrow \infty$ ), the velocity distribution at the kinetic level is bi-modal with two weights at the velocity values of 0.5 and 2, corresponding to the velocity of the clouds. Whereas, this bi-modal distribution could not be accounted for in Section 6.4.2, because of the monokinetic assumption, the Quadrature Method of Moment (QMOM) succeeds at reconstructing these two distinctive velocities, and perfectly reproduces the expected crossing of the two clouds. Meanwhile, the quality of the polydispersity description is preserved, the only source of error being the numerical diffusion, more important than in Section 6.4.2 since the advection scheme employed for the high order velocity moment method is first order in space. The design of a second order scheme requires complex algebra in order to ensure the

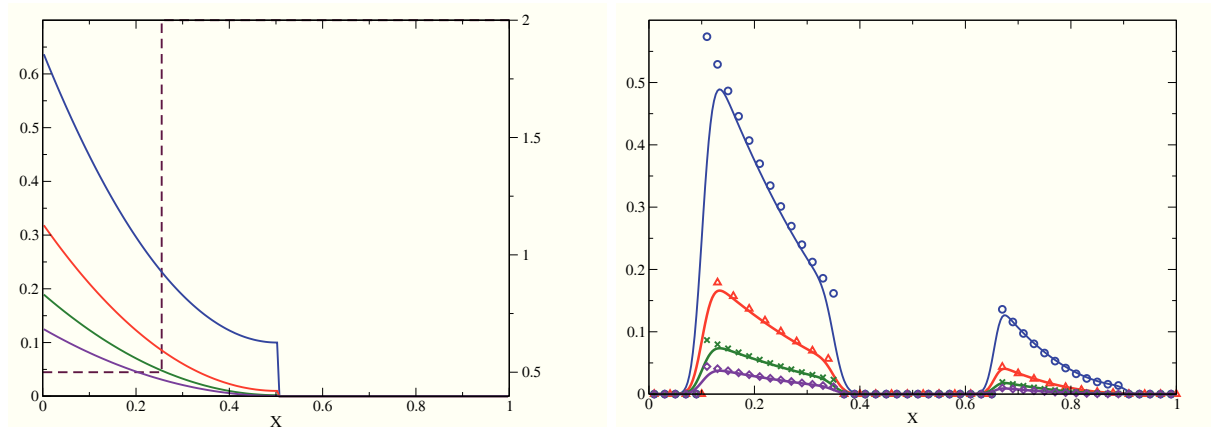


Figure 10.1: Evolution of a spray in a discontinuous velocity field calculated with the multi-fluid multi-velocity model model, compared to the analytical solution of the problem. (left) Initial condition; the plain curves represent, with decreasing ordering in terms of value, the four first moments from the  $0^{th}$  order (highest) to the  $3^{rd}$  (lowest). The plain curves are scaled by the left Y-axis and the dashed curve representing the velocity field, is scaled by the right Y-axis. (right) Solution at  $t = 0.2$  compared to the analytical solution of the problem represented by markers. The computation is carried out in a 300 cell grid

realizability condition for the velocity moments, see Chapter 9 for explanations on this subject.

In conclusion, this first test case demonstrates the feasibility of an Eulerian model able to description PTC, as well as providing efficiency polydispersity description. This result is essential, as it gives a solution to the two limitations of Eulerian models stated in Chapter 3, and consequently bridges the theoretical gap between Eulerian and Lagrangian methods.

### Two-dimensional droplet cloud crossing

This test case challenges the extension to two-dimensions of the high order velocity moment method. As seen in Section 9.3, extending the quadrature method from one to two-dimensions amounts to extend the QMOM from mono-variate to multi-variate distribution functions. This transition represents a theoretical gap. This is the reason why a test case is dedicated to validate the quadrature method proposed in Section 9.3. It involves an elementary case of droplet cloud crossing with opposite velocity at  $CFL = 1$ , in a  $200 \times 200$  cell grid. Figure (10.3)-(top right) displays the initial conditions. The test case involves evaporating droplet clouds, and tests, first the quadrature method for crossing sprays in two dimensions, and also the coupling between transport and evaporation. The distribution function is constant, as illustrated in Section 3.3.2. In addition to the crossing droplet cloud, a third motionless cloud is initialized in the top right corner of the domain in order to evaluate the quality of the resolution of the evaporation term coupled to the description of the crossing, see Fig. (10.3)-(top-left). Results, displayed in Fig. (10.3), show that the quality of polydispersity description is not affected by the velocity moment quadrature. The slight different at time  $t = 0.3$  comes from the numerical diffusion due to the Strang dimensional splitting, see Section 3.2.1. This is obviously the very first test, and others with greater complexity will have to be conducted in order to validate the feasibility of this method for potentially industrial configurations. Nevertheless, this test was necessary since the extension from one to two-dimension is far from being trivial, and its results are encouraging and allow us to go further in the validation process.

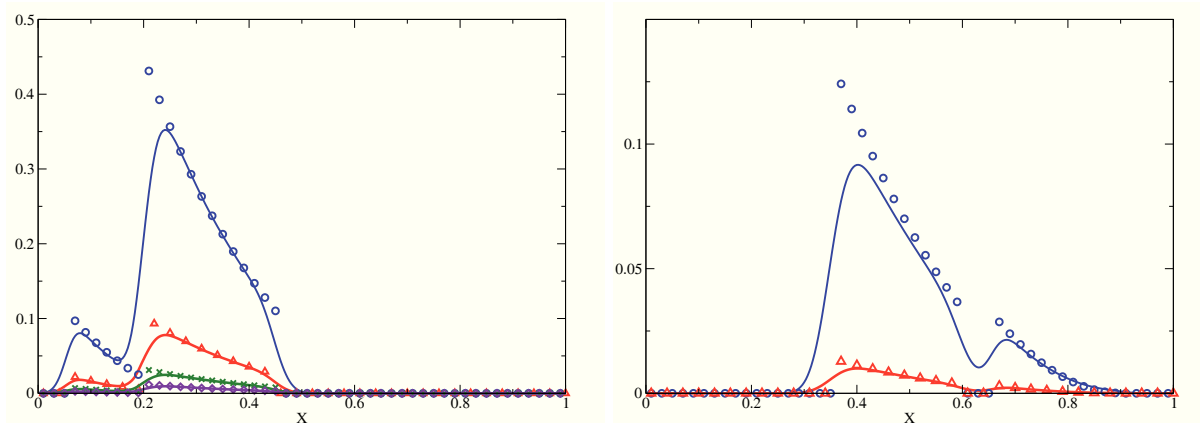


Figure 10.2: Evolution of a spray in a discontinuous velocity field calculated with the multi-fluid multi-velocity model model, compared to the analytical solution of the problem. Solution at time  $t = 0.4$  (left) and  $t = 0.7$  (right) compared to the analytical solution of the problem represented by markers. The computation is carried out in a 300 cell grid.

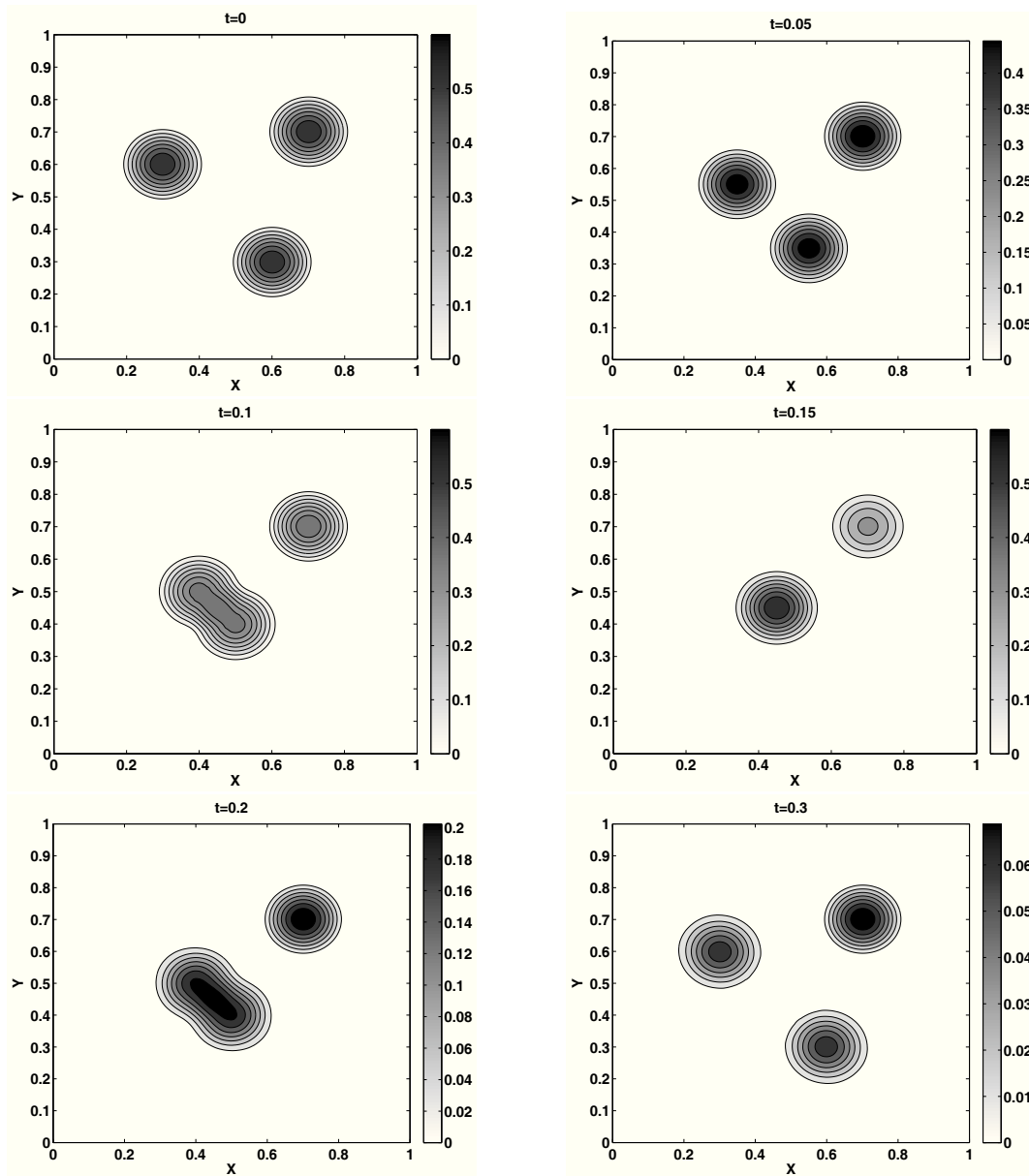


Figure 10.3: Transport and evaporation of droplet clouds with PTC. (Top-left) Initial condition: the cloud at the top-right of the domain is motionless and is hold as the reference to evaluate the quality of the evaporation resolution for moving clouds. The computation is carried out in  $200 \times 200$  cell grid.

## Conclusion

This chapter concludes the presentation of the modeling work done during this PhD, begun with the design of the EMSM model, and continued with the design of the EMVM model. It provides a theoretical solution to the two limitations formulated in Section 3.4 in the context of the multi-fluid model : an efficient description of polydispersity and the capacity to describe PTC with an Eulerian model. Fig. (10.4) gives an illustration of the nature of the models designed during this PhD, in the present hierarchy of Eulerian spray models.

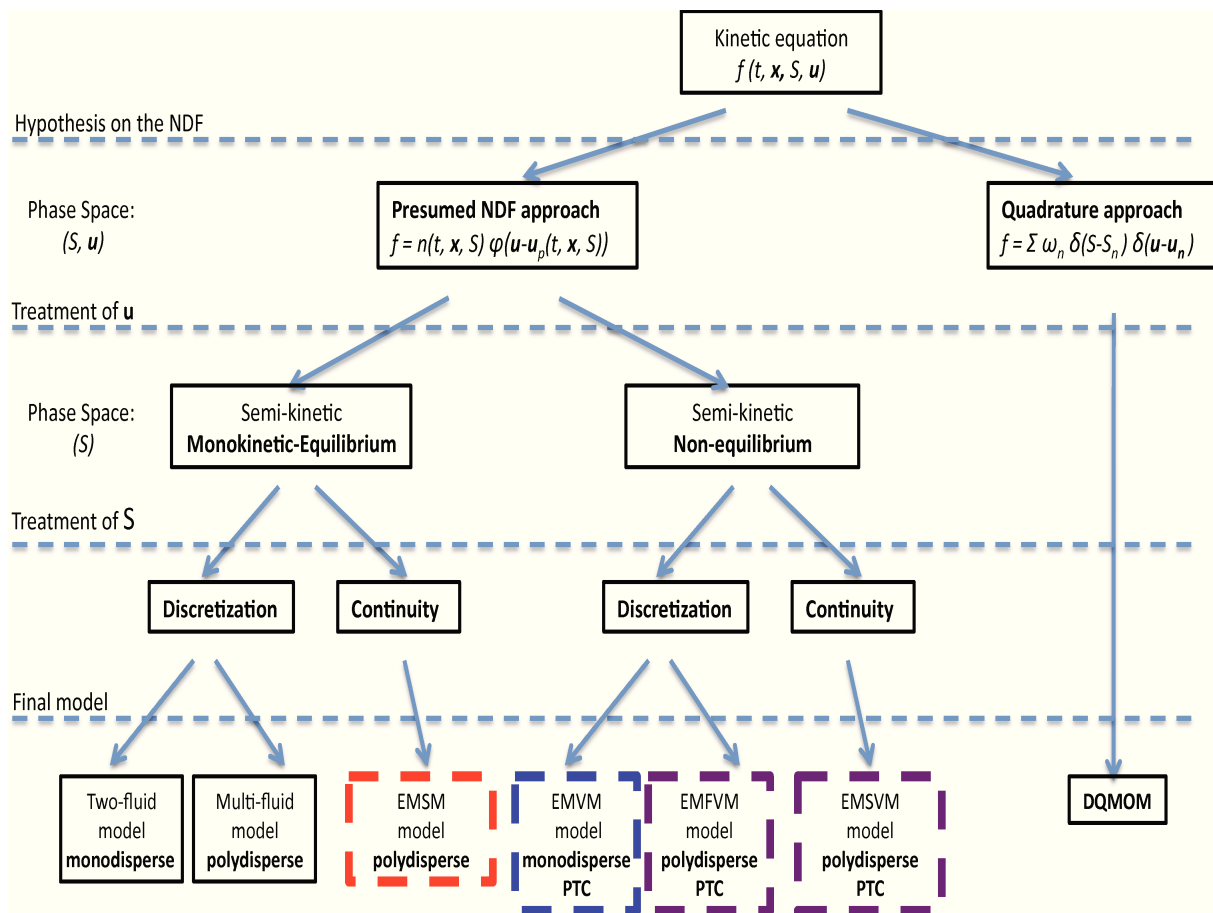


Figure 10.4: Overview of spray models, augmented with the models designed in this PhD. The EMSM model is discussed in Chapter 4. The EMVM model is discussed in Chapter 9. The EMFVM and EMSVM models are discussed in this chapter

## Chapter 11

# Implementation of the EMFVM model in MUSES3D

This chapter presents a synthetic vision of the implementation work of EMFVM model in the MUSES3D code presented in Chapter 7. As for the implementation of the EMSM model, the present developments have to meet three requirements : the preservation of the code genericity, of the algorithm capacity to ensure low diffusion, and its easy adaptation to High Performance Computing (HPC) algorithm of the code. The purpose of this work is the same as for the implementation of the EMSM model : assess its feasibility on challenging test cases. This chapter is organized as follows. At first, based on the exiting structure of the MUSES3D code, an inventory of the needed modifications is proposed. Then the computing implementation strategy is discussed and organized between the three following aspects : data structure and corresponding tools, initialization, numerical scheme.

We recall here the convention chosen for the notations.

**Notation:** The various kinds of structure considered in the MUSES3D code are denoted with the following convention:

- arrays are written with normal characters,
- derived data types are written in italic characters,
- routines are written in italic bold charaters
- module names are written in bold characters.

**Notation:** For the sake of legibility, the profil of the arrays contained in the derived data types, which is noted in Section 7.1.4  $array(1 : N_x, 1 : N_y, 1 : N_z, 1 : N_S, 1 : N_{mom}, 1 : N)$  is written, in the algorithm illustrations under a simplified form. Indeed, given the framework described in Section 3.2, the physical transport is done in the context of a dimensionalized splitting, so there is only one transported dimension implying that  $N = 1$  and only one space dimension is mapped. Moreover, only one size section is considered, so  $N_S = 1$ . Thus, without loss of generality, the slope and the flux arrays are noted  $array_i(1 : N_{mom})$ , denoting the value of  $array$  in the  $i^{th}$  cell of the transported dimension.

### 11.1 Inventory of needed modifications

In order to fulfill the three conditions formulated in the introduction, and according to the code structure, presented in Chapter 7, five intervention locations are identified:

- The first one concerns the data structure. As seen in Chapter 7, the data structure relies on a single data type, *Field*, illustrated in Algo. (1). Yet, in the context of the EMFVM, the quadrature

procedure, on the basis of this model, computes abscissas and weights resulting from the quadrature of the velocity moment vector, see Section 9.3. These two arrays have thus to be included in the data structure to run computations with the EMFVM model. Moreover, one has to take into account that the velocity moment set contains four moments in one dimension and ten moments in two dimensions (see Section 9.2 and Section 9.3).

- The corresponding inversion procedure, or quadrature procedure goes hand in hand with the presence of abscissas and weights. We refer to it as inversion algorithm, relative to the projection algorithm performing the inverse work, i.e computing the moments from the abscissas and weights.
- These new arrays have to be initialized.
- Concerning the numerical scheme for physical transport resolution, Section 9.5 presents and justifies the use of a first order kinetic scheme. Yet, at present, only the second order advection schemes are implemented. The intervention location of finite volume schemes has been clearly identified in Section 7.1.2.
- Chapter 10.2.1 has highlighted some difficulties when directly using the multi-fluid resolution algorithm for phase space transport. An adapted algorithm has then been proposed in order to use the multi-fluid algorithm for resolution with the EMFVM model.

## 11.2 Data structure modification and associated numerical tools implementation

### 11.2.1 Data structure

Two new aspects, explained in the previous section, concerning the data structure are brought by the EMFVM. The first requires to include arrays of *abscissas* and *weights* in the generic data type *Field*. This is illustrated in Algo. (11.2.1). In the context of the EMFVM model, the vector *sizemom*, dedicated

---

**Algorithm 10** Generic data structure with weights and abscissas

---

```

structure Field
  array sizemom, velmom, wgt, abs
end structure Field

```

---

to EMSM model, is not used. Moreover, all the developments explained in this chapter are done in the context of third order moment quadrature. The profil of *velmom*, *wgt*, and *abs* is generic and corresponds, as explained in Section 7.1.4, to:

$$\text{array}(N_x, N_y, N_z, N_S, N_{mom}), \quad (11.1)$$

but  $N_{mom}$  has different values for each of the abovementioned arrays:

- For the velocity moment vector, *velmom*,  $N_{mom} = 4$ , for a one-dimensional case, and the components the array are defined this way:

$$\begin{aligned}
 \text{velmom}(1) &= M_0, \\
 \text{velmom}(2) &= M_1, \\
 \text{velmom}(3) &= M_2, \\
 \text{velmom}(4) &= M_3.
 \end{aligned} \quad (11.2)$$

In a two dimensions case,  $N_{mom} = 10$ , and the components of the array are defined this way:

$$\begin{aligned} \text{velmom}(1) &= M_{0,0}, \\ \text{velmom}(2) &= M_{1,0}, \text{velmom}(3) = M_{0,1}, \\ \text{velmom}(4) &= M_{2,0}, \text{velmom}(5) = M_{1,1}, \text{velmom}(6) = M_{0,2}, \\ \text{velmom}(7) &= M_{3,0}, \text{velmom}(8) = M_{2,1}, \text{velmom}(9) = M_{1,2}, \text{velmom}(10) = M_{0,3}. \end{aligned} \quad (11.3)$$

where the  $M_k$  and  $M_{l,m}$  are the velocity moments defined in Chapter 9.

- For the *weight* array *wgt*,  $N_{mom} = \beta$ , where  $\beta$ , defined in Chapter 9, is the total number of quadrature points. In two dimensions, *wgt* reads:

$$\text{wgt}(1) = n_1, \text{wgt}(2) = n_2, \text{wgt}(3) = n_3, \text{wgt}(4) = n_4.$$

- For the *abscissas* array *abs*,  $N_{mom} = \beta N_{\text{dim}}$ . The vector *abs* then writes in its fifth dimension:

$$\text{abs}(1) = U_{(1)1}, \text{abs}(2) = U_{(2)2}, \text{abs}(3) = U_{(3)1}, \text{abs}(4) = U_{(4)2}, \quad (11.4)$$

$$\text{abs}(5) = U_{(1)1}, \text{abs}(6) = U_{(2)2}, \text{abs}(7) = U_{(3)1}, \text{abs}(8) = U_{(4)2}. \quad (11.5)$$

$$(11.6)$$

### 11.2.2 Associated numerical tools

As explained in Section 9.3, the critical step of the EMFVM model, derived from the EMVM model, is the inversion algorithm. This algorithm, by far the most challenging to design, goes hand in hand with the projection algorithm. The general structure of the inversion algorithm *inversion*, is presented in Algo. (11), in the two-dimensional case. This algorithm proceeds in three steps. The two first steps are singularity detection steps, corresponding to cases where the Cholesky matrix used in the decomposition of the covariance matrix (see Section 9.3) is singular. A distinction is made between singularities occurring in direction  $x$  or  $y$  with  $\sigma_{1,1} = 0$  or  $\sigma_{2,2} = 0$ , and the case where the singularity occurs in another direction, when  $\sigma_{1,2}^2 = \sigma_{1,1}\sigma_{2,2}$ . The third step corresponds to the quadrature in regular cases.

Within the routine *inversion* calls to different subroutines are made :

- *selec\_mom* is called in the case where the velocity dispersion is null in the first or second space direction. This routine extracts the set of moments in the direction of non null dispersion from the global moment set.
- *mom\_chol1D* is called in the same context. This routine performs the one-dimensional Cholesky decomposition in the direction where the dispersion is non null. Its input arguments are *selected\_mom* and its output are the reduced moments *reduced\_mom*.
- *pds\_chol* computes the set of weight, and abscissas of the set of reduced moments, in each direction of the Cholesky decomposition.
- *treat\_singularity* is called in the case where the velocity dispersion is null in a direction different from the canonical directions of the referential frame, and performs the quadrature on that particular case.
- *mom\_chol* is the routine for the two-dimensional Cholesky decomposition

The structure of the projection algorithm is displayed in Algo. (12).

This tools being particular to the EMFVM model, they are included in a dedicated module called **Tools\_emvm**.



---

**Algorithm 11** Routine *inversion*

---

```

procedure inversion(velmom, abs, wgt)
  input velmom
  output wgt, abs
  % Case where  $\sigma_{1,1} = 0$ 
  if (velmom(4) * velmom(0) - velmom(2)2 <  $\epsilon$ ) then
    % The quadrature is done in the second direction
    call selec_mom(velmom,2,1,selected_mom)
    call mom_cholD(selected_mom,reduced_mom)
    call pds_chol(reduced_mom)
    ...
    % Computation of wgt abs
    ...
    % Case where  $\sigma_{2,2} = 0$ 
  else if (velmom(6) * velmom(0) - velmom(3)2 <  $\epsilon$ ) then
    % The quadrature is done in the first direction
    call selec_mom(velmom,1,2,selected_mom)
    call mom_cholD(selected_mom,reduced_mom)
    call pds_chol(reduced_mom)
    ...
    % Computation of wgt abs
    ...
  else if (velmom(5) * velmom(0) - velmom(2) * velmom(3) <  $\epsilon$ ) then
    call treat_singularity(velmom,abs,wgt)
  else
    % Regular case call mom_chol(velmom,reduced_mom)
    call pds_chol(reduced_mom)
    ...
    % Computation of wgt abs
    ...
  end if
end procedure inversion

```

---



---

**Algorithm 12** Projection algorithm

---

```

procedure projection(mom_vel, wgt, abs)
  % Example of a two-dimensional case
  velmom(1) =  $\sum_{i=1}^{\beta} \text{wgt}(i)$ 
  ...
  velmom(10) =  $\sum_{i=1}^{\beta} \text{wgt}(i) * \text{abs}^3(N_{\text{pic}} + i)$ 
  ...
end procedure projection

```

---

## 11.3 Modification of the initialization process

The initialization of the arrays `mom_vel`, `abs` and `wgt` is discussed here. First, referring to Algo. (3), the initialization in the EMFVM case is included in the condition  $N_{mom\_sizes} = 0$ , like the multi-fluid initialization. Then, a flag is introduced in order to distinguish the two types of initialization within the condition  $N_{mom\_sizes} = 0$ .

Since the first component of the velocity vector `velmom` is identical in the cases of multi-fluid or EMFVM resolution, its initialized is taken up. The abscissas and the weights are then initialized. Finally, the whole velocity moment vector is initialized, through a projection algorithm. This is illustrated in Algo. (13). The code offers the possibility to initialize velocity distribution with dispersion around the mean velocity in each direction. The array `dispersion` accordingly modifies the value of the corresponding abscissa from the mean velocity (velocity in Algo. (13)).

---

**Algorithm 13** Initialization of `Spray%vel`, `Spray%abs` and `Spray%wgt`

---

```

% multi-fluid initialization
if (multi-fluid) then
  ...
  % EMFVM initialization
else if (EMFVM) then
  ...
  % Initialization of velmom(1) as done in Algo. (3)
  ...
  for  $i = 1, N_{dim}$  do
     $abs((i - 1) * \beta + 1 : \beta * i) = velocity(i) + dispersion((i - 1) * \beta + 1 : \beta * i)$ 
  end for
   $wgt(1 : \beta) = velmom(1) / \beta$ 
  ...
  call projection(Spray,wgt,abs)
  ...
end if

```

---

## 11.4 Numerical scheme adaptation

### 11.4.1 Physical transport resolution

The first order scheme designed in Section 9.5 for advection requires only slight modifications in the modules of the successive finite volume scheme steps : **Slope\_tools**, **Recons\_tools**, **Flux\_tools**, **Update\_tools** (see Chapter 7). Indeed, a first order scheme does not involve any slope computation. Therefore the changes concern fluxes computations, and the update procedure. The input argument vector is particularly lighter than in the multi-fluid or EMSM context, since, referring to Section 9.5, it only involves the values of the abscissas and weights on both sides of an interface. The updated flux computation, routine structure is illustrated in Algo. (14).

Some changes are also brought in the update procedure in comparison to the multi-fluid model. In order to ensure the stability of the scheme, the update moment vector is inverted and then projected. Indeed, as discussed in Section 9.3, the moment set realizable through the set of abscissas and weights is a subspace included in the velocity moment space. This final step of inversion-projection ensures that the moment vector `velmom` is consistent with the set of computed abscissas and weights. The implementation of the EMFVM model for physical transport can be seen in Fig. (11.1).

---

**Algorithm 14** Flux computation

---

**procedure** *flux\_comp*(*Flux*,*Spray*,*Slope*,*Recons*,*Mean*)

```

...
if ( $N_{mom\_sizes} = 0$ ) then
  % multi-fluid model resolution
  if (multi-fluid) then
    ...
    % EMFVM model resolution
  else if (EMFVM) then
    for  $i = 1, N_x(N_y \text{ or } N_z)$  do
      call vel_flux(Flux%veli,Spray%absi, Spray%wgti, Spray%absi-1, Spray%wgti-1)
    end for
  end if
...
end if
...
end procedure flux_comp

```

---



---

**Algorithm 15** Update procedure

---

**procedure** *update\_field*(*Spray*<sup>*n*</sup>, *Spray*<sup>*n+1*</sup>)

```

...
if ( $N_{mom\_sizes} = 0$ ) then
  % multi-fluid model resolution
  if (multi-fluid) then
    ...
    % EMFVM model resolution
  else if (EMFVM) then
    for  $i = 1, N_x(N_y \text{ or } N_z)$  do
      Spray*%veli = Sprayn%veli
      call euler(Spray*%veli)
      Sprayn+1%veli = Sprayn%veli
      call inversion(Spray,wgt,abs)
      call projection(Spray,wgt,abs)
    end for
  end if
...
end if
...
end procedure update_field

```

---

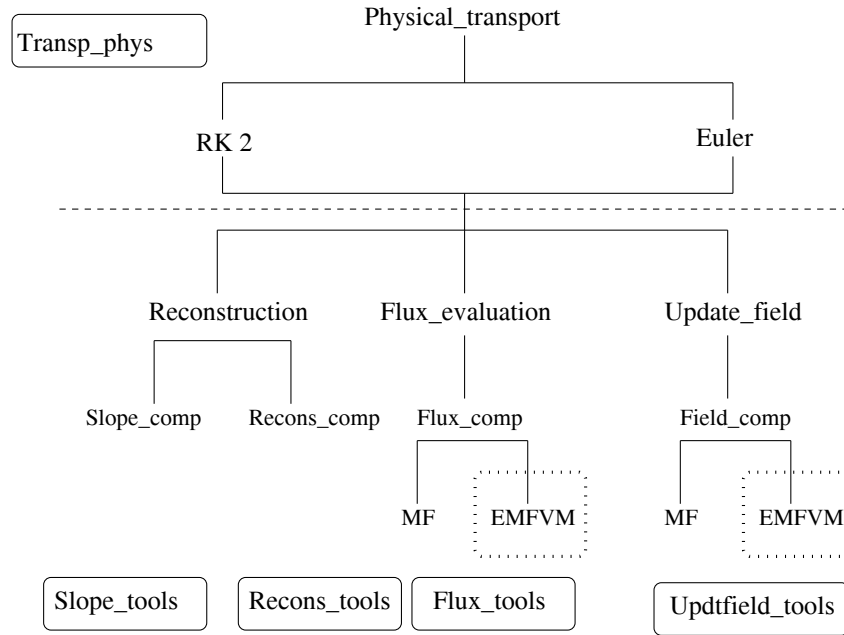


Figure 11.1: Implementation of EMFVM model in the structure for physical transport. The dashed line distinguishes the different modules. The dotted borders locate the contributions. The signe MF denotes the multi-fluid model

### 11.4.2 Phase space transport resolution

As seen in Section 10.2, the resolution of phase space transport can rely on the ODE solver Radau5 designed for the multi-fluid model, with some adjustments. Then, two possibilities were then given. One could either create a new routine dedicated to the EMFVM model at the level of the routine *phase\_tr\_mf*. This would have brought the advantage of a clear structure distinguishing the multi-fluid and the EMFVM model resolution. But this would have needed to create a new routine from scratch as well as its interfaces with the module *spray\_eq* used to compute the source term  $\Phi$  in Eq. (7.3). The second option has thus been held, consisting in adjusting the multi-fluid algorithm in order to handle the resolution with the EMFVM when needed.

This has required two modifications. The first one has consisted in initializing the vector  $\mathbf{Y}$  or initial conditions for the Radau5 solver, in Eq. (7.3) with the centered moments defined in Section 10.2. The updated structure of *phase\_tr\_mf* is displayed in Algo. (16). The second modification has consisted in creating routines to analytically compute the Jacobian of the source terms  $\Phi$ . This has been handled by the routine *mf\_jeq*, the equivalent of *mf\_eq* for Jacobian computation. The output of these two routines, the sources term  $\Phi(\mathbf{Y})$ , from *mf\_eq*, and its Jacobian from *mf\_jeq*, is then transferred to the routine *driver\_radau*, performing the actual resolution through the Radau5 solver. The structure of the routine *mf\_jeq* is displayed in Algo. (17). The structure update of the code structure needed by the implementation of the EMFVM model is illustrated in Fig. (11.2).

## 11.5 Conclusion

This chapter is dedicated to the implementation of the EMFVM model in the MUSES3D code. It presents the computing strategy in order to cope with the three requirements formulated in the introduction. The new functionality of the MUSES3D code has allowed to evaluate the EMFVM model on challenging test cases, where the results are discussed in Chapter 12.

---

**Algorithm 16** Transport in phase space

---

```

procedure phase_tr_mf(Spray)
  ...
  if (EMFVM) then
    call mom_to_mom_center(Spray,centered_velmom)
    ...
    %Computation of  $\mathbf{Y}$ 
    call driver_radau( $\mathbf{Y}$ ,  $t_0$ ,  $t_{end}$ )
    %Update of centered_velmom
    centered_velmom =  $\mathbf{Y}$ 
    ...
    call mom_center_to_mom(Spray,centered_velmom)
    ...
    call inversion(Spray,wgt,abs)
    call projection(Spray,wgt,abs)
    ...
  end if
  ...
end procedure phase_tr_mf

```

---



---

**Algorithm 17** Jacobians computation

---

```

procedure mf_jeq...
  % Computation of the Jacobianof the drag and evaporation terms
  call drop_model( $t$ )
  ...
  if (evaporation) then
    call Fill_mat_Jac_evap(Jac_evap)
     $\mathbf{Jac}(\mathbf{Y}) = \text{Jac\_evap}$ 
  end if
  ...
  if (drag) then
    call Fill_mat_Jac_drag(Jac_drag)
     $\mathbf{Jac}(\mathbf{Y}) = \mathbf{Jac}(\mathbf{Y}) + \text{Jac\_drag}$ 
  end if
  ...
end procedure mf_jeq

```

---

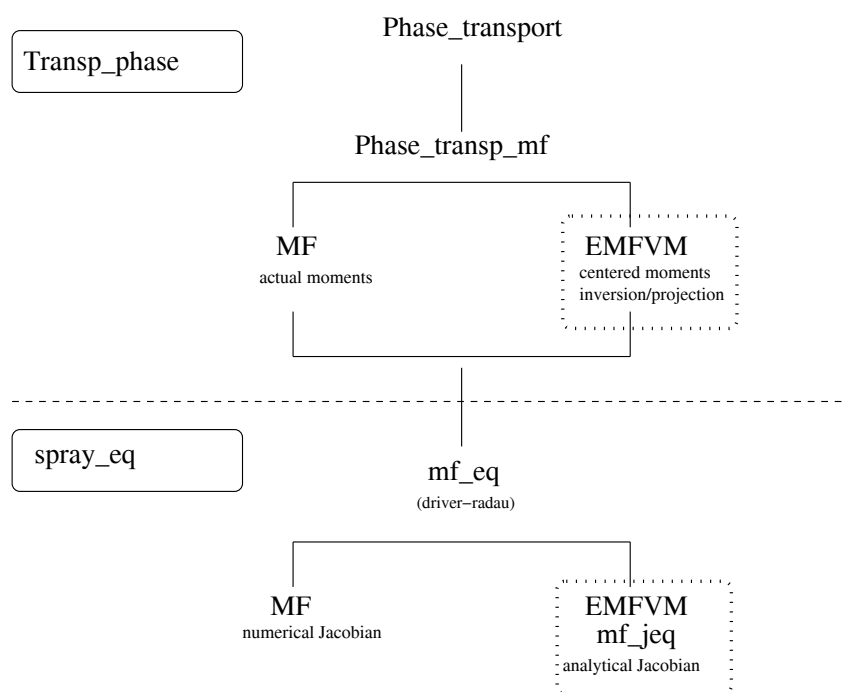


Figure 11.2: Implementation of EMFVM model in the structure for phase space transport. The dashed line distinguishes the different modules. The dotted border locates the contributions.

# Chapter 12

## Validation and results

This chapter is dedicated to the evaluation of the Eulerian Multi Fluid and Velocity Moment (EMFVM) model implemented in the MUSES3D code, see Chapter 11. Its implementation in MUSES3D allows to use more challenging test case than the ones presented in Chapter 10. In the first test case, focusing on droplet clouds dynamics in the Taylor-Green configuration for the gaseous phase, the behavior of the quadrature method is assessed where substantial numerical diffusion is present. Eventually, a second test case, involving a free jet, shows the ability of the model to description areas of significant velocity dispersion, i.e when Particle Trajectory Crossings (PTC) occur. The corresponding results lead to a first conclusion about the potential of the method towards further extension to industrial configurations.

### 12.1 Dynamics of a droplet cloud in a Taylor-Green configuration

The studied configuration is designed to assess the robustness of the high order velocity moment method in a challenging context, since a two-dimensional Taylor-Green configuration for the gas phase is considered. This configuration is illustrated in Fig. (3.2)-left. Two motionless clouds are initialized, one at the top, the other at the bottom of  $200 \times 200$  domain, with periodic boundary conditions on its edges. A first case, involving a non-evaporating monodisperse spray, is run in order to assess the single EMVM method and associate schemes in this particular configuration.

What is particularly interesting is the behavior of the quadrature method in this gas field in a case where numerical diffusion is present. Indeed, in area with very low density, due to numerical approximations, quadrature methods may lead to multi-modal distributions where one node, despite its low weight, has an uncontrolled associated velocity values. These situation can cause unexpected  $\delta$ -shocks. The computation CFL remains 1, thanks to perfectly well adapted resolution algorithms contained in the MUSES3D code (see Chapter 7). Then, a second test case shows the capacity of the EMFVM model to solve a polydisperse evaporating spray experiencing PTC in this Taylor-Green configuration.

The reader must be aware of the fact that this tests, assessing the model robustness, are a first step towards a full validation of the EMFVM model. Comparison with experiments or validated approach, such as Lagrangian approaches have to be carried out in order to draw definitive conclusions. This is done in Section 12.2.

#### 12.1.1 Non evaporating case

In this first case, the spray is initialized with a Stokes number of  $St = 0.31$ . Since the particle Stokes number is greater than the critical Stokes number of this configuration  $St_c$ , the particles will be ejected from the vortices, so that PTC are highly probable.

This first test involves a non evaporating monodisperse spray. The computation is run until the dimensionless time  $t = 2$ . Results of the dynamics of this spray are shown on Fig. (12.1) to Fig. (12.4). Fig. (12.1) presents the successive mass fields until  $t = 1$ , and Fig. (12.3) between time  $t = 1$  and  $t = 2$ . Fig. (12.2) and Fig. (12.2) displays, for some instants, the x- and y-velocity fields as well as the spray temperature, in the sense defined in Section 9.3. Areas of high value of temperature are significant of velocity dispersion, where crossing trajectories may occur. Dragged by the gaseous Taylor-Green vortices, the clouds begin their movement at  $t = 0.25$ , and one can here notice that they are going to impinge. They begin to cross at time  $t = 0.5$ , according to their y-velocity values in Fig. (12.2)-medium left. This is confirmed by the field of temperature shown in in Fig. (12.2)-bottom left. The particle temperature is defined by the following relation:

$$T = \frac{\sigma_{1,1} + \sigma_{2,2}}{2}. \quad (12.1)$$

This temperature associated to the velocity dispersion, should not be confused with the temperature of the liquid, which is not resolved in this work. Since droplet collisions are excluded from this case, a non-zero droplet temperature automatically implies the presence of droplet clouds with different velocities at the same location.

Particles have finished to cross at  $t = 0.75$ , and, since the Stokes number is much higher than the critical Stokes number  $St_c$  (see Section 3.3.1) above which particles are ejected from the vortices, the cloud initialized at the bottom part of the domain finds itself at the top part of the domain. The effect of drag exerted by the vortices has led to the accumulation of droplets on the two thin layers, at  $t = 0.75$ . At  $t = 1$ , two parts can now be distinguished. The first part one, at the center of the domain, is ejected from the vortices and the corresponding clouds are to cross the same way as at time  $t = 0.5$ . This movement is an oscillatory phenomenon. But in addition, a new part is ejected at the right and left edges of the domain. If one focuses on the region such as  $y > 0.5$ , it is important to notice that the y-velocity of the extreme part of the flow field ( $x < 0.2$  and  $x > 0.8$ ) is positive, and opposed to the y-velocity of the center part of the flow field. This is due to the particle inertia. Indeed, these particles originates from the bottom cloud, with positive y-velocity. During the crossing, they enter the top vortices with negative y-velocity field. But their inertia is high enough so that they are advected to positive y-velocity fields in a time lower than their relaxation time. Therefore, because of periodic boundary conditions, two types of crossing occurs according to Fig. (12.2)-left : in the x- and y-directions. These crossings are seen at time  $t = 1.25$  and  $t = 1.5$  in Fig. (12.3). The velocity and temperature field structures at time  $t = 1.5$  indicate that particles will impinge at  $y = 0$ , and  $y = 1$ . This is confirmed at time  $t = 1.75$  and  $t = 2$  and Fig. (12.4)-left highlights the new areas of high temperature predicted at  $t = 1.5$ . Let us finally focuses on the singularities which occur at time  $t = 1.5$  at  $x = 0.08$  and  $x = 0.92$ . This singularity occurrence corresponds to the presence of locally three distinct velocities. In one considers the top part of the domain, the velocity distribution is made of the velocity of the branch going toward the top of the domain, and the two velocities of the central layers with an oscillating movement between the tops and the bottom vortices. We will come back to this singularity in the next paragraph.

This test case validates the good behavior of the EMVM model, and particularly of the quadrature method and its implementation in the MUSES3D code. But the major conclusion to be drawn from this test case is the fact that we have for the first time demonstrated that an Eulerian model can account for PTC. Still, this method has two important limitations. The first one lies in the number of different velocity abscissas that can locally be reconstructed. The EMVM model as devised in Section 9.3 transports velocity moments up to third order in velocity. This allows to reconstruct locally only two distinct velocity vectors. In case more than two particles impinge, which happens in our illustration at  $t = 1.5$ , the advection system becomes weakly hyperbolic, like in the pressureless gas formalism, explained in Section 3.1.3, so that a  $\delta$ -shock is engendered. Extensions of the method to fifth or seventh order can be envisaged in order to reconstruct three or four different velocity vectors, if absolutely needed. This limitation is not to prevent the use of the EMVM method in industrial context, since the occurrence probability of a crossing involving three particles with three different velocities can reasonably be considered much lower than the probability occurrence of only two particles. Moreover, Fig. (12.3) demonstrates that the designed kinetic-based numerical schemes are perfectly stable through



these singularities. The following limitation is the most serious. It has been explained in Section 9.3, that different quadrature methods can be proposed, but the choice of the quadrature impacts the solution, which is not acceptable. That is why, on the basis of this work, further studies have been pursued, and some very promising method have been proposed in [233] and [37].

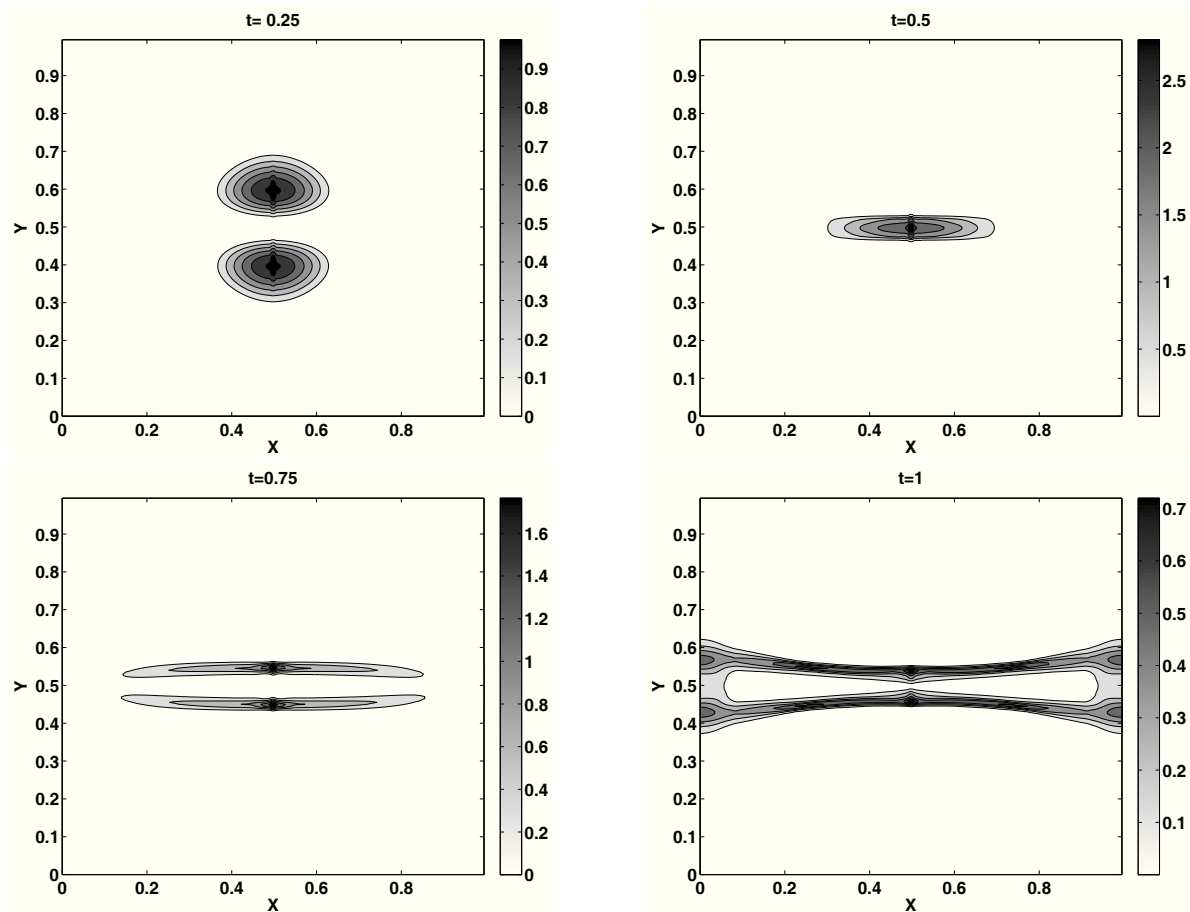


Figure 12.1: Dynamics of a monodisperse spray ( $St = 0.31$ ) in Taylor-Green vortices, solved with the EMFVM model, until  $t = 1$ . Corresponding droplet mass density with 6 equi-distributed iso-contours. The computation is run in a  $200 \times 200$  cell grid.

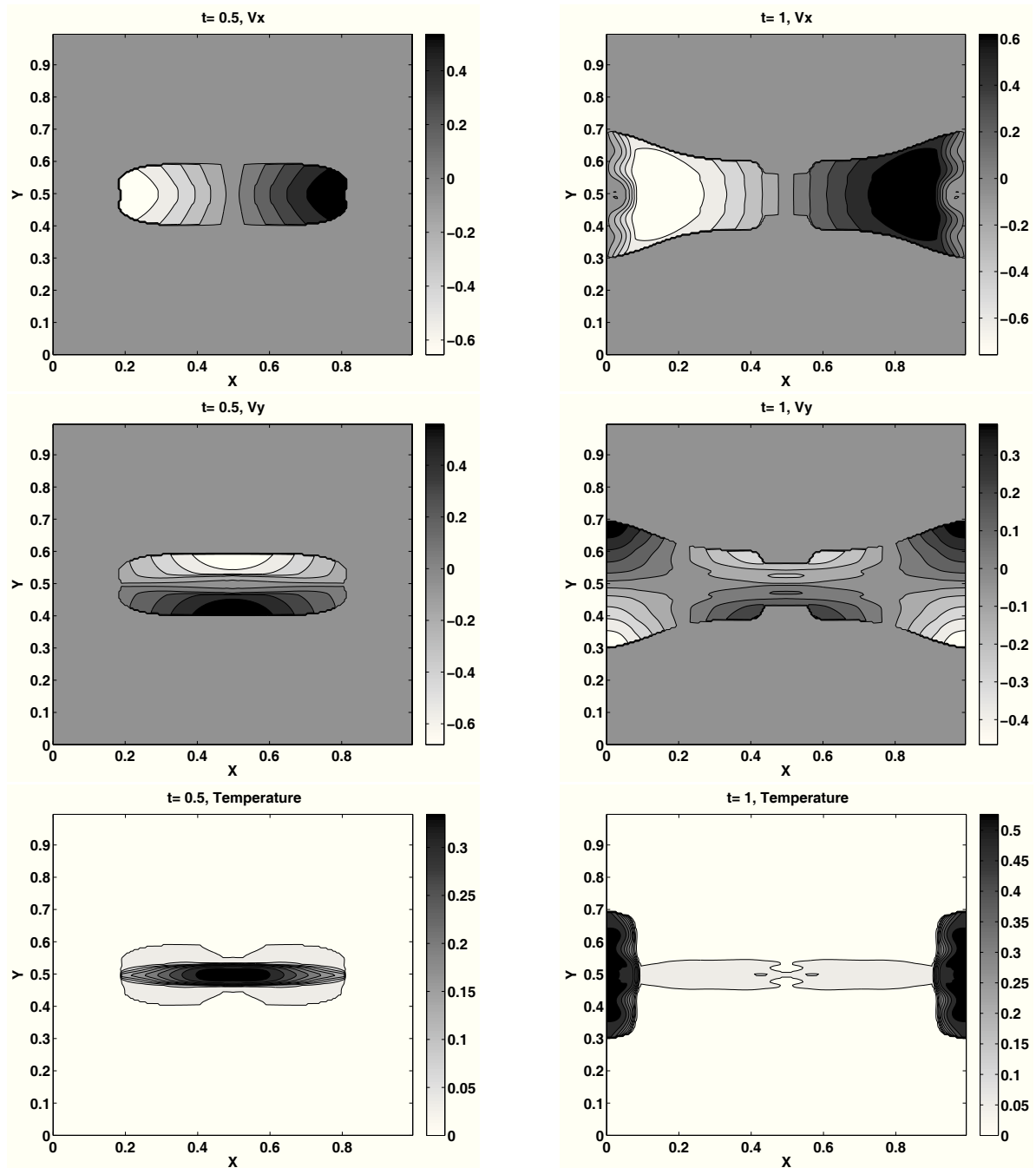


Figure 12.2: Dynamics of a monodisperse spray ( $St = 0.31$ ) in Taylor-Green vortices, solved with the EMFVM model. Corresponding x-velocity, y-velocity, and temperature with 10 equi-distributed isocontours. (Left) results for  $t = 0.5$ . (Right) results for  $t = 1$ . The computation is run in a  $200 \times 200$  cell grid.

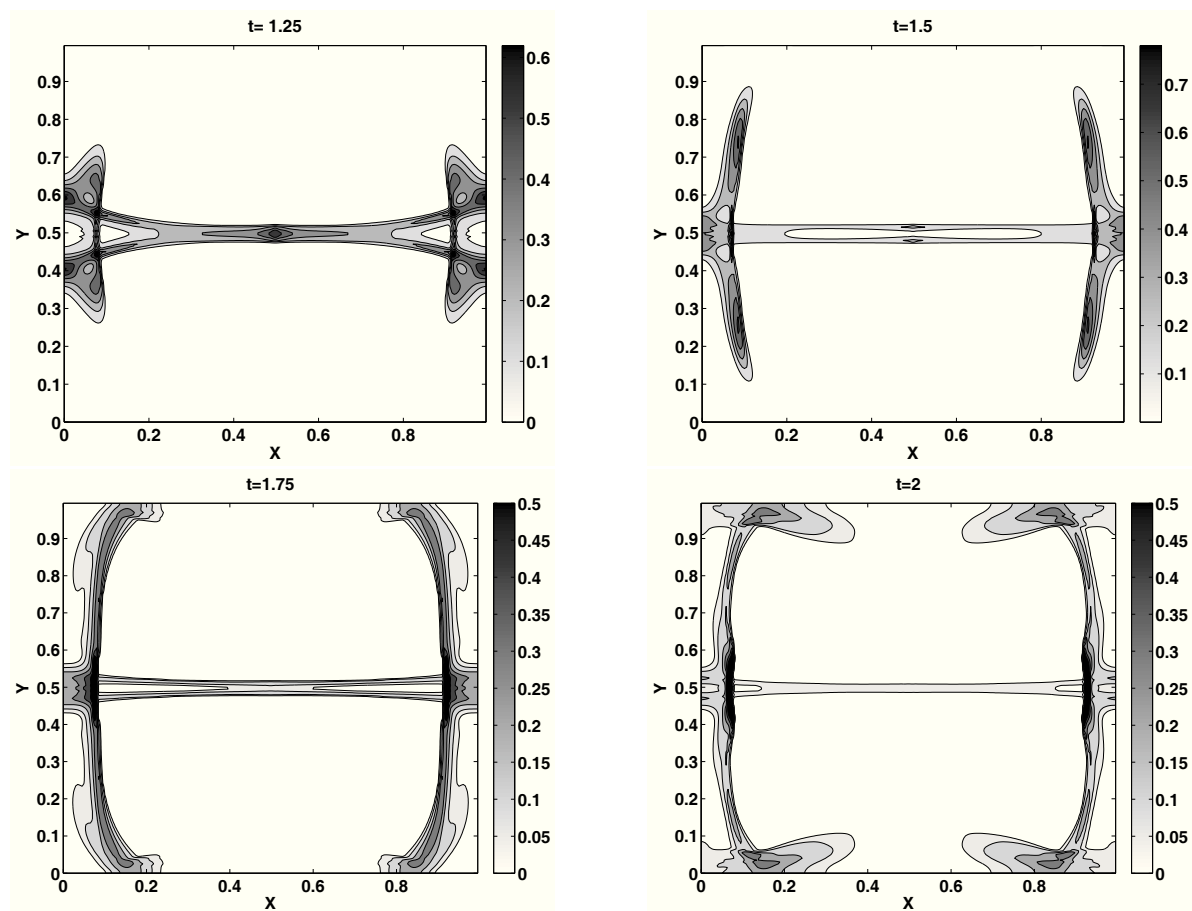


Figure 12.3: Dynamics of a monodisperse spray ( $St = 0.31$ ) in Taylor-Green vortices, solved with the EMFVM model, from  $t = 1.25$  to  $t = 2$ . Corresponding droplet mass density with 6 equi-distributed iso-contours. The computation is run in a  $200 \times 200$  cell grid.

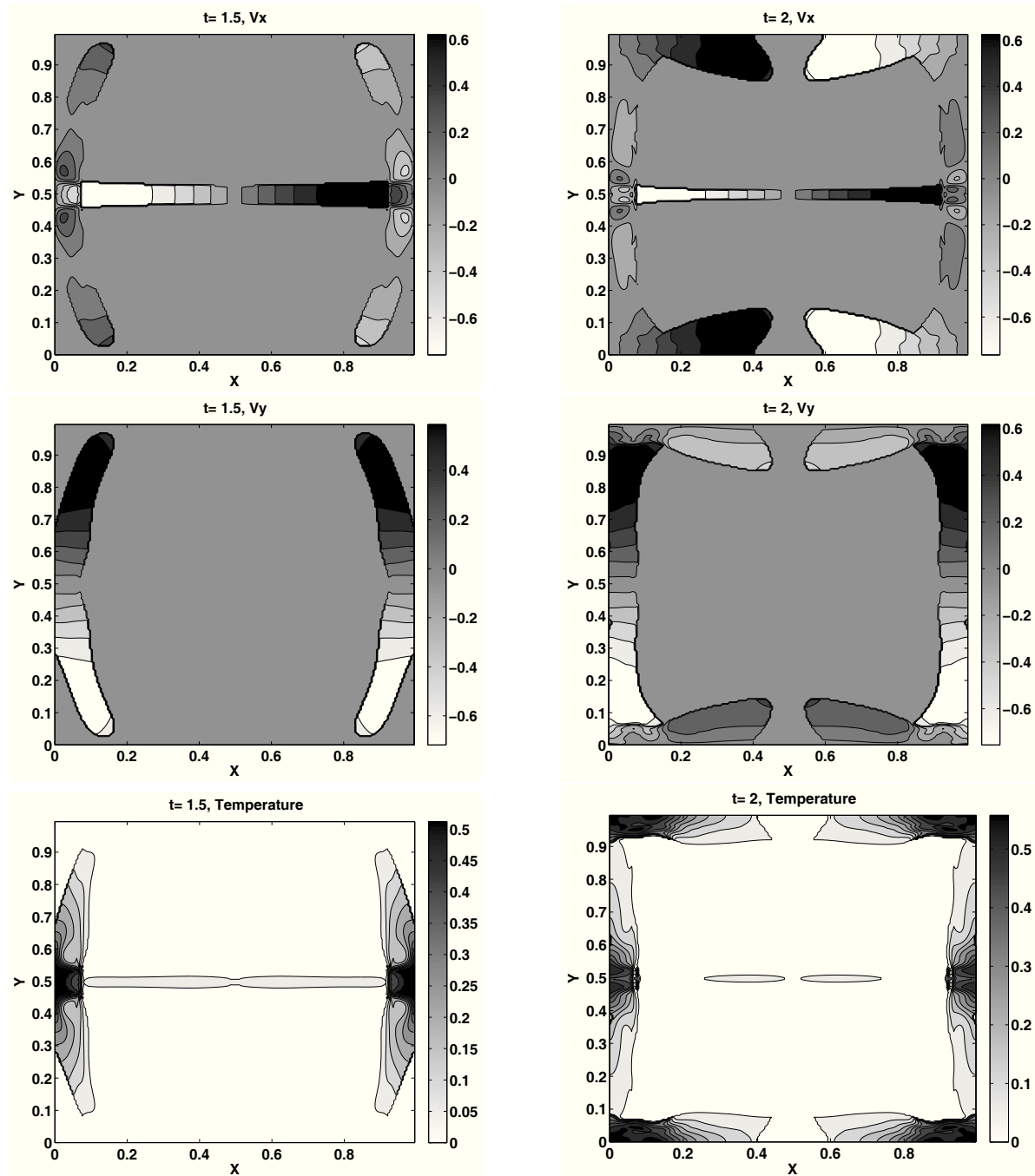


Figure 12.4: Dynamics of a monodisperse spray ( $St = 0.31$ ) in Taylor-Green vortices, solved with the EMFVM model. Corresponding x-velocity, y-velocity, and temperature with 10 equi-distributed isocontours. (Left) results for  $t = 1.5$ . (Right) results for  $t = 2$ . The computation is run in a  $200 \times 200$  cell grid.

### 12.1.2 Case of a polydisperse evaporating spray

We take up the same configuration as before with the same initial and boundary conditions but we consider now a polydisperse evaporating spray, described with the EMFVM model. The size phase space is made of five sections, with Stokes number ranging from  $St = 0.061$  to  $St = 0.46$ . The size distribution is illustrated in Fig. (8.2). The evaporation coefficient is set at  $K = 0.12$ . Fig. (12.5) displays the result for the total mass, at instants  $t = 0.5, 1, 1.5$  and  $2$ , whereas Fig. (12.6) shows results section by section at time  $t = 1$ . By comparing Fig. (12.5) with the corresponding results exposed at Fig. (12.1) and Fig. (12.3), the first conclusion is the good behavior of the model relative to evaporation, inheriting the stability features of the multi-fluid model. Moreover, the importance of the role of size-velocity correlations in this particular case explains the different of structure of the fields. The stripes appearing in Fig. (12.1)-top left, and which are clear on Fig. (12.1)-bottom right display this size-velocity correlation: each stripe on Fig. (12.1)-bottom right corresponds to one size section.

Fig. (12.6) very nicely describes the size-conditionned dynamics showing that the mass field of the lower sections, when still containing some mass are more developed than the mass field of the higher section containing particles with a higher relaxation time and thus harder to drag.

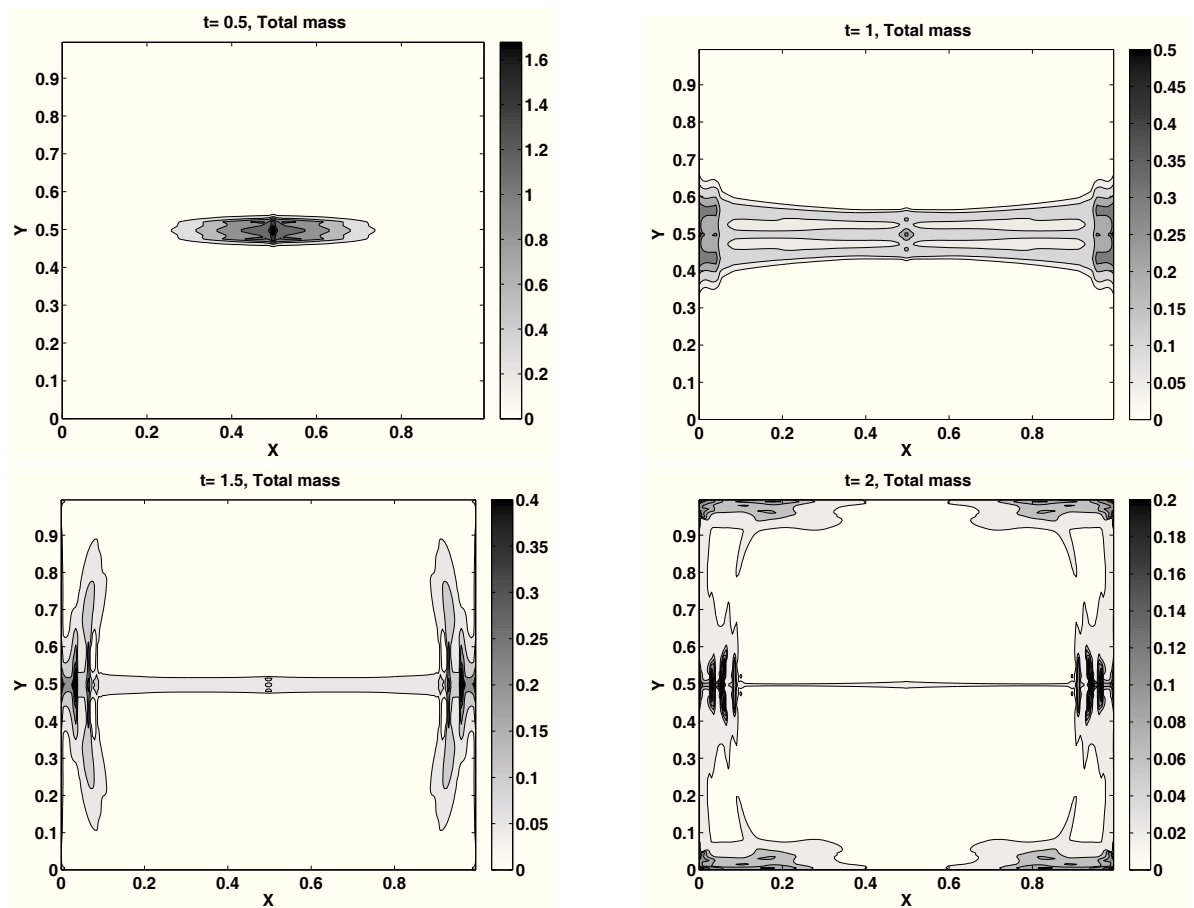


Figure 12.5: Dynamics of a polydisperse evaporating spray in Taylor-Green vortices, solved with the EMFVM model, for  $t = 0.5, 1, 1.5, 2$ . Corresponding droplet mass density with 6 equi-distributed isocontours. The computation is run in a  $200 \times 200$  cell grid.

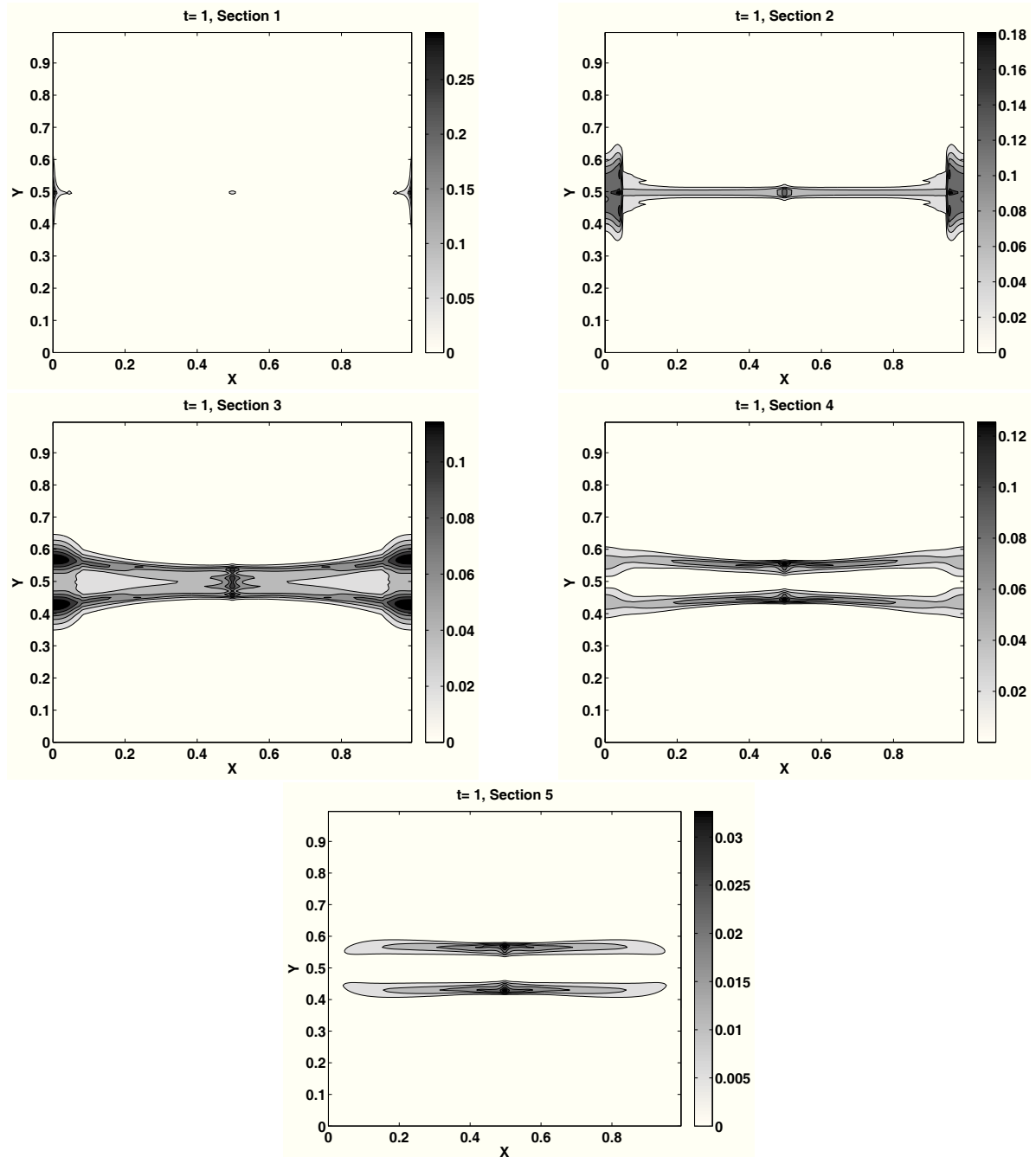


Figure 12.6: Dynamics of a polydisperse evaporating spray in Taylor-Green vortices, solved with the EMFVM model. Corresponding droplet mass density for each size section, from section 1 (top-left) to section 5 (bottom) at time  $t = 1$  with 6 equi-distributed iso-contours. The computation is run in a  $200 \times 200$  cell grid.

## 12.2 Free-jet configuration

### 12.2.1 EMFVM model versus Lagrangian models for free-jet configuration

The configuration chosen for the simulation with the multi-fluid, multi-velocity model is the same free-jet configuration with gas-phase instabilities as described in Section 3.3.2. The unstationary gas-phase velocity field destabilizes the liquid phase, and because spatially separate droplet clouds will interact with different gas-phase vortices, the droplets may impinge at a later time. Nonetheless, the intensity of crossings is relatively low as only a small amount of liquid interacts with the vortices. Indeed, the range of eligible Stokes numbers for which droplet crossing can be observed is small. On the one hand, the Stokes number must be greater than a minimum value,  $St_{\min}$ , above which droplets can be ejected from the vortices. On the other hand, the Stokes number must be lower than a maximum value,  $St_{\max}$ , above which the liquid phase does not interact with the gas phase. In the free-jet configuration, the range of Stokes numbers is  $[0.48, 1.1]$ . Nevertheless, this configuration precisely highlights an important property of our model, which is the ability to capture simultaneously regions where the droplet ‘temperature’ (or velocity variance)

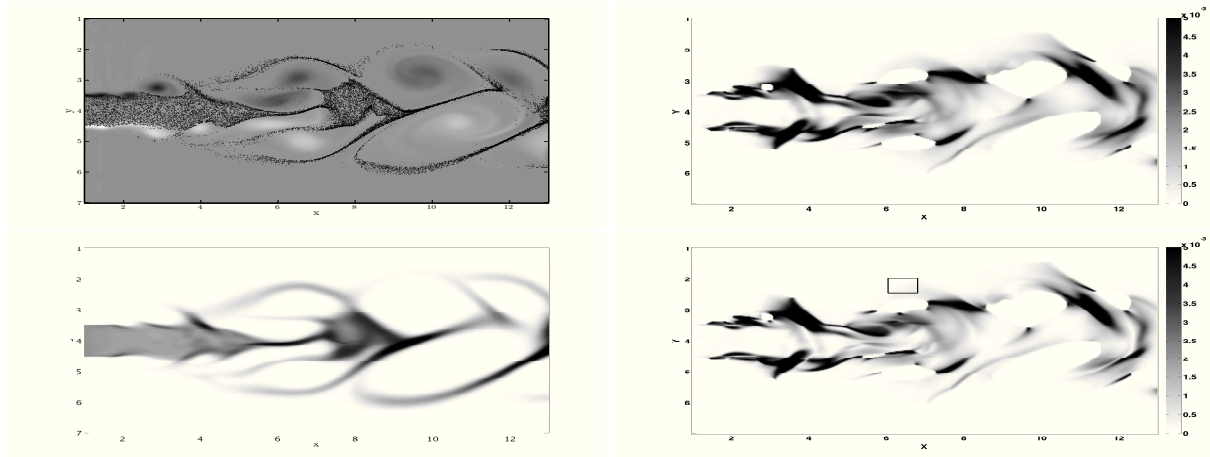


Figure 12.7: Non-evaporating polydisperse spray with high-inertia droplets (Stokes 0.48 to 1.1 corresponding to diameters from 60 to 90  $\mu\text{m}$ ) at time  $t = 20$ . (Top left) Lagrangian particle positions with 20,000 particles over gas vorticity. (Bottom left) Eulerian number density on  $400 \times 200 \times 5$  grid. (Top right) Trace of velocity covariance matrix. (Bottom right) Absolute value of the difference between the two eigenvalues of the velocity covariance matrix.

For the simulations with the multi-velocity model, the first step is to show a good level of agreement between the Eulerian and Lagrangian simulations for the non-evaporating test case. Fig. (12.7)-left presents a fair comparison between the droplet number density fields with a level of agreement similar to the level obtained in earlier figures. In order to quantify the ability of the method to capture droplet crossing, we have also plotted in Fig. (12.7)-(top right) one-half the trace of the velocity covariance matrix, which amounts to a droplet ‘temperature’ in the case of an isotropic velocity distribution. However, the droplet temperature is defined for all types of velocity distributions, including isotropic and anisotropic ones, and therefore the crossings may be difficult to discern from the temperature field. In order to characterize regions of anisotropy, and thus regions where droplet crossings might be more easily observed, we have also plotted the absolute value of the difference of the two eigenvalues of the velocity covariance matrix in Fig. (12.7)-(bottom right). This figure very beautifully complements the plot in Fig. (12.7)-(top right), indicating that droplet crossings occur throughout the flow field.

Next, we focus a specific region of the flow domain in order to discuss details of the actual droplet velocity field. The region of interest is highlighted in Fig. (12.7)- (bottom right) and contains both a zone with large differences between the two eigenvalues of the velocity covariance matrix and a zone

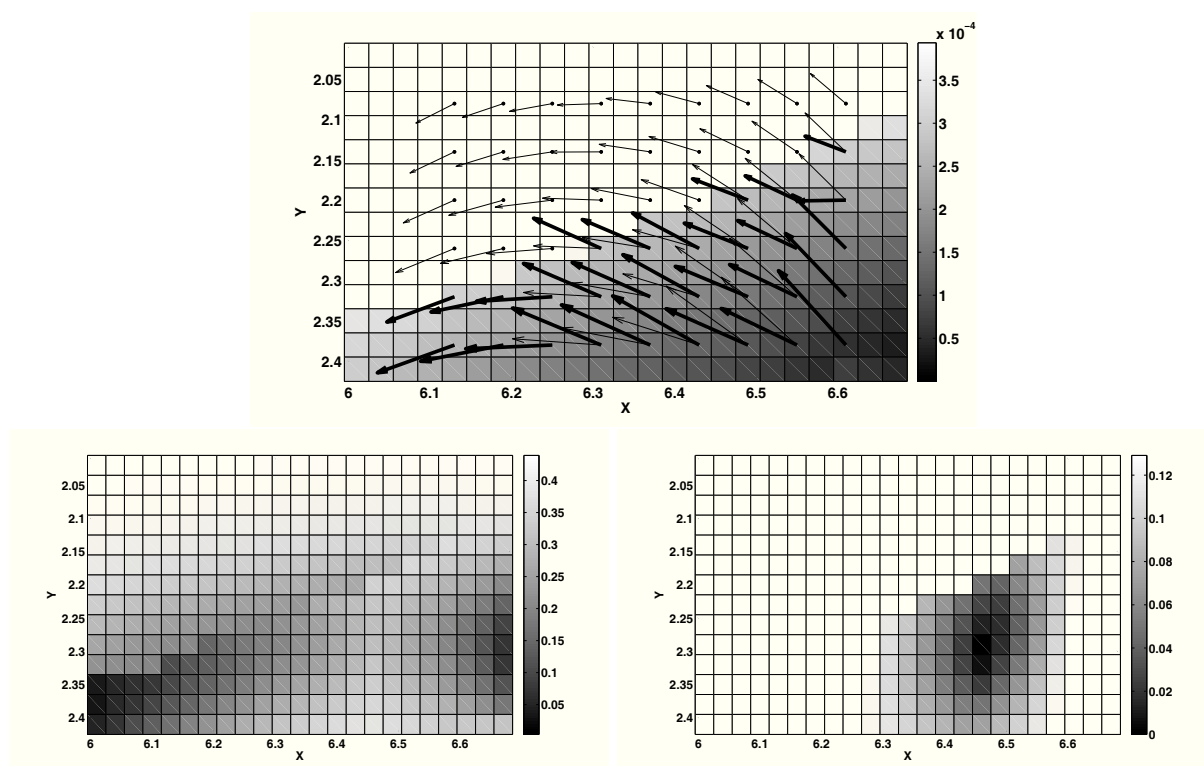


Figure 12.8: Focus on region of the spray outlined by the rectangle in Fig. (12.7)-(bottom right). (Top) Region where a significant and a null field of absolute value of the difference between the two eigenvalues of the velocity covariance matrix coexist. The two types of arrows (solid, bold) represent two different velocities and highlight droplet crossing in the zone where the absolute value of the difference between the two eigenvalues of the velocity covariance matrix is non-zero. In the zone where the droplet temperature is close to zero, the velocity field degenerates to one velocity. (Bottom left) Higher weights associated with the solid arrows. (Bottom right) Lower weights associated with the bold arrows.

where the temperature is null. Figure 12.8-(top) represents the velocity vectors in the first zone. The associated weights are displayed in Fig. (12.8)-(bottom left) for the highest weights and in Fig. (12.8)-(bottom right) for the lowest weights and correspond, respectively, to the solid and bold arrows. As the order of magnitude between the two sets of weights is five, these figures show the ability of the multi-velocity model to capture the fine structure of the droplet jet. It can be easily seen that the two different types of velocity vectors correspond to two droplet clouds dragged by two different gas-phase vortices. Let us note that there can only be (except for very specific cases) two dominant velocity vectors, due to the fact that in the model we invert the velocity moment set using a two-node quadrature for each dimension. In the zero-temperature zone, it can be seen in Fig. (12.8)-(top) that the velocity field consists of a single vector at each point. The important conclusion drawn from these figures is that the multi-velocity model (when carefully implemented) is able to capture both regions of droplet crossings as well as regions of zero temperature.

Finally, we have plotted the results of the multi-fluid, multi-velocity model with evaporation in the case of the polydisperse spray jet in Fig. (12.9). Once again, this figure demonstrates the ability of the proposed method to capture the dynamics conditioned on size as well as evaporation for a range of small to moderate Stokes numbers



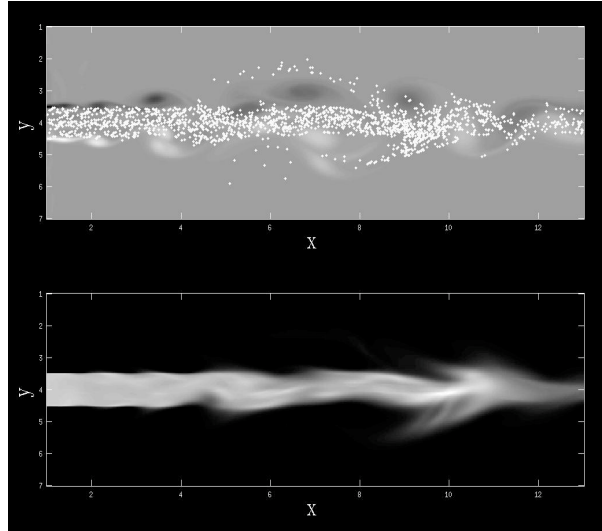


Figure 12.9: Evaporating polydisperse spray with high-inertia droplets (Stokes 0.48 to 1.1 corresponding to diameters from 60 to 90  $\mu\text{m}$ ) at time  $t = 15$ . (Top) Lagrangian particle positions with 7,000 particles over gas-phase vorticity. (Bottom) Eulerian number density on  $400 \times 200 \times 10$  grid.

### 12.2.2 EMFVM model versus multi-fluid model for crossing jets

In order to illustrate the behavior of the multi-velocity model in the context of a realistic jet, we use the same configuration as in Section 12.2, with the addition of a vertical jet of droplets that will cross the horizontal jet. The gas phase is exactly the same as before and the droplets in the two jets are injected with the same velocity ( $U_0$ ), density and size. The particles in the vertical jet are inertial enough to cross the horizontal jet, even though they are decelerated by the gas. Their Stokes number is 4.05, corresponding to a diameter of 175  $\mu\text{m}$ . For comparison, the same configuration is simulated with a multi-fluid model with one section. In addition, separate simulations with only the horizontal or the vertical jet using the multi-velocity model are presented.

Results from the four simulations are given in Fig. (12.10). The number density of the spray with two crossings jets obtained from the multi-velocity model is shown in Fig. (12.10)-(top right). Results for the vertical jet are shown in Fig. (12.10)-(top left) and for the horizontal jet in Fig. (12.10)-(bottom left). One can see that the simulation of the two crossing jets corresponds to the superposition of the independent simulations of each jet. This behavior clearly illustrates the ability of the multi-velocity model to capture particle crossing. In contrast, the multi-fluid model in Fig. (12.10)-(bottom right) is unable to reproduce this kind of crossing (i.e. it cannot capture the exact solution to the Williams-Boltzmann equation) and instead produces a  $\delta$ -shock. As discussed in Section 3.4.2, the presence of  $\delta$ -shocks in a two-way coupled system will produce unphysical gas-phase flow structures.

## Conclusion

This series of study configurations have assessed the feasibility of the quadrature method employed to description PTC, in one and also two-dimensions. It also shows the feasibility of an Eulerian model able to account for polydispersity and PTC in the same time. This is an essential result, as it provides the evidence that the two limitations described in Section 3.4 of Eulerian models relative to Lagrangian methods can be overcome. The robustness of QMOM in two-dimensions has been challenged in a Taylor-Green configuration for the gas phase. The critical point were the behaviour of the quadrature with numerical diffusion and also with more than two characteristics crossing at the same point. The latter point resulted, as expected from the study of Section 9.3, in the creation of  $\delta$ -shocks, while the results turn out to be satisfactory for the first point. However, in more complex configurations as numerical

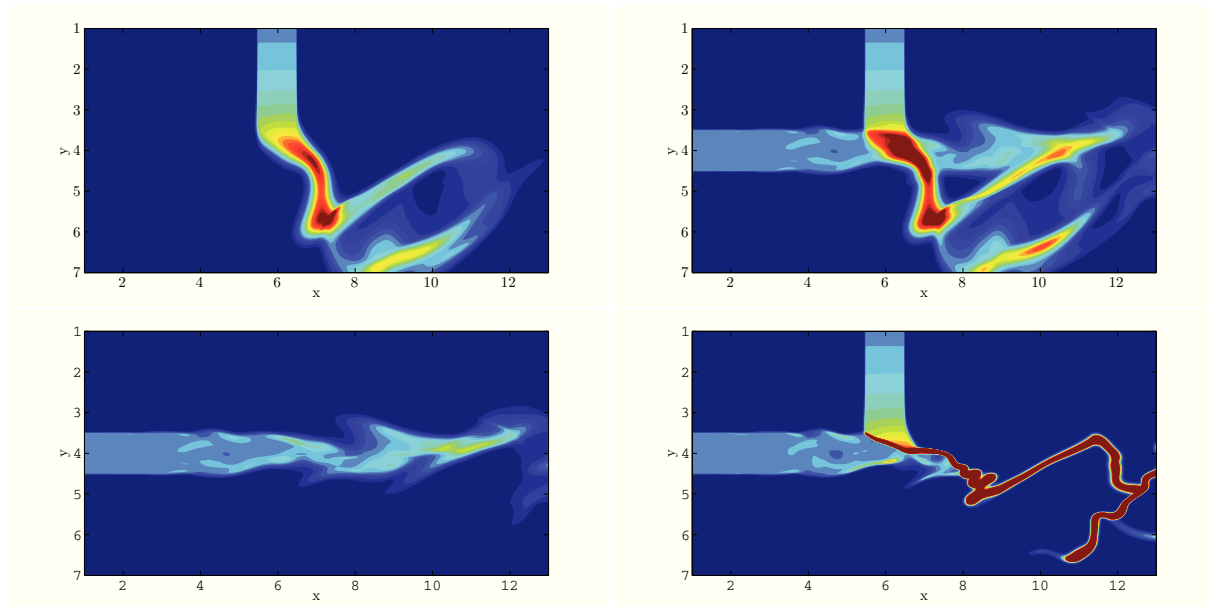


Figure 12.10: Total number density of the non-evaporating spray at time  $t = 20$ . (Top left) Vertical jet with the multi-velocity model. (Bottom left) Horizontal jet with the multi-velocity model. (Top right) Two crossing jets with the multi-velocity model. (Bottom right) Two crossing jets with the multi-fluid model.

diffusion creates locally uncontrolled velocities, it may locally engenders several values of velocities and create artificial  $\delta$ -shocks, even in flow areas not concerned by any crossing. But the high order velocity moment method can do very nice achievements, as shown in the free test case. It is able to predict areas of high temperature, when crossing occur, and is also able to reconstruct the velocity vectors in a crossing area, as Lagrangian methods would do. This work and these results have led to some publications in [51, 87, 50]. They are very encouraging for further developments. Indeed, the application of this kind of methods in industrial cases will require more evolved models. Some very promising methods, based on the quadrature method, have been designed, which do not reconstruct bi-modal distribution any more, but complete Gaussian velocity distributions [37]. In conclusion, this chapter has pointed out the breakthrough brought by the quadrature method in the simulation of PTC by Eulerian models.

## Part IV

# Introduction of the size moment method in the code IFP-C3D

# Introduction

The second aspect of this work concerning the implementation of an Eulerian spray model in the industrial code of IFP Energies nouvelles, IFP-C3D, is investigated. The strategy consists in transferring the model for polydisperse spray and the associated numerical schemes exposed in Part II. This requires answering the two following questions. First, the numerical schemes designed in Chapter 5 and Chapter 6 are designed in an Eulerian framework involving fix grids. However the algorithm used in the IFP-C3D code relies on an Arbitrary Lagrangian Eulerian (ALE) approach, with the essential characteristic of involving mesh movement in the resolution. If the evaporation term can be easily transferred in the context of an operator splitting approach, the critical issue consists in adapting the advection scheme to this new context. This implies preserving its property of stability, satisfying the realizability condition for the size moments and capturing  $\delta$ -shocks in the context of pressureless gas formalism dynamics. This other requirement is accuracy with the design of a second order transport scheme in the ALE context. The second challenge is to define a whole computing strategy in order to properly integrate, from scratch, the Eulerian spray model in the IFP-C3D code.

The answers to this two questions are explained in this part. In the first case, the advection scheme for the moment is adapted to the ALE cell-vertex formalism used in the IFP-C3D code. On the other hand, a new scheme is proposed for the momentum in order to preserve the stability property in the case now where the dynamical variables are defined on the vortices of the mesh. This work is explained in Chapter 13. Then the computing strategy is defined in order to fulfill the three requirements: it has to respect the general algorithm of the IFP-C3D code; it must not introduce regressions, and keep the stability properties of the schemes designed in Chapter 5 and Chapter 6 through evaporation and transport. The accurate behavior of this new functionality implemented in IFP-C3D is assessed through specific test cases and comparisons with DNS computations through the MUSES3D code. Finally the feasibility of the Eulerian spray model is demonstrated for the injection of a polydisperse evaporating spray. This work is explained in Chapter 14. This work has been presented during the ICMF Conference, Tampa, USA (2010) [130], and is the object of an article in preparation in the International Journal of Multiphase Flows [131].

## Chapter 13

# Adaptation of the moment method to the Arbitrary Lagrangian Eulerian formalism

This chapter focuses on the adaptation of the EMSM model to describe polydispersity to the mesh movement formalism used in the industrial CFD code IFP-C3D.

In order to capture polydispersity in a formalism where the size phase space is not discretized, we have designed in Part II, the EMSM model with adapted numerical schemes meeting the requirements of stability and accuracy. Its potential has been assessed in Chapter 8.

But so far, the EMSM model has been devised in an Eulerian formalism, where the mesh is supposed to be fixed. However, in the context of internal combustion engines, the configurations studied at IFP Energies nouvelles may involve a changing computational geometry, due to the potential movement of the piston. Therefore the numerical scheme in the code IFP-C3D is based on a formalism coping with mesh movement: the Arbitrary Lagrangian Eulerian (ALE) formalism.

Since the ALE formulation is imposed to us, the task is then to be able to adapt our moment method to this particular configuration, with the desire to keep the order of accuracy of the schemes designed in the Eulerian formalism. The difficulty of this work arises from the strong stability requirements of the moment system, already in a fix grid formalism. Therefore, in a first time we consider only structured meshes.

The remainder of this chapter is the following. In a first part, we derive the equations from a fixed mesh to a moving mesh. The general strategy for the numerical scheme is then explained in this chapter. Section 13.2 is dedicated to the resolution for the gas phase. In Section 13.4 we explain how the realizability condition is met in aerosol dynamics. Finally, in Section 13.5 is explained how the discrete maximum is ensured for the resolution of spray dynamics.

Practically, we want to be able to design, in the ALE formalism, numerical schemes to solve the

dynamical system on size moments of a spray, defined in Chapter 4:

$$\begin{aligned}
\partial_t(m_0) + \nabla_{\mathbf{x}} \cdot (m_0 \mathbf{u}_p) &= -Kn(t, \mathbf{x}, 0), \\
\partial_t(m_1) + \nabla_{\mathbf{x}} \cdot (m_1 \mathbf{u}_p) &= -Km_0, \\
\partial_t(m_2) + \nabla_{\mathbf{x}} \cdot (m_2 \mathbf{u}_p) &= -2Km_1, \\
&\vdots \\
\partial_t(m_N) + \nabla_{\mathbf{x}} \cdot (m_N \mathbf{u}_p) &= -NKm_{N-1}, \\
\partial_t(m_1 \mathbf{u}_p) + \nabla_{\mathbf{x}} \cdot (m_1 \mathbf{u}_p \otimes \mathbf{u}_p) &= -Km_0 \mathbf{u}_p + m_0 \frac{(\mathbf{u}_g - \mathbf{u}_p)}{St_0},
\end{aligned} \tag{13.1}$$

coupled to the Euler system for compressible gas:

$$\begin{aligned}
\partial_t(\rho_g) + \nabla_{\mathbf{x}} \cdot (\rho_g \mathbf{u}_g) &= 0, \\
\partial_t(\rho_g \mathbf{u}_g) + \nabla_{\mathbf{x}} \cdot (\rho_g \mathbf{u}_g \otimes \mathbf{u}_g) &= -\nabla_{\mathbf{x}} P_g, \\
\partial_t(\rho_g E_g) + \nabla_{\mathbf{x}} \cdot (\rho_g E_g \mathbf{u}_g) &= -\nabla_{\mathbf{x}} \cdot (P_g \mathbf{u}_g),
\end{aligned} \tag{13.2}$$

where  $\rho_g$ ,  $P_g$ ,  $E_g$  are respectively the gas density, pressure, and total energy. The gas is assumed to be a perfect gas and so follows the corresponding equation of state.

The system of equations on the gas is written in SI units. In order to perform simulation with reasonable values of moments, the size moments are nondimensionalized relative to  $S_0$ , a characteristic droplet size. In this context,  $St_0 = \frac{\rho_l S_0}{18\Pi\mu_g}$ , where  $\rho_l$  is the density of the liquid, and  $\mu_g$  the gas viscosity. Besides,  $K = R/S_0$ , where  $R$  is the evaporation coefficient, defined in Section 1.2.3. Moreover, the fact that spray momentum is defined by  $m_1 \mathbf{u}_p$  and not by  $m_0 \mathbf{u}_p$  is justified in Section 4.1.4. The derivation of system (13.1) can be found in Chapter 4.

## 13.1 Equations in frame change

### 13.1.1 Description of motion

Because of the shortcomings of purely Lagrangian and purely Eulerian descriptions, a technique has been developed that succeeds to a certain extent in combining the best features of both the Lagrangian and the Eulerian approaches. Such a technique is known as the Arbitrary Lagrangian-Eulerian (ALE) description [62]. In the ALE description, the nodes of the computational mesh may be moved with the continuum in normal Lagrangian way, or be held fixed in the Eulerian manner, or be moved in some arbitrarily specified way to give a continuous rezoning capability. Because of this freedom in moving the computational mesh offered by the ALE description, greater distortions of the continuum can be handled than would be allowed by a purely Lagrangian method, with more resolution than is afforded by a purely Eulerian approach.

The Lagrangian viewpoint consists in following the material particles of the continuum in their motion. To this end, one introduces, as suggested in Fig. (13.1), a computational grid which follows the continuum in its motion, the grid nodes being permanently connected to the same material points. The material coordinates  $\mathbf{X}$ , allow us to identify the material configuration  $R_{\mathbf{X}}$ . The motion of the material points

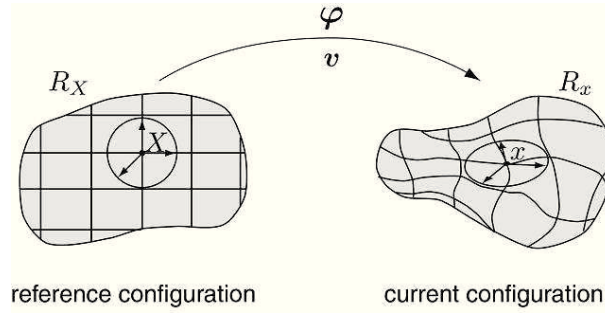


Figure 13.1: Lagrangian description of motion. Source Donea [62]

relates the material coordinates  $\mathbf{X}$  to the spatial ones  $\mathbf{x}$ . It is defined by an application  $\phi$  such that:

$$\begin{aligned} \phi : R_{\mathbf{X}} \times [t_0, t_{end}[ &\rightarrow R_{\mathbf{x}} \times [t_0, t_{end}[, \\ (\mathbf{X}, T) &\mapsto \phi(\mathbf{X}, T) = (\mathbf{x}, t) \end{aligned} \tag{13.3}$$

which allows to link  $\mathbf{X}$  and  $\mathbf{x}$  by the law of motion and to deduce the material velocity, namely:

$$\mathbf{x} = \mathbf{x}(\mathbf{X}, T), \quad t = T, \quad \mathbf{v}_{\mathbf{X}}(\mathbf{X}, T) = \partial_t \mathbf{x}|_{\mathbf{X}}, \tag{13.4}$$

which explicitly states the particular nature of  $\phi$ . The vector  $\mathbf{u}$  can refer either to the liquid or gaseous velocity. The spatial coordinates  $\mathbf{x}$ , depend both on the material particle  $\mathbf{X}$ , and time  $t$ , and, second, physical time is measured by the same variable  $t$  in both material and spatial domains.

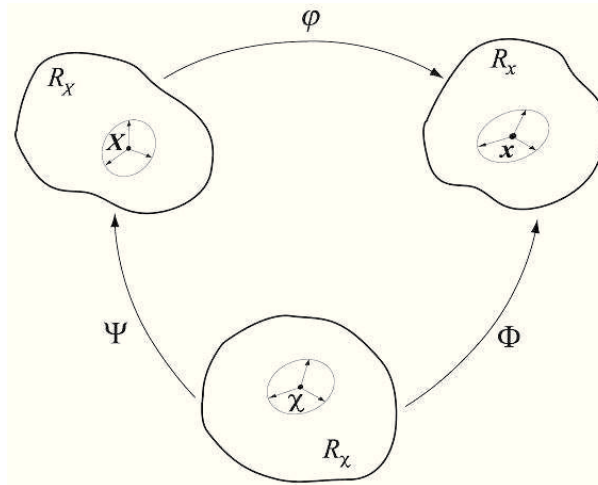


Figure 13.2: Lagrangian description of motion. Source Donea [62]

However, in the ALE description of motion, neither the material configuration  $R_{\mathbf{X}}$  nor the spatial one  $R_{\mathbf{x}}$  is taken as a reference. Thus, a third domain is needed : the referential configuration  $R_{\chi}$ , where the reference coordinates,  $\chi$  are introduced to identify the grid points. The relation between these configuration is shown in Fig. (13.2). The referential domain  $R_{\chi}$  is mapped into the spatial domain by  $\Phi$ . The mapping  $\Phi$  from the referential domain to the spatial domain, which can be understood as the motion of the grid points in the spatial domain, is represented by:

$$\Phi : R_{\chi} \times [t_0, t_{end}[ \rightarrow R_{\mathbf{x}} \times [t_0, t_{end}[ (\chi, t) \mapsto \Phi(\chi, t) = (\mathbf{x}, t), \tag{13.5}$$

and its gradient is defined by:

$$\partial_{(\mathbf{x},t)}\Phi = \begin{pmatrix} \nabla_{\mathbf{x}}\mathbf{x} & \mathbf{v}_{\mathbf{x}} \\ 0^T & 1 \end{pmatrix}, \quad \mathbf{J} = \nabla_{\mathbf{x}}\mathbf{x}, \quad \mathbf{v}_{\mathbf{x}}(\boldsymbol{\chi}, t) = \partial_t\mathbf{x}|_{\boldsymbol{\chi}}, \quad (13.6)$$

where  $\mathbf{v}_{\mathbf{x}}$  is the mesh velocity. We define also the quantity  $J(\boldsymbol{\chi}, t) = \det(\nabla_{\boldsymbol{\chi}}\mathbf{x}) = \det(\mathbf{J})$ , which is the dilatation rate of a volume  $d^3\boldsymbol{\chi}$  with time. The functions  $\phi$  and  $\Phi$  are sufficient to be able to write equations in  $R_{\boldsymbol{\chi}}$  from equations written in  $R_{\mathbf{x}}$ . Nevertheless, if we want to fully characterize the relationship between the three frames of reference, it is interesting to introduce the function  $\Psi$  or more precisely its inverse  $\Psi^{-1}$  defined by:

$$\begin{aligned} \Psi^{-1} : R_{\mathbf{X}} \times [t_0, t_{end}[ &\rightarrow R_{\boldsymbol{\chi}} \times [t_0, t_{end}[ \\ (\mathbf{X}, T) &\mapsto \Psi^{-1}(\mathbf{X}, T) = (\boldsymbol{\chi}, t), \end{aligned} \quad (13.7)$$

and its gradient is defined by:

$$\partial_{(\mathbf{X},t)}\Psi^{-1} = \begin{pmatrix} \nabla_{\mathbf{X}}\boldsymbol{\chi} & \mathbf{u}_{\mathbf{X}} \\ 0^T & 1 \end{pmatrix}, \quad \mathbf{u}_{\mathbf{X}}(\boldsymbol{\chi}, t) = \partial_t\boldsymbol{\chi}|_{\mathbf{X}}, \quad (13.8)$$

and is interpreted as the particle velocity in the mesh frame. The relation between velocities  $\mathbf{u}$ ,  $\mathbf{v}_{\mathbf{x}}$  and  $\mathbf{u}_{\mathbf{X}}$  can be obtained by differentiating  $\phi = \Phi \circ \Psi^{-1}$ :

$$\partial_{(\mathbf{X},t)}\phi(\mathbf{X}, t) = \partial_{(\boldsymbol{\chi},t)}\Phi(\Psi^{-1}(\mathbf{X}, t))\partial_{(\mathbf{X},t)}\Psi^{-1}(\mathbf{X}, t) \quad (13.9)$$

$$= \partial_{(\boldsymbol{\chi},t)}\Phi(\boldsymbol{\chi}, t)\partial_{(\mathbf{X},t)}\Psi^{-1}(\mathbf{X}, t), \quad (13.10)$$

or, in its matrix format:

$$\begin{pmatrix} \nabla_{\mathbf{X}}\mathbf{x} & \mathbf{u} \\ 0^T & 1 \end{pmatrix} = \begin{pmatrix} \nabla_{\boldsymbol{\chi}}\mathbf{x} & \mathbf{v}_{\mathbf{x}} \\ 0^T & 1 \end{pmatrix} \begin{pmatrix} \nabla_{\mathbf{X}}\boldsymbol{\chi} & \mathbf{u}_{\mathbf{X}} \\ 0^T & 1 \end{pmatrix}, \quad (13.11)$$

which yields, after block multiplication:

$$\mathbf{u} = \mathbf{v}_{\mathbf{x}} + \nabla_{\boldsymbol{\chi}}\mathbf{x} \cdot \mathbf{u}_{\mathbf{X}}. \quad (13.12)$$

This equation is rewritten as

$$\mathbf{w} = \mathbf{v}_{\mathbf{X}} - \mathbf{v}_{\mathbf{x}} = \nabla_{\boldsymbol{\chi}}\mathbf{x} \cdot \mathbf{u}_{\mathbf{X}}, \quad (13.13)$$

defining the convective velocity  $\mathbf{w}$  that is the relative velocity between the material and the mesh.

The convective velocity  $\mathbf{w}$  should not be confused with  $\mathbf{u}_{\mathbf{X}}$ . As stated before,  $\mathbf{u}_{\mathbf{X}}$  is the particle velocity as seen from the mesh frame reference  $R_{\boldsymbol{\chi}}$ , whereas  $\mathbf{w}$  is the particle velocity relative to the mesh as seen from the spatial frame reference  $R_{\mathbf{x}}$  (both  $\mathbf{u}$  and  $\mathbf{u}_{\mathbf{X}}$  are variations of coordinate  $\mathbf{x}$ ). Physically, if  $\mathbf{u}_{\mathbf{X}} = 0$ , then the particle is motionless in  $R_{\boldsymbol{\chi}}$ , and therefore, it is also motionless in  $R_{\mathbf{x}}$ . But if  $\mathbf{u}_{\mathbf{X}} \neq 0$ , then  $\mathbf{u}_{\mathbf{X}}$  is the particle velocity seen by the mesh. But if this mesh expands at the rate  $\nabla_{\boldsymbol{\chi}}\mathbf{x} > 1$  (respectively compresses at the rate  $\nabla_{\boldsymbol{\chi}}\mathbf{x} < 1$ ), then seen from  $R_{\mathbf{x}}$ , the particle velocity is multiplied by this expansion rate of the mesh (respectively by the compression rate of the mesh).

In fact, equation (13.13) implies that  $\mathbf{w} = \mathbf{u}_{\mathbf{X}}$  if and only if  $\partial_{\boldsymbol{\chi}}\mathbf{x} = \mathbf{I}$ , that is, when the mesh motion is purely translational, without rotations or deformations of any kind.

In the ALE formulation, the freedom of moving the mesh is very attractive. It helps to combine the respective advantages of the Lagrangian and Eulerian formulations. This could however be overshadowed by the burden of specifying grid velocities well suited to the particular problem under consideration. Consequently, the practical implementation of the ALE description requires that an automatic mesh displacement prescription algorithm be supplied.



### 13.1.2 Equations in a moving frame

The conservation equations in the ALE formalism are derived starting from the Eulerian viewpoint. There are two different final formulations (one in conservative form and one in non conservative form) depending on whether the dilatation rate  $J$  is considered. The first one that does not use the dilatation rate is non conservative and is called the *quasi-Eulerian* description. The second uses the dilatation rate and is conservative. The starting point for both of the methods is the time derivative of integrals over moving volumes.

#### 13.1.2.1 Quasi-Eulerian description

Consider a material volume  $V_t$  bounded by a smooth closed surface  $S_t$  whose points at time  $t$  move with the material velocity  $\mathbf{u} = \mathbf{u}(\mathbf{x}, t)$  where  $\mathbf{x} \in S_t$ . A material volume is a volume that permanently contains the same amount of particles. The material time derivative of the integral of a scalar function  $f(\mathbf{x}, t)$  over the time-varying material volume  $V_t$  is given by the following well-know expression, often referred to as Reynolds transport theorem (see for example [31] for a detailed proof):

$$\frac{d}{dt} \int_{V_t} f(\mathbf{x}, t) dV = \int_{V_c \equiv V_t} \partial_t f(\mathbf{x}, t) dV + \int_{S_c \equiv S_t} f(\mathbf{x}, t) \mathbf{u} \cdot \mathbf{n} dS, \quad (13.14)$$

which holds for some functions  $f(\mathbf{x}, t)$ . The volume integral in the right-hand side is defined over a control volume  $V_c$  (fixed in space) which coincides with the moving material volume  $V_t$  at the considered instant  $t$ , in time. Similarly, the fixed control surface  $S_c$  coincides at time  $t$  with the closed surface  $S_t$  bounding the material volume  $V_t$ . In the surface integral,  $\mathbf{n}$  denotes the unit outward normal to  $S_t$  and  $\mathbf{u}$  is the material velocity of points of the boundary  $S_t$ . The first term in the right-hand side of Eq. (13.14) is the local time derivative. The boundary integral represents the flux of the scalar quantity  $f$  across the fixed boundary of the control volume  $V_c \equiv V_t$ .

Noting that:

$$\int_{S_c} f(\mathbf{x}, t) \mathbf{u} \cdot \mathbf{n} dS = \int_{V_c} \nabla_{\mathbf{x}} \cdot (f \mathbf{u}) dV, \quad (13.15)$$

one obtains the alternative form of Reynolds transport theorem:

$$\frac{d}{dt} \int_{V_t} f(\mathbf{x}, t) dV = \int_{V_c \equiv V_t} \partial_t f(\mathbf{x}, t) + \nabla_{\mathbf{x}} \cdot (f \mathbf{u}) dV. \quad (13.16)$$

The ALE integral form of the conservation equations is Reynolds transport theorem applied to an arbitrary volume  $V_t = V(\phi(\boldsymbol{\chi}, t))$  whose boundary  $S_t = \partial V_t$  moves with the mesh velocity  $\mathbf{v}_{\boldsymbol{\chi}}$ :

$$\partial_t|_{\boldsymbol{\chi}} \int_{V(\phi(\boldsymbol{\chi}, t))} f(\mathbf{x}, t) d^3 \mathbf{x} = \int_{V_t} \partial_t f(\mathbf{x}, t) d^3 \mathbf{x} + \int_{S_t} f(\mathbf{x}, t) \mathbf{v}_{\boldsymbol{\chi}} \cdot \mathbf{n} d^2 \mathbf{x}. \quad (13.17)$$

Combining (13.17) and (13.14), one obtains:

$$\partial_t|_{\boldsymbol{\chi}} \int_{V(\phi(\boldsymbol{\chi}, t))} f(\mathbf{x}, t) d^3 \mathbf{x} + \int_{S_t} f(\mathbf{x}, t) (\mathbf{u} - \mathbf{v}_{\boldsymbol{\chi}}) \cdot \mathbf{n} d^2 \mathbf{x} = \frac{d}{dt} \int_{V_t} f(\mathbf{x}, t) dV. \quad (13.18)$$

In order to obtain the differential form of the equation we need to relate the time derivative in the material, spatial and mesh frame references. Let a scalar physical quantity be described by  $f(\mathbf{x}, t)$ ,  $f^*(\boldsymbol{\chi}, t)$  and  $f^{**}(\mathbf{X}, t)$  in the spatial, mesh, and material frame references.

Using the mapping  $\phi$ , the spatial description  $f(\mathbf{x}, t)$  and the material description  $f(\mathbf{X}, t)^{**}$  can be related as:

$$f(\mathbf{X}, t)^{**} = f(\phi(\mathbf{X}, t), t). \quad (13.19)$$

Resolving the composed derivative of  $f(\phi(\mathbf{X}, t), t)$  relative to time, one obtains:

$$\partial_t f^{**} = \partial_t f + \nabla_{\mathbf{x}} f \cdot \mathbf{u}. \quad (13.20)$$

Similarly, using the mapping  $\Psi$ , the mesh description  $f^*(\mathbf{x}, t)$  and the material description  $f(\mathbf{X}, t)^{**}$  can be related as:

$$f(\mathbf{X}, t)^{**} = f^*(\Psi^{-1}(\mathbf{X}, t), t). \quad (13.21)$$

Resolving the composed derivative of  $f(\Psi^{-1}(\mathbf{X}, t), t)$  relative to time, one obtains:

$$\partial_t f^{**} = \partial_t f + \nabla_{\boldsymbol{\chi}} f \cdot \mathbf{u}_{\boldsymbol{\chi}}. \quad (13.22)$$

This equation relates the material and mesh time derivative. However constitutive relations are naturally expressed in the spatial configuration. Thus, using the definition of  $\mathbf{u}_{\boldsymbol{\chi}}$  given in Eq. (13.13), the previous equation may be rearranged into:

$$\partial_t f^{**} = \partial_t f + \nabla_{\mathbf{x}} f \cdot \mathbf{w}. \quad (13.23)$$

Let  $\alpha$  be a quantity per unit mass of the fluid, and let us consider that  $\alpha$  verifies the equation:

$$\rho \frac{d\alpha}{dt} = \rho(\partial_t \alpha|_{\mathbf{x}} + \mathbf{u} \cdot \nabla_{\mathbf{x}} \alpha) = \nabla_{\mathbf{x}} \cdot \boldsymbol{\sigma} + S, \quad (13.24)$$

where  $\boldsymbol{\sigma}$  is the stress tensor for  $\alpha$  and  $S$  the source term for  $\alpha$ .

The ALE form of the above conservation equation is obtained by considering the time derivative of  $\alpha$  not at constant  $\mathbf{x}$  any more, but at constant  $\boldsymbol{\chi}$ . This leads to replace in the convective term the material velocity  $\mathbf{u}$  with the particle velocity relative to the mesh  $\mathbf{w} = \mathbf{u} - \mathbf{v}_{\boldsymbol{\chi}}$ :

$$\rho \frac{d\alpha}{dt} = \rho(\partial_t \alpha|_{\boldsymbol{\chi}} + \mathbf{w} \cdot \nabla_{\mathbf{x}} \alpha) = \nabla_{\mathbf{x}} \cdot \boldsymbol{\sigma} + S. \quad (13.25)$$

### 13.1.2.2 Description using the dilatation rate

In order to derivate this version of ALE formulation, the starting point is the integral Eq. (13.18). The volume  $V(\phi(\boldsymbol{\chi}, t))$  over which the integral is calculated has a dependence relative to time. This derivation consists in writing the integral over a fixed volume, and therefore to perform the change of variable  $\mathbf{x} = \Phi(\boldsymbol{\chi}, t)$ , with a fixed  $\boldsymbol{\chi}$ . If we consider  $\boldsymbol{\chi}$  at time  $t = 0$ , then the resulting volume, over the mesh frame reference, writes  $V_{\boldsymbol{\chi}}(\boldsymbol{\chi}, 0)$ . Doing this variable changes leads to the change of elementary volume  $d^3 \mathbf{x} = \det(\nabla_{\boldsymbol{\chi}} \boldsymbol{\Phi}) d^3 \boldsymbol{\chi}$  where the quantity  $\det(\nabla_{\boldsymbol{\chi}} \boldsymbol{\Phi}) = J$  which is namely the dilatation rate. Equation (13.18) rewrites, for the quantity  $\alpha$  per unit mass:

$$\partial_t|_{\boldsymbol{\chi}} \int_{V_{\boldsymbol{\chi}}(\boldsymbol{\chi}, 0)} J \alpha(\mathbf{x}, t) d^3 \boldsymbol{\chi} + \int_{S_t} \alpha(\mathbf{x}, t) (\mathbf{u} - \mathbf{v}_{\boldsymbol{\chi}}) \cdot \mathbf{n} d^2 \mathbf{x} = 0. \quad (13.26)$$

Now that  $V_{\boldsymbol{\chi}}(\boldsymbol{\chi}, 0)$  does not depend on time, it is possible to invert the time derivative with the integral:

$$\int_{V_{\boldsymbol{\chi}}(\boldsymbol{\chi}, 0)} \partial_t J \alpha(\mathbf{x}, t)|_{\boldsymbol{\chi}} d^3 \boldsymbol{\chi} + \int_{S_t} \alpha(\mathbf{x}, t) (\mathbf{u} - \mathbf{v}_{\boldsymbol{\chi}}) \cdot \mathbf{n} d^2 \mathbf{x} = 0. \quad (13.27)$$

Noting that

$$\int_{S_t} \alpha(\mathbf{x}, t) (\mathbf{u} - \mathbf{v}_{\boldsymbol{\chi}}) \cdot \mathbf{n} d^2 \mathbf{x} = \int_{V(\phi(\boldsymbol{\chi}, t))} \nabla_{\mathbf{x}} \cdot (\alpha(\mathbf{x}, t) (\mathbf{u} - \mathbf{v}_{\boldsymbol{\chi}})) d^3 \mathbf{x}, \quad (13.28)$$

and performing the change of variable on this integral leads to the final form of the integral equation for  $\alpha$ :

$$\int_{V_{\chi}(\chi,0)} \partial_t J \alpha(\mathbf{x}, t) |_{\chi} + J \nabla_{\mathbf{x}} \cdot (\alpha(\mathbf{x}, t)(\mathbf{u} - \mathbf{v}_{\chi})) d^3 \chi = \int_{V_{\chi}(\chi,0)} J \nabla_{\mathbf{x}} \cdot \boldsymbol{\sigma} + J S d^3 \chi. \quad (13.29)$$

As a new quantity (the dilatation rate) has been introduced, an additional equation, on the dilatation rate has to be introduced meanwhile, for the system to be closed. This equation is obtained considering the evolution of the volume  $V(\phi(\chi, t))$  with time. Using the Reynolds theorem leads to:

$$\partial_t \int_{V(\phi(\chi, t))} d^3 \mathbf{x} = \int_{\partial V(\phi(\chi, t))} \mathbf{v}_{\chi} \cdot \mathbf{n} d^2 \mathbf{x} = \int_{V(\phi(\chi, t))} \nabla_{\mathbf{x}} \cdot \mathbf{v}_{\chi} d^3 \mathbf{x}. \quad (13.30)$$

Performing the change of variable  $\mathbf{x} = \Phi(\chi, t)$  on both sides of the integral leads to:

$$\int_{V_{\chi}(\chi,0)} \partial_t J d^3 \chi = \int_{V_{\chi}(\chi,0)} J \nabla_{\mathbf{x}} \cdot \mathbf{v}_{\chi} d^3 \chi. \quad (13.31)$$

In their differential form, the equations in this version in the ALE formulation read:

$$\begin{aligned} \partial_t J &= J \nabla_{\mathbf{x}} \cdot \mathbf{v}_{\chi} \\ \partial_t J \alpha(\mathbf{x}, t) |_{\chi} + J \nabla_{\mathbf{x}} \cdot (\alpha(\mathbf{x}, t)(\mathbf{u} - \mathbf{v}_{\chi})) &= 0. \end{aligned} \quad (13.32)$$

This form is preferable than the first one as it enables to clearly see how the dynamic equations are coupled with the evolution of the mesh. Therefore we use this form to design the numerical scheme.

Applying to system (13.1), system (13.2) the modification displayed in order to derivate a system in the ALE formulation, leads to:

$$\begin{aligned} \partial_t (J) |_{\chi} - J \nabla_{\mathbf{x}} \cdot (\mathbf{v}_{\chi}) &= 0, \\ \partial_t (J \rho_g) |_{\chi} + J \nabla_{\mathbf{x}} \cdot (\rho_g \mathbf{w}_g) &= 0, \\ \partial_t (J \rho_g \mathbf{u}_g) |_{\chi} + J \nabla_{\mathbf{x}} \cdot (\rho_g \mathbf{u}_g \mathbf{w}_g) + J \nabla_{\mathbf{x}} (P) &= 0, \\ \partial_t (J \rho_g E_g) |_{\chi} + J \nabla_{\mathbf{x}} \cdot (\rho_g E_g \mathbf{w}_g) + J \nabla_{\mathbf{x}} (P \mathbf{u}_g) &= 0, \\ \partial_t (J m_0) |_{\chi} + J \nabla_{\mathbf{x}} \cdot (m_0 \mathbf{w}_p) + J K \tilde{n}_{ME} &= 0, \\ \partial_t (J m_k) |_{\chi} + J \nabla_{\mathbf{x}} \cdot (m_k \mathbf{w}_p) + J K (k-1) m_{k-1} &= 0, \\ \partial_t (J m_1 \mathbf{u}_p) |_{\chi} + J \nabla_{\mathbf{x}} \cdot (m_1 \mathbf{u}_p \mathbf{w}_p) + J K m_0 \mathbf{u}_p &= J m_0 \frac{(\mathbf{u}_g - \mathbf{u}_p)}{\text{St}_0}, \end{aligned} \quad (13.33)$$

where the coefficient  $k$  ranges in  $[1, N]$ , and where  $\mathbf{w}_g = \mathbf{u}_p - \mathbf{v}_{\chi}$  is the gas velocity relative to the mesh, and  $\mathbf{w}_p = \mathbf{u}_g - \mathbf{v}_{\chi}$  is the particle velocity relative to the mesh.

In order to design numerical schemes for the resolution of the moment dynamics, two difficulties arise, like in the Eulerian case:

- The realizability condition for the moments has to be preserved. This condition has been defined in Section 4.3. Let us recall that it states that one must be able, at any time, to reconstruct a distribution function from the moment vector  $(m_0, m_1, \dots, m_N)^t$ . What makes it difficult to meet is the fact that not every  $N + 1$  component vector can be associated with a distribution function and that the geometry of the moment space is complex.

- The advection scheme has to be stable through the singularities brought by the pressureless gas formalism for the moments have to be captured.

## 13.2 Numerical scheme

### 13.2.1 Outline of peculiarities introduced by the ALE formalism

In the field of fluid dynamics, the majority of ALE computer codes are based on finite volumes, which is the case here. Nevertheless, in structural mechanics area, the other field where the ALE method is popular, codes are based on finite elements. Writing a numerical scheme in ALE formulation requires to face new difficulties not encountered in the case of fixed grids. As already mentioned, the basis and the main advantage of the ALE method is to couple the Lagrangian and Eulerian descriptions. This involves to have a mesh update procedure that assigns mesh node velocities or displacement at each time step. There basically exist two mesh update strategies: mesh regularization and mesh adaptation. The objective of mesh regularization is of geometrical nature. It consists in keeping the computational mesh as regular as possible during the whole calculation, thereby avoiding excessive distortions and squeeze of the computing zones and preventing mesh entanglement. This procedure decreases the numerical errors due to mesh distortion. These mesh updating procedures are classified depending on whether the boundary-motion is prescribed *a priori* or its motion is unknown. The interested reader can consult [112, 156, 111]. On the other hand when using mesh adaptation technique, the objective is to optimize the computational mesh to achieve an improved accuracy, possibly at low computing cost (the total number of elements in a mesh remains unchanged throughout the computation, as well as the element connectivity). Mesh refinement is typically carried out by moving the nodes towards zones of strong solution gradient, such as localization zones in large deformation problems involving softening materials. See for example [8]. In fluid dynamics, the most obvious influence of an ALE formalism is that the convective term must account for the mesh motion. Thus the convective velocity  $\mathbf{w}$  replaces the material velocity  $\mathbf{u}$ , which appears in the convective term of Eulerian formulations. It is interesting to note that the mesh motion may increase or decrease the convection effects by impacting the diffusion on the solution (we will come back to that later). In the standard fluid dynamic case already, stabilizations techniques need to be implemented. This is even truer when it comes to the very sensitive system of moment dynamics. The rest of the specificities of ALE formalism concerns boundary conditions. In fact boundary conditions are related to the problem, not to the description employed. Thus the same boundary conditions, be it in Eulerian or Lagrangian formalism, are implemented. That is, along the boundary of the domain, kinematical and dynamical conditions must be defined. The peculiarity of the ALE form does not lie on boundary condition themselves, but on their enforcement on moving grids. Some strategies can be found in the problems of free surfaces [113, 28] and fluid-structure interactions [157, 192]. The last specificity, we can put in the class of boundary conditions, concerns the notion of geometric conservation laws for unsteady flow computation on moving and deforming finite element or finite volume grids. This notion has been studied in [76] [103]. The basic requirement is that any ALE computational method should be able to predict exactly the trivial solution of a uniform flow. The ALE equation of mass balance is usually taken as a starting point to derive the geometric conservation law. Assuming uniform fields of density  $\rho$  and material velocity  $\mathbf{u}$ , it reduces to the continuous geometric conservation law:

$$\partial_t|_{\mathcal{X}} \int_{V(\phi(\mathcal{X},t))} d^3x = \int_{V_t} \mathbf{w} \cdot \mathbf{n} d^2x. \quad (13.34)$$

Integrating Eq. (13.34) in time from  $t^n$  to  $t^{n+1}$  renders the discrete geometric conservation law (DGCL):

$$|\Omega_e^{n+1}| - |\Omega_e^n| = \int_{t^n}^{t^{n+1}} \left( \int_{V_t} \mathbf{w} \cdot \mathbf{n} d^2x \right) dt, \quad (13.35)$$

stating that the change in volume of each element from  $t^n$  to  $t^{n+1}$  must be equal to the volume swept by the element boundary during the time interval. Assuming that the volumes  $\Omega_e$  in the left-hand side of

Eq. (13.35) can be computed exactly, this amounts to requiring also the exact computation of the flux in the right-hand side. This poses some restrictions on the update procedure for the grid position and velocity.

However, the link between DGCLs and the stability of ALE and accuracy of ALE schemes is still a controversial topic of current research.

### 13.2.2 Dimensional and operator splitting numerical scheme inspired from IFP-C3D

The previous section was a brief outline of the conditions in order to reach an optimized level of accuracy for CFD codes involving a moving computational geometry. But the question to answer in our case is more upstream as we are interested in the feasibility study of applying moment method to an ALE formulation. When the crucial difficulty of stability is solved, then it will be possible to address meshing strategies afterwards. Therefore the purpose of this section is to show to what extent we are able to export the stability and accuracy properties of the schemes designed for the EMSM model in Section 6 from the Eulerian to the ALE formalism.

In this context, we restrict ourselves to cartesian meshes to show some results for the design of first and second order in time and space schemes for the transport of moments. Meanwhile, the continuous phase (gas) is solved with second order in space scheme. The general algorithm is based on the one implemented in the code IFP-C3D. It is indeed in this code that the moment method has to be finally implemented. All the schemes presented in the following are written and tested in a dedicated one-dimensional code.

In one space dimension, the system can easily be rewritten in the mesh frame reference, as  $dx = Jd\chi$ :

$$\begin{aligned}
\partial_t(J)|_\chi - \partial_\chi(u_\chi) &= 0, \\
\partial_t(J\rho_g)|_\chi + \partial_\chi(\rho_g w_g) &= 0, \\
\partial_t(J\rho_g u_g)|_\chi + \partial_\chi(\rho_g u_g w_g) + \partial_\chi(P) &= 0, \\
\partial_t(J\rho_g E_g)|_\chi + \partial_\chi(\rho_g E_g w_g) + \partial_\chi(Pu_g) &= 0, \\
\partial_t(Jm_0)|_\chi + \partial_\chi(m_0 w_p) + J K \tilde{n}_{ME} &= 0, \\
\partial_t(Jm_k)|_\chi + \partial_\chi(m_k w_p) + J(k-1)m_{k-1} &= 0, \\
\partial_t(Jm_1 u_p)|_\chi + \partial_\chi(m_1 u_p w_p) + J K m_0 u_p &= J m_0 \frac{(u_g - u_p)}{St_0}.
\end{aligned} \tag{13.36}$$

*Remark:* Obtaining these kinds of conservative equations in three dimensions in space is much more tedious, as the relation between  $\nabla_{\mathbf{x}}$  and  $\nabla_{\chi}$  is matricial and  $\mathbf{J}$  does not coincide with its determinant any more. The derivation in three dimensions is done in Appendix D.2.

The formulation (13.36) turns out to separate acoustic waves of the gas from kinematic waves. Therefore, the basic idea of ALE approaches is to perform a splitting of Eq. (13.36), within a time-step  $\Delta t$ . Indeed, because of the different nature of the waves introduced in the equation systems for the gas and the particles in system (13.36), each step is solved with dedicated solvers for each phase. This approach is fully accurate when the kinematic waves speed is negligible compared to the acoustic waves speed. This hypothesis is not obvious in the context of injection in Diesel engines, where the highest speeds of injection can now reach more than  $600 \text{ ms}^{-1}$ . Nevertheless, this is the strategy adopted in the IFP-C3D code [18].

We use a Lie fractional time-step algorithm decomposed in three steps. The first step (phase A) corresponds to the resolution of the source terms of the system, which in our case are the evaporation and the drag term:

$$\begin{aligned}
\partial_t(J)|_\chi &= 0, \\
\partial_t(J\rho_g)|_\chi &= 0, \\
\partial_t(J\rho_g u_g)|_\chi &= 0, \\
\partial_t(J\rho_g E_g)|_\chi &= 0, \\
\partial_t(Jm_0)|_\chi &= JK\tilde{n}_{ME}, \\
\partial_t(Jm_k)|_\chi &= J(k-1)m_{k-1}, \\
\partial_t(Jm_1 u_p)|_\chi &= -JKm_0 u_p + Jm_0 \frac{(u_g - u_p)}{St_0}.
\end{aligned} \tag{13.37}$$

The second step (phase B) is called the Lagrange step, taking into account only acoustic effects due to the gaseous pressure, which is the only source of acoustic effects as the spray is treated as a pressureless gas. The system solved in during that step reads:

$$\begin{aligned}
\partial_t(J_g)|_{X_g} - \partial_\chi(u_g) &= 0, \\
\partial_t(J_g \rho_g)|_{X_g} &= 0, \\
\partial_t(J_g \rho_g u_g)|_{X_g} + \partial_\chi(P) &= 0, \\
\partial_t(J_g \rho_g E_g)|_{X_g} + \partial_\chi(P u_g) &= 0, \\
\partial_t(J_p)|_{X_p} - \partial_\chi(u_p) &= 0, \\
\partial_t(J_p m_k)|_{X_p} &= 0, k = 0..N \\
\partial_t(J_p m_1 u_p)|_{X_p} &= 0,
\end{aligned} \tag{13.38}$$

$J_g$  denotes the dilatation due to the gaseous velocity field and  $J_p$  the dilatation due to the liquid velocity field. This step corresponds to the resolution of two p-systems, one for each the gaseous and the liquid phase. As the mesh nodes moves at the speed of each phase, two virtual meshes coexist at the end of this step. This is possible as there is no coupling term in this computational step. The presence of a coupling term would cause a problem with this approach as the quantities from each phase intervening in would be defined on two different meshes.

In the last step (phase C), the convective terms are solved in an Eulerian formalism. The two virtual meshes, output of the Lagrange phase, are moved to their common final location corresponding to a displacement with the velocity  $u_\chi$ . With  $\mathbb{U}_g = (\rho, \rho u_g, \rho E_g)$ ,  $\mathbb{U}_p = (m_{k., k=1..N}, m_0 u_p)$ , and the subscript  $m \in g, p$  either referring to the gas or the particles. The dynamical system during phase C reads:

$$\begin{aligned}
\partial_t J_m|_\chi + \partial_\chi w_m &= 0, \\
\partial_t J_m \mathbb{U}_m|_\chi + \partial_\chi \mathbb{U}_m w_m &= 0.
\end{aligned} \tag{13.39}$$

Combining the equations of system (13.39), we obtain the componentwise advection equation. One gets:

$$\partial_t \mathbb{U}_m + \frac{w_m}{J_m} \partial_\chi \mathbb{U}_m = 0, \quad w_m = u_m - u_\chi. \tag{13.40}$$

At the discrete level, the transport velocity for the gas should be taken equal to  $u_m^* - u_\chi$ , where  $u_m^*$  is the output of phase B. This ensures that after phase A and B, the mesh has moved exactly at velocity  $u_\chi$ . The projection step is merely a remap of the variables contained in  $\mathbb{U}_m$ , at the velocity relative to the referential domain.

The quantities are expressed in this final mesh, which is the reason why this step is also called the projection step, or the rezoning step.

We divide the domain,  $[0, Z]$  into  $N$  cells  $[x_{i-1/2}, x_{i+1/2}]$ , each cell having its own size  $\Delta x_i$ . The inner cells are numbered from 1 to  $N$ . We also define two ghost cells labeled 0 and  $N+1$ . The thermodynamical quantities are defined on the cells, so for example  $\rho_i$  is defined as:  $\rho_i = \frac{1}{\Delta x_i} \int_{x_{i-1/2}}^{x_{i+1/2}} \rho(x) dx$ . The velocities are defined on the nodes, we write them:  $u_{g,i-1/2}, u_{g,i+1/2}, u_{p,i-1/2}, u_{p,i+1/2}, u_{\chi,i+1/2}, u_{\chi,i-1/2}$ . Moreover we denote by  $(J_m^n, \mathbb{U}_m^n), (J_m^A, \mathbb{U}_m^A), (J_m^B, \mathbb{U}_m^B), (J_m^C, \mathbb{U}_m^C) = (J_m^{n+1}, \mathbb{U}_m^{n+1})$  the values of  $(J_m, \mathbb{U}_m)$  respectively at time  $t = n\Delta t$ , at the end of phase A, at the end of phase B, and at the end of phase C which are also the updated values at time  $t = (n+1)\Delta t$ .

### 13.3 Resolution for the gas phase

In the configuration studied, insofar as a one-way coupling is between the gas and the particles, no source term associated to the gas is taken into account. The operator associated with phase A is thus identity.

#### 13.3.1 Lagrangian phase

For the gas, the Lagrangian step corresponds to the resolution of a p-system, with the treatment of the acoustic waves. In order to avoid small time steps leading to high computational costs, an implicit time integration is an essential requirement.

From the mass conservation equation, we first use mass conservation in a material volume:  $(J_g \rho_g)^B = (J_g \rho_g)^A = \rho_g^A$ , since  $J_g^A = 1$ . Extracting this relation in the three other equations leads to:

$$\begin{aligned} \partial_t \tau - \frac{1}{\rho} \partial_\chi u_g &= 0, \quad \tau = 1/\rho_g, \\ \partial_t u_g + \frac{1}{\rho} \partial_\chi P &= 0, \\ \partial_t E_g + \frac{1}{\rho} \partial_\chi P u &= 0. \end{aligned} \tag{13.41}$$

System (13.41) only takes into account the acoustic waves. Let us calculate the eigenvalues of this system. Indeed, the eigenvalues of the system are  $0, \pm \rho c$ , where  $c$  is the speed of sound in the gas phase.

System (13.41) can be rewritten:

$$\partial_t W + \mathbf{A}(W) \partial_m W = 0, \tag{13.42}$$

where the matrix  $\mathbf{A}(W)$  reads:

$$\mathbf{A} = \begin{pmatrix} 0 & -1 & 0 \\ -\rho_g^2 c^2 & 0 & 0 \\ -u \rho_g^2 c^2 & P & 0 \end{pmatrix}. \tag{13.43}$$

Its characteristic polynomial writes:  $\theta = -X(X - \rho_g c)(X + \rho_g c)$ . The eigenvalues of  $\mathbf{A}$  are then  $0, \rho_g c, -\rho_g c$ .

Before discretizing these equations, let us remark that the total energy  $E_g$  is not well defined on the grid, as the internal energy is defined on a cell, and the kinetic energy on a node. We will then work with the gas internal energy  $e_g$ , the equation of which is deduced from a combination of the equations of system (13.41). We assume that all the quantities are  $C^1$ , and so that no shock-wave occurs. This assumption is relevant as we consider the spray downstream the injector, with a substantially lower velocity in comparison to its injection velocity. Besides, we are not interested in the description of the shock waves in the gas. The equation of internal energy  $e_g$  is extracted from the equation on total energy and momentum:

$$\partial_t e_g + p \frac{1}{\rho_g} \partial_\chi u_g = 0.$$

But:

$$\partial_t \tau - \frac{1}{\rho_g} \partial_\chi u_g = 0.$$

So we get:

$$\partial_t e_g + p \partial_t \tau = 0. \quad (13.44)$$

The numerical scheme used to solve system (13.41) is a simplified version of the standard acoustic Godunov scheme [98], which can be interpreted as a relaxation scheme [46]. The discretized equations read:

$$\begin{aligned} \tau_i^B - \tau_i^A - \frac{\Delta t (u_{g,i+1/2}^* - u_{g,i-1/2}^*)}{\rho_{g,i}^A \Delta x_i^A} &= 0, \\ u_{g,i+1/2}^B - u_{g,i-1/2}^A + \frac{\Delta t (P_{i+1}^* - P_i^*)}{\rho_{g,i}^A \Delta x_i^A} &= 0, \\ e_{g,i}^B - e_{g,i}^A + P_i^B (\tau_i^B - \tau_i^A) &= 0, \end{aligned} \quad (13.45)$$

where

$$\begin{aligned} u_{g,i+1/2}^* &= u_{g,i+1/2}^B - \frac{P_{i+1}^B - P_i^B}{2a}, \\ P_i^* &= P_i^B - a \frac{u_{g,i+1/2}^B - u_{g,i-1/2}^B}{2}. \end{aligned} \quad (13.46)$$

The parameter  $a$  is homogeneous to  $\rho_g c$ , the Lagrangian speed of sound in the gas. However, it can be shown that  $a$  must be subjected to the subcharacteristic condition  $a > \max_i (\rho_g c)_i$ .

The resulting non-linear matrix equation is inverted by the Newton method.

### 13.3.2 Eulerian phase

The outcome of the Lagrange step is now the input data for the projection step.

*Notation:* In the following, to keep the formulas quite clear, we are going to omit the superscript B denoting quantities computed at the end of phase B. Consequently quantities written without a time superscript implicitly refer to the end of phase B. There is one exception, concerning the cell volume  $\Delta x_i$ , always taken at time  $t = n\Delta t$ . For the sake of clarity, we will use  $\Delta x_i$  to refer to  $\Delta x_i^n$ , omitting the superscript  $n$ .

Let  $\psi$  refer to a cell-defined quantity. As  $\psi$  is a solution of a conservative equation, a finite volume discretization is appropriate for its discretization. Integrating the second equation of system (13.39) over the  $i^{\text{th}}$  cell, we get the discretized equation:

$$\psi_i^{n+1} \Delta x_i^{n+1} = \psi_i \Delta x_i - \Delta t ((\psi w_g)_{i+1/2} - (\psi w_g)_{i-1/2}). \quad (13.47)$$



The cell volume of the mesh associated to the gas phase is  $\Delta x_{g,i} = J_{g,i} \Delta x_i$  at the end of the Lagrange step, and  $\Delta x_{g,i}^{n+1} = J_{g,i}^{n+1} \Delta x_i^n$  at the end of the Eulerian phase. In the following the expression of the cell volume is expanded relative to the dilatation coefficient. This makes the impact on the mesh dilatation clearer in the equations. Thus Eq. (13.47) rewrites:

$$\psi_i^{n+1} = \psi_i - \frac{\Delta t}{\Delta x_i} ((\psi w_g)_{i+1/2} - (\psi w_g)_{i-1/2}). \quad (13.48)$$

The values  $(\psi w_g)_{i+1/2}$  and  $(\psi w_g)_{i-1/2}$  are computed using a first order upwind scheme:

$$(\psi w_g)_{i+1/2} = \psi_i w_{g,i+1/2}^+ + \psi_{i+1} w_{g,i+1/2}^-. \quad (13.49)$$

The discretized equation on the dilatation rate  $J_g$  writes:

$$J_{g,i}^{n+1} = J_{g,i} - \frac{\Delta t}{\Delta x_i} (w_{g,i+1/2} - w_{g,i-1/2}). \quad (13.50)$$

From the equations (13.47) and (13.50) one can derive the stability condition of that basic first order scheme.

Expressing  $J_{g,i}$  relative to  $J_{g,i}^{n+1}$  in Eq. (13.47) leads to:

$$(J_g \psi)_i^{n+1} = (J_g \psi)_i - \frac{\Delta t}{\Delta x_i} \left( w_{g,i+1/2}^- (\psi_{i+1} - \psi_i) - w_{g,i-1/2}^+ (\psi_{i-1} - \psi_i) \right). \quad (13.51)$$

Finally:

$$\psi_i^{n+1} = \psi_i \left[ 1 + \frac{\Delta t}{J_{g,i}^{n+1} \Delta x_i^n} (w_{g,i+1/2}^- - w_{g,i-1/2}^+) \right] - \frac{\Delta t}{J_{g,i}^{n+1} \Delta x_i^n} w_{g,i+1/2}^- \psi_{i+1} + \frac{\Delta t}{J_{g,i}^{n+1} \Delta x_i^n} w_{g,i-1/2}^+ \psi_{i-1}. \quad (13.52)$$

In order to have a convex sum of  $\psi_i, \psi_{i+1}, \psi_{i-1}$ , the term  $1 + \frac{\Delta t}{J_{g,i}^{n+1} \Delta x_i^n} (w_{g,i+1/2}^- - w_{g,i-1/2}^+)$  must be positive. This leads to the CFL criterion:

$$\frac{\Delta t}{J_{g,i}^{n+1} \Delta x_i} \max_{i \in \mathbb{Z}} |w_{g,i+1/2}^- - w_{g,i-1/2}^+| \leq 1, \quad (13.53)$$

or, expressing  $J_{g,i}^{n+1}$  relative to  $u_\chi$ :

$$\frac{\Delta t}{\Delta x_i^n + (u_{\chi,i+1/2} - u_{\chi,i-1/2}) \Delta t} \max_{i \in \mathbb{Z}} |w_{g,i+1/2}^- - w_{g,i-1/2}^+| \leq 1. \quad (13.54)$$

The resolution of the momentum equations are more tedious, as the first thing is to define the quantity  $(\psi u_g)_{i+1/2}$ . This is not *a priori* obvious as  $\rho_g$ , and  $u_g$  are not defined on the same domain. We define the momentum on the nodes. This means that we solve the momentum on a dual mesh with respect to the regular one. The dual cell centers are the nodes of the regular cells, and the dual cell interfaces are the regular cell centers. Using a weighted average by  $\rho_g$  on each side of the node. For the gas, phase, this writes:

$$(\rho_g u_g)_{i+1/2} = u_{g,i+1/2} \frac{(J_g \rho_g)_i + (J_g \rho_g)_{i+1}}{J_{g,i} + J_{g,i+1}}. \quad (13.55)$$

The discretized equation leads, for the gas:

$$(J_g \rho_g u_g)_{i+1/2}^{n+1} = (J_g \rho_g u_g)_{i+1/2} - \frac{\Delta t}{\Delta x} [(\rho_g u_g w_g)_{i+1} - (\rho_g u_g w_g)_i]. \quad (13.56)$$

As before we use a first order upwind scheme to compute the fluxes:

$$(\rho_g u_g w_g)_i = (\rho_g u_g)_{i-1/2} w_{g,i}^+ + (\rho_g u_g)_{i+1/2} w_{g,i}^-, \quad (13.57)$$

where  $w_{g,i} = \frac{w_{g,i+1/2} + w_{g,i-1/2}}{2}$ .

We may also want to have a scheme with a higher order in space and time. For the gas phase, a classical linear reconstruction with a minmod limiter is used for the cell-defined quantities. The momentum, expressed on each node from the velocity and the density, are reconstructed on the dual mesh, with the same type of reconstruction as for the cell-defined quantities. This scheme guarantees the *sine qua non* condition: positivity of the density and internal energy.

## 13.4 Resolution for aerosol and realizability condition

The preliminary step for the resolution of the spray dynamics is the resolution for aerosol dynamics. As aerosol particles have the same velocity as the gas, its resolution only involves the respect of realizability condition, defined in Section 4.3.

### 13.4.1 Adaptation of the numerical scheme in the Eulerian phase

In Chapter 6, a scheme has been proposed, relying on the reconstruction of canonical moments, in order to preserve the realizability condition directly during the convection process. This scheme can be found in [129]. But these developments have been done in an Eulerian framework. This part presents the adaptation of this scheme to the ALE formulation.

Defining the discrete values of the moments over the mesh at the end of the Lagrangian step:

$$m_{k,i}^B = \frac{1}{\Delta x^B} \int_{x_{i-1/2}^B}^{x_{i+1/2}^B} m_k^B(x) dx, \quad k = 0, \dots, N. \quad (13.58)$$

The discretization of the convection part in the equations on moments in system (13.36) leads to:

$$\mathbf{m}_i^{n+1} \Delta x_i^{n+1} = \mathbf{m}_i^B \Delta x_i^B - \Delta t (\mathbf{F}_{i+1/2} - \mathbf{F}_{i-1/2}), \quad (13.59)$$

where  $\mathbf{F}_{i+1/2}$ , the moment flux, writes:

$$\mathbf{F}_{i+1/2} = \int_0^{\Delta t} \int_{\mathbb{R}} u \begin{pmatrix} m_0 \\ m_1 \\ \vdots \\ m_N \end{pmatrix} (x_{i+1/2}) du dt. \quad (13.60)$$

In order to design a second order scheme in space, one chooses to reconstruct the moments linearly in the  $i^{\text{th}}$  cell. Two difficulties are encountered, as explained in Chapter 6. The first one is that, given the complexity of the moment space, we are not sure that the reconstructed vector at the point  $x_{i+1/2}$  is still a moment vector. Moreover, assuming that we can be sure of that, there is no guarantee that, after adding the fluxes, the updated moment is still a moment vector. Indeed, the moment space is not a vectorial space.

Both difficulties are solved when considering the kinetic level of description and looking at the macroscopic equations as derived from the kinetic equation:

$$\partial_t(f) + u\partial_\chi(f) = 0, \text{ in } \mathbb{R}_\chi \times \mathbb{R}_u \times \mathbb{R}_S \times ]t_n, t_{n+1}[, \quad (13.61)$$

so that  $f(t, x, u, S) = f(0, x - ut, u, S)$ .

Thus, expressing the moments according to  $f$  leads to the following expression for  $\mathbf{F}_{i+1/2}$ :

$$\mathbf{F}_{i+1/2} = \frac{1}{\Delta t} \int_0^{\Delta t} \int_{\mathbb{R}} \int_0^1 \begin{pmatrix} 1 \\ S \\ \vdots \\ S^N \end{pmatrix} u f(t, x_{i+1/2}, S, u) \, dS du dt. \quad (13.62)$$

We can compute the integrals over  $\mathbb{R}^+$  and  $\mathbb{R}^-$  separately, and then the numerical flux can be written in the flux vector splitting form:  $\mathbf{F}_{i+1/2} = \mathbf{F}_{i+1/2}^+ + \mathbf{F}_{i+1/2}^-$ , where the distinction is made between positive and negative velocities.

Using the fact that  $f$  is transported at the velocity  $u$  enables to make a change of variable in the expression (13.62), so that  $\mathbf{F}_{i+1/2}^+$  can be expressed as a space integral of the moments over the  $i^{\text{th}}$  cell. Provided that the reconstruction of  $f$  ensures that the scheme is conservative and that the realizability condition is satisfied  $\forall x \in [x_{i-1/2}, x_{i+1/2}]$ , the updated vector  $\mathbf{m}_i^{n+1}$  belongs to the moment space. In fact, in that case, when considering positive velocities with no loss of generality, the quantity  $\mathbf{m}_i^B - \frac{\Delta t}{\Delta x_i^B} \mathbf{F}_{i+1/2}^+$  is a moment vector.

To achieve a reconstruction meeting the two above requirements, we reconstruct the canonical moments, in  $]x_{j-1/2}, x_{j+1/2}[$  taking benefit from the fact that they are transported and they lie in  $[0, 1]$ :

$$\begin{cases} m_0(x) &= m_{0,j} + D_{m_{0j}}(x - x_j), \\ p_1(x) &= \overline{p_{1j}} + D_{p_{1j}}(x - x_j), \\ &\vdots \\ p_N(x) &= \overline{p_{Nj}} + D_{p_{Nj}}(x - x_j). \end{cases}$$

where  $D_{p_{1,i}}$  and  $D_{p_{n,i}}$  are the slopes and the quantities with bars, called the modified averages, are different from their real mean value in order for the scheme to be conservative.

Indeed, given  $\mathcal{T}$  a transported quantity and  $\mathcal{C}$  the corresponding conserved quantity, the scheme is conservative if:

$$\begin{cases} \mathcal{C}(x) = m_0(x)\mathcal{T}(x), \\ \mathcal{C}_i = \mathcal{T}_i m_{0,i} = \frac{1}{\Delta x} \int_{x_{i-1/2}}^{x_{i+1/2}} m_0(x)\mathcal{T}(x) \, dx \end{cases}$$

The recursive dependance of higher order canonical moments makes their modified average more difficult to express. High order polynomial must be integrated, (up to order 4 for  $\overline{p_2}$ , and 6 for  $\overline{p_3}$ ). The quantity  $\overline{p_{k,i}}$  writes  $\overline{p_{k,i}} = a_{k,i} + b_{k,i} D_{p_{k,i}}$ . The calculation of the coefficients  $a_{2j}, a_{3j}$  and  $b_{2j}, b_{3j}$  is achieved using Maple (Maplesoft, a division of Waterloo Maple, Inc 2007), and implemented in the code written in Fortran. Their expression is quite heavy, but, as it is just an algebraic relation, the corresponding CPU cost is low.

The slopes for the canonical moments are determined using limiters in order to satisfy maximum principles:

$$r_{ki} \leq p_k(x) \leq R_{ki}, \quad x \in (x_{i-1/2}, x_{i+1/2}),$$

where  $r_{ij} = \min(p_{k,i-1}, p_{k,i}, p_{k,i+1})$  and  $R_{ij} = \max(p_{k,i-1}, p_{k,i}, p_{k,i+1})$ . We must have:

$$\begin{cases} r_{ki} \leq a_{k,i} + b_{k,i} D_{p_{k,i}} + \frac{\Delta x_i^B}{12} D_{p_{k,i}} \leq R_{ki}, \\ r_{ki} \leq a_{k,i} + b_{k,i} D_{p_{k,i}} - \frac{\Delta x_i^B}{12} D_{p_{k,i}} \leq R_{ki}. \end{cases}$$

The slopes must then verify:

$$\begin{cases} D_{p_{k,i}} \leq \min\left(\frac{R_{ki} - a_{k,i}}{b_{k,i} + \Delta x_i^B/2}, \frac{a_{k,i} - r_{ki}}{\Delta x_i^B/2 - b_{k,i}}\right), \\ D_{p_{k,i}} \geq \min\left(\frac{r_{ki} - a_{k,i}}{b_{k,i} + \Delta x_i^B/2}, \frac{a_{k,i} - R_{ki}}{\Delta x_i^B/2 - b_{k,i}}\right). \end{cases}$$

In practice, we use the following slope limiter to satisfy all the conditions:

$$D_{p_{k,i}} = \frac{1}{2} (\text{sgn}(p_{k,i+1} - p_{k,i}) + \text{sgn}(p_{k,i} - p_{k,i-1})) \times \min\left(\frac{|p_{k,i+1} - a_{k,i}|}{2(\frac{\Delta x_i^B}{2} + b_{k,i})}, \frac{|a_{k,i} - p_{k,i-1}|}{2(\frac{\Delta x_i^B}{2} - b_{k,i})}\right).$$

The same limiter is used for the slope on the droplet number  $m_0$ . In order to ensure the non-negativity of  $m_0$ , one adds the following condition:  $D_{m_0,i} \Delta x_i^B/2 \leq m_{0,i}$ .

In practice, we set  $N = 3$ , so we work with the four first size moments. The final expression of the size flux containing the canonical moments is:

$$\mathbf{F}_{i+1/2}^+ = \frac{1}{\Delta t} \int_{x_{i+1/2}^L}^{x_{i+1/2}^R} m_0^n \begin{pmatrix} 1 \\ p_1 \\ (p_1((1-p_1)p_2 + p_1)) \\ p_1\{(1-p_1)(1-p_2)p_2p_3 + [p_1 + p_2(1-p_1)]^2\} \end{pmatrix} (x) dx,$$

where  $x_{i+1/2}^L = x_{i+1/2} - w_{g,i+1/2}^+ \Delta t$ , where  $w_{g,i+1/2}^+$  either represents the gas velocity in the case of aerosols, or the particle velocity in the case of sprays. This scheme is second order in space and time for the moments.

### 13.4.2 Results

In order to assess the numerical efficiency of our method, some computations have been performed with a code especially written to validate the use of moment methods in the ALE formalism in one dimension. A first result shows the possibility to transport and evaporate and aerosol. The interest for a second order in space scheme is then highlighted when the grid moves.

The particles are considered as tracers for the gas phase initiated in the condition of a Riemann problem. The left state is set as  $P_l = 3 Pa$ ,  $\rho_l = 1 kg m^{-3}$  and for the right state  $P_r = 1 Pa$ ,  $\rho_r = 0.125 kg m^{-3}$ . The gas constant of the EOS is set as  $1 J kg^{-1} K^{-1}$ . From now on we omit the units of the quantities, the dimensioned ones being written in the international system. The NDF for the polydisperse aerosol is set as constant with the value  $n(x, S) = \rho'$ ,  $S \in [0, 1]$  so that  $m_0 = \rho'$ . The initial conditions are displayed in Fig. (13.3). Physically,  $m_0$  and  $\rho$  have no reason to be equal. The quantity  $m_0$  is the droplet number density and  $\rho$  is the gas density, and both quantities are initialized with the same value only for a numerical reason. That way, the profil of  $m_0$  can be easily compared to the profil of  $\rho$ . Neumann

boundary conditions are set on the space interval  $[0, 1]$ , on the grid with 200 cells. The CFL has to be chosen with caution. Indeed the time step is determined at the beginning of the resolution, before phase A. However, during the Lagrangian phase, the acoustic effects on the gas modify the gas velocity field and so, locally, the CFL condition set at the beginning may turn out not to be met. Actually, in addition to the convective CFL number, we introduce another CFL number, the acoustic CFL number, for the Lagrangian resolution. We set the acoustic CFL number to 10, and the convective CFL a little bit below one, at 0.9, to ensure a stable resolution.

Figures (13.4)-left and (13.4)-right show the results for the gas density,  $m_0$ , and the analytical solution for this case at  $t = 0.1$ . In Fig. (13.4)-left the spatial resolution for the aerosol is first order, and it is second order in Fig. (13.4)-right, whereas the resolution of the gas is second order in both cases. We have only displayed the results for  $m_0$  and  $m_1$  for the sake of legibility, but  $m_2$  and  $m_3$  are also solved. The difference of resolution of the moments between the two results is conform to what one would expect. The first conclusion to draw is that the method explained in this section works in the ALE formalism and gives convincing results. Besides, the difference of resolution between the gas and the moments is quite interesting to note in Fig. (13.4)-right. It is slightly more precise for the moments than for the gas. In Fig. (13.5)-left the particles are evaporated with the coefficient  $K = 2$ .  $K$  is such as  $\Delta S = K \Delta t$ , so that all the droplets must be evaporated at  $t = \Delta S / K$ . Focusing on the result for  $m_0$ , it is everywhere equal to  $0.8\rho'$ . This is coherent with the initial NDF, and the evaporation rate  $K = 2$ , implying that 20% of the total droplet number must have been evaporated.

Figure (13.5)-right displays the results for  $m_0$  of the same test case, but comparing a first order scheme with the second order scheme. The accuracy of these schemes is compared on a fixed grid but also in a moving grid. The displacement of the grid follows the law :  $x(t) = 0.2 \sin(2\pi/0.1t)$ . The results focused on the interface region. When no grid movement is involved, the second order scheme is already more accurate than the first order. This conclusion validates the implementation of our high order moment method. But the interest of a second order scheme becomes obvious when the grid moves. In our case, the high grid velocity leads to small CFL numbers for the fluids. Therefore the profil of  $m_0$  is much more diffused with the first order scheme than with the second order scheme.

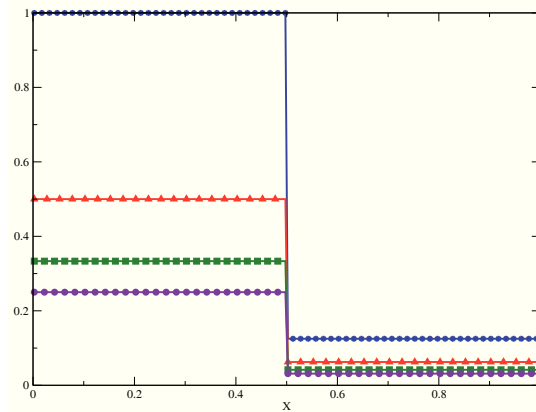


Figure 13.3: Initial condition for the moments. The blue curve with stars refers to  $m_0$ , the red curve with up triangles to  $m_1$ , the green curve with squares to  $m_2$ , and the violet curve with circles to  $m_3$ .

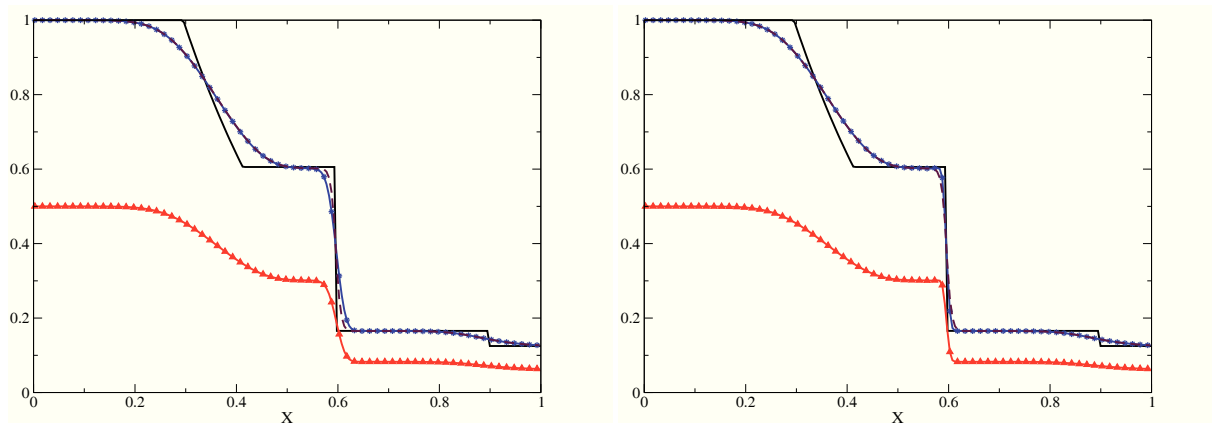


Figure 13.4: (left) Solution of the Riemann problem at  $t = 0.1$  for the gas and the aerosol, with the first order in space scheme for the aerosol and second order for the gas. The analytical solution is represented by the solid black line, the dashed maroon line represents the numerical solution for the gas, the blue curve with stars markers and the red curve with up triangle markers respectively stands for  $m_0$  and  $m_1$ . (right) Solution of the Riemann problem on a moving grid, comparison between the different orders of resolution of the gas and  $m_0$ . The computation is carried out on a 200 cell grid.

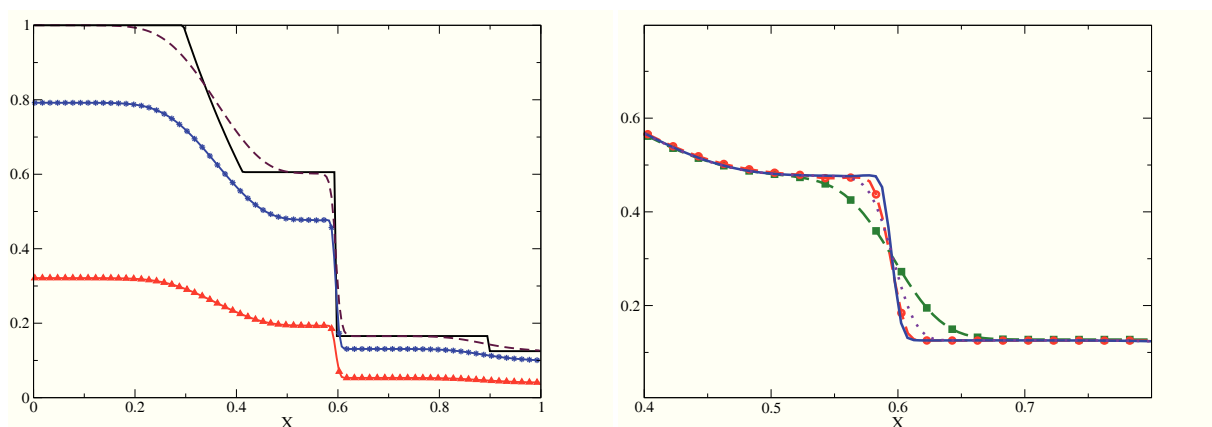


Figure 13.5: (left) Solution of the Riemann problem at  $t = 0.1$  for the gas and the evaporating aerosol, with second order for both phases. The analytical solution is represented by the solid black line, the dashed maroon line represents the numerical solution for the gas, the blue curve with stars markers and the red curve with up triangle markers respectively stands for  $m_0$  and  $m_1$ . (right) Solution of the Riemann problem on a moving grid, comparison between the different orders of resolution of the gas and  $m_0$ . The result is focus on the interfacial area of Fig.(13.4). Same configuration, but now with second order for the aerosol. The computation is carried out on a 200 cell grid.

## 13.5 Transport of spray and preservation of the discrete maximum principle

Spray particles have their own inertia. This is accounted for by an equation on their momentum  $m_1 u_p$ , in addition to the equations on moments. The solution for the moment space preservation has been solved in the case of aerosols, detailed in the precedent section. The purpose of this part is to focus on the processes affecting the spray velocity: the drag term, treated as a source term in phase A, the dilatation term in phase B due to the spray velocity, and especially the rezoning step where the respect of the discrete maximum principle for the velocity is crucial.

### 13.5.1 Treatment of the drag term in phase A

In this step the following equation system is resolved:

$$\begin{aligned}\partial_t J_p &= 0, \\ \partial_t (J_p m_k) &= 0, \\ \partial_t (m_1 u_p) &= m_0 \frac{(u_g - u_p)}{St_0},\end{aligned}\tag{13.63}$$

and reduces to:

$$\partial_t u_p = \frac{m_0}{m_1} \frac{(u_g - u_p)}{St_0}.\tag{13.64}$$

During that phase, due to the assumption of one-way coupling,  $u_g$  stays constant. Thus the ODE (13.64) can be easily solved and the result for the spray velocity is:

$$u_p^A = u_p^n \exp\left(-\frac{m_0}{m_1 St_0} \Delta t\right) + u_g^n \left(1 - \exp\left(-\frac{m_0}{m_1 St_0} \Delta t\right)\right).\tag{13.65}$$

### 13.5.2 Phase B

In the particle phase, there is no pressure term in the momentum equation. This implies that the dilatation coefficient  $J_p$  is modified only by the divergence of the particle velocity field which is unchanged during this phase. The involved characteristic wave speeds are only the particle speed. We can thus use an explicit method for the resolution of the system concerning the moments. If one writes  $\tau_{k,i} = 1/m_{k,i}$ ,  $k = 1 \dots N$ , one gets:

$$\tau_{k,i}^B = \tau_{k,i}^A \left(1 - \frac{\Delta t}{\Delta x_i} (u_{p,i+1/2} - u_{p,i-1/2})\right).\tag{13.66}$$

For  $\tau_{k,i}$  to remain positive, we impose  $\Delta t \leq \frac{\Delta x_i}{u_{p,i+1/2} - u_{p,i-1/2}}$ .

From the values of  $\tau_{k,i}$  can be deduced the value of  $J_p^B$  in virtue of the relation  $(J_p m_{k,i})^B = (J_p m_{k,i})^A$ .

### 13.5.3 Phase C: first attempt for a stable advection scheme

*Notation:* In this section, we denote by  $J_{p,i}$  the discrete value at the  $i^{th}$  cell of the dilatation coefficient of the mesh associated to the spray,  $m_{k,i}$  the discrete value of  $m_k$ ,  $\Delta x_i$  the cell size at  $t = n\Delta t$ , and  $w_{p,i+1/2}$  and  $u_{p,i+1/2}$  the values respectively of  $w_p$  and  $u_p$  at the point  $x_{i+1/2}$ . As previously for the case of gas quantities, the superscript  $B$ , referring to quantities computed at the end of phase B, will be omitted for

the sake of legibility; hence quantities with no superscript are the output of phase B.

For the resolution of phase C, the first idea, for a first order scheme, is to apply the first order scheme for the resolution of the gas in the case of spray. The important property of system (13.39) is that the quantities are transported.

It can be therefore proven that  $m_{k,i}$  is transported in virtue of the discretized equation (13.47) which, applied to  $m_{k,i}$ , leads to:

$$(J_p m_k)_i^{n+1} = (J_p m_k)_i - \frac{\Delta t}{\Delta x} \left[ m_{k,i+1} w_{p,i+1/2}^- + m_{k,i} w_{p,i+1/2}^+ - (m_{k,i} w_{p,i-1/2}^- + m_{k,i-1} w_{p,i-1/2}^+) \right], \quad (13.67)$$

combined to the equation:

$$J_{p,i}^{n+1} = J_{p,i}^B - \frac{\Delta t}{\Delta x} (w_{p,i+1/2} - w_{p,i-1/2}). \quad (13.68)$$

As previously for the case of gas quantities, under the CFL condition  $\Delta t \max_i \frac{|w_{p,i+1/2}^- - w_{p,i-1/2}^+|}{\Delta x_i J_{p,i}^{n+1}} \leq 1$ ,  $m_{k,i}^{n+1}$  is a convex sum of  $m_{k,i}$ ,  $m_{k,i+1}$  and  $m_{k,i-1}$ . This conclusion holds without assuming the sign of the velocity. This equality shows that the discrete maximum principle is respected for cell-centered quantities.

To demonstrate the same property for the velocity, we start from the discretized equation of momentum conservation (13.56):

$$(J_p m_1 u_p)_{i+1/2}^{n+1} = (J_p m_1 u_p)_{i+1/2} - \frac{\Delta t}{\Delta x} [(m_1 u_p w_p)_{i+1} - (m_1 u_p w_p)_i], \quad (13.69)$$

where  $(J_p m_1 u_p)_{i+1/2}$  is defined, similarly to Eq. (13.55), as:

$$(J_p m_1 u_p)_{i+1/2} = (J_p m_1)_{i+1/2} u_{p,i+1/2} = \frac{(J_p m_1)_i + (J_p m_1)_{i+1}}{2} u_{p,i+1/2}, \quad (13.70)$$

and, by definition:

$$m_{1,i+1/2} = \frac{(J_p m_1)_{i+1/2}}{J_{p,i+1/2}} = \frac{(J_p m_1)_i + (J_p m_1)_{i+1}}{J_{p,i} + J_{p,i+1}}, \quad (13.71)$$

so that:

$$(J_p m_1 u_p)_{i+1/2} = J_{p,i+1/2} m_{1,i+1/2} u_{p,i+1/2}. \quad (13.72)$$

In order to obtain the same relation as in (13.52) where  $u_{p,i+1/2}^{n+1}$  expresses as a convex sum of the  $u_{p,i+1/2}$ ,  $(J_p m_1)_{i+1/2}^{n+1}$  should write:

$$\begin{aligned} (J_p m_1)_{i+1/2}^{n+1} &= (J_p m_1)_{i+1/2} - \frac{\Delta t}{\Delta x} \left[ w_{p,i+1}^+ m_{1,i+1/2} + w_{p,i+1/2}^- m_{1,i+3/2} \right. \\ &\quad \left. - (w_{p,i-1}^+ m_{1,i-1/2} + w_{p,i-1}^- m_{1,i+1/2}) \right]. \end{aligned} \quad (13.73)$$

As the relation between  $(J_p m_1)_{i+1/2}$  and  $(J_p m_1)_i$  is linear, the equation verified by  $(J_p m_1)_{i+1/2}^{n+1}$  is



obtained summing the equations on  $(J_p m_1)_i^{n+1}$  and  $J_i^{n+1}$ :

$$(J_p m_1)_{i+1/2}^{n+1} = (J_p m_1)_{i+1/2} - \frac{\Delta t}{\Delta x} \left[ \frac{m_{1,i} w_{p,i+1/2}^+ + m_{1,i+1} w_{p,i+1/2}^- + m_{1,i+1} w_{p,i+3/2}^+ + m_{1,i+2} w_{p,i+3/2}^-}{2} - \frac{m_{1,i-1} w_{p,i-1/2}^+ + m_{1,i} w_{p,i-1/2}^- + m_{1,i} w_{p,i+1/2}^+ + m_{1,i+1} w_{p,i+1/2}^-}{2} \right]. \quad (13.74)$$

Comparing Eq. (13.73) and (13.74), we should have:

$$\begin{aligned} w_{p,i+1}^+ m_{1,i+1/2} &= \frac{m_{1,i} w_{p,i+1/2}^+ + m_{1,i+1} w_{p,i+3/2}^+}{2}, \\ w_{p,i}^+ m_{1,i-1/2} &= \frac{m_{1,i-1} w_{p,i-1/2}^+ + m_{1,i} w_{p,i+1/2}^+}{2}. \end{aligned} \quad (13.75)$$

*Remark:* The same type of relations also hold for  $w_{p,i+1}^-$  and  $w_{p,i}^-$  but we did not write them for the sake of legibility.

But, analysing the first term:

$$\begin{aligned} w_{p,i+1}^+ m_{1,i+1/2} - \frac{m_{1,i} w_{p,i+1/2}^+ + m_{1,i+1} w_{p,i+3/2}^+}{2} &= \\ \frac{1}{2} w_{p,i+1/2}^+ \left( \frac{(J_p m_1)_i + (J_p m_1)_{i+1}}{J_{p,i} + J_{p,i+1}} - m_{1,i} \right) + \frac{1}{2} w_{p,i+1/2}^+ \left( \frac{(J_p m_1)_i + (J_p m_1)_{i+1}}{J_{p,i} + J_{p,i+1}} - m_{1,i+1} \right), \end{aligned} \quad (13.76)$$

is not null in the general case and vanishes only when  $J_{p,i}$  and  $J_{p,i+1}$  are equal to 1, which is a consequence of  $w_{p,i+1/2}^+ = w_{p,i+3/2}^+$  stating that there is no dilatation or compaction of the mesh. This result has far reaching consequences, because due to dilatation effects, this scheme does not guarantee the discrete maximum principle on the velocity. In Appendix D.1, we provide a counter-example where the discrete maximum principle is not respected by this scheme.

*Remark:* This results is also true for the gas phase, namely the discrete maximum principle is not guaranteed for the gas velocity. But this does not impact the algorithm stability, because the velocity field is then smoothen by the pressure field in phase C. This is not the case for the spray as it follows the pressureless gas formalism.

### 13.5.4 Stable second order scheme with flux coherence between $m_1$ and $\psi u_p$

The problem with the initial scheme is that the fluxes for the cell centered quantities ( $m_1$ ) and the off-centered quantities ( $u_p$ ) are not coherent. Indeed, the fluxes write:

$$\begin{aligned} (m_1 u_p w_p)_i &= (m_1 u_p)_{i-1/2} w_{p,i}^+ + (m_1 u_p)_{i+1/2} w_{p,i}^-, \\ (m_1 w_p)_{i+1/2} &= m_{1,i} w_{p,i+1/2}^+ + m_{1,i+1} w_{p,i+1/2}^-, \end{aligned} \quad (13.77)$$

with different values of  $m_1$  in the two expressions.

The idea developed here is to be able to derive the flux for the momentum from the flux for  $m_1$ . For that purpose our strategy is to adapt to off-centered grids the scheme developed by Larrourou for fixed grids in [142]. The very property of this scheme is, given the system of conservation equations:

$$\begin{aligned} \partial_t m_1 + \partial_x m_1 w_p &= 0, \\ \partial_t m_1 Y + \partial_x m_1 Y w_p &= 0, \end{aligned} \quad (13.78)$$

to conserve the density  $m_1$  and  $m_1 Y$  and to ensure the maximum principle on the transported quantity  $Y$ .

In order to achieve this property, the scheme writes:

$$\begin{aligned} m_{1,i}^{n+1} &= m_{1,i} - \frac{\Delta t}{\Delta x_i} [(m_1 w_p)_{i+1/2} - (m_1 w_p)_{i-1/2}] = 0, \\ (m_1 Y)_i^{n+1} &= (m_1 Y)_i - \frac{\Delta t}{\Delta x_i} [(m_1 Y w_p)_{i+1/2} - (m_1 Y w_p)_{i-1/2}] = 0, \end{aligned} \quad (13.79)$$

with:

$$(m_1 Y w_p)_{i+1/2} = (m_1 w_p)_{i+1/2}^+ Y_i + (m_1 w_p)_{i+1/2}^- Y_{i+1}. \quad (13.80)$$

Here the variable  $Y$  is decentered relative to the sign of the flux for density. This is the key difference with the previous scheme, where  $m_1 Y$  was decentered relative to the value of the velocity. It is easy to show that this structure of flux guarantees the maximum principle on  $Y$ .

$$\begin{aligned} (m_1 Y)_i^{n+1} &= (m_1 Y)_i - \frac{\Delta t}{\Delta x_i} \left[ (m_1 w_p)_{i+1/2}^+ Y_i + (m_1 w_p)_{i+1/2}^- Y_{i+1} - \right. \\ &\quad \left. ( (m_1 w_p)_{i-1/2}^+ Y_{i-1} + (m_1 w_p)_{i-1/2}^- Y_i ) \right]. \end{aligned} \quad (13.81)$$

Expressing  $m_1^{n+1}$  in (13.81) leads to:

$$\begin{aligned} Y_i^{n+1} &= Y_i \left[ 1 + \frac{\Delta t}{\Delta x m_{1,i}^{n+1}} ((m_1 w_p)_{i+1/2}^- - (m_1 w_p)_{i-1/2}^+) \right] - \\ &\quad \frac{\Delta t}{\Delta x m_{1,i}^{n+1}} \left[ (m_1 w_p)_{i+1/2}^- Y_{i+1} - (m_1 w_p)_{i-1/2}^+ Y_{i-1} \right], \end{aligned} \quad (13.82)$$

and provided the CFL condition  $\max_i \frac{\Delta t}{\Delta x_i} |(m_1 w_p)_{i+1/2}^+ - (m_1 w_p)_{i-1/2}^-| \leq 1$ ,  $Y_i^{n+1}$  is a convex sum of  $Y_{i-1}$ ,  $Y_i$ ,  $Y_{i+1}$  and hence the discrete maximum principle is enforced.

Considering now a decentered scheme with a moving mesh, the discretized equation read:

$$\begin{aligned} (J_p m_1)_i^{n+1} &= (J_p m_1)_i - \frac{\Delta t}{\Delta x} ((m_1 w_p)_{i+1/2} - (m_1 w_p)_{i-1/2}), \\ J m_1 Y_{i+1/2}^{n+1} &= J m_1 Y_{i+1/2} - \frac{\Delta t}{\Delta x} ((m_1 Y w_p)_{i+1} - (m_1 Y w_p)_i). \end{aligned} \quad (13.83)$$

The difficulty here lies in the fact that the flux for density and for momentum are not defined on the same points. Hence we define the quantity

$$(m_1 w_p)_i^* = \frac{1}{2} ((m_1 w_p)_{i+1/2} + (m_1 w_p)_{i-1/2}), \quad (13.84)$$

so that:

$$(m_1 Y w_p)_i = (m_1 w_p)_i^{*+} Y_{i-1/2} + (m_1 w_p)_i^{*-} Y_{i+1/2}. \quad (13.85)$$

The update of the momentum reads:

$$\begin{aligned} J m_1 Y_{i+1/2}^{n+1} &= J m_1 Y_{i+1/2} - \frac{\Delta t}{\Delta x_i} \left[ (m_1 w_p)_{i+1}^{*+} Y_{i+1/2} + (m_1 w_p)_{i+1}^{*-} Y_{i+3/2} - \right. \\ &\quad \left. ((m_1 w_p)_i^{*+} Y_{i-1/2} + (m_1 w_p)_i^{*-} Y_{i+1/2}) \right], \end{aligned} \quad (13.86)$$

and with the definition (13.70) and (13.71), we get:

$$(J_p m_1)_{i+1/2}^{n+1} = (J_p m_1)_{i+1/2} - \frac{\Delta t}{\Delta x_i} \left[ \underbrace{\frac{1}{2} ((m_1 w_p)_{i+1/2} + (m_1 w_p)_{i+3/2})}_{(m_1 w_p)_{i+1}^*} - \underbrace{\frac{1}{2} ((m_1 w_p)_{i-1/2} + (m_1 w_p)_{i+1/2})}_{(m_1 w_p)_i^*} \right], \tag{13.87}$$

and after some algebra we obtain that:

$$Y_{i+1/2}^{n+1} = Y_{i+1/2} \left[ 1 - \frac{\Delta t}{\Delta x_i} ((m_1 w_p)_i^{*,+} - (m_1 w_p)_{i+1}^{*, -}) \right] - \frac{\Delta t}{\Delta x} ((m_1 w_p)_{i+1}^{*, -} Y_{i+3/2} - (m_1 w_p)_i^{*,+} Y_{i-1/2}), \tag{13.88}$$

which, under the CFL condition  $\max_i \frac{\Delta t}{\Delta x_i} |(m_1 w_p)_i^{*,+} - (m_1 w_p)_{i+1}^{*, -}| \leq 1$ , is a convex sum.

### 13.5.5 Results

The numerical feasibility of the transport of a spray with its own inertia respecting the discrete maximum principle on the velocity is assessed through some elementary test cases.

#### 13.5.5.1 Convection at uniform velocity

The stability of the method is proven first on a convection test case with uniform velocity. A crenel is initiated in a 100 cell domain, moving at velocity  $u_p = 1$ . The final time of the computation is  $t_{max} = 0.3$ . The initial conditions are represented in Fig. (13.6)-left that also shows the result for the first and the second order scheme, at  $CFL = 0.8$ . In Fig. (13.6)-left these results correspond to the expected results and prove that the discrete maximum principle is respected for the velocity. Figure (13.6)-right deals with the same configuration, but now the mesh moves with the same law as in the test cases for aerosol (13.4.2):  $x(t) = 0.2 \sin(\frac{2\pi}{0.1}t)$ . Three different results are displayed, for the second order scheme with  $CFL = 0.8$ ,  $CFL = 0.5$ , and for the first order scheme with  $CFL = 0.5$ . If the solutions for the second order scheme are understandable, the difference of the result with the first order scheme is a direct consequence of the mesh movement and Neumann boundary conditions. In the beginning of the computation, according to its movement law, the domain left border goes forward to the point 0.2. The initial conditions are such that, at this time, the left edge of the kernel is located a bit further than this point. But the first order scheme diffuses the crenel such that a part of it lies before the left border of the domain, is ejected of the computational domain because of the type of boundary conditions. The same explication hold for the right side of the crenel. This very simple example highlights first the advantage of the second order scheme in terms of accuracy especially when mesh movement is involved, but also the importance of the choice mesh movement law that can potentially alter the solution.

#### 13.5.5.2 Ability to capture $\delta$ -shocks

The second case tests this ability of the numerical method to capture  $\delta$ -shocks, singularities that are engendered by the pressureless gas formalism. For that purpose, a velocity discontinuity is initiated at the point  $x = 0.25$  with  $v = 2, x \leq 0.25$  and  $v = 1, x > 0.25$ , whereas the field of moments is constant ( $m_0 = 1$ ), the size distribution being the same as in previous cases. Two results are displayed at time  $t = 0.1$ , the first one without mesh movement, and the second one with mesh movement (with the same law as in the previous tests), with  $CFL = 1$  and a 200 cell grid. Figure (13.7)-left shows the resulting  $\delta$ -shock for the first and second order schemes where it can be seen that its dynamics is the same in both cases. Moreover this dynamics is the expected one. Indeed the analytical solution of this simple case leads to the shock moving at the average velocity between the two initial states, which is 1.5, and

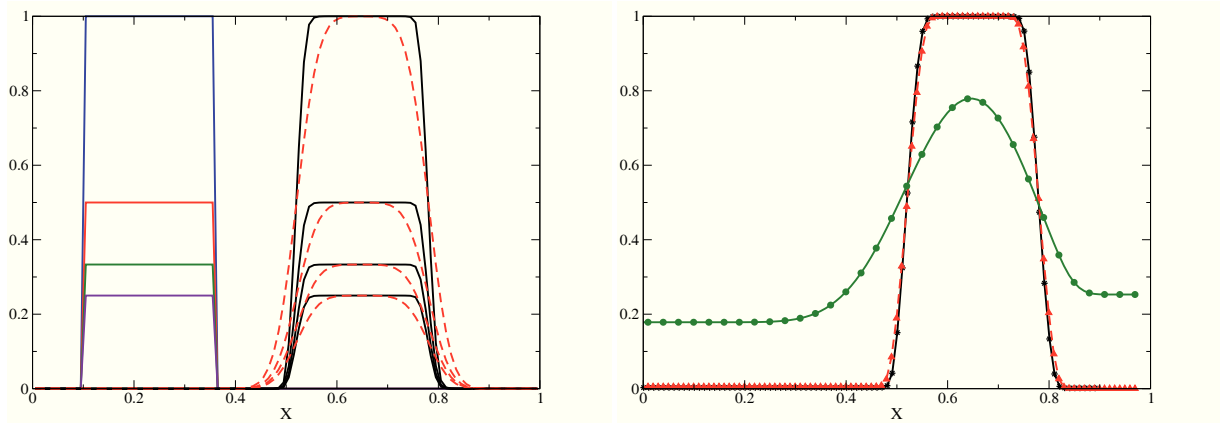


Figure 13.6: Convection of the spray at uniform velocity with and without mesh movement. (left) Initial condition for  $m_0$  (blue curve),  $m_1$  (red curve),  $m_2$  (green curve),  $m_3$  (violet curve), and solution of the convection case without mesh movement at time  $t = 0.3$  at  $CFL = 0.8$  with the first order scheme (dashed red curves) and the second order scheme (black curve). (right) Solution of the convection case with mesh movement at  $CFL = 0.8$  with the second order scheme (black curve) and at  $CFL = 0.5$  for the second order scheme (red curve with triangle) and the first order scheme (green curve with circles). The computation is carried out on a 100 cell grid.

consequently at time  $t = 0.1$ , the shock initiated at  $x = 0.25$  should be at  $x = 0.4$ , corresponding to the results of Fig. (13.7)-left. The focus on this area of interest done in Fig. (13.7)-right shows the difference of accuracy between the first and second order scheme. This difference is amplified in the moving mesh configuration, increasing the diffusive effects by reducing the time step, as seen on Fig. (13.8). This test assesses the ability of our methods to capture  $\delta$ -choc, the second major stability condition with the preservation of the moment space. This is all the more an achievement since these methods are designed on off-centered meshes introducing the concept of dual meshes for which the methods designed for centered meshes cannot be adapted.

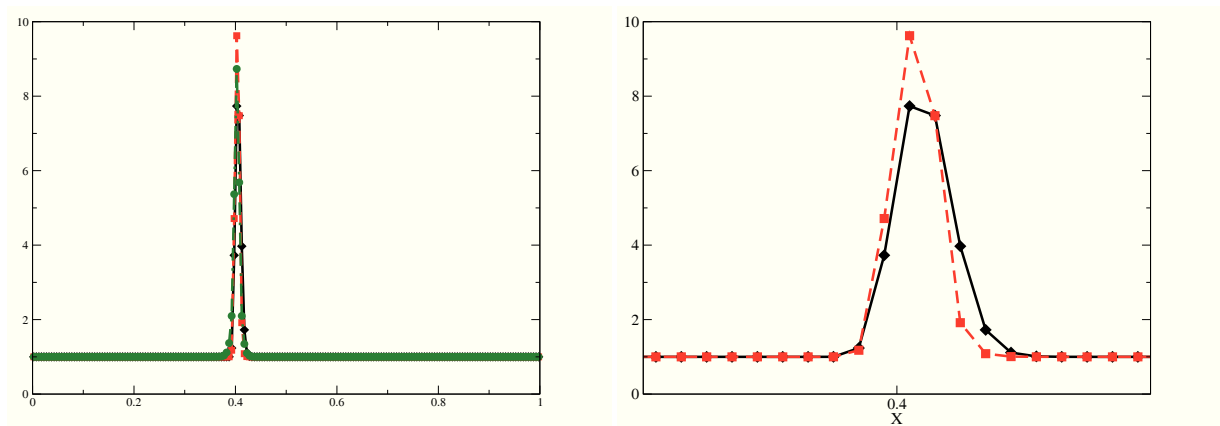


Figure 13.7: (left)  $\delta$ -shock dynamics at time  $t = 0.1$  for the first (black curve with diamonds) and second order scheme (dashed red curve with squares) without mesh movement. (right) Focus on the  $\delta$ -shock. The computation is carried out on a 200 cell grid.

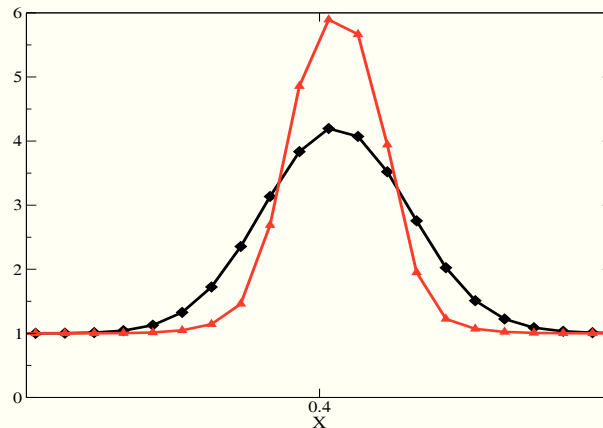


Figure 13.8: (left)  $\delta$ -shock dynamics at time  $t = 0.1$  for the first (black curve with diamonds) and second order scheme (dashed red curve with squares) with mesh movement. The computation is carried out on a 200 cell grid.

### 13.5.5.3 Resolution coupling transport and evaporation

The aim of this case is to show that the stability and accuracy properties of the numerical tools designed for fixed grid and centered meshes are preserved in the resolution of an evaporating spray with mesh movement on an off-centered mesh. For that purpose the configuration studied in Section 6.4.2 is reused here.

The distribution function is more complex than before, in order to show that the evaporation solver does not presume any type of NDF:

$$n = \begin{cases} \lambda(x) \sin(\pi s) + (1 - \lambda(x)) \exp(-10s) & \text{if } x \leq 0.5, \\ 0 & \text{otherwise.} \end{cases}$$

where  $\lambda(x) = 4(0.5 - x)^2$ .

The particles velocity is initiated by:

$$u(x) = \begin{cases} 0.5 & \text{if } x \leq 0.25, \\ 2 & \text{if } x > 0.25 \end{cases} .$$

Periodic boundary conditions are set on the space interval  $[0, 1]$ . The analytical solution is the translation of the two parts of the density profile corresponding to each value of the velocity. Figure (13.9) displays the initial condition for the size moments and the velocity.

At  $t = 0.225$ , Fig.(13.10)-left, the initial distribution breaks into two parts. Vacuum is created at the initial velocity discontinuity. The numerical solutions are represented by solid lines with decreasing ordering in terms of value, meaning that the highest curve stands for the  $0^{th}$  order moment, and the lowest curve stands for the  $3^{rd}$  order moment. The analytical solutions for the corresponding moments are represented by markers. It can be seen that the numerical solution very accurately matches the analytical one.

At  $t = 0.45$ , Fig.(13.10)-right, because of periodic boundary conditions, the fastest portion catches up the slower one. In this figure, the numerical solutions are represented by dashed line, the numerical

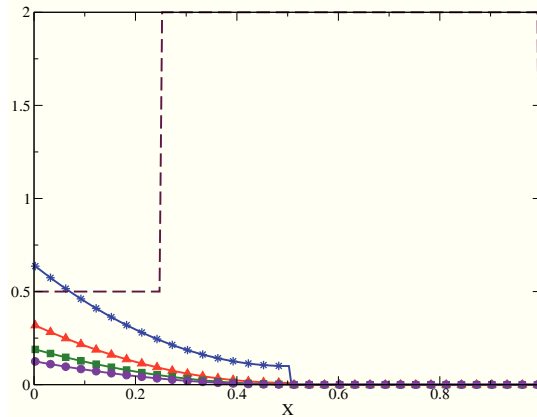


Figure 13.9: Initial condition for the moment and the velocity.

solution by solid lines, and only  $m_0$  and  $m_1$  are represented for the sake of legibility. The two types of solution are very different. Indeed, the models corresponding to each type of solution are different. The numerical solution corresponds to the resolution of system (13.36), written in the pressureless gas formalism. In this context, as the pressure is considered to be null, nothing prevents the particles from accumulating. A  $\delta$ -shock is therefore engendered when two droplet clouds with different velocity meet [21]. On the other hand, the analytical solution of this problem in the infinite Knudsen limit for the particles corresponds to the solution at the kinetic level, where the droplets cross. One can notice though that in the region where only one droplet cloud is considered (in the interval  $[0.4, 0.5]$ ), the numerical and analytical solution match. However our purpose is to show that system (13.36) can be implemented in the ALE formalism. With respect to this objective, Fig.(13.10)-right validates our numerical approach for sprays as the dynamic of the shock is well captured. Nevertheless simulating jet crossing is an issue in Eulerian models and methods and has been recently resolved in the literature. We refer to Chapter 9 and references therein for details on this matter.

Figure (13.11) shows that the results are still very satisfying with a mesh movement.

#### 13.5.5.4 Resolution coupling transport and drag

In this last test case, we test the coupling between transport and drag. The behavior of the particle according to their Stokes number is studied.

For that purpose, a Riemann problem (with the same parameters as in the test case presented in Section 13.4.2) is initiated for the gas phase with the discontinuity lying at  $x = 0.25$ . A discontinuity for the moments (only represented by  $m_0$ ) is initiated at the same point as well. Both phases are initially motionless. Different computations are run for different values of Stokes numbers ( $2 \cdot 10^{-3}$ , 0.2, 20), based on a gas time scale of  $5 \cdot 10^{-2}$  s. Neumann boundary conditions are set on the domain. The final time of the computation is  $t = 0.05$ , with  $CFL = 0.9$ , in a 100 cell grid. Figure (13.12) represents the initial conditions. For very small particles ( $St = 2 \cdot 10^{-3}$ ), Fig.(13.13), their velocity quasi instantaneously relaxes to the gas one. Two different instants are displayed in order to understand the evolution of the moment field. In Fig.(13.13)-left, one notices that, although the velocity fields correspond, the density fields ( $\tau$  and  $m_0$ ) are different in interfacial area. In the velocity increasing part, the decreasing moment field makes one think of an expansion wave as for the gas phase. But the profile of  $m_0$  is stiffer than the profile of  $\tau$  in that zone, because the inertial effects of the pressureless particle. Indeed this profile ends on a singularity, typical of a vacuum zone. The opposite situation occurs right after the maximum velocity point, in the velocity decreasing part, where the particle accumulation engender a  $\delta$ -shock. In Fig. (13.13)-right the velocity field getting smoother tends to smooth the singularities as well. Figure (13.14)-left displays

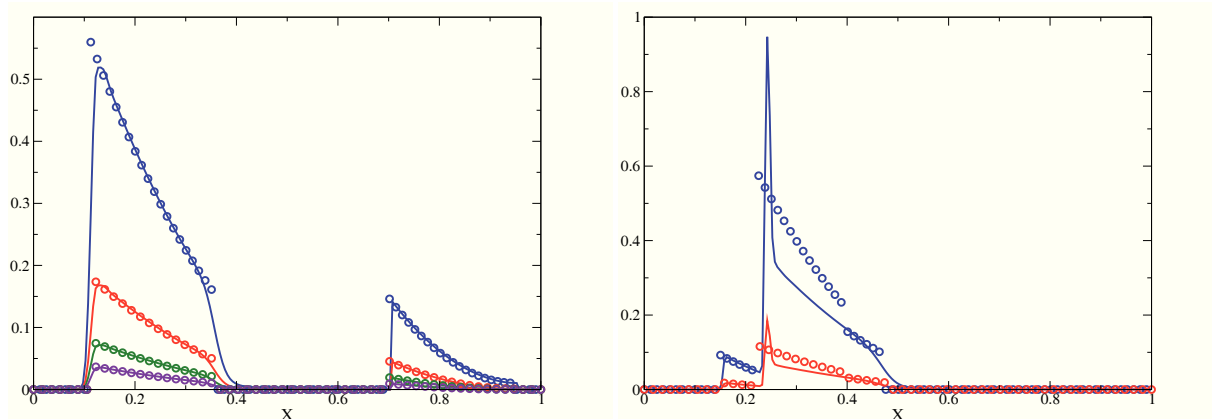


Figure 13.10: Evolution of a spray in a discontinuous velocity field calculated with the moment method, compared to the analytical solution of the problem. (left) Solution at time  $t = 0.2$ . The plain curves represent, with decreasing ordering in terms of value, the four first moments from the  $0^{th}$  order  $m_0$  (blue curve with circles) to the  $3^{rd}$   $m_3$  (violet curve with diamonds). The analytical solution is represented by markers. (right) Solution at time  $t = 0.45$ . For legibility, only  $m_0$  (blue curve) and  $m_1$  (red curve) are represented. The numerical solution is represented by dashed lines, the analytical solution by solid line. (Top) Solution in the space interval  $[0, 1]$ . (Bottom) Focus on the interest area from the top figure. The computation is carried out on a 200 grid. The computation is carried out on a 200 grid.

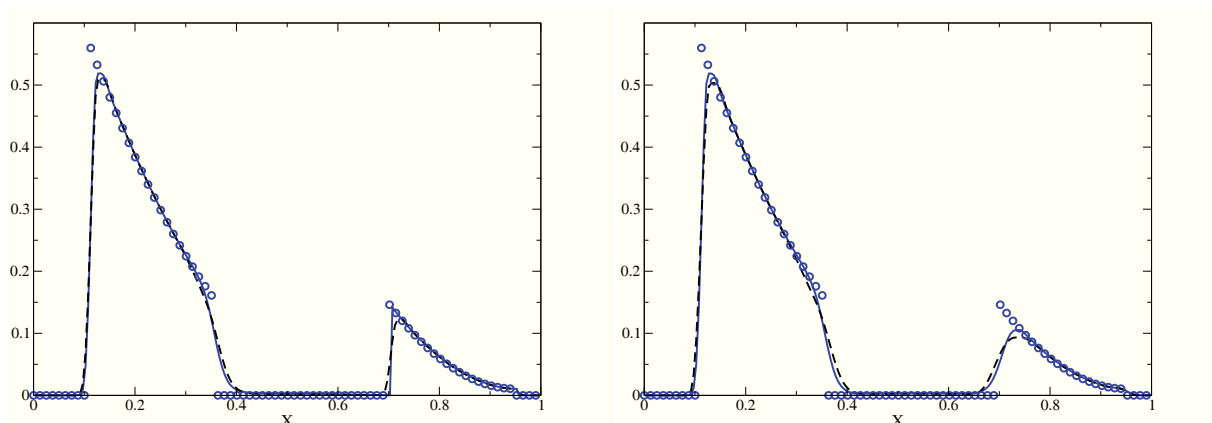


Figure 13.11: Evolution of a spray in a discontinuous velocity field calculated with the moment method, compared to the analytical solution of the problem. Solution at time  $t = 0.2$  with mesh movement. The plain curves represent, with decreasing ordering in terms of value, the four first moments from the  $0^{th}$  order  $m_0$  (blue curve with circles) to the  $3^{rd}$   $m_3$  (violet curve with diamonds). The analytical solution is represented by markers. (left) Computation with  $CFL = 1$ . (right) Computation with  $CFL = 0.8$ . The computation is carried out on a 200 grid.

the results for particles with  $St = 0.2$ . The process is similar to the previous case, but here the particle velocity finite relaxation time is noticeable and explain why singularities are sharper than for particles with very small Stokes number. Particles with a high Stokes number ( $St = 20$ ) are almost insensitive to drag force within the computation time, so that the moment field is barely modified (Fig. (13.14)-right). In conclusion to that test case, the particle velocity relaxes more or less fast according to the value of the Stokes number, which is the expected result. Moreover, due to pressureless gas effects (even for small Stokes particles), singularities still occur in the moment field.

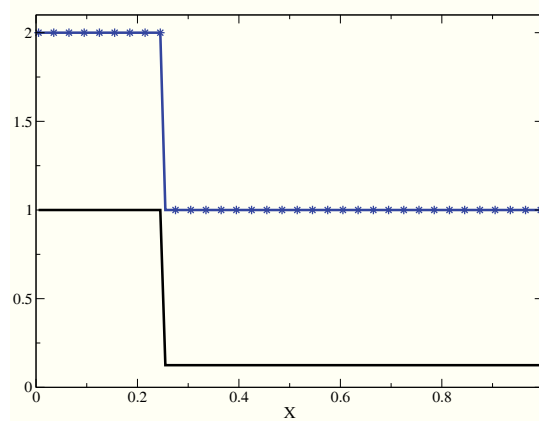


Figure 13.12: Coupled transport and drag resolution. Initial condition for the moment and the gas. The blue line with stars corresponds to  $m_0$ , the black line to the gas density  $\rho_g$ .

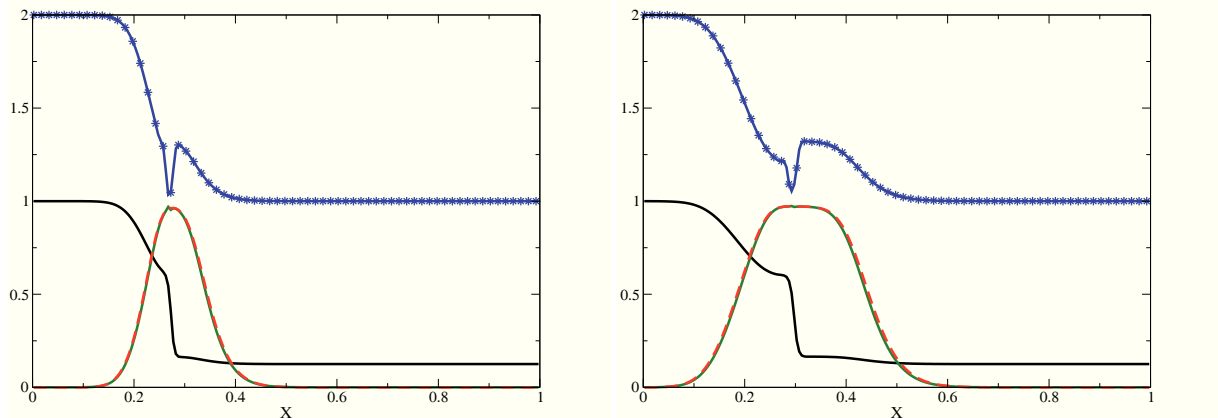


Figure 13.13: Solution for particles with  $St = 2.10^{-3}$ . The blue line with stars corresponds to  $m_0$ , the black line to the gas density  $\tau$ , the green line to the particle velocity, and the dashed red line to the gas velocity. (left) Solution at time  $t = 0.025$ . (right) Solution at time  $t = 0.05$ . The computation is carried out on a 100 grid.



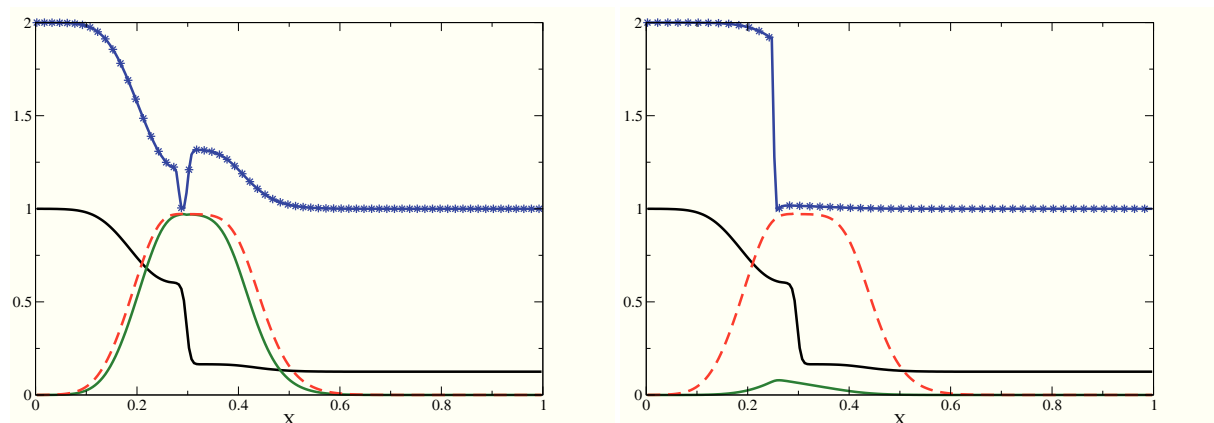


Figure 13.14: Solution at time  $t = 0.05$ . The blue line with stars corresponds to  $m_0$ , the black line to the gas density  $\tau$ , the green line to the particle velocity, and the dashed red line to the gas velocity. (left) Solution for particles with  $St = 0.2$ . (right) Solution for particles with  $St = 20$ . The computation is carried out on a 100 grid.

## Conclusion

This chapter presents one of the contributions done during this PhD, in order to extend the EMSM model to the IFP-C3D code. It addresses the theoretical issue of the adaptation of the high order schemes designed in Chapter 5 and Chapter 6. Indeed, the two stability conditions the realizability condition and stability through  $\delta$ -shocks had to be ensured. This has been achieved, for the first case, by adapting the kinetic scheme tools to the ALE formalism. For the second case though, a new scheme has to be considered, in order to ensure the discrete maximum principle for velocity in a cell-vertex structure. These very satisfying results are a first positive answer towards the use of high order schemes for the EMSM in an industrial context based on the ALE formalism. This work has been presented during the ICMF Conference, Tampa, USA (2010) [130], and an article is in preparation in the International Journal of Multiphase Flows [131].

## Chapter 14

# Introduction of the EMSM model in an industrial code, IFP-C3D

This chapter is dedicated to the second aspect of the extension of the Eulerian Multi Size Moments (EMSM) in an industrial framework. The first part, addressed in Chapter 13 was about the extension of the proprieties of the numerical schemes designed in Chapter 5 and Chapter 6 to the Arbitrary Lagrangian Eulerian (ALE) framework. The work presented here concerns the computing strategy for the implementation of the EMSM model in the IFP-C3D code. It is then presented in the same spirit as in Chapter 7, i.e a synthetic presentation of the IFP-C3D code highlights the critical points of the code and leads to a check list of the areas where modifications were brought. The computing strategy will then be explained. Finally validation test cases assess the model, specially with mesh movement, and the feasibility of spray resolution with the EMSM model in injection condition is demonstrated.

### 14.1 Presentation of IFP-C3D

#### 14.1.1 General characteristics of the IFP-C3D code

The IFP-C3D code has been developed at IFP Energies nouvelles over the last few years. The purpose of this code is to simulate compressible reactive flows with combustion and sprays. The principal features of this code are the following:

- The gas phase resolution is based on the Navier-Stokes equation system, with source terms related to spray and combustion.
- These equations are written in the ALE formalism, to take into account the potential grid motion, due to the piston movement occurring in engine simulations.
- The computations are performed with unstructured meshes containing hexahedral computational cells.
- Turbulent phenomena in the gas phase are taken into account by a RANS formalism.
- The spray is simulated with a Lagrangian approach [104], a Stochastic Parcel approach, explained In Section 2.1. Note that our developments are made in a version where the liquid phase is simulated with a purely Lagrangian approach.

In the following, we focus on the general algorithm and the connectivity.

#### 14.1.2 General algorithm and numerical scheme

The conservation equations are solved using the Arbitrary Lagrangian Eulerian formalism, which takes into account the moving geometric parts. The IFP-C3D code uses the operator splitting algorithm described in Chapter 13. The resolution algorithm is divided into three steps, or phases:

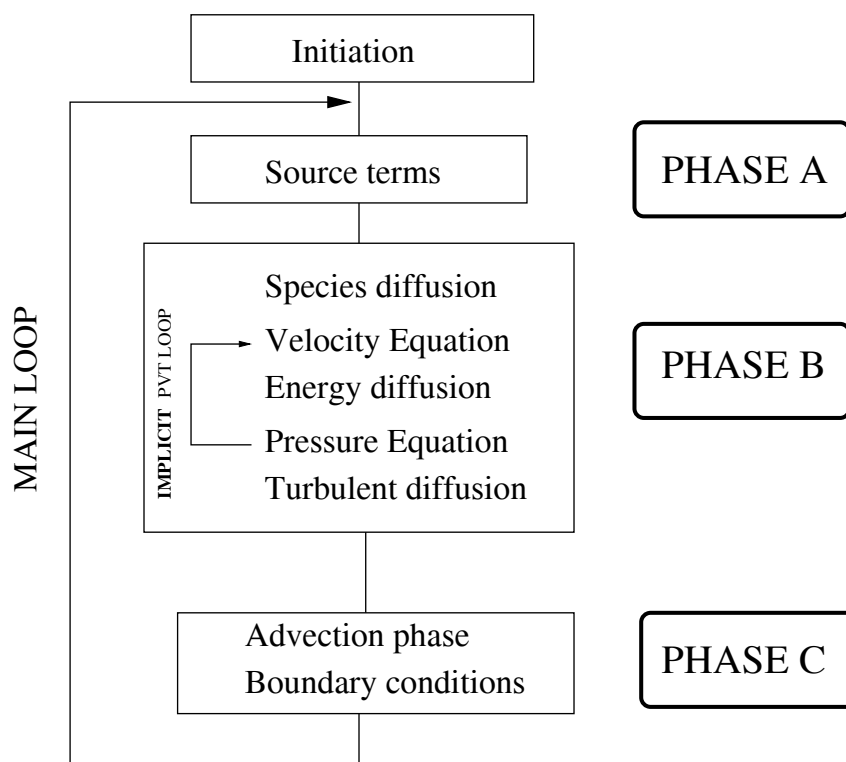


Figure 14.1: General algorithm of the IFP-C3D code.

- In phase A, source terms of the chemical reactions on gas (auto-ignition, combustion, post oxidation, chemical equilibrium, etc.) of the Lagrangian fuel injection spray and of the spark ignition are calculated and added to the conservation equations.
- In phase B, all the diffusion terms are solved implicitly, with first the species mass, internal energy term, and turbulent terms. The method introduced in [195] is retained in its fully implicit version. The coupled implicit equations (momentum, temperature and pressure) are solved with the SIMPLE algorithm [215]: this is called the PVT (Pressure Temperature Velocity) loop. The pressure equation is solved using the BiCGSTAB iterative method with ILU preconditioning [18]. The temperature and velocity equations are solved using the residual conjugate gradient with Jacobi preconditioning. The diffusion terms of the turbulent equation ( of the  $k-\epsilon$  model) are solved when the SIMPLE algorithm has converged.
- In phase C, the vertices are moved from the Lagrangian trajectory calculated during phase B to their final position calculated by the moving grid algorithm for the next time step. This translation needs the finite volume fluxes to be calculated. The fluxes of the scalar like mass, internal energy and turbulence quantities are computed between cells using a Quasi Second Order Upwind Scheme (QSOU) [6]. Using connectivity of cells/faces, slopes are calculated with the Superbee limiter. The faces of the control volume surrounding the vertex are also moving and the momentum advection step calculates fluxes through each facet of the volume. The slopes for the momentum fluxes are computed with the Van Leer limiter. The computed slopes allow the calculation of scalar fluxes at the center of faces and vector fluxes at the middle of the edge. These slope calculations ensure a second-order upwind advection for every scalar and momentum. As no convective CFL-like number is calculated for that phase, sub-cycles have to be considered in order to ensure the stability of this phase.

The general algorithm of the IFP-C3D code is illustrated in Fig. (14.1).

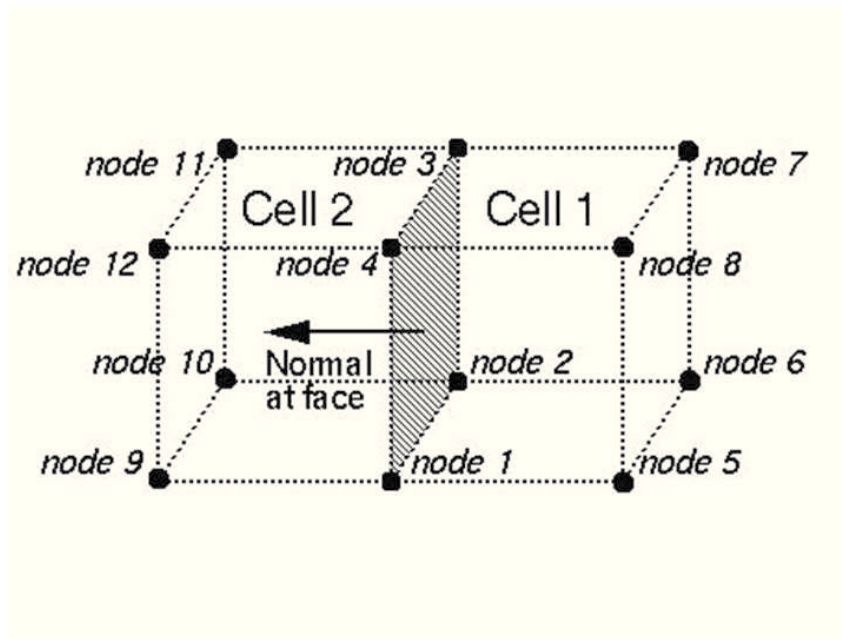


Figure 14.2: Illustration of connectivity.

### 14.1.3 Connectivity aspect and grid evolution

As stated above in the introduction of this chapter, the code IFP-C3D is unstructured. This formalism reduces constraints during the grid process generation and avoids the difficult numerical processing of cells located at the corner of two blocks present in the structured multiblock formalism. Cells have a better shape with unstructured grids, and local refinement of zones where the gradients are suspected to be high, is less expensive. With hexahedral grids, gradients calculations are accurate, and moving algorithms can maintain a good grid quality when the geometry is moving.

In the unstructured approach, the connectivity (node, cell and face) must be computed and registered. Nodes can have any number of neighbors, while hexahedrons have six neighbors respectively, to their six faces. The staggered hexahedral description with cell centered scalar and node-centered vectors is used. The topological element face is widely used in the solver. This element can be linked easily to hexahedrons and nodes. It is defined by one or two hexahedrons (fluid or boundary faces) and four nodes, nodes 1 to 4 in Fig. (14.2). Sorting cells and nodes indexes for a given face can give the orientation that we need for solving the transport equations. The eight sorted border nodes, node 5 to 12 in Fig. (14.2), are also registered and used for raising numerical accuracy in convection terms. The use of the unstructured approach necessitates to compute and register the connectivity between the nodes, faces and cells. Nodes can have any number of neighbors, while a hexahedron can only have six neighbors, respectively to its six faces. For the reader interested in parallel computing performance, a discussion relative to the connectivity can be found in [18].

As stated in the previous chapter, in order to adapt to the moving computational geometry, the peculiarity of the ALE formalism relative to scientific computation is the grid evolution strategy. In the design of a corresponding algorithm, one must ensure that it does not lead to cells with a negative determinant, and also that it is accomplished in a reasonable time. The method used in IFP-C3D relies on an iterative algorithm, which for a given node uses an average of the displacement of every neighbor. A temporal interpolation methodology [68] is used. In this method, a target grid at a final angle is fully computed outside the solver, by external grid generators. Then during the run, the position of a node at a given time is computed by an interpolation between its former position and its final position, weighted by its proximity from the piston and the valves. The full description of this method can be found in [18]. Moreover, when considering moving boundaries (intake/exhaust valves, piston), the risk of extremely

distorted meshes makes the use of a remapping method mandatory. Consequently, remeshing techniques are needed to ensure good mesh quality over the entire engine cycle. The technique adopted in IFP-C3D is then a mesh regularization. According to the instant in the engine cycle, some geometrical parts can be added or removed relative to the initial mesh. For example when intake valve is closed, the intake pipe can be removed from the calculation. Finally, a turbulent wall law and a heat transfer law should be used, because the grid resolution is generally low near the walls. See [7] for a precise description of the wall laws computed in IFP-C3D.

#### 14.1.4 Introduced models

A list of the principal models implemented in the IFP-C3D code is provided here. A detailed description of these models can be found in [18] :

- It was already mentioned that the liquid fuel spray is simulated with a Lagrangian approach [104], and turbulent phenomena are taken into account by a RANS formalism ( $k-\epsilon$  model),
- The spray impact at the wall can lead to the formation of a liquid film. Spray/wall interaction processes are described using a submodel described in [188],
- Because of the wide range of engine configurations, there are numerous physical sub-models available to compute combustion, with different fuels such as Diesel or gasoline:
  - For gasoline engines, the ECFM model (Extended Coherent Flame Model) is used conjointly with the AKTIM (Arc and Kernel Tracking Ignition Model) model [68] to compute the spark ignition,
  - The combustion process for diesel engines is simulated by the ECFM3Z model (3-Zones Extended Coherent Flame Model) [45],
- The pollutant modeling is obtained by coupling two models: the first one called CORK (CO Reduced Kinetics) [120] dedicated to the CO modeling and the second one called PSK (Phenomenological Soot Kinetics) [163] devoted to soot modeling. Other approaches based on tabulated techniques are currently begin developed [121].

#### 14.1.5 Mapping of the intervention areas for the implementation of the EMSM model

The numerical strategy developed for the implementation of the EMSM model in the IFP-C3D code is different from the one defined in the context of of the MUSES3D code, see Chapter 7 and Chapter 11. Because of development constrains due to the industrial context, the genericity level of the code is lower than the MUSES3D code presented in Chapter 7.

Consequently the required adjustments in the IFP-C3D code involve more modifications in the code structure than in the MUSES3D code:

- The data structure: the arrays specific to the EMSM model will have to be defined (for example the array of moments or velocity),
- The initialization procedure, in interaction with the input data file (params.kin),
- The boundary condition computation. If periodic boundary conditions can be easily adapted, the injection boundary conditions have to be written from scratch,
- The three phases of the numerical scheme.

## 14.2 Implementation of the EMSM model

This section presents the numerical developments upgrading the code IFP-C3D to a polydisperse Eulerian spray solver. The detail of this work is presented under four different topics. The first point concerns the evolution of the data structure. The second point concerns the upgrade of the initialization procedure. The third point deals with the adaptation of injection boundary conditions to the EMSM model. The final point focuses on the modifications brought in the numerical scheme. These developments were made on a the Lagrangian V201 version of the code.

### 14.2.1 Data structure

As mentioned in Section 14.1.5, the whole data structure has to be created for the implementation of the EMSM model. The principal arrays created are displayed here. Their spacial index differs whether they refer to a cell, a face or a vertex. We use here the following convention:

- the index  $i$  refers to a cell. The total cell number is denoted by  $nhex$
- the index  $j$  refers to a node. The total node number is denoted by  $nnode$
- the index  $l$  refers to a face. The total node number is denoted by  $nface$

The principal arrays defined in the context of the EMSM are:

```
real(kind(0.d0)), dimension( $nhex, N_{mom\_sizes}$ ) :  $mom$ 
real(kind(0.d0)), dimension( $nhex$ ) : :  $volliq$ 
real(kind(0.d0)), dimension( $nnod$ ) : :  $uliq, vliq, wliq$ 
real(kind(0.d0)), dimension( $nface, N_{mom\_sizes}$ ) : :  $fluxliq$ 
real(kind(0.d0)), dimension( $nface$ ) : :  $fluxmomliq, axliq, ayliq, azliq$ 
```

The number  $N_{mom\_sizes}$  denotes the number of considered moments, the array  $mom$  refers to the size moment field,  $volliq$  represents the cell volume in the mesh resulting from the Lagrange step (phase B) applied to the liquid phase. These arrays are defined on cells. The arrays  $uliq, vliq, wliq$ , are the spray velocity field in the x, y, and z direction respectively, and are defined on the mesh vertices. The arrays  $fluxliq$ , and  $fluxmomliq$  represent the flux associated to the moments and the momentum respectively. The arrays  $axliq, ayliq$ , and  $azliq$  represent the face surface area of the mesh resulting from the Lagrange step (phase B) applied to the liquid phase. These quantites are defined on faces.

### 14.2.2 Initialization

This paragraph presents the new options introduced in the code during the initialization procedure:

- `idimom`: This switch is activated for a computation with the high order moment method. This model can either compute a spray or an aerosol.
- `idispray`: This is the switch to activate the aerosol model or the spray model.
- `iscalmom`: This switch sets the initial conditions for the moment fields.
- `iuvwmom`: This switch sets the initial conditions for the velocity field.
- `ievap`: This switch must be 'on' to activate the evaporation model.
- `idrag`: This switch must be 'on' to activate the drag model.

### 14.2.3 Implementation of injection boundary conditions

If periodic boundary conditions were transparent for our developments, injection boundary conditions had to be designed from scratch to be able to inject spray quantities in the computational domain. The corresponding parameters introduced in the data file are:

- `ins-mom`: this flag locate the border area where the injection condition is activated.
- `moment-field`: this array monitors the rate of moment injected with respect to time.
- `moment-vel`: this array monitors the particles velocity with respect to time.

These developments concern the routines *begin* and *rinput\_2*.

### 14.2.4 Numerical scheme implementation

The core of the developments has consisted in the implementation of the numerical schemes into the general ALE algorithm of the code. Given the complex architecture of the code, it was chosen to stick as close as possible to it. The developments are presented relative to each of the three phases. Recalling system (13.33), we aim at solving the evolution of the spray described by the following system:

$$\begin{aligned}
\partial_t(J)|_{\mathcal{X}} - J \nabla_{\mathbf{x}} \cdot (\mathbf{v}_{\mathcal{X}}) &= 0, \\
\partial_t(J\rho)|_{\mathcal{X}} + J \nabla_{\mathbf{x}}(d\rho \mathbf{w}_g) &= 0, \\
\partial_t(J\rho \mathbf{u}_g)|_{\mathcal{X}} + J \nabla_{\mathbf{x}} \cdot (\rho \mathbf{u}_g \mathbf{w}_g) + J \nabla_{\mathbf{x}}(P) &= 0, \\
\partial_t(J\rho E_g)|_{\mathcal{X}} + J \nabla_{\mathbf{x}} \cdot (\rho E_g \mathbf{w}_g) + J \nabla_{\mathbf{x}}(P \mathbf{u}_g) &= 0, \\
\partial_t(Jm_0)|_{\mathcal{X}} + J \nabla_{\mathbf{x}} \cdot (m_0 \mathbf{w}_p) + JK \tilde{n}_{ME} &= 0, \\
\partial_t(Jm_k)|_{\mathcal{X}} + J \nabla_{\mathbf{x}} \cdot (m_k \mathbf{w}_p) + JK(k-1)m_{k-1} &= 0, \\
\partial_t(Jm_1 \mathbf{u}_p)|_{\mathcal{X}} + J \nabla_{\mathbf{x}} \cdot (m_1 \mathbf{u}_p \mathbf{w}_p) + JK m_0 \mathbf{u}_p &= J m_0 \frac{(\mathbf{u}_g - \mathbf{u}_p)}{St_0},
\end{aligned} \tag{14.1}$$

where  $St_0$ , is the droplet characteristic Stokes number, defined in Chapter 13.

**Notation:** If one considers  $\mathbb{U}_g = (\rho, \rho \mathbf{u}_g, \rho E_g)$ ,  $\mathbb{U}_p = (m_{k.,k=1..N}, m_0 \mathbf{u}_p)$  one denotes by  $(J_m^n, \mathbb{U}_m^n)$ ,  $(J_m^A, \mathbb{U}_m^A)$ ,  $(J_m^B, \mathbb{U}_m^B)$ ,  $(J_m^C, \mathbb{U}_m^C) = (J_m^{n+1}, \mathbb{U}_m^{n+1})$  the values of  $(J_m, \mathbb{U}_m)$  respectively at time  $t = n\Delta t$ , at the end of phase A, at the end of phase B, and at the end of phase C which are also the updated values at time  $t = (n+1)\Delta t$ .

#### 14.2.4.1 Developments in phase A

In the framework considered for the EMSM model, phase A corresponds to the resolution of the evaporation and drag terms. As done in Chapter 7, the contribution of these two terms are splitted, by using the code modular structure.

The evaporation term is solved in the module specially introduced in the code, **Evaporation\_emsm**. The interface with the main routine `c3d`, is illustrated in Algo. (18)

For the drag resolution, as discussed in Section 3.2.3 we consider, a one-way coupling, we therefore only consider the influence of the gas phase on the spray. In this context, since the gas velocity is constant during phase A, as explained in Section 3.2.3, the spray velocity can be solved analytically. The solution  $\mathbf{u}_p$  reads:

$$\mathbf{u}_{p_j}^A = \mathbf{u}_{p_j}^n \exp\left(-\frac{m_{0,j}^n}{m_{1,j}^n \theta} \Delta t\right) + \left(1 - \exp\left(-\frac{m_{0,j}^n}{m_{1,j}^n \theta} \Delta t\right)\right) (\mathbf{u}_{g_j}^n - \mathbf{u}_{p_j}^n). \tag{14.2}$$



---

**Algorithm 18** Resolution of the evaporation term implementation.
 

---

```
procedure c3d
```

```
...
```

```
% Phase A
```

```
...
```

```
if EMSM then
```

```
  if evap then
```

```
    call evap_emsm(mom,dt)
```

```
  ...
```

```
  end if
```

```
end if
```

```
...
```

```
end procedure c3d
```

---

Keeping in mind that the velocity vector is defined on nodes, whereas the moments are defined on cells, one has to express the moments on the nodes of the mesh. Therefore,  $m_{0,j}^n$  is defined by:

$$m_{0,j}^n = \frac{\sum_{i=1}^8 m_{0,i}^n \Delta \mathbf{x}_i^A}{\sum_{i=1}^8 \Delta \mathbf{x}_i^A}, \quad (14.3)$$

where the sum is performed on the eight cells surrounding the vertex  $j$ , in three dimensions, and  $\Delta \mathbf{x}_i^A$  is the volume of cell  $i$  at the end of phase A.

#### 14.2.4.2 Developments in phase B

We make the distinction between aerosol and spray particles. In the case of aerosol particles, they are transported at the gas velocity, and consequently, the moments are updated relative to the cell volume change, in relation to the equation:  $(Jm_k)^B = m_k^A$ . The actual relation written in the IFP-C3D code is  $\Delta \mathbf{x}_i^B m_{k,i}^B = m_{k,i}^A \Delta \mathbf{x}_i^A$ , where  $\Delta \mathbf{x}_i^B$  is the result of the acoustic phase applied to the gas. Spray resolution during phase B needs further developments, since the system to be solved for the particles writes:

$$\begin{aligned} \partial_t(J_p)|_{\mathbf{x}_p} - J_p \nabla_{\mathbf{x}} \cdot (\mathbf{u}_p) &= 0, \\ \partial_t(J_p m_k)|_{\mathbf{x}_p} &= 0, \\ \partial_t(J_p m_1 \mathbf{u}_p)|_{\mathbf{x}_p} &= 0, \end{aligned} \quad (14.4)$$

where  $\partial_t(\cdot)|_{\mathbf{x}_p}$  represents the time derivative along the characteristics of the material frame reference associated to the particles.

In the one-dimensional case, the solution of system (14.4) is given by Eq. (13.66):

$$\tau_{k,i}^B = \tau_{k,i}^A \left( 1 - \frac{\Delta t}{\Delta x_i} (u_{p,i+1/2} - u_{p,i-1/2}) \right), \quad (14.5)$$

where  $\tau_{k,i} = 1/m_{k,i}$ ,  $k = 1 \dots N_{mom\_sizes}$ , and  $(J_p m_{k,i})^B = (J_p m_{k,i})^A$ . Moreover, for  $\tau_{k,i}$  to remain positive, we must have  $\Delta t \leq \frac{u_{p,i+1/2} - u_{p,i-1/2}}{\Delta x_i^n}$ . The challenge consists in implementing this relation in three dimensions. The only difference then is that the velocity difference becomes a divergence, localized at cell  $i$ . Thus, the previous relations are straightforward to compute, provided the velocity divergence is correctly computed. The computing strategy for the velocity divergence is displayed in Algo. (19), for

a cartesian mesh. In this context, the hexahedral cells are regular and the orientation of their faces is such that they are parallel two by two, and orthogonal to the vector  $\mathbf{e}_x$ ,  $\mathbf{e}_y$  and  $\mathbf{e}_z$ . The faces orthogonal to  $\mathbf{e}_x$  are denoted by the indexed 1, and 2, the ones orthogonal to  $\mathbf{e}_y$  are denoted by the indexed 3, and 4, and the ones orthogonal to  $\mathbf{e}_z$  are denoted by the indexed 5, and 6. Thus, the faces  $l_1$  and  $l_2$  are the two faces orthogonal to  $\mathbf{e}_x$ . Moreover, we assume that  $x(l_1) < x(l_2)$ ,  $y(l_3) < y(l_4)$ ,  $z(l_5) < z(l_6)$ , which justifies the expression of the term Divergence in Algo. (19). In Algo. (19), the term  $uliq(j/l)$  denotes the x-velocity of the  $j^{th}$  node of face  $l$ . Thus, in this algorithm  $j$  ranges from 1 to 4. The computation of the velocity divergence is also implemented, since it is needed for injection case using an axi-symmetrical mesh, see Section 14.4.1.

---

**Algorithm 19** Computation of the velocity divergence.

---

```

procedure phaseb
...
  if EMSM then
...
    if spray then
      % Loop on the cells
      for  $i = 1, nhex$  do
        % Computation of couples of faces parallel to each other
         $l_1 = face(i, 1)$ 
         $l_2 = face\_opposite(i, 1)$ 
        ...
         $l_5 = face(i, 3)$ 
         $l_6 = face\_opposite(i, 3)$ 
        ...
        % Computation of the velocity on the faces
         $uliq\_face(l_1) = 0.25 (uliq(1/l_1) + uliq(2/l_1) + uliq(3/l_1) + uliq(4/l_1))$ 
         $uliq\_face(l_2) = 0.25 (uliq(1/l_2) + uliq(2/l_2) + uliq(3/l_2) + uliq(4/l_2))$ 
         $vliq\_face(l_3) = 0.25 (vliq(1/l_3) + vliq(2/l_3) + vliq(3/l_3) + vliq(4/l_3))$ 
         $vliq\_face(l_4) = 0.25 (vliq(1/l_4) + vliq(2/l_4) + vliq(3/l_4) + vliq(4/l_4))$ 
         $wliq\_face(l_5) = 0.25 (wliq(1/l_5) + wliq(2/l_5) + wliq(3/l_5) + wliq(4/l_5))$ 
         $wliq\_face(l_6) = 0.25 (wliq(1/l_6) + wliq(2/l_6) + wliq(3/l_6) + wliq(4/l_6))$ 
        ...
        % Computation of the velocity divergence of cell  $i$  ...
         $Divergence = 1/\Delta x_i * (uliq\_face(l_2) - uliq\_face(l_1)) + 1/\Delta y_i * (vliq\_face(l_4) - vliq\_face(l_3)) +$ 
         $1/\Delta z_i * (wliq\_face(l_6) - wliq\_face(l_5))$ 
      end for...
    end if
  end if...
end procedure phaseb

```

---

The computation of the updated cell volume  $volliq_i^B$ , moments  $mom_i^B$ , and the associated CFL condition do not bring any additional difficulty.

The mesh modification due to the Lagrange phase is accounted for, not only by the cell volume change, but also by the changes of its faces surface area. For that purpose, we compute the updated node coordinates, given by the relation  $\mathbf{x}_j^B = \mathbf{x}_j^n + \mathbf{u}_p dt$ . The update surface area  $S_{faceliquid,l}$  is given using a dedicated routine already implemented.

#### 14.2.4.3 Developments in phase C

The phase C, or projection phase, is divided in two steps:

- In the first step, the volume swept by a face  $l$ ,  $fxf_l$ , is computed with the relation  $fxf_l = \Delta V_{mesh,i} + S_{face,l} \mathbf{u}_l \cdot \mathbf{n}_l$ . The right-hand side expression includes first the part of the volume swept by face  $l$

due to the mesh movement at velocity  $\mathbf{v}_\chi$ , and the second part, due to the fluid convection ( $\mathbf{u}_l$  can refer to the gas or particle velocity) through the interface. The quantity  $S_{face,l}$  is the face surface,  $\mathbf{n}$  its outgoing normal vector, and  $\mathbf{u}_l$  the velocity computed at its center, obtained by averaging the velocities of the nodes composing the face, as done in Algo. (19). The number of required sub-cycles  $n_{flux}$  is computed during this step, to ensure stability. This step is performed in the routine *flux\_init*.

- The second step is the actual finite volume scheme, with the slope computation, reconstruction steps, fluxes computation, combining  $fxfl_i$  calculated in the first step, and the reconstructed values at the faces, and finally the update step. Because of the different spatial definition of thermodynamic quantities and velocity there are two routines, *flxsca* and *flxmom*, with the dedicated advection scheme for each case. This step is performed in the routine *euleri*.

In our strategy, we aim, at first, to implement a first order advection scheme for the EMSM model. According to Chapter 6, piecewise constant reconstructions ensure the realizability condition for the moments.

The computation of  $fxfl_i$  is transparent for aerosol particles, since their dynamics is monitored by the gas dynamics. But a structure for the advection of moments has to be created in the second step. This structure is based on the routine *flxsca* that is generic to any cell-defined scalar quantity.

The developments are much heavier in the case of spray particles. Since they have their own dynamics the first step has to be adapted to the spray, leading to the computation of the new array  $fxfliq_j$ . Besides, an advection scheme for the particles has to be implemented, in addition to the moments advection scheme.

Let us first focus on the first step. Following the example of  $fxfl_j$ , the volume swept by the faces of the mesh associated to the liquid phase  $fxfliq_j$  is composed of two terms: the first one, resulting from the global mesh movement at velocity  $\mathbf{v}_\chi$  (unchanged from the previous case), and the second one resulting from the convective movement of the spray velocity  $\mathbf{u}_p$ . The following expression for  $fxfliq_j$  is then:

$$fxfliq_j = \Delta V_{mesh,i} + S_{face,l} \mathbf{u}_{p,l} \mathbf{n}_l. \quad (14.6)$$

The velocity, defined on the  $l^{th}$  face center  $\mathbf{u}_{p,l}$ , has been computed during phase B, see Algo. (19). The same goes for the updated surface area, resulting from the movement of the mesh associated to the particle phase during phase B. Accordingly, a new condition arise in the computation of  $n_{flux}$ , taking into account the fluxes for the liquid phase. This new condition writes:

$$\frac{|fxfliq_l|}{\max(volliq_{i1}^B, volliq_{i2}^B)} < CFL, \quad (14.7)$$

where  $volliq_{i1}^B$  and  $volliq_{i2}^B$  are the volume of the cells on both sides of face  $l$ .

Secondly, the adaption of the advection scheme requires to:

- update the moment field *mom*,
- update the spray velocity field *uliq*, *vliq*, *wliq*,
- adapt the boundary conditions to the spray quantities.

In the sub-cycle process, the update field at iteration  $\beta + 1$  are obtained from the field at iteration  $\beta$  through the relations:

$$\begin{aligned} volliq_i^{\beta+1} (m_k)_i^{\beta+1} &= volliq_i^\beta (J_p m_k)_i^\beta - \sum_l F_l, \\ volliq_j^{\beta+1} (m_1 \mathbf{u}_p)_j^{\beta+1} &= volliq_j^\beta (m_1 \mathbf{u}_p)_j^\beta - \sum_i \mathbf{G}_i. \end{aligned} \quad (14.8)$$

The first equation concerns the evolution of the moment field of the mesh cell  $i$ , whereas the second equation concerns the evolution of the moment field of the dual cell  $j$ , centered on the node  $j$ . In order to define the nodal quantity  $volliq_j^{\beta+1}(m_1 \mathbf{u}_p)_j^{\beta+1}$  the relation of Eq. (13.70) is extended to the three dimensional case by:

$$volliq_j m_{1,j} \mathbf{u}_p^{(j)} = \left( \frac{1}{8} \sum_i^8 volliq_i m_{1,i} \right) \mathbf{u}_p^{(j)}, \quad (14.9)$$

where  $volliq_j$  is the volume of the dual cell centered on the node  $j$ , and the sum is made on the eight neighbor cells of node  $j$ . The moment flux  $F_l$  writes:

$$F_l = \frac{1}{n_{flux}} (m_{k,l}^\beta f_{xfliq_l}), \quad (14.10)$$

where  $m_{k,l}^\beta$  is the value of the reconstructed value of moment  $m_k$  at the interface  $l$ . In the context of the (QSOU) Scheme [6], the momentum flux  $\mathbf{G}_i$  in three dimensions writes:

$$\mathbf{G}_i = \frac{1}{4} \sum_i^8 \left( \frac{(F_{l_1} + F_{l_2})_i}{2} + \frac{(F_{l_3} + F_{l_4})_i}{2} + \frac{(F_{l_5} + F_{l_6})_i}{2} \right) \mathbf{u}_p^{(j)}, \quad (14.11)$$

where a sum of the moment flux is made over the eight neighbor cells of node  $j$ , and for each cell  $i$ , the moment fluxes in the three spatial directions are considered. As previously, indexes 1 – 2 refers to the x-direction, indexes 3 – 4 refers to the y-direction, and indexes 5 – 6 refers to the z-direction. The interested reader can find details in [6]. The general structure of the updated advection procedure is displayed in Algo. (20).

The last step concerns the adaptation of velocity boundary conditions during phase C. So far, boundary conditions have been assumed to apply exclusively to the gas phase, since it was the only Eulerian phase of the code. Now that a Eulerian spray is introduced, one has to adapt the boundary conditions so that it can potentially apply to spray. The most efficient way considered is, when boundary conditions apply to the spray, to replace the arrays accessed by the corresponding routine by temporary arrays, containing the required data from the spray. This is illustrated in Algo. (21).

A synthetic vision of the implementation of the EMSM model in the code structure is presented in Fig. (14.3)

---

**Algorithm 20** General structure of the new advection scheme.

---

```

procedure euleri
...
% Gas species advection
...
% Particle advection
if EMSM then

  if aero then
    ...
    call flasca(mom,fxf)
    ...
  else if spray then
    ...
    % Advection of spray, and computation of the moment fluxes F call flasca(mom,fxfliq)
    ...
    % Preparation of the computation of momentum fluxes
    for i = 1, nhex do
      G(i,1) = 0.25*(F(i, 1) + F(1, 2))
      G(i,3) = 0.25*(F(i, 3) + F(1, 4))
      G(i,5) = 0.25*(F(i, 5) + F(1, 6))
    end for
  end if
end if % Gas momentum advection
...
% Spray momentum advection
if EMSM then
  ...
  call flxmom(uliq,vliq,wliq,G)
  ...
  % Boundary condition for spray velocity
  ...
end if
...
end procedure euleri

```

---



---

**Algorithm 21** Computation of velocity boundary conditions for the spray.

---

```

procedure euleri
...
% Boundary condition for spray velocity
gas_velocity_temp = gas_velocity
gas_array_temp = gas_array
gas_velocity = spray_velocity
gas_array = spray_array
call bcvel
spray_velocity = gas_velocity
gas_array = gas_array_temp
gas_velocity = gas_velocity_temp
...
end procedure euleri

```

---

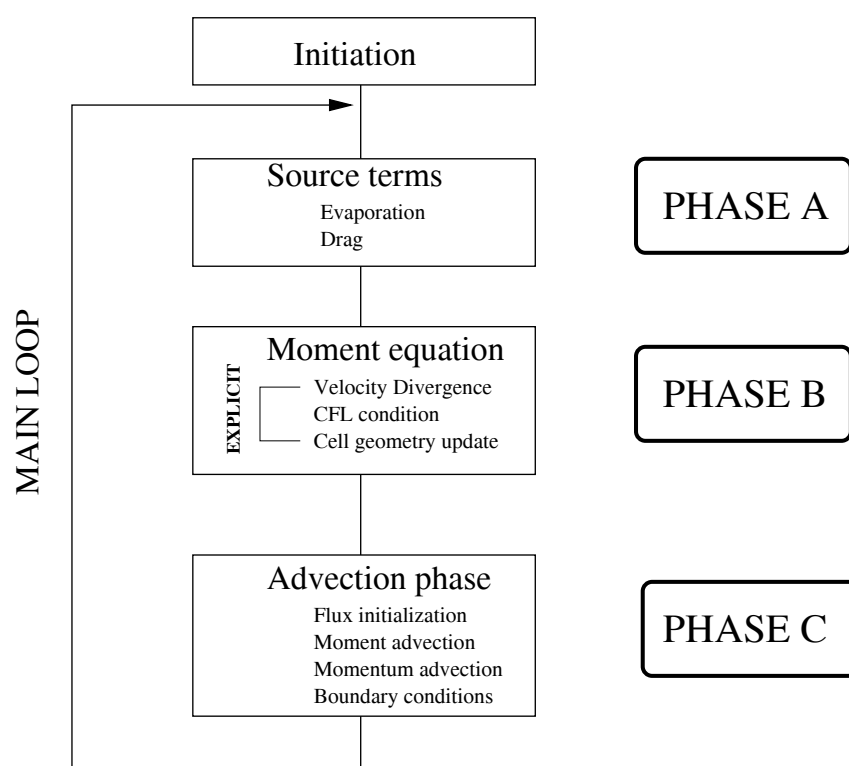


Figure 14.3: Synthetic vision of the implementation of the EMSM in the IFP-C3D code structure.

## 14.3 Numerical validations

The purpose of this section is to validate the implementation of the EMSM model for aerosol and spray in IFP-C3D. The first test case, a one dimensional Riemann problem, ensures that the spray dynamics is correct. In the second test case, the robustness of the scheme is tested when mesh movement is involved. Then the spray dynamics with evaporation, transport and drag is validated in the Taylor-Green configuration for the gaseous velocity field. Finally an injection case of a polydisperse droplet spray is realized and compared with the corresponding Lagrangian result, confirming the feasibility of engine computations with the implemented model.

### 14.3.1 One-dimensional Riemann problem

In this test case a Riemann problem consisting in a velocity discontinuity in initiated for a spray. The initial conditions are represented in Fig. (14.5):

$$\left\{ \begin{array}{l} (m_0, m_1, m_2, m_3) = (1, 0.5, 0.333, 0.25), \forall x \in [0, 1], \\ u_p = 1000 \text{ ms}^{-1}, x \in [0.4, 0.6], \\ u_p = 500 \text{ ms}^{-1} \text{ otherwise.} \end{array} \right. \quad (14.12)$$

The number density function (NDF) is assumed to be constant, as represented in Fig. (14.4). Since the moment field is constant over the whole domain, the solution for the velocity reduces to the solution of the Burgers equation [152]. Thus a  $\delta$ -shock occurs at the discontinuity at  $x = 0.6 \text{ m}$  and propagates at the average velocity between the left and the right states, that is  $750 \text{ ms}^{-1}$ . At the other discontinuity, a vacuum zone appears, since the left state velocity is lower than the right state one. Figure. (14.6) displays the solution at two instants, at  $t = 10^{-4} \text{ s}$  and  $t = 10^{-3} \text{ s}$ . On the top are represented the fields of  $m_0$  and  $m_1$ ; the velocities are represented on the bottom. The first instant,  $t = 10^{-4} \text{ s}$  is chosen so that potentially, the state at velocity  $1000 \text{ ms}^{-1}$  can cover the whole computational domain. Since periodic boundary conditions are set on the edges of the domain, the second instant,  $t = 10^{-3} \text{ s}$  is chosen so that, if the velocity field was constant, the particles at velocity  $1000 \text{ ms}^{-1}$  would exactly cover the domain, and would recover their initial location. Focusing on Fig. (14.6), at time  $t = 10^{-3} \text{ s}$ , a  $\delta$ -shock is created which propagates at velocity  $750 \text{ ms}^{-1}$  since it is at location  $x = 0.65 \text{ m}$ . Meanwhile a vacuum zone appears at the other discontinuity, which is the expected behavior. At time  $t = 10^{-3} \text{ s}$ , the vacuum zone has developed and the  $\delta$ -shock has amplified. The  $\delta$ -shock velocity has decreased because all the particles at velocity  $u_p = 1000 \text{ ms}^{-1}$  have entered it, and consequently, there is only a negative momentum flux relative to the shock velocity entering it. These tests confirm that the EMSM model has correctly been implemented in the context of a one-dimensional fixed grid.

### 14.3.2 Validation of the scheme robustness through mesh movement

The objective of this second test case is to ensure that the implemented model is stable with mesh movement. The evolution of homogeneous fields of liquid and gas are considered in a closed high pressure cell. The bottom boundary of this cell corresponds to a moving piston being at the bottom dead center. The gas is taken as air, and the particles are initially stationary. No ignition occurs, and no thermic effect is considered. Also, no special treatment of the boundary is considered. The computation ends after a revolution of the crank, with the crank angle degree (cad) ranging in  $[-180, 180]$ . The high pressure cell and the movement of the piston are described in Fig. (14.7).

The boundary condition are  $(\mathbf{u}_p - \mathbf{u}_{piston}) \cdot \mathbf{n} = 0$  on the surface of the piston, and  $\mathbf{u}_p \cdot \mathbf{n} = 0$  at the upper edge of the domain. The size distribution is constant and similar to the one-dimensional tests with aerosol. During the compression and expansion of the high pressure cell, the computational cell volumes change is homothetic. The results are displayed for the number density  $m_0$  and the surface density  $m_1$  with a 1200 ( $30 \times 40$ ) cell grid. Computations are successively run for an aerosol and a spray. Figure (14.8) displays the results for the moments, in the case of an aerosol,  $cad = -100, -30, 50, 180$ . In the

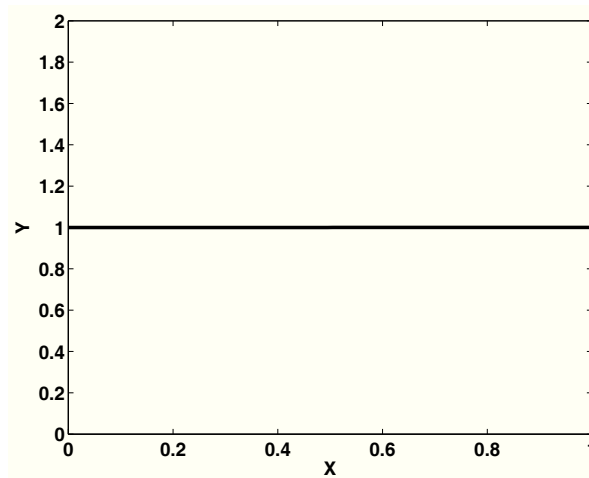
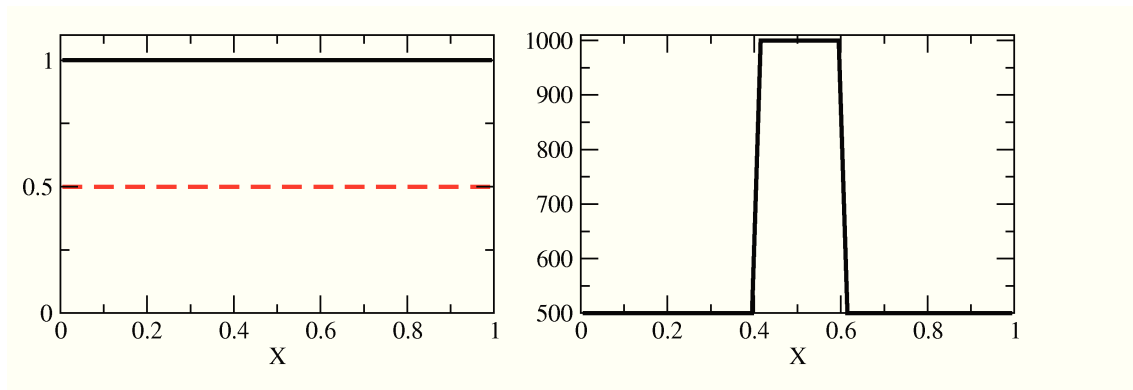


Figure 14.4: Initial size distribution.

Figure 14.5: Initial conditions for the spray. (Left) Initial moment fields. The solid black line represents  $m_0$ , while the dashed red line represents  $m_1$ . (Right) Initial velocity field.

various graphs, the distance where the value of the moments is null is the distance traveled by the piston. These graphs show that the flow stays homogeneous during the whole computation. This is a typical case where the operator splitting done in the algorithm of IFP-C3D is legitimate since the speed of sound is at least one order of magnitude higher than the convective speed of the fluid. In fact, the speed of sound exceeds  $300 \text{ m s}^{-1}$ . At the same time, with a rating of  $1200 \text{ trmn}^{-1}$ , and stroke of about  $10 \text{ cm}$ , the piston average velocity and that of the dragged fluid is much smaller than the speed of sound in the gas. Mass conservation impose that the gas density and consequently the particle number increase as the piston heads to the top dead center, because the volume of the high pressure cell decreases, Fig. (14.8)-(top right), Fig. (14.8)-(bottom left) . The moments recover their initial values at the end of the computation.

Figure (14.9) displays results for spray at different instants. The two first ones ( $cad = -100$  and  $cad = -30$ ) correspond to the compression of the high pressure cell. The two following ones ( $cad = 50$  and  $cad = 180$ ) correspond to the expansion of the domain. The case of spray is dramatically different from the previous one. Indeed inertial particles within the infinite Stokes limit are considered now, since no interaction with the gas phase is taken into account. They stick to the piston as it moves forward. This behavior is observed in Fig. (14.9)-top and is responsible for the singularity present at the piston surface. Meanwhile, the moment field downstream of the piston is unchanged. This is a direct consequence of the



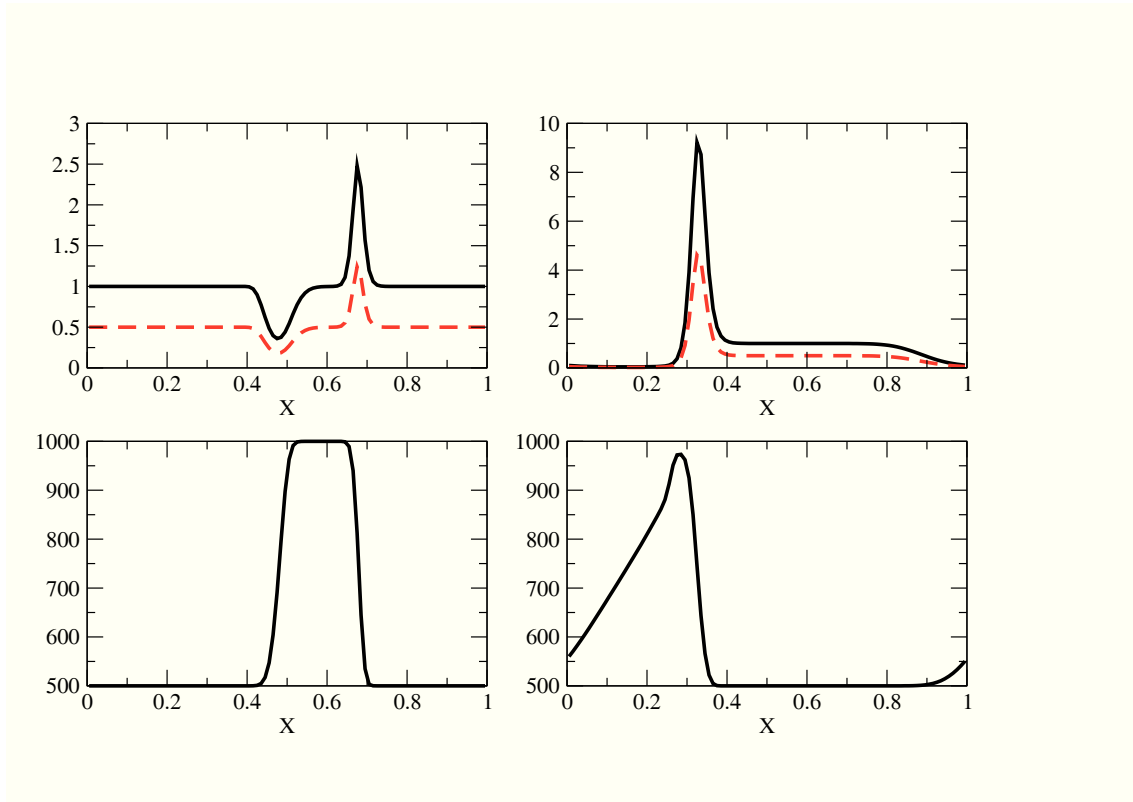


Figure 14.6: Solution for spray particles for the Riemann problem. (Top) Solution for  $m_0$  (solid black line) and  $m_1$  (dashed red line). (Bottom) Solution for the velocity field. (left) solution at time  $t = 10^{-4}$ . (Right) Solution at time  $t = 10^{-3}$ . The computation is carried out on a 100 grid.

assumption made for pressureless gas dynamics, wherein the speed of sound is null, and consequently no pressure waves modify the field. In Fig. (14.9)-bottom, the  $\delta$ -shock moves forward relatively to the mesh. The enlargement of the  $\delta$ -shock has two explanations. The first one is the numerical diffusion. Secondly, the computational cell volume expansion contributes to the  $\delta$ -shock enlargement. Meanwhile, upstream of the  $\delta$ -shock, in the wake of the piston, a vacuum zone is created, which is the expected behavior.

This test case assesses the robustness of the scheme implemented in IFP-C3D in the context of moving grids. This is a substantial achievement since one recalls that this scheme has to preserve two critical stability conditions: the realizability condition on the moments, and the discrete maximum principle on the spray velocity. This example amply illustrates that even within the algorithm of an industrial code, sensitive stability conditions are respected.

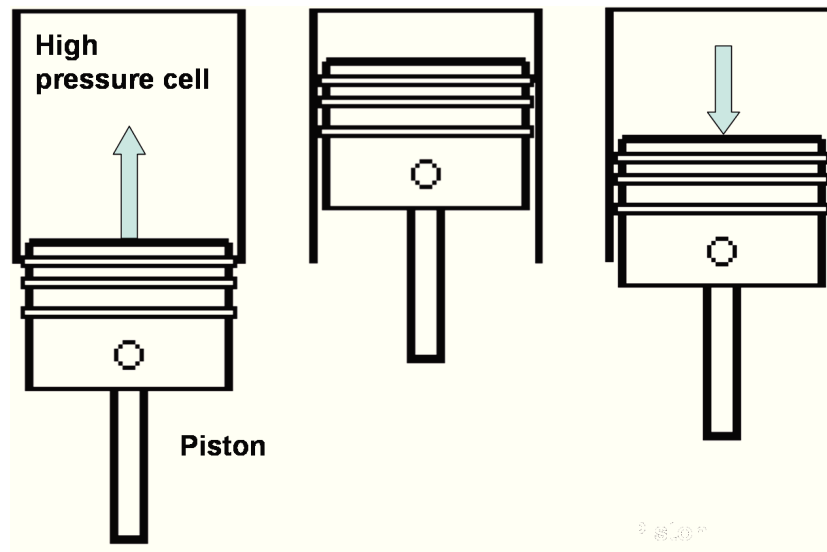


Figure 14.7: Considered piston movement during the computation. The computation starts at  $cad = -180$  and ends at  $cad = 180$ .

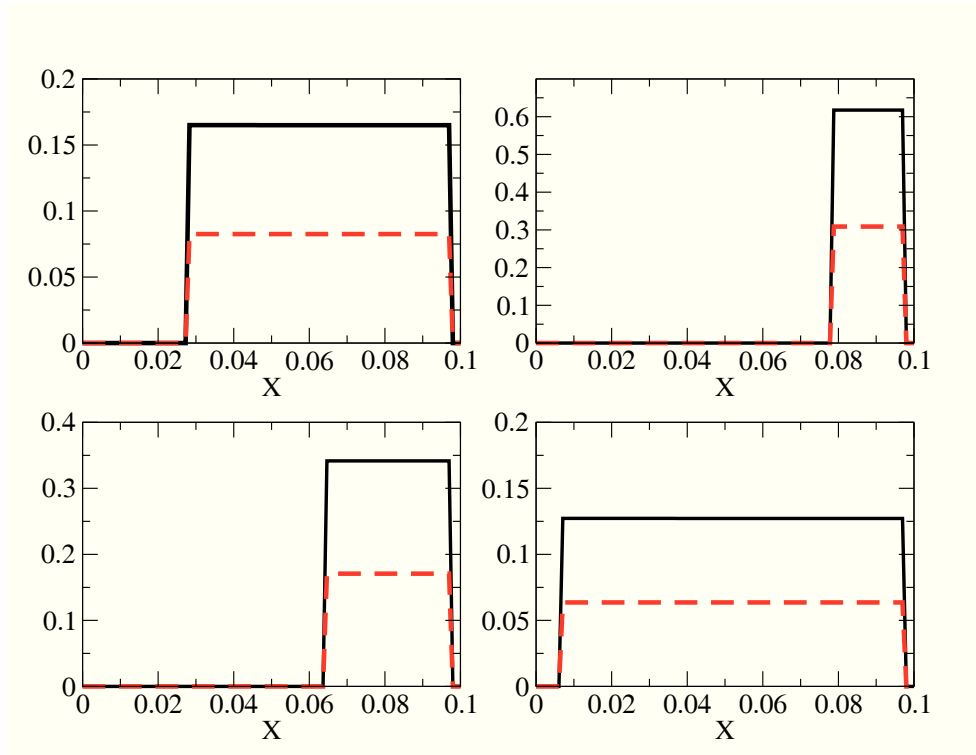


Figure 14.8: Results in the case of an aerosol, for  $m_0$  (solid black line) and  $m_1$  (dashed red line). Results for  $cad = -100, -30, 50, 180$ .

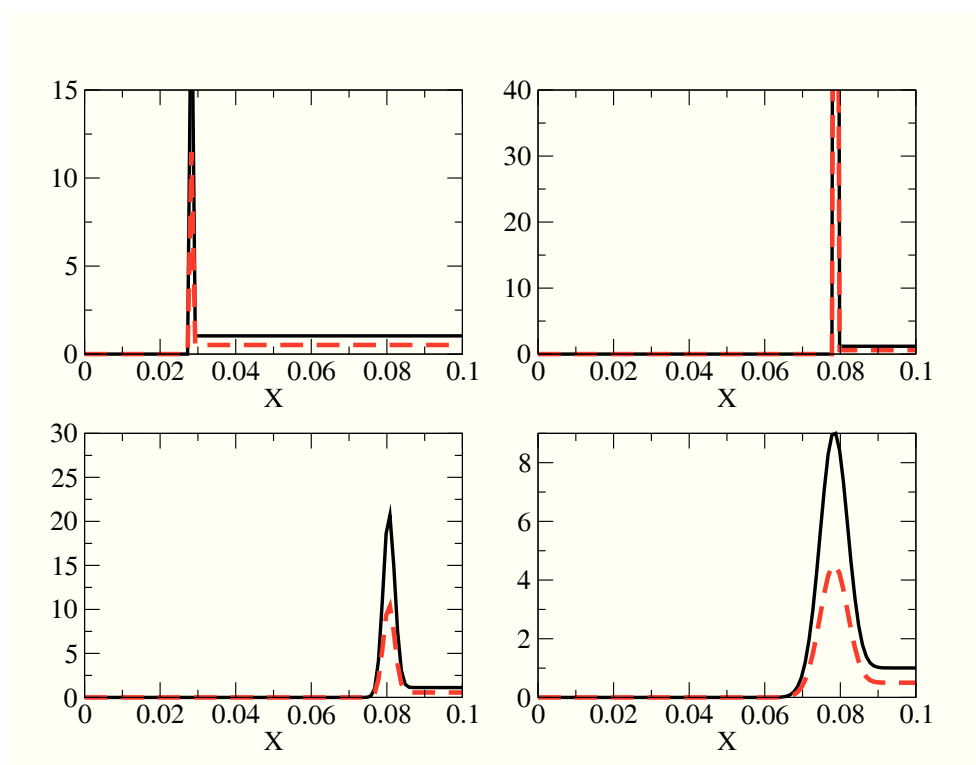


Figure 14.9: Results in the case of a spray, for  $m_0$  (solid black line) and  $m_1$  (dashed red line). Results for  $cad = -100, -30, 50, 180$ .

### 14.3.3 Validation of the spray dynamics through evaporation and drag, by comparison with the MUSES3D code

The objective of this test case is to study and validate the behavior of spray particles, undergoing evaporation and drag. Therefore no mesh movement is considered. The chosen test case involves, the Taylor-Green vortices for the gas velocity field in a square and periodic domain, wherein a motionless droplet cloud is initiated, which can be seen in Fig. (14.10). The results obtained with IFP-C3D are validated by comparison with the results obtained for the same configuration with the MUSES3D code, an academic solver for polydisperse spray [49], wherein the EMSM model has been implemented and validated, see Chapter 7.

When comparing two codes, the difficulty lies in ensuring that there is a coherent relation between the quantity values of each system. The system solved in IFP-C3D is system (14.1), whereas the system solved in Muses 3D can be found in Section 4.1. Therefore the adopted strategy in this work is to take up entirely, both the description of gas as well as the reference quantities defined in Muses3D, and accordingly calculate the dimensional values of the coupling coefficient between the gas and the particles, present in the drag term and in the evaporation term. The final difficulty is to determine coherent final computation times. In MUSES3D, the Reynolds number based on  $U_0$ ,  $\nu_0$  and  $L_0$  is 1000, where  $U_0$  is a typical vortex velocity and  $L_0$  the dimension of the computational domain. The dimensional quantities are based on a velocity of  $U_0 = 1ms^{-1}$ ,  $L_0 = 1.5 \cdot 10^{-2}m$  and  $\nu_0 = 1.6 \cdot 10^{-5}m^2s^{-1}$ . The gas and the liquid phase are such that  $\frac{\rho_l}{\rho_g} = 565$ . The non dimensional kinetic equation from which the equation system solved in MUSES3D is derivated writes (see Section 1.2.4):

$$\partial_t \bar{f} + \partial_{\mathbf{x}}(\bar{\mathbf{u}}\bar{f}) + \partial_{\bar{\mathbf{u}}}(\overline{\mathbf{D}_r f}) - \partial_{\bar{S}}(K\bar{f}) = 0. \quad (14.13)$$

The terms  $\overline{\mathbf{D}_r}$  and  $K$  are written:

$$\begin{aligned} \overline{\mathbf{D}_r} &= \frac{18\pi\mu^*}{\rho_l \bar{S}} \frac{L_0^2}{S_0} (\overline{\mathbf{u}_g} - \bar{\mathbf{u}}) = \frac{1}{St} (\overline{\mathbf{u}_g} - \bar{\mathbf{u}}), \\ K &= \frac{L_0^2}{S_0} 4\pi Sh_c \frac{\rho_g'}{\rho_l'} D^* \ln(1 + B_m). \end{aligned} \quad (14.14)$$

In the same time, the equation solved in IFP-C3D writes:

$$\partial_t f + \partial_x(\mathbf{u}f) + \partial_{\mathbf{u}}(D_r f) - \partial_S(Rf) = 0. \quad (14.15)$$

The first choice is to consider the same characteristic time for the gas,  $\tau_g = 1.5 \cdot 10^{-2}s$ . The corresponding choice of characteristic time and length are  $U_0 = 100ms^{-1}$  and  $L_0 = 1.5m$ , where  $U_0$  is the characteristic vortex velocity and  $L_0$  is the domain length, so that  $\tau_g$  is the time taken to cover the domain. The velocity field then writes:

$$\begin{aligned} u_{g,x} &= U_0 \cos\left(\frac{2\pi}{L_0}\left(x - \frac{L_0}{4}\right)\right) \sin\left(\frac{2\pi}{L_0}\left(y - \frac{L_0}{4}\right)\right), \\ u_{g,y} &= -U_0 \sin\left(\frac{2\pi}{L_0}\left(x - \frac{L_0}{4}\right)\right) \cos\left(\frac{2\pi}{L_0}\left(y - \frac{L_0}{4}\right)\right). \end{aligned} \quad (14.16)$$

The characteristic droplet diameter is taken as  $d_0 = 100 \mu m$  which amounts to a droplet surface  $S_0 = 10^{-2}mm^2$ . We focus now on the expression of  $\overline{\mathbf{D}_r}$  and  $K$  in IFP-C3D. In order to simplify matters, the same gas with the same properties is considered, so that the values of  $\nu_0$ ,  $Sh_c$  and  $D^*$  are unchanged. In MUSES3D,  $\overline{\mathbf{D}_r} = f L_0 U_0^2 \mathbf{D}_r$ , so that,  $\tau_p^{-1}$ , the drag coefficient, inverse of the droplet time relaxation to the gas velocity, writes

$$\tau_p^{-1} = \frac{U_0}{L_0 St} = \frac{U_0}{L_0} \frac{L_0^2 18\pi\mu^*}{\rho_l \bar{S} S_0}, \quad (14.17)$$

so that  $\theta$ , the drag parameter in system (14.1), writes:

$$\theta = \frac{\tau_p}{S} = \frac{L_0}{U_0} \frac{\rho_l S_0}{L_0^2 18\pi\mu^*}. \quad (14.18)$$

This relation defines the drag term defined in IFP-C3D. As for the evaporation coefficient,  $K = \frac{L_0}{U_0 S_0} R$ , so that  $R$  writes:

$$\frac{R}{S_0} = \frac{U_0}{L_0} K = \frac{U_0 L_0}{S_0} 4\pi \text{Sh}_c \frac{\rho'_g}{\rho'_l} D^* \ln(1 + B_m). \quad (14.19)$$

For numerical applications, for droplets with a characteristic diameter of  $d_0 = 100 \mu\text{m}$  corresponding to a characteristic Stokes number of 1.4, the dimensionless quantity  $\frac{S}{\text{St}} = 0.426$ , so that  $\theta = 0.035$  in IFP-C3D. The dimensionless evaporation coefficient yields  $K = 0.21$  in MUSES3D, so that the time dimensionalized evaporation coefficient yields  $\frac{R}{S_0} = 14.16\text{s}^{-1}$ .

For the representation of the results with IFP-C3D, the domain length is reduced to  $[0, 1]$  by an homothetic transformation, and the moments displayed  $\overline{m_k}$  are nondimensionalized by  $S_0$ , so that  $\overline{m_k} = \frac{m_k}{S_0^k}$ .

Four different instants are represented. The resolution of the IFP-C3D code is compared to the one of the MUSES3D code at  $t = 0.4$ , Fig. (14.11),  $t = 1$ , Fig. (14.12),  $t = 1.4$ , Fig. (14.13), and  $t = 2$ , Fig. (14.14). The displayed field is  $m_0$ , the  $0^{\text{th}}$  size moment, equal to the total droplet number.

Since the droplet cloud is initialized in two different vortices, a main part is dragged in the top-left vortex, whereas a small part is dragged by the top-right vortex, as seen in at  $t = 1$ . The droplet Stokes number is much higher than the critical Stokes number  $\text{St}_c$ , below which the particles stay in the vortices, so that their characteristics do not cross, see Section 3.3.1. At  $t = 1.4$ , particles are ejected from the vortices because of the periodic boundary conditions, especially particles dragged by the top-left vortex which enter the bottom-right vortex. In this region, the gas velocity field is opposed to the droplet velocity. As seen at  $t = 2$ , this leads to the creation of a discontinuity in the velocity and thus to the formation of a  $\delta$ -shock in the particle size moment field. We reiterate that this is a typical effect of the pressureless gas formalism used in the EMSM model. Meanwhile, the residual portion of the small part dragged by the top-right vortex is ejected from this vortex and enters the  $\delta$ -shock.

Although the code structures are very different, one can assess that the level of similarity between the results given by the two codes is very high. Indeed there are three paramount differences between the numerical schemes implemented in MUSES3D and in IFP-C3D. The first one concerns the formalism used. The MUSES3D code is an academic solver dedicated to spray resolution in an Eulerian formalism, whereas in IFP-C3D the ALE formalism is implemented. Secondly, the numerical scheme for transport in physical space is second order in space and time in the MUSES3D code, whereas it is only first order in the IFP-C3D code. This is the reason why the moment field is more diffused at time  $t = 1, 1.4$  and  $2$ . Finally, in the structured MUSES3D code, a dimensional splitting algorithm handles transport in multi-dimensions, whereas in the IFP-C3D code which is an unstructured code, it is fully multi-dimensional. Thus, in the IFP-C3D code during a time step, the state of a cell can only impact its neighboring cells sharing a common face. But in the MUSES3D code due to the transport in alternated directions, even neighboring cells with a common node can be impacted. That is why, at time  $t = 2$ , in the result given with MUSES3D, the particles, dragged by their inertia, penetrate further in the bottom-right vortex than in the result given in the IFP-C3D code. Despite these unavoidable differences caused by the intrinsic difference between the two codes, this comparison case is a success and validates the implementation of the EMSM code in the IFP-C3D code in terms of spray dynamics through transport coupled to drag and evaporation.

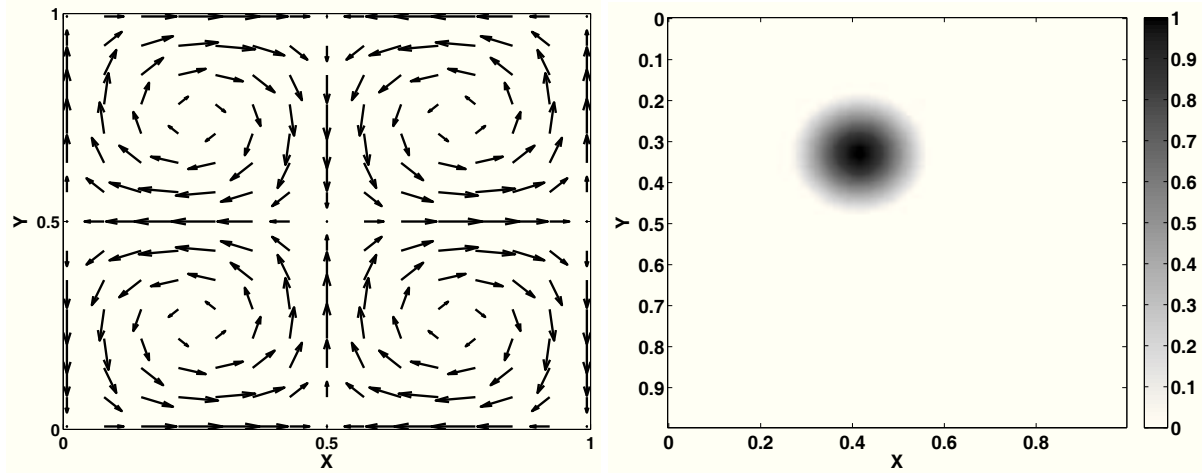


Figure 14.10: Taylor-Green configuration for the gaseous flow (left) and initial condition for the moment  $m_0$  of the spray (right).

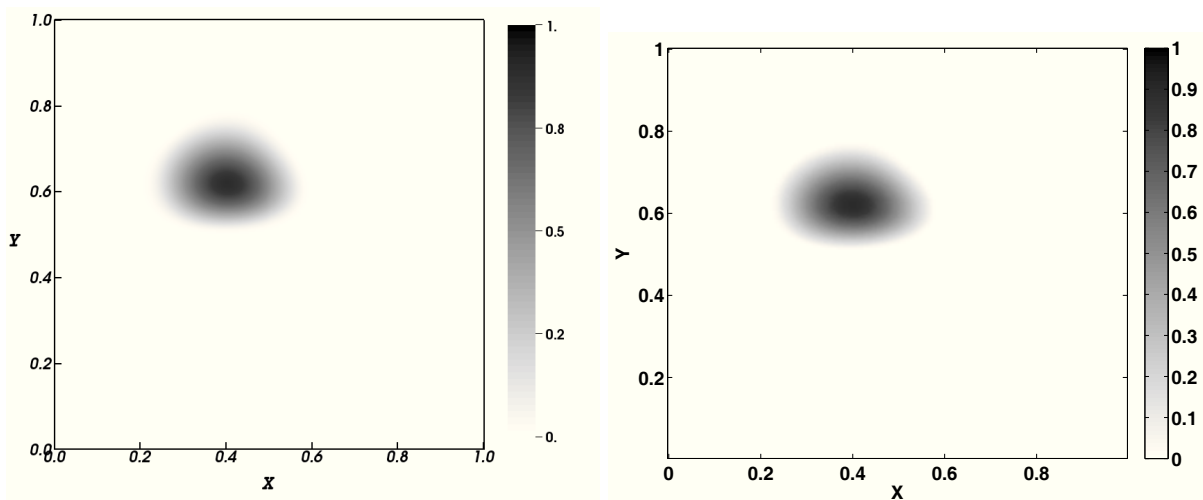


Figure 14.11: Comparison of the results of the IFP-C3D and MUSES3D codes. Results for  $m_0$  at time  $t = 0.4$ . (Left) results with the IFP-C3D code. (Right) results with the MUSES3D code.

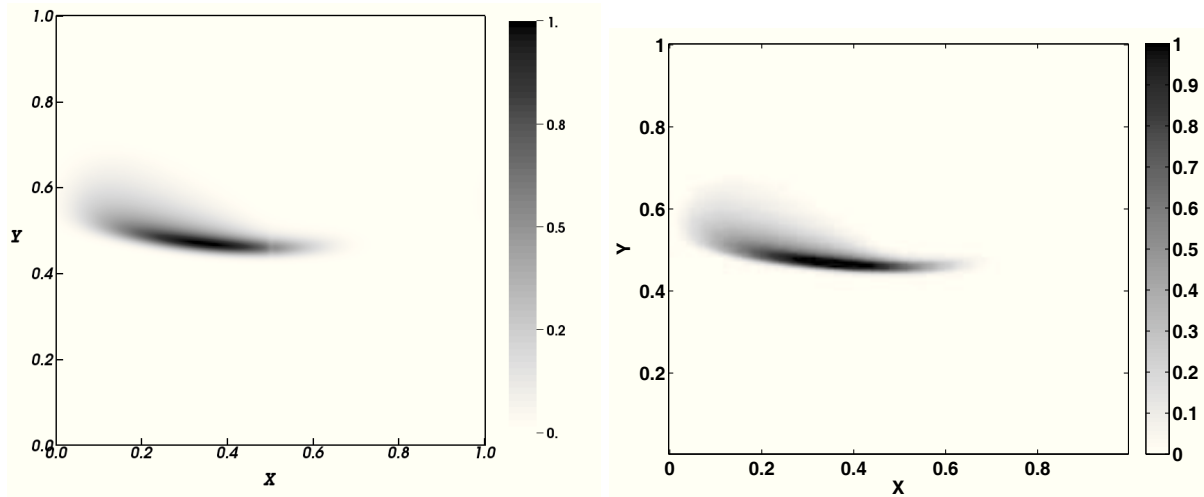


Figure 14.12: Comparison of the results of the IFP-C3D and MUSES3D codes. Results for  $m_0$  at time  $t = 1$ . (Left) results with the IFP-C3D code. (Right) results with the MUSES3D code.

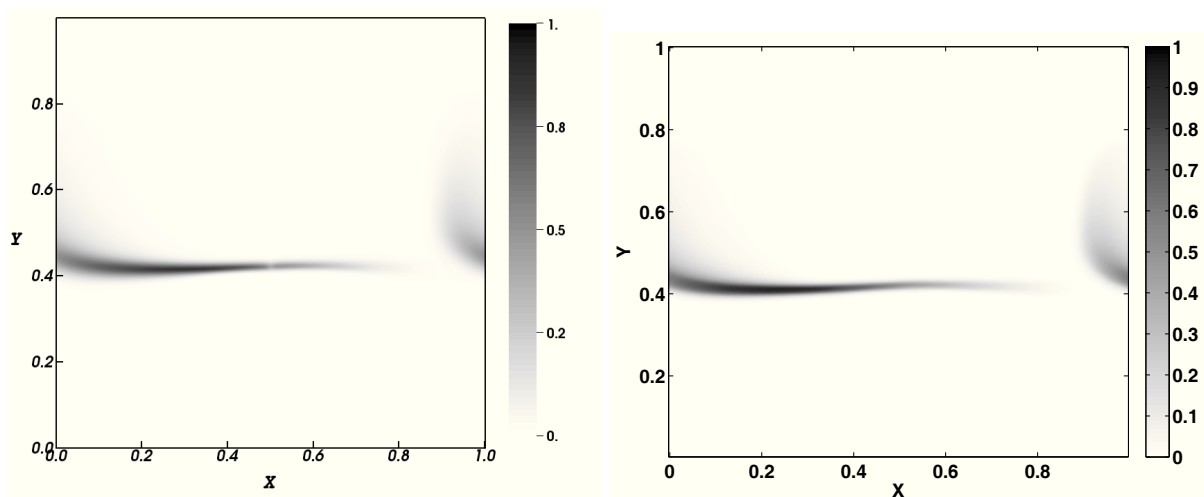


Figure 14.13: Comparison of the results of the IFP-C3D and MUSES3D codes. Results for  $m_0$  at time  $t = 1.4$ . (Left) results with the IFP-C3D code. (Right) results with the MUSES3D code.

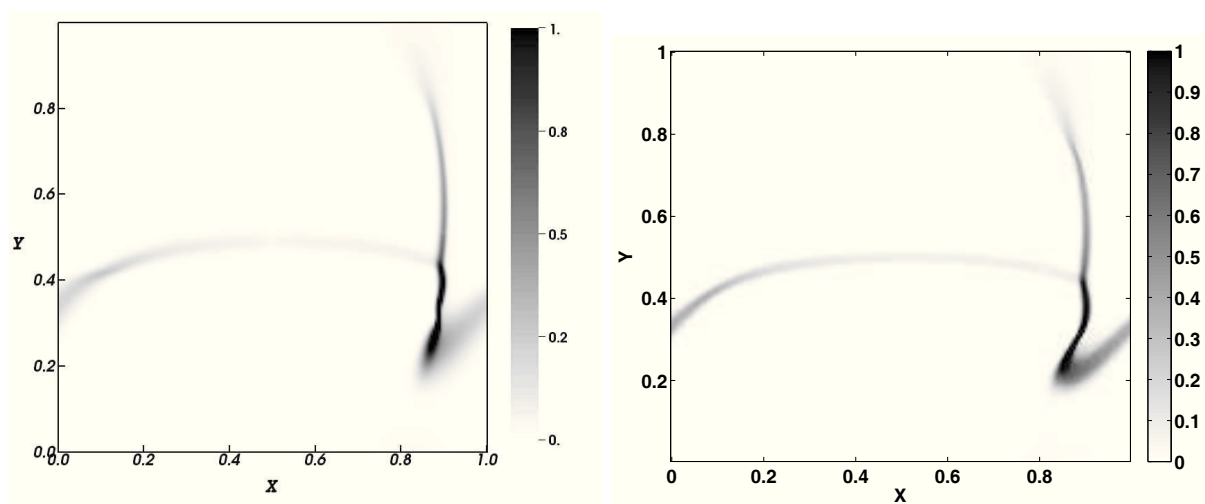


Figure 14.14: Comparison of the results of the IFP-C3D and MUSES3D codes. Results for  $m_0$  at time  $t = 2$ . (Left) results with the IFP-C3D code. (Right) results with the MUSES3D code.



## 14.4 Feasibility of injection cases with Eulerian spray model

This section concludes the developments of the Eulerian spray model in the IFP-C3D code by answering to the initial objective formulated by IFP Energies nouvelles, that is assessing the feasibility of the method in injection cases. Evidences of the success of this development are shown through two types of results. The first one tests the Eulerian spray model on an injection case of an evaporating spray. These computations are conducted in the context of a one-way coupling, formulated in Section 1.3. Secondly, the accurate behavior of the Eulerian model in injection cases is validated through comparisons with the Lagrangian method implemented in IFP-C3D.

### 14.4.1 Description of the case

The test case considered is taken up from the study conducted in [220]. It relies on the experimental work of Ferrand [78], focusing on turbulent interactions occurring in a particle laden turbulent jet. Our interest in this case is to be able to reproduce the conditions of this experiment, but in a laminar flow context. The computations are run with a polydisperse droplet population, following the Rosin-Rammler distribution:

$$f(D) = q_{rr} \frac{D^{q_{rr}-1}}{D_{smr}^{q_{rr}}} \exp\left(-\frac{D}{D_{smr}}\right), \quad (14.20)$$

where  $D$  is the particle radius,  $D_{smr}$  is the Sauter mean radius, and  $q_{rr}$  is a coefficient determining the sharpness of the distribution. Fig. (14.15), displays two Rosin-Rammler distributions with  $q_{rr} = 2$  and  $q_{rr} = 3.5$  respectively. The distribution considered here is the distribution with  $q_{rr} = 3.5$ .

The computations are run with the mesh presented in Fig. (14.16). This is a two-dimensional mesh in the axial and radial direction  $z$  and  $x$ , respectively. In the direction  $y$ , it represents the angular portion of a circular injector, with an angle of 0.05 rad. It is composed of square cells with a length of 1 mm, (80 in the  $x$ -direction, and 200 in the  $z$ -direction). The  $4 \times 4$  cell additional part at the top of the mesh is dedicated to injection, its justification can be found in [220]. Symmetric boundary conditions are imposed on the mesh axis,  $y = 0, x = 0$ , whereas periodic boundary conditions are set on faces orthogonal to the  $y$  axis, and free exit boundary conditions are set for the part localized at  $z = 0$ .

This cases involves injection of a fuel spray and gas with velocity  $18 \text{ m s}^{-1}$ . The gas phase is taken as air, with initial pressure  $P_g = 10^5 \text{ Pa}$ , temperature  $T_g = 293 \text{ K}$ , and viscosity  $\mu_g = 1.99 \cdot 10^{-5} \text{ kg m}^{-1} \text{ s}^{-1}$ , whereas the fuel is taken as the  $C_{14}H_{30}$  species, with a density  $\rho_l = 760 \text{ kg m}^{-3}$ . The disperse flow is injected with a liquid volume fraction of  $\alpha_l = 1.12 \cdot 10^{-3}$  in a chamber initially filled with air.

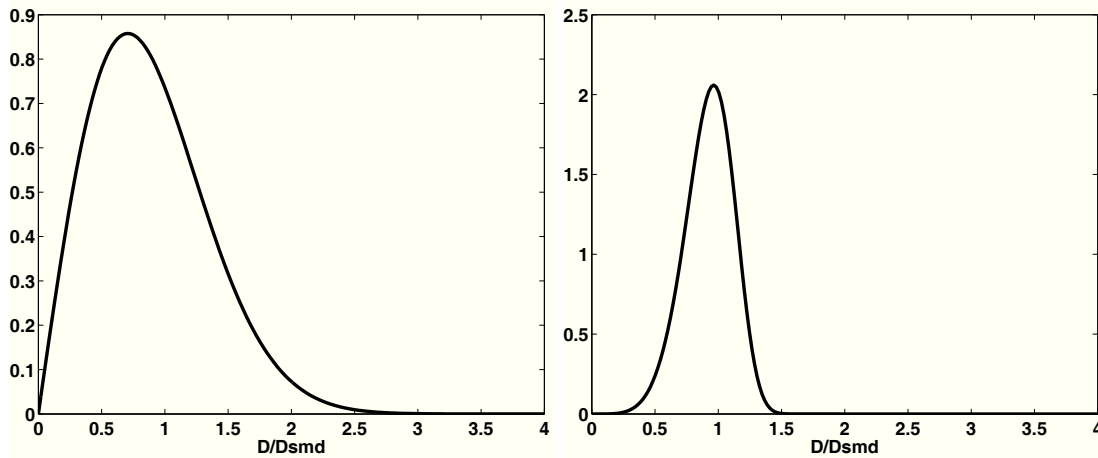


Figure 14.15: Illustration of Rosin-Rammler distributions, for two values of  $q_{rr}$ . Left : distribution with  $q_{rr} = 2$ ; Right : distribution with  $q_{rr} = 3.5$ , actually used in the computations.

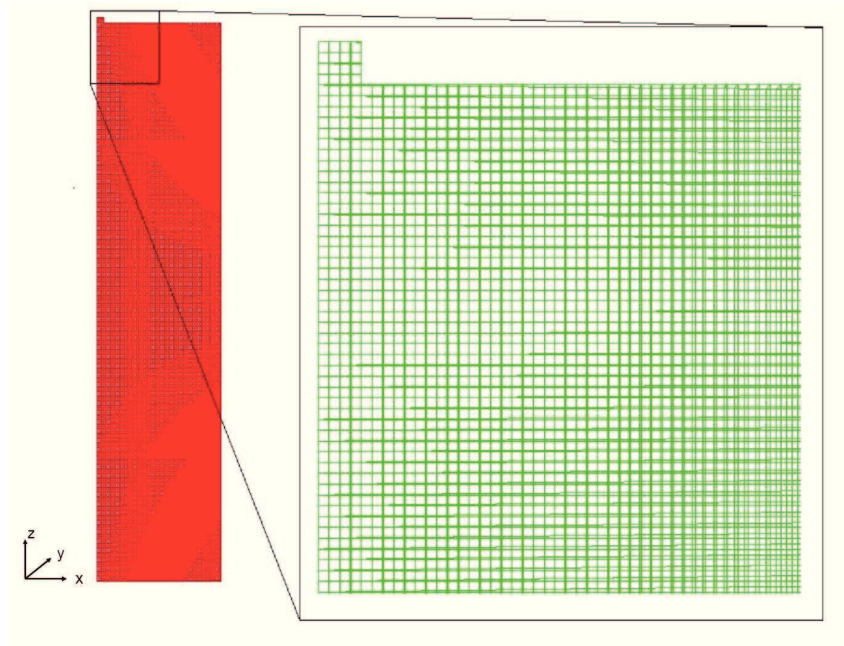


Figure 14.16: Mesh used for the Lagrangian, and Eulerian numerical simulations. Left: complete mesh; Right: focus of the area close to the injector.

#### 14.4.2 Computations of the size moments, and drag coefficients

As justified in Section 13.4, the size moments are nondimensionalized relative to a characteristic size of the system  $S_0$ .

##### Polydisperse distribution

In order to compute the size moments of the Rosin-Rammler distribution the first step is to express the distribution in Eq. (14.20) relative to the droplet surface variable. For that purpose, we use the relation:  $f(D)dD = f(S)dS = f(S)4\pi dD$ , so that Eq. (14.20) becomes:

$$f(S) = q_{rr} \frac{S^{q_{rr}/2-1}}{S_{smr}^{q_{rr}/2}} \exp \left[ - \left( \frac{S}{S_{smr}} \right)^{q_{rr}/2} \right], \quad (14.21)$$

where  $S_{smr}$  is the Sauter mean surface of the droplets. As illustrated in Fig. (14.15), for  $D = 4 \times D_{smr}$ , the values of the NDF can be considered null. Therefore, the characteristic size values of the distribution is taken as  $S_0 = 16 \times S_{smr}$ . Given that  $f(S)dS = f(S_0 \bar{S})S_0 d\bar{S}$ , the dimensionless Rosin-Rammler distribution function writes:

$$f(\bar{S}) = q_{rr} 16^{q_{rr}/2} (\bar{S})^{q_{rr}/2-1} \exp \left[ - (16\bar{S})^{q_{rr}/2} \right]. \quad (14.22)$$

From now on, the bar sign will be omitted. The moments vector corresponding to the NDF Eq. (14.22), and actually injected in the domain, writes:

$$\mathbf{m} = (2.5066, 0.1272, 7.9 \cdot 10^{-3}, 5.58 \cdot 10^{-4})^T. \quad (14.23)$$

The characteristic droplet number  $N_0$ , is given by writing that the injected liquid volume fraction must be equal to  $\alpha_l$ :

$$N_0 S_0 \int_0^1 \frac{S^{3/2}}{6\sqrt{\pi}} f(S) dS = \alpha_l. \quad (14.24)$$

For example, for a droplet population such as  $D_{smr} = 5 \mu m$ , we have  $S_0 = 5 \cdot 10^{-9} m^2$  and  $N_0 = 9.5 \cdot 10^9 m^{-3}$ , and for  $D_{smr} = 20 \mu m$ , we get  $S_0 = 8 \cdot 10^{-8} m^2$ , and  $N_0 = 1.48 \cdot 10^8 m^{-3}$ .

Let us compute now the drag coefficients, i.e. the particle characteristic time response  $\tau_p$ , and the particle Reynolds number  $Re_p$ . The expression of  $\tau_p$  is given by

$$\tau_p = \frac{m_1}{m_0} \theta, \quad (14.25)$$

where  $\theta = \rho_l S_0 / 18 \pi \mu_g$ . The particle Reynolds number is given by

$$Re_p = \frac{2 \rho_g \|\mathbf{u}_g - \mathbf{u}_p\|}{\mu_g} \sqrt{\frac{S_0}{4\pi}} \sqrt{\frac{m_1}{m_0}}. \quad (14.26)$$

### Monodisperse distribution

For a monodisperse population, we consider  $S_0 = 2\pi(D_{smr})^2$ , so that the dimensionless NDF reads  $f(S) = \delta(S - 0.5)$ , in order to recover the mean droplet surface:

$$\pi(D_{smr})^2 = S_0 \frac{\int_0^1 \bar{S} f(\bar{S}) d\bar{S}}{\int_0^1 f(\bar{S}) d\bar{S}} = S_0 \frac{m_1}{m_0}. \quad (14.27)$$

The moment vector corresponding to this NDF writes:

$$\mathbf{m} = (1, 0.5, 0.25, 0.125)^T. \quad (14.28)$$

The characteristic droplet number  $N_0$ , is given by Eq. (14.24), and the values of  $\theta$  and  $Re_p$  are given by Eq. (14.25) and Eq. (14.26).

### 14.4.3 Comparison with the Lagrangian resolution method

The first set of test cases consist in comparing results given by the implemented Eulerian spray model and the Lagrangian model of IFP-C3D. The Lagrangian relies on a Stochastic Particle method (Section 2.1). When implementing the Eulerian spray model, we have made sure that the Eulerian variables does not interfere with the Lagrangian variable, so that we introduce the capacity to simultaneously run a computation with the Lagrangian model and the Eulerian one. What is interesting is this approach is that the Lagrangian model considers a two-way coupling. Our strategy is to use the resulting gaseous velocity field in order to compute the drag interaction with the spray Eulerian field, expecting then that the resulting Lagrangian particles and the Eulerian particle number field coincide. This will then validate the spray dynamics through injection.

*Remark:* Let us emphasize that this comparison allows us to validate only the Eulerian spray dynamics though interaction with the gas phase in the context of one-way coupling. We do not claim to solve the Eulerian spray dynamics in a two-way coupling which would require to actually develop and implement a two-coupling model in the Eulerian framework.

Computations are run successively with monodisperse and polydisperse droplet populations. In the case of a monodisperse population, two computations are run, with  $D_{smr} = 5 \mu m$  and  $D_{smr} = 20 \mu m$ . Results for  $D_{smr} = 5 \mu m$  are displayed in Fig. (14.17), Fig. (14.18), Fig. (14.19), Fig. (14.20) for instants  $t = 5 \cdot 10^{-3} s$ ,  $t = 10^{-2} s$ ,  $t = 1.5 \cdot 10^{-2} s$ , and  $t = 2 \cdot 10^{-2} s$ , respectively. On these figures, the left side corresponds to the particle number comparison, and the right side to the velocity field comparison, where the absolute value of the velocity is represented.

The overall remark is that comparisons are qualitatively satisfying, in the sense that the fields of particle number and velocity coincide quite well. The penetration length is the same for the Lagrangian and the Eulerian result. When focusing on the particle number field at  $t = 2 \cdot 10^{-2} s$ , at Fig. (14.20), some

of the relatively fine structure of the particle flow found with the Lagrangian method are captured by the Eulerian method. This is very encouraging, since the Eulerian method is first order, and thus promising for the future development of higher order schemes. The same conclusion holds for the velocity field where, for example, at  $t = 2 \cdot 10^{-2} s$ , the fine structure of maximum velocity is captured by the Eulerian model. The effect of two-way coupling effect present in the Lagrangian model are highlighted in Fig. (14.21) and Fig. (14.22) displaying the gas density fields at times  $t = 5 \cdot 10^{-3} s$ ,  $t = 10^{-2} s$ ,  $t = 1.5 \cdot 10^{-2} s$ .

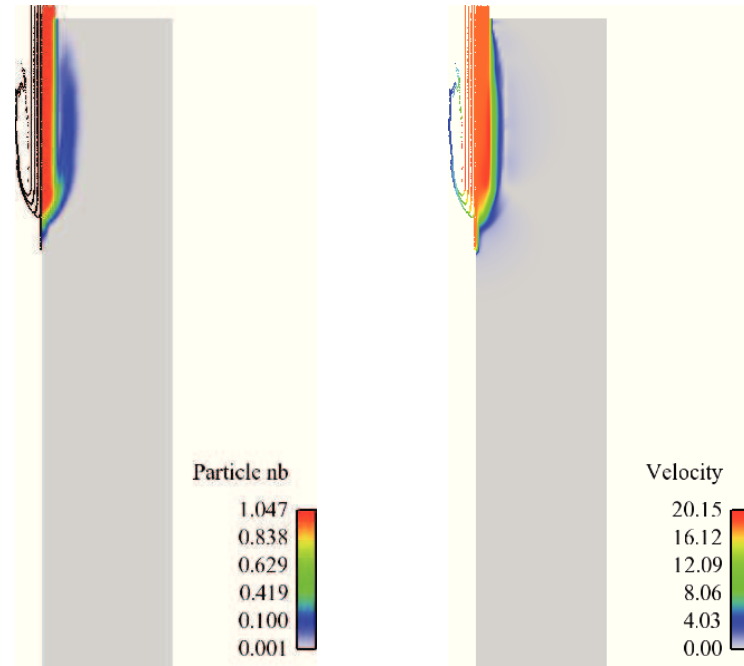


Figure 14.17: Comparison of Lagrangian and Eulerian results for a monodisperse flow made of droplets of  $D = 5 \mu m$ , at time  $t = 5 \cdot 10^{-3} s$ . In each figure, the Lagrangian particles are displayed on the left side on the domain, and the Eulerian field on the right side. Left : particle number ( $m_0$ ); Right : particle velocity.

The same conclusion holds for the case of a droplet population of  $D_{smr} = 20 \mu m$ , displayed at Fig. (14.23) and Fig. (14.24), at time  $t = 5 \cdot 10^{-3} s$ ,  $t = 10^{-2} s$ . One can notice the difference of penetration lengths between this case, and the case where  $D_{smr} = 5 \mu m$ , significant of the difference of inertia. The corresponding gaseous density fields are displayed in Fig. (14.25).

The next case considers a droplet population with  $D_{smr} = 20 \mu m$  again, but this time the population is assumed to be polydisperse with the Rosin-Rammler distribution displayed at Fig. (14.15). The impact of the size-conditioned dynamics can be assessed in Fig. (14.26) where the Lagrangian field of particles is significantly different from the particle field of Fig. (14.23) for a monodisperse population. Due to the uniform droplet dynamics in the monodisperse case, they are concentrated on the same structure, whereas in the polydisperse the different of inertia is responsible for the disperse cloud that can be observed in Fig. (14.26) and Fig. (14.27). On the other hand, there is only a very slight difference between the Eulerian fields displayed in Fig. (14.26) and Fig. (14.27) in the polydisperse case and the fields displayed in Fig. (14.23) and Fig. (14.24) in the monodisperse case. This is due to the fact that the Eulerian spray model considers a single dynamics for the entire droplet population, based on the mean surface density and the number density, as explained in Section 4.1.4. The difference between the two fields comes from the fact that the computation of the characteristic time response and particle Reynolds number leads to a mean drag force a bit lower than in the monodisperse case.

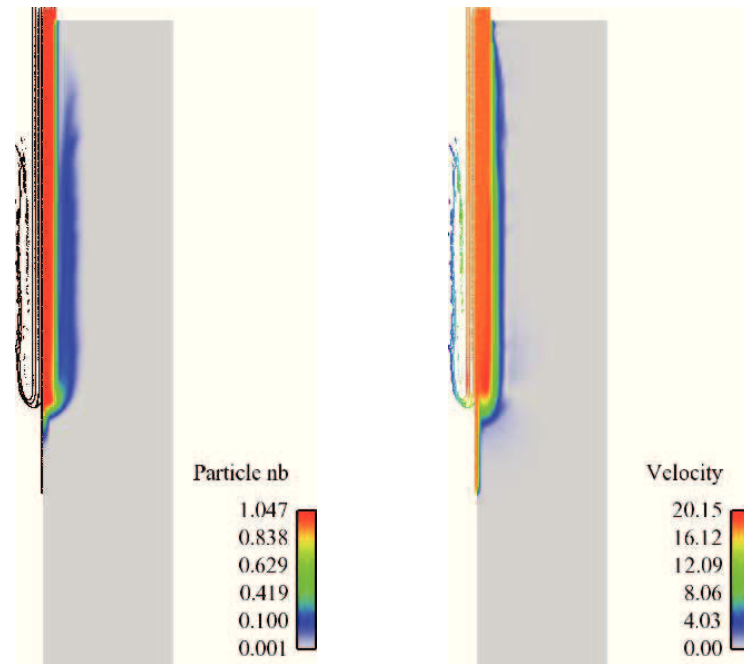


Figure 14.18: Comparison of Lagrangian and Eulerian results for a monodisperse flow made of droplets of  $D = 5 \mu m$ , at time  $t = 10^{-2} s$ . In each figure, the Lagrangian particles are displayed on the left side on the domain, and the Eulerian field on the right side. Left : particle number ( $m_0$ ); Right : particle velocity.

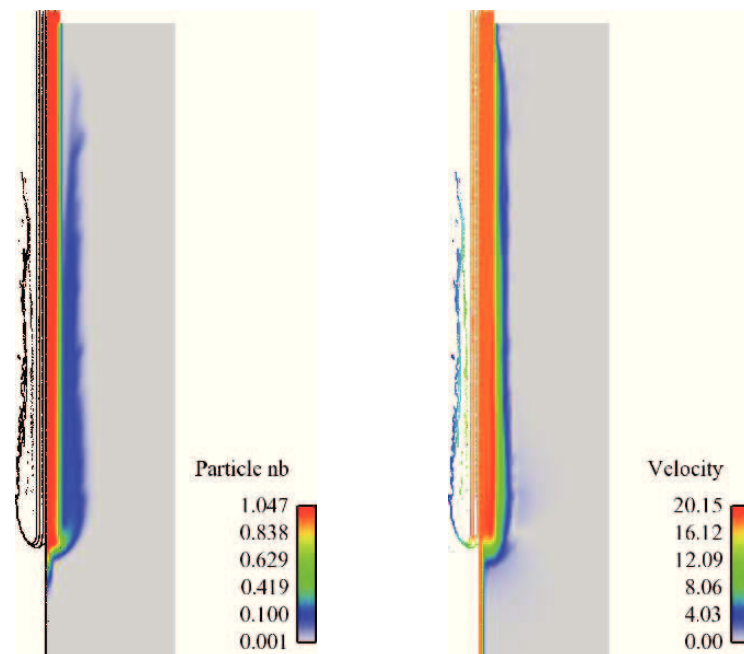


Figure 14.19: Comparison of Lagrangian and Eulerian results for a monodisperse flow made of droplets of  $D = 5 \mu m$ , at time  $t = 1.5 \cdot 10^{-2} s$ . In each figure, the Lagrangian particles are displayed on the left side on the domain, and the Eulerian field on the right side. Left : particle number ( $m_0$ ); Right : particle velocity.

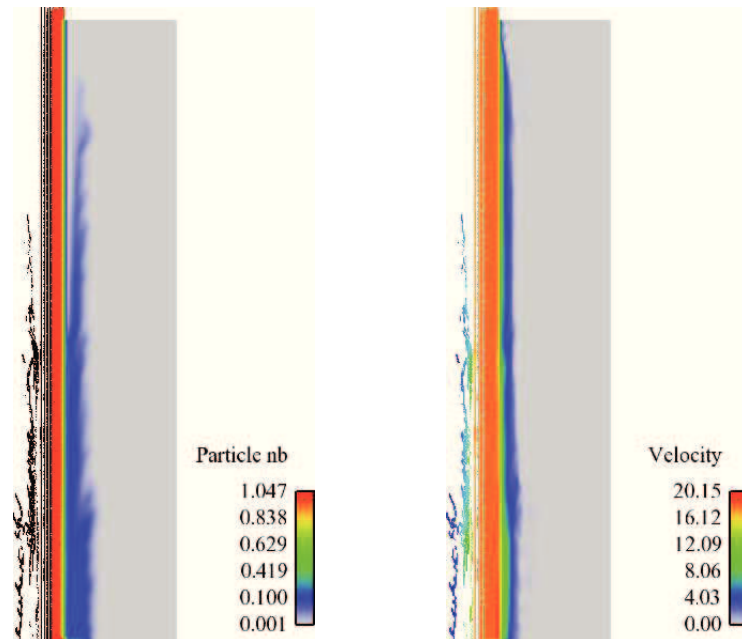


Figure 14.20: Comparison of Lagrangian and Eulerian results for a monodisperse flow made of droplets of  $D = 5 \mu m$ , at time  $t = 2.10^{-2} s$ . In each figure, the Lagrangian particles are displayed on the left side on the domain, and the Eulerian field on the right side. Left : particle number ( $m_0$ ); Right : particle velocity.

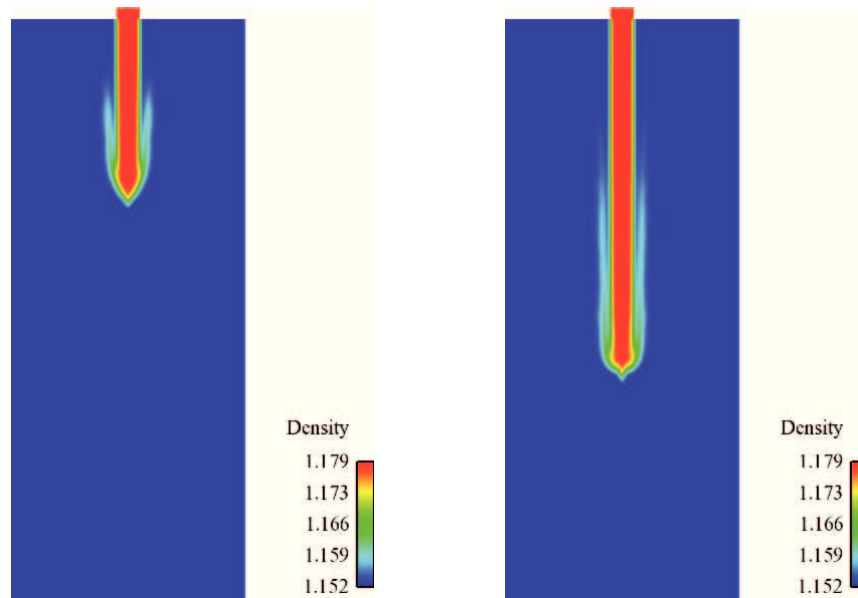


Figure 14.21: Gas density field in the context of the two-way coupling considered in the Lagrangian resolution. Results for a monodisperse flow made of droplets of  $D = 5 \mu m$ . Left : results for  $t = 5.10^{-3} s$ ; Right : results for  $t = 10^{-2} s$ .

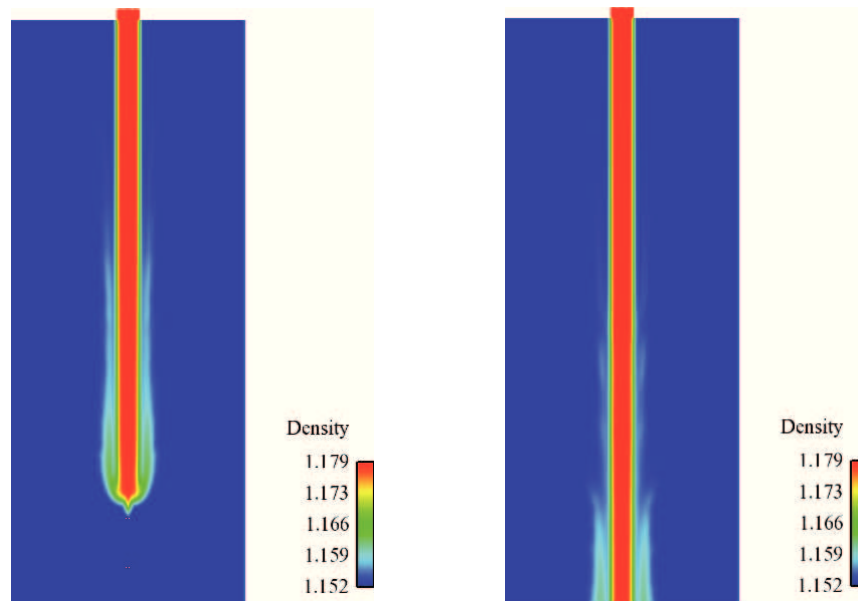


Figure 14.22: Gas density field in the context of the two-way coupling considered in the Lagrangian resolution. Results for a monodisperse flow made of droplets of  $D = 5 \mu m$ . Left : results for  $t = 1.5 \cdot 10^{-2} s$ ; Right : results for  $t = 2 \cdot 10^{-2} s$ .

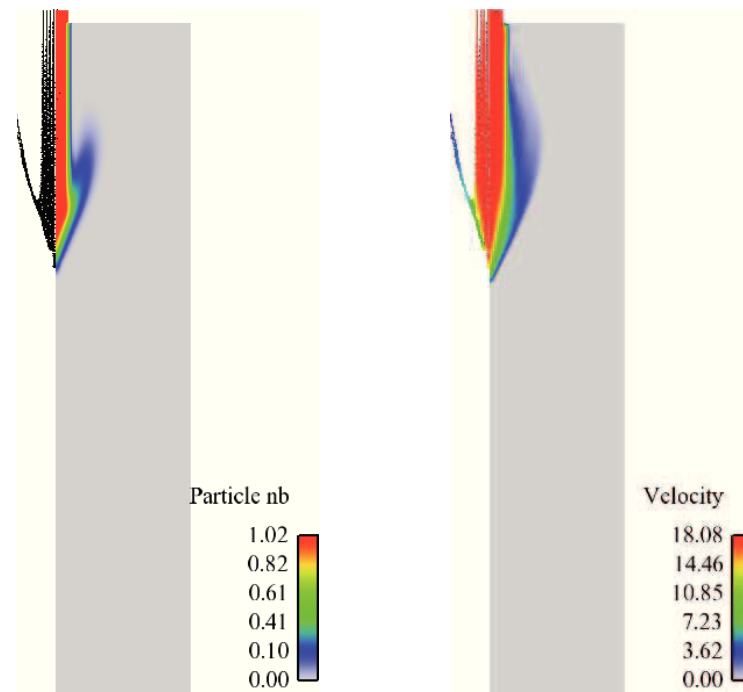


Figure 14.23: Comparison of Lagrangian and Eulerian results for a monodisperse flow made of droplets of  $D = 20 \mu m$ , at time  $t = 5 \cdot 10^{-3} s$ . In each figure, the Lagrangian particles are displayed on the left side on the domain, and the Eulerian field on the right side. Left : particle number ( $m_0$ ); Right : particle velocity.

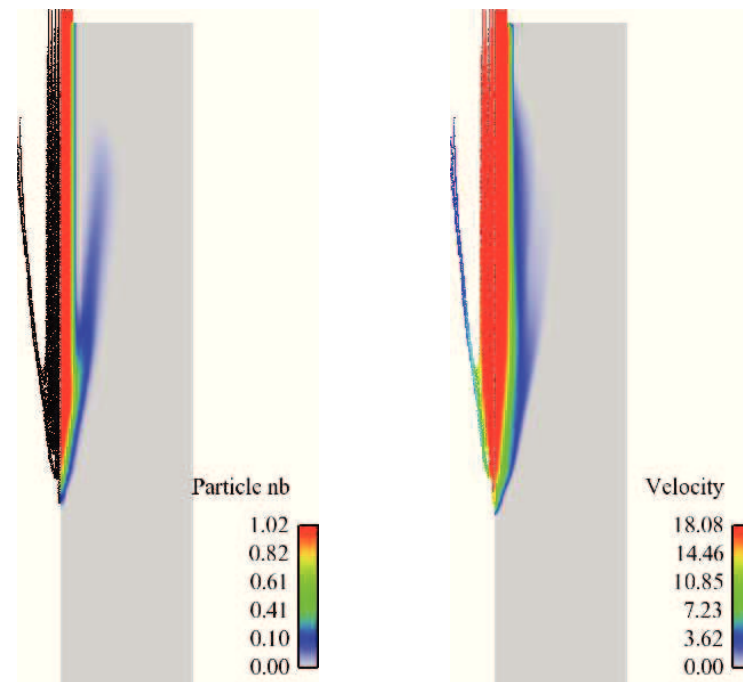


Figure 14.24: Comparison of Lagrangian and Eulerian results for a monodisperse flow made of droplets of  $D = 20 \mu m$ , at time  $t = 10^{-2} s$ . In each figure, the Lagrangian particles are displayed on the left side on the domain, and the Eulerian field on the right side. Left : particle number ( $m_0$ ); Right : particle velocity.

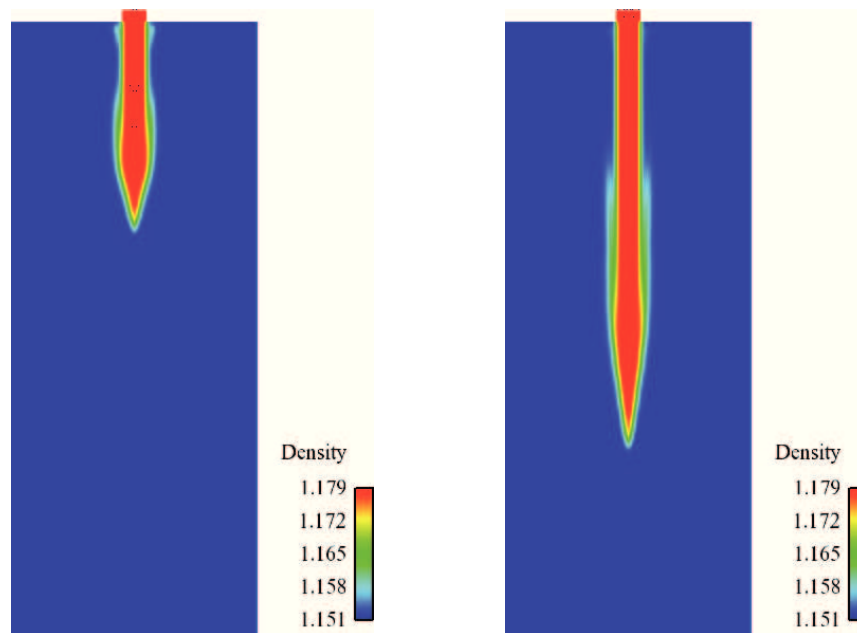


Figure 14.25: Gas density field in the context of the two-way coupling considered in the Lagrangian resolution. Results for a monodisperse flow made of droplets of  $D = 20 \mu m$ . Left : results for  $t = 5.10^{-3} s$ ; Right : results for  $t = 10^{-2} s$ .



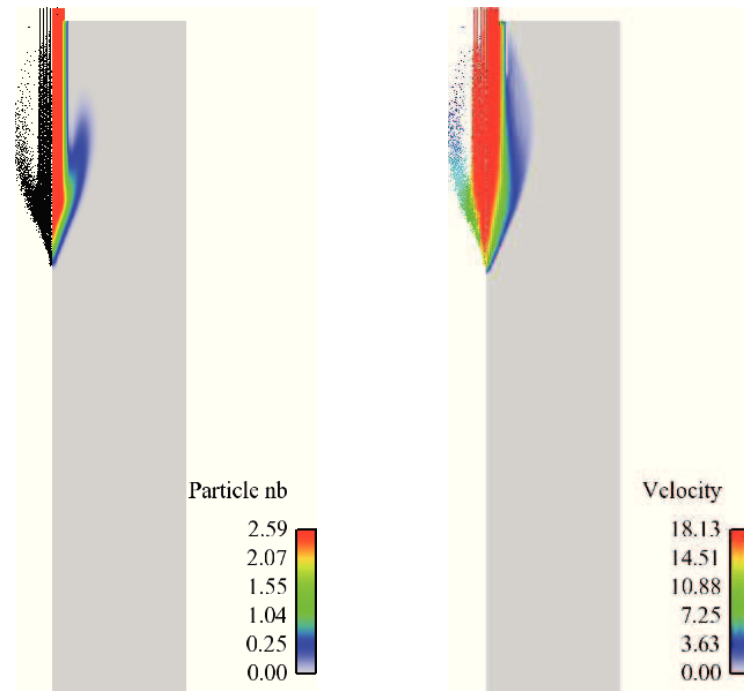


Figure 14.26: Comparison of Lagrangian and Eulerian results for a polydisperse flow made of droplets of  $D = 20 \mu m$ , at time  $t = 5.10^{-3} s$ . In each figure, the Lagrangian particles are displayed on the left side on the domain, and the Eulerian field on the right side. Left : particle number ( $m_0$ ); Right : particle velocity.

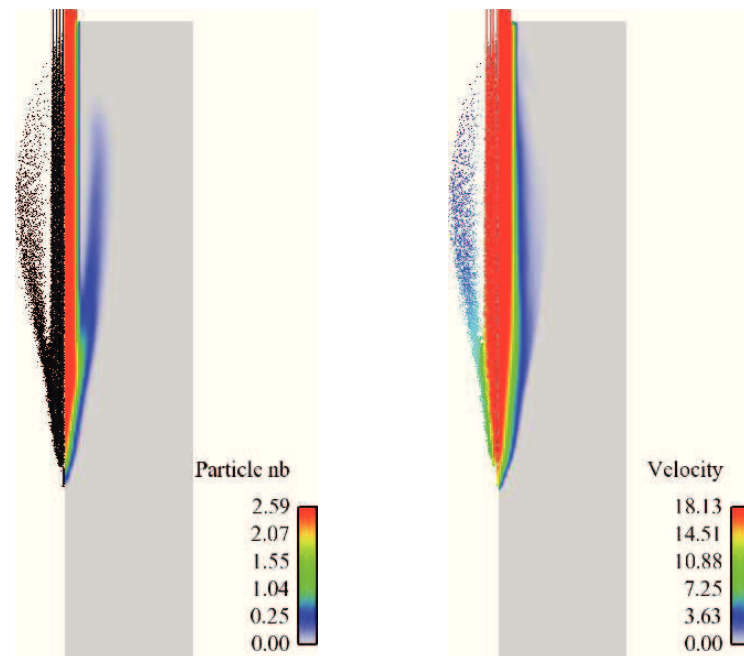


Figure 14.27: Comparison of Lagrangian and Eulerian results for a polydisperse flow made of droplets of  $D = 20 \mu m$ , at time  $t = 10^{-2} s$ . In each figure, the Lagrangian particles are displayed on the left side on the domain, and the Eulerian field on the right side. Left : particle number ( $m_0$ ); Right : particle velocity.

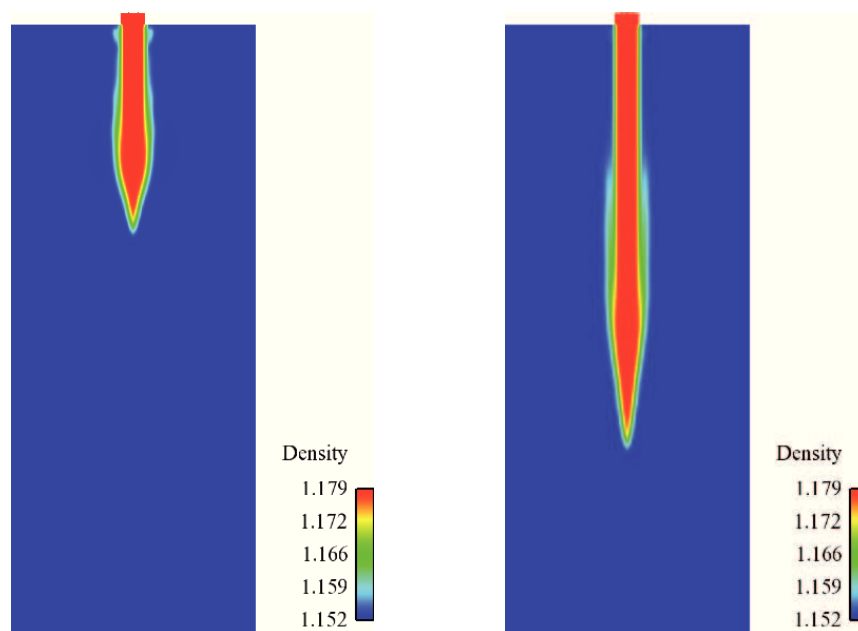


Figure 14.28: Gas density field in the context of the two-way coupling considered in the Lagrangian resolution. Results for a polydisperse flow made of droplets with a Sauter mean radius  $D_{smr} = 20 \mu m$ . Left : results for  $t = 5.10^{-3} s$ ; Right : results for  $t = 10^{-2} s$ .

#### 14.4.4 Spray description with the Eulerian spray model

This second set of injection cases assesses the capacity of the Eulerian spray model to describe evaporating polydisperse sprays in the IFP-C3D code. In this section, since we consider only the Eulerian spray model, the computation is run in the context of a one-way coupling.

Our validation strategy consists in comparing the behavior of an evaporative spray, with the same spray injected with evaporation. Three polydisperse droplet populations are successively injected. The profile of their NDF is the same, and is illustrated in Fig. (14.15)-right. They differ by their Sauter mean radius,  $D_{smr}$ :  $5 \mu m$ ,  $20 \mu m$ ,  $80 \mu m$ , corresponding to low, medium, and high inertia droplets, respectively. The remaining conditions of the computations are explained in Section 14.4.1.

We focus first on the non-evaporative computations, with results displayed in Fig. (14.29) to Fig. (14.34). Fig. (14.29), Fig. (14.30) and Fig. (14.31) display the particle number field  $m_0$  for the spray with  $D_{smr} = 5 \mu m$  (left) and the gas phase (right) at instants  $t = 10^{-2} s$ ,  $t = 5 \cdot 10^{-2} s$  and  $t = 0.1 s$ . Other moments  $m_1, m_2, m_3$ , have exactly the same structure as the field of  $m_0$ , because, since there is no evaporation, the size distribution is unchanged and has the same profile everywhere in space. The field of particles is to be compared to the gas field. One can indeed notice the similarity between the two fields, that is a consequence of the low-inertia character of the injected droplets. Nevertheless, disparities can be observed, specially in Fig. (14.31) at the created gaseous vortices where preferential concentration of the particles occurs at the edges of these vortices. This is significant of the fact that, even though the particles are small, yet they are not tracers for the gas flow.

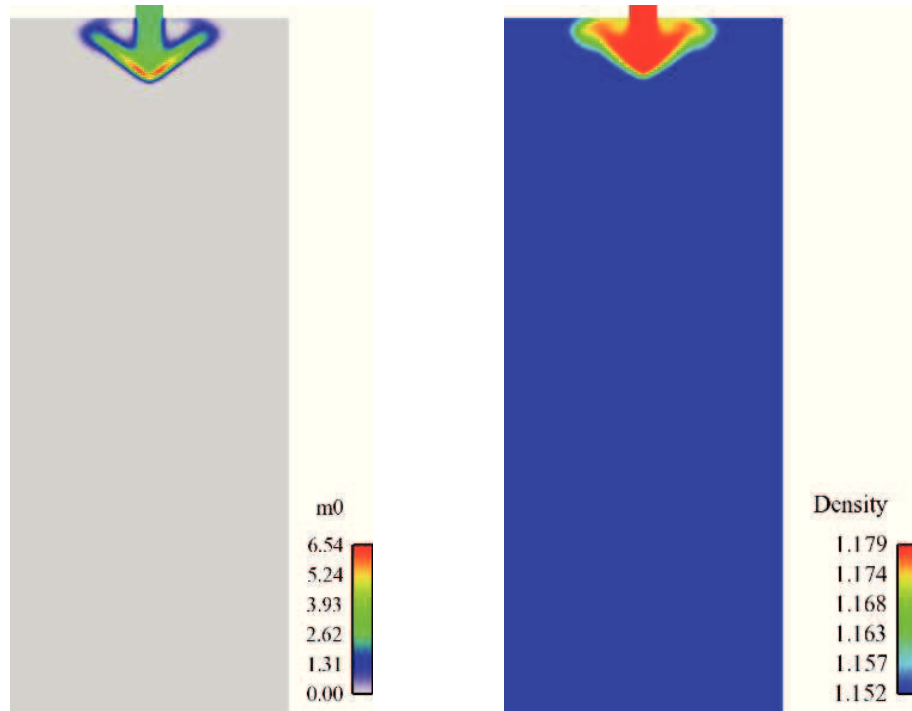


Figure 14.29: Results obtained with the EMSM model for a polydisperse flow made of droplets with a Sauter mean radius of  $D_{smr} = 5 \mu m$ , at time  $t = 10^{-2} s$ . Left : particle number ( $m_0$ ); Right : gas density field.

Particle population with  $D_{smr} = 20 \mu m$  is considered in Fig. (14.32) and Fig. (14.33). The gas field is unchanged. As particles are much more inertial than before (the Stokes number is 16 times higher), he spray is much less dragged by the gas phase. However, the spray is stopped quite fast, so that the penetration length is relatively small. It is interesting to note the high droplet concentration at the edge

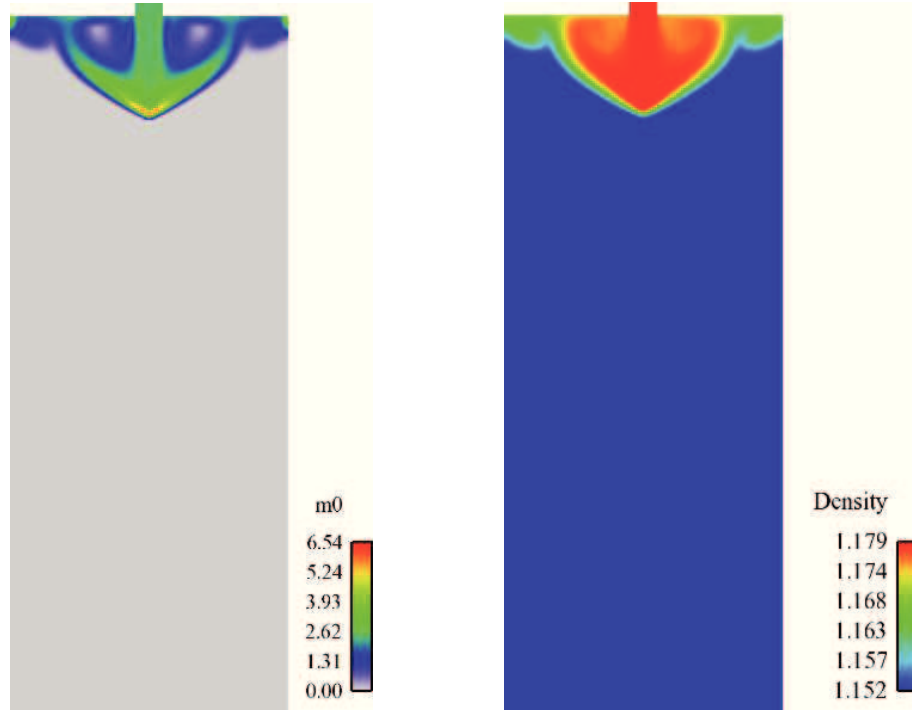


Figure 14.30: Results obtained with the EMSM model for a polydisperse flow made of droplets with a Sauter mean radius of  $D_{smr} = 5 \mu m$ , at time  $t = 5.10^{-2} s$ . Left : particle number ( $m_0$ ); Right : gas density field.

of the jet, revealing of a  $\delta$ -shock creation, resulting from the important velocity gradient due to the drag exerted by the gas phase that stops the path of the droplets in the chamber.

In the case of particles with  $D_{smr} = 80 \mu m$ , illustrated in Fig. (14.34), for instants  $t = 10^{-2} s$  and  $t = 5.10^{-2} s$ , their high inertial character makes them flow in the chamber almost without seeing the gas flow. This regime is called the ballistic regime. Moreover, since the particle velocity field is barely impacted by the gas, there is no singularity in the field of  $m_0$ .

The evaporative cases are now displayed in Fig. (14.35) to Fig. (14.40). The evaporation coefficient is set at  $K = 5$ , so that, according to the profile of the distribution shown in Fig. (14.15)-right, all the droplets should largely be evaporated, after a residence time in the chamber of  $t = 0.1 s$ . The results for the three cases are displayed now only for the final instants  $t = 0.1 s$  for  $D_{smr} = 5 \mu m$ , and  $D_{smr} = 20 \mu m$ , and  $t = 5.10^{-2} s$  for  $D_{smr} = 80 \mu m$ . Contrary to the non-evaporative cases, the four size moments are considered, since the evaporation term may have changed the size distribution profile. The scale established for the representation of the moments is based on the values of the moments of the initial size distribution. This means that the scale for  $m_k$  is proportional to the scale of  $m_0$  by the coefficient  $(m_k/m_0)_{Rosin-Rammler}$ , where  $(m_k/m_0)_{Rosin-Rammler}$  is the fraction of moments of the initial Rosin-Rammler distribution considered. The interest of using this scale is that the structure of the different moment fields are exactly matching in case the size distribution is spatially homogeneous, but they differ in the opposite case, so that is it very easy to notice spatial differences in the size distribution.

The general observation confirms that evaporation modifies the profile of the NDF, as a drift velocity in the size phase space from higher values to lower values. This is why, the relative field values of  $m_{k+1}$  are lower than for  $m_k$ .

In the case of  $D_{smr} = 5 \mu m$ , on can observe that the fields are much less widespread than in the non-evaporating case. This is due to the fact that droplets, with sufficient residence time in the chamber,

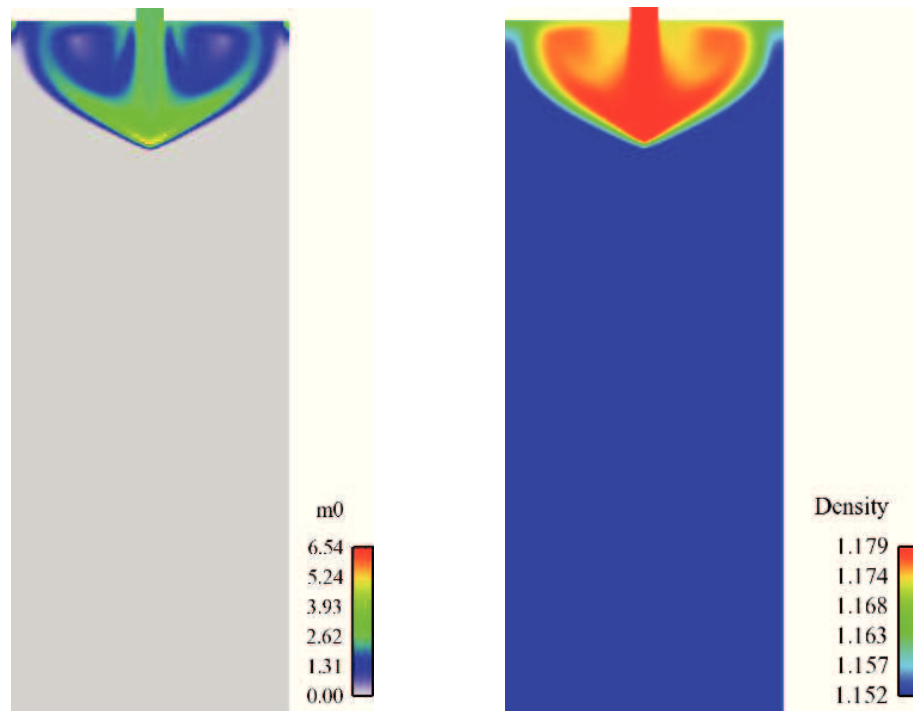


Figure 14.31: Results obtained with the EMSM model for a polydisperse flow made of droplets with a Sauter mean radius of  $D_{smr} = 5 \mu m$ , at time  $t = 0.1 s$ . Left : particle number ( $m_0$ ); Right : gas density field.

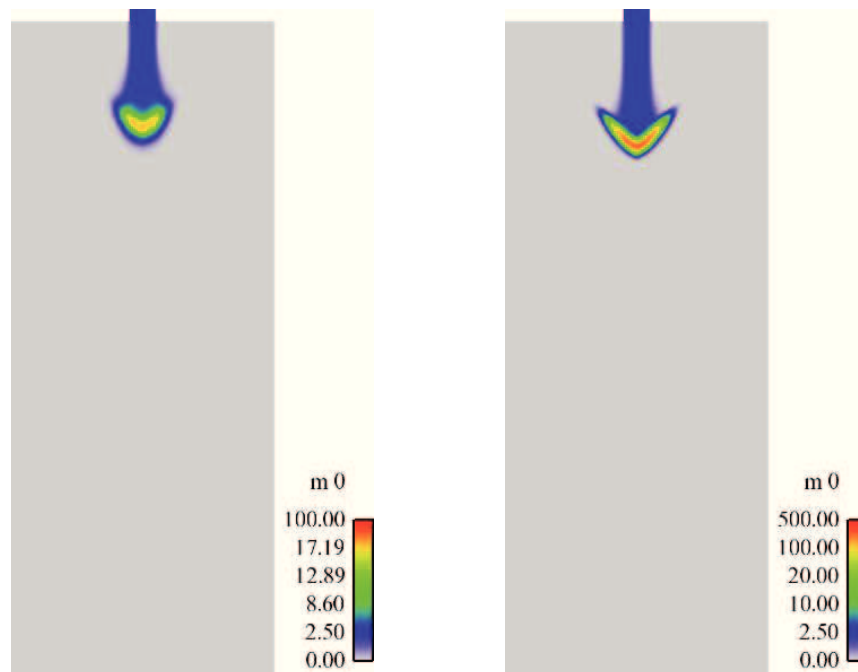


Figure 14.32: Results obtained with the EMSM model for a polydisperse flow made of droplets with a Sauter mean radius of  $D_{smr} = 20 \mu m$ . Left : particle number ( $m_0$ ) at time  $t = 10^{-2} s$ ; Right : particle number ( $m_0$ ) at time  $t = 5.10^{-2} s$

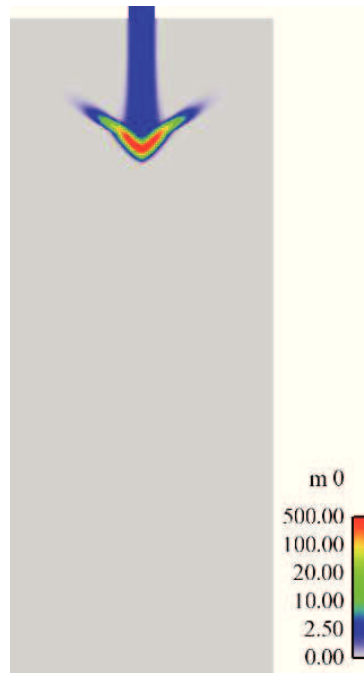


Figure 14.33: Results obtained with the EMSM model for a polydisperse flow made of droplets with a Sauter mean radius of  $D_{smr} = 20 \mu m$ : particle number at time  $t = 0.1 s$

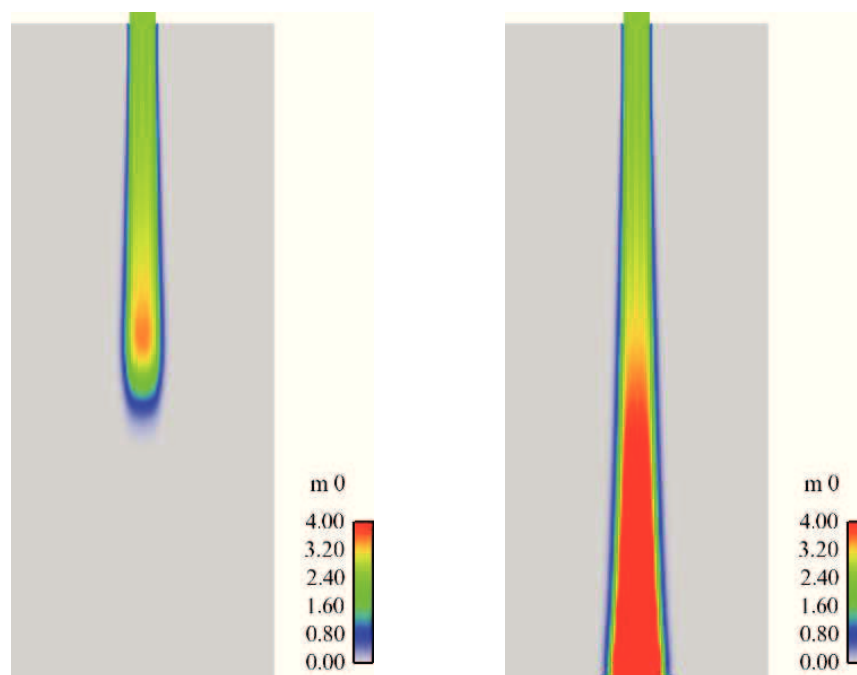


Figure 14.34: Results obtained with the EMSM model for a polydisperse flow made of droplets with a Sauter mean radius of  $D_{smr} = 80 \mu m$ . Left : particle number ( $m_0$ ) at time  $t = 10^{-2} s$ ; Right : particle number ( $m_0$ ) at time  $t = 5.10^{-2} s$

have been completely evaporated. This is an important observation, since it gives the evidence that the

Eulerian spray model implemented is able to evaporate droplets until they disappear. This was not the case with the Eulerian two-fluid model implemented by [220]. The same conclusions holds for the cases  $D_{smr} = 20 \mu m$  displayed in Fig. (14.37) and Fig. (14.38)., and for the case of  $D_{smr} = 80 \mu m$ , displayed in Fig. (14.39) and Fig. (14.40). These test cases demonstrate the ability of the Eulerian spray model implemented in IFP-C3D to treat injection cases involving polydisperse evaporating sprays.

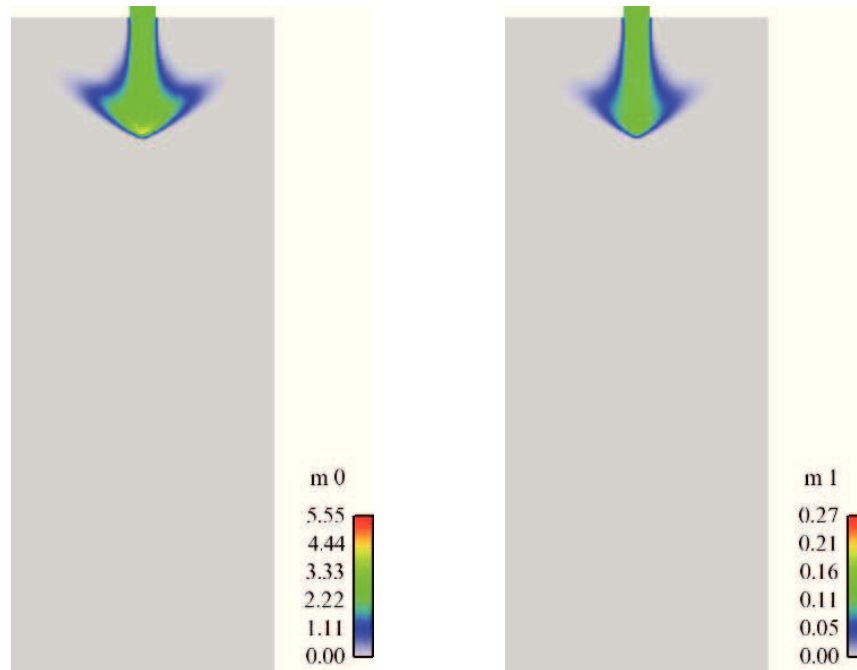


Figure 14.35: Results obtained with the EMSM model for a polydisperse evaporating spray made of droplets with a Sauter mean radius of  $D_{smr} = 5 \mu m$ , at time  $t = 0.1 s$ . Left : particle number ( $m_0$ ); Right : particle surface density ( $m_1$ ).

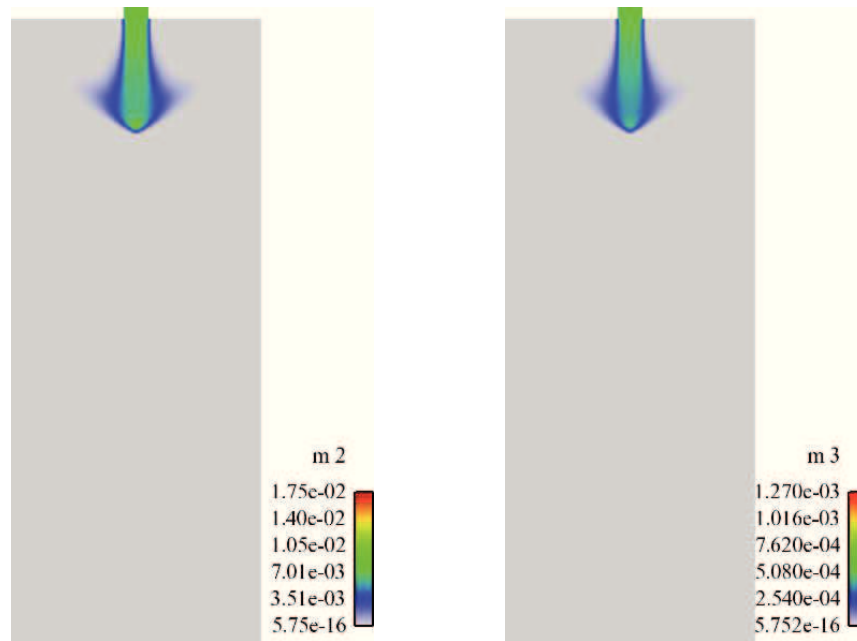


Figure 14.36: Results obtained with the EMSM model for a polydisperse evaporating spray made of droplets with a Sauter mean radius of  $D_{smr} = 5 \mu m$ , at time  $t = 0.1$  s. Left : second order size moment ( $m_2$ ); Right : third order size moment ( $m_3$ ).

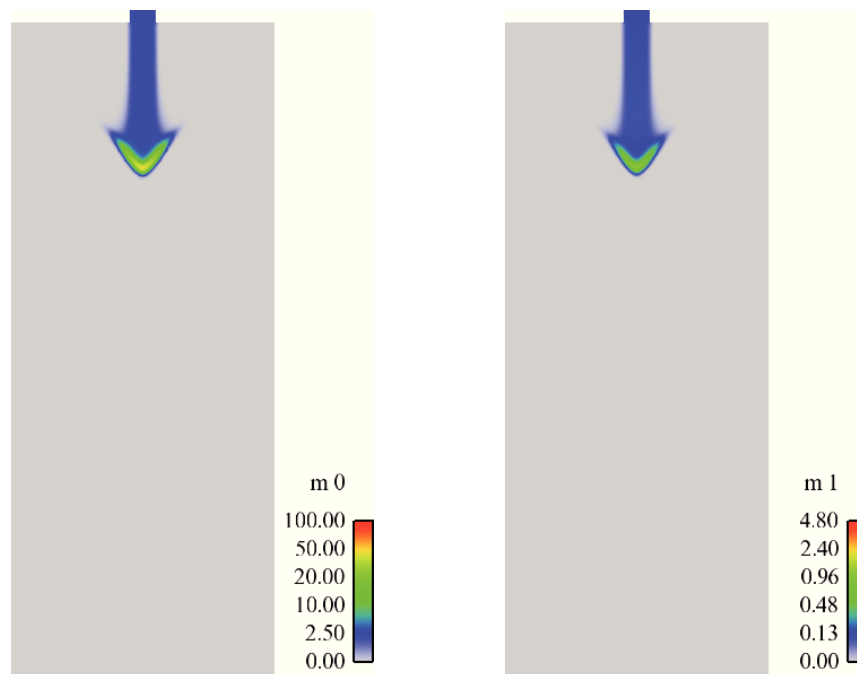


Figure 14.37: Results obtained with the EMSM model for a polydisperse evaporating spray made of droplets with a Sauter mean radius of  $D_{smr} = 20 \mu m$ , at time  $t = 0.1$  s. Left : particle number ( $m_0$ ); Right : particle surface density ( $m_1$ ).



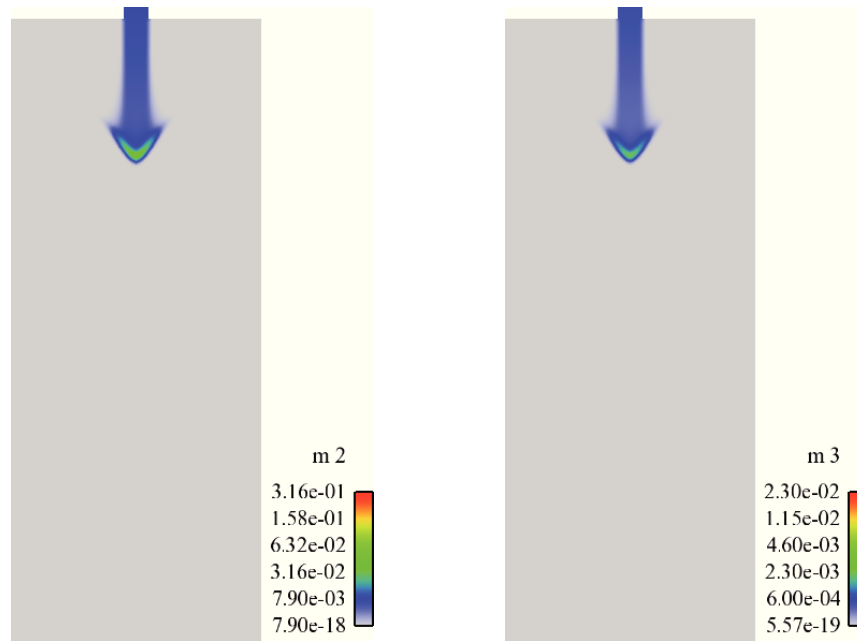


Figure 14.38: Results obtained with the EMSM model for a polydisperse evaporating spray made of droplets with a Sauter mean radius of  $D_{smr} = 20 \mu m$ , at time  $t = 0.1$  s. Left : second order size moment ( $m_2$ ); Right : third order size moment ( $m_3$ ).

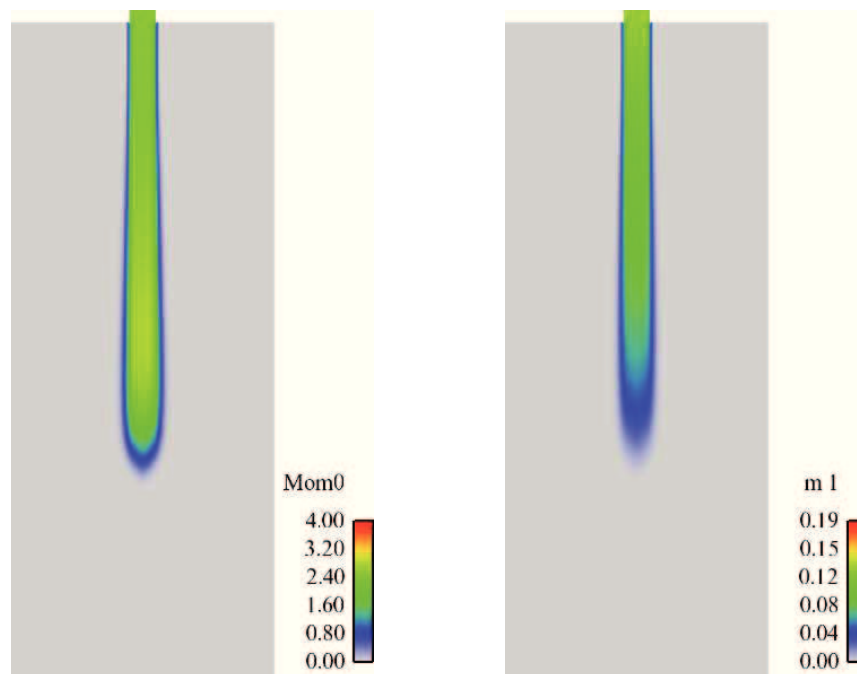


Figure 14.39: Results obtained with the EMSM model for a polydisperse evaporating spray made of droplets with a Sauter mean radius of  $D_{smr} = 80 \mu m$ , at time  $t = 0.1$  s. Left : particle number ( $m_0$ ); Right : particle surface density ( $m_1$ ).

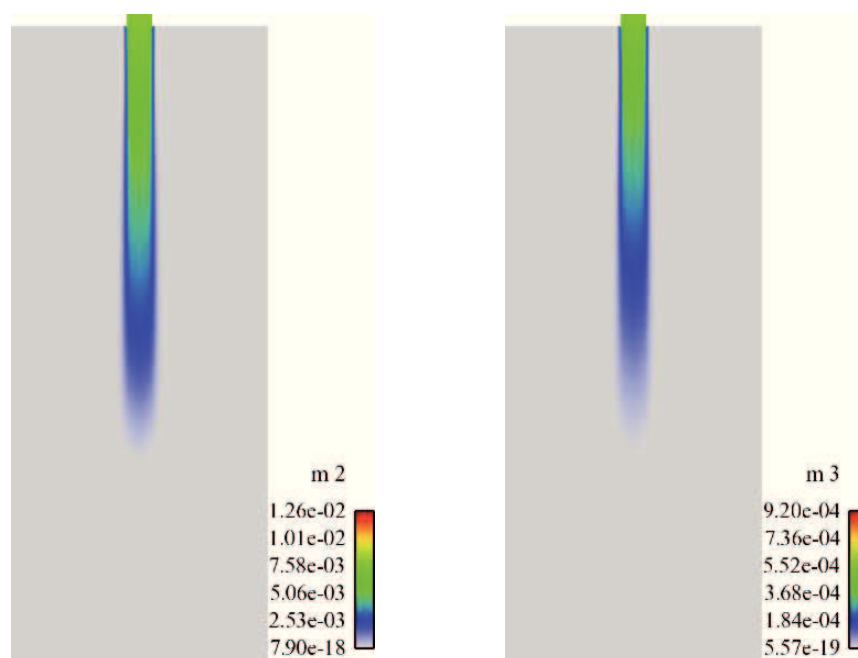


Figure 14.40: Results obtained with the EMSM model for a polydisperse evaporating spray made of droplets with a Sauter mean radius of  $D_{smr} = 80 \mu m$ , at time  $t = 0.1 s$ . Left : second order size moment ( $m_2$ ); Right : third order size moment ( $m_3$ ).

## 14.5 Conclusion

The purpose of this chapter is to highlight the critical points of the challenge consisting in implementing from scratch a whole spray model (the Eulerian spray model explained in Part II) in the industrial IFP-C3D code. The computing strategy is presented, and answers the two following difficulties: the first one is to integrate the numerical tools of the EMSM model preserving the general algorithmic of the ALE formalism; the second one is to ensure that no regression has been brought. The test cases conducted have successively lead to the validation of the implemented model ensuring the stability conditions induced by the system of equations on the moments, see Section 4.3. Eventually, the last tests demonstrate the feasibility of the EMSM model in injection case, and pave the way for further developments.

## Part V

# Synthesis of two-fluid models for separate-phase flows

# Introduction

As pointed out in the general introduction, this PhD is a contribution towards the project of IFP Energies nouvelles that is to couple, in an Eulerian framework, a description of the separate-phase flow close to the injector, and a description of the polydisperse spray resulting for secondary breakup, downstream of the injector. The core of this PhD work in this context has been to design a spray model able to describe polydispersity with sufficient precision, in a reasonable amount of time for industrial computations, see Part II. Moreover, this model and associated numerical schemes have been implemented in the IFP-C3D code developed at IFP Energies nouvelles, in preparation for further coupling with the existing separate-phase two-fluid model (see Part IV).

In order to couple these two models, one may have to bring some adaptations to them, not only in terms of computing, but also in terms of modeling. A good knowledge of the two-fluid model in the IFP-C3D code is then a first necessary condition. Descriptions of this model can be found in [215, 220, 12]. But more than the mere knowledge of this model, a sufficient background on the field of two-fluid models is required, since, in the further purpose of coupling with the Eulerian spray model, some adaptations will have to be done.

Therefore, the purpose of this chapter, is twofold:

- to present a general derivation methodology on two-fluid models, highlighting the critical steps where physical assumptions are made. A classification of the resulting models is proposed on the basis of these different assumptions. Then, general conditions are given to ensure the model consistency. This work is done in Chapter 15.
- to provide a review on two-fluid models in order to justify the model introduced in the IFP-C3D code in the perspective of these existing models. This work is done in Chapter 16.

# Chapter 15

## Derivation of a two-fluid model

For the purpose of coupling the Eulerian spray model introduced in Part II and Chapter 14, and the separate-phase two-fluid model already implemented in the IFP-C3D code [215, 220, 12], some background of these types of model is required. Yet, as mentioned in the introduction, Eulerian separate-phase two-fluid models and spray models are based on fundamentally different assumptions so that they represent distinct research fields.

The purpose of this chapter is therefore to provide a derivation methodology of separate-phase two-fluid models. The various assumptions made to tackle these issues are studied, which lead to models of different types. Despite the wide range of existing models, general conditions are required to ensure stability.

This chapter is organized as follows. First, the derivation strategy is discussed. The starting point consists in writing Navier-Stokes equations for both phase with jump condition: this is called the local instantaneous formulation. These equations can be directly solved in the context of sharp interface methods (VOF, Level Set). In other cases, and in ours in particular, averaged equations are derived. These averaged equations are further studied. A classification of these models is presented, according to the type of equilibrium assumed between phases. And finally, *sine qua non* conditions that must be fulfilled by a two-fluid model are given and explained.

### 15.1 Local instantaneous formulation

The starting point is to assume that each phase involved can be described as a continuum governed by the partial differential equations of continuum mechanics. The materials are separated by an interface, which we assume to be a surface. At the interface, jump conditions express conservation of mass and momentum. The equations of motion in each phase are:

$$\partial_t \rho \phi + \nabla_{\mathbf{x}} \cdot (\rho \phi \mathbf{u}) = \nabla_{\mathbf{x}} \cdot \boldsymbol{\psi} + S, \quad (15.1)$$

where the successive values of  $\phi$ ,  $\boldsymbol{\psi}$  and  $S$  are:

	Mass	Momentum	Energy
$\phi$	1	$\mathbf{u}$	$E = e + 1/2 \mathbf{u}^2$
$\boldsymbol{\psi}$	0	$-\mathbf{T} = -P\mathbf{I} + \boldsymbol{\tau}$	$-\mathbf{T} \cdot \mathbf{u} + \mathbf{q}$
$S$	0	$\mathbf{F}$	$\mathbf{F} \cdot \mathbf{u}$

These equations are valid in the interior of each phase. Here  $\rho$  denotes the density,  $\mathbf{u}$  the velocity,  $\mathbf{T}$  the stress tensor, and  $\mathbf{F}$  the body force density. Conservation of angular momentum becomes  $\mathbf{T} = \mathbf{T}^T$ , where the superscript T denotes transpose. At the interface one has:

1. jump condition for mass

$$[\rho(\mathbf{u} - \mathbf{u}_i) \cdot \mathbf{n}] = 0, \quad (15.2)$$

2. jump condition for momentum

$$[\rho \mathbf{u}(\mathbf{u} - \mathbf{u}_i) \cdot \mathbf{n} - \mathbf{T} \cdot \mathbf{n}] = \sigma \kappa \mathbf{n}. \quad (15.3)$$

Here,  $[\ ]$  denotes the jump condition across the interface,  $\mathbf{u}_i$  is the velocity of the interface,  $\sigma$  is the surface tension,  $\kappa$  is the mean curvature of the interface, and  $\mathbf{n}$  is the unit normal. We assume that  $\mathbf{n}$  points out of phase  $k$  and that the jump between  $f$  in phase  $k$  and  $f$  in phase  $l$  is defined by  $[f] = f^l - f^k$ . The mass of the interface has been neglected. Constitutive equations must be supplied to describe the behavior of each material involved. For example, if one material is an incompressible liquid, then specifying the value of  $\rho$  and assuming  $\boldsymbol{\tau} = \mu(\nabla_{\mathbf{x}}\mathbf{u} + (\nabla_{\mathbf{x}}\mathbf{u})^T)$  determines the nature of the fluid behavior in that phase. Similar considerations are possible for solid and gas. The resulting differential equations along with jump conditions provide a fundamental description of the detailed or exact flow.

At this stage, two strategies can be considered. First, one can directly solve the local instantaneous equations presented above in the context of a DNS. Since a key element of this system is the existence of an interface separating phases and associated discontinuities of properties across the fluid interface, sharp interface tracking methods have been designed. These methods rely on techniques such as Volume of Fluid (VOF), Level Set, Ghost Fluid, or a combination of these techniques. Recent advances can be found in [236, 91, 36, 109, 110]. At this level, any type of two-phase flow can be resolved, i.e there is no distinction between separate-phase and disperse-phase flows, since all the flow details are solved.

However, these methods are expensive in terms of computational cost, and usually, in an industrial context, the details of the flow are not required. For most purposes, averaged, or macroscopic flow information is sufficient. Fluctuations, or details in the flow must be resolved only to the extent that they impact the mean flow (like the Reynolds stresses does on the mean flow in a turbulent flow). In this case, no procedure is universally accepted and thus mainly two different approaches have been employed to obtain averaged equations.

A first approach involves bypassing the discrete nature of the separate phases through the use of averaging methods. In practise, averaging operators are applied to Eq. (15.1). In the averaging process, the various terms appearing in the macroscopic equations are shown to arise from appropriate microscopic considerations. For example, stress terms arise from microscopic stresses (pressure for instance) and also from velocity fluctuations (Reynolds stresses). Knowledge of this fact does give some insight into the formulation of constitutive equations. This method is used for example by authors such as Ishii [115] or Delhaye [53]. In the other approach, equations are postulated without the link with the microscopic description. In this case, conservation laws are determined for each phase and they account for the exchange of mass, momentum and energy between phase. Closures are provided through a thermodynamic analysis of the resulting system. This approach is used for example by Marle [162] or Baer and Nunziato [10] and is taken up by authors such as Saurel and Abgrall [206, 207]. Both approaches have been very fruitful but also complimentary. The averaged equations for both phases can be fully justified by an averaging process from the microscopic level of description. Yet, for a key quantity, the volume fraction, the link between the two levels of description is less obvious, so that a postulated approach has preferably been adopted. Therefore, as a first step, the derivation process of the averaged flow quantities is presented, and then the derivation of the other equations potentially involved in a two-fluid model are discussed as a second step.

## 15.2 Averaged two-fluid equations

### 15.2.1 Averaging procedure

An averaging operator is applied to the equations of the local instantaneous formulation. Averaged equations should be as simple as possible. Therefore, averaging operations must fulfill some calculation

rules:

$$\begin{aligned}
\langle f + \alpha \rangle &= \langle f \rangle + \langle \alpha \rangle, \\
\langle \langle f \rangle \alpha \rangle &= \langle f \rangle \langle \alpha \rangle, \\
\langle \theta \rangle &= \theta, \\
\langle \partial_t f \rangle &= \partial_t \langle f \rangle, \\
\langle \nabla_{\mathbf{x}} f \rangle &= \nabla_{\mathbf{x}} (\langle f \rangle),
\end{aligned} \tag{15.4}$$

where  $\theta$  is a coefficient. The first three of these relations are called Reynolds rules, the fourth is called Leibniz rule, and the fifth is called Gauss rule.

Some examples of commonly used averages are time averaging:

$$\langle f \rangle (t, \mathbf{x}) = \frac{1}{T} \int_{t-T}^t f(t, \mathbf{x}) dt, \tag{15.5}$$

where  $T$  is an averaging time scale; the space average

$$\langle f \rangle (t, \mathbf{x}) = \frac{1}{\|\mathbf{L}\|^3} \int_{\mathbf{x}-L/2}^{\mathbf{x}+L/2} \langle f \rangle (t, \mathbf{x}) d\mathbf{x}, \tag{15.6}$$

where  $\|\mathbf{L}\|$  is an averaging length scale; and the ensemble average:

$$\langle f \rangle (t, \mathbf{x}) = \frac{1}{N} \sum_{\mu=1}^N f(t, \mathbf{x}, \mu), \tag{15.7}$$

where  $f(t, \mathbf{x}, \mu)$  denotes a realization of the quantity  $f$  for the  $\mu^{\text{th}}$  sample.

The relations to experiments of the different types of averaging procedure are discussed in [53].

In this chapter, the governing equations are derived by the ensemble averaging process, as it appears to be the most general. Nevertheless, if there is a conceptual different between the nature of the filter used, yet, in the actual derivation of the two-fluid equations, this different has no impact since interaction terms will be formally written and will have to be closed. The closure of this terms characterizes the two-fluid model. This point is discussed at the end of this section.

Two different methods to derive two-fluid equations from the microscopic level of description exist. Both are exposed here.

### Direct application of the averaging operator

The first one consists in directly applying the averaging operator to Eq. (15.1). This method is used in [115, 53] for example. In order to describe it, let us consider, among the  $N$  samples, that  $N_k$  samples being such that the point  $\mathbf{x}$  pertains to phase  $k$  at time  $t$  and  $N_i$  such that point  $\mathbf{x}$  pertains to the interface at time  $t$ . In two-phase flows, index  $k$  can either be  $g$  or  $l$  representing gas or liquid respectively. It follows from these definitions, that:

$$N = N_1(t, \mathbf{x}) + N_2(t, \mathbf{x}) + N_i(t, \mathbf{x}). \tag{15.8}$$

The residence statistical-fraction, called the volume fraction in this manuscript,  $\alpha_k$ , and the  $k$ -weighted statistical average  $\langle f \rangle_k$  are defined by the following relations:



$$\begin{aligned}\alpha_k(t, \mathbf{x}) &= \frac{N_k(t, \mathbf{x})}{N}, \\ \langle f \rangle_k(t, \mathbf{x}) &= \frac{1}{N_k} \sum_{\mu=1}^{N_k(t, \mathbf{x})} f_k(t, \mathbf{x}, \mu).\end{aligned}\tag{15.9}$$

The term  $\alpha_k$  is also the probability of finding phase  $k$  at a given point in space and at a given time. It is recognized [53] that the finite sum

$$\sum_{\mu=1}^{N_k(t, \mathbf{x})} f_k(t, \mathbf{x}, \mu),\tag{15.10}$$

is a piecewise continuous function of  $\mathbf{x}$  and  $t$ . By adding term by term this balance equation written for each of the  $N_k(t, \mathbf{x})$  samples where point  $\mathbf{x}$  belongs to phase  $k$  at time  $t$ , we obtain

$$\sum_{\mu=1}^{N_k(t, \mathbf{x})} \partial_t(\rho_k \phi_k) + \sum_{\mu=1}^{N_k(t, \mathbf{x})} \nabla_{\mathbf{x}} \cdot (\rho_k \phi_k \mathbf{u}_k) = \sum_{\mu=1}^{N_k(t, \mathbf{x})} \nabla_{\mathbf{x}} \cdot \psi_k + \sum_{\mu=1}^{N_k(t, \mathbf{x})} S_k.\tag{15.11}$$

Applying the particular form of the Leibniz and Gauss theorems given in [53], and thanks to definitions Eq. (15.9), we obtain:

$$\begin{aligned}\partial_t \alpha_k \langle \rho \phi \rangle_k + \nabla_{\mathbf{x}} \cdot (\alpha_k \langle \rho \phi \mathbf{u} \rangle_k) &= \nabla_{\mathbf{x}} \cdot (\alpha_k \langle \psi \rangle_k) + \alpha_k \langle \rho S \rangle_k \\ &\quad - \frac{1}{N_i} \sum_{\mu=1}^{N_i(t, \mathbf{x})} \frac{N_i}{N} \frac{1}{|\mathbf{u} \cdot \mathbf{n}_k|_j} (\dot{m}_k \phi_k + \psi_k \cdot \mathbf{n}_k) |\partial_t \chi_k|,\end{aligned}\tag{15.12}$$

where  $\dot{m}_k$  is the mass flux of phase  $k$  across the interface, and  $\chi_k$  is the phase function, defined to be:

$$\chi_k = \begin{cases} 1 & \text{if } \mathbf{x} \text{ is in phase } k, \\ 0 & \text{otherwise.} \end{cases}\tag{15.13}$$

A specific length  $\mathcal{L}_j(t, \mathbf{x})$  can be introduced, defined by

$$\mathcal{L}_j(t, \mathbf{x}) = \frac{N}{N_i} \mathbf{u}_i \cdot \mathbf{n}_k|_j \frac{1}{|\partial_t \chi_k|},\tag{15.14}$$

where  $j$  denotes the  $j^{\text{th}}$  interface passing through point  $\mathbf{x}$  at time  $t$  among the  $N$  samples. In order for  $\mathcal{L}_j(t, \mathbf{x})$  to have a physical significance and since  $|\partial_t \chi_k|$  is infinite,  $N$  must be chosen to be infinite and in such way that  $\frac{N}{N_i}$  is infinite. In that case, Eq. (15.12) becomes

$$\partial_t \alpha_k \langle \rho \phi \rangle_k + \nabla_{\mathbf{x}} \cdot (\alpha_k \langle \rho \phi \mathbf{u} \rangle_k) = \nabla_{\mathbf{x}} \cdot (\alpha_k \langle \psi \rangle_k) + \alpha_k \langle \rho \phi \rangle_k - \frac{1}{N_i} \sum_{j=1}^{\infty} \frac{1}{\mathcal{L}_j} (\dot{m}_k \phi_k + \psi_k \cdot \mathbf{n}_k),\tag{15.15}$$

where  $\sum_{j=1}^{\infty}$  means that we deal with an infinite sum.

### Use of the phase function in the averaging procedure

The second method of derivation suggests to use the phase function  $\chi_k(t, \mathbf{x})$  directly in the local instantaneous equations. This method is used by Marle [162], Drew [64, 65], or Iyer [116] and exposed here. The phase function follows the instantaneous interface between the two fluids or the two phase and is

thus convected by the instantaneous interface velocity  $\mathbf{u}_i$ . So  $\chi_k$  is governed by the following transport equation:

$$\partial_t \chi_k + \mathbf{u}_i \cdot \nabla_{\mathbf{x}} \chi_k = 0. \quad (15.16)$$

Another property of the phase indicator function is that the gradient of  $\chi_k$  identifies the interface so that any quantity multiplying  $\nabla_{\mathbf{x}} \chi_k$  is evaluated at the phase  $k$  side of the interface. The function  $\chi_k$  is actually a generalized function, a Heavyside function precisely. The proper demonstration of Eq. (15.16) with a set of test functions  $\Phi$  can be found in [64]. It can also be shown that  $\nabla_{\mathbf{x}} \chi_k$  is a Dirac distribution localized at the interface:

$$\nabla_{\mathbf{x}} \chi_k = -\mathbf{n}_{k,i} \delta_i. \quad (15.17)$$

where  $\mathbf{n}_{k,i}$  is the unit vector normal to the interface pointing outside phase  $k$ .

Now consider the instantaneous single-phase transport equation Eq. (15.1). The procedure here is first to multiply this equation by  $\chi_k$  and then the whole equation is ensemble averaged. The resulting equation is:

$$\partial_t \langle \chi_k \rho \phi \rangle + \nabla_{\mathbf{x}} \cdot \langle \chi_k \rho \phi \mathbf{u} \rangle = \nabla_{\mathbf{x}} \cdot \langle \chi_k \boldsymbol{\psi} \rangle + \langle \chi_k S \rangle + \langle \rho \phi (\partial_t \chi_k + \mathbf{u} \cdot \nabla_{\mathbf{x}} \chi_k) \rangle - \nabla_{\mathbf{x}} \cdot (\boldsymbol{\psi} \cdot \nabla_{\mathbf{x}} \chi_k), \quad (15.18)$$

The symbol has the same significance as in the first method. Substituting the relation from Eq. (15.16), we get:

$$\partial_t \langle \chi_k \rho \phi \rangle + \nabla_{\mathbf{x}} \cdot \langle \chi_k \rho \phi \mathbf{u} \rangle = \nabla_{\mathbf{x}} \cdot \langle \chi_k \boldsymbol{\psi} \rangle + \langle \chi_k S \rangle + \langle [\rho \phi (\mathbf{u} - \mathbf{u}_i) - \boldsymbol{\psi}] \cdot \nabla_{\mathbf{x}} \chi_k \rangle. \quad (15.19)$$

The last term in Eq. (15.19) represents the averaged interface transport source term as  $\nabla_{\mathbf{x}} \chi_k$  identifies the interface and causes the discontinuous quantities multiplying it to be evaluated on the phase- $k$  side of the interface. This term usually requires modeling from physical considerations and it depends on the quantity  $\phi$  which is being evaluated. The averaging procedure described in this section will now be applied to formulate the mass, momentum and energy equations of the two-fluid model. The description of mass, momentum, and energy follows that of [64] and [116].

### 15.2.1.1 Conservation of mass

The conservation of mass for phase  $k$  is obtained by setting  $\phi = 1$  in Eq. (15.19). The following relations are used:

$$\begin{aligned} \alpha_k &= \langle \chi_k \rangle, \\ \alpha_k \tilde{\rho}_k &= \langle \chi_k \rho \rangle, \\ \alpha_k \tilde{\rho}_k \tilde{\mathbf{u}}_k &= \langle \rho \chi_k \mathbf{u} \rangle. \end{aligned} \quad (15.20)$$

The quantity  $\alpha_k$ , the volume fraction of phase  $k$  is defined in Eq. (15.9). The term  $\tilde{\rho}_k$  is the phase averaged material density of phase  $k$  and  $\tilde{\mathbf{u}}_k$  is the density Favre-weighted average of the velocity of phase  $k$ . Using the relations given in Eq. (15.1), the ensemble averaged conservation of mass equation for phase  $k$  is written as

$$\partial_t (\alpha_k \tilde{\rho}_k) + \nabla_{\mathbf{x}} \cdot (\alpha_k \tilde{\rho}_k \tilde{\mathbf{u}}_k) = \Gamma_k, \quad (15.21)$$

where  $\Gamma_k = \langle \rho [\mathbf{u} - \mathbf{u}_i] \cdot \nabla_{\mathbf{x}} \chi_k \rangle$  is the source term due to phase-change, i.e. evaporation or condensation. So  $\Gamma_k$  is an average mass flow rate due to the difference in the instantaneous velocity of phase  $k$  and the instantaneous interfacial velocity that occurs due to phase change. The evaluation of this source term requires further modeling, discussed in Chapter 16. Given the assumption of interface with a null mass, the jump condition at the interface requires that

$$\Gamma_g + \Gamma_l = 0. \quad (15.22)$$

Eq. (15.22) ensures that the total mass is conserved. Volume conservation requires that:

$$\alpha_g + \alpha_l = 0. \quad (15.23)$$

### 15.2.1.2 Conservation of momentum

The ensemble-average momentum equation is obtained by setting  $\phi = \mathbf{u}$  in Eq. (15.19). The convective term in Eq. (15.19) then becomes

$$\begin{aligned} \langle \chi_k \rho \mathbf{u} \mathbf{u} \rangle &= \alpha_k \tilde{\rho}_k \mathbf{u}_k \tilde{\mathbf{u}}_k \\ &= \alpha_k \tilde{\rho}_k \tilde{\mathbf{u}}_k \tilde{\mathbf{u}}_k + \alpha_k \rho_k (\mathbf{u}_k \tilde{\mathbf{u}}_k - \tilde{\mathbf{u}}_k \tilde{\mathbf{u}}_k). \end{aligned} \quad (15.24)$$

The term  $\chi_k \tilde{\rho}_k (\mathbf{u}_k \tilde{\mathbf{u}}_k - \tilde{\mathbf{u}}_k \tilde{\mathbf{u}}_k)$  is usually called the turbulent stress tensor in the context of two-fluid models. The turbulent stress tensor arises due to the correlation between the fluctuating velocity components and it is analogous to the Reynolds stress tensor in single-phase turbulent flows. Using this representation for the turbulent stress and dropping the overbars for the averaged quantities, the convective term can be written as:

$$\langle \chi_k \rho \mathbf{u} \mathbf{u} \rangle = \alpha_k \tilde{\rho}_k \tilde{\mathbf{u}}_k \tilde{\mathbf{u}}_k + \alpha_k \boldsymbol{\tau}_k^t, \quad (15.25)$$

where  $\boldsymbol{\tau}_k^t$  is the turbulent stress tensor of phase  $k$ . The diffusive flux  $\boldsymbol{\psi}$  in this case is the stress tensor  $\mathbf{T} = -P\mathbf{I} + \boldsymbol{\tau}$ , where  $P$  is the instantaneous pressure and  $\mathbf{T}$  is the shear stress tensor. The interfacial momentum transfer term is given by:

$$\mathbf{M}_k = \langle [\rho \mathbf{u}(\mathbf{u} - \mathbf{u}_i) - \mathbf{T}] \cdot \nabla_{\mathbf{x}} \chi_k \rangle. \quad (15.26)$$

*Remark:* It would be however interesting to draw a parallel with the kinetic model for disperse flow derived in Chapter 9. In this context,  $\chi_k \tilde{\rho}_k (\mathbf{u}_k \tilde{\mathbf{u}}_k - \tilde{\mathbf{u}}_k \tilde{\mathbf{u}}_k)$  represents the covariance matrix of the velocity distribution function, with no relation to turbulence. The EMVM model described in Chapter 9 solves this term in order to capture particle crossings. But in the case of two-fluid models, fluids are considered continuous media so that no kinetic approach can be considered. This is why the term  $\chi_k \tilde{\rho}_k (\mathbf{u}_k \tilde{\mathbf{u}}_k - \tilde{\mathbf{u}}_k \tilde{\mathbf{u}}_k)$  is always considered a fluctuation term due to turbulence and is always modeled. This explains why no crossing can be described in the context of two-fluid models.

The interfacial momentum term can be split into contributions from the phase change, the pressure and the interfacial shear [64]:

$$\mathbf{M}_k = \Gamma_k \mathbf{u}_{k,i} + P_{k,i} \nabla_{\mathbf{x}} \alpha_k + \mathbf{M}_k^d, \quad (15.27)$$

where  $\mathbf{M}_k \mathbf{u}_{k,i} = \langle [\rho \mathbf{u}(\mathbf{u} - \mathbf{u}_i)] \cdot \nabla_{\mathbf{x}} \chi_k \rangle$  is the momentum source term due to the phase change,  $\mathbf{u}_{k,i}$  is the averaged interfacial velocity and  $P_{k,i}$  is the averaged interfacial pressure. The term  $\mathbf{M}_k^d$  is referred to as the interfacial force density.

$$\mathbf{M}_k^d = \langle (P - P_i) \nabla_{\mathbf{x}} \chi_k - \boldsymbol{\tau} \cdot \nabla_{\mathbf{x}} \chi_k \rangle, \quad (15.28)$$

where  $\mathbf{M}_k^d$  represents the transfer of momentum from one phase to the other due to shear forces at the interface. It includes the forces of drag, virtual mass, lift, Basset and Magnus forces. This term requires modeling from a physical perspective and depends upon the type of flow. For many authors, among them [10, 206], a closure of  $\mathbf{M}_k^d$  is to introduce a drag term between the two phases, although both fluids are considered to be inviscid. This interaction term is therefore sometimes called non viscous drag term. Using the manipulations performed till now, the ensemble-averaged momentum equation for phase  $k$  is written as:

$$\partial_t (\alpha_k \tilde{\rho}_k \tilde{\mathbf{u}}_k) + \nabla_{\mathbf{x}} \cdot (\alpha_k \tilde{\rho}_k \tilde{\mathbf{u}}_k \tilde{\mathbf{u}}_k) = -\alpha_k \nabla_{\mathbf{x}} \tilde{P}_k + \nabla_{\mathbf{x}} \cdot \alpha_k (\tilde{\boldsymbol{\tau}}_k + \boldsymbol{\tau}_k^t) + \Gamma_k \mathbf{u}_{k,i} + (P_{k,i} - \tilde{P}_k) \nabla_{\mathbf{x}} \alpha_k + \mathbf{M}_k^d, \quad (15.29)$$

The momentum jump condition at the interface requires that the sum of the interfacial forces for both phases be equal to the average surface tension force [115]. After summing Eq. (15.27) for the gas and liquid phases, we get:

$$\mathbf{M}_g^d + P_{g,i} \nabla_{\mathbf{x}} \alpha_g + \mathbf{M}_l^d - P_{l,i} \alpha_g = \sigma \kappa \nabla_{\mathbf{x}} \alpha_g, \quad (15.30)$$

where  $\kappa$  is the average mean curvature of the interface and  $\sigma$  is the surface tension. The average surface tension force per unit area is equal to the different in the pressures of the two phases [115]

$$(P_{g,i} - P_{l,i}) \nabla_{\mathbf{x}} \alpha_g = \sigma \kappa. \quad (15.31)$$

Combining Eq. (15.30) and Eq. (15.31) we get the momentum jump condition:

$$\mathbf{M}_g^d + \mathbf{M}_l^d = 0. \quad (15.32)$$

Therefore, only one of the interface forces  $\mathbf{M}_g^d$  or  $\mathbf{M}_l^d$  need to be specified. Moreover, in Eq. (15.29), the pressure of phase  $k$  at the interface  $P_{k,i}$  is distinguished from the pressure in phase  $k$ , which is noted  $P_k$ . This distinction proves to be paramount when the hyperbolic character of the two-fluid system is discussed in Section 15.4. Nevertheless, a common assumption made in the literature is to neglect surface tension effect as done in [115], so that the interfacial pressures can be equaled

$$P_{g,i} = P_{l,i}. \quad (15.33)$$

One should be fully aware that this assumption is absolutely not related to the distinction between interface pressure of phase  $k$   $P_{k,i}$  and pressure in phase  $k$ ,  $P_k$ . This completes the formulation of the momentum equation. The turbulent stress and the interfacial transfer terms need to be modeled, according to the physical context the model is designed for.

### 15.2.1.3 Energy equation

The ensemble-averaged energy equation is obtained by setting  $\phi = E = e + \mathbf{u} \cdot \mathbf{u} / 2$  in Eq. (15.19), where  $E$  is the total energy that is the sum of the internal energy  $e$  and the kinetic energy. Following [115], the averaged energy equation is written as

$$\begin{aligned} \partial_t (\alpha_k \tilde{\rho}_k \tilde{E}_k) + \nabla_{\mathbf{x}} \cdot (\alpha_k \tilde{\rho}_k \tilde{E}_k \tilde{\mathbf{u}}_k) &= -\nabla_{\mathbf{x}} \cdot (\alpha_k \tilde{\rho}_k \tilde{\mathbf{u}}_k \tilde{P}_k) - \nabla_{\mathbf{x}} \cdot (\alpha_k (\tilde{\mathbf{q}}_k + \mathbf{q}_k^t)) \\ &+ \nabla_{\mathbf{x}} \cdot (\alpha_k (\tilde{\boldsymbol{\tau}}_k + \boldsymbol{\tau}_k^t) \cdot \tilde{\mathbf{u}}_k) + \Pi_k. \end{aligned} \quad (15.34)$$

The two terms of the LHS of Eq. (15.34) are the unsteady and the convective transfer terms. The first term on the RHS is the pressure work, the second term is the sum of the molecular and turbulent heat flux, the third term is the work done by molecular shear forces and turbulent stresses and the fourth term is the interface energy transfer. The interface transport source term can be split into different components arising from different physical processes:

$$\Pi_k = \Gamma_k E_{k,i} + \Pi_k^d + \mathbf{M}_k^d \cdot \mathbf{u}_{k,i}. \quad (15.35)$$

where  $E_{k,i}$  is the total energy localized at the interface, and  $\Pi_k^d$  is the total energy production at the interface. The first term represents the energy transferred from one phase to the other due to the mass source resulting from phase change. The second term represents the production of total energy at the interface. The interested reader can refer to [115] for details. The third term represents the work done by shear forces at the interface and it is the product of the interface force density and the interface velocity. A distinction is made between the interfacial velocity of phase  $k$   $\mathbf{u}_{k,i}$ , and the velocity of phase  $k$ , like for the pressure, and in the same way, authors postulate the equality of interfacial velocities:

$$\mathbf{u}_{g,i} = \mathbf{u}_{l,i} = \mathbf{u}_i. \quad (15.36)$$

In subsequent discussions the symbols for the averages will be dropped for convenience and all quantities will be ensemble-averaged unless otherwise stated. The final two-fluid system of equations is summarized here:

$$\begin{aligned} \partial_t(\alpha_k \rho_k) + \nabla_{\mathbf{x}} \cdot (\alpha_k \rho_k \mathbf{u}_k) &= \Gamma_k, \\ \partial_t(\alpha_k \rho_k \mathbf{u}_k) + \nabla_{\mathbf{x}} \cdot (\alpha_k \rho_k \mathbf{u}_k \mathbf{u}_k) &= -\alpha_k \nabla_{\mathbf{x}} P_k + \nabla_{\mathbf{x}} \cdot \alpha_k (\boldsymbol{\tau}_k + \boldsymbol{\tau}_k^t) \\ &\quad + \underbrace{\Gamma_k \mathbf{u}_{k,i} + (P_{k,i} - P_k) \nabla_{\mathbf{x}} \alpha_k + \mathbf{M}_k^d}_{\mathbf{M}_k}, \end{aligned} \quad (15.37)$$

$$\begin{aligned} \partial_t(\alpha_k \rho_k E_k) + \nabla_{\mathbf{x}} \cdot (\alpha_k \rho_k E_k \mathbf{u}_k) &= -\nabla_{\mathbf{x}} \cdot (\alpha_k \rho_k \mathbf{u}_k P_k) - \nabla_{\mathbf{x}} \cdot (\alpha_k (\mathbf{q}_k + \mathbf{q}_k^T)) + \nabla_{\mathbf{x}} \cdot (\alpha_k (\boldsymbol{\tau}_k + \boldsymbol{\tau}_k^t) \cdot \mathbf{u}_k) \\ &\quad + \underbrace{\Gamma_k E_{k,i} + \Pi_k^d + \mathbf{M}_k^d \cdot \mathbf{u}_{k,i}}_{\Pi_k}, \end{aligned}$$

with the interfacial terms verifying:

$$\begin{aligned} \Gamma_l + \Gamma_g &= 0, \\ \mathbf{M}_l + \mathbf{M}_g &= 0, \\ \Pi_l + \Pi_g &= 0. \end{aligned} \quad (15.38)$$

Systems (15.37) and (15.38) represent the first step of a two-fluid model derivation. However, the path is still long before finalizing a completely closed model. Among the numerous unclosed terms, the volume fraction  $\alpha_k$  is an essential quantity when dealing with multi-phase flows, with the same importance as classical terms of mass, momentum and energy. The way it is written does not allow to solve  $\alpha_k$  as an independent variable. On the other hand, it is not possible to properly derive a formal equation on  $\alpha_k$  through averaging operators like it has been done for mass or momentum. Two different strategies to write a transport equation on the volume fraction were thus suggested in the literature. They are presented in the next paragraph.

### 15.2.2 The volume fraction equation: taking into account non equilibrium between the phases

Two different cases have first to be distinguished, whether the liquid phase is considered incompressible or not. The problem becomes trivial when the liquid phase is considered incompressible, since  $\rho_l$  is constant, and so the mass equation degenerates into the equation on  $\alpha$ . But, things are much more complicated in the case of two compressible flows. This comes from the fact that it has not been possible so far to properly derivate the macroscopic equation on the volume fraction from the microscopic equation by averaging process. In order to point out this difficulty, we try to apply a space averaging operator to Eq. (15.16):

$$\partial_t \langle \chi_k \rangle + \langle \mathbf{u} \cdot \nabla_{\mathbf{x}} \chi_k \rangle = 0. \quad (15.39)$$

The term  $\langle \mathbf{u} \cdot \nabla_{\mathbf{x}} \chi_k \rangle = \frac{1}{\|\mathbf{L}\|^3} \int_{\mathbf{x}-\mathbf{L}/2}^{\mathbf{x}+\mathbf{L}/2} \mathbf{u} \cdot (-\mathbf{n}_k) \delta_i d\mathbf{x}$  writes:

$$\langle \mathbf{u} \cdot \nabla_{\mathbf{x}} \chi_k \rangle = \frac{1}{\|\mathbf{L}\|^3} \int_{S_i} \mathbf{u} \cdot (-\mathbf{n}_i) dS, \quad (15.40)$$

since  $\mathbf{u}_i$  is only defined on the interface, where  $\int_{S_i}$  represents the integral along the interface. Therefore, there is no possibility to give a differential expression for the term  $\langle \mathbf{u} \cdot \nabla_{\mathbf{x}} \chi_k \rangle$  in order to write the equation on  $\alpha$  as a conservative equation. Consequently, there is no relation between the microscopic interfacial velocity  $\mathbf{u}_i$  depending on the interactions between the phase at a microscopic scale, and the

averaged interfacial velocity  $\langle \mathbf{u} \rangle$ , appearing in the resulting averaged equation of the two-fluid system in Eq. (15.37).

Historically, two different perspectives were adopted. The first one was to write the *a priori* equation

$$\partial_t \alpha + \mathbf{u} \cdot \nabla_{\mathbf{x}} \alpha = S, \quad (15.41)$$

where  $\mathbf{u}$  and  $S$  are a velocity and a source terms that have to be closed so that the system stayed hyperbolic. These closures were done through the use of the so-called 'topological relations'. The origin of this appellation comes from the fact that the averaging operator loses some information on the interface topology [25, 13]. In the second approach, people adopted a completely different point of view considering that the equation on  $\alpha$  must be deduced from the equations of state (EOS). The term  $\alpha$  becomes an internal variable, like energy, pressure or density, and the resulting closed equation must be admissible, i.e it should ensure the second principle of thermodynamics. This approach is more consistent than the first one since the hyperbolic character of the system of equations is also ensured. Baer and Nunziato [10] were the first authors to derive the equation on  $\alpha$  this way. This approach was taken up by Saurel [207] or Lallemand [139]. The resulting equation reads:

$$\partial_t \alpha + \mathbf{u}_i \cdot \nabla_{\mathbf{x}} \alpha = S_{\alpha}. \quad (15.42)$$

The terms  $\mathbf{u}_i$  and  $S_{\alpha}$  are discussed in Section 15.5. One notes that  $\mathbf{u}_i$  here refers to the averaged interfacial velocity and is *a priori* different from the averaged phase velocities  $\mathbf{u}_l$  and  $\mathbf{u}_g$ .

### 15.2.3 The notion of area density to better account for the flow topology

The aim of the surface density  $\Sigma$  is to better account for the interface topology. This quantity may be involved in cases where the volume fraction  $\alpha$  is accessed, in order to provide a more accurate closure of the interaction terms. Indeed, with these two quantities, a mean droplet size can be reconstructed by the relation  $d = \frac{6\alpha}{\Sigma}$ . This approach is particularly suited to account for any physical process responsible for surface density variation. One can mention coalescence, atomization, nucleation, condensation. The study of the surface density equation was not investigated in this PhD. We refer to [182, 220] for discussions about this topic. Let us nevertheless note that the concept of surface area density was initially a concept used in the combustion field [33].

### 15.2.4 Closure challenges and consistency conditions

At this level, the dynamic equations of a two-fluid model have been written. As it is seen in system (15.37), numerous terms have to be closed. The actual modeling work then begins, depending on the physical process studied. Since multi-phase flows occur in a lot of various physical phenomena, various closures and then various models have been proposed. It is therefore a tedious work to put the models now proposed in the literature in perspective and to do a comparative study of their strengths and weaknesses. This work is however essential in order to identify the most suitable solutions already proposed for a given physical problem. The purpose of this chapter is to provide a methodology for the design of a two-fluid model by distinguishing different steps of the closure procedure.

The first aspect to be aware of when dealing with multi-phase flows is that the number of equations is not set, and can vary from three with the same system of equations as for a single-phase, to seven with each conservation equation written for both phase and the transport equation for the volume fraction, or even eight if one adds the equation on surface density. These differences are significant of the different equilibrium hypotheses made between the phases. The strongest of these assumptions is the complete kinematic and thermodynamical equilibrium, i.e. equilibrium of velocities, pressures and temperatures (and chemical potentials in case reactive flows are concerned). Within this assumption, the phases are considered two species of a same fluid, and the multi-phase flow reduces to a multi-species flow. In other contexts, no equilibrium assumption is made, so that all the primary quantities for both phases

have to be solved. The volume fraction plays a key role in the assessment of equilibrium between phases. When  $\alpha$  is solved as a primary variable of the system, i.e. when the model contains a transport equation on  $\alpha$ , its resolution allows to reach quantities of each phase, and not of the mixture. By doing that, the volume fraction introduces the notion of a separating interface between the two phases. On the other hand, if  $\alpha$  is derived from other quantities of the system, or when  $\alpha$  cannot even be reached, the notion of interface disappears. A classification of two-fluid models relying on the equilibrium assumption is provided in Section 15.3.

If we consider the two-fluid system (15.37) and Eq. (15.42), we highlight some necessary conditions the two-fluid model has to verify in order to be consistent. First, a two-fluid model has to be conservative. This means that the model has to conserve the total mass, momentum and energy of the fluids. By summing on the two phases equations of system (15.37), the resulting system should formally write like the Euler or Navier-Stokes equations. Physically, the fluid considered is the mixture of the two phases, with the characteristic:

$$\begin{aligned}\rho_m &= \sum_k \alpha_k \rho_k, \\ \rho_m \mathbf{u}_m &= \sum_k \alpha_k \rho_k \mathbf{u}_k, \\ \rho_m E_m &= \sum_k \alpha_k \rho_k E_k.\end{aligned}\tag{15.43}$$

Note that no interfacial term or exchange term between phases should appear in the resulting system. The other property linked to this one is that the model should degenerate correctly when only one fluid is present.

Focusing now on the unclosed terms in system (15.37), one can identify different types of closure. The first one concerns, for each phase, terms closed through the Equation of State (EOS) and fluctuating terms due to turbulence:  $\boldsymbol{\tau}_k^t$  and  $\mathbf{q}_k^t$ . They are closed following the same approaches developed for single-phase flows. The second type concerns interfacial terms:  $P_{k,i}$  and  $\mathbf{u}_i$ . They are factors of differential terms, in the momentum and energy conservation equations. Consequently their expression conditions the wave dynamics of the system. The second step of the methodology is then to express  $P_{k,i}$  and  $\mathbf{u}_i$  in a way that ensures the hyperbolic character of the system. The third type of unclosed terms gathers all the exchange terms:  $\Gamma_k$ ,  $\mathbf{M}_k$ , and  $\Pi_k$ . Their closure obviously depends on the type of phenomenon studied. Nonetheless, irrespective of the physical process studied, they should ensure the system to be dissipative, i.e. to satisfy the second principle of thermodynamics. The fulfillment of this third condition provides admissible closure for the exchange terms. As stated by Baer and Nunziato [10] these expressions provide useful information in formulating the constitutive equations for the final determination of the exchange terms.

### 15.3 General classification of two-fluid models

The previous section was dedicated to the derivation of the formal equation resulting in system (15.37), and Eq. (15.42). Yet, in the literature, the number of equations solved may be different from one model to another. This is due to the nature of the equilibrium assumption made between the phases. The purpose of this section is to provide a classification of models in terms of the equilibrium assumptions made. This classification ranges from models with the strongest assumption to models making no assumption. The critical importance of the role played by the volume fraction  $\alpha$  is highlighted, since it enables the treatment of an interface between the phases. In this section, only models considering both phases compressible are considered. When one phase is considered incompressible, the equation on the volume fraction reduces to the equation on partial masses, so the description of an interface flow becomes straightforward. This is the case for the multi-fluid and EMSM model derived in Chapter 3 and Chapter 4, where not only we assumed that the liquid was incompressible, but we also assumed spherical particles, and so spherical interfaces.

We define the different equilibrium notions used in the following:

- kinematic equilibrium:  $\mathbf{u}_l = \mathbf{u}_g$ ,
- mechanical equilibrium:  $P_l = P_g$ ,
- thermal equilibrium:  $T_l = T_g$ ,
- the thermodynamic equilibrium includes mechanical and thermal equilibria.

### 15.3.1 The critical issue of interface description

For numerical simulation of multi-species flows, as done, for example, in combustion problems, the model that is mostly used is written in terms of mass fraction equations and partial pressures. But the notion of partial pressure is valid only at local thermodynamic equilibrium. When a control volume contains several gases perfectly mixed together, this notion is valid in most cases. In the case of multi-phase flows, when fluids are not well mixed, as when an interface exists, physics of thermal exchange occurs only in a tiny part of the control volume: at the interface. So each fluid has its own temperature and the assumption of local thermodynamic equilibrium is no longer valid. The numerical errors induced by such an assumption were pointed out by Abgrall [2] on a one-dimensional shock tube test case with two gases of different specific heat ratios. Given this consideration, it appears that a critical characteristic of a two-fluid model is its ability to reproduce the thermodynamic conditions at an interface.

### 15.3.2 Mono-fluid models

The first type of two-fluid model consist in the Euler or Navier-Stokes system of equations written for neither of the phases but for a mixture fluid corresponding to an average of the phase, with quantities defined in system (15.43). This is the easiest two-fluid model being found in the literature. The EOS is written for this mixture phase, and can be obtained through several ways. The law can either be tabulated, reproduce the phase diagram liquid-vapor (cubic law), or be a linear combination of the EOS of the pure fluids. Since the equations are written for the averaged quantities, no interfacial nor exchange terms appear. However, the reduced number of equations goes hand in hand with strong assumptions between phases. As only the characteristics of the mixture fluid can be assessed, the phases are considered to be in thermodynamic equilibrium (equality of pressures and temperatures) and velocity equilibrium. These assumptions go at odds with the description of an interface. As justified by Saurel and Abgrall in [206], the interfacial conditions are equality of pressures and normal velocities. This type of model can only be used when only the characteristics of the mixture are needed, and not the details of each phase. This model is also known as Homogeneous Equilibrium Model (HEM).

### 15.3.3 Two-fluid mixture models

In this kind of models, the three equations of the mixture model are taken up, and are augmented with an additional equation. This equation can be a conservation equation of one of the partial masses

$$\partial_t \alpha_k \rho_k + \nabla_{\mathbf{x}} \cdot (\alpha_k \rho_k \mathbf{u}_m) = \Gamma_k, \quad (15.44)$$

where a term of mass exchange appears [77]. This model is inspired from models designed for multi-species flows. If details of the partial mass of the flow  $\alpha_k \rho_k$  are provided, when both phases are considered compressible, quantities of phase  $k$  still cannot be assessed, and therefore the equilibrium assumptions are the same as for the mixture model : thermodynamic and kinematic.

On the other hand, some authors like Karni [133] or Abgrall [2] succeed in describing an interface between phases, even at thermodynamic equilibrium. They consider that both fluids follow the same kind of EOS, but with parameters which may differ. Therefore, instead of adding a conservative equation on the partial mass, they introduce non-conservative transport equations for the parameters of the EOS. If a perfect



gas EOS is considered like in [5], only one parameter is transported. In the case a stiffened gas EOS is considered like in [206], two parameters are transported. But, since this method is still based on a thermodynamic equilibrium, it fails to describe interface between gas and liquid for example. Moreover, it leads to conservation errors regarding the partial mass of the various fluids yielding inaccurate internal energies and temperatures at the interface. We chose to classify this model as a two-fluid mixture model and not an interface model, since it does not respect the interface conditions, and is not able to treat an interface for any physical situation.

To illustrate what happens with these models, we examine a simplified example using the notion of mass fraction and partial pressures. Consider a control volume  $V$  filled with a volume  $V_1$  of fluid 1 and a volume  $V_2$  of fluid 2, Fig. (15.1). Volume  $V_k$  contains the mass  $m_k = n_k \tilde{M}_k$ , where  $n_k$  and  $\tilde{M}_k$  represent respectively the number of moles and the molar mass of the fluid  $k$  ( $k = 1$  or  $2$ ). The notion of partial pressures is based on local thermodynamic equilibrium. Partial pressure  $P_{p1}$  is the pressure that fluid 1 would have if it occupied all the volume  $V$ . Assuming that the whole fluid is governed by the ideal gas law, and noting that  $\tilde{R}$  is the molecular gas constant, we get:

$$P_{pk} = n_k \tilde{R} T / V = \alpha_k \rho_k R T, \quad (15.45)$$

where  $R$  represent the gas constant per unit mass. The mixture density then reads  $\rho = \sum \alpha_k \rho_k$ . It is convenient to introduce mass fractions  $Y_k = \alpha_k \rho_k / \rho$ . Then the pressure reads

$$P = \rho R T, \quad (15.46)$$

where the gas constant is  $\tilde{R} / \bar{M}$  with  $\bar{M} = 1 / \sum (Y_k / \tilde{M}_k)$ . Imagine now that volume  $V$  corresponds to a computational cell in the numerical diffusion zone of a contact discontinuity. For example, fluid 1 is air and fluid 2 is liquid water. There is no reason why the temperatures of these fluids should be in equilibrium during the numerical diffusion process of the computational method. The same remark holds even if the two fluids are two gases. The reason why this type of model fails to describe interfacial conditions is that they can access some of the partial quantities  $\alpha_k \rho_k$ , but not the primitive quantities of phase  $k$  like  $\rho_k$ . As stated by Allaire [5], this supposes to know the value of  $\alpha_k$ .

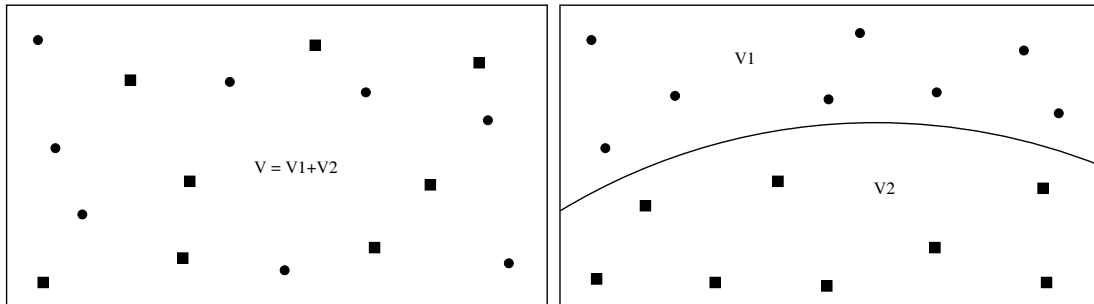


Figure 15.1: Multi-species (left) vs multi-fluid configuration (right)

The six-equation model developed by Ishii [115] can also be classified in this category. This is a six equation model, composed of the equations contained in system (15.37), with equations of mass, momentum and energy for each phase. Contrary to the previous models mentioned in this paragraph, this model allows to have different velocities and pressures between phases, so it gets over the cinematic and mechanical equilibrium. But, as before, the fact that it does not allow to determine the value of the volume fraction makes it unable to describe thermal non equilibrium at an interface. Also, as stated in [30], when both phases are considered compressible, the model closure is given by pressure equality.

### 15.3.4 Two-fluid interface models

The shortage pointed out in the previous paragraph has lead scientists to consider an approach based on the volume fraction  $\alpha_k = V_k / V$ , taking up the example of the previous paragraph. The mixture density

is obtained by  $\rho = \sum \alpha_k \rho_k$ , where the densities of each phase are defined by  $\rho_k = n_k \tilde{M}_k / V_k = m_k / V_k$ . The pressure of each phase is given by  $P_k = \rho_k R_k T_k$  and the mixture pressure is defined by

$$P = \sum \alpha_k P_k. \quad (15.47)$$

Note that if the temperatures are in equilibrium,  $T_k = T$ , then the pressure given by Eq. (15.47) is equal to the pressure given by Eq. (15.46). The advantage of the formulation using volume fractions is clear: it is not necessary to have temperature equilibrium to compute the pressures. On the other hand, this formulation requires the knowledge of two temperatures or internal energies and also of the two densities. This is achieved only if the volume fraction can be assessed.

That is why models able to treat interface, that we call here two-fluid interface models, contain a transport equation on the volume fraction. In our review, two models have been identified, that are able to treat an interface. The first one is the model designed by Baer and Nunziato [10]. It contains the six conservation equations of system (15.37) plus the non-conservative transport equation for the volume fraction Eq. (15.42): this model contains seven equations. A thermal non-equilibrium between the phases can then be described. Besides, as an equation on momentum is written for both phases, different velocities and pressures for each phase can be supposed. This model assumes no equilibrium of any type between the phases. On the other hand, as seen in Section 15.2.2, the derivation of a transport equation on the volume fraction is not straightforward, and this equation turns out to be non-conservative which leads to additional difficulties in the design of a suitable numerical scheme. Moreover, it requires to provide closure to interfacial and exchange terms, coping with some conditions focused on in Section 15.4 and in Section 15.5. These difficulties are most probably the reason why the first consistent model of this type was released by Baer and Nunziato in 1986.

The second type of model, called five-equation model, is derived from the seven-equation model. It considers a single equation on momentum and on energy. It thus considers a cinematic and mechanical equilibrium between the phases. This model can also be seen as the relaxed version of the seven-equation model.

This study points out the link between the type of equilibrium hypothesis made between the phases and the number of equations of the model. As one could expect, the less equilibrium assumptions are made, the more equations have to be written, and the more unclosed terms appear. It also highlights the critical role of the volume fraction  $\alpha$  in the description of the interface. The conclusion of this study are summarized in Fig. (15.2).

## 15.4 Mathematical structure

In this section, we analyze the necessary conditions on phase pressures  $P_k$  and on interfacial terms  $\Pi$  and  $\mathbf{u}_i$ , for the system composed of Eq. (15.42) and system (15.37) to be hyperbolic. In mathematical terms, if one rewrites this system in one-dimension:

$$\partial_t \mathbf{U} + \mathbf{A}(\mathbf{U}) \partial_x \mathbf{U} = S(\mathbf{U}), \quad (15.48)$$

where  $\mathbf{U} = (\alpha_g, \alpha_g \rho_g, \alpha_g \rho_g u_g, \alpha_g \rho_g E_g, \alpha_l \rho_l, \alpha_l \rho_l u_l, \alpha_l \rho_l E_l)$  is the state vector,  $\mathbf{A}(\mathbf{U})$  is the matrix associated to the spatial derivatives, and  $S(\mathbf{U})$  is the source term, the model should be such that  $\mathbf{A}(\mathbf{U})$  is diagonalizable with real eigenvalues. Physically, this means that the waves of the system travel at a defined real velocity. If this is not the case, i.e. if at least one wave velocity is imaginary, then singularities called "resonances" occur. A corresponding study can be found in [189]. Two cases are distinguished whether one of the phases is considered incompressible or both phases are supposed to be compressible. We first focus on the incompressible case, and suppose that the multi-phase flow is made of a liquid with  $\rho_l = \text{constant}$  and a compressible gas. When assuming the liquid is incompressible, the thermodynamic pressure  $P_l$  is homogeneous and the pressure term in the momentum equation is a mechanical pressure determined such that the velocity divergence is null,  $\nabla_{\mathbf{x}} \cdot \mathbf{u}_l = 0$  holds [186]. The interfacial pressure is

	Mixture Model	Two-Fluid mixture Model		Two-Fluid Interface Model	
Mixture variables	$\rho_m$ $\mathbf{v}_m$ $E_m$	$\rho_m$ $\mathbf{v}_m$ $E_m$		$\mathbf{v}_m$ $E_m$	
Phase variables		$\alpha_l \rho_l$ or $\Omega$	$\rho_k, k=l,g$ $\mathbf{v}_k, k=l,g$ $E_k, k=l,g$	$\alpha_l \rho_l$ $\alpha_l$	$\alpha_k \rho_k, k=l,g$ $\mathbf{v}_k, k=l,g$ $E_k, k=l,g$ $\alpha_l$
Type of equilibrium hypothesis	Thermodynamic kinetic	Thermodynamic kinetic	Thermodynamic	kinetic mechanical	none

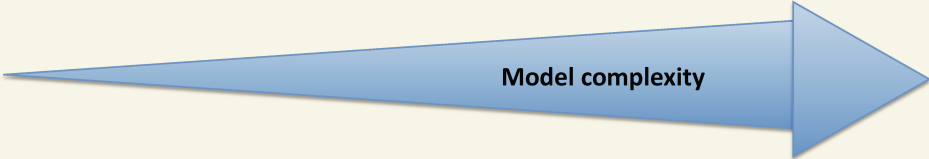


Figure 15.2: Hierarchy of two-fluid models according to the nature of the considered equilibrium. For each model, the solved quantities are represented. The term  $\Omega$  represents the parameter(s) of the EOS chosen for both phases.

taken equal to the gas pressure [65]. If one considers the momentum equations for both phases, omitting the diffusion terms (written in one dimension, without loss of generality)

$$\begin{aligned}\partial_t(\alpha_g \rho_g u_g) + \partial_x(\alpha_g \rho_g u_g) &= -\alpha_g \partial_x P_g - (P_g - \Pi) \partial_x \alpha_g, \\ \partial_t(\alpha_l \rho_l u_l) + \partial_x(\alpha_l \rho_l u_l) &= -\alpha_l \partial_x P_l - (P_l - \Pi) \partial_x \alpha_g,\end{aligned}\tag{15.49}$$

it becomes, with the incompressible assumption for the liquid phase

$$\begin{aligned}\partial_t(\alpha_g \rho_g u_g) + \partial_x(\alpha_g \rho_g u_g) &= -\alpha_g \partial_x P, \\ \partial_t(\alpha_l \rho_l u_l) + \partial_x(\alpha_l \rho_l u_l) &= -\alpha_l \partial_x P,\end{aligned}\tag{15.50}$$

where  $P = P_g$ . As noted in [205, 207, 22], this choice yields an ill-posed mathematical problem, which results in numerical instabilities during numerical resolution, or in the necessity of using an extremely large numerical viscosity yielding unrealistic solutions. This is why some authors have proposed introducing a non-equilibrium pressure effect  $\Pi(\alpha_l)$  to enable the system to be hyperbolic. Sainsaulieu [205] adds a pressure term  $\theta = \theta_0 \alpha_l^\delta$  to the pressure term for the liquid phase in Eq. (15.50), so that the pressure term, initially  $\alpha_l \partial_x P$ , becomes  $\alpha_l \partial_x P + \partial_x \theta$ . In [22], Bouchut adds the corrective term  $C_p \rho_l (u_g - u_l)^2 \partial_x \alpha_l$  to the momentum equation for the liquid.

In the second case, both fluids are considered compressible. If each phase is considered to have its own pressure, then, according to Saurel [207], this guarantees hyperbolicity. So, there is some freedom in the choice of closure relations for interfacial pressure and velocity with respect to hyperbolicity. But for physical reasons, the interfacial pressure and velocity must be estimated as accurately as possible. Unfortunately, this is nearly impossible in the general case. For the specific context of stratified flows, it is possible to estimate an interfacial pressure on the basis of the velocity and density differences [14]. For gases and solid particles flows under weak solid compressibility, it is reasonable to assume the interfacial pressure to be the gas one, and interfacial velocity to be the solid one [10]. For compressible multi-phase flows with interface, Saurel [207] suggests the following expression for the interfacial pressure

$$P_i = \sum_k \alpha_k (P_k + \rho_k (u_i - u_k)^2),\tag{15.51}$$

and for the interfacial velocity

$$u_i = \sum_k \alpha_k \rho_k u_k / \sum_k \alpha_k \rho_k,\tag{15.52}$$

These expressions are discussed in Chapter 16. In fact, for each physical situation, there are choices better than others, but none is entirely satisfactory. The fundamental idea of this section is that introducing extra closure relations decreases the number of degrees of freedom of a system. If the system was already well-posed, i.e. there was enough relations to solve the problem, the extra closure relations can cause a consistency problem and then lead to some mathematical problems. This goes hand in hand with the idea, in the applied mathematics community, that a model physically sound is most likely to have good mathematical properties.

## 15.5 Thermodynamic consistency

The purpose in this section is to give some restrictions to the closure of the exchange terms, and more generally to the dissipative terms of the system (viscous stress tensor  $\mathbf{T}$  or heat flux  $\mathbf{q}_k$ ). These restrictions will be given by enforcing sufficient conditions in order to ensure the second principle of thermodynamics. The developments leading to these restrictions rely on the theory of irreversible processes. The procedure shown in this section reproduces the developments made by Baer and Nunziato [10]. These are not the only authors who have done this derivation (see [162]), but their work has become a reference in the

multi-phase flow community. Indeed, they deduced the transport equation on the volume fraction that is being used by many authors nowadays [206, 207] with success for treatment of multi-phase flows with interfaces. The main steps of the developments are the following:

- Statement of the system of equations and relations between exchange terms,
- Derivation of the evolution equation of the entropy, using the Gibbs law,
- Derivation of the evolution equation of the Helmholtz free energy, using the Clausius-Duhem inequality,
- Determination of the internal variables of the system, and the dependence of the functions and exchange terms on these variables,
- Expansion of the Helmholtz free energy relatively to the internal variables, and statement of the sufficient conditions, finally leading to the restrictions on the dissipative term expression.

The system of equations considered by Baer and Nunziato is the non-conservative version of system (15.37), the equation of internal energy substituting the equation of total energy. On the basis of that system, the two assumptions are, first, that each phase behaves as if it were a single material except when it is interacting and hence exchanging mass, momentum and energy with the other phase. The second one is that the system must be conservative. These two assumptions allow to write the following system

$$\begin{aligned}
 D_t \alpha_k \rho_k &= -\alpha_k \rho_k \nabla_{\mathbf{x}} \cdot \mathbf{u}_k + \Gamma_k, \\
 \alpha_k \rho_k D_t \mathbf{u}_k &= -\nabla_{\mathbf{x}} (\alpha_k P_k) + \mathbf{M}_k - \Gamma_k \mathbf{u}_k, \\
 \alpha_k \rho_k D_t e_k &= -\alpha_k P_k \nabla_{\mathbf{x}} \cdot \mathbf{u}_k - \nabla_{\mathbf{x}} \cdot \alpha_k \mathbf{q}_k + \alpha_k r_k + \pi_k - \mathbf{M}_k \mathbf{u}_k - \Gamma_k (e_k - 1/2 \mathbf{u}_k^2),
 \end{aligned} \tag{15.53}$$

where  $e_k$  is the internal energy and  $r_k$  the external heat sources for phase  $k$ . The term  $\pi_k$  denotes the internal energy exchange. Fluids are considered inviscid here. Note that system (15.53) slightly differs from the original system of equations written by Baer and Nunziato. We bypass some developments that are not essential for the point we want to make. The interested reader can refer to [10] for all the details. The second assumption leads to:

$$\begin{aligned}
 \sum_k \Gamma_k &= 0, \\
 \sum_k \mathbf{M}_k &= 0, \\
 \sum_k \pi_k &= 0.
 \end{aligned} \tag{15.54}$$

In order to derive an entropy equation for the system, a legitimate question is how to define entropy of the multi-phase system. Baer and Nunziato sum the entropies of each single phase. The entropy equations of each phase are derived using the Gibbs relation for each phase:

$$ds_k = \frac{de_k}{T_k} + \frac{P_k}{T_k} d\left(\frac{1}{\rho_k}\right). \tag{15.55}$$

Following the work of Woods [230], after summing the entropy condition, the second law of thermodynamics can be stated as an entropy inequality:

$$\sum_k [\alpha_k \rho_k D_t s_k + \Gamma_k s_k + \nabla_{\mathbf{x}} \cdot (1/T_k \mathbf{q}_k) - \frac{\alpha_k r_k}{T_k}] \geq 0. \tag{15.56}$$

Rather than working with entropy, where the volumic heat source is present, it is more convenient to introduce the phase Helmholtz free energy  $\Psi_k$  given by

$$\Psi_k = e_k - T_k s_k. \quad (15.57)$$

The purpose is then to write the Clausius-Duhem inequality for the two-phase flow, using the same strategy for its derivation for a single-phase flow. The advantage of this formulation is that it only involves internal phenomena of the two-fluid system. The Clausius-Duhem inequality of the multi-phase flow can be written as

$$\sum_k \frac{1}{T_k} \left[ \alpha_k \rho_k (s_k D_t T_k + D_t \Psi_k) - \alpha_k P_k \nabla_{\mathbf{x}} \cdot \mathbf{u}_k - \frac{1}{T_k} \alpha_k \mathbf{q}_k \cdot \nabla_{\mathbf{x}} T_k - \mathbf{M}_k \cdot \mathbf{u}_k + \pi_k - (\Psi_k - 1/2 \mathbf{u}_k^2) \Gamma_k \right] \geq 0. \quad (15.58)$$

Equation (15.58) is the basis equation from which restrictions on the dissipative terms (called "mixture response" in [10]) are determined. However, in order that Eq. (15.58) provides explicit conditions, the free energies  $\Psi_k$  have to be expressed relatively to the system state variables. More generally, all the functions appearing in Eq. (15.58) have to be expressed the same way. In order to do that, the authors of [10] use the principle of phase separation [66, 194]. This principle expresses the idea that in a mixture of discrete phases, the free energy  $\Psi_k$ , the pressure  $P_k$ , the entropy  $s_k$  and the heat flux  $\mathbf{q}_k$  of a given constituent  $k$  depend only on the properties and the thermodynamic state of that constituent. On the other hand, the interaction, i.e the mass, momentum, and energy exchange,  $\Gamma_k$ ,  $\mathbf{M}_k$ ,  $\pi_k$ , between the two phases depend on the properties and the thermodynamic states of both constituents. These statements can be expressed mathematically by writing constitutive equations of the form:

$$\begin{aligned} \Psi_k &= \Psi_k(\mathcal{S}_k), & P_k &= P_k(\mathcal{S}_k), & s_k &= s_k(\mathcal{S}_k), & \mathbf{q}_k &= \mathbf{q}_k(\mathcal{S}_k), \\ \Gamma_k &= \Gamma_k(\mathcal{S}_l, \mathcal{S}_g), & \mathbf{M}_k &= \mathbf{M}_k(\mathcal{S}_l, \mathcal{S}_g), & \pi_k &= \pi_k(\mathcal{S}_l, \mathcal{S}_g), \end{aligned} \quad (15.59)$$

$$(15.60)$$

where the thermodynamic state of constituent  $k$  is the array

$$\mathcal{S}_k = [\alpha_k, T_k, \rho_k, \mathbf{u}_k, \nabla_{\mathbf{x}} T_k], \quad (15.61)$$

containing all the variables present in Eq. (15.58). The next assumption is essential, since the evolution equation on  $\alpha_k$  originates from it, and is used by many authors nowadays. It is important to note that if the quantities of Eq. (15.59) depend on the fields  $\alpha_k, \rho_k, \mathbf{u}_k, T_k, \nabla_{\mathbf{x}} T_k$ , then the six conservation equations of system (15.53) are not sufficient to close the system. In the introduction of [10], Baer and Nunziato pointed out solutions proposed in the literature, and highlighted the shortage of each for the physics they study. Therefore, they proposed their own closure, based on the addition of a new evolution equation for the volume fraction of one of the constituents

$$D_t \alpha_k = S(\mathcal{S}_l, \mathcal{S}_g). \quad (15.62)$$

the volume fraction of the other constituent being found out by the relation  $\sum_k \alpha_k = 1$ . Equation (15.62) allows to account for both the compressibility of the constituents and the compaction of the granular bed by recognizing the volume fraction as an independent internal degree of freedom within the mixture. The free energy is expanded in Eq. (15.58), using the chain rule:

$$D_t \Psi_k = \partial_{\alpha_k} \Psi_k D_t \alpha_k + \partial_{T_k} \Psi_k D_t T_k + \partial_{\rho_k} \Psi_k D_t \rho_k + \partial_{\mathbf{u}_k} \Psi_k D_t \mathbf{u}_k + \nabla_{\nabla_{\mathbf{x}} T_k} \Psi_k \nabla_{\mathbf{x}} (T_k). \quad (15.63)$$

There are now two steps of resolution. By requiring that the Clausius-Duhem inequality be true for every possible thermodynamic process, it enables to consider that the coefficients of the terms  $D_t T_k, \nabla_{\mathbf{x}} \cdot$

$\mathbf{u}_k, D_t \mathbf{u}_k, D_t \nabla_{\mathbf{x}}(T_k)$  vanish, since it is possible to construct certain processes such that these terms can take arbitrary large values so that the Clausius Duhem inequality can be violated. We conclude that the Helmholtz free energy is a function only of the state variables  $\rho_k, T_k, \alpha_k$ , and that Eq. (15.58) becomes

$$\sum \frac{1}{T_k} \left[ \pi_k - \mathbf{M}_k \cdot \mathbf{u}_k - \Gamma_k (\Psi_k + \frac{P_k}{\rho_k} - \frac{1}{2} \mathbf{u}_k^2) (\beta_k - P_k) D_t \alpha_k - \frac{1}{T_k} \mathbf{q}_k \cdot \nabla_{\mathbf{x}}(T_k) \right] \geq 0, \quad (15.64)$$

where  $\beta_k = \alpha_k \rho_k \partial_{\alpha_k} \Psi_k$  is called *configuration pressure* in [10], and is a consequence of changes in the packing of the granular bed. Hence, it must reflect the contact force between the grains.

The dissipation inequality Eq. (15.63) actually provides information useful in formulating specific constitutive equations for the exchange functions  $\Gamma_k, \mathbf{M}_k, \pi_k$ , the evolution of the volume fraction  $D_t \alpha_k$  and the heat flux  $\mathbf{q}_k$ . The expansion of Eq. (15.63) relative to the sum sign and an organization of the terms based on physical intuition and experimental observation suggest specific constitutive equations for the above-mentioned terms. For the sake of legibility, we do not write the expanded equation as well as the constitutive equations for its terms, since they can be found in [10]. Among all these fundamental results, we expose the resulting equation on the volume fraction, as it is, in our sense, the most impressive breakthrough, and as it has been included in most of the proposed two-fluid interface models nowadays in the literature. The transport equation on  $\alpha_l$  reads

$$\partial_t \alpha_l + \mathbf{u}_i \cdot \nabla_{\mathbf{x}} \alpha_l = \mu [P_l - (P_g - \beta_g)] + \frac{\Gamma_k}{\rho_k}. \quad (15.65)$$

Equation (15.65) expresses that changes in the volume fraction are due to combustion (more generally mass transfer between phases), but also to pressure differences existing between phases and the configuration pressures. In this context,  $\beta_s$  is a pressure which resists changes in the packing of the bed and hence compaction. It is physically sound to ascribe this resistance to the contact forces acting on the solid and hence set  $\beta_g = 0$ . The coefficient  $\mu_c$  is interpreted as the *compaction viscosity* and if it vanishes, then Eq. (15.65) implies that the pressure in the solid grains equal the pressure in the gas plus the pressure due to contact forces between the grains  $P_l = P_g + \beta_s$ .

Another fundamental result is the apparition of relaxation terms in the momentum and energy exchange terms:

$$\begin{aligned} \mathbf{M}_k &= \lambda(\mathbf{u}_s - \mathbf{u}_g) + \dots, \\ \pi_k &= \lambda \mathbf{u}_i (\mathbf{u}_s - \mathbf{u}_g). \end{aligned} \quad (15.66)$$

The term  $\lambda(\mathbf{u}_s - \mathbf{u}_g)$  can be considered as a *non viscous drag term* between the phases. Indeed, let us recall that we assumed the gas phase to be inviscid.

This development shows that from the enforcement of the second principle of thermodynamic, numerous relations can be deduced in order to close the exchange terms and the dissipative terms of a two-fluid model. One has to be aware that if they lead to admissible forms, yet they are not sufficient to give explicit expressions of this. This final step corresponds to the modeling work regarding the nature of the physical process studied. Among the advances brought by the work done in [10], the relaxation terms in pressure, and velocity are very important, since they are not limited to transition-to-detonation problems but they have proven to be very useful in all situations involving an interface between phases, as developed in Chapter 16. The other remark concern the assumptions made through all this development. The phase separation principle used to express in particular the free energy for phase  $k$  is quite understandable from a physical viewpoint. But it has also a very important practical interest since it leads to constitutive equations that are workable for the modeling step. Second, the equation on the entropy of system (15.56) is obtained by simply summing the entropy equation for each phase, no effect of the interface being taken into account. Some authors, for example Marle [162], have a different approach, since they consider an interface with a non zero mass and write the total entropy evolution of the system as the sum of the entropy of each phase and the entropy of the interface. Finally, the *a priori* evolution equation written for the volume fraction Eq. (15.62) presumes that  $\alpha$  is a transported quantity, and not a conserved quantity.

## Conclusion

The aim of this chapter was to show how to write a consistent two-fluid model for separate-phase flows, which is a process very different from writing a model for a single-phase flow, for two main reasons: the existence of exchange terms between phases, and the notion of volume fraction and interface. Therefore, if a two-fluid, model system of equations can be quite easily written

$$\begin{aligned} \partial_t(\alpha_k \rho_k) + \nabla_{\mathbf{x}} \cdot (\alpha_k \rho_k \mathbf{u}_k) &= \Gamma_k, \\ \partial_t(\alpha_k \rho_k \mathbf{u}_k) + \nabla_{\mathbf{x}} \cdot (\alpha_k \rho_k \mathbf{u}_k \mathbf{u}_k) &= -\alpha_k \nabla_{\mathbf{x}} P_k + \nabla_{\mathbf{x}} \cdot \alpha_k (\boldsymbol{\tau}_k + \boldsymbol{\tau}_k^t) \\ &\quad + \underbrace{\Gamma_k \mathbf{u}_{k,i} + (P_{k,i} - P_k) \nabla_{\mathbf{x}} \alpha_k + \mathbf{M}_k^d}_{\mathbf{M}_k}, \\ \partial_t(\alpha_k \rho_k E_k) + \nabla_{\mathbf{x}} \cdot (\alpha_k \rho_k E_k \mathbf{u}_k) &= -\nabla_{\mathbf{x}} \cdot (\alpha_k \rho_k \mathbf{u}_k P_k) - \nabla_{\mathbf{x}} \cdot (\alpha_k (\mathbf{q}_k + \mathbf{q}_k^t) + \nabla_{\mathbf{x}} \cdot (\alpha_k (\boldsymbol{\tau}_k + \boldsymbol{\tau}_k^t) \cdot \mathbf{u}_k) \\ &\quad + \underbrace{\Gamma_k E_{k,i} + \Pi_k^d + \mathbf{M}_k^d \cdot \mathbf{u}_{k,i}}_{\Pi_k}, \end{aligned} \tag{15.67}$$

with the interfacial terms verifying:

$$\begin{aligned} \Gamma_l + \Gamma_g &= 0, \\ \mathbf{M}_l + \mathbf{M}_g &= 0, \end{aligned} \tag{15.68}$$

$$\Pi_l + \Pi_g = 0, \tag{15.69}$$

where these equations are obtained from an averaging process of the single-phase ones, and

$$\partial_t \alpha + \mathbf{u}_i \cdot \nabla_{\mathbf{x}} \alpha = S_{\alpha}. \tag{15.70}$$

which is the *a priori* form of the evolution equation for the volume fraction, the actual design of a consistent two-fluid model lies in the closure of the numerous exchange and interfacial terms. Three major steps were thus identified. The first one consists in defining the nature of the equilibrium between the phases. This condition determines the number of evolution equations required. Second, one has to ensure that the two-fluid model is hyperbolic. This implies a consistent closure of the differential terms. Finally, the model has to be dissipative, i.e. the resulting entropy equation of the system should have a positive sign. This study provides admissible formulations for the exchange term. In particular, the enforcement of this dissipation inequality done by Baer and Nunziato in [10] has provided an expression for the source term of the transport equation for the volume fraction. Once this step has been achieved, explicit expressions have to be given to the unclosed terms on the basis of physical considerations. The interfacial pressure and velocity are expressed through combinations of pressure and velocity of the phases. Exchange terms are determined by constitutive equations. The next chapter contains a non-exhaustive review of two-fluid models proposed in the literature. The different steps on a two-fluid model derivation are illustrated in Fig. (15.3).



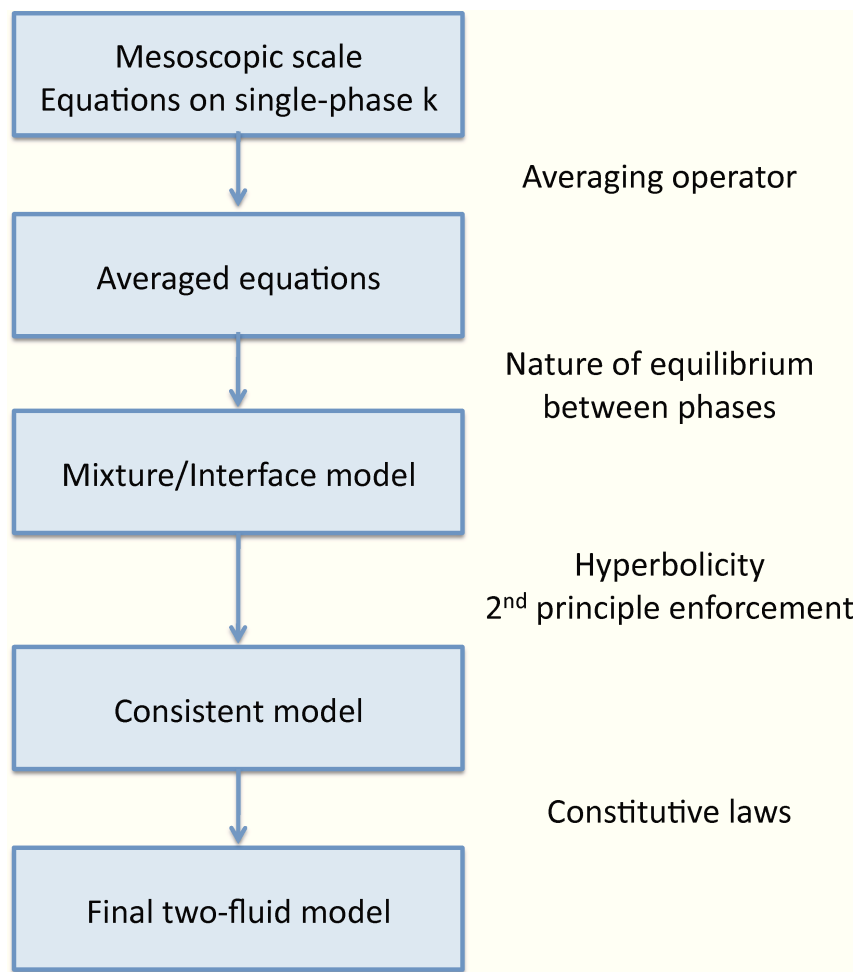


Figure 15.3: Derivation of a two-fluid model

## Chapter 16

# Review on models for multi-phase flows

The previous chapter has highlighted the key steps for a two-fluid model derivation:

- the determination of the type of equilibrium between phases,
- a coherent closure of the interfacial pressures in order to ensure that the system is hyperbolic,
- the derivation of admissible formulations for the dissipative terms, in order to ensure the second principle of thermodynamic.

The final step consists in giving a precise expression for the constitutive relations, according to the physical process under investigation. This final closure concerns two types of law: the equation of state for each phase, and constitutive laws for all the dissipation terms of the system, be they inside a phase like  $\boldsymbol{\tau}_k$  or  $\mathbf{q}_k$ , or exchange terms. We propose here a (non-exhaustive) review of two-fluid models used in the literature. The purpose of this review is to justify the choice made for the model implemented in the IFP-C3D code. Hereafter, we list some of the various physical processes treated in the literature:

- The study of bubble flows in vertical columns: this mainly concerns the nuclear industry faced with the problematic of flow in the cooling circuit. Among others, Ishii [115], Delhaye [53] and Morel [182] have proposed suitable models for this case.
- The propagation of evaporation fronts, and of cavitation, studied by Saurel and Le Metayer [149, 207]. In particular, Bayoro [12] studied the cavitation phenomena in Diesel injection.
- The deflagration-to-detonation transition, studied by Baer and Nunziato [10], and propagation of detonation waves in heterogeneous media studied by Chinnayya [43].
- The primary and secondary atomization studied by Vallet and Borghi [217, 216] or Jay [122].
- Primary atomization in the context of Diesel injection studied by Moreau [181].
- Study of sloshing in fuel tank at high Bond number [39].

### 16.1 Mixture model

As explained in Chapter 15, mixture models are based on a thermodynamic and kinetic equilibrium assumption between the phases. Mean physical quantities are solved (density, velocity, viscosity, temperature) and the studied fluid is a mixture of the two phases. This fluid is solution of a system of equations for a single-phase flow. Therefore, classical resolution techniques for fluid mechanics can be used. The equation of state (EOS) applies then to the mixture, and is different from the pure fluid EOS. Various types of EOS have been proposed. The first type corresponds to cubic equations reproducing

the liquid-vapor phase diagram. Some authors also use combinations of EOS of pure fluids to build the mixture EOS. Tabulated equations can also be used. In the case of a cubic EOS, for example the Van der Waals equation, the hyperbolic character of the system might be lost in the mixture domain, where the two phases coexist [174]. This problem does not occur when a tabulated equation or an equation resulting from a combination of EOS for pure fluid is considered. But on the other hand, other problems appear, for example the inability of the model to take into account metastable states [149]. Moreover, no exchange term is explicitly solved. However, as explained in the following, mixture models have been used in processes where exchanges between phases are important, but in special contexts with particular assumptions on the kinetic of these transfers. Although the use of mixture models is limited to very special cases, under clear and identified assumptions on the flow, it allows an efficient resolution of the flow.

The first model we focus on is designed in the context of fuel injection in internal combustion engines. The problem faced by Moreau in [181] is to determine the impact of the flow inside the injector in the primary atomization process. His purpose is to describe cavitation effects occurring in the injector, right before the fuel penetrates the combustion chamber. He then focuses on the interaction between the fuel jet with vapor pockets due to cavitation and the gas phase, when it enters the combustion chamber. We only focus on the first aspect of his work. He supposes that the kinetic of the mass, momentum, and energy transfer between the phases is fast, notably because the cavitation zones are considered disperse within the liquid fuel zone. Consequently he states that the flow can be considered at equilibrium, i.e at thermodynamic and kinematic equilibrium. Besides, he assumes that thermal phenomena are not important. This hypothesis, combined with the fact that cavitation is a purely dynamical effect, justifies that his study does not require to solve a conservation equation on energy, and thus to work at constant temperature.

The mixture model (also called Homogeneous Equilibrium Model or HEM) contains then only two equations, on mass and momentum

$$\begin{aligned}\partial_t \rho_m + \nabla_{\mathbf{x}} \cdot (\rho_m \mathbf{u}) &= 0, \\ \partial_t (\rho_m \mathbf{u}_m) + \nabla_{\mathbf{x}} \cdot (\rho_m \mathbf{u} \mathbf{u}) &= -\nabla_{\mathbf{x}} P_m + \nabla_{\mathbf{x}} \cdot \boldsymbol{\tau}_m,\end{aligned}\tag{16.1}$$

where the terms with the subscript m denote the mixture variables. Thus, taking the example of density,

$$\rho_m = \sum_k \alpha_k \rho_k.\tag{16.2}$$

In particular,  $\boldsymbol{\tau}_m$ , the viscous stress tensor of the mixture, is closed by the Boussinesq constitutive equation [181]. This involves the values of the mixture viscosity  $\mu_m$ , taken as

$$\mu_m = \sum_k \alpha_k \mu_k.\tag{16.3}$$

From the number of unknowns and the number of relations, at least one more relation has to be determined in order to close the problem. This relation is the mixture state equation. The equation of state built by Moreau is a barotrope equation  $P_m = P_m(\rho_m)$ , relying on a combination of EOS of the pure phases. The essential point to notice is that postulating this form of EOS allows the pressure  $P_m$  to vary, even if a liquid and vapor phases of the same fluid are considered under a constant temperature. That is not possible if the state equation for perfect gas is considered. The state equation of Moreau is defined by integrating the relation

$$dP_m = c_m^2 d\rho_m,\tag{16.4}$$

where  $c_m$  is the speed of sound in the mixture. Note that Eq. (16.4) implies that the process is isentropic. Since the temperature is constant, the thermodynamic quantities of each phase are constant. This allows Moreau to highlight an explicit relation between the mixture pressure  $P_m$  and density  $\rho_m$ . This also

entirely closes the problem since the knowledge of  $\rho_m$  enables to access the volume fraction  $\alpha$  and to close  $\mu_m$ . This is one example of equation of state for a mixture. In the field of cavitating flow, Dumont [72] gathers various state equations used in the literature.

The simplicity of the mixture model (made of the Euler or Navier-Stokes system of equations, plus an EOS for the mixture) goes hand in hand with important limitations.

For cavitation problems, the thermodynamic equilibrium assumption forbids the study of metastable cases. Besides, as assumed by Moreau, mass transfer is assumed to be instantaneous, but this is not always correct (see for example evaporation front in liquid phase studied in [149]). Moreover, some cavitation problems can be solved making the exact opposed hypothesis, i.e. that the kinetic of transfer is very slow, even null. An example of these models can be found in [107, 48]. The mixture equations are actually the exact Euler equations for the liquid, the vapor being considered as vacuum. The liquid volumic expansion results then in vacuum. Nevertheless, the common point between these models is their inability to describe evaporative fronts, since an interface description is then required. Finally, this mixture EOS is valid only for flows where the liquid and its vapor only are present. If an uncondensable gas (air in water for example) is present in the flow, the mixture EOS no longer holds. In many practical situations, the liquid is not a pure fluid and some uncondensable gases are present. They strongly influence the mixture compressibility and modify the mass transfer dynamics.

In gaseous detonation, there is no phase change but only a change in the chemical composition of the mixture. Also, the molecular collisions are so intense that the assumption of temperature equilibrium between the various components is valid. For detonations in solid explosives this no longer holds. Indeed, the detonation is composed of a shock wave propagating in the solid material and followed by a reaction zone where energy is liberated with a finite rate. During the energy liberation, the reactive solid material transforms to product gases. When the reaction ends, the flow is a pure gas mixture. But the reaction zone always corresponds to a multi-phase mixture. In this multi-phase mixture, the assumption of equilibrium is totally wrong since the solid phase has a very different temperature from the burnt gases. For many applications, the details of the reaction zone has no importance because this zone is very steep (a few micrometers), and the detonation can be considered as a discontinuity connecting a pure unreacted solid to a mixture of reacted gases. But there are lots of applications for which the details of this reaction zone are important. For example, with non-ideal explosives, this reaction zone can be of the order of 1cm to 1m. This is why mixture models, and the thermodynamic equilibrium assumption between phases, are completely inadapted. The first assumption, the pressure equilibrium can be justified for the problem under study. But the second equilibrium, the thermal equilibrium is completely wrong as the gas phase during combustion can reach temperatures above  $3000K$ , whereas the solid phase after the shock front does not exceed  $1000K$ .

## 16.2 Two-fluid models

In this section, we consider problems solved by two-fluid models in the sense given in Chapter 15, that is to say that the system of equations is more complex than the simple Euler system of equations for a mixture flow. The classification we follow in this section is relative to non-interface and interface problems.

### 16.2.1 Resolution of problems without an interface

#### Six equation model

One of the most famous two-fluid models, the model of Ishii [115] is dedicated to liquid-vapor bubble flows occurring in cooling networks of nuclear plants, in normal or accidental functioning. This model

is composed of six equations which are the equations of system (15.37) we recall here:

$$\begin{aligned}
\partial_t(\alpha_k \rho_k) + \nabla_{\mathbf{x}} \cdot (\alpha_k \rho_k \mathbf{u}_k) &= \Gamma_k, \\
\partial_t(\alpha_k \rho_k \mathbf{u}_k) + \nabla_{\mathbf{x}} \cdot (\alpha_k \rho_k \mathbf{u}_k \mathbf{u}_k) &= -\alpha_k \nabla_{\mathbf{x}} P_k + \nabla_{\mathbf{x}} \cdot \alpha_k (\boldsymbol{\tau}_k + \boldsymbol{\tau}_k^t) + \mathbf{M}_k, \\
\partial_t(\alpha_k \rho_k E_k) + \nabla_{\mathbf{x}} \cdot (\alpha_k \rho_k E_k \mathbf{u}_k) &= -\nabla_{\mathbf{x}} \cdot (\alpha_k \rho_k \mathbf{u}_k P_k) - \nabla_{\mathbf{x}} \cdot (\alpha_k (\mathbf{q}_k + \mathbf{q}_k^t)) \\
&\quad + \nabla_{\mathbf{x}} \cdot (\alpha_k (\boldsymbol{\tau}_k + \boldsymbol{\tau}_k^t) \cdot \mathbf{u}_k) + \Pi_k.
\end{aligned} \tag{16.5}$$

In the literature, this model can be found under two different options:

- One of the phases is considered incompressible. Thus only the gas phase has a state equation, and the pressure of the mixture is taken as the gas mixture.
- Both phases are compressible, and the closure is realized by forcing mechanical equilibrium (pressure equilibrium) between the phases.

According to Section 15.4, these two versions of the six equation model lead to an ill posed system of equations. In his PhD Thesis, Morel [182] used the incompressible version of this model, although it was already discussed by some authors like [26]. His choice is justified by the fact that wave propagation is not paramount in his study. Plus, by adding diffusion terms, the problem can become parabolic. His research field was the improvement of exchange term closure. Accordingly, he pointed out the fact that they generally depend upon the contact area between the phases per unit volume, namely the volumetric interfacial area, also called interfacial surface density. Thus, his work was dedicated to a correct prediction of this surface density [182]. Ishii [115] suggested that the interface surface density  $\Sigma$  should obey a transport equation having the following form:

$$\partial_t \Sigma + \nabla_{\mathbf{x}} \cdot (\Sigma \mathbf{u}_{\Sigma}) = S_{\Sigma}. \tag{16.6}$$

where  $\mathbf{u}_{\Sigma}$  is the transport velocity of the interface surface density (equal to  $\mathbf{u}_i$ , the transport velocity of the volume fraction defined in Section 15.2.2), and  $S_{\Sigma}$  a source term taking into account the different phenomena creating or destroying interfacial area, such as coalescence or breakup of bubbles or droplets, phase change or interfacial stretching. Ishii wrote this equation for a population of identical (but not necessary spherical) bubbles. Morel's objective was to derive such an equation without assuming any particular geometrical configuration in the interfaces, and therefore to prove that it could be applied independently of the flow regime. This development was based on the work of Candel and Poinot [33], who wrote an equation on a flame surface density, in order to account for its stretching. As a by-product of his work, the rigorous mathematical expression of the transport velocity  $\mathbf{u}_{\Sigma}$  was established.

## 16.2.2 Resolution of interface problems

We consider the simulation of interfaces between two immiscible fluids. This situation occurs in many physical processes such as fuel injection in a combustion chamber, atomization, evaporation front, detonation front, deflagration-to-detonation transition. The problem is modeled by the Euler equations in each fluid domain and the usual jump conditions across the interface. The major numerical difficulty is to compute accurately the motion of the interface.

### 16.2.2.1 Incompressible case

The model of Vallet and Borghi [216, 217] is often referred to by people studying atomization of high pressure liquid jets. Its resolution is based on a two-fluid equilibrium model, where the Euler equations are written for the mixture, augmented by an equation on the partial density of the liquid. The important assumption made on the flow is that the liquid is considered incompressible. The mixture density is then constant in the case of pure liquid, whereas it varies when gas is present. Only one equation of state has to be considered, and applies to the gas phase. The main consequence of this assumption is that

the evolution equation for the partial liquid mass density coincides with the liquid volume fraction  $\alpha_l$ . Moreover this modeling considers turbulent flows with high variation in density and energy, and hence, is well suited for atomization regimes (with high Reynolds and Weber number). The system of equations writes:

$$\begin{aligned}\partial_t \rho_m Y + \nabla_{\mathbf{x}} \cdot (\rho_m Y \mathbf{u}) &= -\nabla_{\mathbf{x}} \cdot (\rho_m \widetilde{\mathbf{u}' Y'}), \\ \partial_t \rho_m + \nabla_{\mathbf{x}} \cdot (\rho_m \mathbf{u}) &= 0, \\ \partial_t \rho_m \mathbf{u} + \nabla_{\mathbf{x}} \cdot (\rho_m \mathbf{u} \otimes \mathbf{u}) &= -\nabla_{\mathbf{x}} P_m - \nabla_{\mathbf{x}} \cdot (\rho_m \widetilde{\mathbf{u}' \otimes \mathbf{u}'}),\end{aligned}\tag{16.7}$$

where  $P_m$ , the mixture pressure, is taken as the gas pressure, and  $f'$  is the fluctuation of the quantity  $f$  around its mean value  $\bar{f}$  due to turbulence, such that  $f' = f - \bar{f}$ . Let us note that  $Y$  does not represent the volume fraction, but the mass fraction, so that it can easily be related to the volume fraction by  $\alpha_l = \rho_m Y / \rho_l$ . The perfect gas EOS is considered.

The atomization process leads big liquid entities to break into smaller entities, so that, with a constant volume fraction, the liquid surface density increases. The authors have introduced an evolution equation for surface density  $\Sigma$  to take this phenomenon into account:

$$\partial_t \Sigma + \nabla_{\mathbf{x}} \cdot (\Sigma \mathbf{u}) = \nabla_{\mathbf{x}} \cdot (D_s \nabla_{\mathbf{x}} \Sigma) + (A + a) \Sigma - V_s \Sigma^2.\tag{16.8}$$

where  $D_s$  is a diffusion coefficient,  $1/A$  and  $1/a$  are two different production time scales and  $V_s$  is a destruction coefficient homogeneous to a velocity. The production term has two origins: the macroscopic contribution  $A$  due to the stretching of the interface caused by gradients of the mean velocity (corresponding to the Kelvin-Helmholtz instability), and the microscopic contribution  $a$  of the small turbulence scale. The purpose of the destruction term is to counteract the linear production term when  $\Sigma$  reaches saturation.

Jay [119] developed a similar model and also introduces an equation for  $\Sigma$  with different closures for the diffusion, production, and destruction terms.

### 16.2.2.2 Compressible case

Compressible multi-phase flows occur in many situations in which fluids have different physical or thermodynamic properties and are separated by interfaces. A classical example is an interface between air and helium under a shock wave. Other well-known examples are the Richtmyer-Meshkov instabilities between two gases and the behavior of a gas bubble in a liquid under shock wave. Many numerical simulations of such processes are based on the Euler or Navier-Stokes equations augmented by one or several species of conservation equations in order to build reasonable EOS parameters at the interface. Indeed, classical numerical methods produce artificial diffusion of contact discontinuities, resulting in artificial fluid mixing at the interface. In this artificial mixture, pressure and temperature computations lead to instabilities with this approach.

As explained in Section 15.3, the ground reason for these instabilities to occur is that the model assumes thermodynamic equilibrium between phases, whereas there is no thermal equilibrium at the interface. Often, the EOS found in the literature have only a limited range of validity (specially for solids and liquid). When the thermodynamic parameters provided by a numerical method are slightly outside this domain of validity, the pressure, entropy, sound speed, etc., that are computed have no physical meaning (negative pressures for example).

When the fluid properties are close (low density variations and low parameters of the EOS change), these methods induce low deviations. But in many circumstances, the fluid parameters are very different, as are the densities from one fluid to another. Consider, for example, an interface separating a liquid and a gas, or as in many applications with detonations, an interface between a gas and a solid. Under such conditions, methods based on the Euler equations augmented by species conservation equations or transport equations for the EOS parameters are ill-adapted. It has been shown that even when the fluid properties are close, standard algorithms based upon species conservation equations induce large errors in the pressure and velocity computations [1, 132, 2]. These observations make mandatory a precise and

physically sound treatment of the interface.

A way to circumvent the limitations of mixture models expressed in Section 16.1 is to determine more thermodynamic variables for the multi-phase mixture, and to be able to access the own variables of each phase. In this context, each phase, considered compressible, will be governed by its own set of partial differential equations closed by the EOS of the corresponding pure material. The flow is no longer dependent on the mixture EOS model. This type of model corresponds to the two-fluid interface model defined in Section 15.3.

### Seven equation model

To our knowledge, the so-called seven equation model, proposed by Baer and Nunziato was the first consistent two-fluid interface model. Their purpose was to describe deflagration-to-detonation transition in reaction granular materials, involving then a solid phase (represented by the subscript  $s$ ) and a gas phase. The system of equations writes:

$$\begin{aligned}
\partial_t \alpha_s + \mathbf{u}_s \cdot \nabla_{\mathbf{x}} \alpha_s &= \frac{\alpha_s \alpha_g}{\mu_c} [P_s - (P_g + \beta_s)] + \frac{\Gamma_s}{\rho_s}, \\
\partial_t \rho_s + \nabla_{\mathbf{x}} \cdot (\rho_s \mathbf{u}_s) &= \Gamma_s, \\
\partial_t \rho_g + \nabla_{\mathbf{x}} \cdot (\rho_g \mathbf{u}_g) &= -\Gamma_s, \\
\rho_s [\partial_t \mathbf{u}_s + \mathbf{u}_s \cdot \nabla_{\mathbf{x}} \mathbf{u}_s] &= -\alpha_s \nabla_{\mathbf{x}} P_s + (P_g - P_s) \nabla_{\mathbf{x}} \alpha_s - (\delta + \frac{1}{2} \Gamma_s) (\mathbf{u}_s - \mathbf{u}_g), \\
\rho_g [\partial_t \mathbf{u}_g + \mathbf{u}_g \cdot \nabla_{\mathbf{x}} \mathbf{u}_g] &= -\alpha_g \nabla_{\mathbf{x}} P_g - (\delta + \frac{1}{2} \Gamma_s) (\mathbf{u}_g - \mathbf{u}_s), \\
\rho_s [\partial_t e_s + \mathbf{u}_s \cdot \nabla_{\mathbf{x}} e_s] &= -\alpha_s P_s \nabla_{\mathbf{x}} \cdot \mathbf{u}_s + \nabla_{\mathbf{x}} \cdot (k_s \nabla_{\mathbf{x}} T_s) + h(T_g - T_s) - (P_s - \beta_s) (\alpha'_s - \frac{\Gamma_s}{\rho_s}), \\
\rho_g [\partial_t e_g + \mathbf{u}_g \cdot \nabla_{\mathbf{x}} e_g] &= -\alpha_g P_g \nabla_{\mathbf{x}} \cdot \mathbf{u}_g + \nabla_{\mathbf{x}} \cdot (k_g \nabla_{\mathbf{x}} T_g) - h(T_g - T_s), \\
&\quad - [P_g \nabla_{\mathbf{x}} \alpha_s - \delta (\mathbf{u}_s - \mathbf{u}_g)] \cdot (\mathbf{u}_s - \mathbf{u}_g) + (P_s - \beta_s) (\alpha'_s - \frac{\Gamma_s}{\rho_s}) + \Gamma_s (e_g - e_s),
\end{aligned} \tag{16.9}$$

where  $\mu_c$  is the compaction viscosity,  $\beta_s$  is the configuration pressure between the solid grains. These terms are explained in Section 15.5. Let us point out that  $\mu$  is a non null finite parameter. The term  $\Gamma_s$  denotes the mass gained by the solid phase. The term  $\delta$  represents the drag term between the phases. The term  $k_s$  and  $k_g$  are the thermal conductivities in each phase,  $h$  represents the heat-transfer coefficient. Finally  $\alpha'_s$  is the particular derivative of  $\alpha_s$  at velocity  $\mathbf{u}_s$ .

The existence of a transport equation for  $\alpha_s$  allows to access the thermodynamic variables of each pure material. One can verify that this system is conservative, i.e. if the conservation equations are summed phase by phase, the Euler equations for the mixture are found. This system of equations is particularly remarkable, since it is the first time that relaxation terms in pressure appear in a two-fluid model. These terms are the results of the application to this problem of the irreversible processes thermodynamic theory (see Section 15.5). One can notice that the momentum and energy equations are not symmetric. This is due to the fact that the closure of the interfacial terms is not done in a symmetric manner. Indeed, the authors have set  $P_i = P_g$ ,  $\mathbf{u}_i = \mathbf{u}_s$ ,  $e_i = e_s$ . As explained in Section 15.4, there is no unique closure of the interfacial terms. This set makes the problem hyperbolic and appears to be the best suited for the particular process studied [10]. The authors point out that this model is able to describe two important effects governing flame spread and the subsequent formation of shock waves which lead to detonation. In the momentum equation for the solid, the term involving the pressure difference represents the forces associated with the motion of the grains when they are no longer in contact. In that instance, the pressure gradient term becomes small as  $\alpha_s \rightarrow 0$ . Secondly, the compressional energy term associated with the pressure in the solid  $(P_s - \beta_s) (\alpha'_s - \frac{\Gamma_s}{\rho_s})$  influences the behavior of both the solid particles and the gas. The authors also remark that both energy equations include convective energy transport.

The readers interested in the determination of the constitutive equations for this problem can consult [10].

### *Two-fluid interface model with pressure and velocity relaxation*

Saurel and Abgrall [207] proposed a model taking basis ideas from the one proposed by Baer and Nunziato.

$$\begin{aligned}
 \partial_t \alpha_k + \mathbf{u}_i \cdot \nabla_{\mathbf{x}} \alpha_k &= \mu (P_k - P_{k'}) + \frac{\Gamma_k}{\rho_X}, \\
 \partial_t (\alpha_k \rho_k) + \nabla_{\mathbf{x}} \cdot (\alpha_k \rho_k \mathbf{u}_k) &= \Gamma_k, \\
 \partial_t (\alpha_k \rho_k \mathbf{u}_k) + \nabla_{\mathbf{x}} \cdot (\alpha_k \mathbf{u}_k \otimes \mathbf{u}_k) &= -\nabla_{\mathbf{x}} (\alpha_k P_k) + P_i \nabla_{\mathbf{x}} \alpha_k + \lambda (\mathbf{u}_{k'} - \mathbf{u}_k), \\
 \partial_t (\alpha_k \rho_k E_k) + \nabla_{\mathbf{x}} \cdot (\alpha_k \rho_k E_k \mathbf{u}_k) &= -\nabla_{\mathbf{x}} (\alpha_k P_k \mathbf{u}_k) - P_i \mathbf{u}_i \cdot \nabla_{\mathbf{x}} \alpha_k - \mu P_i (P'_k - P_k) - \lambda \mathbf{u} \cdot (\mathbf{u}_k - \mathbf{u}'_k),
 \end{aligned} \tag{16.10}$$

where  $\mu$  and  $\lambda$  are the pressure and velocity relaxation coefficient respectively, and the subscript  $k'$  denotes the complementary phase to phase  $k$ . One can notice that two equations on the volume fraction are written, whereas a single equation on the volume fraction for one phase  $\alpha_k$  would be enough, the other volume fraction being deduced by  $\alpha'_k = 1 - \alpha_k$ . The three following main characteristics of system (16.10) are discussed:

- the significance of the non-conservative interaction terms,
- the relaxation procedure in pressure and velocity,
- the closure of the interface terms.

#### *Non-conservative terms*

Saurel and Abgrall [207] give a simple picture of the physical meaning of the non-conservative terms  $P_i \nabla_{\mathbf{x}} \cdot \alpha_k$  and  $P_i \mathbf{u}_i \cdot \nabla_{\mathbf{x}} \alpha_k$ . The one-dimensional Euler equations averaged over a duct of variable cross-section  $A$ , in the absence of mass, momentum and heat transfer are

$$\begin{aligned}
 \partial_t (A\rho) + \partial_x (A\rho u) &= 0, \\
 \partial_t (A\rho u) + \partial_x (A\rho u^2 + P) &= P \partial_x A, \\
 \partial_t (A\rho E) + \partial_x [A u (\rho E + P)] &= -P \partial_t A.
 \end{aligned} \tag{16.11}$$

In the two-phase system, the volume fraction  $\alpha$  is sometimes used as a surface fraction, specially in the nozzle problems, where  $\alpha_k$  represents the surface fraction occupied by phase  $k$ . These problems can be reduced to a one-dimensional problem in the nozzle longitudinal direction [53]. If one makes the analogy between  $A$  and  $\alpha_k$ , and replace the temporal derivative  $\partial_t A$  by a space derivative  $u \partial_x A$ , using the first equation of Eq. (16.10), one recovers the same equations from the one-dimensional averaged Euler equations and the two-fluid model. This means that the non-conservative terms in the two-fluid model have the same effect as the duct variation cross-section terms: nozzling terms. Their effects are well known in steady flows: acceleration of subsonic flows in area restriction for example. This also means that the two-fluid model, in a certain sense, couples several Euler systems in 'ducts' of variable cross-section. These 'ducts' have permeable walls for the various transfers, are moving with the flow at velocity  $\mathbf{u}_i$  and are expanding with the pressure differential  $\mu(P_k - P'_k)$  at a rate controlled by  $\mu$ .

#### *Pressure and velocity relaxation*

The relaxation coefficient  $\lambda$ , also called homogenization variable by Saurel and Abgrall [207], depends on the compressibility of each fluid (and so on their EOS), on the nature of each fluid, and on the two-phase mixture topology. Therefore, at this point, it is important to distinguish two different two-phase topologies. The first one is the interface flow, implying a clear interface between two compressible fluids. This paragraph is dedicated to this configuration. Indeed, this topology is the most challenging



to describe, as interfacial conditions have to be satisfied. The second topology is the non equilibrium homogeneous flows. This situation is rather different from that of interface flow where phases are separated by well-defined interfaces. In non equilibrium homogeneous flow, a control volume contains a large number of individual particles with many interfaces, while in interface flows, nearly all the control volumes contain pure phases, except for the computational cells around the interface. Meanwhile in this configuration like in interface flows, non thermodynamic equilibrium nor kinetic equilibrium assumption is *a priori* done. The distinction between these two types of flow is schematically represented in Fig. (16.1).

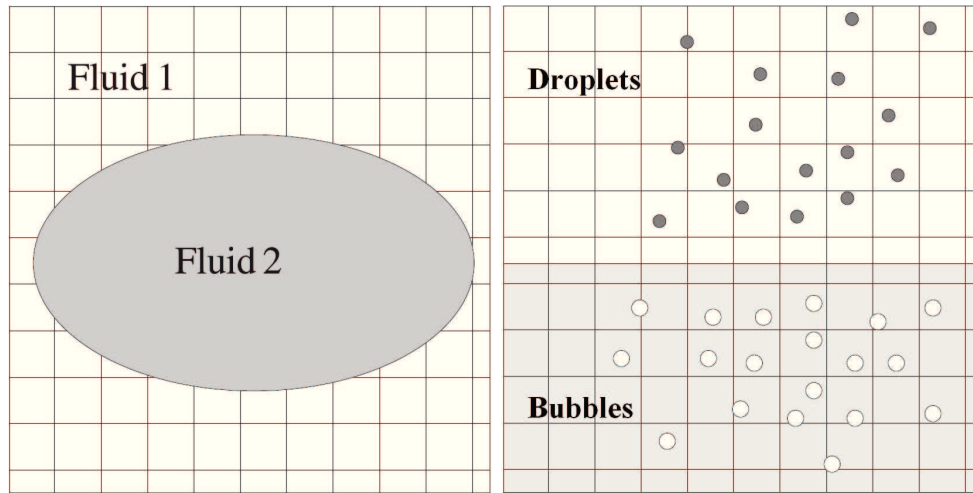


Figure 16.1: Illustration of the two types of visions. Left: multi-fluid vision; Right: multi-phase vision.

Let us examine now the physical grounds of pressure relaxation in both contexts. In non-equation homogeneous flows, after wave propagation, the fluids are in a non-equilibrium pressure state ( $P_g \neq P_l$ ) and a pressure relaxation process will develop so that pressure will tend to equilibrium,  $P_g = P_l$ . Locally, after the wave propagation, the fluids undergo a three-dimensional motion. This motion, at microscopic scale (droplet scale for example) creates a volume variation of each fluid, accompanied by an internal energy variation, so that pressure tends to equilibrium. This motion is due to the three-dimensional propagation of the various waves. Thus, locally, after wave propagation, the pressure relaxation process undergoes a volume variation given by the equation

$$\partial_t \alpha_k = \mu(P_k - P'_k). \quad (16.12)$$

This volume variation induces energy variations due to the interfacial pressure work

$$\partial_t (\alpha_k \rho_k E_k) = -\mu P_i (P_k - P'_k). \quad (16.13)$$

The compaction viscosity is a positive coefficient or a more complicated positive function. The right-hand side of Eq. (16.13) represents the pressure work during the pressure relaxation process.

For interface flows, Saurel and Abgrall justify pressure equality between the phases by the fact that it restores boundary conditions at the interface, necessary to close the moving boundary problem [206]. The relaxation procedure must therefore ensure  $P_g = P_l$  at the interface. The authors note that it is possible to force pressure equality at the interface by solving the same system as that proposed in Eq. (16.12) and Eq. (16.13). Since pressure equality must be satisfied at each time, it is necessary that the pressure relaxation be instantaneous, so that the compaction viscosity tends to infinity. It is essential to notice that this is completely different from *a priori* supposing mechanical equilibrium. In summary, the compaction viscosity has a finite value in the non-equilibrium homogeneous flow, while it becomes infinite at the interface. This gives the capacity of this model to describe both phases at the same time.

We now focus on velocity relaxation introduced by the term  $\lambda(\mathbf{u}'_k - \mathbf{u}_k)$ . In non-equilibrium homogeneous flows, the velocity relaxation process may have a long characteristic time compared to that of the pressure relaxation. On the one hand, it depends on the pressure relaxation process, which in general is fast compared to the longitudinal wave propagation dynamics. On the other hand, it depends on effects related to fluid viscosity. These last effects may be very slow compared to the others. Therefore, in non-equilibrium homogeneous flows,  $\lambda$  has a finite value. For interface flows, the second interface condition imposes velocity equality at the interface [206]. It implies velocity equilibrium  $\mathbf{u}_g = \mathbf{u}_l$ . A way to impose this condition is to solve system (16.10) with the drag force and an infinite velocity relaxation coefficient  $\lambda$ . It is interesting to compare this relaxation term in two-phase flows, with the one in single-phase flow. If, for a single-phase flow, this term is a pure viscous effect, whereas in two-phase flow, such a term appears even though both fluids are considered inviscid. Indeed, with a two-fluid model, details of the flow microstructure are not available because only averaged quantities are determined. The drag force over an elementary particle (bubble, droplet) corresponds to the sum of constraints induced by the various materials at the interface. There is a part due to viscosity or deviatoric constraints (viscous drag force) and a part due to the spherical part of the strain tensor (pressure drag force). Inside a two-fluid control volume, expressions for these forces need knowledge of the microscopic flow structure, which is not available. Consequently, in general, drag force is introduced as an empirical relation coming from experiments, or from a submodel.

#### *Closure of the interfacial terms*

Let us examine now the closure of the interfacial terms, in the context of interface problems. For these applications, the velocities and pressures of all phases will be relaxed instantaneously during numerical resolution. So, the strategy adopted by Saurel and Abgrall is to choose interfacial variables close to the relaxed state. Because each phase is compressible, a choice preserving symmetry is preferable. A reasonable estimate that considers compressibility of each phase and preserves symmetry is to take the interfacial pressure equal to a mixture total pressure

$$P_i = \sum_k \alpha_k (P_k + \rho_k (\mathbf{u}_i - \mathbf{u}_k)^2). \quad (16.14)$$

The phase pressures  $P_k$  are given by appropriate EOS for each phase.

The second interface variable is the average interfacial velocity. In most references,  $\mathbf{u}_i$  is taken equal to the velocity of the incompressible or the less compressible phase [10, 205, 22]. As mentioned previously regarding the interfacial pressure, determining the interface velocity is not obvious at all. Again, in the context of compressible flows, the choice of the interfacial velocity does not affect the mathematical structure of the overall system, provided that each phase has its own pressure. There is thus some freedom in this choice. But again, for symmetry reasons, we set the velocity of the center of mass as the estimate for the average interfacial velocity:

$$\mathbf{u}_i = \frac{\sum_k \alpha_k \rho_k \mathbf{u}_k}{\sum_k \alpha_k \rho_k}. \quad (16.15)$$

#### *Seven equation model using a "mean-field" description for the description of a disperse-phase*

We highlight here some of the work of Lhuillier consisting in writing a "symmetric system of equations which acknowledges for the existence of a disperse-phase while not prescribing at the outset which phase it is". The disperse-phase is here considered monodisperse, i.e. all particles have the same size. We present here the general ideas of the developments which can be found in [154, 153]. As explained in Section 15.2.1, equations of a two-fluid model can be obtained by an ensemble averaging process of the local instantaneous formulation, multiplied by the phase function  $\chi_p$ , where the subscript p denotes the particles, whereas the subscript f denotes the surrounding fluid. The mass and momentum equations,

assuming no phase change and no gravity, read:

$$\begin{aligned} \partial_t(\alpha_p \rho_p) + \nabla_{\mathbf{x}} \cdot (\alpha_p \rho_p \mathbf{u}_p) &= 0, \\ \partial_t(\alpha_p \rho_p \mathbf{u}_p) + \nabla_{\mathbf{x}} \cdot (\alpha_p \rho_p \mathbf{u}_p \mathbf{u}_p + \alpha_p \rho_p \langle \mathbf{u}' \mathbf{u}' \rangle) &= \nabla_{\mathbf{x}} \cdot (\langle \chi_p \mathbf{T}_p \rangle) - \langle \mathbf{T}_f \cdot \mathbf{n}_p \delta_I \rangle. \end{aligned} \quad (16.16)$$

For the particulate phase however, the kinetic theory can be used, as explained in Chapter I. Hence, instead of  $\chi_p$ , the relevant function of presence is a sum of Dirac delta functions peaked on the particle centers and denoted by  $\delta_p$ :

$$\delta_p = \sum_{i=1}^N \delta_i(\mathbf{x} - \mathbf{R}_i), \quad (16.17)$$

where  $\mathbf{R}_i$  denotes the  $i^{\text{th}}$  particle center location. The number density  $n$  of the particles and the average particle velocity  $\mathbf{v}_p$  are defined as:

$$n = \langle \delta_p \rangle, \quad n \mathbf{v}_p = \langle \delta_p \mathbf{v} \rangle. \quad (16.18)$$

From the kinetic equation of evolution of  $\delta_p$ , the averaged mass and momentum equations read:

$$\begin{aligned} \partial_t(nm) + \nabla_{\mathbf{x}} \cdot (nm \mathbf{v}_p) &= 0, \\ \partial_t(nm \mathbf{v}_p) + \nabla_{\mathbf{x}} \cdot (nm \mathbf{v}_p \mathbf{v}_p + nm \langle \mathbf{v}' \mathbf{v}' \rangle) &= n \mathbf{F}, \end{aligned} \quad (16.19)$$

where  $m$  represents the mass of a particle,  $\mathbf{F}$  represents the forces exerted by the surrounding fluid phase on a particle:  $\mathbf{F} = \langle \oint \mathbf{T}_f \cdot \mathbf{n}_p dS \rangle$ . The average velocity is *a priori* different in each case. Their relationship is explained in the following.

The author's aim is to write a symmetric system of equations for the particles and the fluid. Since the two-fluid formalism is the only applicable one for the fluid phase, there is no choice but to adopt this formalism. However, when it comes to the particulate phase, the kinetic based model provides immediate closures. Therefore, the idea is to express, in the two-fluid model, some quantities pertaining to the particles by their expression derived from the kinetic theory. The challenge then is to relate the two averages:  $\langle \chi_p \rangle$  and  $\langle \delta_p \rangle$ . This is done in [154], where  $\langle \chi_p \psi \rangle$  is expressed as a multipole expansion:

$$\langle \chi_p \psi \rangle = \langle \delta_p \int \psi dV \rangle - \nabla_{\mathbf{x}} \cdot \langle \delta_p \int \mathbf{r} \psi dV \rangle + \frac{1}{2} \nabla_{\mathbf{x}} \nabla_{\mathbf{x}} : \langle \delta_p \int \mathbf{r} \mathbf{r} \psi dV \rangle + \dots, \quad (16.20)$$

and similarly for quantities defined over the interfaces:

$$\langle \delta_I \psi \rangle = \langle \delta_p \int \psi dS \rangle - \nabla_{\mathbf{x}} \cdot \langle \delta_p \int \mathbf{r} \psi dS \rangle + \frac{1}{2} \nabla_{\mathbf{x}} \nabla_{\mathbf{x}} : \langle \delta_p \int \mathbf{r} \mathbf{r} \psi dS \rangle + \dots \quad (16.21)$$

Here,  $\psi$  denotes a flow variable,  $\mathbf{r}$  is the position vector relative to the particle center,  $V$  and  $S$  denote respectively the particle volume and surface. These multipole expansions, over the volume or the surface of a test-particle, are inspired from the macroscopic description of electromagnetic media.

As a consequence of Eq. (16.20), the exact link between the volume fraction  $\alpha_p$  and the number density  $n$  for sphere of radius  $a$  can be found to be:

$$\alpha_p = nV + \frac{a^2}{10} \nabla_{\mathbf{x}}^2 (nV), \quad (16.22)$$

and the relation between  $\mathbf{u}_p$  and  $\mathbf{v}_p$  is:

$$\alpha_p \mathbf{u}_p = nV \mathbf{v}_p + \frac{a^2}{5} \nabla_{\mathbf{x}} \times (nV \Omega_p) + \frac{a^2}{10} \nabla_{\mathbf{x}}^2 (nV \mathbf{v}_p) + \dots \quad (16.23)$$

where  $\Omega_p$  defined by  $\langle \delta_p \Omega \rangle = n \Omega_p$ , is the average angular velocity of the particles.

The link between the two averages being established, let us close the equations of Eq. (16.16). The mass conservation equation is already closed. In the momentum conservation equation we aim at closing the term  $\langle \mathbf{T}_f \cdot \mathbf{n}_p \delta_I \rangle$ . Applying the multipole expansion for this term leads to:

$$\begin{aligned} \langle \mathbf{T}_f \cdot \mathbf{n}_p \delta_I \rangle &= n \langle \oint \mathbf{T}_f \cdot \mathbf{n}_p dS \rangle - \nabla_{\mathbf{x}} \cdot [n \langle \oint (\mathbf{T}_f \cdot \mathbf{n}_p) \mathbf{r} dS \rangle] + \dots, \\ &= n \mathbf{f} - \nabla_{\mathbf{x}} \cdot [n \mathbf{S}] + \dots \end{aligned} \quad (16.24)$$

Then, introducing this expression into the momentum conservation equation of the particulate and the fluid phase leads to (all the small scale fluctuation around the average velocity are neglected):

$$\begin{aligned} \partial_t (\alpha_p \rho_p \mathbf{u}_p) + \nabla_{\mathbf{x}} \cdot (\alpha_p \rho_p \mathbf{u}_p \mathbf{u}_p) &= \nabla_{\mathbf{x}} \cdot (\langle \chi_p \mathbf{T}_p \rangle - n \mathbf{S}) + n \mathbf{f}, \\ \partial_t (\alpha_f \rho_f \mathbf{u}_f) + \nabla_{\mathbf{x}} \cdot (\alpha_f \rho_f \mathbf{u}_f \mathbf{u}_f) &= \nabla_{\mathbf{x}} \cdot (\langle \chi_f \mathbf{T}_f \rangle + n \mathbf{S}) - n \mathbf{f}, \end{aligned} \quad (16.25)$$

and

$$\begin{aligned} \partial_t (\alpha_p \rho_p \mathbf{u}_p) + \nabla_{\mathbf{x}} \cdot (\alpha_p \rho_p \mathbf{u}_p \mathbf{u}_p) &= \nabla_{\mathbf{x}} \cdot (\mathbf{T}^{col}) + n \mathbf{f}, \\ \partial_t (\alpha_f \rho_f \mathbf{u}_f) + \nabla_{\mathbf{x}} \cdot (\alpha_f \rho_f \mathbf{u}_f \mathbf{u}_f) &= \nabla_{\mathbf{x}} \cdot (\mathbf{T}) - n \mathbf{f}, \end{aligned} \quad (16.26)$$

where  $(\mathbf{T}^{col})$  is the tensor due to collisions in the particulate phase. The expression of  $n \mathbf{f}$  is given by [191, 118]:

$$n \mathbf{f} = \alpha_p \nabla_{\mathbf{x}} \cdot \mathbf{T} + \mathbf{F}_r, \quad \mathbf{T} = -p_f \mathbf{I} + \boldsymbol{\tau}, \quad (16.27)$$

where  $p_f$  is the pressure in the fluid phase, and  $\boldsymbol{\tau}$  is the viscous stress of the mixture. The final expressions of the momentum conservation equations are:

$$\begin{aligned} \partial_t (\alpha_p \rho_p \mathbf{u}_p) + \nabla_{\mathbf{x}} \cdot (\alpha_p \rho_p \mathbf{u}_p \mathbf{u}_p) &= \nabla_{\mathbf{x}} \cdot (\mathbf{T}^{col}) + \alpha_p \nabla_{\mathbf{x}} \cdot \mathbf{T} + \mathbf{F}_r, \\ \partial_t (\alpha_f \rho_f \mathbf{u}_f) + \nabla_{\mathbf{x}} \cdot (\alpha_f \rho_f \mathbf{u}_f \mathbf{u}_f) &= \alpha_f \nabla_{\mathbf{x}} \cdot \mathbf{T} - \mathbf{F}_r. \end{aligned} \quad (16.28)$$

If one neglects the collision tensor, the equations are symmetric. The right-hand side terms mean that each phase interacts with the other through a mutual interaction  $\mathbf{F}_r$ , and through the "mean-field" stress  $\mathbf{T}$  created by both phases. The force associated with the mean-field stress acts on each phase in proportion to their volume fraction. The detailed model can be found in [155].

The ideas presented here are very interesting in the perspective of designing a comprehensive model accounting for either the separate flow and the spray. Since this work provides a common formalism for both types of flows, it could be taken benefit from, specially in the transition zone between primary and secondary atomization.

### 16.2.2.2.1 Reduced model: five equation model

To our knowledge, the model proposed by Saurel and Abgrall [207] is the most advanced, since it can simultaneously treat two different types of flows. This is why the spectrum of reachable applications by this model is very large. Among the principal applications we can mention detonation waves [10], cavitation involving evaporation fronts [149], or atomization. For the latter application, nothing prevents to

consider an additional evolution equation on the volumic surface density  $\Sigma$ . Nevertheless, some authors argue that this model may generate important computational cost. Thus, Massoni et al. [166] point out that the hyperbolic, or transport operator is twice as expensive as in the case of a mixture model. This is the reason why Massoni et al. [166] and Allaire et al. [5] proposed a reduced model that is able to treat only interface problems:

$$\begin{aligned}
 \partial_t \alpha_k + \mathbf{u} \cdot \nabla_{\mathbf{x}} \alpha_k &= 0, \\
 \partial_t (\alpha_k \rho_k) + \nabla_{\mathbf{x}} \cdot (\alpha_k \rho_k \mathbf{u}_k) &= \Gamma_k, \\
 \partial_t (\rho \mathbf{u}) + \nabla_{\mathbf{x}} \cdot (\mathbf{u} \otimes \mathbf{u}) &= -\nabla_{\mathbf{x}}(P), \\
 \partial_t (\rho E) + \nabla_{\mathbf{x}} \cdot (\rho E \mathbf{u}) &= -\nabla_{\mathbf{x}}(P_k \mathbf{u}).
 \end{aligned} \tag{16.29}$$

As pointed out by Le Metayer [149] this interface model is an asymptotic reduction of the previously described interface model, where kinetic and mechanical equilibrium are assumed. Note that since less transport equations are considered, less characteristics waves are considered, so that this model is hyperbolic with this set of equilibrium assumptions.

This five equation model is also used in [39] to describe the physical behavior of a free surface between two fluids, and particularly to reproduce sloshing in spatial rocket tank. The configuration described is isothermal, so that the model does not contain an equation on energy. Moreover, the equation on the volume fraction contains a relaxation term based on the pressure difference between the two phases, as written in system (16.10), with an infinite relaxation velocity. In order to assess the pressure in each phase, a linearized equation of state is used :  $P_k(\rho_k) = P_0 + c_k^2(\rho_k - \rho_{0,k})$ , where  $P_0$  and  $\rho_{0,k}$  are respectively a reference pressure and a reference density for phase  $k$ .

#### Numerical methods

Concerning the numerical methods for the averaged five and seven-equation model, the critical aspect is the treatment of the interface. There exist two types of methods. The first type of methods allows numerical diffusion at the interface. Contrary to methods used in a DNS context, using VOF or Level Set method, the interface is not reconstructed. As explained in [207], numerical diffusion is considered as a drawback for numerical schemes, but is usually a necessary feature to capture discontinuities in gas dynamics applications. In the context of flows with interfaces, numerical schemes, based on Riemann solvers have been designed in [207, 206, 166, 149] that possess a similar simplicity: a scheme that works on a fixed grid, that allows interface deformations, that deals with inflow and outflow boundary conditions in a simple way, that uses the same numerical scheme for all computational cells, and also predicts interface formation. These methods usually create a numerical transition zone for the volume fraction  $\alpha$  which requires to introduce a mixture model. This can be problematic for the five-equation model, since no mixture is *a priori* considered. Solutions have been provided to this issue in [5, 4]. Numerical diffusion can be reduced by techniques used in gas dynamics applications: mesh refinements or high-order differencing for example.

The second type of methods preserves the interface sharpness. We underline here the recent advances made in [136] by designing an anti-diffusive numerical scheme for the simulation of interfaces between compressible fluids in the context of a five-equation model. It is interesting to note that these methods does not involve any interface reconstruction method.

## 16.3 Two-fluid model implemented in the IFP-C3D code

This section focuses on the model designed for the simulation of injection with the IFP-C3D code. It exposes the main justifications for the model choice, stated in [215, 220]. The configuration targeted is a fuel injection in car engine conditions. The pressure injection can rise up to 2000 bar, whereas the velocity can reach  $600 \text{ m s}^{-1}$ . Under these conditions, the liquid phase compressibility is considered. An interface model for compressible phases is then required in order to take into account the non-thermodynamic

equilibrium between the gas in the chamber and the injected fuel. A five-equation or seven-equation models are then good candidates for this problem. Besides, one wants to model the multi-phase area coming from primary and secondary break-up. Therefore a seven-equation model is finally chosen. This model, presented in [12] is similar to the model of Baer and Nunziato presented before. An EOS for each phase is considered: perfect gas for the gas phase, and rigid gas [215, 220] for the liquid phase. Moreover, in order to provide more information about the liquid phase topology than the single volume fraction, an evolution equation on surface area density has been added [220]. In terms of numerical methods, the strategy of Truchot [215] has consisted in taking up the general algorithm and the schemes designed for the gas phase, and to adapt it to the liquid phase. This algorithm is based on the ALE formalism and an operator splitting algorithm. The algorithm as well as the numerical schemes are presented in Section 14.1.

## Conclusion

This review on averaged models, based on the classification made in Chapter 15 is intended to provide a background substantial enough to understand the principal features of the two-fluid model implemented in the IFP-C3D code.

This two-fluid model implemented progressively by [215, 220, 12], is a seven-equation model similar to the model designed in [10], augmented with an equation on the surface area density. The same numerical methods are applied to the gas and the liquid phase in the context of the ALE formalism.

On the other hand, the developments made in the context of this PhD Thesis on this topic have led to the implementation of an Eulerian spray model, the EMSM model (see Part 4), with the same numerical methods. Thus, at present, the IFP-C3D code contains, at the same time, a separate-phase two-fluid model, and a spray model. The challenge now is to couple these descriptions into a comprehensive description of fuel injection, that can meanwhile describe the physics of the two-fluid flow area close to the injector, and also provide precise information of the topology of the droplet flow after atomization. Such a coupling between a separate-phase two-fluid model and a spray model has already been attempted. Let us mention the work done in [54] for fuel injection consisting in coupling an Homogeneous Equilibrium Model for the simulation of the liquid core primary break-up with a Lagrangian description of the disperse phase. This coupling is done in the solver Eulerian Lagrangian Spray Atomization (ELSA). Nevertheless coupling a Eulerian approach with a Lagrangian approach leads some difficulties. The first one concerns the nature of the quantities considered, which are averaged values throughout a cell in the Eulerian approach, and punctual values in the Lagrangian approach. This difference may lead, during the coupling, to problems regarding the conservation of mass, momentum and energy of the liquid phase. Moreover the initialization of the Lagrangian particles is done through a sampling of the number density function (NDF). This step requires to explicitly reconstruct a NDF, whereas the information transported by the Eulerian model concerns at most fewer moments of the NDF. The choice of coupling two Eulerian models in the context of this PhD is to have precisely the same approach in both models in order to circumvent these two difficulties.

At present, the flow topology is described through the volume fraction  $\alpha$ , and the surface area density  $\Sigma$ . This description does not suppose a particular droplet geometry, but accesses only a mean diameter in the case of spherical droplets. On the other hand, the spray model considers four size moments, supposing the droplets spherical. The first issue to address is then to define equivalent quantities in both models that can be transferred from the two-fluid model to the spray model. The first possible way to explore is to enrich the description of the flow topology by the separate-phase two-fluid model. Secondly, in the context of the spray model, to account for more complex droplet geometries, so that droplets are not assumed spherical any more. The second issue to address is the criteria definition triggering the model switch. Corresponding studies can be found in [54].

# General Conclusion and Perspectives

The studies conducted in this work had to answer two questions. The first aspect was to address the limitations of Eulerian spray models compared to Lagrangian models. We are indeed more than convinced of the promising potential of Eulerian models, as a serious alternative for Lagrangian methods currently used in industry for simulations of two-fluid flows. The separate area of the flow, where the liquid phase is a continuum, is naturally described by Eulerian separate-phase two-fluid models. In the context of a complete description of liquid injection, because they are based on the same framework, Eulerian spray models for the disperse phase appear to ensure a much easier coupling with the separate-phase description than Lagrangian approaches. Besides, the computational cost needed for the simulation by Lagrangian methods of an instantaneous flow can be very important, whereas the adaptation of these methods to parallel architecture is far from being obvious. On the other hand, Stéphane de Chaisemartin and Lucie Fréret [49, 88, 86] have proven the high optimization capacity of the Eulerian multi-fluid model. However two theoretical difficulties have to be answered preliminarily: the ability to describe a polydisperse flow with only one size section, and non-equilibrium flows, where particle trajectory crossing (PTC) may occur. Secondly, in the context of the project conducted by IFP Energies nouvelles, consisting in the simulation of a full spray injection in internal combustion engines, the purpose of this work was to implement an Eulerian spray model able to account for spray polydispersity and meeting the requirements of an industrial computation in terms of computational cost.

By reaching these two objectives, this work has brought three major contributions. It has answered the two theoretical difficulties of Eulerian spray models emphasized in the previous paragraph. This has resulted in the design of groundbreaking models, based on high order moment methods. The first one, developed in Part II, the EMSM model, provides a very efficient description of polydispersity, and validation results show that it has come to a very interesting degree of maturity. On the other hand, Part III is dedicated to overcome the theoretical barrier preventing Eulerian spray model to describe PTC. This has resulted in a breakthrough in Eulerian modeling: the EMVM model. This work has been done in the context of research work towards a future use in an industrial context.

Second, two coupled models are proposed, the first one by associating the multi-fluid model to the EMVM model, resulting in the EMFVM model, and the second one by associating the EMSM to the EMVM model, resulting in the EMSVM model. Furthermore, it has answered the need formulated by IFP Energies nouvelles by implementing the EMSM previously mentioned in the code IFP-C3D, in the ALE formalism.

What is particularly interesting in this work is the fact that it has covered all the innovation steps from the actual design of the model resolving mathematical and physical difficulties, to its feasibility in an industrial context, resolving difficulties in terms of engineering. Eventually, new innovative numerical algorithms have emerged, in order to ensure accuracy and stability proprieties for dynamical systems with peculiar mathematical structure and a narrow stability domain. Some have been devised in Eulerian framework and some other in Arbitrary Eulerian Lagrangian framework,

By combining mathematical, physical, and numerical analysis as well as computer science and engineering work, this work has brought the following results:

- In terms of mathematical analysis, the determination of the EMVM system weakly hyperbolic character, the equilibrium statement between the kinetic and macroscopic levels of description, and the characterization of the entropy solution in case of singularities. This work has been submitted in the journal *Communication in Mathematical Sciences* [125].

- In terms of modeling:
  - The creation of the EMSM model with stable closure. The evaporative term is closed using an Entropy Maximization technique [177]. For that purpose, the moment space properties are investigated. In order to close the drag term in the momentum dynamics equation we consider the size-averaged velocity instead of the number-averaged velocity.
  - The design of the EMVM model based on a Quadrature Method of Moment (QMOM) [84], with the critical algorithm of inversion of the moment sequence to compute the corresponding set of weights and abscissas. One and two-dimensional cases are presented, which leads to different types of problems.
  - The coupling of the multi-fluid and the EMVM models leading to an Eulerian model overcoming the two difficulties of Eulerian spray models, and also the coupling of the EMSM and the EMVM models. These models rely on the assumption of independence of size and velocity distributions in each size section, simplifying their derivation.
- In terms of numerical scheme:
  - An original numerical scheme for the description of the size phase space dynamics of an evaporative spray, combining a kinetic-based scheme [196] with a Direct Quadrature Method of Moment (DQMOM) [159]. This scheme is of high order accuracy in space and time. This model and this scheme are not limited to liquid droplet, but can be used for the resolution of aerosol or soots dynamics. This work has been published in the SIAM Journal of Applied Mathematics [173], and presented during the SIAM International Conference on Numerical Combustion, Monterrey, USA (2008) [127].
  - A new numerical scheme for the resolution on the advection of a moment sequence, based on the reconstruction of canonical moments in the context of a kinetic-based scheme. To our knowledge, this scheme is the first one able to preserve the realizability condition for the integrity of the moment sequence *per se*. Indeed, this question has already been investigated [176, 231] but, always, additional algorithms were used to satisfy this condition. This work has been published in a Lectures Series of the Von Karman Institute [172] and presented during the ICLASS Conference, Vail, USA (2009) [128].
  - Robust algorithms for the high order velocity moment method towards its implementation in the platform MUSES3D, preserving its genericity.
  - Adaptation of transport algorithms for the EMSM model for its extension to the ALE framework used in the IFP-C3D code, involving moving meshes. This work has been presented during the ICMF Conference, Tampa, USA (2010) [130], and is in preparation in the International Journal of Multiphase Flows [131].
- In terms of computing:
  - Creation of new functionalities in the code MUSES3D, by defining computing strategies for the implementation of the EMSM and the EMVM models.
  - Creation of a new functionality, Eulerian spray resolution, in the IFP-C3D code, by defining computing strategies for the implementation of the EMSM model.
  - Assessment of the efficiency of the EMSM model by time resolved comparisons with the multi-fluid model, in a DNS framework. This work has been submitted in Journal of Computational Physics [129].
  - Assessment of the feasibility of computations with the EMVM model. This work has been published in the journal Flow, Turbulence and Combustion [126], in two proceedings of the Summer Program 2008 at Stanford [51, 87] and in a special number of the Comptes Rendus Mécanique [50].



- Validation of this functionality, and assessment of its feasibility in injection cases, towards full engine computation, in the IFP-C3D code. First results have been presented during the ICMF Conference, Tampa, USA (2010) [130], and the complete results are to be published in an article in preparation in the International Journal of Multiphase Flows [131].

As far as the perspectives of this work are concerned, three types of extensions can be thought of. The first one represents a direct continuation of the work provided in this study, developing the physical analysis of evaporating spray dispersion in turbulent flows. The second one is related to the improvement of spray models and their extension to other resolution contexts. Finally, the third one concerns the coupling between separate-phase two-fluid models and Eulerian spray models.

- The developments made in the IFP-C3D code have been validated through comparison with the Lagrangian model used in the IFP-C3D code, for injection cases. This validation has been done, first, in a low velocity injection case. If the validation through real injection cases does not bring any additional difficulties, it could bring a final demonstration of the feasibility of the implemented spray model in the IFP-C3D code. Besides, the Eulerian spray model has been introduced, first, in a context of a simplified framework: one-way coupling,  $d^2$  law for evaporation. Yet this framework differs from the Lagrangian model one [18]. A study needs to be conducted to consider the same framework for both models in order to do quantitative comparisons. This involves, in particular, the extension of the Eulerian spray model to the RANS framework of the IFP-C3D code. Additional terms will then have to be considered like turbulent dispersion. This is studied by Oguz Emre in his PhD [74].
- The second point is related to research work in Eulerian spray models. The first aspect is to propose, on the basis the mathematical analysis done in Section 9.2, a fully high order advection scheme for the simulation of spray flows with potential occurrence of PTC. On the basis of the work presented in Section 9.3, the second aspect consists in improving the quadrature method in multi-dimensional configurations. The Conditional Quadrature Method of Moment (CQMOM) has been proposed [233] in that perspective. Besides, one point that should be improved in the EMSM model is the size-velocity correlation which is on its way [222] and the method should be a powerful method in order to capture the dynamics and evaporation of polydisperse sprays.

Moreover, the extension to LES should be considered. This work has already begun with methods considering a velocity dispersion provided by LES sub-models [37], instead of the monokinetic assumption done here. A third aspect is that the numerical schemes for advection are presented in this work for structured meshes. Their extension to non-structured mesh is required in order to extend the accuracy level to industrial code like IFP-C3D. Finally, despite the simplified framework considered in this work, it is important to note that Eulerian spray models can be extended to more complex frameworks. Let us mention for example the work of François Doisneau, taking into account the coalescence operator [59, 60].

- The last perspective corresponds to the last stage of the project conducted by IFP Energies nouvelles: the coupling between the existing separate-phase model, and the Eulerian spray model implemented during this PhD. Two questions have to be answered in terms of modeling. First, this coupling objective points out the difficulty to take into account the compressibility of each phase. In the two-fluid model, both phase are considered as compressible, but droplets are considered incompressible in the spray model. Based on physical grounds, the relevance of taking into account the disperse phase compressibility will have to be first answered, since this assumption will condition the modeling as well as the numerical scheme. The second question concerns the representation of the liquid topology done in each model. On the one hand, the two-fluid model considers the volume fraction and surface area density, with an undefined geometry of the liquid phase. On the other hand, the EMSM model considers moments of a size distribution of droplets assumed to be spherical. The challenge is then to enrich the description done by both models in order to define equivalent quantities that can be exchanged from the two-fluid model to the EMSM model. This aspect is related to primary atomization, studied at IFP Energies nouvelles by Bejoy Mandupala in his PhD [158], breaking the dense liquid core into ligaments and not necessarily into droplets.

# Appendices

## Appendix A

# Chapman-Enskog development for the resolution of the Fokker-Planck equation

The Fokker-Planck equation introduced in Section 1.2.5 reads:

$$\partial_t f + \nabla_{\mathbf{x}} \cdot (\mathbf{u}f) = \frac{1}{\epsilon} \mathcal{J}(f), \quad \mathcal{J}(f) = \nabla_{\mathbf{u}} \cdot [(\mathbf{u} - \mathbf{u}_g)f + \boldsymbol{\sigma} \nabla_{\mathbf{u}} f] \quad (\text{A.1})$$

where the differential operator  $\mathcal{J}$  appears to be a singular perturbation for Eq. (A.1) in the case  $\epsilon \rightarrow 0$ . The NDF is solved in that case using a Chapman-Enskog development.

The basic idea of the Chapman-Enskog method [40], [41], is to expand the NDF  $f$  into a series in the formal smallness parameter  $\epsilon$  as :

$$f = f^{(0)} + \epsilon f^{(0)} \phi^{(1)} + \epsilon^2 f^{(0)} \phi^{(2)} + \dots \quad (\text{A.2})$$

where each order of  $\epsilon$  is recursively solved from the lower orders of  $\epsilon$ .

*Remark:* For the sake of simplicity and ease, the Chapman-Enskog development is performed in one-dimension.

The first step in a Chapman-Enskog development is to determine the invariants of the operator  $\mathcal{J}$ . From Eq. (A.1), it follows that the total number density  $\rho_p$  is the only invariant, as:

$$\int \mathcal{J}(f) du = 0, \quad \forall f. \quad (\text{A.3})$$

Introducing the expansion Eq. (A.2) in Eq. (A.1) leads to the following equation:

$$\begin{aligned} \partial_t f^{(0)} + \partial_x (u f^{(0)}) + \epsilon (\partial_t f^{(0)} \phi^{(1)} + \partial_x (u f^{(0)} \phi^{(1)})) + \epsilon^2 (\partial_t f^{(0)} \phi^{(2)} + \partial_x (u f^{(0)} \phi^{(2)})) + \dots = \\ \frac{1}{\epsilon} J(f^{(0)}) + J(f^{(0)} \phi^{(1)}) + \epsilon J(f^{(0)} \phi^{(2)}) + \dots, \end{aligned} \quad (\text{A.4})$$

Since the coefficient of each order of magnitude of  $\epsilon$  must be null in Eq. (A.4), it follows that  $J(f^{(0)}) = 0$ , and so that  $f^{(0)}$  must be Maxwellian:

$$f^{(0)} = \frac{\rho_p}{\sqrt{2\pi\sigma}} \exp\left(-\frac{C^2}{2\sigma}\right), \quad (\text{A.5})$$

where  $C = u - u_g$ .

The terms of higher order with respect to  $\epsilon$  in the Chapman-Enskog expansion Eq. (A.2) satisfy differential equations, the left-hand side of which involve the lower order terms and the kernel of which is associated to the only macroscopic quantity conserved by the  $J$  operator, that is total number density of particles.

## Zeroth order derivation

At the zeroth order in  $\epsilon$ , Eq. (A.4) reads:

$$\partial_t f^{(0)} + \partial_x (u f^{(0)}) = J(f^{(0)} \phi^{(1)}), \quad (\text{A.6})$$

Let us rewrite Eq. (A.6):

$$\partial_t \log(f^{(0)}) + \partial_x (u \log(f^{(0)})) = \frac{1}{\epsilon} \mathcal{F}(\phi^{(1)}), \quad \mathcal{F}(\phi^{(1)}) = \frac{\mathcal{J}(f^{(0)} \phi^{(1)})}{f^{(0)}}. \quad (\text{A.7})$$

It can be shown, after some algebra, that:

$$\mathcal{F}(\phi^{(1)}) = (u_g - u) \partial_v \phi^{(1)} + \sigma \partial_v^2 \phi^{(1)}. \quad (\text{A.8})$$

A key property of  $\mathcal{F}$  will be very useful in the following. First, let us denote the scalar product  $\int f^{(0)} \Phi \Psi du$  in the Hilbert space of the  $L^2$  functions of the velocity  $\mathbb{H}$  by  $\langle \Phi, \Psi \rangle$ . The demonstration that  $\int f^{(0)} \Phi \Psi du$  is a scalar product is straightforward. It comes that:

**Proposition 9** *The operator  $\mathcal{F}$  is self-adjoint for the scalar product  $\langle \cdot, \cdot \rangle$ , i.e.  $\langle \Phi, \mathcal{F}(\Psi) \rangle = \langle \mathcal{F}(\Phi), \Psi \rangle$ .*

**Proof 9**

$$\begin{aligned} \langle \Phi, \mathcal{F}(\Psi) \rangle &= \int f^{(0)} \Phi \mathcal{F}(\Psi) du \\ &= \int f^{(0)} \Phi (u_g - u) \partial_v \Psi du + \sigma \int f^{(0)} \Phi \partial_v^2 \Psi du \\ &= - \int \Psi \frac{(u_g - u)}{\sigma} f^{(0)} \Phi (u_g - u) du - \int \Phi f^{(0)} \partial_v \Psi (u_g - u) du + \int \Psi f^{(0)} \Phi du \\ &\quad - \sigma \int \frac{(u_g - u)}{\sigma} f^{(0)} \Phi \partial_v \Psi du - \sigma \int f^{(0)} \partial_v \Phi \partial_v \Psi du \\ &= - \int \Phi f^{(0)} \Psi du + \int \phi f^{(0)} \Phi du \\ &\quad + \int \frac{(u_g - u)^2}{\sigma} f^{(0)} \Phi \Psi du - \int \Psi \frac{(u_g - u)}{\sigma} f^{(0)} \Phi (u_g - u) du \\ &\quad + \int (u_g - u) f^{(0)} \partial_v \Phi \Psi du - \int \Psi f^{(0)} \partial_v \Phi (u_g - u) du \\ &\quad + \int f^{(0)} \Psi (u_g - u) \partial_v \Phi du + \sigma \int f^{(0)} \Psi \partial_v^2 \Phi du - \int \Psi f^{(0)} \partial_v \Phi (u_g - u) du \\ &= \sigma \int f^{(0)} \Psi \partial_v^2 \Phi du - \int \Psi f^{(0)} \partial_v \Phi (u_g - u) du \\ &= \int f^{(0)} \Psi \mathcal{F}(\Phi) du \\ &= \langle \Psi, \mathcal{F}(\Phi) \rangle. \end{aligned} \quad (\text{A.9})$$

■

In this context, we end up with a self-adjoint compact differential operator with a one dimensional kernel in the proper Hilbert space, for which a Fredholm alternative guarantees the resolvability of  $\phi^{(1)}$  and leads to the following proposition.

**Proposition 10** *The function  $\partial_t \log(f) + \partial_x(u \log(f))$ , verifies*

$$\int \partial_t \log(f) + \partial_x(u \log(f)) \, du = 0, \quad (\text{A.10})$$

so that the equation on the macroscopic quantities reads:

$$\partial_t \rho_p + \partial_x(\rho_p u_g) = 0. \quad (\text{A.11})$$

This condition is called the resolvability condition.

**Proof 10** *The function  $\partial_t \log(f) + \partial_x(u \log(f))$  belongs to the image of  $\mathcal{F}$ , so, given the self-adjoint character of  $\mathcal{F}$ , it must be orthogonal to its kernel. It comes that  $\langle \partial_t \log(f) + \partial_x(u \log(f)), 1 \rangle = 0$ .*

■

## First order derivation

To obtain the first order expression of the total number density, we need to consider the terms of order  $\epsilon$  in Eq. (A.4):

$$\partial_t(f^{(0)}\phi^{(1)}) + \partial_x(u f^{(0)}\phi^{(1)}) = \mathcal{J}(f^{(0)}\phi^{(2)}). \quad (\text{A.12})$$

Extending the resolvability condition defined in Prop. (10), to the first order of  $\epsilon$  in Eq. (A.4) leads to:

$$\partial_t \rho_p + \partial_x(\rho_p u_g) = -\epsilon \partial_x \int f^{(0)} \phi^{(1)} u \, du. \quad (\text{A.13})$$

The explicit expression of  $\phi^{(1)}$  has to be given to determine Eq. (A.13). It needs the resolution of Eq. (A.6). The left-hand side of Eq. (A.6) can be expressed according to the macroscopic quantities of the particles through the expression of  $f^{(0)}$  given in Eq. (A.5):

$$\begin{aligned} \partial_t \log(f^{(0)}) + \partial_x(u \log(f^{(0)})) &= \partial_t \log(f^{(0)}) + u_g \partial_x(\log(f^{(0)})) + C \partial_x(\log(f^{(0)})) \\ &= D_t(\log(f^{(0)})) + C \partial_x(\log(f^{(0)})) \\ &= \frac{1}{\rho_p} D_t \rho_p + \frac{C}{\sigma} D_t u_g + C \frac{\partial_x \rho_p}{\rho_p} + \frac{C^2}{\sigma} \partial_x u_g \\ &= \underbrace{\left(\frac{C^2}{\sigma} - 1\right)}_{\Phi_1} \partial_x u_g + \underbrace{\frac{C}{\sigma}}_{\Phi_2} D_t u_g + \underbrace{\frac{C}{\Phi_3}}_{\Phi_3} \frac{\partial_x \rho_p}{\rho_p}. \end{aligned} \quad (\text{A.14})$$

where  $D_t = \partial_t + u_g \partial_x$ .

The function  $\phi^{(1)}$  is then decomposed into:

$$\phi^{(1)} = \phi_1^{(1)} \partial_x u_g + \phi_2^{(1)} D_t u_g + \phi_3^{(1)} \frac{\partial_x \rho_p}{\rho_p}, \quad (\text{A.15})$$

leading to the system of three equations:

$$\mathcal{F}(\phi_1^{(1)}) = \left(\frac{C^2}{\sigma} - 1\right), \quad \mathcal{F}(\phi_2^{(1)}) = D_t u_g, \quad \mathcal{F}(\phi_3^{(1)}) = \frac{\partial_x \rho_p}{\rho_p}, \quad (\text{A.16})$$

where the solution writes:

$$\phi_1^{(1)} = \frac{C^2}{\sigma}, \quad \phi_2^{(1)} = -\frac{u}{\sigma}, \quad \phi_3^{(1)} = -u. \quad (\text{A.17})$$

The flux in Eq. (A.13) writes then:

$$\int f^{(0)} \phi^{(1)} u \, du = \left[ \int f^{(0)} C \, du \right] \frac{\partial_x \rho_p}{\rho_p} + \left[ \int f^{(0)} \frac{C^2}{\sigma} C \, du \right] \partial_x u_g + \left[ \int f^{(0)} - \frac{u}{\sigma} C \, du \right] D_t u_g, \quad (\text{A.18})$$

so that

$$\int f^{(0)} \phi^{(1)} u \, du = -\sigma \partial_x \rho_p - n D_t u_g, \quad (\text{A.19})$$

which leads to the explicit formulation of Eq. (A.13):

$$\partial_t \rho_p + \partial_x (\rho_p u_g) = \epsilon \partial_x (\sigma \partial_x \rho_p) + \epsilon \partial_x (\rho_p D_t u_g). \quad (\text{A.20})$$

This equation is called the Schmoluchovski equation [89].

Another way to obtain this result would be to consider the momentum from Eq. (A.6), in the reference frame moving with the mean gas velocity  $u_g$ :

$$\int C [\partial_t f + \partial_x (u f)] \, du = \int C \left[ \frac{1}{\epsilon} \mathcal{J}(f) \right] \, du. \quad (\text{A.21})$$

# Appendix B

## EMSM model

### B.1 Resolution of the ODE system with classical methods

The purpose of this appendix is to show the instabilities of a resolution of ODE systems of type (4.15) with classical schemes and a pointwise reconstruction. We use the ME reconstruction with  $N = 3$  and  $S_{\min} = 0$ ,  $S_{\max} = 1$ . If  $\mathbf{m}(t) = (m_0(t), m_1(t), m_2(t), m_3(t))$ , the system that must be solved is the following one :

$$\begin{cases} \mathrm{d}_t m_0 = -\tilde{n}_{ME} \\ \mathrm{d}_t m_1 = -m_0 \\ \mathrm{d}_t m_2 = -m_1 \\ \mathrm{d}_t m_3 = -m_2 \end{cases} \quad (\text{B.1})$$

We will thus compare the results given by some classical ODE solvers with the analytical solution of the equation (4.12). The functions that we choose as references are a smooth and a singular one given in Fig. 5.2 and Fig. 5.5 respectively.

#### Explicit Runge Kutta scheme

We use a solver based on an explicit Runge-Kutta (4,5) formula with an adaptative time step [63]. We present the results of the resolution scheme at two different times in order to illustrate the amplification of the errors generated.

For the smooth distribution, we can see in Fig. B.1-left that the ODE solution at  $t = 0.15$  becomes substantially different from the solution obtained by the reconstruction from the moments of the analytical solution. It clearly breaks down (Fig. B.1-right) at  $t = 0.2$ . The calculations give the same results, regardless of the relative tolerance (we launched resolution with tolerance of  $10^{-6}$ ,  $10^{-10}$ ,  $10^{-16}$ ). At each time step, an error is made for the evaporative flux. This error amplifies as it can be seen at the two times  $t = 0.15$  and  $t = 0.2$ , and finally the moment vector doesn't belong to the moment space any more. In other words, there is no function whose successive moments are equal to the components of the moment vector and it exemplifies the stability problem encountered in the moment method. The problem of the solver is not a problem of stiffness of the system, but a problem of preservation of the moment space, as it is explained in the next subsection (Section B.1).

The same conclusions hold for the singular distribution. We present the situation in Fig. B.2 at  $t = 0.6$ . Indeed when we compute the solution for a longer time, the resolution collapses.

#### Explicit Euler method

Let us use the explicit Euler method with a fixed time step. We show that, as for the Runge-Kutta solver, the resolution breaks down, and we study now the cause of this collapse. Indeed, we see what happens for the canonical moments. As seen in Section 4.2.2, the canonical moments indicate the position of the moment vector relative to the moment space boundaries. If the vector goes out of the moment space, that

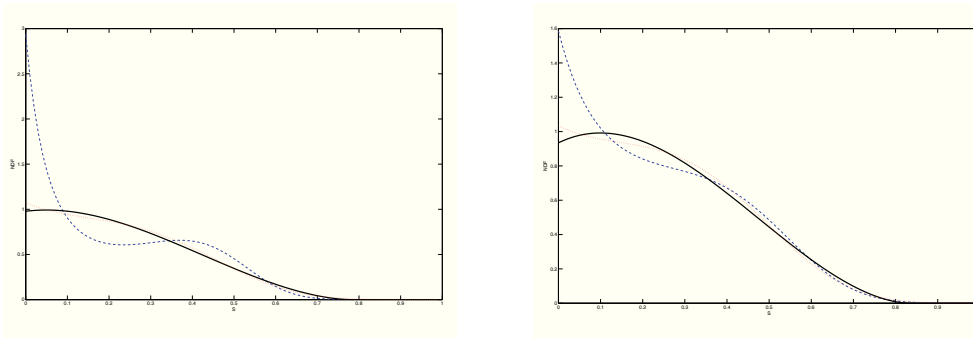


Figure B.1: Analytical solution (solid lines), its reconstruction from its moments by maximization of entropy (dotted lines) and solution of (B.1) computed with the Runge-Kutta method for the smooth initial distribution (dashed lines), at  $t = 0.15$  (left) and  $t = 0.20$  (right).

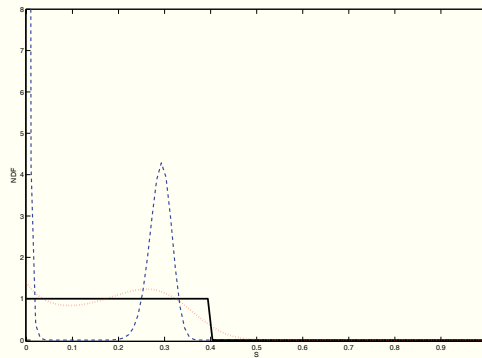


Figure B.2: Analytical solution (solid lines), its reconstruction from its moments by maximization of entropy (dotted lines) and solution of (B.1) computed with the Runge-Kutta method for the singular initial distribution, at  $t = 0.6$ .

means that there is no function whose successive moments are equal to the components of the vector, and thus no more ME reconstruction is available. The canonical moments must stay between 0 and 1.

In order to show that the resolution does lead to an improper solution regardless of the time step, we present two results obtained with three different time steps :  $dt = 0.1$  ,  $dt = 0.01$ , and  $dt = 0.001$ . The evolution of the canonical moments is represented to show that the collapse is due to the (negative) value of one of them.

For the smooth distribution, it can be seen in Fig. B.3 the canonical moments of the analytical solution. The moment space becomes narrower and narrower as time goes on. This is due to the fact that support of the distribution decreases as time goes on. For  $dt = 0.1$ , we can notice that the resolution collapses when the third canonical moment becomes negative (Fig. B.3-left). The error made by considering the evaporative flux constant during a whole time step is too big to preserve the moment space. When we consider a time step equal to 0.001, the stop time is bigger than 1 (Fig. B.3-right), because contrary to the analytical solution where all the droplets have been evaporated, there are still droplets left in the Explicit Euler solution because of the numerical diffusion. The Explicit Euler solution sticks very well to the analytical solution. That is not amazing because the smaller the time step is, the more accurate the Explicit Euler solution is, because the error made on the evaporative flux is smaller. It must be noticed that this result is possible because the initial distribution we consider has its canonical moments quite far from the moment space boundaries. So, even if there is a small error, the moment space will be preserved for a longer time. But problems appear when there is almost no droplets left. Indeed, the moment space becomes always narrower, and there is a time when the moment space is not preserved, which is revealed by the fact that at least one canonical moment becomes negative (Fig. B.3-right). Nevertheless, one can



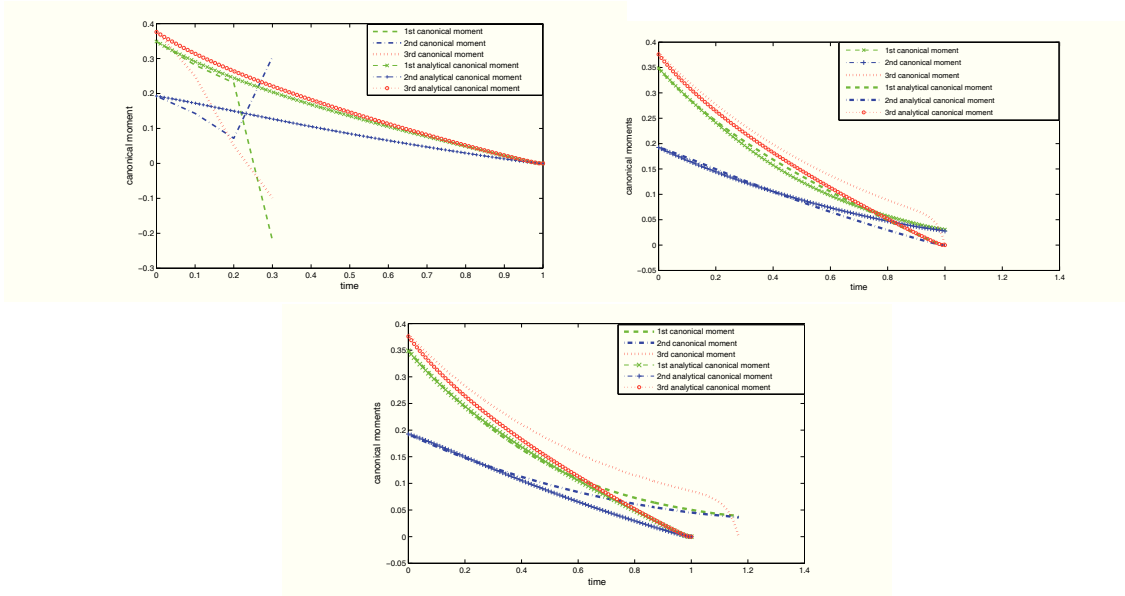


Figure B.3: canonical moments of the Euler Explicit solution for  $dt = 0.1$  and  $dt = 0.001$  for the smooth initial distribution.

argue that this method gives precise results, before the moment space is no more preserved. However, its cost becomes prohibitive without insuring a global stability property. Thus the scheme breeds an intrinsic error which inevitably leads to the collapse of the resolution.

We present in Fig. B.4 the canonical moments for the exact solution with the singular distribution. The conclusions are the same as the one for the smooth distribution. The smaller the time step is, the longer the space moment is preserved, but there is always a time when the errors make the moment space not preserved any more, as we can see for the time steps  $dt = 0.05$  and  $dt = 0.001$ .

The direct resolution of system (B.1) with classical ODE solvers leads then to stability problems due to the fact that the moment space is not conserved. That is why kinetic scheme is developed in Section 5.1.

## B.2 ME reconstruction and boundaries of the moment space

The aim of this part is to show the behavior of the ME reconstruction close to the boundary of the moment space. In order to evaluate the distance to this boundary, we use the canonical moments presented in Section 4.2.2

At the boundary of  $\mathbb{M}_1$ , the first canonical moment is equal to 0 or 1. The solution of the Hausdorff problem is then a Dirac delta function  $\delta_0$  if  $p_1 = 0$  or  $\delta_1$  if  $p_1 = 1$ , for a moment of order 0  $m_0$  equal to 1. The ME reconstructions with 4 moments for two moment vectors close to these boundaries are plotted in Fig. B.5; they correspond to the canonical moments  $p_1 = 0.01$  or  $p_1 = 0.99$ ,  $p_2 = 0.5$  and  $p_3 = 0.5$ . The lower principal representations are also plotted (with an arbitrary scale). We can see that the ME reconstructions, as well as the lower principal representations, give NDF close to the expected Dirac delta functions. It can also be shown that the moment of order 0 over an interval  $[0, S_b]$  with  $S_b$  bigger than 0.02 of the two reconstructions only differ of less than 0.3% and are equal to 1 (the value for the corresponding point of the boundary) with an accuracy greater than 1%. Moments of order bigger than 1 over  $[0, S_b]$  are very small in two cases. In the context of a kinetic scheme for the resolution of the evaporation, like in Section 5.1.4 or Section 5.4.2, it is quite easy to see that, for moment vector close to the boundary (even close enough so that the Newton algorithm of the ME reconstruction does not converge) the flux can be computed with the lower principal representation, or eventually with the NDF corresponding to the point of the boundary.

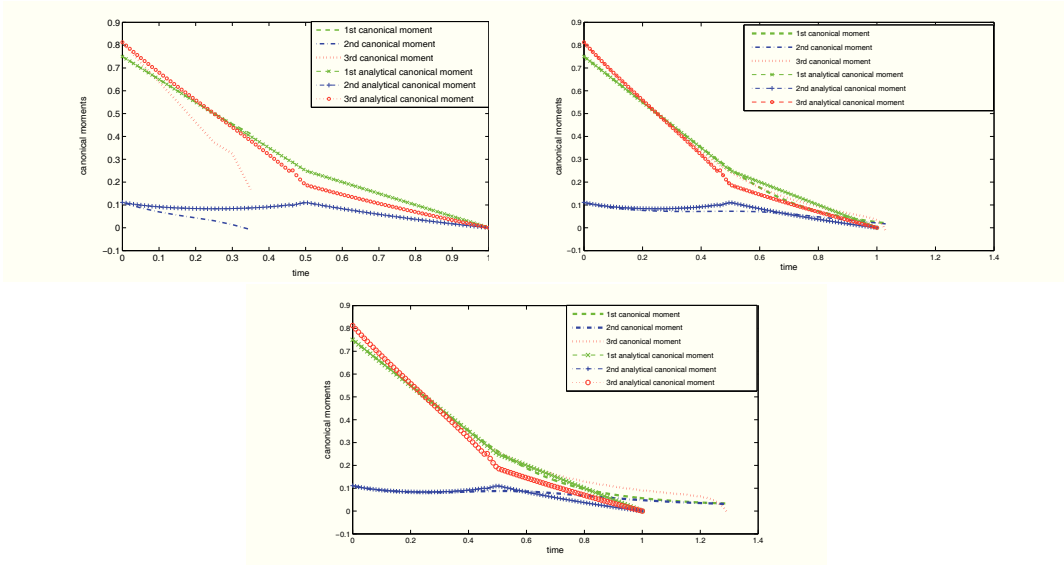


Figure B.4: canonical moments of the Euler Explicit solution for  $dt = 0.05$  and  $dt = 0.001$  for the singular initial distribution.

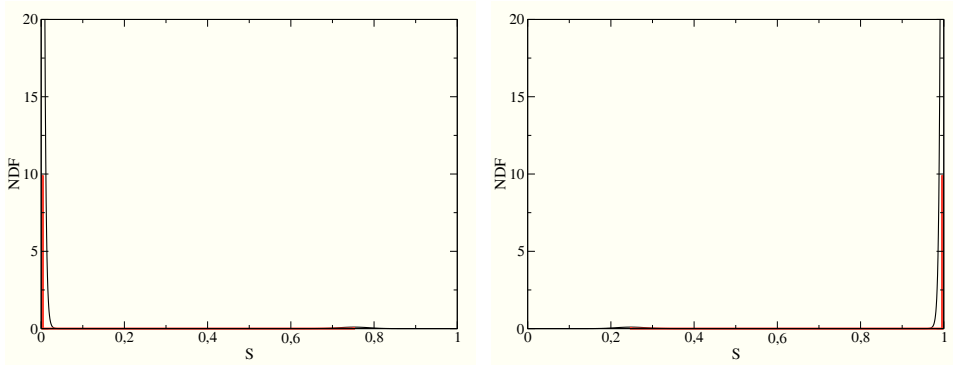


Figure B.5: ME reconstruction with 4 moments, for  $p_1 = 0.01$  (left) or  $p_1 = 0.99$  (right),  $p_2 = 0.5$  and  $p_3 = 0.5$  and the Dirac delta functions corresponding to the lower principal representation.

At the boundary of  $\mathbb{M}_2$ , the second canonical moment is equal to 0 or 1. The solution of the Hausdorff problem is then a Dirac delta function at  $\delta_{p_1}$  if  $p_2 = 0$  or a sum of two Dirac delta functions  $(1-p_1)\delta_0 + p_1\delta_1$ , if  $p_2 = 1$ . The ME reconstructions with 4 moments, as well as the lower principal representations, are plotted in Fig. B.6 for two moment vectors close to these boundaries : they correspond to the canonical moments  $p_1 = 0.8$ ,  $p_2 = 0.01$  or  $p_2 = 0.99$  and  $p_3 = 0.5$ . Like previously, the ME reconstructions and the lower principal representations give NDF close to the expected Dirac delta functions. Moreover, for the first case,  $p_2 = 0.01$ , the moments of the two reconstructions over an interval  $[0, S_b]$ , with  $S_b$  small enough are close to 0 with an accuracy greater than 2%. For the second case,  $p_2 = 0.99$ , the moments of order 0 of the two reconstructions over  $[0, S_b]$ , with  $S_b$  bigger than 0.03, only differ of less than 0.04% and differ of the value  $1 - p_1 = 0.2$  (the moment of order 0 of the NDF corresponding to the point of the boundary of  $\mathbb{M}_2$ ) of less than 0.04%. The other moments are close to zero with the same level of accuracy. Finally, in both cases, the flux can still be computed from the lower principal representation or eventually with the NDF corresponding to the moment vector at the boundary, with a good accuracy. And we can expect that the accuracy will increase when the moment vector will be closer of the boundary.

At the boundary of  $\mathbb{M}_3$ , the third canonical moment is equal to 0 or one. The solution of the Hausdorff

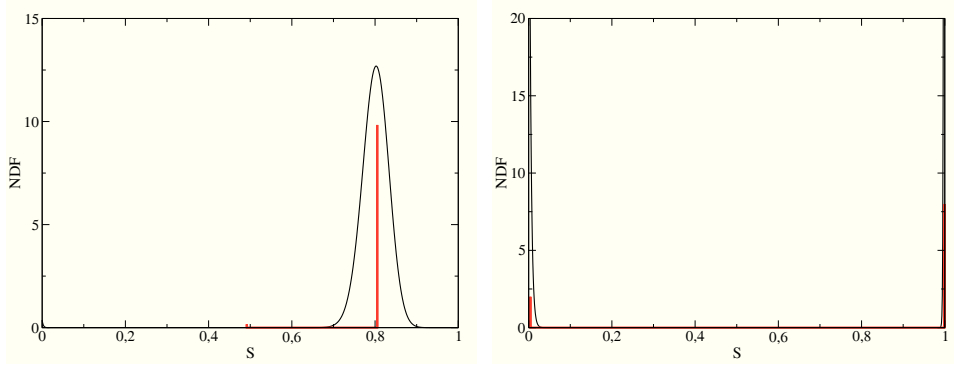


Figure B.6: ME reconstruction with 4 moments, for  $p_1 = 0.2$ ,  $p_2 = 0.01$  (left) or  $p_2 = 0.99$  (right) and  $p_3 = 0.5$  and the Dirac delta functions corresponding to the lower principal representation.

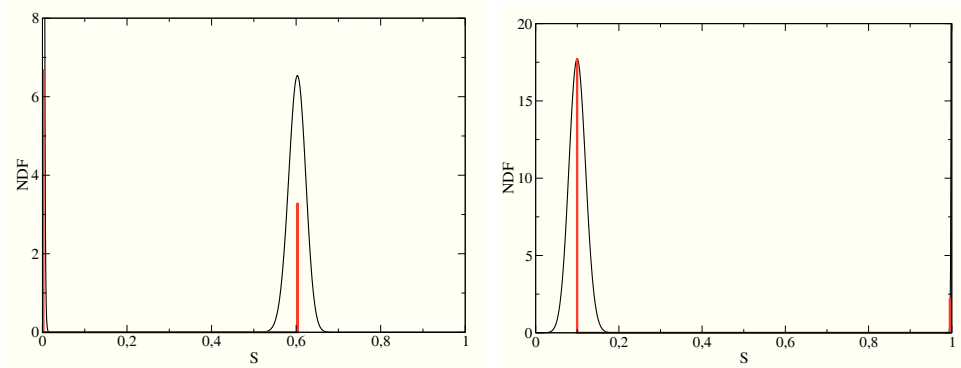


Figure B.7: ME reconstruction with 4 moments, for  $p_1 = 0.2$ ,  $p_2 = 0.5$  and  $p_3 = 0.01$  (left) or  $p_3 = 0.99$  (right) and the Dirac delta functions corresponding to the lower principal representation.

problem is then a sum of two Dirac delta functions. If  $p_3 = 0$ , it is written :

$$\frac{p_2(1-p_1)}{p_1+p_2-p_1p_2}\delta_0 + \frac{p_1}{p_1+p_2-p_1p_2}\delta_{p_1+p_2-p_1p_2},$$

and if  $p_3 = 1$ , it is written :

$$\frac{1-p_1}{1-p_1+p_1p_2}\delta_{p_1(1-p_2)} + \frac{p_1p_2}{1-p_1+p_1p_2}\delta_1.$$

The ME reconstructions with 4 moments, as well as the lower principal representations, are plotted in Fig. B.7 for two moment vectors close to these boundaries : they correspond to the canonical moments  $p_1 = 0.2$ ,  $p_2 = 0.5$  and  $p_3 = 0.01$  or  $p_3 = 0.99$ . The same conclusion on the fluxes can be done.

In order to have function close to bimodal distribution, that is to say at the boundary of  $\mathbb{M}_4$ , we have to consider a larger number of moment. It is done in Fig. B.8 with 6 moments.

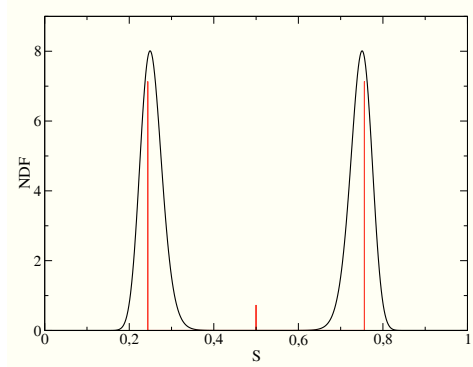


Figure B.8: ME reconstruction with 6 moments, for  $p_1 = 0.5$ ,  $p_2 = 0.25$  and  $p_3 = 0.5$ ,  $p_4 = 0.0171$  and  $p_5 = 0.5$  and the Dirac delta functions corresponding to the lower principal representation.

### B.3 Moment vector advection scheme in the context of a non-structured grid

Although the article focuses on a numerical scheme for the advection of a moment vector in a structured mesh, it is possible, with some adjustments, to extend this scheme to a non-structured mesh. This appendix gives the principle of a second order scheme for any type of cell geometry. Let  $\mathcal{T}$  denote the grid, composed of cells denoted by  $K$ , delimited by the area  $\partial K$ . A face of the cell is denoted by  $e$ , and  $\vec{n}_{K,e}$  is the unitary outwards vector through  $e$ , as illustrated in Fig B.9. If the moment vector of cell  $K$  is  $\mathcal{M}_K = (m_{0,K}, m_{1,K}, m_{0,K}, m_{0,K})^T$ , then a first order scheme writes:

$$\mathcal{M}_K^{n+1} = \mathcal{M}_K^n - \frac{\Delta t}{V_K} \sum_{e \in \partial K} \Phi(\mathcal{M}_K^n, \mathcal{M}_{K,e}^n, \vec{n}_{K,e}) |e| \tag{B.2}$$

where  $V_K$  is the volume of cell  $K$ ,  $|e|$  is the area of the face  $e$ ,  $\mathcal{M}_K^n$  is the value of the vector  $\mathcal{M}$  in cell  $K$  at iteration  $n$ , and  $\mathcal{M}_{K,e}^n$  is the value of the vector  $\mathcal{M}$  of the neighbor cell through the face  $e$ . The quantity  $\Phi(\mathcal{M}_K^n, \mathcal{M}_{K,e}^n, \vec{n}_{K,e})$  is the numerical flux corresponding to the direction of vector  $\vec{n}_{K,e}$ .

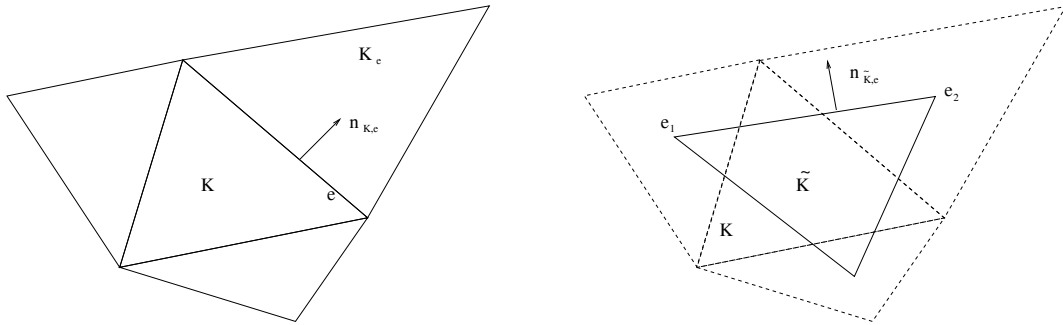


Figure B.9: Primary (left) and dual (right) mesh

For the second order scheme, the vector  $\mathcal{W}_K = (m_{0,K}, p_{1,K}, p_{2,K}, p_{3,K})^T$  is considered for linear reconstruction:

$$\mathcal{W}(x) = \overline{\mathcal{W}_K} + \vec{\nabla} \mathcal{W}_K \cdot (x - x_K) \tag{B.3}$$

where,  $\overline{\mathcal{W}_K}$  is a modified average value of the quantities computed in order for the scheme to be conservative, as explained in the structured grid case, and  $x_K$  is the center of cell  $K$ . The gradient of  $\mathcal{W}$ , is estimated using a Green formula for a cell of the dual mesh (see Fig. (B.9)-right):

$$\int_{\tilde{K}} \vec{\nabla} \mathcal{W}_K \, dx = \int_{\partial \tilde{K}} \mathcal{W} \cdot \vec{n}_{K,e} \, ds \tag{B.4}$$

Considering that  $\vec{\nabla} \mathcal{W}_K$  is constant on cell  $K$  (because of the linear reconstruction), one gets an estimate of it using a linear interpolation on the face of  $\tilde{K}$  through the expression:

$$\begin{aligned} V_K \vec{\nabla} \mathcal{W}_K &= \sum_{e \in \partial K} \left( \int_0^1 (1-\lambda) \mathcal{W}^n(e_1) + \lambda \mathcal{W}^n(e_2) d\lambda \right) |e| \vec{n}_{K,e} \\ &= \sum_{e \in \partial K} \frac{1}{2} (\mathcal{W}^n(e_1) + \mathcal{W}^n(e_2)) |e| \vec{n}_{K,e} \end{aligned} \quad (\text{B.5})$$

In order to ensure that  $\mathcal{W}_{min} \leq \mathcal{W}(x) \leq \mathcal{W}_{max}$  for any  $x$  in the cell  $K$ ,  $\vec{\nabla} \mathcal{W}_K$  is limited with the following expression:

$$\widetilde{\vec{\nabla}} \mathcal{W}_K = \min \left( 1, \frac{\mathcal{W}_{max} - \mathcal{W}_K}{\max_{x \in K} |\vec{\nabla} \mathcal{W}_K \cdot (x - x_K)|}, \frac{\mathcal{W}_K - \mathcal{W}_{min}}{\min_{x \in K} |\vec{\nabla} \mathcal{W}_K \cdot (x - x_K)|} \right) \vec{\nabla} \mathcal{W}_K \quad (\text{B.6})$$

where  $\mathcal{W}_{max} = \max_{e \in \partial K} (\mathcal{W}_{K_e})$  is the maximum value of  $\mathcal{W}$  in the cell  $K$ , and  $\mathcal{W}_{min} = \min_{e \in \partial K} (\mathcal{W}_{K_e})$  is the minimum value,  $\mathcal{W}_{K_e}$  denoting the value of the vector  $\mathcal{W}$  on the edge of the cell  $K$ . Then, the value of  $\mathcal{W}_{e,K}$ , taken at the center of the face  $e$  is assessed through:

$$\mathcal{W}_{e,K} = \overline{\mathcal{W}_K} + \vec{\nabla} \mathcal{W}_K \cdot (x_e - x_K) \quad (\text{B.7})$$

The computation of the bar values follows the same logic as in the structured case, that is to say that the mean value in cell  $K$  of the moments expressed as a function of the canonical moments must be equal to the mean value of the moments.

Given this reconstruction with this slope limiter, the maximum principle for the canonical moments is satisfied and the moment space is preserved throughout the whole cell  $K$ .

The temporal integration is performed using an explicit second order Runge-Kutta method. In this context, the solution reads:

$$\mathcal{M}_K^{n+1} = \frac{1}{2} \mathcal{M}_K^n + \frac{1}{2} \widetilde{\mathcal{M}}_K^{n+1} - \frac{\Delta t}{2V_K} \sum_{e \in \partial K} \Phi(\widetilde{\mathcal{M}}_K^{n+1}, \widetilde{\mathcal{M}}_{K,e}^{n+1}, \vec{n}_{K,e}) |e| \quad (\text{B.8})$$

where

$$\widetilde{\mathcal{M}}_K^{n+1} = \mathcal{M}_K^n - \frac{\Delta t}{V_K} \sum_{e \in \partial K} \Phi(\mathcal{M}_{K,e}^n, \mathcal{M}_K^n, \vec{n}_{K,e}) |e| \quad (\text{B.9})$$

As it is classical for non-structured grid, restrictions on the CFL number apply. The maximum possible CFL value enforcing the scheme properties (positivity of density, of the moments and preservation of the moment space) depends on the considered mesh geometry.

# Appendix C

## EMVM model

### C.1 Generalized Cholesky matrices decomposition

Here we will take advantage of the fact that the Cholesky matrix is not unique. Indeed, the equality

$$\boldsymbol{\sigma} = \mathbf{L}^T \mathbf{L} \tag{C.1}$$

is still true if one considers  $\mathbf{R}\mathbf{L}$ , where  $\mathbf{R}$  is a rotation matrix. Thus, the set of the Cholesky matrices is invariant by rotation, and is periodic with the period  $\pi$ , since

$$\mathbf{R}(\theta + \pi)\mathbf{L} = -\mathbf{R}(\theta)\mathbf{L} \tag{C.2}$$

And if we consider a Gaussian distribution, then the set of nodes associate to these matrices describes an ellipse.

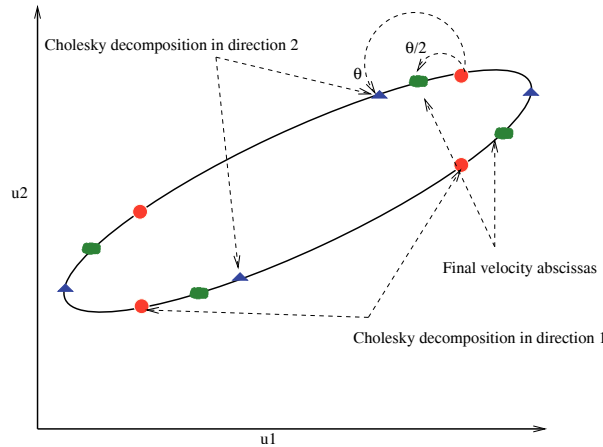


Figure C.1: Generalized Cholesky decomposition

The basic idea motivated by this statement is to launch a study on the error made by the quadrature-based method on third order moments among all the different rotation  $\rho_l(\theta)$ ,  $\theta \in [0, \pi]$  of the Cholesky decomposition. Practically, an inversion-projection step is applied to a moment vector  $\mathbf{W}_2 \in \mathcal{W}_2$ , and the error is computed between the initial moment vector, and the reconstructed moment vector from  $\mathcal{V}_4 \in \mathcal{V}_4$ . We expect to find a rotation angle where the error is the lowest. We consider the set of velocity distribution with a  $\boldsymbol{\sigma}$  writing:

$$\boldsymbol{\sigma} = \sigma \begin{bmatrix} 1 & r \\ r & 1 \end{bmatrix} \tag{C.3}$$

where  $\sigma_{1,1} = \sigma_{2,2} = \sigma = 1$ . The characteristic parameters of a distribution are then

- the value of the correlation coefficient  $r_{12}$
- the value of the centered third order moments, writing:

$$\begin{aligned} - m_{30} &= \frac{M_{3,0}}{M_{0,0}} - u_{p,1}^3 \\ - m_{21} &= \frac{M_{2,1}}{M_{0,0}} - u_{p,1}^2 u_{p,2} \\ - m_{12} &= \frac{M_{1,2}}{M_{0,0}} - u_{p,1} u_{p,2}^2 \\ - m_{03} &= \frac{M_{0,3}}{M_{0,0}} - u_{p,2}^3 \end{aligned}$$

Three different tests are conducted. First, the case of an equilibrium distribution is considered, for which  $r = 0.9$ , all the centered third order moments are null. Then a non-equilibrium distribution with  $r = 0$  and  $m_{30} = 1$  is considered. Finally a non equilibrium distribution with  $r = 0.9$  and  $m_{30} = 1$  is studied. Two figures are displayed for each test case. The first result is the set all the velocity abscissas of the decomposition with matrix  $\mathbf{R}(\theta)\mathbf{L}$ ,  $\theta \in [0, \pi]$ . Among all these node sets, three are pointed out, that minimize errors on the reconstructed centered moments defined such as:

$$\begin{aligned} err1 &= (m_{30} - \sum_{\alpha=1}^4 n_{\alpha} U_{(\alpha)1}^3)^2 + (m_{21} - \sum_{\alpha=1}^4 n_{\alpha} U_{(\alpha)1}^2 U_{(\alpha)2})^2 \\ &\quad (m_{12} - \sum_{\alpha=1}^4 n_{\alpha} U_{(\alpha)1} U_{(\alpha)2}^2)^2 + (m_{03} - \sum_{\alpha=1}^4 n_{\alpha} U_{(\alpha)2}^3)^2 \\ err2 &= (m_{30} + m_{21} - \sum_{\alpha=1}^4 n_{\alpha} U_{(\alpha)1}^3 - \sum_{\alpha=1}^4 n_{\alpha} U_{(\alpha)1}^2 U_{(\alpha)2})^2 \\ &\quad (m_{12} + m_{03} - \sum_{\alpha=1}^4 n_{\alpha} U_{(\alpha)1} U_{(\alpha)2}^2 - \sum_{\alpha=1}^4 n_{\alpha} U_{(\alpha)2}^3)^2 \\ err3 &= (m_{30} - \sum_{\alpha=1}^4 n_{\alpha} U_{(\alpha)1}^3)^2 + (m_{03} - \sum_{\alpha=1}^4 n_{\alpha} U_{(\alpha)2}^3)^2 \end{aligned} \tag{C.4}$$

For the equilibrium distribution Fig. (C.2), the set of velocity abscissas of  $\mathcal{V}_4$  describes an ellipse, and all the *centered* moment are null. For the case where  $m_{30} = 1$  and  $r = 0$ , Fig. (C.2), some errors occur, and impact not only  $m_{30}$ , but the other third order moments as well. According to the definition of the error, different sets of nodes are the best adapted. This is confirmed in Fig. (C.2)-right, as the minima of the error curves do not correspond to the same rotation angle. This result reveals that the notion of most adapted Cholesky decomposition, does not exist. This is confirmed by the third test case, in Fig. (C.3) with a distribution such as  $r = 0.9$ , and  $m_{30} = 1$ . Here again, different sets of nodes minimize the different errors.

Studying different Cholesky decomposition for quadrature-based moment method, we have not found a decomposition leading to be set of weights and abscissas  $\mathbf{V}_4$  that is either permutation-invariant and minimizes the distance from  $\mathbf{W}_2$ . Accordingly, the closure system (9.43), and the result depend on the type of decomposition chosen. Besides, no guarantee has been provided that these quadrature methods ensure the maximum principle applying to the velocity abscissas in virtue of Eq. (9.26). Moreover, like in the one-dimensional case,  $\delta$ -shocks appear when three different velocity nodes have to be reconstructed in a direction. This represents an issue in configurations where numerical diffusion is important. Indeed, in areas of numerical diffusion, uncontrolled velocity can be reconstructed from the momentum conservation, so that erratic  $\delta$ -shocks might appear. In order to prevent these anomalies, one has to enrich the

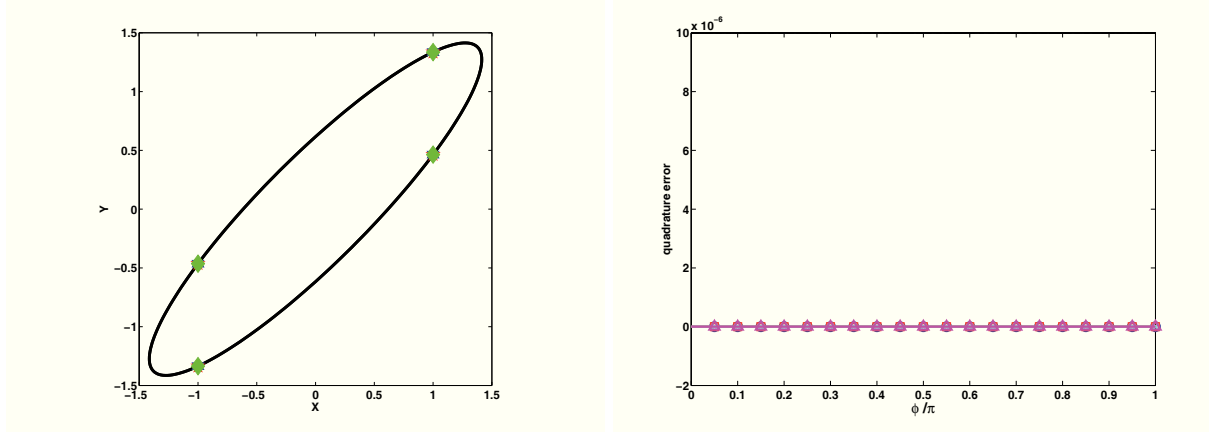


Figure C.2: Quadrature method and associated error for a distribution with  $r = 0.9$ ,  $m_{30} = 0$ . Left: set of all velocity abscissas for quadrature in  $[0, \pi]$ ; All the nodes are equivalent. Right: reconstructed centered third order moments and error made by the quadrature on these moments: all the centered third order moments stay null, as well as the error made.

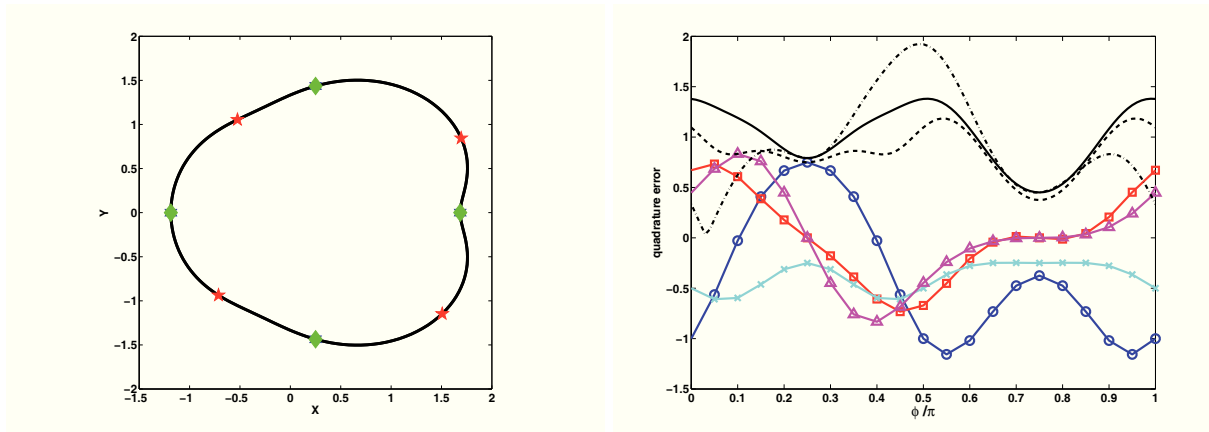


Figure C.3: Quadrature method and associated error for a distribution with  $r = 0$ ,  $m_{30} = 1$ . Left: set of all velocity abscissas for quadrature in  $[0, \pi]$ ; the blue squares are the set of nodes which minimizes  $err1$ , the red stars are the set of nodes which minimizes  $err2$ , and the green diamonds are the set of nodes which minimizes  $err3$ . Right: reconstructed centered third order moments:  $m_{30}$  (blue curve with circles),  $m_{21}$  (red curve with squares),  $m_{12}$  (cyan curve with crosses),  $m_{03}$  (magenta curve with triangles); error made by the quadrature on these moments:  $err1$  (solid black line),  $err2$  (dashed dotted black line),  $err3$  (dashed black line).



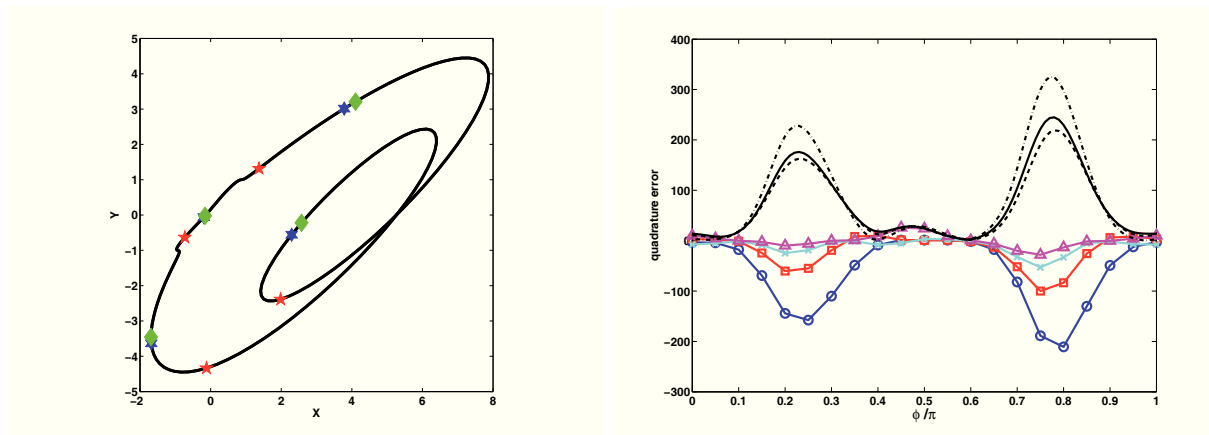


Figure C.4: Quadrature method and associated error for a distribution with  $r = 0.9$ ,  $m_{30} = 1$ . Left: set of all velocity abscissas for quadrature in  $[0, \pi]$ ; the blue squares are the set of nodes which minimizes  $err1$ , the red stars are the set of nodes which minimizes  $err2$ , and the green diamonds are the set of nodes which minimizes  $err3$ . Right: reconstructed centered third order moments:  $m_{30}$  (blue curve with circles),  $m_{21}$  (red curve with squares),  $m_{12}$  (cyan curve with crosses),  $m_{03}$  (magenta curve with triangles); error made by the quadrature on these moments:  $err1$  (solid black line),  $err2$  (dashed dotted black line),  $err3$  (dashed black line).

representation of the distribution function that is reconstructed, to take into account these new velocities. Increasing the number  $N_{pic}$  of nodes is not a satisfactory solution, as it only delays the problem, not to mention the increase of variables in the system and of the CPU cost. Perspective to that issue can be found in [233].

## C.2 Equations on centered moments

The time derivative of the centered moments is expressed according to the moments:

$$\begin{aligned}
\partial_t \left( m_{3/2}^{(j)} \tilde{M}_{2,0}^{(j)} \right) &= \partial_t \left( m_{3/2}^{(j)} M_{2,0}^{(j)} \right) - 2M_{1,0}^{(j)} \partial_t \left( m_{3/2}^{(j)} M_{1,0}^{(j)} \right) + (M_{1,0}^{(j)})^2 \partial_t \left( m_{3/2}^{(j)} \right) \\
\partial_t \left( m_{3/2}^{(j)} \tilde{M}_{1,1}^{(j)} \right) &= \partial_t \left( m_{3/2}^{(j)} M_{1,1}^{(j)} \right) - M_{1,0}^{(j)} \partial_t \left( m_{3/2}^{(j)} M_{0,1}^{(j)} \right) - M_{0,1}^{(j)} \partial_t \left( m_{3/2}^{(j)} M_{1,0}^{(j)} \right) + M_{1,0}^{(j)} M_{0,1}^{(j)} \partial_t \left( m_{3/2}^{(j)} \right) \\
\partial_t \left( m_{3/2}^{(j)} \tilde{M}_{0,2}^{(j)} \right) &= \partial_t \left( m_{3/2}^{(j)} M_{0,2}^{(j)} \right) - 2M_{0,1}^{(j)} \partial_t \left( m_{3/2}^{(j)} M_{0,1}^{(j)} \right) + (M_{0,1}^{(j)})^2 \partial_t \left( m_{3/2}^{(j)} \right) \\
\partial_t \left( m_{3/2}^{(j)} \tilde{M}_{3,0}^{(j)} \right) &= \partial_t \left( m_{3/2}^{(j)} M_{3,0}^{(j)} \right) - 3M_{1,0}^{(j)} \partial_t \left( m_{3/2}^{(j)} M_{2,0}^{(j)} \right) - 3M_{2,0}^{(j)} \partial_t \left( m_{3/2}^{(j)} M_{1,0}^{(j)} \right) \\
&\quad + 6(M_{1,0}^{(j)})^2 \partial_t \left( m_{3/2}^{(j)} M_{1,0}^{(j)} \right) + \left( 3M_{2,0}^{(j)} M_{1,0}^{(j)} - 4(M_{1,0}^{(j)})^3 \right) \partial_t \left( m_{3/2}^{(j)} \right) \\
\partial_t \left( m_{3/2}^{(j)} \tilde{M}_{2,1}^{(j)} \right) &= \partial_t \left( m_{3/2}^{(j)} M_{2,1}^{(j)} \right) - M_{0,1}^{(j)} \partial_t \left( m_{3/2}^{(j)} M_{2,0}^{(j)} \right) - 2M_{1,0}^{(j)} \partial_t \left( m_{3/2}^{(j)} M_{1,1}^{(j)} \right) \\
&\quad - 2 \left( M_{1,1}^{(j)} - 2M_{1,0}^{(j)} M_{0,1}^{(j)} \right) \partial_t \left( m_{3/2}^{(j)} M_{1,0}^{(j)} \right) - \left( M_{2,0}^{(j)} - 2(M_{1,0}^{(j)})^2 \right) \partial_t \left( m_{3/2}^{(j)} M_{0,1}^{(j)} \right) \\
&\quad + \left( M_{2,0}^{(j)} M_{0,1}^{(j)} + 2M_{1,1}^{(j)} M_{1,0}^{(j)} - 4(M_{1,0}^{(j)})^2 M_{0,1}^{(j)} \right) \partial_t \left( m_{3/2}^{(j)} \right) \\
\partial_t \left( m_{3/2}^{(j)} \tilde{M}_{1,2}^{(j)} \right) &= \partial_t \left( m_{3/2}^{(j)} M_{1,2}^{(j)} \right) - M_{1,0}^{(j)} \partial_t \left( m_{3/2}^{(j)} M_{0,2}^{(j)} \right) - 2M_{0,1}^{(j)} \partial_t \left( m_{3/2}^{(j)} M_{1,1}^{(j)} \right) \\
&\quad - 2 \left( M_{1,1}^{(j)} - 2M_{0,1}^{(j)} M_{1,0}^{(j)} \right) \partial_t \left( m_{3/2}^{(j)} M_{0,1}^{(j)} \right) - \left( M_{0,2}^{(j)} - 2(M_{0,1}^{(j)})^2 \right) \partial_t \left( m_{3/2}^{(j)} M_{1,0}^{(j)} \right) \\
&\quad + \left( M_{0,2}^{(j)} M_{1,0}^{(j)} + 2M_{1,1}^{(j)} M_{0,1}^{(j)} - 4(M_{0,1}^{(j)})^2 M_{1,0}^{(j)} \right) \partial_t \left( m_{3/2}^{(j)} \right) \\
\partial_t \left( m_{3/2}^{(j)} \tilde{M}_{0,3}^{(j)} \right) &= \partial_t \left( m_{3/2}^{(j)} M_{0,3}^{(j)} \right) - 3M_{0,1}^{(j)} \partial_t \left( m_{3/2}^{(j)} M_{0,2}^{(j)} \right) - 3M_{0,2}^{(j)} \partial_t \left( m_{3/2}^{(j)} M_{0,1}^{(j)} \right) + 6(M_{0,1}^{(j)})^2 \partial_t \left( m_{3/2}^{(j)} M_{0,1}^{(j)} \right) \\
&\quad + \left( 3M_{0,2}^{(j)} M_{1,0}^{(j)} - 4(M_{0,1}^{(j)})^3 \right) \partial_t \left( m_{3/2}^{(j)} \right) \tag{C.5}
\end{aligned}$$

So that the equations on centered moments read:

$$\begin{aligned}
\partial_t \left( m_{3/2}^{(j)} \right) &= - (E_1^{(j)} + E_2^{(j)}) m_{3/2}^{(j)} + E_1^{(j+1)} m_{3/2}^{(j+1)} \\
\partial_t \left( m_{3/2}^{(j)} \tilde{M}_{1,0}^{(j)} \right) &= - (E_1^{(j)} + E_2^{(j)}) m_{3/2}^{(j)} \tilde{M}_{1,0}^{(j)} + E_1^{(j+1)} m_{3/2}^{(j+1)} \tilde{M}_{1,0}^{(j+1)} + m_{3/2}^{(j)} \frac{u_{g,x} - \tilde{M}_{1,0}^{(j)}}{\theta S_p^{(j)}} \\
\partial_t \left( m_{3/2}^{(j)} \tilde{M}_{0,1}^{(j)} \right) &= (E_1^{(j)} + E_2^{(j)}) m_{3/2}^{(j)} \tilde{M}_{0,1}^{(j)} + E_1^{(j+1)} m_{3/2}^{(j+1)} \tilde{M}_{0,1}^{(j+1)} + m_{3/2}^{(j)} \frac{u_{g,y} - \tilde{M}_{0,1}^{(j)}}{\theta S_p^{(j)}} \\
\partial_t \left( m_{3/2}^{(j)} \tilde{M}_{2,0}^{(j)} \right) &= - (E_1^{(j)} + E_2^{(j)}) m_{3/2}^{(j)} \tilde{M}_{2,0}^{(j)} + E_1^{(j+1)} m_{3/2}^{(j+1)} \tilde{M}_{2,0}^{(j+1)} - 2m_{3/2}^{(j)} \frac{\tilde{M}_{2,0}^{(j)}}{\theta S_p^{(j)}} \\
&\quad + E_1^{(j+1)} m_{3/2}^{(j)} \left( \tilde{M}_{1,0}^{(j+1)} - \tilde{M}_{1,0}^{(j)} \right)^2 \\
\partial_t \left( m_{3/2}^{(j)} \tilde{M}_{1,1}^{(j)} \right) &= - (E_1^{(j)} + E_2^{(j)}) m_{3/2}^{(j)} \tilde{M}_{1,1}^{(j)} + E_1^{(j+1)} m_{3/2}^{(j+1)} \tilde{M}_{1,1}^{(j+1)} - 2m_{3/2}^{(j)} \frac{\tilde{M}_{1,1}^{(j)}}{\theta S_p^{(j)}} \\
\partial_t \left( m_{3/2}^{(j)} \tilde{M}_{0,2}^{(j)} \right) &= - (E_1^{(j)} + E_2^{(j)}) m_{3/2}^{(j)} \tilde{M}_{0,2}^{(j)} + E_1^{(j+1)} m_{3/2}^{(j+1)} \tilde{M}_{0,2}^{(j+1)} - 2m_{3/2}^{(j)} \frac{\tilde{M}_{0,2}^{(j)}}{\theta S_p^{(j)}} \\
&\quad + E_1^{(j+1)} m_{3/2}^{(j+1)} \left( \tilde{M}_{0,1}^{(j+1)} - \tilde{M}_{0,1}^{(j)} \right)^2 \\
\partial_t \left( m_{3/2}^{(j)} \tilde{M}_{3,0}^{(j)} \right) &= - (E_1^{(j)} + E_2^{(j)}) m_{3/2}^{(j)} \tilde{M}_{3,0}^{(j)} + E_1^{(j+1)} m_{3/2}^{(j+1)} \tilde{M}_{3,0}^{(j+1)} - 3m_{3/2}^{(j)} \frac{\tilde{M}_{3,0}^{(j)}}{\theta S_p^{(j)}} \\
&\quad + E_1^{(j+1)} m_{3/2}^{(j+1)} \left[ 3 \left( \tilde{M}_{2,0}^{(j+1)} - \tilde{M}_{2,0}^{(j)} \right) \left( \tilde{M}_{1,0}^{(j+1)} - \tilde{M}_{1,0}^{(j)} \right) + \left( \tilde{M}_{1,0}^{(j+1)} - \tilde{M}_{1,0}^{(j)} \right)^3 \right] \\
\partial_t \left( m_{3/2}^{(j)} \tilde{M}_{2,1}^{(j)} \right) &= - (E_1^{(j)} + E_2^{(j)}) m_{3/2}^{(j)} \tilde{M}_{2,1}^{(j)} + E_1^{(j+1)} m_{3/2}^{(j+1)} \tilde{M}_{2,1}^{(j+1)} - 3m_{3/2}^{(j)} \frac{\tilde{M}_{2,1}^{(j)}}{\theta S_p^{(j)}} \\
&\quad + E_1^{(j+1)} m_{3/2}^{(j+1)} \left[ \left( \tilde{M}_{2,0}^{(j+1)} - \tilde{M}_{2,0}^{(j)} \right) \left( \tilde{M}_{0,1}^{(j+1)} - \tilde{M}_{0,1}^{(j)} \right) \right. \\
&\quad \left. + 2 \left( \tilde{M}_{1,1}^{(j+1)} - \tilde{M}_{1,1}^{(j)} \right) \left( \tilde{M}_{1,0}^{(j+1)} - \tilde{M}_{1,0}^{(j)} \right) + \left( \tilde{M}_{0,1}^{(j+1)} - \tilde{M}_{0,1}^{(j)} \right) \left( \tilde{M}_{1,0}^{(j+1)} - \tilde{M}_{1,0}^{(j)} \right)^2 \right] \\
\partial_t \left( m_{3/2}^{(j)} \tilde{M}_{1,2}^{(j)} \right) &= - (E_1^{(j)} + E_2^{(j)}) m_{3/2}^{(j)} \tilde{M}_{1,2}^{(j)} + E_1^{(j+1)} m_{3/2}^{(j+1)} \tilde{M}_{1,2}^{(j+1)} - 3m_{3/2}^{(j)} \frac{\tilde{M}_{1,2}^{(j)}}{\theta S_p^{(j)}} \\
&\quad + E_1^{(j+1)} m_{3/2}^{(j+1)} \left[ \left( \tilde{M}_{0,2}^{(j+1)} - \tilde{M}_{0,2}^{(j)} \right) \left( \tilde{M}_{1,0}^{(j+1)} - \tilde{M}_{1,0}^{(j)} \right) \right. \\
&\quad \left. + 2 \left( \tilde{M}_{1,1}^{(j+1)} - \tilde{M}_{1,1}^{(j)} \right) \left( \tilde{M}_{0,1}^{(j+1)} - \tilde{M}_{0,1}^{(j)} \right) + \left( \tilde{M}_{0,1}^{(j+1)} - \tilde{M}_{0,1}^{(j)} \right) \left( \tilde{M}_{1,0}^{(j+1)} - \tilde{M}_{1,0}^{(j)} \right)^2 \right] \\
\partial_t \left( m_{3/2}^{(j)} \tilde{M}_{0,3}^{(j)} \right) &= - (E_1^{(j)} + E_2^{(j)}) m_{3/2}^{(j)} \tilde{M}_{0,3}^{(j)} + E_1^{(j+1)} m_{3/2}^{(j+1)} \tilde{M}_{0,3}^{(j+1)} - 3m_{3/2}^{(j)} \frac{\tilde{M}_{0,3}^{(j)}}{\theta S_p^{(j)}} \\
&\quad + E_1^{(j+1)} m_{3/2}^{(j+1)} \left[ 3 \left( \tilde{M}_{0,2}^{(j+1)} - \tilde{M}_{0,2}^{(j)} \right) \left( \tilde{M}_{0,1}^{(j+1)} - \tilde{M}_{0,1}^{(j)} \right) + \left( \tilde{M}_{0,1}^{(j+1)} - \tilde{M}_{0,1}^{(j)} \right)^3 \right] \quad (C.6)
\end{aligned}$$

## Appendix D

# Arbitrary Lagrangian Eulerian formalism

### D.1 Counter-example of Section 13.5.3

We show here a counterexample where the first order advection scheme designed in Section 13.5.3 fails to preserve the discrete maximum principle on velocity, in the context of a cell-vertex mesh. Let us consider where we suppose that  $m_1$  is uniform and equal to  $m$  and that

$$w_p = \begin{cases} w > 1 & x \leq x_{i-1/2} \\ 1 & x > x_{i-1/2} \end{cases} \quad (\text{D.1})$$

Moreover, the mesh is assumed to be regular and fixed, so  $u_\chi = 0$ , and  $w_p = u_p$ . In this context,  $J_{p,i}^n$  is constant.

We are interested in the value of  $u_{p,i+3/2}^{n+1}$ . Therefore, we compute  $(J_p m_1 u_p)_{i+3/2}^{n+1}$  and  $(J_p m_1)_{i+3/2}^{n+1}$ . First of all, let us remark that

$$J_{p,i}^{n+1} = 1 + \frac{\Delta t}{\Delta x}(1 - w) \quad (\text{D.2})$$

$$(J_p m_1 u_p)_{i+3/2}^{n+1} = (J_p m_1 u_p)_{i+3/2} - \frac{\Delta t}{\Delta x}((m_1 u_p)_{i+3/2} - (m_1 u_p)_{i+1/2}) \quad (\text{D.3})$$

$$= m u_{p,i+3/2} - \frac{\Delta t}{\Delta x} (m u_{p,i+3/2} - \frac{m}{1 + \frac{\Delta t}{2\Delta x^n}(1-w)} u_{p,i+1/2})$$

$$= m \left( \left(1 - \frac{\Delta t}{\Delta x}\right) + \frac{\frac{\Delta t}{\Delta x}}{1 + \frac{\Delta t}{2\Delta x^n}(1-w)} \right)$$

$$= m \frac{1 + \frac{\Delta t}{2\Delta x} \left(1 - \frac{\Delta t}{\Delta x}\right) (1-w)}{1 + \frac{\Delta t}{2\Delta x} (1-w)}$$

(D.4)

In the same time

$$(J_p m_1)_{i+3/2}^{n+1} = \frac{1}{2} ((J_p m_1)_{i+1}^{n+1} + (J_p m_1)_{i+2}^{n+1}) \quad (\text{D.5})$$

where

$$\begin{aligned} (J_p m_1)_{i+1}^{n+1} &= (J_p m_1)_{i+1} - \frac{\Delta t}{\Delta x} ((m_1 u_p)_{i+1/2} - (m_1 u_p)_{i+3/2}) \\ &= m \frac{1 + \frac{\Delta t}{\Delta x} (1 - \frac{\Delta t}{\Delta x})(1 - w)}{1 + \frac{\Delta t}{\Delta x} (1 - w)} \end{aligned} \quad (D.6)$$

and

$$(J_p m_1)_{i+2}^{n+1} = (J_p m_1)_{i+2} = m \quad (D.7)$$

So that

$$(J_p m_1)_{i+3/2}^{n+1} = m \frac{1 + \frac{\Delta t}{\Delta x} (1 - w) - \frac{1}{2} \frac{\Delta t^2}{\Delta x^2} (1 - w)}{1 + \frac{\Delta t}{\Delta x} (1 - w)} \quad (D.8)$$

And finally

$$u_{p,i+3/2}^{n+1} = \frac{1 + \lambda(1 - \lambda)(1 - w)}{1 + \frac{\lambda}{2}(1 - w)} \frac{1 + \lambda(1 - w)}{1 + \lambda(1 - w) - \frac{\lambda^2}{2}(1 - w)} \quad (D.9)$$

The question is then to figure out if  $u_{p,i+3/2}^{n+1}$  lies outside  $[1, w]$ . In particular,  $u_{p,i+3/2}^{n+1}$  is lower than 1 if

$$(1 + \lambda(1 - \lambda)(1 - w))(1 + \lambda(1 - w)) < (1 + \frac{\lambda}{2}(1 - w))(1 + \lambda(1 - w) - \frac{\lambda^2}{2}(1 - w)) \quad (D.10)$$

leading to the condition

$$\frac{\lambda}{2} > \frac{\lambda}{4} \quad (D.11)$$

which is indeed verified.

This counterexample shows then a case where the discrete maximum principle is not guaranteed for the velocity.

## D.2 Derivation of equations in ALE formalism in three dimensions

In this appendix, we show how to write the equation in ALE formalism in 3 dimension in space. Starting from the conservation equation for a scalar quantity  $\alpha$  in the ALE formalism:

$$\partial_t (J\alpha)|_{\mathcal{X}} + J\nabla_{\mathbf{x}} \cdot (\alpha(\mathbf{u} - \mathbf{v}_{\mathcal{X}})) = J\nabla_{\mathbf{x}} \cdot \boldsymbol{\sigma} + JS \quad (D.12)$$

We would like to write  $J$  into the differential operator.

In one space dimension, this is very easy to do, as  $Jdx = d\chi$ . But in 3 dimensions in space we have the following relationship:  $J\nabla_{\mathbf{x}} \cdot \alpha = \nabla_{\chi} \cdot (J\mathbf{J}^{-1}\alpha)$ , where  $\mathbf{J} = \nabla_{\chi}\mathbf{x}$ .

We are going to demonstrate this relation in 2 dimensions in space, and assume its extension to three dimensions. Let us first express  $\nabla_{\chi}\alpha$  relative to  $\nabla_{\mathbf{x}}\alpha$ .

$$\begin{aligned} \partial_{\chi_1}\alpha &= \partial_{\chi_1 x_1}\partial_{x_1}\alpha + \partial_{\chi_1 x_2}\partial_{x_2}\alpha \\ \partial_{\chi_2}\alpha &= \partial_{\chi_2 x_1}\partial_{x_1}\alpha + \partial_{\chi_2 x_2}\partial_{x_2}\alpha \end{aligned} \quad (D.13)$$

In matricial form, we can write:

$$(\partial_{\chi_1}\alpha, \partial_{\chi_2}\alpha) = (\partial_{x_1}\alpha, \partial_{x_2}\alpha)\mathbf{J} \text{ or } \nabla_{\chi}\alpha = \nabla_{\mathbf{x}}\alpha\mathbf{J} \quad (\text{D.14})$$

We write

$$\mathbf{J} = \begin{pmatrix} a & b \\ c & d \end{pmatrix} \quad (\text{D.15})$$

So that

$$J\mathbf{J}^{-1} = \begin{pmatrix} d & -b \\ -c & a \end{pmatrix} \quad (\text{D.16})$$

where

$$\begin{aligned} a &= \partial_{\chi_1}x_1 & b &= \partial_{\chi_2}x_1 \\ c &= \partial_{\chi_1}x_2 & d &= \partial_{\chi_2}x_2 \end{aligned} \quad (\text{D.17})$$

We consider now a vector  $\alpha$ . Using the relation (D.14) for each of its components leads to:

$$\begin{aligned} J(\partial_{x_1}\alpha_1, \partial_{x_2}\alpha_1) &= (\partial_{\chi_1}\alpha_1, \partial_{\chi_2}\alpha_1)J\mathbf{J}^{-1} \\ J(\partial_{x_1}\alpha_2, \partial_{x_2}\alpha_2) &= (\partial_{\chi_1}\alpha_2, \partial_{\chi_2}\alpha_2)J\mathbf{J}^{-1} \end{aligned} \quad (\text{D.18})$$

So that

$$\begin{aligned} J\partial_{x_1}\alpha_1 &= d\partial_{\chi_1}\alpha_1 - c\partial_{\chi_2}\alpha_1 \\ J\partial_{x_2}\alpha_2 &= -b\partial_{\chi_1}\alpha_2 + a\partial_{\chi_2}\alpha_2 \end{aligned} \quad (\text{D.19})$$

In the same time,

$$\begin{aligned} \nabla_{\chi} \cdot \begin{pmatrix} d & -b \\ -c & a \end{pmatrix} \begin{pmatrix} \alpha_1 \\ \alpha_2 \end{pmatrix} &= \nabla_{\mathbf{x}} \cdot \begin{pmatrix} d\alpha_1 - b\alpha_2 \\ -c\alpha_1 + a\alpha_2 \end{pmatrix} \\ &= d\partial_{\chi_1}\alpha_1 - c\partial_{\chi_2}\alpha_1 + \alpha_1(\partial_{\chi_1}d - \partial_{\chi_2}c) \\ &= -b\partial_{\chi_1}\alpha_2 + a\partial_{\chi_2}\alpha_2 + \alpha_2(\partial_{\chi_2}a + \partial_{\chi_1}b) \end{aligned} \quad (\text{D.20})$$

Because of the Schwarz theorem:

$$\begin{aligned} \partial_{\chi_1}d - \partial_{\chi_2}c &= 0 \\ \partial_{\chi_2}a + \partial_{\chi_1}b &= 0 \end{aligned} \quad (\text{D.21})$$

And consequently

$$J\nabla_{\chi} \cdot \alpha = \nabla_{\mathbf{x}} \cdot (J\mathbf{J}^{-1}\alpha) \quad (\text{D.22})$$

# Bibliography

- [1] R. ABGRALL, *Generalization of the Roe scheme for the computation of a mixture of perfect gases*, La Recherche Aéronautique (English Edition), 6 (1988), pp. 31–43.
- [2] ———, *How to prevent pressure oscillations in multicomponent flow calculations: A quasi conservative approach*, Journal of Computational Physics, 125 (1996), pp. 150–160.
- [3] R. ABRAMOV, *A practical computational framework for the multidimensional moment-constrained maximum entropy principle*, J. Comput. Phys., 211 (2006), pp. 198–209.
- [4] G. ALLAIRE, S. CLERC, AND S. KOKH, *A five-equation model for the numerical simulation of interfaces in two-phase flows*, Comptes Rendus de l'Académie des Sciences - Series I - Mathematics, 331 (2000), pp. 1017 – 1022.
- [5] G. ALLAIRE, S. CLERC, AND S. KOKH, *A five-equation model for the simulation of interfaces between compressible fluids*, J. Comput. Phys., 181 (2002), pp. 577–616.
- [6] A. AMSDEN, P. J. O'ROURKE, AND T. D. BUTLER, *KIVA II, a computer program for chemically reactive flows with sprays*, Tech. Rep. LA-11560-MS, Report Los Alamos National Laboratory, Los Alamos, New Mexico, 1989.
- [7] A. A. ANGELBERGER, T. POINSOT, AND B. DELHAYE, *Improving near-wall combustion and wall heat transfer modeling in si-engine computation*, SAE paper 972881, (1997).
- [8] H. ASKES AND A. RODRIGUEZ-FERRAN, *A combined rh-adaptative scheme based on domain subdivision. Formulation and linear examples*, Int. J. Numer. Methods Eng., 51(3) (2001), pp. 253–273.
- [9] E. BABINSKY AND P. E. SOJKA, *Modeling drop size distribution*, Progress in Energy and Combustion Science, 28 (2002), pp. 303–329.
- [10] M. R. BAER AND J. W. NUNZIATO, *A two-phase mixture theory for the deflagration-to-detonation transition (DDT) in reactive granular materials*, International journal of multiphase flow, 12 (1986), pp. 861–889.
- [11] C. BARDOS, F. GOLSE, AND D. LEVERMORE, *Fluid dynamic limits of kinetic equations. I. Formal derivations*, J. Statist. Phys., 63 (1991), pp. 323–344.
- [12] F. BAYORO, *Prise en compte de l'écoulement du liquide dans l'injecteur dans la modélisation de jets de carburant Diesel*, tech. rep., Rapport de thèse à mi-parcours, 2008.
- [13] A. E. BERGLES, J. G. COLLIER, J. M. DELHAYE, G. F. HEWITT, AND F. MAYINGER, *Basic equations for two-phase flow modeling*, vol. Two-phase flow and heat transfer in the power and process industries, Chap.2, p 40-97, Hemisphere Publ. Corp., 1981.
- [14] D. BESTION, *The physical closure laws in the CATHARE code*, Nuclear Engineering and Design, 124 (1990), pp. 229–245.
- [15] P. L. BHATNAGAR, E. P. GROSS, AND M. KROOK, *A model for collision processes in gases. I. Small amplitude processes in charged and neutral one-component systems*, Physical Review, 94 (1954), pp. 511–525.

- [16] G. A. BIRD, *Molecular gas dynamics and the direct simulation of gas flows*, Oxford Science Publications, 42 (1994).
- [17] A. V. BOBYLEV AND T. OHWADA, *The error of the splitting scheme for solving evolutionary equations*, Applied Mathematics Letters, 14 (2001), pp. 45–48.
- [18] J. BOHBOT, N. GILLET, AND A. BENKENIDA, *IFP-C3D: An unstructured parallel solver for reactive compressible gas flow with spray*, Oil and Gas Science and Technology, 64 (2009), pp. 309–355.
- [19] M. BOILEAU, *Simulation aux grandes échelles de l'allumage diphasique des foyers aéronautiques*, PhD thesis, Institut National Polytechnique de Toulouse, 2007.
- [20] R. BORGHI AND M. DESTRIAU, *La combustion et les flammes*, Technip, 1995.
- [21] F. BOUCHUT, *On zero pressure gas dynamics*, in Advances in kinetic theory and computing, World Sci. Publishing, River Edge, NJ, 1994, pp. 171–190.
- [22] F. BOUCHUT, Y. BRENIER, J. CORTES, AND J. RIPOLI, *A hierarchy of models of two-phase flows*, Journal of NonLinear Science, 10 (2000), pp. 639–600.
- [23] F. BOUCHUT AND F. JAMES, *One-dimensional transport equations with discontinuous coefficients*, Nonlinear Anal., 32 (1998), pp. 891–933.
- [24] F. BOUCHUT, S. JIN, AND X. LI, *Numerical approximations of pressureless and isothermal gas dynamics*, SIAM J. Num. Anal., 41 (2003), pp. 135–158.
- [25] J. BOURÉ, *Les lois constitutives des modèles d'écoulements diphasiques monodimensionnels à deux fluides: Formes envisageables, restrictions résultant d'axiomes fondamentaux*, tech. rep., CEA-R-4915, 1978.
- [26] ———, *Wave phenomena and one dimensional two-phase flow models*, Multiphase Science & Technology, 9 (1997), pp. 1–107.
- [27] S. BOVE, T. SOLBERG, AND B. H. HJERTAGER, *A novel algorithm for solving population balance equations: the parallel parent and daughter classes. Derivation, analysis and testing*, Chemical Engineering Science, 60 (2005), pp. 1449–1464.
- [28] H. BRAESS AND P. WRIGGERS, *Arbitrary Lagrangian-Eulerian finite element analysis of free surface flow*, Comput. Meth. Appl. Mech., 190(1-2) (2000), pp. 95–110.
- [29] J. E. BROADWELL, *Shock structure in a simple discrete velocity gas*, The Physics of Fluids, 7 (1964), pp. 1243–1247.
- [30] P. BUTLER, M. LEMBECK, AND H. KRIER, *Modeling of shock development and transition to detonation initiated by burning in porous propellant beds*, Combustion and Flame, 46 (1982), pp. 75–93.
- [31] S. CANDEL, *Mécanique des fluides*, Dunod, Paris, second ed., 1990.
- [32] S. CANDEL, F. LACAS, N. DARABIHA, AND J.-C. ROLON, *Group combustion in spray flames*, Multiphase Science and Technology, 11 (1999), pp. 1–18.
- [33] S. CANDEL AND T. POINSOT, *Flame stretch and the balance equation for the flame area*, Combustion Science and Technology, 70 (1990), pp. 1–15.
- [34] C. CERCIGNANI, *The Boltzmann equation and its applications*, Springer-Verlag, New York, 1988.
- [35] C. CERCIGNANI, R. ILLNER, AND M. PULVIRENTI, *The mathematical theory of dilute gases*, Springer-Verlag, New York, 1994.



- [36] A. CERVONE, S. MANSERVISI, R. SCARDOVELLI, AND S. ZALESKI, *A geometrical predictor-corrector advection scheme and its application to the volume fraction function*, Journal of Computational Physics, 228 (2009), pp. 406 – 419.
- [37] C. CHALONS, R. O. FOX, AND M. MASSOT, *A multi-Gaussian quadrature method of moments for gas-particle flows in a LES framework*, in Proceedings of the Summer Program 2010, Center for Turbulence Research, Stanford University, Stanford, 2010.
- [38] S. CHANDRASEKHAR, *Stochastic problems in physics and astronomy*, Rev. Mod. Phys., 15 (1943), pp. 1–89.
- [39] V. J. CHANTEPERDRIX G., VILLEDIEU P., *A compressible model for separated two-phase flows computations*, ASME Fluids Engineering Division Summer Meeting, (2002).
- [40] S. CHAPMAN, *On the law of distribution of molecular velocities, and on the theory of viscosity and thermal conduction, in a non-uniform simple monoatomic gas*, Phil. Trans. R Soc., A (1916), pp. 279–348.
- [41] ———, *On the kinetic theory of a gas. part II: A composite monoatomic gas: Diffusion, viscosity, and thermal conduction*, Phil. Trans. R Soc., A (1918), pp. 115–197.
- [42] S. CHAPMAN AND T. G. COWLING, *The mathematical theory of nonuniform gases*, Cambridge Mathematical Library, Cambridge University Press, Cambridge, third ed., 1990.
- [43] A. CHINNAYYA, E. DANIEL, AND R. SAUREL, *Modeling detonation waves in heterogeneous energetic materials*, Journal of Computational Physics, 196 (2004), pp. 490–538.
- [44] R. CLIFT, J. R. GRACE, AND M. E. WEBER, *Bubbles, Drop and Particles*, Academic Press, New York, 1978.
- [45] O. COLIN AND A. BENKENIDA, *The 3-zones extended coherent flame model (ECFM3Z) for computing premixed diffusion combustion*, Oil and Gas Science and Technology, 59 (2004), pp. 593–609.
- [46] F. COQUEL, Q. L. NGUYEN, M. POSTEL, AND Q. H. TRAN, *Entropy-satisfying relaxation method with large time-steps for Euler IBVPs*, Math. Comp., 79 (2010), pp. 1493–1533.
- [47] C. T. CROWE, M. SOMMERFELD, AND Y. TSUJI, *Multiphase Flows with droplets and particles*, CRC Press, Boca Raton, Florida, 1998.
- [48] G. DAVIES, O. FLANAGAN, R. HILLIER, D. HITCHINGS, AND S. LORD, *Hydraulic shock loading due to supercavitating projectiles*, in Abstract of the 20<sup>th</sup> International Symposium on Shock Waves, 1994.
- [49] S. DE CHAISEMARTIN, *Eulerian models and numerical simulation of turbulent dispersion for polydisperse evaporation sprays*, PhD thesis, Ecole Centrale Paris, France, 2009. Available on TEL : <http://tel.archives-ouvertes.fr/tel-00443982/en/>.
- [50] S. DE CHAISEMARTIN, L. FRÉRET, D. KAH, F. LAURENT, R. FOX, J. REVEILLON, AND M. MASSOT, *Eulerian models for turbulent spray combustion with polydispersity and droplet crossing*, Comptes Rendus Mécanique, 337 (2009), pp. 438–448. Special Issue 'Combustion for Aerospace Propulsion'.
- [51] S. DE CHAISEMARTIN, L. FRERET, D. KAH, F. LAURENT, R. O. FOX, J. REVEILLON, AND M. MASSOT, *Eulerian models for turbulent spray combustion with polydispersity and droplet crossing : modeling and validation*, in Proceedings of the Summer Program 2008, Center for Turbulence Research, Stanford University, 2009, pp. 265–276.
- [52] S. DE CHAISEMARTIN, F. LAURENT, M. MASSOT, AND J. REVEILLON, *Evaluation of Eulerian multi-fluid versus Lagrangian methods for ejection of polydisperse evaporating sprays by vortices*, Journal of Computational Physics, (2007). Submitted, available on HAL : <http://hal.archives-ouvertes.fr/hal-00169721/>.

- [53] J. M. DELHAYE AND J. L. ACHARD, *On the averaging operators introduced in a two-phase flow modeling*, Proceedings CSNI Specialist Meeting in transient two-phase flow, 1 (1976), pp. 5–84.
- [54] F. X. DEMOULIN, G. BLOKKEEL, A. MURA, P. BEAU, AND R. BORGHI, *Modeling of liquid atomization as a turbulent flow with high density fluctuations*, Atomization and Sprays, 17 (2007), pp. 298–313.
- [55] S. DESCOMBES AND M. MASSOT, *Operator splitting for nonlinear reaction-diffusion systems with an entropic structure: singular perturbation and order reduction*, Numer. Math., 97 (2004), pp. 667–698.
- [56] O. DESJARDINS, R. O. FOX, AND P. VILLEDIEU, *A quadrature-based moment closure for the Williams spray equation.*, Proceedings of the Summer Program 2006. Center for Turbulence Research, Stanford, (2006), pp. 223–234.
- [57] ———, *A quadrature-based moment method for dilute fluid-particle flows*, Journal of Computational Physics, 227 (2008), pp. 2514–2539.
- [58] H. DETTE AND W. J. STUDDEN, *The theory of canonical moments with applications in statistics, probability, and analysis*, Wiley Series in Probability and Statistics: Applied Probability and Statistics, John Wiley & Sons Inc., New York, 1997. A Wiley-Interscience Publication.
- [59] F. DOISNEAU, F. LAURENT, A. MURRONE, J. DUPAYS, AND M. MASSOT, *Optimal Eulerian model for the simulation of dynamics and coalescence of alumina particles in solid propellant combustion*, in Proceedings of the 7th International Conference on Multiphase Flows, ICMF 2010 7th International Conference on Multiphase Flows, Tampa - Florida USA, 2010, pp. 1–15.
- [60] ———, *Evaluation of Eulerian Multi-Fluid models for the simulation of dynamics and coalescence of particles in solid propellant combustion*, Journal of Computational Physics (submitted), (2011).
- [61] K. DOMELEVO, *The kinetic sectional approach for noncolliding evaporating sprays*, Atomization and Sprays, 11 (2001), pp. 291–303.
- [62] J. DONEA, A. HUERTA, J.-P. PONTHOT, AND A. RODRIGUEZ-FERRAN, *Arbitrary Lagrangian-Eulerian methods*, Encyclopedia of Computational Mechanics, (2004), pp. 413–437.
- [63] J. R. DORMAND AND P. J. PRINCE, *A family of embedded Runge-Kutta formulae*, J. Comput. Appl. Math., 6 (1980), pp. 19–26.
- [64] D. A. DREW, *Mathematical modeling of two-phase flow*, Ann. Rev. Fluid. Mech., 15 (1983), pp. 261–91.
- [65] D. A. DREW AND S. L. PASSMAN, *Theory of multicomponent fluids*, Applied Mathematical Sciences, 135 (1999).
- [66] D. A. DREW AND L. A. SIEGEL, *Averaged equations for two-phase flows*, Studies in Applied Mathematics, (1), pp. 205–231.
- [67] O. A. DRUZHININ AND S. E. ELGHOBASHI, *A Lagrangian-Eulerian mapping solver for direct numerical simulation of bubble-laden turbulent shear flows using the two-fluid formulation*, J. Comput. Phys., 154 (1999), pp. 174–196.
- [68] J. DUCLOS AND M. ZOLVER, *3D modeling of intake, injection and combustion in a DI-SI engine under homogeneous and stratified operating conditions*, COMODIA, (1998).
- [69] G. DUFOUR, *Modélisation multi-fluide eulérienne pour les écoulements diphasiques à inclusions dispersées*, PhD thesis, Université Paul Sabatier Toulouse III, 2005.
- [70] G. DUFOUR AND P. VILLEDIEU, *A second-order multi-fluid model for evaporating sprays*, M2AN Math. Model. Numer. Anal., 39 (2005), pp. 931–963.

- [71] J. K. DUKOWICZ, *A particle-fluid numerical model for liquid sprays*, J. Comput. Phys., 35 (1980), pp. 229–253.
- [72] N. DUMONT, *Modélisation de l'écoulement diphasique dans les injecteurs Diesel*, PhD thesis, Institut National Polytechnique de Toulouse, 2004.
- [73] S. ELGHOBASHI AND G. C. TRUESDELL, *Direct numerical simulation of particle dispersion in a decaying isotropic turbulence*, J. Fluid Mech., 242 (1992), pp. 655–700.
- [74] O. EMRE, *Modélisation de la polydispersion des sprays denses dans le contexte des modèles diphasiques eulériens à phases séparées*, PhD thesis, Ecole Centrale Paris, 2013.
- [75] A. ERN AND V. GIOVANGIGLI, *Multicomponent transport algorithms*, Springer-Verlag, Berlin, 1994.
- [76] C. FARHAT, P. GUEZAIN, AND C. GRANDMONT, *The discrete geometric conservation law and the nonlinear stability of ALE schemes for the solution of flow problems on moving grids*, J. Comp. Phys., 174(2) (2001), pp. 669–694.
- [77] E. FAUCHER, J. M. HERARD, M. BARRET, AND C. TOULEMONDE, *Computation of flashing flow in variable cross section ducts*, International Journal of Computational Fluid Dynamics, 13 (2000), pp. 365–391.
- [78] V. FERRAND, R. BASILE, AND J. BORÉE, *Gas-droplet turbulent velocity correlations and two-phase interaction in an axisymmetric jet laden with partly responsive droplets*, International journal of multiphase flow, 29 (2003), pp. 195–217.
- [79] J. H. FERZIGER AND H. G. KAPER, *Mathematical Theory of transport processes in gases*, North-Holland, Amsterdam, 1972.
- [80] P. FEVRIER, *Etude numérique des effets de concentration préférentielle et de corrélation spatiale entre vitesses de particules solides en turbulence homogène isotrope stationnaire*, PhD thesis, Institut National Polytechnique de Toulouse, 2000.
- [81] P. FEVRIER, O. SIMONIN, AND K. SQUIRES, *Partitioning of particle velocities in gas-solid turbulent flows into a continuous field and a spatially uncorrelated random distribution theoretical formalism and numerical study*, Journal of Fluid Mechanics, 533 (2005), pp. 1–46.
- [82] R. O. FOX, *Computational Models for Turbulent reacting Flows*, Cambridge Texts in Applied Mathematics, Cambridge University Press, Cambridge, 2003.
- [83] ———, *Introduction and fundamentals of modeling approaches for polydisperse multiphase flows*, in Multiphase reacting flows: modelling and simulation, vol. 492 of CISM Courses and Lectures, Springer Wien, 2007, pp. 1–40. Editors D.L. Marchisio and R. O. Fox, Udine, July 2006.
- [84] ———, *A quadrature-based third-order moment method for dilute gas-particle flow*, Journal of Computational Physics, 227 (2008), pp. 6313–6350.
- [85] R. O. FOX, F. LAURENT, AND M. MASSOT, *Numerical simulation of spray coalescence in an Eulerian framework: direct quadrature method of moments and multi-fluid method*, J. Comput. Phys., 227 (2008), pp. 3058–3088.
- [86] L. FRERET, S. DE CHAISEMARTIN, J. REVEILLON, AND M. MASSOT, *Eulerian models and three-dimensional numerical simulation of polydisperse sprays*, in International Conference on Multiphase Flows, Tampa Bay, Unites-States, 2010.
- [87] L. FRÉRET, F. LAURENT, S. DE CHAISEMARTIN, D. KAH, F. LAURENT, P. VEDULA, R. O. FOX, O. THOMINE, J. REVEILLON, AND M. MASSOT, *Eulerian moment models for polydisperse weakly collisional sprays: model and validation*, in Proceedings of the Summer Program 2008, Center for Turbulence Research, Stanford University, 2009, pp. 277–288.

- [88] L. FRERET, O. THOMINE, J. RÉVEILLON, S. DE CHAISEMARTIN, F. LAURENT, AND M. MASSOT, *On the role of preferential segregation in flame dynamics in polydisperse evaporating sprays*, Proceedings of the Summer Program 2010. Center for Turbulence Research, Stanford, (2010).
- [89] S. K. FRIEDLANDER, *Smoke, Dust, and Haze, Fundamental of Aerosol Dynamics*, Topics in Chemical Engineering, Oxford University Press, second ed., 2000.
- [90] U. FRISCH, D. D'HUMIÈRES, B. HASSLACHER, P. LALLEMAND, Y. POMEAU, AND J. P. RIVET, *Lattice gas hydrodynamics in two and three dimensions*, Complex Systems, 1 (1987), pp. 649–707.
- [91] D. FUSTER, A. BAGUÉ, T. BOECK, L. L. MOYNE, A. LEBOISSETIER, S. POPINET, P. RAY, R. SCARDOVELLI, AND S. ZALESKI, *Simulation of primary atomization with an octree adaptive mesh refinement and VOF method*, International Journal of Multiphase Flow, 35 (2009), pp. 550 – 565.
- [92] M. GARCIA, *Développement et validation du formalisme Euler-Lagrange dans un solveur parallèle non-structuré pour la simulation aux grandes échelles.*, PhD thesis, Institut National Polytechnique de Toulouse, 2009.
- [93] R. GATIGNOL, *Théorie cinétique d'un gaz à répartition discrète de vitesses*, Lecture Notes in Physics, Springer, Berlin, 36 (1975).
- [94] V. GIOVANGIGLI, *Plane laminar flames with multicomponent transport and complex chemistry*, Math. Models Methods Appl. Sci., 9 (1999), pp. 337–378.
- [95] V. GIOVANGIGLI AND M. MASSOT, *Asymptotic stability of equilibrium states for multicomponent reactive flows*, Math. Models Methods Appl. Sci., 8 (1998), pp. 251–297.
- [96] E. GODLEWSKI AND P.-A. RAVIART, *Numerical Approximation of Hyperbolic systems of conservation laws*, Applied Mathematical Sciences, Springer, New-York, 1992.
- [97] G. A. E. GODSAVE, *Studies of the combustion of drops in a fuel spray: the burning of single drops of fuel*, in Proceedings of the 4th Symp. (International) on Combustion, The Comb. Institute, Baltimore, 1953, pp. 818–830.
- [98] S. GODUNOV, *A difference scheme for numerical computation of discontinuous solution of hydrodynamic equations*, Math. Sib, 47 (1959), pp. 271–306.
- [99] L. GOSSE, S. JIN, AND X. LI, *Two moment systems for computing multiphase semiclassical limits of the Schroedinger equation*, Mathematical Models Methods Applied to Science, 13 (2003), pp. 1689–1723.
- [100] H. GRAD, *Principles of the kinetic theory of gases*, in Handbuch der Physik (herausgegeben von S. Flügge), Bd. 12, Thermodynamik der Gase, Springer-Verlag, Berlin, 1958, pp. 205–294.
- [101] J. B. GREENBERG, D. ALBAGLI, AND Y. TAMBOUR, *An opposed jet quasi-monodisperse spray diffusion flame*, Combust. Sci. Technol., 50 (1986), pp. 255–270.
- [102] J. B. GREENBERG, I. SILVERMAN, AND Y. TAMBOUR, *On the origin of spray sectional conservation equations*, Combustion and Flame, 93 (1993), pp. 90–96.
- [103] H. GUILLARD AND C. FARHAT, *On the significance of the geometric conservation law for flow computations on moving meshes*, Comput. Meth. Appl. Mech. Eng., 190(11-12) (2000), pp. 1467–1482.
- [104] C. HABCHI, *Modélisation Tridimensionnelle de l'injection et de la préparation du mélange gaz/carburant dans les moteurs à combustion interne*, PhD thesis, Institut National Polytechnique de Toulouse, 2006.

- [105] E. HAIRER AND G. WANNER, *Solving ordinary differential equations. II*, Springer-Verlag, Berlin, 1991. Stiff and differential-algebraic problems.
- [106] ———, *Solving ordinary differential equations. II*, Springer-Verlag, Berlin, 1996. Stiff and differential-algebraic problems, second revised edition.
- [107] P. HELLUY AND T. BARBERON, *Finite volume simulation of cavitating flow*, tech. rep., Rapport de recherche INRIA, 4824, 2003.
- [108] M. HERRMANN, *A Eulerian level set/vortex sheet method for two-phase interface dynamics*, J. Comput. Phys., 203 (2005), pp. 539–571.
- [109] ———, *A balanced force refined level set grid method for two-phase flows on unstructured flow solver grids*, Journal of Computational Physics, 227 (2008), pp. 2674 – 2706.
- [110] M. HERRMANN, *Detailed numerical simulations of the primary atomization of a turbulent liquid jet in crossflow*, Journal of Engineering for Gas Turbines and Power, 132 (2010), p. 061506.
- [111] C. W. HIRT, A. A. AMSDEN, AND J. L. COOK, *An arbitrary Lagrangian-Eulerian computing method for all flow speeds*, Journal of Computational Physics, 14 (1974), pp. 227–253.
- [112] A. HUERTA AND W. LIU, *Viscous flow structure interaction*, J. Press Vessel Technol.-Trans ASME, 110(1) (1988), pp. 15–21.
- [113] ———, *ALE formulation for large boundary motion*, Trans. 10<sup>th</sup> Int. Conf. Structural Mechanics in Reactor Technology, Anaheim, California, B (1989), pp. 335–346.
- [114] J. HYLKEMA AND P. VILLEDIEU, *A random particle method to simulate coalescence phenomena in dense liquid sprays*, in Lecture Notes in Physics, vol. 515, Arcachon, France, 1998, Proc. 16th Int. Conf. on Num. Meth. in Fluid Dyn., pp. 488–493.
- [115] M. ISHII, *Thermo-Fluid dynamic theory of two-phase flow*, Eyrolles, 1975.
- [116] V. A. IYER, *Modeling of Diesel Sprays Using an Eulerian-Liquid Eulerian-Gas Two-Fluid Model*, PhD thesis, Purdue University West Lafayette, 2001.
- [117] P.-E. JABIN, *Various levels of models for aerosols*, Mathematical Models and Methods in Applied Sciences, 12 (2002), pp. 903–919.
- [118] R. JACKSON, *Locally averaged equations of motion for a mixture of identical spherical particles and a newtonian fluid*, Chemical Engineering Science, 52 (1997), pp. 2457 – 2469. Mathematical modelling of chemical and biochemical processes.
- [119] S. JAY, *Modélisation de la combustion diphasique au moyen de bilan d'aires interfaciale et de surface de flamme. Application à la combustion cryotechnique*, PhD thesis, Ecole Centrale Paris, 2002.
- [120] S. JAY, P. BEARD, AND A. PIRES DA CRUZ, *Modeling coupled processes of CO and soot formation and oxidation for conventional and HCCI Diesel combustion*, SAE paper, 01-0162 (2007).
- [121] S. JAY AND O. COLIN, *A variable volume approach of tabulated detailed chemistry and its applications to multidimensional engine simulations*, Proceedings of the Combustion Institute, available online (2010).
- [122] S. JAY, F. LACAS, AND S. CANDEL, *Combined surface density concepts for dense spray combustion*, Combustion and Flame, 144 (2006), pp. 558–577.
- [123] J. T. JENKINS AND S. B. SAVAGE, *A theory for the rapid flow of indential, smooth, nearly elastic spherical particles*, Journal of Fluid Mechanics, 130 (1983), pp. 187–202.

- [124] S. JIN AND X. LI, *Multi-phase computations of the semiclassical limit of the schrödinger equation and related problems: Whitham vs wigner*, *Physica D: Nonlinear Phenomena*, 182 (2003), pp. 46 – 85.
- [125] D. KAH, C. CHALONS, AND M. MASSOT, *Beyond pressureless gas dynamics: quadrature-based velocity moment models*, *Communication in Mathematical Sciences* (submitted), (2010).
- [126] D. KAH, F. LAURENT, L. FRÉRET, S. DE CHAISEMARTIN, R. O. FOX, J. REVEILLON, AND M. MASSOT, *Eulerian quadrature-based moment models for polydisperse evaporating sprays*, *Flow, Turbulence and Combustion*, 85 (2010), pp. 649–676. "Special Issue Dedicated to Stephen B. Pope".
- [127] D. KAH, F. LAURENT, M. MASSOT, , AND S. JAY, *A Eulerian model for the dynamics of polydisperse evaporating sprays: Combining the multi-fluid model with the quadrature method of moments*, in *12<sup>th</sup> SIAM International Conference on Numerical Combustion*, 31/03-2/04 2008, Monterey, California, 2008.
- [128] D. KAH, F. LAURENT, M. MASSOT, AND S. JAY, *Modeling of polydisperse sprays using a high order size moment method for the numerical simulation of advection and evaporation*, in *Proceedings of the 11th ICLASS, International Conference on Liquid Atomization and Spray Systems Vail, Colorado*, 2009.
- [129] ———, *A high order moment method simulating evaporation and advection of a polydisperse spray*, To be submitted to *Journal of Computational Physics*, (2010).
- [130] D. KAH, M. MASSOT, Q. H. TRAN, S. JAY, AND F. LAURENT, *A high order moment method with mesh movement for the description of a polydisperse evaporating spray*, in *Proceedings of the International Conference on Multiphase Flows*, Tampa, Florida, 2010. available on HAL : <http://hal.archives-ouvertes.fr/hal-00498214/en/>.
- [131] D. KAH, Q. H. TRAN, M. MASSOT, AND F. LAURENT, *A high order moment method with mesh movement for the description of a polydisperse evaporating spray*, To be submitted to *International Journal of Multiphase Flow*, (2011).
- [132] S. KARNI, *Multicomponent flow calculations by a consistent primitive algorithm*, *Journal of Computational Physics*, 112 (1994), pp. 31–43.
- [133] ———, *Hybrid multifluid algorithms*, *SIAM Journal of Scientific Computing*, 17 (1996), pp. 1019–1039.
- [134] A. KAUFMANN, *Vers la simulation des grandes échelles en formulation Euler-Euler des écoulements réactifs diphasiques*, PhD thesis, Institut National Polytechnique de Toulouse, 2004.
- [135] M. KLEIN, A. SADIKI, AND J. JANICKA, *A digital filter based generation of inflow data for spatially developing direct numerical or large eddy simulations*, *J. Comput. Phys.*, 186 (2003), pp. 652–665.
- [136] S. KOKH AND F. LAGOUTIÈRE, *An anti-diffusive numerical scheme for the simulation of interfaces between compressible fluids by means of a five-equation model*, *Journal of Computational Physics*, 229 (2010), pp. 2773 – 2809.
- [137] M. KOSTOGLU, *Extended cell average technique for the solution of coagulation equation*, *Journal of Colloid and Interface Science*, 306 (2007), pp. 143–160.
- [138] K. K. KUO, *Principles of combustion*, John Wiley and sons, 1986.
- [139] M.-H. LALLEMAND, A. CHINNAYYA, AND O. LE METAYER, *Pressure relaxation procedures for multiphase compressible flows*, *Internat. J. Numer. Methods Fluids*, 49 (2005), pp. 1–56.
- [140] P. LALLEMAND AND L.-S. LUO, *Theory of the lattice Boltzmann method: Dispersion, dissipation, isotropy, Galilean invariance, and stability*, *Phys. Rev. E*, 61 (2000), pp. 6546–6562.

- [141] N. LAMARQUE, *Schémas numériques et conditions limites pour la simulation aux grandes échelles de la combustion diphasique dans les foyers d'hélicoptère*, PhD thesis, Institut National Polytechnique de Toulouse, 2007.
- [142] B. LARROUTUROU, *How to preserve the mass fraction positivity when computing compressible multi-component flows*, Journal of Computational Physics, 95(1) (2004), pp. 59–84.
- [143] F. LAURENT, *Analyse numérique d'une méthode multi-fluide Eulérienne pour la description de sprays qui s'évaporent*, C. R. Math. Acad. Sci. Paris, 334 (2002), pp. 417–422.
- [144] ———, *Modélisation mathématique et numérique de la combustion de brouillards de gouttes polydispersés*, PhD thesis, Université Claude Bernard, Lyon 1, 2002.
- [145] ———, *Numerical analysis of Eulerian multi-fluid models in the context of kinetic formulations for dilute evaporating sprays*, M2AN Math. Model. Numer. Anal., 40 (2006), pp. 431–468.
- [146] F. LAURENT AND M. MASSOT, *Multi-fluid modeling of laminar poly-dispersed spray flames: origin, assumptions and comparison of the sectional and sampling methods*, Comb. Theory and Modelling, 5 (2001), pp. 537–572.
- [147] F. LAURENT, M. MASSOT, AND P. VILLEDIEU, *Eulerian multi-fluid modeling for the numerical simulation of coalescence in polydisperse dense liquid sprays*, J. Comput. Phys., 194 (2004), pp. 505–543.
- [148] F. LAURENT, V. SANTORO, M. NOSKOV, A. GOMEZ, M. SMOOKE, AND M. MASSOT, *Accurate treatment of size distribution effects in polydispersed spray diffusion flames: multi-fluid modeling, computations and experiments*, Combust. Theory and Modelling, 8 (2004), pp. 385–412.
- [149] O. LE METAYER, *Modelisation et resolution de la propagation de fronts permeables. Application aux fronts d'évaporation et de detonation*, PhD thesis, Université d'Aix Marseille 1, 2003.
- [150] A. H. LEFEBRE, *Atomization and Sprays*, Combustion : An International Series, Taylor & Francis, Bristol, 1989.
- [151] R. J. LEVEQUE, *Numerical methods for conservation laws*, Birkhäuser Verlag, Basel, second ed., 1992.
- [152] ———, *Finite volume methods for hyperbolic problems*, Cambridge Texts in Applied Mathematics, Cambridge University Press, Cambridge, 2002.
- [153] D. LHUILLIER, *A mean-field description of two-phase flows with phase changes*, International Journal of Multiphase Flow, 29 (2003), pp. 511 – 525.
- [154] D. LHUILLIER AND A. NADIM, *Fluid dynamics of particulate suspensions: selected topics*, in Proceedings of the 9th International Symposium, E. Inan and K. Z. Markov, eds., Continuum Models and Discrete Systems, June 29-July 3, 1998, pp. 180–197.
- [155] D. LHUILLIER, T. G. THEOFANOUS, AND M.-S. LIOU, *Multiphase flows: Compressible multi-hydrodynamics*, in Handbook of Nuclear Engineering, D. G. Cacuci, ed., Springer US, 2010, pp. 1813–1912.
- [156] W. LIU AND H. CHANG, *Efficient computational procedures for long-time duration fluid-structure interaction problems*, J. Press Vessel Technol.-Trans ASME, 106 (1984), pp. 317–322.
- [157] ———, *A method of computation for fluid structure interaction*, Comp. Struct., 20(1-3) (1985), pp. 3039–3067.
- [158] B. MANDUMPALA DAVASSY, *Atomization Modeling of Liquid Jets by an Eulerian Approach*, PhD thesis, Université d'Aix Marseille 1, 2012.

- [159] D. L. MARCHISIO AND R. O. FOX, *Solution of population balance equations using the direct quadrature method of moments*, Journal of Aerosol Science, 36 (2005), pp. 43–73.
- [160] D. L. MARCHISIO, J. T. PIKTURNA, R. O. FOX, R. D. VIGIL, AND A. A. BARRESI, *Quadrature method of moments for population balances with nucleation, growth and aggregation*, AIChE Journal, 49 (2003), pp. 1266–1276.
- [161] D. L. MARCHISIO, R. D. VIGIL, AND R. O. FOX, *Quadrature method of moments for aggregation-breakage processes*, Journal of Colloidal and Interfacial Science, 258 (2003), pp. 322–334.
- [162] C. MARLE, *On macroscopic equations governing multiphase flow with diffusion and chemical reactions in porous media*, Int. J. Eng. Sci., 20 (1982), pp. 643–662.
- [163] S. MARTINOT, P. BÉART, J. ROESLER, AND A. GARO, *Comparison and coupling of homogeneous reactor and flamelet library soot modeling approaches for diesel combustion*, SAE Paper, (2001).
- [164] F. MASHAYEK, *Direct numerical simulations of evaporating droplet dispersion in forced low Mach number turbulence*, Int. J. Heat Mass Transfer, 41 (1998), pp. 2601–2617.
- [165] R. MASHAYEK, F. A. JABERI, R. S. MILLER, AND P. GIVI, *Dispersion and polydispersity of droplets in stationary isotropic turbulence*, Int. J. Multiphase Flow, 23 (1997), pp. 337–355.
- [166] J. MASSONI, R. SAUREL, B. NKONGA, AND R. ABGRALL, *Some models and Eulerian methods for interface problems between compressible fluids with heat transfer*, International journal of Heat and Mass Transfer, 45 (2002), pp. 1287–1307.
- [167] M. MASSOT, *Modélisation Mathématique et Numérique de la Combustion des Mélanges Gazeux*, PhD thesis, Thèse de l'Ecole Polytechnique, 1996.
- [168] ———, *Eulerian multi-fluid models for polydisperse evaporating sprays*, vol. 492 of CISM Courses and Lectures, Springer Wien, 2007, pp. 79–123. Editors D.L. Marchisio and R. O. Fox, Udine, July 2006.
- [169] M. MASSOT, R. KNIKKER, C. PÉRA, AND J. REVEILLON, *Lagrangian/Eulerian analysis of the dispersion of evaporating sprays in non-homogeneous turbulent flows*, in International Conference on Multiphase Flows, Japan, 2004.
- [170] M. MASSOT, M. KUMAR, A. GOMEZ, AND M. D. SMOOKE, *Counterflow spray diffusion flames of heptane: computations and experiments*, in Proceedings of the 27th Symp. (International) on Combustion, The Comb. Institute, 1998, pp. 1975–1983.
- [171] M. MASSOT, F. LAURENT, AND S. DE CHAISEMARTIN, *Eulerian Multi-fluid method for the numerical simulation of evaporating polydisperse sprays : modelling and numerical issues in multi-dimensional configurations*, in Proceedings of the International Conference on Multiphase Flows, Leipzig, Germany, 2007.
- [172] M. MASSOT, F. LAURENT, S. DE CHAISEMARTIN, L. FRÉRET, AND D. KAH, *Eulerian multi-fluid models: modeling and numerical methods*, in Modelling and Computation of Nanoparticles in Fluid Flows, Lectures of the von Karman Institute, NATO RTO, 2009. In Press, available on HAL : <http://hal.archives-ouvertes.fr/hal-00423031/en/>.
- [173] M. MASSOT, F. LAURENT, D. KAH, AND S. DE CHAISEMARTIN, *A robust moment method for evaluation of the disappearance rate of evaporating sprays*, SIAM J. Appl. Math., 70 (2010), pp. 3203–3234.
- [174] H. MATHIS, *Etude théorique et numérique des écoulements avec transition de phase*, PhD thesis, Institut de Recherche Mathématique avancée, Université Louis Pasteur, Strasbourg, 2010.
- [175] R. MCGRAW, *Description of aerosol dynamics by the quadrature method of moments*, Aerosol Science and Technology, 27 (1997), pp. 255–265.



- [176] ———, *Numerical advection of correlated tracers: preserving particle size/composition moment sequences during transport of aerosol mixtures*, J. Phys.: Conf. Ser., 78 (2007), pp. 1–5.
- [177] L. R. MEAD AND N. PAPANICOLAOU, *Maximum entropy in the problem of moments*, J. Math. Phys., 25 (1984), pp. 2404–2417.
- [178] T. MENARD, S. TANGUY, AND A. BERLEMONT, *Coupling level set/VOF/ghost fluid methods: Validation and application to 3D simulation of the primary break-up of a liquid jet*, International Journal of Multiphase Flow, 33 (2007), pp. 510–524.
- [179] R. S. MILLER AND J. BELLAN, *Direct numerical simulation of a confined three-dimensional gas mixing layer with one evaporating hydrocarbon-droplet-laden stream*, Journal of Fluids Mechanics, 384 (1999), pp. 293–338.
- [180] ———, *Direct numerical simulation and subgrid analysis of a transitional droplet laden mixing layer*, Phys. Fluid, 12 (2000), pp. 650–671.
- [181] J. B. MOREAU, *Modélisation de l'écoulement polyphasique à l'intérieur et en sortie des injecteurs Diesel*, PhD thesis, Institut National Polytechnique de Toulouse, 2005.
- [182] C. MOREL, *Modélisation multidimensionnelle des écoulements diphasiques gaz-liquide. Application à la simulation des écoulements à bulles ascendants en conduite verticale*, PhD thesis, Ecole Centrale Paris, 1997.
- [183] J.-B. MOSSA, *Extension polydisperse pour la description euler-euler des écoulements diphasiques réactifs - TH/CFD/05/74*, PhD thesis, Institut National Polytechnique de Toulouse, 2005.
- [184] M. E. MUELLER, G. BLANQUART, AND H. PITSCH, *Hybrid method of moment for modeling soot formation and growth*, Combustion and Flame, 156 (2009), pp. 1143–1155.
- [185] ———, *A joint volume-surface model of soot aggregation with the method of moment*, Proceedings of the Combustion Institute, 32 (2009), pp. 785–792.
- [186] B. MULLER, *Low Mach number asymptotics of the Navier-Stokes equations*, Journal of Engineering Mathematics, 34 (1998).
- [187] A. MURRONE AND H. GUILLARD, *A five equation reduced model for compressible two phase flow problems*, J. Comp. Phys., 205 (2005), pp. 664–698.
- [188] J. D. NABER AND R. D. REITZ, *Modeling engine spray/wall impingement*, SAE Technical Paper Serie, (1988).
- [189] M. NDJINGA, *Quelques aspects de modélisation et d'analyse des systèmes issus des écoulements diphasiques*, PhD thesis, Ecole Centrale Paris, 2007.
- [190] I. NICODIN AND R. GATIGNOL, *Unsteady half-space evaporation and condensation problems on the basis of the discrete kinetic theory*, Physics of Fluids, 18 (2006).
- [191] R. I. NIGMATULIN, *Dynamics of Multiphase Media*, Hemisphere Publ. Corp., 1991.
- [192] T. NOMURA AND T. HUGHES, *An Arbitrary Lagrangian-Eulerian finite element method for interaction of fluid and a rigid body*, Comput. Meth. Appl. Mech. Eng., 95(1) (1992), pp. 115–138.
- [193] P. J. O'ROURKE, *Collective drop effects on vaporizing liquid sprays*, PhD thesis, Princeton University, 1981.
- [194] S. L. PASSMAN, J. W. NUNZIATO, AND E. K. WALSH, *A theory of multiphase mixtures*, In Rational Thermodynamics (Edited by Truesdell, C., New-York), (1984).
- [195] S. V. PATANKAR, *Numerical heat transfer and fluid flow*, Hemisphere Publishing Corp, Washington D.C, (1980).

- [196] B. PERTHAME, *Kinetic formulation of conservation laws*, vol. 21 of Oxford Lecture Series in Mathematics and its Applications, Oxford University Press, Oxford, 2002.
- [197] T. POINSOT AND D. VEYNANTE, *Theoretical and Numerical Combustion*, Edwards, Philadelphia, second ed., 2005.
- [198] W. H. PRESS, S. A. TEUKOLSKY, W. T. VETTERLING, AND B. P. FLANNERY, *Numerical Recipes in Fortran 77*, Cambridge: Cambridge University Press, 1992.
- [199] M. W. REEKS, *On a kinetic equation for the transport of particles in turbulent flows*, Phys. Fluids, 3 (1991), pp. 446–456.
- [200] J. REVEILLON, *Direct numerical simulation of sprays: turbulent dispersion evaporation and combustion*, in *Multiphase reacting flows: modelling and simulation*, vol. 492 of CISM Courses and Lectures, Springer Wien, 2007, pp. 229–273. Editors D.L. Marchisio and R. O. Fox, Udine, July 2006.
- [201] J. REVEILLON, N. BRAY, AND L. VERVISH, *DNS study of spray vaporization and turbulent micro-mixing*, in AIAA 98-1028, 36th Aerospace Sciences Meeting and Exhibit, Reno NV, 1998.
- [202] J. REVEILLON AND L. VERVISCH, *Analysis of weakly turbulent diluted-spray flames and spray combustion regimes*, J. Fluid Mech., 537 (2005), pp. 317–347.
- [203] J. J. RILEY AND G. S. PATTERSON, *Diffusion experiments with numerically intergrated isotropic turbulence*, Physics of Fluids, 17 (1974), pp. 292–297.
- [204] M. RÜGER, S. HOHMANN, M. SOMMERFELD, AND G. KOHNEN, *Euler/Lagrange calculations of turbulent sprays: the effect of droplet collisions and coalescence*, Atomization and Sprays, 10 (2000), pp. 47–81.
- [205] L. SAINSAULIEU, *Finite volume approximation of two phase-fluid flows based on an approximate Roe-type Riemann solver*, Journal of Computational Physics, 121 (1994), pp. 1–28.
- [206] R. SAUREL AND R. ABGRALL, *A multiphase Godunov method for compressible multifluid and multiphase flow*, Journal of Computational Physics, 150 (1999), pp. 425–467.
- [207] R. SAUREL AND O. L. METAYER, *A multiphase model for compressible flows with interfaces, shocks, detonation waves and cavitation*, Journal of Fluid Mechanic, 431 (2000), pp. 239–271.
- [208] W. A. SIRIGNANO, *Fluid Dynamics and Transport of Droplets and Sprays*, Cambridge University Press, Cambridge, 1999.
- [209] J. SLATTERY AND S. CORRISIN, *Momentum, energy and mass transfer in continua*, Physics Today, 26 (1973).
- [210] D. B. SPALDING, *The combustion of liquid fuels*, in *Proceedings of the 4th Symp. (International) on Combustion*, The Comb. Institute, Baltimore, 1953, pp. 847–864.
- [211] K. D. SQUIRES AND J. K. EATON, *Preferential concentration of particles by turbulence*, Physics of Fluids, 3 (1991), pp. 1169–1178.
- [212] G. STRANG, *On the construction and comparison of difference schemes*, SIAM Journal of Numerical Analysis, 5 (1968), pp. 506–517.
- [213] H. STRUCHTRUP, *Macroscopic transport equations for rarefied gas flows*, Interaction of Mechanics and Mathematics, Springer, Berlin, 2005. Approximation methods in kinetic theory.
- [214] A. TAGLIANI, *Hausdorff moment problem and maximum entropy: a unified approach*, Appl. Math. Comput., 105 (1999), pp. 291–305.

- [215] B. TRUCHOT, *Développement et validation d'un modèle eulérien en vue de la simulation des jets de carburants dans les moteurs à combustion interne*, PhD thesis, Institut National Polytechnique de Toulouse, 2005.
- [216] A. VALLET, *Contribution à la modélisation de l'atomisation d'un jet liquide haute pression*, PhD thesis, Faculté des Sciences de l'Université de Rouen, 1997.
- [217] A. VALLET AND R. BORCHI, *An Eulerian model of atomization of a liquid jet*, in Third International Conference on Multiphase Flow, Lyon, France, 1998.
- [218] B. VAN LEER, *Towards the ultimate conservative difference scheme IV. A new approach to numerical convection*, J. Comput. Phys., 23 (1977), pp. 276–299.
- [219] M. VANNI, *Approximate population balance equations for aggregation-breakage processes*, Journal of Colloid and Interface Science, 221 (2000), pp. 143–160.
- [220] C. VESSILLER, *Contribution à l'étude des brouillards denses et dilués par la simulation numérique Euler/Euler et Euler/Lagrange.*, PhD thesis, Ecole Centrale Paris, 2007.
- [221] A. VIE, *Simulation aux grandes échelles d'écoulements diphasiques turbulents à phase liquide dispersée*, PhD thesis, Université Paul Sabatier Toulouse III, 2010.
- [222] A. VIÉ, F. LAURENT, AND M. MASSOT, *Size-velocity correlations in high order moment methods: modelling and numerical issues*, Journal of Computational Physics (submitted), (2011).
- [223] A. VIE, M. SANJOSÉ, S. JAY, C. ANGELBERGER, B. CUENOT, AND M. MASSOT, *Evaluation of a multi-fluid mesoscopic Eulerian formalism on the large eddy simulation of an aeronautical-type configuration*, in Proceedings of the International Conference on Multiphase Flows, Tampa, Florida, 2010.
- [224] V. VIKAS, Z. WANG, A. PASSALACQUA, AND R. O. FOX, *Realizable high-order finite-volume schemes for quadrature-based moment methods*, Journal of Computational Physics, 230 (2011), pp. 5328 – 5352.
- [225] P. VILLEDIEU AND J. HYLKEMA, *Une méthode particulière aléatoire reposant sur une équation cinétique pour la simulation numérique des sprays denses de gouttelettes liquides*, C. R. Acad. Sci. Paris Sér. I Math., 325 (1997), pp. 323–328.
- [226] I. VINKOVIC, C. AGUIRRE, S. SIMOENS, AND M. GOROKHOVSKI, *Large eddy simulation of droplet dispersion for inhomogeneous turbulent wall flow*, International Journal of Multiphase Flow, 32 (2006), pp. 344–364.
- [227] L. WANG, D. L. MARCHISIO, R. D. VIGIL, AND R. O. FOX, *CFD simulation of aggregation and breakage processes in laminar Taylor-Couette flow*, Journal of Colloidal and Interfacial Science, 282 (2005), pp. 380–396.
- [228] F. A. WILLIAMS, *Spray combustion and atomization*, Phys. Fluids, 1 (1958), pp. 541–545.
- [229] ———, *Combustion Theory (Combustion Science and Engineering Series)*, ed F A Williams (Reading, MA: Addison-Wesley), 1985.
- [230] L. C. WOODS, *The thermodynamics of fluid systems*, Oxford, Clarendon Press; New York, Oxford University Press, 1975.
- [231] D. L. WRIGHT, *Numerical advection of moments of the particle size distribution in Eulerian models*, Journal of Aerosol Science, 38 (2007), pp. 352–369.
- [232] C. YOON AND R. MC GRAW, *Representation of generally mixed multivariate aerosols by the quadrature method of moments: I. Statistical foundation*, Journal of Aerosol Science, 35 (2003), pp. 561–576.

- 
- [233] C. YUAN AND R. O. FOX, *Conditional quadrature method of moments for kinetic equations*, Journal of Computational Physics (submitted), (2010).
- [234] L. I. ZAICHIK, O. SIMONIN, AND V. M. ALIPCHENKOV, *An Eulerian approach for large eddy simulation of particle transport in turbulent flows*, Journal of Turbulence, 10 (2009), pp. 1468–5248.
- [235] Y. B. ZEL'DOVICH, *Gravitational instability : an approximate theory for large density perturbations*, Astronomy and Astrophysics, 5 (1970), pp. 84–89.
- [236] P. ZENG, S. SARHOLZ, C. IWAINSKY, B. BINNINGER, N. PETERS, AND M. HERRMANN, *Simulation of primary breakup for diesel spray with phase transition*, in Recent Advances in Parallel Virtual Machine and Message Passing Interface, M. Ropo, J. Westerholm, and J. Dongarra, eds., vol. 5759 of Lecture Notes in Computer Science, Springer Berlin / Heidelberg, 2009, pp. 313–320.
- [237] A. ZUCCA, D. L. MARCHISIO, A. A. BARRESI, AND R. O. FOX, *Implementation of the population balance equation in CFD codes for modelling soot formation in turbulent flames*, Chemical Engineering Science, 61 (2006), pp. 87–95.